

Rolling Bearing Analysis

FIFTH EDITION

Essential Concepts of Bearing Technology

Tedric A. Harris
Michael N. Kotzalas



Taylor & Francis
Taylor & Francis Group

Rolling Bearing Analysis

FIFTH EDITION

Essential Concepts of Bearing Technology

Preface

Ball and roller bearings, together called rolling bearings, are commonly used machine elements. They are used to permit motion of, or about, shafts in simple commercial devices such as bicycles, roller skates, and electric motors. They are also used in complex mechanisms such as aircraft gas turbines, rolling mills, dental drills, gyroscopes, and power transmissions. Until around 1940, the design and application of these bearings involved more art than science. Since 1945, marking the end of World War II and the beginning of the atomic age, scientific progress has occurred at an exponential pace. Since 1958, the date that marks the commencement of space travel, continually increasing demands have been made of engineering equipment. To ascertain the effectiveness of rolling bearings in modern engineering applications, a firm understanding of how these bearings perform under varied and often extremely demanding conditions of operation is necessary.

A substantial amount of information and data on the performance of rolling bearings is presented in manufacturers' catalogs. These data are mostly empirical in nature, obtained from the testing of products by the larger bearing manufacturing companies, or, more likely for smaller manufacturing companies, from information in various standards publications, for example, the American National Standards Institute (ANSI), Deutsches Institut für Normung (DIN), International Organization for Standardizations (ISO), etc. These data pertain only to bearing applications involving slow-to-moderate speed, simple loading, and nominal operating temperatures. To evaluate the performance of bearing applications operating beyond these bounds, it is necessary to return to the basics of rolling and sliding motions over the concentrated contacts that occur in rolling bearings.

One of the first books on this subject was *Ball and Roller Bearing Engineering* by Arvid Palmgren, Technical Director of ABSKF for many years. It explained, more completely than any other book previously, the concept of rolling bearing fatigue life. Palmgren and Gustav Lundberg, Professor of Mechanical Engineering at Chalmers Institute of Technology in Göteborg, Sweden, proposed theory and formulas on which the current national and ISO standards for the calculation of rolling bearing fatigue life are based. Also, A. Burton Jones' text, *Analysis of Stresses and Deflections*, gave a good explanation of the static loading of ball bearing. Jones, who worked in various technical capacities for the New Departure Ball Bearing Division of General Motors Corporation, Marlin-Rockwell Corporation, and Fafnir Ball Bearing Company, and also as a consulting engineer, was among the first to use digital computers to analyze the performance of ball and roller bearing shaft-bearing-housing systems. Other early texts on rolling bearings are largely empirical in their approaches to applications analysis.

Since 1960, much research has been conducted on rolling bearings and rolling contact. The use of modern laboratory equipment such as scanning and transmission electron microscopes, x-ray diffraction devices, and digital computers has shed much light on the mechanical, hydrodynamic, metallurgical, and chemical phenomena involved in rolling bearing operations. Many significant technical papers have been published by various engineering societies, for example, the American Society of Mechanical Engineers, the Institution of Mechanical Engineers, the Society of Tribologists and Lubrication Engineers, and the Japan Society of Mechanical Engineers, among others, analyzing the performance of rolling bearings in exceptional applications involving high-speed, heavy-load, and extraordinary internal design and materials. Substantial attention has been given to the mechanisms of

rolling bearing lubrication and the rheology of lubricants. Notwithstanding the existence of the aforementioned literature, there remains a need for a reference that presents a unified, up-to-date approach to the analysis of rolling bearing performance. That is the purpose of this book.

To accomplish this goal, significant technical papers and texts covering the performance of rolling bearings, their constituent materials, and lubrication were reviewed. The concepts and mathematical presentations contained in the literature have been condensed and simplified in this book for rapidity and ease of understanding. It should not be assumed, however, that this book supplies a complete bibliography on rolling bearings. Only data found useful in practical analysis have been referenced.

The format of *Rolling Bearing Analysis*, Fifth Edition is aimed at understanding the principles of rolling bearing design and operation. In this edition, the material has been separated into two volumes: *Essential Concepts of Bearing Technology* and *Advanced Concepts of Bearing Technology*. The first volume is for the users of bearings who require only a basic understanding, whereas the second volume enables users involved in complex bearing applications to carry bearing performance analysis to the degree necessary for a solution of their application. The first volume is a stand-alone text; however, the second volume frequently refers to basic concepts explained in the first volume.

To amplify the discussion, numerical examples are referenced in several chapters. For each volume, these examples are contained in a CD-ROM provided inside the back cover of the text. Several of the examples deal with a 209 radial ball bearing, a 209 cylindrical roller bearing, a 218 angular-contact ball bearing, and a 22317 spherical roller bearing. Design and performance data for each bearing are accumulated as the reader progresses through the book. The examples are carried out in metric or Standard International (SI) system of units (millimeters, Newtons, seconds, °C, and so on); however, the results are also given parenthetically in the English system of units. In the appendix, the numerical constants for equations presented in SI or metric system units are provided in the English system of units as well.

Also contained on the CD-ROM are many tables of bearing dimensional, mounting, and life rating data obtained from ABMA/ANSI standards. These tables are referenced in the text as, for example, Table CD2.1; data from the tables are used in the solution of many of the numerical examples.

The text material spans many scientific disciplines, for example, geometry, elasticity, statics, dynamics, hydrodynamics, statistics, and heat transfer. Thus, many mathematical symbols have been employed. In some cases, the same symbol has been chosen to represent different parameters. To help avoid confusion, a list of symbols is presented at the beginning of most chapters.

Because these two books span several scientific disciplines, the treatment of topics varies in scope and manner. Where feasible, mathematically developed solutions to problems are presented. On the other hand, empirical approaches to problems are used where it is more practical. The combination of mathematical and empirical techniques is particularly evident in chapters covering lubrication, friction, and fatigue life.

As stated previously, the material presented herein exists substantially in other publications. The purpose of these books is to concentrate that knowledge in one place for the benefit of both the student and the rolling bearing user who needs or wants a broader understanding of the technical field and the products. The references provided at the end of each chapter enable the curious reader to go into further detail.

Since 1995, the American Bearing Manufacturers Association (ABMA) has sponsored short courses on rolling bearing technology at The Pennsylvania State University. The one-week course, “Advanced Concepts of Bearing Technology,” is based on the material in

Rolling Bearing Analysis, Third and Fourth Editions. Some students, however, believed that a preliminary three-day course, “Essential Concepts of Bearing Technology,” was required to provide sufficient background to successfully complete the advanced course. The latter course is now presented annually; this *Essential Concepts of Bearing Technology* will be used for that course.

Because of my long-time association with the SKF company, as with the previous editions of this book, several of the illustrations in this fifth edition have previously appeared in SKF publications; for such illustrations, appropriate references are identified. Photographs and illustrations from other rolling bearing manufacturers are included as well. The following companies are gratefully acknowledged for contributing photographic material: INA/FAG, NSK Corporation, NTN Bearing Corporation of America, and The Timken Company. The contributor of each such illustration is identified.

During my time as professor of mechanical engineering at The Pennsylvania State University, I had the pleasure of supervising and guiding the pursuit of the M.S. and Ph.D. degrees by Michael N. Kotzalas. Since graduation in 1999, he has been employed by The Timken Company and has greatly expanded his knowledge of, and activities in, the rolling bearing engineering and research field. It is therefore with great satisfaction that I welcome him as co-author of this fifth edition, to which he has made significant contributions.

Tedric A. Harris

Authors

Tedric A. Harris is a graduate in mechanical engineering from the Pennsylvania State University, having received a B.S. in 1953 and an M.S. in 1954. After graduation, he was employed as a development test engineer at the Hamilton Standard Division, United Aircraft Corporation, and later as an analytical design engineer at the Bettis Atomic Power Laboratory, Westinghouse Electric Corporation. In 1960, he joined SKF Industries, Inc. in Philadelphia, Pennsylvania, as a staff engineer. While at SKF, he held several key management positions: manager, Analytical Services; director, Corporate Data Systems; general manager, Specialty Bearings Division; vice president, Product Technology & Quality; president, SKF Tribonetics; vice president, Engineering & Research, MRC Bearings (all in the United States); director for Group Information Systems at SKF Headquarters, Gothenburg, Sweden; and managing director of the Engineering & Research Center in the Netherlands. He retired from SKF in 1991 and was appointed as a professor of mechanical engineering at The Pennsylvania State University, University Park. He taught courses in machine design and tribology and conducted research in the field of rolling contact tribology at the university until retirement in 2001. Currently, he conducts a consulting engineering practice and, as adjunct professor in mechanical engineering, teaches courses in bearing technology to graduate engineers in the University's Continuing Education Program.

He is the author of 67 technical publications, mostly on rolling bearings. In 1965 and 1968, he received Outstanding Technical Paper awards from the Society of Tribologists and Lubrication Engineers and in 2001 from the American Society of Mechanical Engineers (ASME) Tribology Division. In 2002, he received the Outstanding Research Award from the ASME.

He has served actively in numerous technical organizations, including the Anti-Friction Bearing Manufacturers' Association (now ABMA), ASME Tribology Division, and ASME Research Committee on Lubrication. He was elected ASME Fellow Member in 1973. He has served as chair of the ASME Tribology Division and of the Tribology Division's Nominations and Oversight Committee. He holds three U.S. patents.

Michael N. Kotzalas graduated from The Pennsylvania State University with a B.S. in 1994, M.S. in 1997, and Ph.D. in 1999, all in mechanical engineering. During this time, the focus of his study and research was on the analysis of rolling bearing performance, including quasidynamic modeling of ball and cylindrical roller bearings for high-acceleration applications and spall progression testing and modeling for use in condition-based maintenance algorithms.

Since graduation, he has been employed by The Timken Company in its research and development wing and most recently in the Industrial Bearing Business. His current responsibilities include advanced product design and application support for industrial bearing customers, whereas prior responsibilities included new product and analysis algorithm development. For this work, he received two U.S. patents for cylindrical roller bearing designs.

Outside of work, he is also active in industrial societies. As a member of the American Society of Mechanical Engineers (ASME), Dr. Kotzalas currently serves as the chair of the Publications Committee and as a member of the Rolling Element Bearing Technical Committee. With the Society of Tribologists and Lubrication Engineers (STLE), he is a

member of the Awards Committee. Michael has also published ten articles in peer-reviewed journals and one conference proceeding. For this, he received the ASME Tribology Division's Best Paper Award in 2001 and the STLE's Hodson Award in 2003 and 2006. Also, working with the American Bearing Manufacturer's Association (ABMA), Dr. Kotzalas is one of the many instructors for the short course "Advanced Concepts of Bearing Technology."

Table of Contents

Chapter 1

Rolling Bearing Types and Applications

1.1 Introduction to Rolling Bearings

1.2 Ball Bearings

1.2.1 Radial Ball Bearings

1.2.1.1 Single-Row Deep-Groove Conrad-Assembly Ball Bearing

1.2.1.2 Single-Row Deep-Groove Filling-Slot Assembly Ball Bearings

1.2.1.3 Double-Row Deep-Groove Ball Bearings

1.2.1.4 Instrument Ball Bearings

1.2.2 Angular-Contact Ball Bearings

1.2.2.1 Single-Row Angular-Contact Ball Bearings

1.2.2.2 Double-Row Angular-Contact Ball Bearings

1.2.2.3 Self-Aligning Double-Row Ball Bearings

1.2.2.4 Split Inner-Ring Ball Bearings

1.2.3 Thrust Ball Bearings

1.3 Roller Bearings

1.3.1 General

1.3.2 Radial Roller Bearings

1.3.2.1 Cylindrical Roller Bearings

1.3.2.2 Needle Roller Bearings

1.3.3 Tapered Roller Bearings

1.3.4 Spherical Roller Bearings

1.3.5 Thrust Roller Bearings

1.3.5.1 Spherical Roller Thrust Bearings

1.3.5.2 Cylindrical Roller Thrust Bearings

1.3.5.3 Tapered Roller Thrust Bearings

1.3.5.4 Needle Roller Thrust Bearings

1.4 Linear Motion Bearings

1.5 Bearings for Special Applications

1.5.1 Automotive Wheel Bearings

1.5.2 Cam Follower Bearings

1.5.3 Aircraft Gas Turbine Engine and Power Transmission Bearings

1.6 Closure

References

Chapter 2

Rolling Bearing Macrogeometry

2.1 General

2.2 Ball Bearings

2.2.1 Osculation

2.2.2 Contact Angle and Endplay

2.2.3 Free Angle of Misalignment

- 2.2.4 Curvature and Relative Curvature
- 2.3 Spherical Roller Bearings
 - 2.3.1 Pitch Diameter and Diametral Play
 - 2.3.2 Contact Angle and Free Endplay
 - 2.3.3 Osculation
 - 2.3.4 Curvature
- 2.4 Radial Cylindrical Roller Bearings
 - 2.4.1 Pitch Diameter, Diametral Clearance, and Endplay
 - 2.4.2 Curvature
- 2.5 Tapered Roller Bearings
 - 2.5.1 Pitch Diameter
 - 2.5.2 Endplay
 - 2.5.3 Curvature
- 2.6 Closure

References

Chapter 3

Bearings Fitting and Clearance

- 3.1 General
- 3.2 Industrial, National, and International Standards
 - 3.2.1 Method of Establishment and Scope
 - 3.2.2 Tolerances for Press-Fitting of Bearing Rings on Shafts and in Housings
- 3.3 Effect of Interference Fitting on Clearance.
- 3.4 Press Force
- 3.5 Differential Expansion
- 3.6 Effect of Surface Finish
- 3.7 Closure

References

Chapter 4

Bearing Loads and Speeds

- 4.1 General
- 4.2 Concentrated Radial Loading
 - 4.2.1 Bearing Loads
 - 4.2.2 Gear Loads
 - 4.2.3 Belt-and-Pulley and Chain Drive Loads
 - 4.2.4 Friction Wheel Drives
 - 4.2.5 Dynamic Loading Due to an Eccentric Rotor
 - 4.2.6 Dynamic Loading Due to a Crank-Reciprocating Load Mechanism
- 4.3 Concentrated Radial and Moment Loading
 - 4.3.1 Helical Gear Loads
 - 4.3.2 Bevel Gear Loads
 - 4.3.3 Hypoid Gear
 - 4.3.4 Worm Gear
- 4.4 Shaft Speeds
- 4.5 Distributed Load Systems
- 4.6 Closure

References

Chapter 5

Ball and Roller Loads Due to Bearing Applied Loading

- 5.1 General

- 5.2 Ball–Raceway Loading
- 5.3 Symmetrical Spherical Roller–Raceway Loading
- 5.4 Tapered and Asymmetrical Spherical Roller–Raceway and Roller–Flange Loading
- 5.5 Cylindrical Roller–Raceway Loading
 - 5.5.1 Radial Loading
 - 5.5.2 Roller Skewing Moment
- 5.6 Closure

Chapter 6

Contact Stress and Deformation

- 6.1 General
- 6.2 Theory of Elasticity
- 6.3 Surface Stresses and Deformations
- 6.4 Subsurface Stresses
- 6.5 Effect of Surface Shear Stress
- 6.6 Types of Contacts
- 6.7 Roller End–Flange Contact Stress
- 6.8 Closure

References

Chapter 7

Distributions of Internal Loading in Statically Loaded Bearing

- 7.1 General
- 7.2 Load–Deflection Relationships
- 7.3 Bearings under Radial Load
- 7.4 Bearings under Thrust Load
 - 7.4.1 Centric Thrust Load
 - 7.4.2 Angular-Contact Ball Bearings
 - 7.4.3 Eccentric Thrust Load
 - 7.4.3.1 Single-Direction Bearings
 - 7.4.3.2 Double-Direction Bearings
- 7.5 Bearings under Combined Radial and Thrust Load
 - 7.5.1 Single-Row Bearings
 - 7.5.2 Double-Row Bearings
- 7.6 Closure

References

Chapter 8

Bearing Deflection and Preloading

- 8.1 General
- 8.2 Deflections of Bearings with Rigidly Supported Rings
- 8.3 Preloading
 - 8.3.1 Axial Preloading
 - 8.3.2 Radial Preloading
 - 8.3.3 Preloading to Achieve Isoelasticity
- 8.4 Limiting Ball Bearing Thrust Load
 - 8.4.1 General Considerations
 - 8.4.2 Thrust Load Causing Ball to Override Land

8.4.3 Thrust Load Causing Excessive Contact Stress

8.5 Closure

References

Chapter 9

Permanent Deformation and Bearing Static Capacity

9.1 General

9.2 Calculation of Permanent Deformation

9.3 Static Load Rating of Bearings

9.4 Static Equivalent Load

9.5 Fracture of Bearing Components

9.6 Permissible Static Load

9.7 Closure

References

Chapter 10

Kinematic Speeds, Friction Torque, and Power Loss

10.1 General

10.2 Cage Speed

10.3 Rolling Element Speed

10.4 Rolling Bearing Friction

10.5 Rolling Bearing Friction Torque

10.5.1 Ball Bearings

10.5.1.1 Torque Due to Applied Load

10.5.1.2 Torque Due to Lubricant Viscous Friction

10.5.1.3 Total Friction Torque

10.5.2 Cylindrical Roller Bearings

10.5.2.1 Torque Due to Applied Load

10.5.2.2 Torque Due to Lubricant Viscous Friction

10.5.2.3 Torque Due to Roller End–Ring Flange Sliding Friction

10.5.2.4 Total Friction Torque

10.5.3 Spherical Roller Bearings

10.5.3.1 Torque Due to Applied Load

10.5.3.2 Torque Due to Lubricant Viscous Friction

10.5.3.3 Total Friction Torque

10.5.4 Needle Roller Bearings

10.5.5 Tapered Roller Bearings

10.5.6 High-Speed Effects

10.6 Bearing Power Loss

10.7 Thermal Speed Ratings

10.8 Closure

References

Chapter 11

Fatigue Life: Basic Theory and Rating Standards

11.1 General

11.2 Rolling Contact Fatigue

11.2.1 Material Microstructure before Bearing Operation

11.2.2 Alteration of the Microstructure Caused by Over-Rolling

11.2.3 Fatigue Cracking and Raceway Spalling Caused by Over-Rolling

- 11.2.4 Fatigue Failure-Initiating Stress and Depth
- 11.3 Fatigue Life Dispersion
- 11.4 Weibull Distribution
- 11.5 Dynamic Capacity and Life of a Rolling Contact
 - 11.5.1 Line Contact
- 11.6 Fatigue Life of a Rolling Bearing
 - 11.6.1 Point-Contact Radial Bearings
 - 11.6.2 Point-Contact Thrust Bearings
 - 11.6.3 Line-Contact Radial Bearings
 - 11.6.4 Line-Contact Thrust Bearings
 - 11.6.5 Radial Roller Bearings with Point and Line Contact
 - 11.6.6 Thrust Roller Bearing with Point and Line Contact
- 11.7 Load Rating Standards
- 11.8 Effect of Variable Loading on Fatigue Life
- 11.9 Fatigue Life of Oscillating Bearings
- 11.10 Reliability and Fatigue Life
- 11.11 Closure

References

Chapter 12

Lubricants and Lubrication Techniques

- 12.1 General
- 12.2 Types of Lubricants
 - 12.2.1 Selection of Lubricant Type
 - 12.2.2 Liquid Lubricants
 - 12.2.3 Greases
 - 12.2.4 Polymeric Lubricants
 - 12.2.5 Solid Lubricants
- 12.3 Liquid Lubricants
 - 12.3.1 Types of Liquid Lubricants
 - 12.3.1.1 Mineral Oil
 - 12.3.1.2 Synthetic Oils
 - 12.3.1.3 Environmentally Acceptable Oils
 - 12.3.2 Base Stock Lubricant
 - 12.3.3 Properties of Base Liquid Lubricants
 - 12.3.3.1 Viscosity
 - 12.3.3.2 Viscosity Index
 - 12.3.3.3 Pour Point
 - 12.3.3.4 Flash Point
 - 12.3.3.5 Evaporation Loss
 - 12.3.4 Lubricant Additive
 - 12.3.4.1 Purpose
 - 12.3.4.2 VI Improvers
 - 12.3.4.3 Extreme Pressure/Antiwear
 - 12.3.4.4 Other Additives
- 12.4 Grease
 - 12.4.1 How Grease Lubrication Functions
 - 12.4.2 Advantages of Grease Lubrication
 - 12.4.3 Types of Greases
 - 12.4.3.1 General

- 12.4.3.2 Lithium Soap Greases
- 12.4.3.3 Calcium Soap Greases
- 12.4.3.4 Sodium Soap Greases
- 12.4.3.5 Aluminum Complex Greases
- 12.4.3.6 Nonsoap-Base Greases
- 12.4.3.7 Inorganic Thickeners for Grease
- 12.4.3.8 Combining Greases
- 12.4.4 Grease Properties
 - 12.4.4.1 Properties of Retained Oil
 - 12.4.4.2 Dropping Point
 - 12.4.4.3 Low-Temperature Torque
 - 12.4.4.4 Oil Separation
 - 12.4.4.5 Penetration
- 12.5 Solid Lubricants
- 12.6 Lubricant Delivery Systems
 - 12.6.1 Oil Bath/Splash Oil
 - 12.6.2 Circulating Oil
 - 12.6.3 Air–Oil/Oil Mist
 - 12.6.4 Grease
 - 12.6.5 Polymeric Lubricant
- 12.7 Seals
 - 12.7.1 Function of Seals
 - 12.7.2 Types of Seals
 - 12.7.2.1 Labyrinth Seals
 - 12.7.2.2 Shields
 - 12.7.2.3 Elastomeric Lip Seals
 - 12.7.2.4 Garter Seals
- 12.8 Closure

References

Chapter 13

Structural Materials of Bearings

- 13.1 General
- 13.2 Rolling Bearing Steels
 - 13.2.1 Types of Steels for Rolling Components
 - 13.2.2 Through-Hardening Steels
 - 13.2.3 Case-Hardening Steels
 - 13.2.4 Steels for Special Bearings
- 13.3 Steel Manufacture
 - 13.3.1 Melting Methods
 - 13.3.2 Raw Materials
 - 13.3.3 Basic Electric Furnace Process
 - 13.3.4 Vacuum Degassing of Steel
 - 13.3.5 Ladle Furnace
 - 13.3.6 Methods for Producing Ultrahigh-Purity Steel
 - 13.3.6.1 Vacuum Induction Melting
 - 13.3.6.2 Vacuum Arc Remelting
 - 13.3.6.3 Electroslag Refining
 - 13.3.7 Steel Products

- 13.3.8 Steel Metallurgical Characteristics
 - 13.3.8.1 Cleanliness
 - 13.3.8.2 Segregation
 - 13.3.8.3 Structure
- 13.4 Effects of Processing Methods on Steel Components
- 13.5 Heat Treatment of Steel
 - 13.5.1 Basic Principles
 - 13.5.2 Time-Temperature Transformation Curve
 - 13.5.3 Continuous Cooling Transformation Curves
 - 13.5.4 Hardenability
 - 13.5.5 Hardening Methods
 - 13.5.6 Through-Hardening, High-Carbon-Chromium Bearing Steels
 - 13.5.6.1 General Heat Treatment
 - 13.5.6.2 Martensite
 - 13.5.6.3 Marquenching
 - 13.5.6.4 Bainite
 - 13.5.7 Surface Hardening
 - 13.5.7.1 Methods
 - 13.5.7.2 Carburizing
 - 13.5.7.3 Carbonitriding
 - 13.5.7.4 Induction Heating
 - 13.5.7.5 Flame-Hardening
 - 13.5.8 Thermal Treatment for Structural Stability
 - 13.5.9 Mechanical Properties Affected by Heat Treatment
 - 13.5.9.1 Elasticity
 - 13.5.9.2 Ultimate Strength
 - 13.5.9.3 Fatigue Strength
 - 13.5.9.4 Toughness
 - 13.5.9.5 Hardness
 - 13.5.9.6 Residual Stress
- 13.6 Materials for Special Bearings
- 13.7 Cage Materials
 - 13.7.1 Material Types
 - 13.7.2 Low-Carbon Steel
 - 13.7.3 Brass
 - 13.7.4 Bronze
 - 13.7.5 Polymeric Cage Materials
 - 13.7.5.1 Advantages and Disadvantages
 - 13.7.5.2 Rolling Bearing Polymer Cages
 - 13.7.6 High-Temperature Polymers
- 13.8 Seal Materials
 - 13.8.1 Function, Description, and Illustration
 - 13.8.2 Elastomeric Seal Materials
- 13.9 Tribological Coatings for Bearing Components
 - 13.9.1 Coatings in General
 - 13.9.2 Coating Deposition Processes
 - 13.9.2.1 General
 - 13.9.2.2 Chemical Conversion Coatings
 - 13.9.2.3 Electroplating and Electroless Plating
 - 13.9.2.4 Chemical Vapor Deposition

- 13.9.2.5 Physical Vapor Deposition
- 13.9.3 Surface Treatments for Mitigation of Damage Mechanisms Associated with Severe Operating Conditions
 - 13.9.3.1 General
 - 13.9.3.2 Interruption or Lack of Lubricant Supply to the Bearing
 - 13.9.3.3 False Brinelling
 - 13.9.3.4 Indentations Caused by Hard Particle Contaminants
 - 13.9.3.5 Severe Wear (Galling or Smearing)
 - 13.9.3.6 Surface-Initiated Fatigue

13.10 Closure

References

Chapter 14

Vibration, Noise, and Condition Monitoring

- 14.1 General
- 14.2 Vibration- and Noise-Sensitive Applications
 - 14.2.1 Significance of Vibration and Noise
 - 14.2.2 Noise-Sensitive Applications
 - 14.2.3 Vibration-Sensitive Applications
- 14.3 The Role of Bearings in Machine Vibration
 - 14.3.1 Bearing Effects on Machine Vibration
 - 14.3.2 Structural Elements
 - 14.3.3 Variable Elastic Compliance
 - 14.3.4 Geometric Imperfections
 - 14.3.4.1 General
 - 14.3.4.2 Microscale
 - 14.3.4.3 Waviness and Other Form Errors
 - 14.3.5 Waviness Model
- 14.4 Measurement of Nonroundness and Vibration
 - 14.4.1 Waviness Testing
 - 14.4.2 Vibration Testing
 - 14.4.3 Bearing Pass Frequencies
 - 14.4.4 Relation of Vibration and Waviness or Other Defects
- 14.5 Detection of Failing Bearings in Machines
- 14.6 Condition-Based Maintenance
- 14.7 Closure

References

Appendix

1 Rolling Bearing Types and Applications

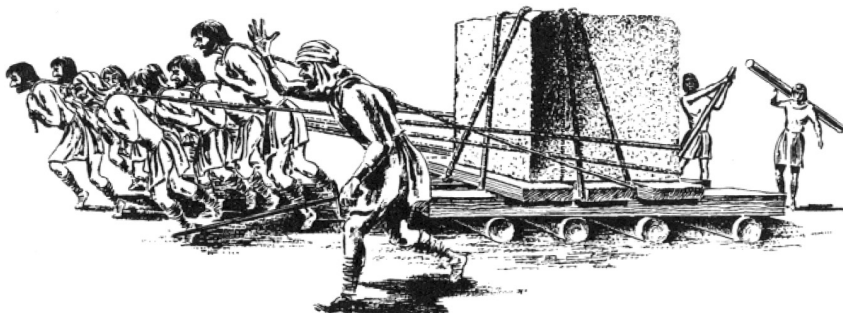
1.1 INTRODUCTION TO ROLLING BEARINGS

After the invention of the wheel, it was learned that less effort was required to move an object on rollers than to slide it over the same surface. Even after lubrication was discovered to reduce the work required in sliding, rolling motion still required less work when it could be used. For example, archeological evidence shows that the Egyptians, ca. 2400 BC, employed lubrication, most likely water, to reduce the manpower required to drag sledges carrying huge stones and statues. The Assyrians, ca. 1100 BC, however, employed rollers under the sledges to achieve a similar result with less manpower. It was therefore inevitable that bearings using rolling motion would be developed for use in complex machinery and mechanisms. [Figure 1.1](#) depicts, in a simplistic manner, the evolution of rolling bearings. Dowson [1] provides a comprehensive presentation of the history of bearings and lubrication in general; his coverage on ball and roller bearings is extensive. Although the concept of rolling motion was known and used for thousands of years, and simple forms of rolling bearings were in use ca. 50 AD during the Roman civilization, the general use of rolling bearings did not occur until the Industrial Revolution. Reti [2], however, shows that Leonardo da Vinci (1452–1519 AD), in his *Codex Madrid*, conceived of various forms of pivot bearings that had rolling elements and even a ball bearing with a device to space the balls. In fact, Leonardo, who among his prolific accomplishments studied friction, stated:

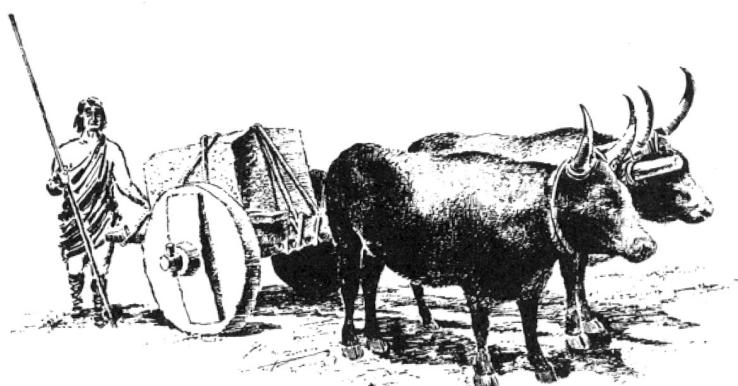
I affirm, that if a weight of flat surface moves on a similar plane their movement will be facilitated by interposing between them balls or rollers; and I do not see any difference between balls and rollers save the fact that balls have universal motion while rollers can move in one direction alone. But if balls or rollers touch each other in their motion, they will make the movement more difficult than if there were no contact between them, because their touching is by contrary motions and this friction causes contrariwise movements.

But if the balls or the rollers are kept at a distance from each other, they will touch at one point only between the load and its resistance... and consequently it will be easy to generate this movement.

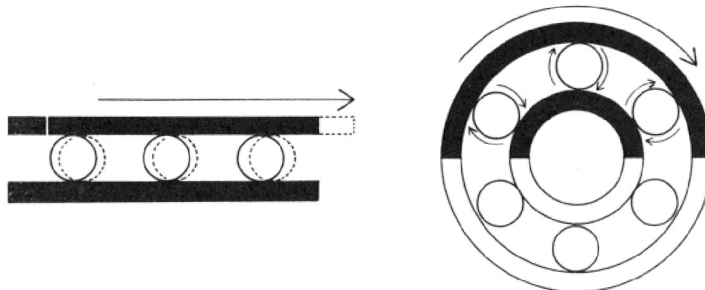
Thus did Leonardo conceive of the basic construction of the modern rolling bearing; his ball bearing design is shown in [Figure 1.2](#). The universal acceptance of rolling bearings by design engineers was initially impeded by the inability of manufacturers to supply rolling bearings that could compete in endurance with hydrodynamic sliding bearings. This situation, however, has been favorably altered during the 20th century, and particularly since 1960, by the development of superior rolling bearing steels and the constant improvement in manufacturing, providing extremely accurate geometry and rolling bearing assemblies with long lives. Initially, this development was triggered by the bearing requirements for high-speed



With the rollers used by the Assyrians to move massive stones in 1100 BC . . .



and later, with crude cart wheels, man strived to overcome friction's drag.

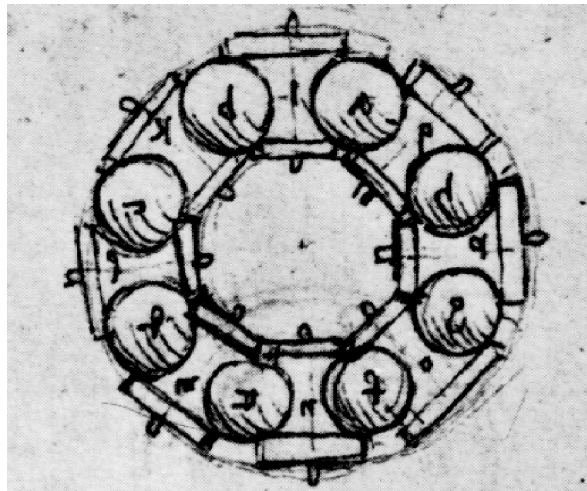


The simple ball bearing for 19th century bicycles marked man's first important victory.

FIGURE 1.1 The evolution of rolling bearings. (Courtesy of SKF.)

aircraft gas turbines; however, competition between ball and roller bearing manufacturers for worldwide markets increased substantially during the 1970s, and this has served to provide consumers with low-cost, standard design bearings of outstanding endurance. The term *rolling bearings* includes all forms of bearings that utilize the rolling action of balls or rollers to permit minimum friction, from the constrained motion of one body relative to another. Most rolling bearings are employed to permit the rotation of a shaft relative to some fixed structure. Some rolling bearings, however, permit translation, that is, relative linear motion, of a fixture in the direction provided by a stationary shaft, and a few rolling bearing designs permit a combination of relative linear and rotary motions between two bodies.

This book is concerned primarily with the standardized forms of ball and roller bearings that permit rotary motion between two machine elements. These bearings will always include a complement of balls or rollers that maintain the shaft and a usually stationary supporting structure, frequently called a *housing*, in a radially or axially spaced-apart relationship.



(a)



(b)

FIGURE 1.2 (a) Thrust ball bearing design (ca. 1500) in *Codex Madrid* by Leonardo da Vinci [2]; (b) Da Vinci bearing with plexiglas upper plate fabricated at Institut National des Sciences Appliquées de Lyon (INSA) as a present for Docteur en Mécanique Daniel Nélia on the occasion of his passing the requirements for “Diriger des Recherches,” December 16, 1999. (Courtesy of Institut National des Sciences Appliquées de Lyon (INSA) December 16, 1999.)

Usually, a bearing will be obtained as a unit that includes two steel rings, each of which has a hardened raceway on which hardened balls or rollers roll. The balls or rollers, also called rolling elements, are usually held in an angularly spaced relationship by a cage, whose function was anticipated by Leonardo. The cage is called a separator or retainer.

Rolling bearings are normally manufactured from steels that harden to a high degree, at least on the surface. In universal use by the ball bearing industry is AISI 52100, a steel

moderately rich in chromium and easily hardened throughout (through-hardened) the mass of most bearing components to 61–65 Rockwell C scale hardness. This steel is also used in roller bearings by some manufacturers. Miniature ball bearing manufacturers, whose bearings are used in sensitive instruments such as gyroscopes, prefer to fabricate components from stainless steels such as AISI 440C. Roller bearing manufacturers frequently prefer to fabricate rings and rollers from case-hardened steels such as AISI 3310, 4118, 4620, 8620, and 9310. For some specialized applications, such as automotive wheel hub bearings, the rolling components are manufactured from induction-hardened steels. In all cases, at least the surfaces of the rolling components are extremely hard. In some high-speed applications, to minimize inertial loading of the balls or rollers, these components are fabricated from lightweight, high-compressive-strength ceramic materials such as silicon nitride. Also, these ceramic rolling elements tend to endure longer than steel at ultrahigh temperatures and in applications with dry film or minimal fluid lubrication.

Cage materials, when compared with materials for balls, rollers, and rings, are generally required to be relatively soft. They must also possess a good strength-to-weight ratio; therefore, materials as widely diverse in physical properties as mild steel, brass, bronze, aluminum, polyamide (nylon), polytetrafluoroethylene (teflon or PTFE), fiberglass, and plastics filled with carbon fibers are used as cage material.

In this modern age of deep-space exploration and cyberspace, many different kinds of bearings have come into use, such as gas film bearings, foil bearings, magnetic bearings, and externally pressurized hydrostatic bearings. Each of these bearing types excels in some specialized field of application. For example, hydrostatic bearings are excellent for applications in which size is not a problem, an ample supply of pressurized fluid is available, and extreme rigidity under heavy loading is required. Self-acting gas bearings may be used for applications in which loads are light, speeds are high, a gaseous atmosphere exists, and friction must be minimal. Rolling bearings, however, are not quite so limited in scope. Consequently, miniature ball bearings such as those shown in Figure 1.3 are found in precision applications such as inertial guidance gyroscopes and high-speed dental drills. Large roller bearings, such as those shown in Figure 1.4, are utilized in mining applications,

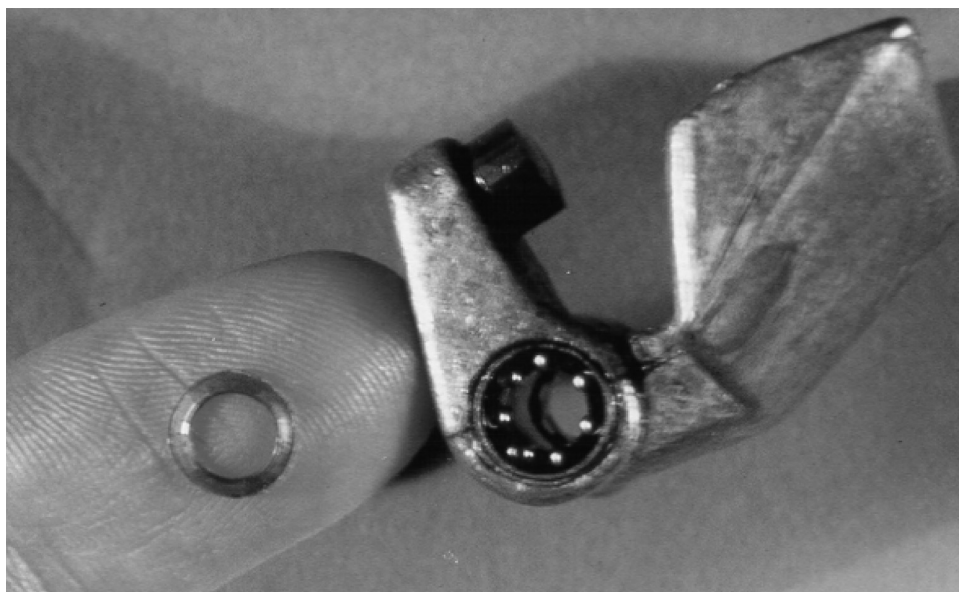


FIGURE 1.3 Miniature ball bearing. (Courtesy of SKF.)



FIGURE 1.4 A large spherical roller bearing for a ball mill (mining) application. (Courtesy of SKF.)

and even larger slewing bearings, as illustrated in [Figure 1.5](#), were used in tunneling machines for the “Chunnel” (English Channel tunneling) project.

Moreover, rolling bearings are used in diverse precision machinery operations, for example, the high-load, high-temperature, dusty environment of steel making ([Figure 1.6](#)); the dirty environments of earthmoving and farming ([Figure 1.7](#) and [Figure 1.8](#)); the life-critical applications in aircraft power transmissions ([Figure 1.9](#)); and the extreme low–high temperature and vacuum environments of deep space ([Figure 1.10](#)). They perform well in all of these applications. Specifically, rolling bearings have the following advantages compared with other bearing types:

- They operate with much less friction torque than hydrodynamic bearings and therefore there is considerably less power loss and friction heat generation.
- The starting friction torque is only slightly greater than the moving friction torque.
- The bearing deflection is less sensitive to load fluctuation than it is with hydrodynamic bearings.
- They require only small quantities of lubricants for satisfactory operation and have the potential for operation with a self-contained, lifelong supply of lubricant.
- They occupy shorter axial lengths than conventional hydrodynamic bearings.
- Combinations of radial and thrust loads can be supported simultaneously.
- Individual designs yield excellent performance over a wide load–speed range.
- Satisfactory performance is relatively insensitive to fluctuations in load, speed, and operating temperature.

Notwithstanding the advantages listed above, rolling bearings have been considered to have a single disadvantage when compared with hydrodynamic bearings. In this regard Tallian [3]

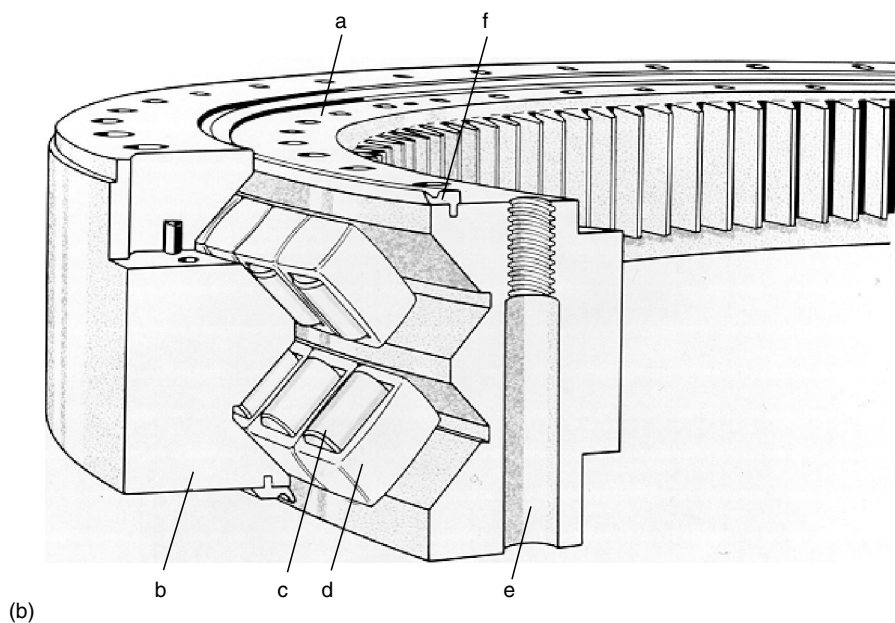


FIGURE 1.5 Large slewing bearing used in an English Channel tunneling machine. (a) Photograph; (b) schematic drawing of the assembly. (Courtesy of SKF.)

defined three eras of modern rolling bearing development: the “empirical” era, extending through the 1920s; the “classical” era, lasting through the 1950s; and the “modern” era, occurring thereafter. Through the empirical, classical, and even into the modern eras, it was said that even if rolling bearings are properly lubricated, properly mounted, properly protected from dirt and moisture, and otherwise properly operated, they will eventually fail because of fatigue of the surfaces in rolling contact. Historically, as shown in [Figure 1.11](#), rolling bearings have been considered to have a life distribution statistically similar to that of light bulbs and human beings.

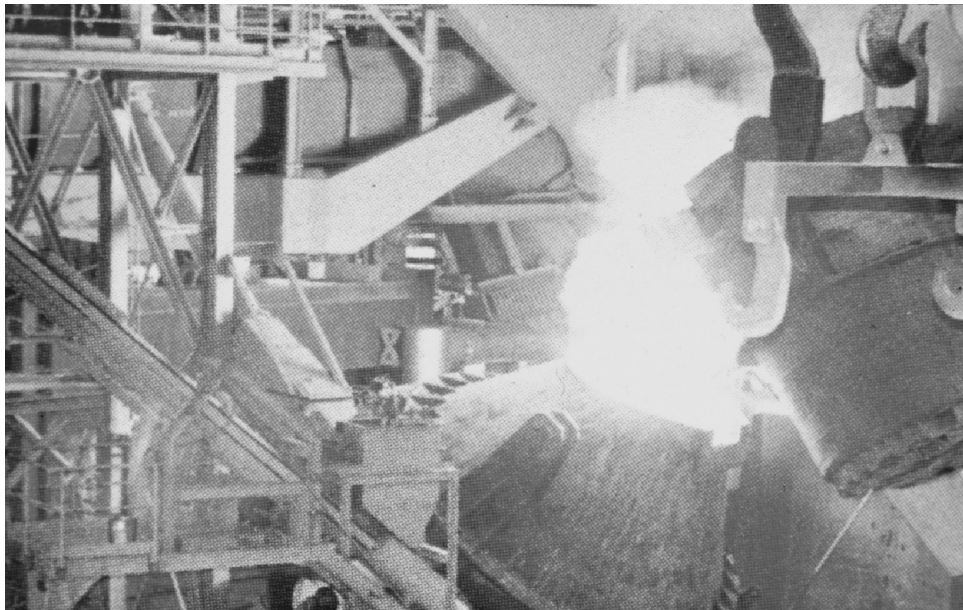


FIGURE 1.6 Spherical roller bearings are typically used to support the ladle in a steel-making facility. (Courtesy of SKF.)



FIGURE 1.7 Many ball and roller bearings must function in the high-contamination environment of earthmoving vehicle operations. (Courtesy of SKF.)



FIGURE 1.8 Agricultural applications employ many bearings with special seals to provide long bearing life. (Courtesy of SKF.)



FIGURE 1.9 CH-53E Sikorsky Super Stallion heavy-lift helicopters employ ball, cylindrical roller, and spherical roller bearings in transmissions that power the main and tail rotors. (Courtesy of Sikorsky Aircraft, United Technologies Corp.)



FIGURE 1.10 The ball bearings in the Lunar Excursion Module and Lunar Rover operated well in the extreme temperatures and hard vacuum on the lunar surface. (Courtesy of SKF.)

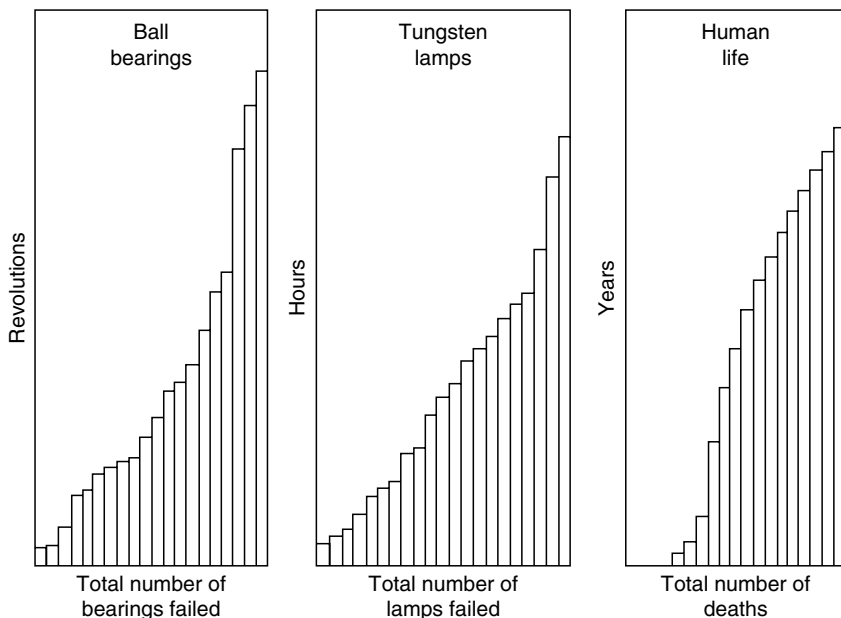


FIGURE 1.11 Comparison of rolling bearing fatigue life distribution with those of humans and light bulbs.

Research in the 1960s [4] demonstrated that rolling bearings exhibit a minimum fatigue life; that is, “crib deaths” due to rolling contact fatigue do not occur when the foregoing criteria for good operation are achieved. Moreover, modern manufacturing techniques enable the production of bearings with extremely accurate internal and external component geometries and extremely smooth rolling contact surfaces. Modern steel-making processes provide rolling bearing steels of outstanding homogeneity with few impurities, and modern sealing and lubricant filtration methods minimize the incursion of harmful contaminants into the rolling contact zones. These methods, which are now used in combination in many applications, can virtually eliminate the occurrence of rolling contact fatigue, even in some applications involving very heavy applied loading. In many lightly loaded applications, for example, most electric motors, fatigue life need not be a major design consideration.

There are many different kinds of rolling bearings, and before embarking on a discussion of the theory and analysis of their operation, it is necessary to become somewhat familiar with each type. In the succeeding pages, a description for each of the most popular ball and roller bearings in current use is given.

1.2 BALL BEARINGS

1.2.1 RADIAL BALL BEARINGS

1.2.1.1 Single-Row Deep-Groove Conrad-Assembly Ball Bearing

A single-row deep-groove ball bearing is shown in [Figure 1.12](#); it is the most popular rolling bearing. The inner and outer raceway grooves have curvature radii between 51.5 and 53% of the ball diameter for most commercial bearings.

To assemble these bearings, the balls are inserted between the inner and outer rings as shown in [Figure 1.13](#) and [Figure 1.14](#). The assembly angle ϕ is given as

$$\phi = 2(Z - 1)D/d_m \quad (1.1)$$

where Z is the number of balls, D is the ball diameter, and d_m is the pitch diameter. The inner ring is then snapped to a position concentric with the outer ring, the balls are separated uniformly, and a riveted cage as shown in [Figure 1.12](#) or a plastic cage as illustrated in [Figure 13.18a](#) is inserted to maintain the separation. Because of the high osculation and the need for an appropriate ball diameter and ball complement to substantially fill the bearing pitch circle, the deep-groove ball bearing has a comparatively high load-carrying capacity when accurately manufactured from good-quality steel and operated in accordance with good lubrication and contaminant-exclusion practices. Although it is designed to carry a radial load, it performs well under combined radial and thrust loads and under thrust alone. With a proper cage design, deep-groove ball bearings can also withstand misaligning loads (moment loads) of small magnitude. By making the outside surface of the bearing a portion of a sphere as illustrated in [Figure 1.15](#), however, the bearing can be made externally self-aligning and, thus, incapable of supporting a moment load.

The deep-groove ball bearing can be readily adapted with seals as shown in [Figure 1.16](#) or shields as shown in [Figure 1.17](#) or both as illustrated in [Figure 1.18](#). These components function to keep the lubricant in the bearing and exclude contaminants. Seals and shields come in many different configurations to serve general or selective applications; those shown in [Figure 1.16](#) through [Figure 1.18](#) should be taken only as examples. In [Chapter 12](#), seals are discussed in greater detail.

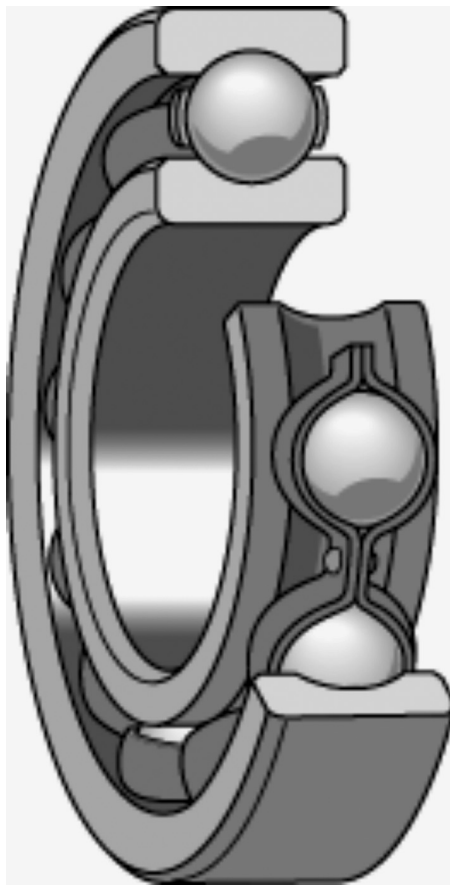


FIGURE 1.12 A single-row deep-groove Conrad-assembly radial ball bearing. (Courtesy of SKF.)

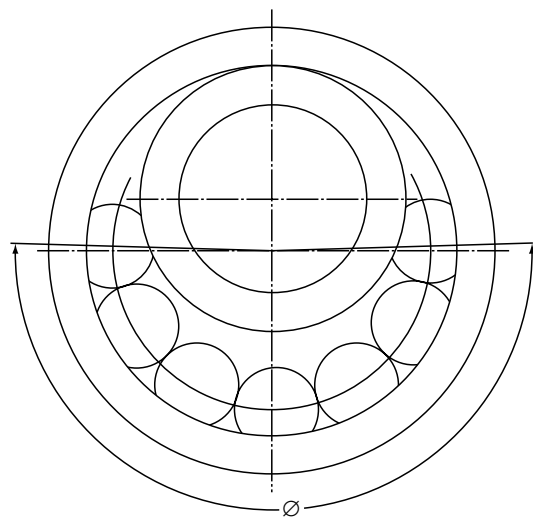


FIGURE 1.13 Diagram illustrating the method of assembly of a Conrad-type, deep-groove ball bearing.



FIGURE 1.14 Photograph showing Conrad-type ball bearing components just before snapping the inner ring to the position concentric with the outer ring.

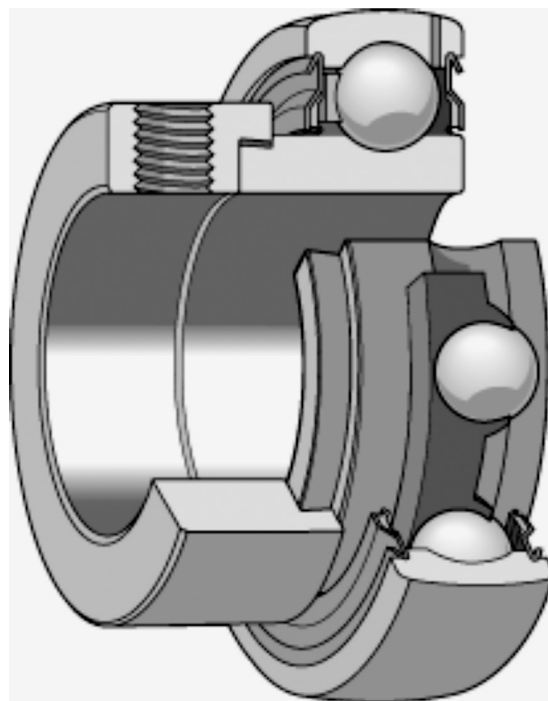


FIGURE 1.15 A single-row deep-groove ball bearing assembly that has a spherized outer surface to make it externally aligning. (Courtesy of SKF.)

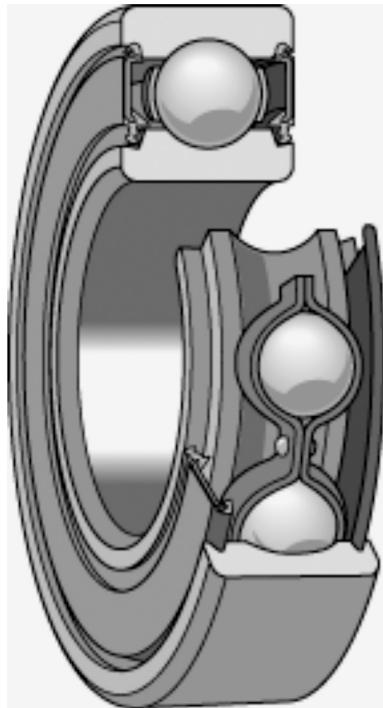


FIGURE 1.16 A single-row deep-groove ball bearing that has two seals to retain lubricant (grease) and prevent ingress of dirt into the bearing. (Courtesy of SKF.)

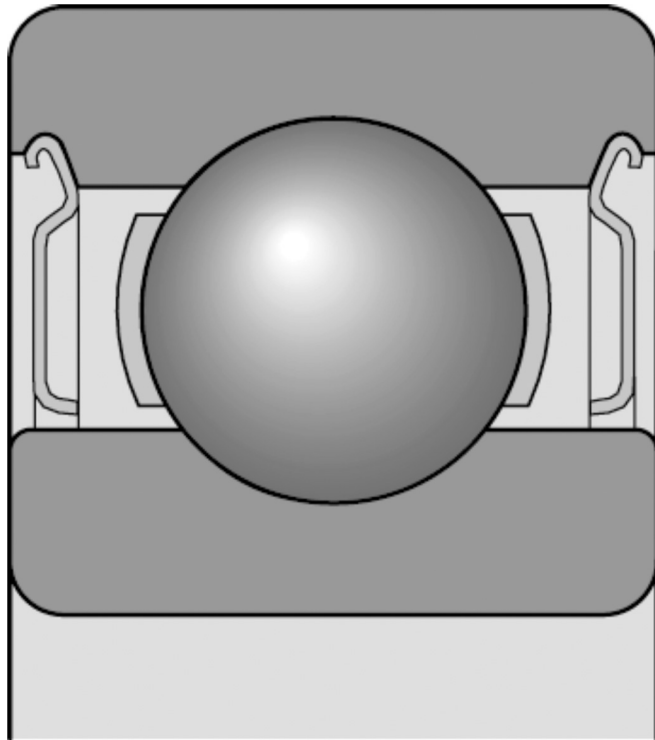


FIGURE 1.17 A single-row deep-groove ball bearing that has two shields to exclude dirt from the bearing. (Courtesy of SKF.)

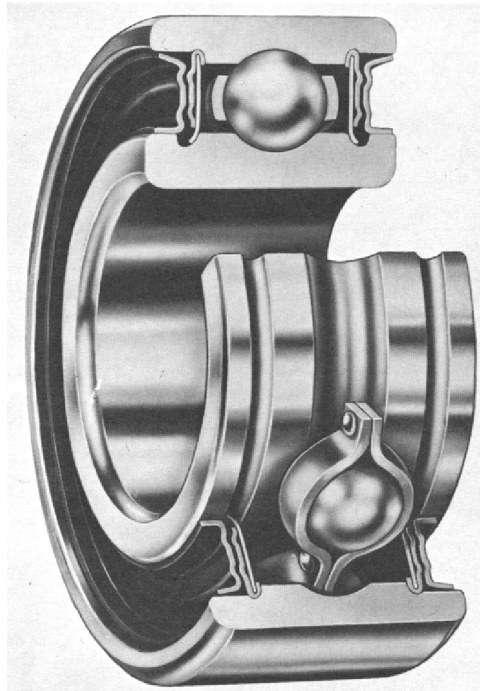


FIGURE 1.18 A single-row deep-groove ball bearing assembly with shields and seals. The shields are used to exclude large particles of foreign matter. (Courtesy of SKF.)

Deep-groove ball bearings perform well at high speeds, provided adequate lubrication and cooling are available. Speed limits shown in manufacturers' catalogs generally pertain to bearing operation without the benefit of external cooling capability or special cooling techniques.

Conrad-assembly bearings can be obtained in different dimension series according to ANSI and ISO standards. Figure 1.19 shows the relative dimensions of various ball bearing series.

1.2.1.2 Single-Row Deep-Groove Filling-Slot Assembly Ball Bearings

A single-row deep-groove filling-slot assembly ball bearing as illustrated in Figure 1.20 has a slot machined in the side wall of each of the inner and outer ring grooves to permit the assembly of more balls than the Conrad type does, and thus it has more radial-load-carrying capacity. Because the slot disrupts the groove continuity, the bearing is not recommended for thrust load applications; otherwise, the bearing has characteristics similar to those of the Conrad type.

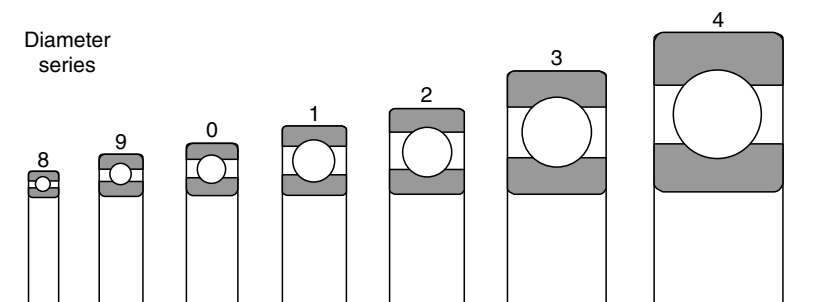


FIGURE 1.19 Size comparison of popular deep-groove ball bearing dimension series.

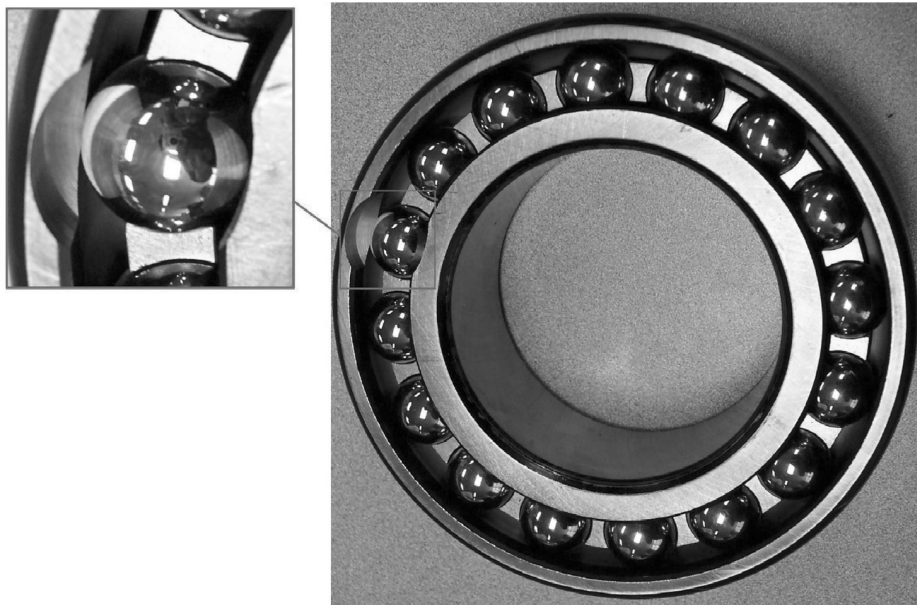


FIGURE 1.20 View of a single-row deep-groove filling slot-type ball bearing assembly. (Courtesy of the Timken Company.)

1.2.1.3 Double-Row Deep-Groove Ball Bearings

A double-row deep-groove ball bearing as shown in [Figure 1.21](#) has greater radial-load-carrying capacity than the single-row types. Proper load-sharing between the rows is a function of the geometrical accuracy of the grooves. Otherwise, these bearings behave similarly to single-row ball bearings.

1.2.1.4 Instrument Ball Bearings

In metric designs, the standardized form of these bearings ranges in size from 1.5-mm (0.05906-in.) bore and 4-mm (0.15748-in.) o.d. to 9-mm (0.35433-in.) bore and 26-mm (1.02362-in.) o.d. (see Ref. [5]). As detailed in Ref. [6], standardized form, inch design instrument ball bearings range from 0.635-mm (0.0250-in.) bore and 2.54-mm (0.100-in.) o.d. to 19.050-mm (0.7500-in.) bore and 41.275-mm (1.6250-in.) o.d. Additionally, instrument ball bearings have extra-thin series that range up to 47.625-mm (1.8750-in.) o.d. and thin series that range up to 100-mm (3.93701-in.) o.d. Those bearings having less than 9-mm (0.3543-in.) o.d. are classified as miniature ball bearings according to ANSI [6] and can use balls as small as 0.6350-mm (0.0250-in.) diameter. These bearings are illustrated in [Figure 1.3](#). They are fabricated according to more stringent manufacturing standards, such as for cleanliness, than are any of the bearings previously described. This is because minute particles of foreign matter can significantly increase the friction torque and negatively affect the smooth operation of the bearings. For this reason, they are assembled in an ultra-clean environment as illustrated in [Figure 1.22](#).

Groove radii of instrument ball bearings are usually not smaller than 57% of the ball diameter. The bearings are usually fabricated from stainless steels since corrosion particles will seriously deteriorate bearing performance.

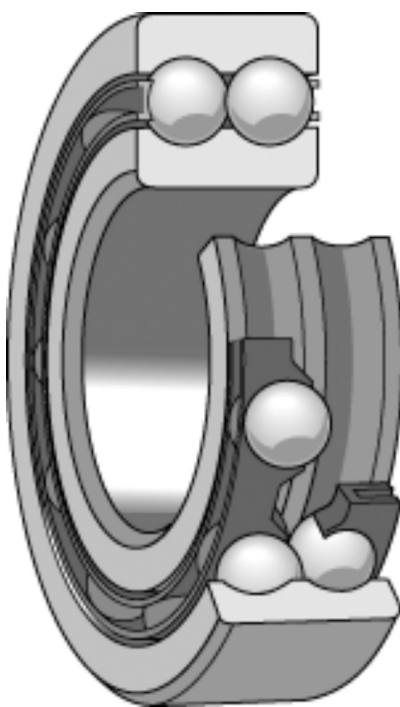


FIGURE 1.21 A double-row deep-groove radial ball bearing. (Courtesy of SKF.)

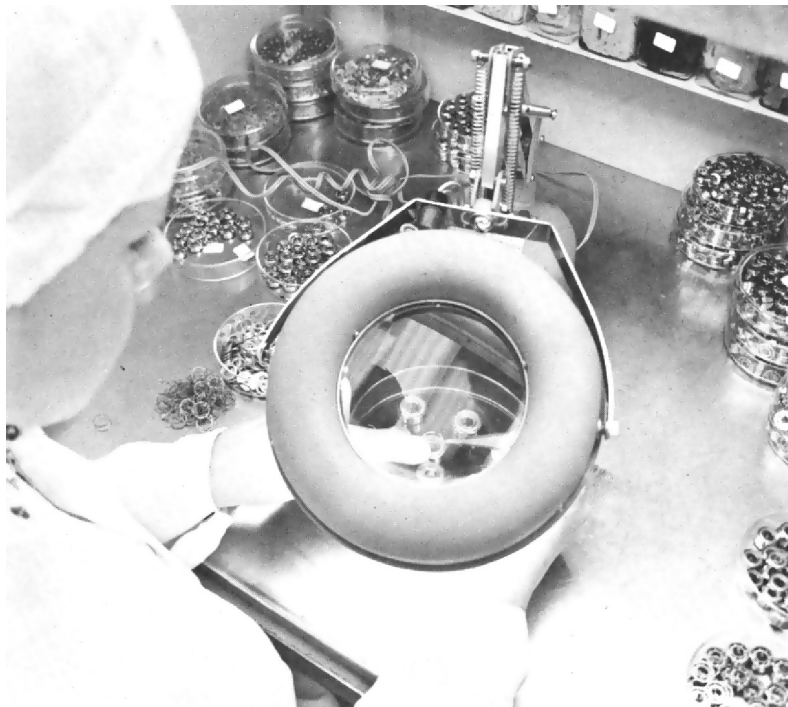


FIGURE 1.22 A delicate final assembly operation on an instrument ball bearing assembly is performed under magnification in a “white room.”

1.2.2 ANGULAR-CONTACT BALL BEARINGS

1.2.2.1 Single-Row Angular-Contact Ball Bearings

Angular-contact ball bearings as shown in Figure 1.23 are designed to support combined radial and thrust loads or heavy thrust loads, depending on the contact angle magnitude. Bearings having large contact angles can support heavier thrust loads. Figure 1.24 shows bearings that have small and large contact angles. The bearings generally have groove curvature radii in the range of 52–53% of the ball diameter. The contact angle does not usually exceed 40°. The bearings are usually mounted in pairs with the free endplay removed as shown in Figure 1.25. These sets may be preloaded against each other to stiffen the assembly in the axial direction. The bearings may also be mounted in tandem as illustrated in Figure 1.26 to achieve greater thrust-carrying capacity.

1.2.2.2 Double-Row Angular-Contact Ball Bearings

Double-row angular-contact ball bearings, as depicted in Figure 1.27, can carry thrust loads in either direction or a combination of radial and thrust loads. Bearings of the rigid type can withstand moment loading effectively. Essentially, the bearings perform similarly to duplex pairs of single-row angular-contact ball bearings.



FIGURE 1.23 An angular-contact ball bearing. (Courtesy of SKF.)

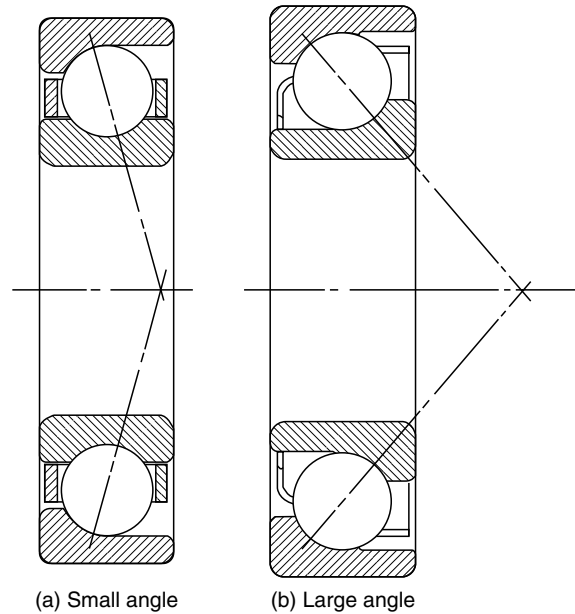


FIGURE 1.24 Angular-contact ball bearings.

1.2.2.3 Self-Aligning Double-Row Ball Bearings

As illustrated in [Figure 1.28](#), the outer raceway of a self-aligning double-row ball bearing is a portion of a sphere. Thus, the bearings are internally self-aligning and cannot support a moment load. Because the balls do not conform well to the outer raceway (it is not grooved),

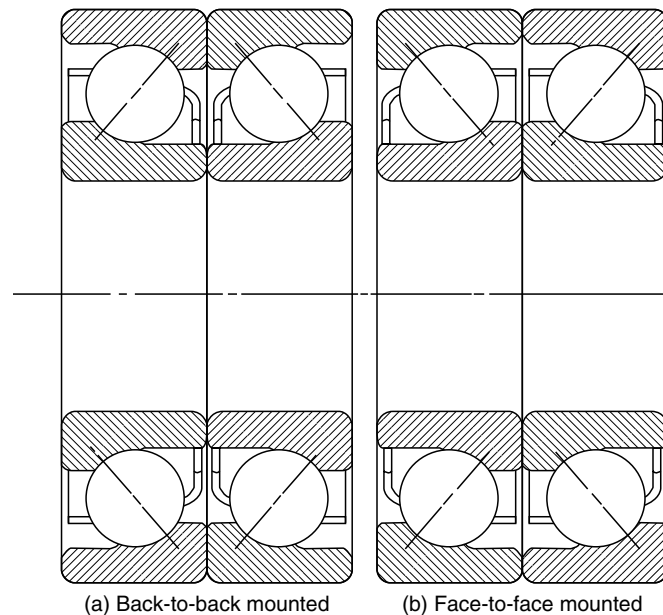


FIGURE 1.25 Duplex pairs of angular-contact ball bearings.

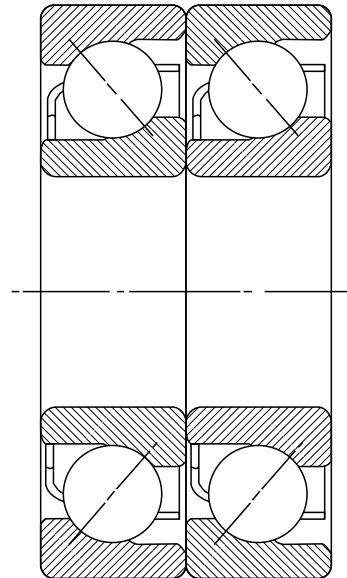


FIGURE 1.26 A tandem-mounted pair of angular-contact ball bearings.

the outer raceway has reduced load-carrying capacity. This is compensated somewhat by the use of a very large ball complement that minimizes the load carried by each ball. The bearings are particularly useful in applications in which it is difficult to obtain exact parallelism between the shaft and housing bores. Figure 1.29 shows this bearing with a tapered sleeve and locknut adapter. With this arrangement, the bearing does not require a locating shoulder on the shaft.

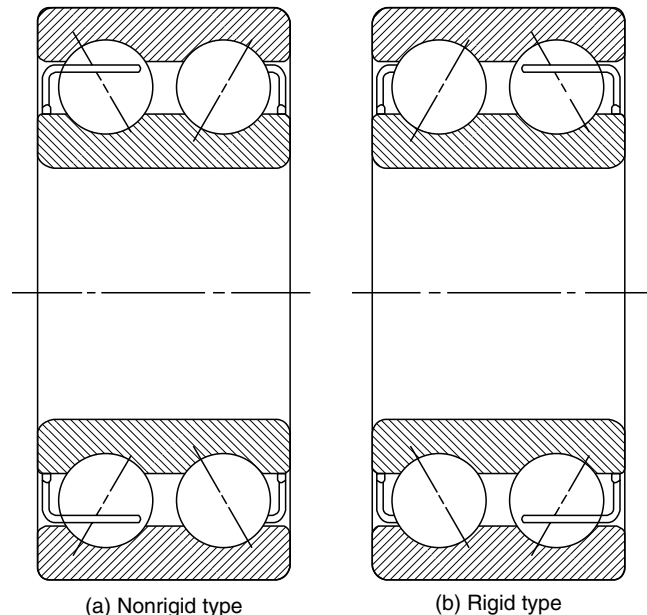


FIGURE 1.27 Double-row angular-contact ball bearings.

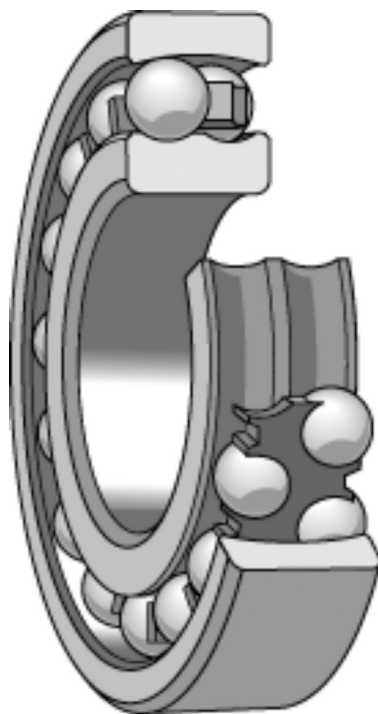


FIGURE 1.28 A double-row internally self-aligning ball bearing assembly. (Courtesy of SKF.)

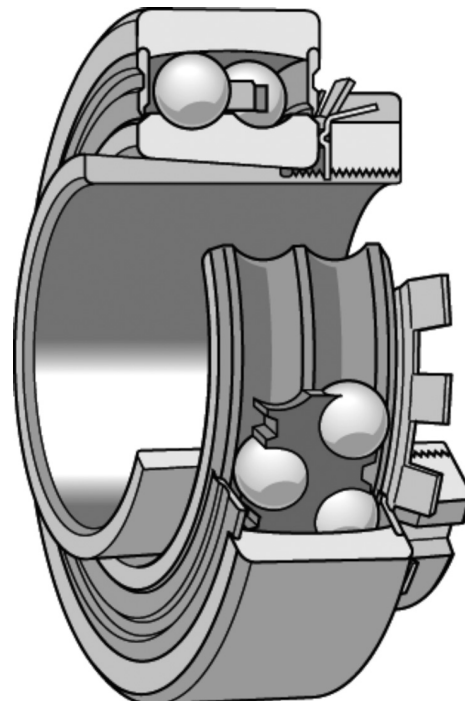


FIGURE 1.29 A double-row internally self-aligning ball bearing assembly with a tapered sleeve and locknut adapter for simplified mounting on a shaft of uniform diameter. (Courtesy of SKF.)

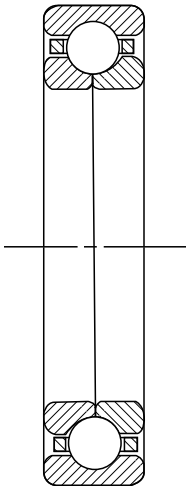


FIGURE 1.30 A split inner-ring ball bearing assembly.

1.2.2.4 Split Inner-Ring Ball Bearings

Split inner-ring ball bearings are illustrated in Figure 1.30, where it can be seen that the inner ring consists of two axial halves such that a heavy thrust load can be supported in either direction. They may also support, simultaneously, moderate radial loading. The bearings have found extensive use in supporting the thrust loads acting on high-speed, gas turbine engine mainshafts. Figure 1.31 shows the compressor and turbine shaft ball bearing locations in a high-performance aircraft gas turbine engine. Obviously, both the inner and outer rings must be locked up on both axial sides to support a reversing thrust load. It is possible with accurate flush grinding at the factory to utilize these bearings in tandem as shown in Figure 1.32 to share a thrust load in a given direction.

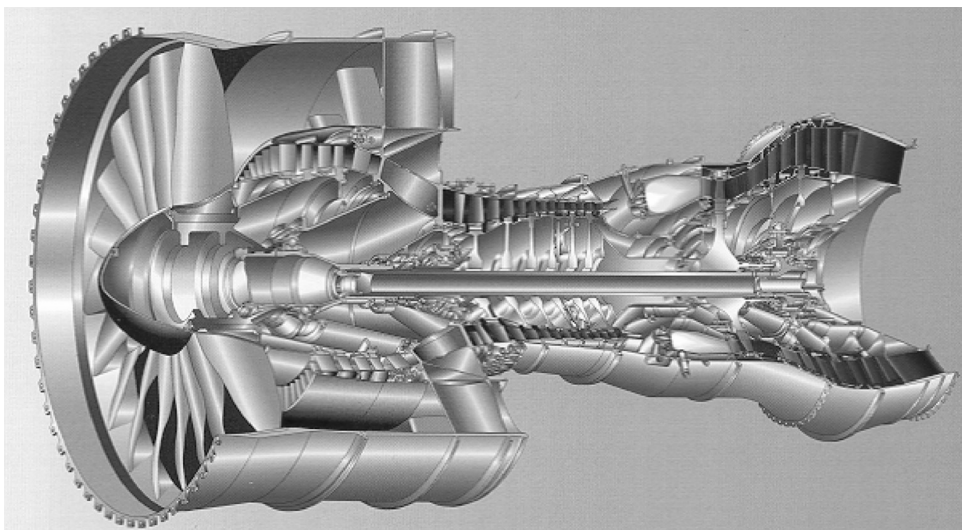


FIGURE 1.31 Cutaway view of turbofan gas turbine engine showing mainshaft bearing locations. (Courtesy of Pratt and Whitney, United Technologies Corp.)

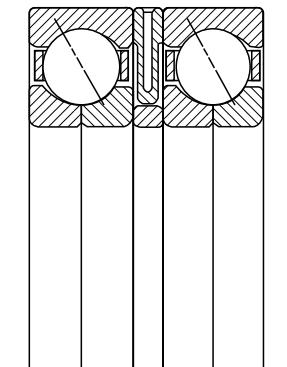


FIGURE 1.32 A tandem-mounted pair of split inner-ring ball bearings.

1.2.3 THRUST BALL BEARINGS

The thrust ball bearing illustrated in Figure 1.33 has a 90° contact angle; however, ball bearings whose contact angles exceed 45° are also classified as thrust bearings. As for radial ball bearings, thrust ball bearings are suitable for operation at high speeds. To achieve a degree of externally aligning ability, thrust ball bearings are sometimes mounted on spherical seats. This arrangement is demonstrated in Figure 1.34. A thrust ball bearing whose contact angle is 90° cannot support any radial load.

1.3 ROLLER BEARINGS

1.3.1 GENERAL

Roller bearings are usually used for applications requiring exceptionally large load-supporting capabilities, which cannot be feasibly obtained using ball bearing assemblies. Roller bearings are usually much stiffer structures (less deflection per unit loading) and provide greater fatigue endurance than do ball bearings of comparable sizes. In general, they also cost more to manufacture, and hence purchase, than comparable ball bearing assemblies. They usually

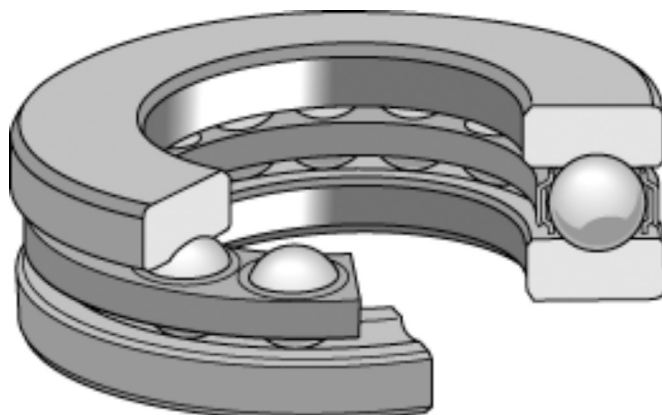


FIGURE 1.33 A 90° contact angle thrust ball bearing assembly. (Courtesy of SKF.)

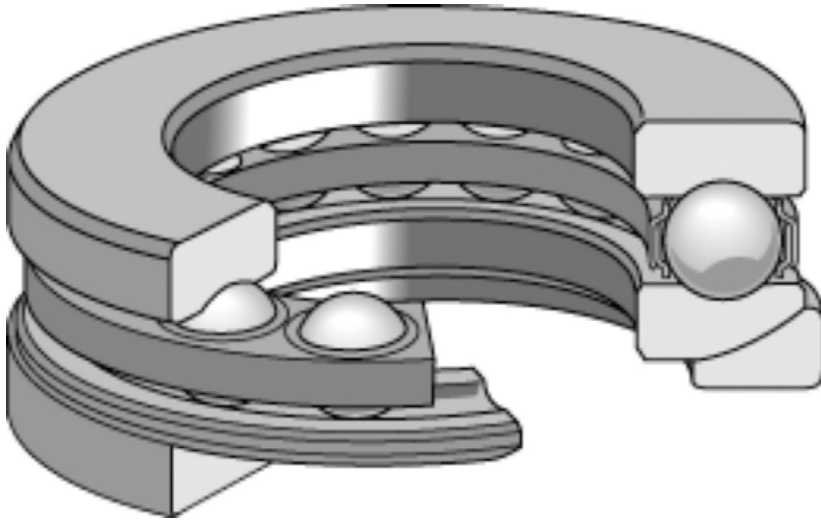


FIGURE 1.34 A 90° contact-angle thrust ball bearing with a spherical seat to make it externally aligning. (Courtesy of SKF.)

require greater care in mounting than do ball bearing assemblies. Accuracy of alignment of shafts and housings can be a problem in all but self-aligning roller bearings.

1.3.2 RADIAL ROLLER BEARINGS

1.3.2.1 Cylindrical Roller Bearings

Cylindrical roller bearings, as illustrated in [Figure 1.35](#), have exceptionally low-friction torque characteristics that make them suitable for high-speed operations. They also have high radial-load-carrying capacities. The usual cylindrical roller bearing is free to float axially. It has two roller-guiding flanges on one ring and none on the other, as shown in [Figure 1.36](#). By equipping the bearing with a guide flange on the opposing ring (illustrated in [Figure 1.37](#)), the bearing can be made to support some thrust load.

To prevent high stresses at the edges of the rollers, the rollers are usually crowned as shown in [Figure 1.38](#). This crowning of rollers also gives the bearing protection against the effects of a slight misalignment. The crown is ideally designed for only one condition of loading. Crowned raceways may be used in lieu of crowned rollers.

To achieve greater radial-load-carrying capacities, cylindrical roller bearings are frequently constructed of two or more rows of rollers rather than of longer rollers. This is done to reduce the tendency of the rollers to skew. [Figure 1.39](#) shows a small double-row cylindrical roller bearing designed for use in precision applications. [Figure 1.40](#) illustrates a large multirow cylindrical roller bearing for a steel rolling mill application.

1.3.2.2 Needle Roller Bearings

A needle roller bearing is a cylindrical roller bearing that has rollers of considerably greater length than diameter. This bearing is illustrated in [Figure 1.41](#). Because of the geometry of the rollers, they cannot be manufactured as accurately as other cylindrical rollers, nor can they be guided as well. Consequently, needle roller bearings have relatively greater friction than other cylindrical roller bearings.

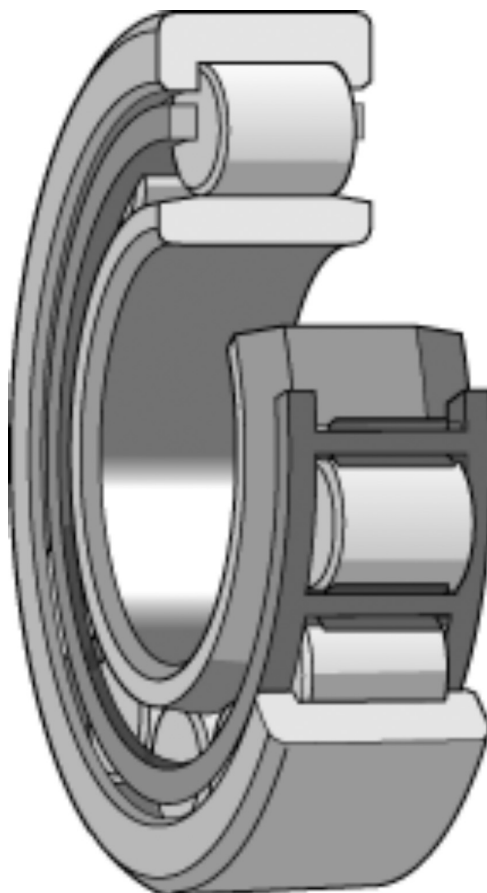


FIGURE 1.35 A radial cylindrical roller bearing. (Courtesy of SKF.)

Needle roller bearings are designed to fit in applications in which the radial space is at a premium. Sometimes, to conserve space, the needles are set to bear directly on a hardened shaft. They are useful for applications in which oscillatory motion occurs or in which continuous rotation occurs but loading is light and intermittent. The bearings may be assembled without a cage, as shown in [Figure 1.42](#). In this full-complement-type bearing, the rollers are frequently retained by turned-under flanges that are integral with the outer shell. The raceways are frequently hardened but not ground.

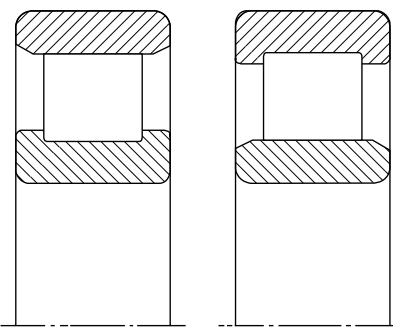


FIGURE 1.36 Cylindrical roller bearings without thrust flanges.

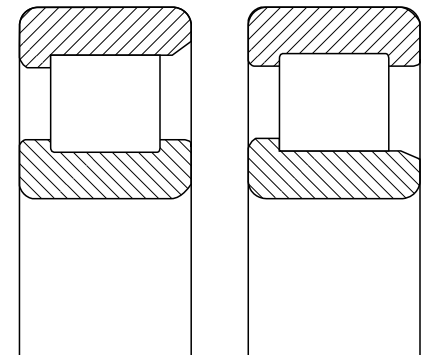


FIGURE 1.37 Cylindrical roller bearings with thrust flanges.

1.3.3 TAPERED ROLLER BEARINGS

The single-row tapered roller bearing shown in [Figure 1.43](#) has the ability to carry combinations of large radial and thrust loads or to carry a thrust load only. Because of the difference between the inner and outer raceway contact angles, there is a force component that drives the tapered rollers against the guide flange. Because of the relatively large sliding friction generated at this flange, the bearing is not suitable for high-speed operations without paying special attention to cooling and lubrication.

Tapered roller bearing terminology differs somewhat from that pertaining to other roller bearings, with the inner ring called the cone and the outer ring the cup. Depending on the magnitude of the thrust load to be supported, the bearing may have a small or steep contact angle, as shown in [Figure 1.44](#). Because tapered roller bearing rings are separable, the bearings are mounted in pairs, as indicated in [Figure 1.45](#), and one bearing is adjusted against the other. To achieve greater radial-load-carrying capacities and to eliminate problems of axial adjustment due to the distance between bearings, tapered roller bearings can be combined, as shown in [Figure 1.46](#), into two-row bearings. [Figure 1.47](#) shows a typical double-row tapered roller bearing assembly for a railroad car wheel application. Double-row bearings can also be combined into four-row or quad bearings for exceptionally heavy radial-load applications such as rolling mills. [Figure 1.48](#) shows a quad bearing that has integral seals.

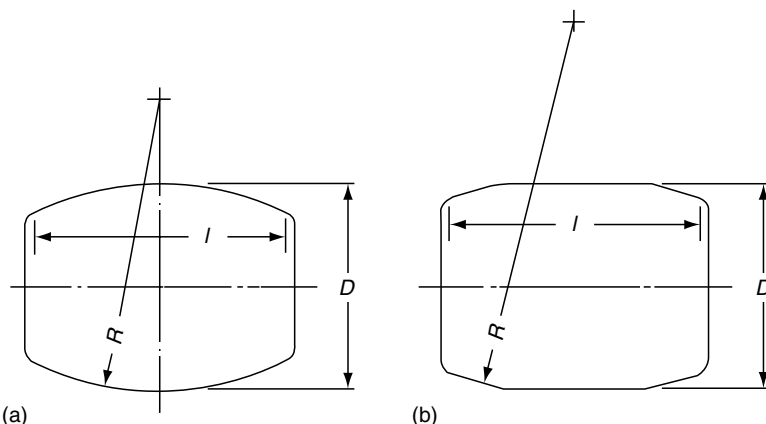


FIGURE 1.38 (a) Spherical roller (fully crowned); (b) partially crowned cylindrical roller (crown radius is greatly exaggerated for clarity).

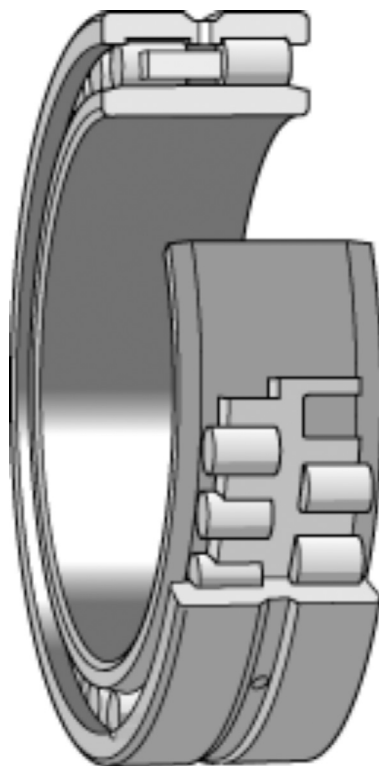


FIGURE 1.39 A double-row cylindrical roller bearing for precision machine tool spindle applications. (Courtesy of SKF.)

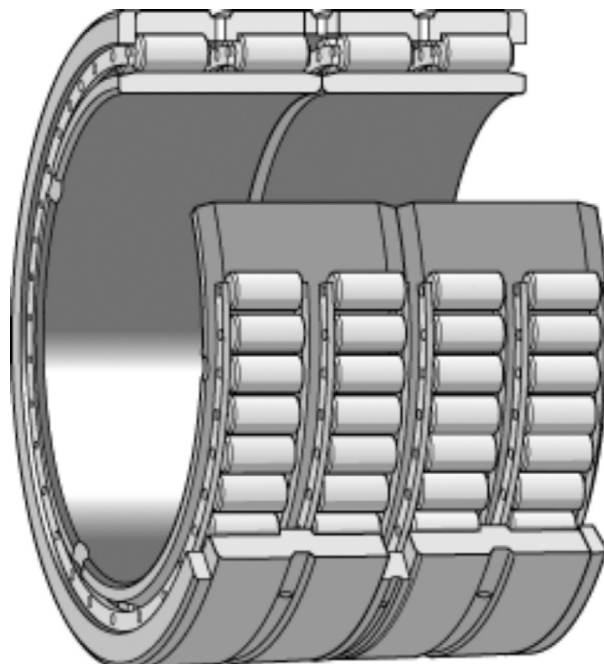


FIGURE 1.40 A multirow cylindrical roller bearing for a steel rolling mill application. (Courtesy of SKF.)



FIGURE 1.41 Needle roller bearing, nonseparable outer ring, cage, and roller assembly. (Courtesy of the Timken Company.)

As with cylindrical roller bearings, tapered rollers or raceways are usually crowned to relieve heavy stresses on the axial extremities of the rolling contact members. By equipping the bearing with specially contoured flanges, a special cage, and lubrication holes, as shown in [Figure 1.49](#), a tapered roller bearing can be designed to operate satisfactorily under high-load–high-speed conditions. In this case, the cage is guided by lands on both the cone rib and the cup, and oil is delivered directly by centrifugal flow to the roller end-flange contacts and cage rail–cone land contact.



FIGURE 1.42 Full-complement needle roller bearings. (a) Drawn cup assembly with trunnion-end rollers and inner ring; (b) drawn cup assembly with rollers retained by grease pack. (Courtesy of the Timken Company.)



FIGURE 1.43 Single-row tapered roller bearing showing separable cup and nonseparable cone, cage, and roller assembly. (Courtesy of the Timken Company.)

1.3.4 SPHERICAL ROLLER BEARINGS

Most spherical roller bearings have an outer raceway that is a portion of a sphere; hence, the bearings, as illustrated in Figure 1.50, are internally self-aligning. Each roller has a curved generatrix in the direction transverse to rotation that conforms relatively closely to the inner

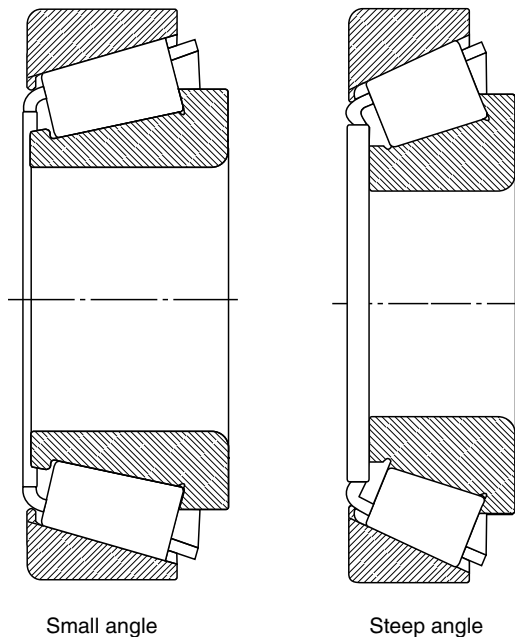


FIGURE 1.44 Small and steep contact angle tapered roller bearings.

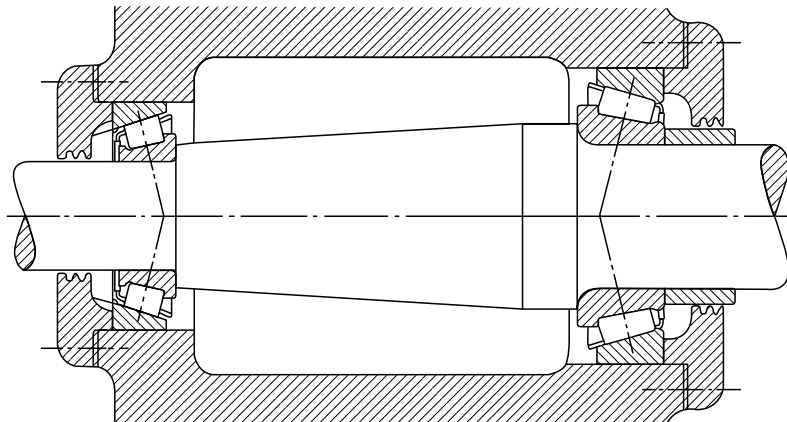


FIGURE 1.45 Typical mounting of tapered roller bearings.

and outer raceways. This gives the bearing a high load-carrying capacity. Various executions of double-row spherical roller bearings are shown in Figure 1.51.

Figure 1.51a shows a bearing with asymmetrical rollers. This bearing, similar to tapered roller bearings, has force components that drive the rollers against the fixed central guide flange. Bearings such as those illustrated in Figure 1.51b and Figure 1.51c have symmetrical (barrel- or hourglass-shaped) rollers, and these force components tend to be absent except under high-speed operations. Double-row bearings that have barrel-shaped, symmetrical rollers frequently use an axially floating central flange as illustrated in Figure 1.51d. This eliminates undercuts in the inner raceways and permits the use of longer rollers, thus increasing the load-carrying capacity of the bearing. Roller guiding in such bearings tends to be accomplished by the raceways in conjunction with the cage. In a well-designed bearing, the roller-cage loads due to roller skewing may be minimized.

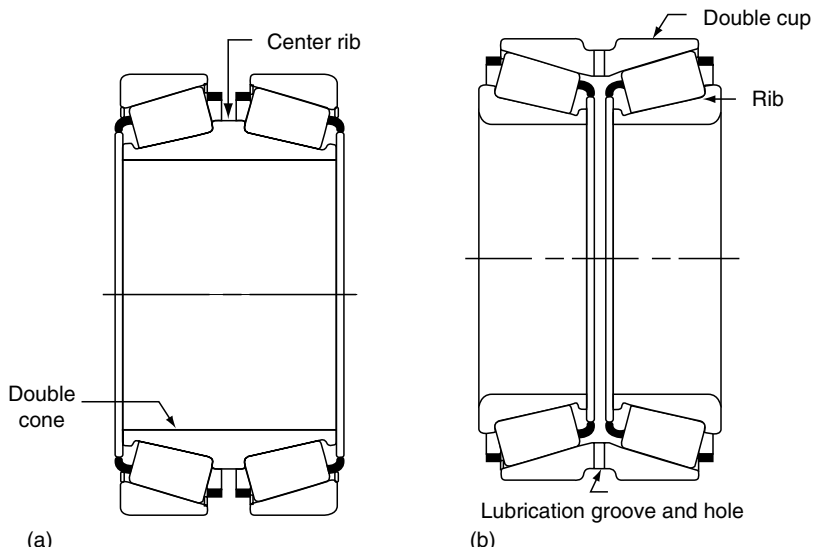


FIGURE 1.46 Double-row tapered rolling bearings. (a) Double cone assembly; (b) double cup assembly. (Courtesy of the Timken Company.)



FIGURE 1.47 Sealed, greased, and preadjusted double-row tapered roller bearing for railroad wheel bearings. (Courtesy of the Timken Company.)

Because of the close osculation between rollers and raceways and curved generatrices, spherical roller bearings have inherently greater friction than cylindrical roller bearings. This is due to the degree of sliding that occurs in the roller–raceway contacts. Spherical roller bearings are therefore not readily suited for use in high-speed applications. They perform well in heavy duty applications such as rolling mills, paper mills, and power transmissions and in marine applications. Double-row bearings can carry combined radial and thrust loads; they cannot support moment loading. Radial, single-row, spherical roller bearings have a basic contact angle of 0° . Under thrust loading, this angle does not increase appreciably; consequently, any amount of thrust loading magnifies the roller–raceway loading substantially. Therefore, these bearings should not be used to carry combined radial and thrust loading when the thrust component of the

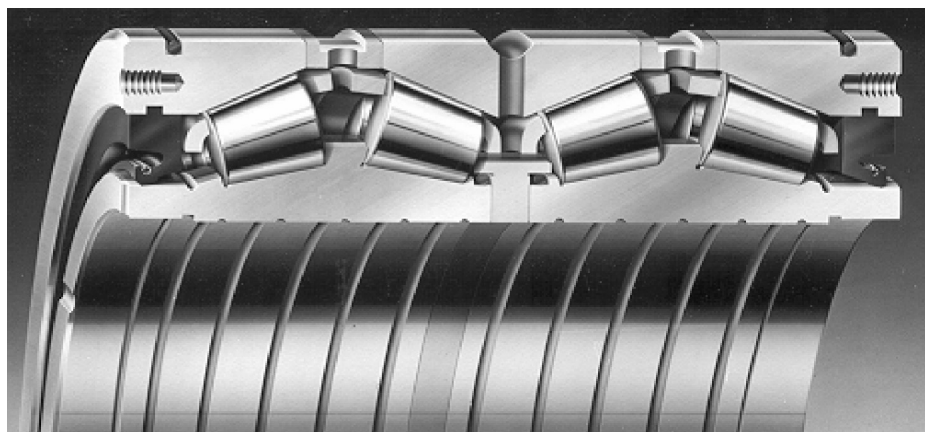


FIGURE 1.48 A four-row tapered roller bearing with integral seals for a hot strip mill application. (Courtesy of SKF.)

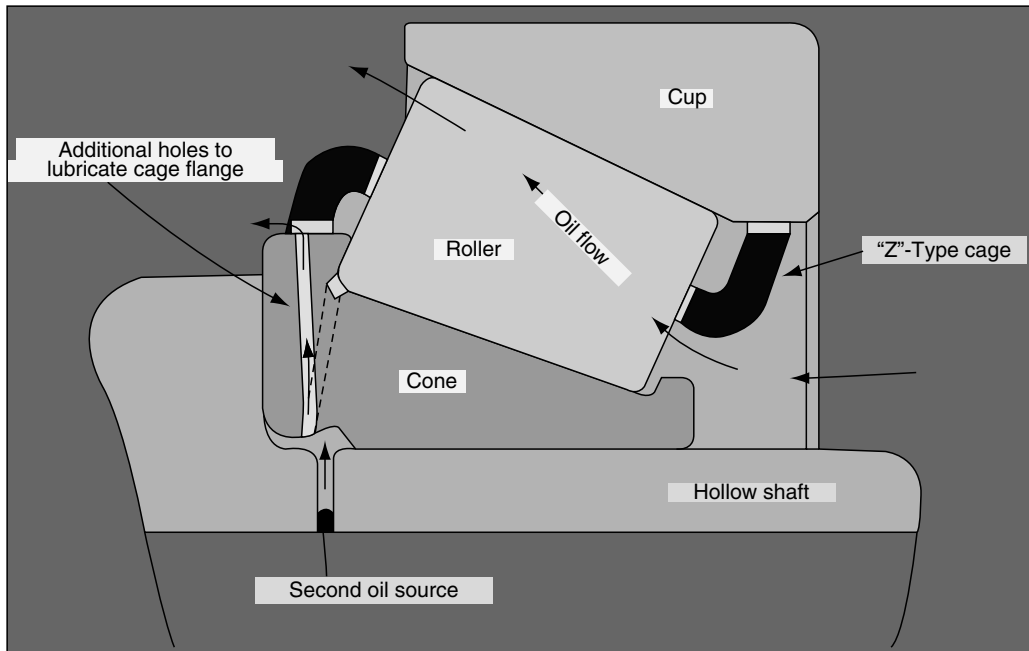


FIGURE 1.49 High-speed tapered roller bearing with radial oil holes and manifold. The “Z”-type cage is guided on the cone rib and cup lands. (Courtesy of the Timken Company.)

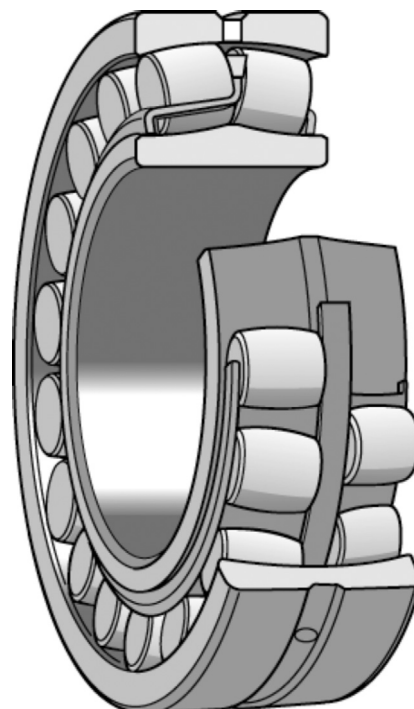


FIGURE 1.50 Cutaway view of a double-row spherical roller bearing with symmetrical rollers and a floating guide flange. (Courtesy of SKF.)

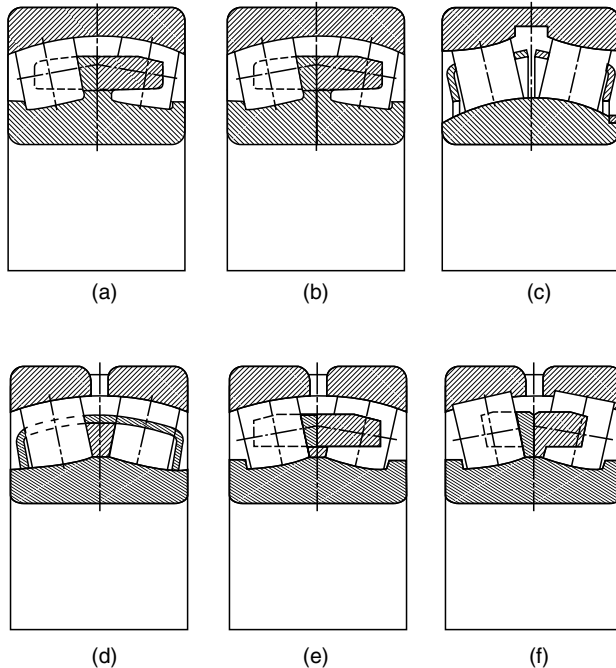


FIGURE 1.51 Various executions of double-row spherical roller bearings.

load is relatively large compared with the radial component. A special type of single-row bearing has a toroidal outer raceway (this is illustrated in [Figure 1.52](#)). It can accommodate radial loads together with some moment loads; however, little thrust loads.

1.3.5 THRUST ROLLER BEARINGS

1.3.5.1 Spherical Roller Thrust Bearings

The spherical roller thrust bearing shown in [Figure 1.53](#) has a very high load-carrying capacity due to high osculation between the rollers and raceways. It can carry a combination thrust and radial load and is internally self-aligning. Because the rollers are asymmetrical, force components occur, which drive the sphere ends of the roller against a concave spherical guide flange. Thus, the bearings experience sliding friction at this flange and do not lend themselves readily to high-speed operations.

1.3.5.2 Cylindrical Roller Thrust Bearings

Because of its geometry, the cylindrical roller thrust bearing, shown in [Figure 1.54](#), experiences a large amount of sliding between the rollers and raceways, also called washers. Thus, the bearings are limited to slow-speed operations. Sliding is reduced somewhat by using multiple short rollers in each pocket rather than a single integral roller. This is illustrated in [Figure 1.55](#).

1.3.5.3 Tapered Roller Thrust Bearings

Tapered roller thrust bearings, illustrated in [Figure 1.56](#), have an inherent force component that drives each roller against the outboard flange. The sliding frictional forces generated at the contacts between the rollers and the flange limit the bearing to relatively slow-speed applications.

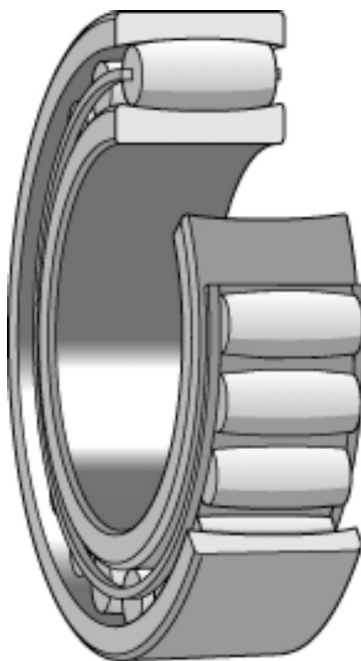


FIGURE 1.52 Single-row, radial, toroidal roller bearing. (Courtesy of SKF.)

1.3.5.4 Needle Roller Thrust Bearings

Needle roller thrust bearings, as illustrated in [Figure 1.57](#), are similar to cylindrical roller thrust bearings except that needle rollers are used in lieu of normal sized rollers. Consequently, roller-washer sliding is prevalent to a greater degree and loading must be light. The principal advantage of the needle roller thrust bearing is that it requires only a narrow axial space. [Figure 1.58](#) illustrates a needle roller–cage assembly that may be purchased in lieu of an entire bearing assembly.

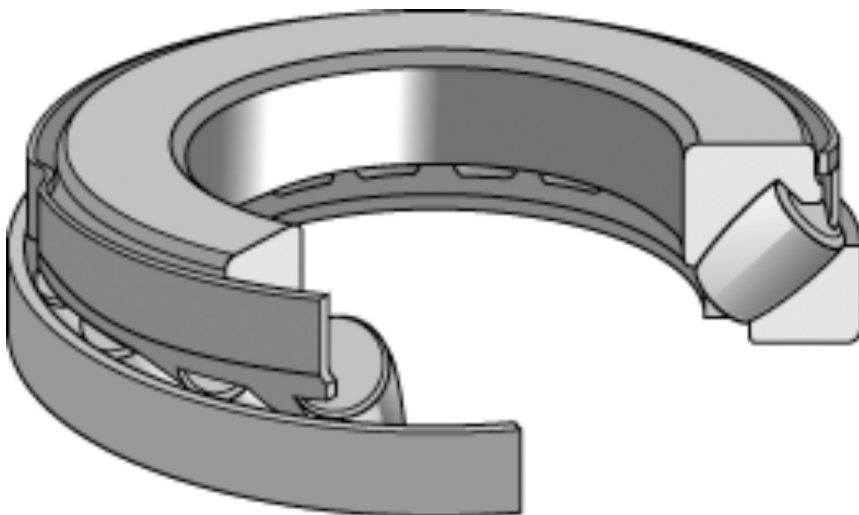


FIGURE 1.53 Cutaway view of a spherical roller thrust bearing assembly. (Courtesy of SKF.)

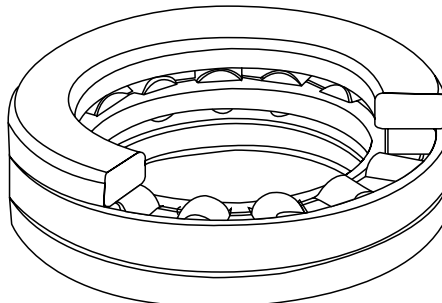


FIGURE 1.54 Cylindrical roller thrust bearing.

1.4 LINEAR MOTION BEARINGS

Linear motion bearings, such as those used in machine tool “ways”—for example, V-ways—generally employ only lubricated sliding action. These sliding actions are subject to relatively high stick-slip friction, wear, and subsequent loss of locational accuracy. Ball bushings operating on hardened steel shafts, illustrated schematically in [Figure 1.59](#), provide many of the low friction, minimal characteristics of radial rolling bearings.

The ball bushing, which provides linear travel along the shaft, limited only by built-in motion stoppers, contains three or more oblong circuits of recirculating balls. As illustrated in [Figure 1.60](#), one portion of the oblong ball complement supports the load on the rolling balls while the remaining balls operate with clearance in the return track.

Ball retainer units can be fabricated relatively inexpensively with pressed steel or nylon (polyamide) materials. [Figure 1.61](#) is a photograph showing an actual unit with its components. Ball bushings of instrument quality are made to operate on shaft diameters as small as 3.18 mm (0.125 in.).

Ball bushings can be lubricated with medium–heavy weight oils or with a light grease to prevent wear and corrosion; for high linear speeds, light oils are recommended. Seals can be provided; however, friction is increased significantly.

As with radial ball bearings, life can be limited by subsurface-initiated fatigue of the rolling contact surfaces. A unit is usually designed to perform satisfactorily for several million units of linear travel. As the hardened shaft is subject to surface fatigue or wear or both, provision can be made for rotating the bushing or shaft to bring new bearing surface into play.

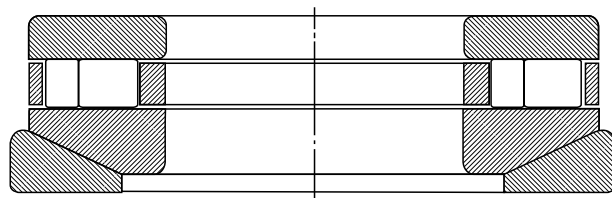


FIGURE 1.55 Cylindrical roller thrust bearing that has two rollers in each cage pocket; the bearing has a spherical seat for external alignment capability.

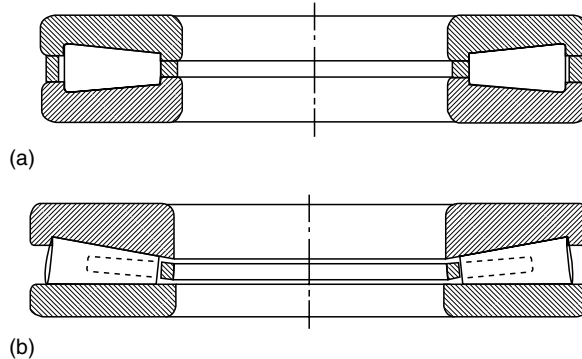


FIGURE 1.56 Tapered roller thrust bearing. (a) Both washers tapered; (b) one washer tapered.



FIGURE 1.57 Needle roller thrust bearing. (Courtesy of the Timken Company.)



FIGURE 1.58 Thrust needle roller-cage assembly. (Courtesy of the Timken Company.)

1.5 BEARINGS FOR SPECIAL APPLICATIONS

1.5.1 AUTOMOTIVE WHEEL BEARINGS

Angular-contact ball bearings for automobile wheels used to be individual bearings mounted in duplex sets, as shown in [Figure 1.25](#). On assembly in the vehicle, these had to be adjusted to eliminate bearing endplay. The same was true for tapered roller, truck wheel bearing sets. To

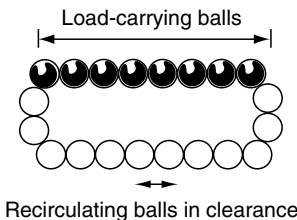
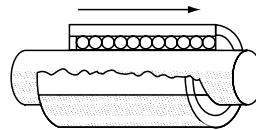


FIGURE 1.59 Schematic illustration of a ball bushing.

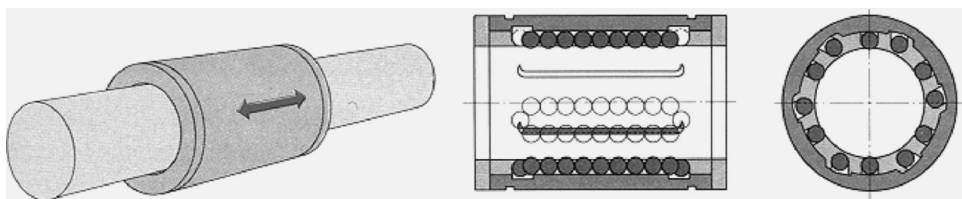


FIGURE 1.60 Schematic diagram of a ball bushing showing a recirculating ball set.



FIGURE 1.61 Linear ball bushing showing various components. (Courtesy of SKF.)

exclude contaminants from the bearings, external seals were required. The bearings were grease-lubricated and, owing to the grease deterioration in this difficult application, needed to be regreased periodically. If this was not accomplished with care, inevitably contamination was introduced into the bearings and their longevity was substantially curtailed. To overcome this situation, many bearings were provided as preadjusted, greased, and sealed-for-life duplex sets, as shown in [Figure 1.62a](#). These units needed to be press-fitted into the wheel hubs. To simplify

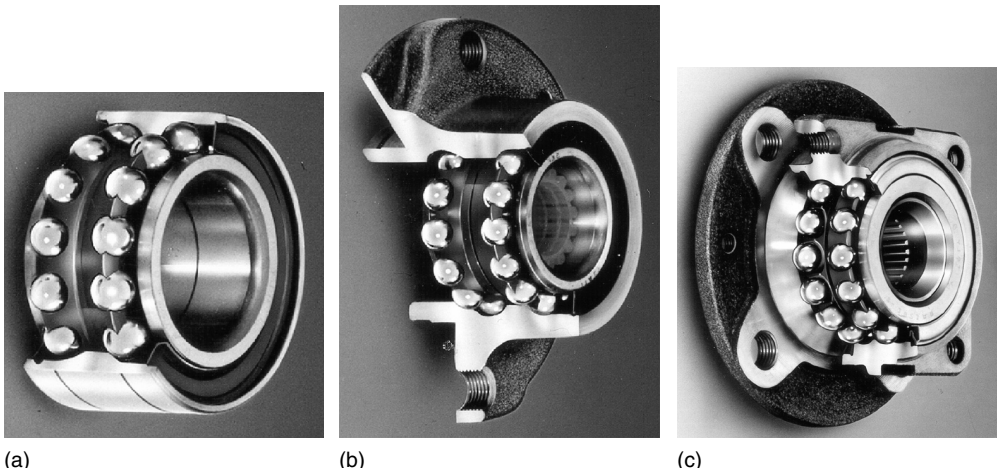


FIGURE 1.62 Modern automobile wheel preadjusted, greased, and sealed-for life, ball bearing units. (a) Without flanges; unit is press-fitted into wheel hub and slip-fitted onto the axle; (b) with a single flange integral with the outer ring of the bearing; (c) with flanges integral with the outer and inner rings of the bearing. (Photographs courtesy of SKF.)

The assembly for the automobile manufacturer and to minimize size, a flange was made integral with the outer ring of the bearing, as shown in Figure 1.62b; thus, the unit could be bolted to studs on the wheel. Subsequently, a self-contained unit with a flange integral with each ring, as shown in Figure 1.62c, came into use; the unit can be bolted to the vehicle frame and the wheel for simple assembly. For heavier duty vehicles such as trucks, tapered roller bearings (Figure 1.63) are used instead of ball bearings.

Function can also be added to the bearing unit, as shown by the tapered roller bearing unit in [Figure 1.64](#). This compact, preadjusted, self-contained bearing unit is equipped with an



FIGURE 1.63 Modern truck wheel preadjusted, greased, and sealed-for-life, tapered roller bearing unit. (Courtesy of SKF.)

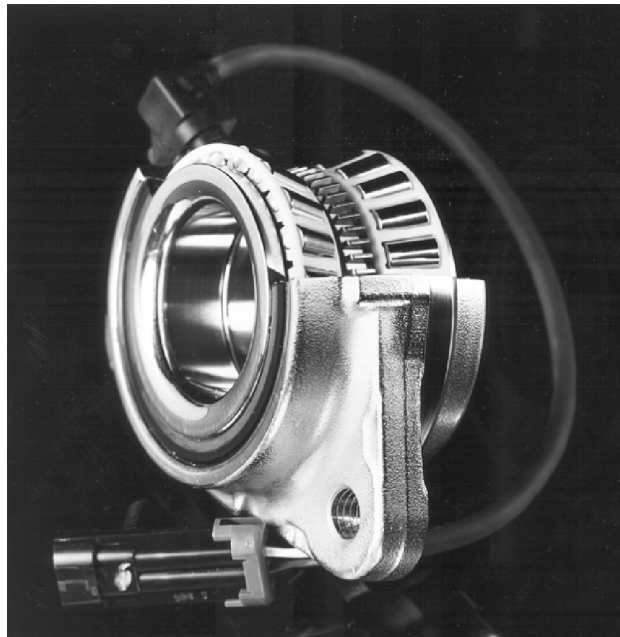


FIGURE 1.64 Self-contained, tapered roller bearing with an integral speed sensor to provide signal to the antilock braking system. (Courtesy of the Timken Company.)

integral speed sensor to provide a signal to the antilock braking system (ABS). Sensors are also placed in rolling bearings to measure the loading applied.

1.5.2 CAM FOLLOWER BEARINGS

To reduce the friction associated with the follower contact on cams, rolling motion may be employed. Needle roller bearings are particularly suited to this application because they are radially compact. Figure 1.65 shows a needle roller bearing, cam follower assembly.

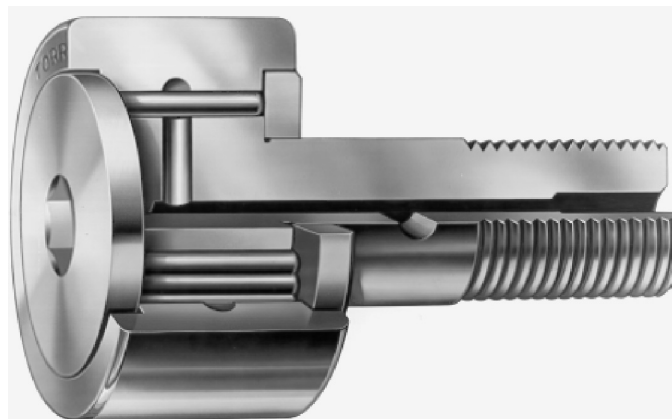


FIGURE 1.65 Needle roller cam follower assembly. (Courtesy of the Timken Company.)

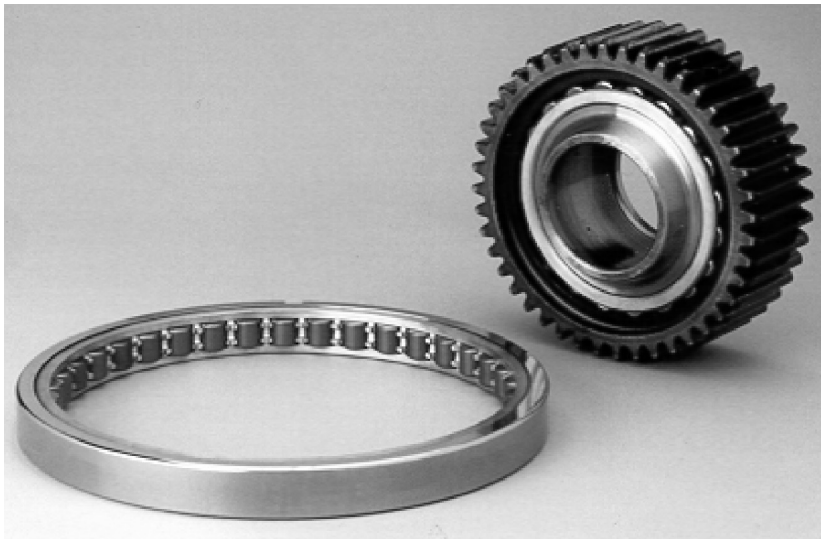


FIGURE 1.66 Aircraft power transmission bearings: (left) cylindrical roller bearing; (right) spherical planet gear bearing. (Courtesy of NTN.)

1.5.3 AIRCRAFT GAS TURBINE ENGINE AND POWER TRANSMISSION BEARINGS

Airplane and helicopter power transmission bearing applications are generally characterized by the necessity to carry heavy loads at high speeds while minimizing bearing size. The bearings are generally manufactured from special high-strength, high-quality steels. Though the weight of a steel bearing itself is significant, minimizing the width of the bearing and the outside diameter aids compactness in engine design, allowing the surrounding engine components to be smaller and weigh less. Thus, aircraft power train bearings have slimmer rings, as illustrated by the cylindrical roller bearing in Figure 1.66. Moreover, bearings are made integral with other components to reduce weight. This is shown by the planetary gear transmission, spherical roller planet bearing in Figure 1.66. The gas turbine engine cylindrical roller bearing in Figure 1.67 has a slender, hollowed out, flange integral with the bearing outer ring; the flange is bolted to the engine frame for ease of assembly.

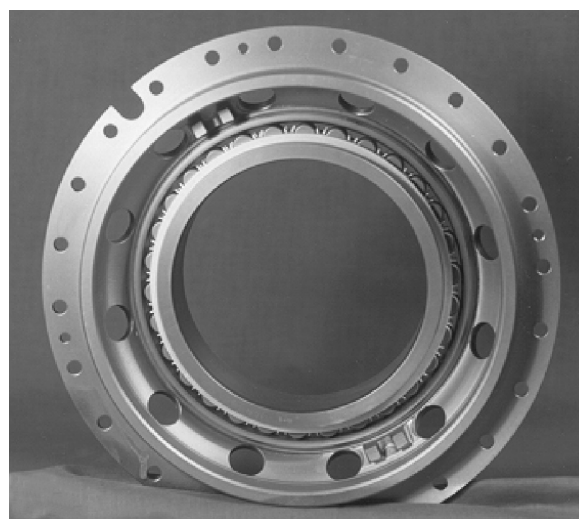


FIGURE 1.67 Aircraft gas turbine engine, cylindrical roller bearing. (Courtesy of SKF.)



FIGURE 1.68 Aircraft gas turbine engine mainshaft bearing components: lower left—split inner-ring ball bearing; center and upper right—cylindrical roller bearing's inner and outer ring units. (Courtesy of FAG OEM und Handel AG.)

Figure 1.68 shows a gas turbine mainshaft, split inner-ring ball bearing with an outer ring that bolts to the housing assembly; it also depicts a cylindrical roller bearing's inner and outer ring units specially fabricated for a turbine engine application.

1.6 CLOSURE

This chapter has illustrated and described various types and executions of ball and roller bearings. It is not to be construed that every type of rolling bearing has been described; discussion has been limited to the most popular and basic forms. For example, there are cylindrical roller bearing designs that use snap rings, instead of machined and ground flanges. ANSI/ABMA and ISO standards on terminology [7] and [8] illustrate many of the more common bearing designs. It is also apparent that many rolling bearings are specially designed for applications. Some of these have been discussed herein only to indicate that special design bearings are sometimes warranted by the application. In general, special bearing designs entail additional cost for the bearing or bearing unit; however, such a cost increase is usually offset by overall efficiency and cost reduction brought to the mechanism and machinery design, manufacture, and operation.

REFERENCES

1. Dowson, D., *History of Tribology*, 2nd ed., Longman, New York, 1999.
2. Reti, L., Leonardo on bearings and gears, *Scientific American*, 224(2), 101–110, 1971.
3. Tallian, T., Progress in rolling contact technology, SKF Report AL690007, 1969.
4. Tallian, T., Weibull distribution of rolling contact fatigue life and deviations there-from, *ASLE Trans.*, 5(1), 183–196, 1962.
5. American National Standards Institute, *American National Standard (ANSI/ABMA) Std. 12.1-1992, Instrument ball bearings—metric design* (April 6, 1992).

6. American National Standards Institute, *American National Standard (ANSI/ABMA) Std. 12.2-1992*, Instrument ball bearings—inch design (April 6, 1992).
7. American National Standards Institute, *American National Standard (ANSI/ABMA) Std. 1-1990*, Terminology for anti-friction ball and roller bearings and parts (July 24, 1990).
8. International Organization for Standards, *International Standard ISO 5593*, Rolling bearings—vocabulary (1984-07-01).

2 Rolling Bearing Macrogeometry

LIST OF SYMBOLS

Symbol	Description	Units
A	Distance between raceway groove curvature centers	mm (in.)
B	A/D	
d	Raceway diameter	mm (in.)
d_m	Bearing pitch diameter	mm (in.)
D	Ball or roller nominal diameter	mm (in.)
D_m	Mean diameter of tapered roller	mm (in.)
D_{\max}	Diameter of tapered roller at large end	mm (in.)
D_{\min}	Diameter of tapered roller at small end	mm (in.)
f	r/D	
l	Roller effective length	mm (in.)
l_f	Distance between cylindrical roller guide flanges	mm (in.)
P_d	Bearing diametral clearance	mm (in.)
P_e	Bearing free endplay	mm (in.)
r	Raceway groove curvature radius	mm (in.)
r_c	Roller corner radius	mm (in.)
R	Roller contour radius	mm (in.)
S_d	Assembled bearing diametral play	mm (in.)
Z	Number of rolling elements	
α	Contact angle	°
α°	Free contact angle	°
α_f	Tapered roller bearing flange angle	°
α_R	Tapered roller included angle	°
α_s	Shim angle	°
γ	$D \cos \alpha / d_m$	
θ	Misalignment angle	°
ρ	Curvature	
$F(\rho)$	Curvature difference	
$\Sigma\rho$	Curvature sum	$\text{mm}^{-1} (\text{in.}^{-1})$
ϕ	Osculation	
ω	Rotational speed	rad/s
Subscripts		
c	Cage	
i	Inner ring or raceway	
o	Outer ring or raceway	
r	Roller	

2.1 GENERAL

Although ball and roller bearings appear to be simple mechanisms, their internal geometries are quite complex. For example, a radial ball bearing subjected to thrust loading assumes angles of contact between the balls and raceways in accordance with the relative conformities of the balls to the raceways and the diametral clearance. On the other hand, the ability of the same bearing to support the thrust loading depends on the contact angles formed. The same diametral clearance or play produces an axial endplay that may or may not be tolerable to the bearing user. In later chapters, it will be demonstrated that diametral clearance affects not only contact angles and endplay but also stresses, deflections, load distributions, and fatigue life.

In the determination of stresses and deflections, the relative conformities of balls and rollers to their contacting raceways are of vital interest. In this chapter, the principal macrogeometric relationships governing the operation of ball and roller bearings will be developed and examined.

2.2 BALL BEARINGS

Ball bearings can be illustrated in the most simple form as in Figure 2.1. From Figure 2.1, one can easily see that the bearing pitch diameter is approximately equal to the mean of the bore and O.D. or

$$d_m \approx \frac{1}{2}(\text{bore} + \text{O.D.}) \quad (2.1)$$

More precisely, however, the bearing pitch diameter is the mean of the inner- and outer-ring raceway contact diameters. Therefore,

$$d_m \approx \frac{1}{2} (d_i + d_o) \quad (2.2)$$

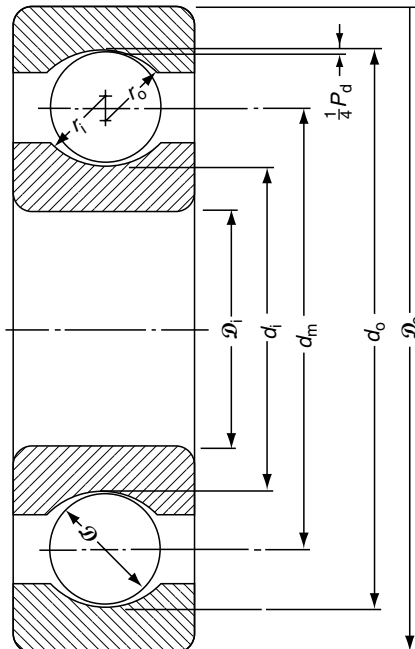


FIGURE 2.1 Radial ball bearing showing diametral clearance.

Generally, ball bearings and other radial rolling bearings such as cylindrical roller bearings are designed with clearance. From [Figure 2.1](#), the diametral* clearance is as follows:

$$P_d = d_m - d_i - 2D \quad (2.3)$$

Table CD2.1 from Ref. [1] gives the values of radial internal clearance for radial contact ball bearings under no load.

See Example 2.1.

2.2.1 OSCULATION

The ability of a ball bearing to carry load depends in large measure on the osculation of the rolling elements and raceways. Osculation is the ratio of the radius of curvature of the rolling element to that of the raceway in a direction transverse to the direction of rolling. From Figure 2.1, it can be seen that for a ball mating with a raceway, osculation is given by

$$\phi = \frac{D}{2r} \quad (2.4)$$

Letting $r = fD$, osculation is

$$\phi = \frac{1}{2f} \quad (2.5)$$

It is to be noted that the osculation is not necessarily identical for inner and outer contacts.

See Example 2.2.

2.2.2 CONTACT ANGLE AND ENDPLAY

Because a radial ball bearing is generally designed to have a diametral clearance in the no-load state, the bearing also can experience an axial play. Removal of this axial freedom causes the ball–raceway contact to assume an oblique angle with the radial plane; hence, a contact angle different from 0° will occur. Angular-contact ball bearings are specifically designed to operate under thrust loads, and the clearance built into the unloaded bearing along with the raceway groove curvatures determines the bearing free contact angle. [Figure 2.2](#) shows the geometry of a radial ball bearing with the axial play removed. From Figure 2.2, it can be seen that the distance between the centers of curvature O' and O'' of the inner- and outer-ring grooves is

$$A = r_o + r_i - D \quad (2.6)$$

Substituting $r = fD$ yields

$$A = (f_o + f_i - 1)D = BD \quad (2.7)$$

where $B = f_o + f_i - 1$, defined as the total curvature of the bearing.

*Clearance is always measured on a diameter, however, because measurement is in a radial plane, it is commonly called radial clearance. This text uses diametral and radial clearance interchangeably.

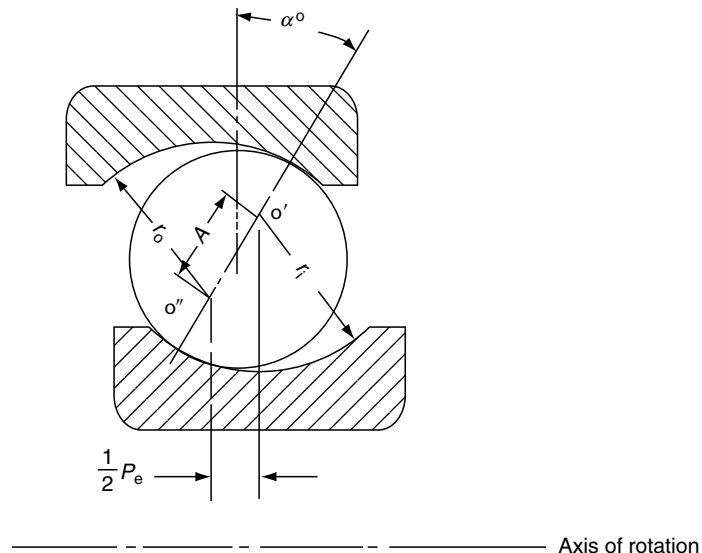


FIGURE 2.2 Radial ball bearing showing ball–raceway contact due to axial shift of inner and outer rings.

Also from Figure 2.2, it can be seen that the free contact angle is the angle made by the line passing through the points of contact of the ball and both raceways and a plane perpendicular to the bearing axis of rotation. The magnitude of the free contact angle can be described as follows:

$$\cos \alpha^\circ = \frac{\frac{1}{2}A - \frac{1}{4}P_d}{\frac{1}{2}A} \quad (2.8)$$

or

$$\alpha^\circ = \cos^{-1} \left(1 - \frac{P_d}{2A} \right) \quad (2.9)$$

If in mounting the bearing an interference fit is used, then the diametral clearance must be diminished by the change in ring diameter to obtain the free contact angle. Hence,

$$\alpha^\circ = \cos^{-1} \left(1 - \frac{P_d + \Delta P_d}{2A} \right) \quad (2.10)$$

See Example 2.3.

Because of diametral clearance, a radial bearing is free to float axially under the condition of no load. This free endplay may be defined as the maximum relative axial movement of the inner ring with respect to the outer ring under zero load. From Figure 2.2,

$$\frac{1}{2}P_e = A \sin \alpha^\circ \quad (2.11)$$

$$P_e = 2A \sin \alpha^\circ \quad (2.12)$$

Figure 2.3 shows the free contact angle and endplay versus P_e/D for single-row ball bearings.

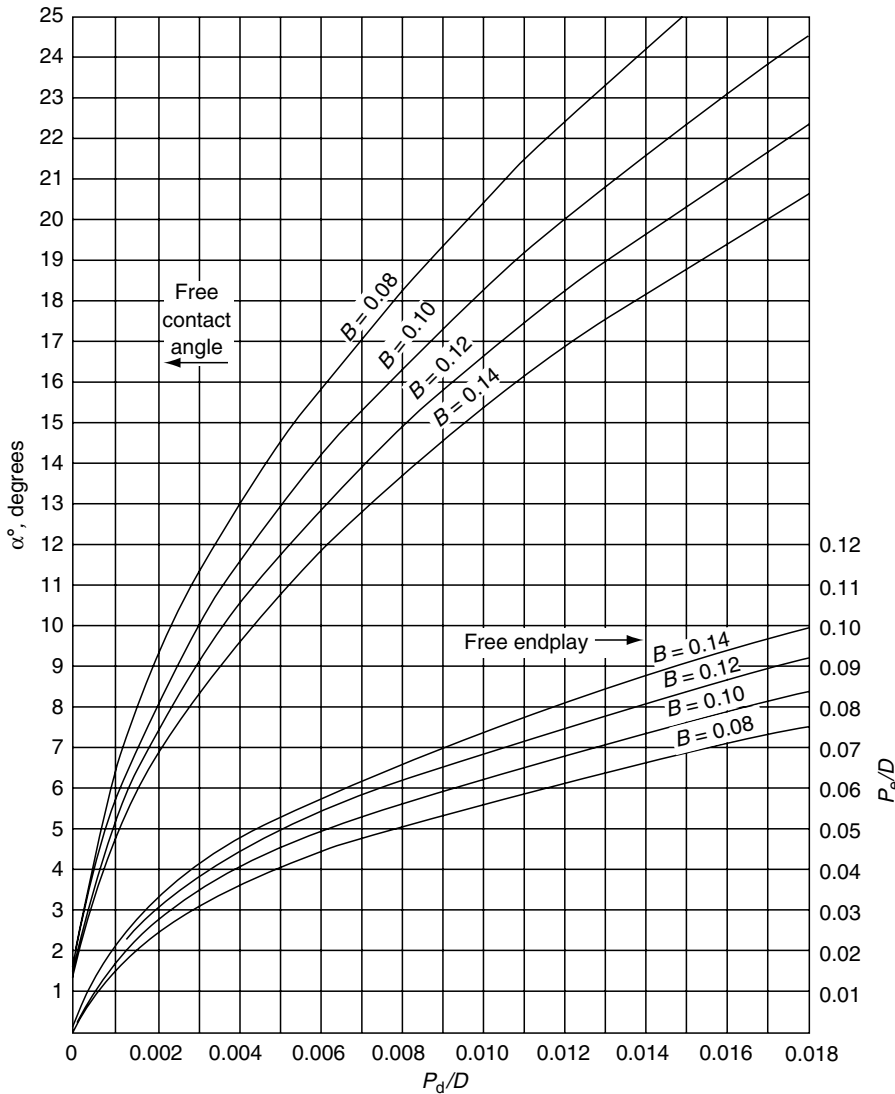


FIGURE 2.3 Free contact angle and endplay versus $B=f_o+f_i-1$ for single-row ball bearings.

Double-row angular-contact ball bearings are generally assembled with a certain amount of diametral play (smaller than diametral clearance). It can be determined that the free endplay for a double-row bearing is

$$P_e = 2A \sin \alpha^\circ - 2 \left[A^2 - \left(A \cos \alpha^\circ + \frac{S_d}{2} \right)^2 \right]^{1/2} \quad (2.13)$$

Split inner-ring ball bearings, illustrated in [Figure 2.4](#), have inner rings that are ground with a shim between the ring halves. The width of this shim is associated with the shim angle that is obtained by removing the shim and abutting the ring halves.

From [Figure 2.5](#), it can be determined that the shim width is given by

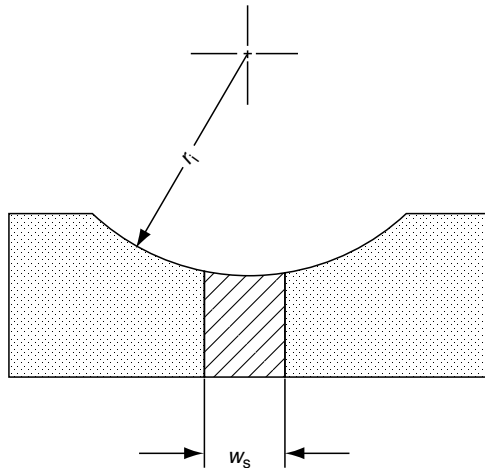


FIGURE 2.4 Inner rings of split inner-ring ball bearings showing shim for grinding.

$$w_s = (2r_i - D)\sin \alpha_s \quad (2.14)$$

Since $f_i = r_i/D$, Equation 2.14 becomes

$$w_s = (2f_i - 1)D \sin \alpha_s \quad (2.15)$$

The shim angle α_s and the assembled diametral play S_d of the bearing accordingly dictate the free contact angle. The effective clearance P_d of the bearing may be determined from Figure 2.5 to be

$$P_d = S_d + (2f_i - 1)(1 - \cos \alpha_s)D \quad (2.16)$$

Thus, the bearing contact angle shown in Figure 2.2 is given by

$$\alpha^\circ = \cos^{-1} \left(1 - \frac{S_d}{2BD} - \frac{(2f_i - 1)(1 - \cos \alpha_s)}{2B} \right) \quad (2.17)$$

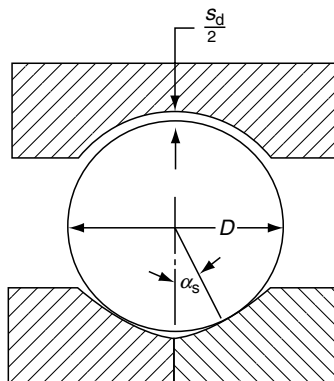


FIGURE 2.5 Split inner-ring ball bearing assembly showing bearing shim angle.

2.2.3 FREE ANGLE OF MISALIGNMENT

Furthermore, diametral clearance can allow a ball bearing to misalign slightly under no load. The free angle of misalignment is defined as the maximum angle through which the axis of the inner ring can be rotated with respect to the axis of the outer ring before stressing bearing components. From Figure 2.6, using the law of cosines it can be determined that

$$\cos \theta_i = 1 - \frac{P_d[(2f_i - 1)D - (P_d/4)]}{2d_m[d_m + (2f_i - 1)D - (P_d/2)]} \quad (2.18)$$

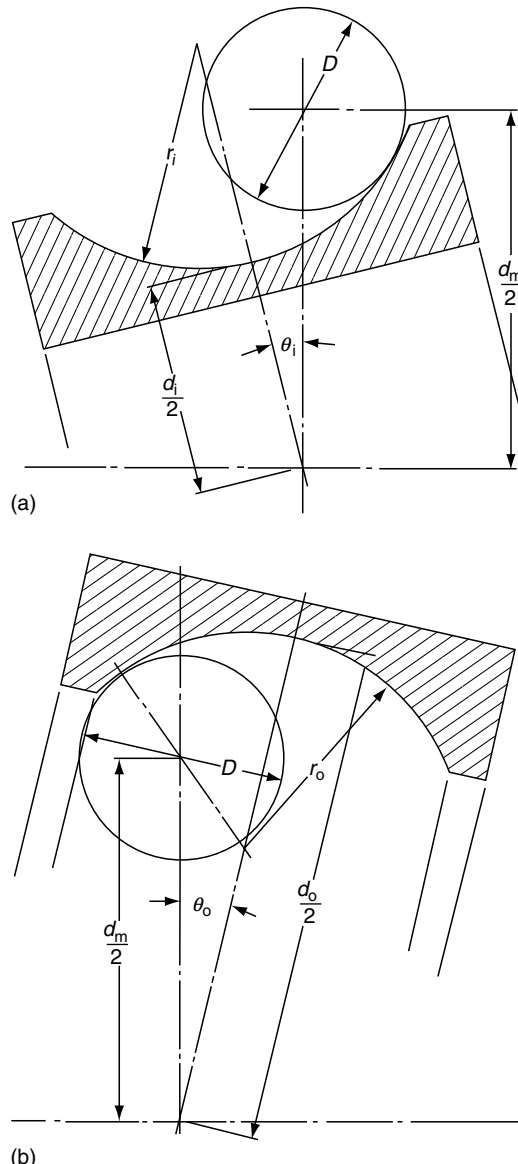


FIGURE 2.6 (a) Free misalignment of inner ring of single-row ball bearing and (b) free misalignment of outer ring of single-row ball bearing.

$$\cos \theta_o = 1 - \frac{P_d[(2f_o - 1)D - (P_d/4)]}{2d_m[d_m - (2f_i - 1)D + (P_d/2)]} \quad (2.19)$$

Therefore, θ , the free contact angle of misalignment, is

$$\theta = \theta_i + \theta_o \quad (2.20)$$

As the following trigonometric identity

$$\cos \theta_i + \cos \theta_o = 2 \cos\left(\frac{\theta_i + \theta_o}{2}\right) \cos\left(\frac{\theta_i - \theta_o}{2}\right) \quad (2.21)$$

is true, and since $\theta_i - \theta_o$ approaches zero, therefore,

$$\theta = 2 \cos^{-1} \left(\frac{\cos \theta_i + \cos \theta_o}{2} \right) \quad (2.22)$$

or

$$\theta = 2 \cos^{-1} \left[1 - \frac{P_d}{4d_m} \left(\frac{(2f_i - 1)D - (P_d/4)}{d_m + (2f_i - 1)D - (P_d/2)} + \frac{(2f_o - 1)D - (P_d/4)}{d_m - (2f_o - 1)D + (P_d/2)} \right) \right] \quad (2.23)$$

See Example 2.4.

2.2.4 CURVATURE AND RELATIVE CURVATURE

Two bodies of revolution having different radii of curvature in a pair of principal planes passing through the contact between the bodies may contact each other at a single point under the condition of no applied load. Such a condition is called point contact. [Figure 2.7](#) demonstrates this condition.

In Figure 2.7, the upper body is denoted by I and the lower body by II; the principal planes are denoted by 1 and 2. Therefore, the radius of curvature of body I in plane 2 is denoted by r_{I2} . As r denotes the radius of curvature, the curvature is defined as

$$\rho = \frac{1}{r} \quad (2.24)$$

Although the radius of curvature is always positive, curvature may be positive or negative, with the convex surfaces positive and concave surfaces negative.

To describe the contact between mating surfaces of revolution, the following definitions are used:

1. Curvature sum:

$$\Sigma\rho = \frac{1}{r_{I1}} + \frac{1}{r_{I2}} + \frac{1}{r_{II1}} + \frac{1}{r_{II2}} \quad (2.25)$$

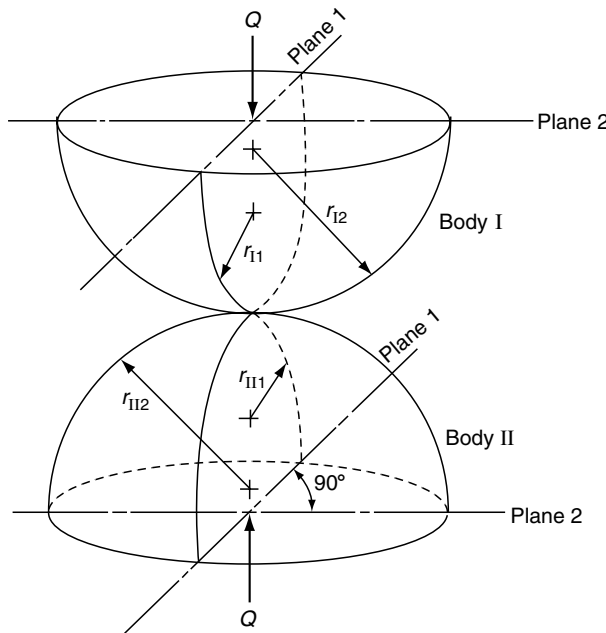


FIGURE 2.7 Geometry of contacting bodies.

2. Curvature difference:

$$F(\rho) = \frac{(\rho_{II} - \rho_{I2}) + (\rho_{III} - \rho_{II2})}{\Sigma\rho} \quad (2.26)$$

In [Equation 2.25](#) and [Equation 2.26](#), the sign convention for convex and concave surfaces is used. Furthermore, care must be exercised to see that $F(\rho)$ is positive.

The purpose of defining the curvature sum and the difference is to analyze two bodies in contact as an equivalent ellipsoid contacting a flat plane. Using this concept, the sign convention described previously becomes more obvious. A concave surface will conform to contacting bodies, thus increasing the equivalent radius or reducing the curvature. Conversely, convex surfaces decrease the equivalent radius or increase the curvature. Finally, since this is an ellipsoid, the curvature difference relates to the difference between the equivalent radii in orthogonal planes. If the radii are equal (sphere), the difference is zero. If the difference is infinitely large, the equivalent ellipsoid approaches a cylinder.

By way of example, $F(\rho)$ is determined for a ball–inner raceway contact as follows ([see Figure 2.8](#)):

$$r_{II} = \frac{1}{2}D$$

$$r_{I2} = \frac{1}{2}D$$

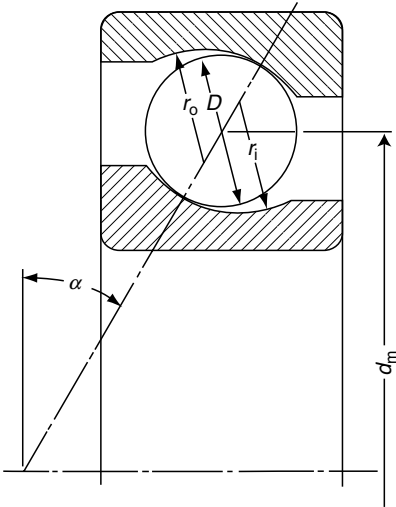


FIGURE 2.8 Ball bearing geometry.

$$r_{II1} = \frac{1}{2}d_i = \frac{1}{2}\left(\frac{d_m}{\cos \alpha} - D\right)$$

$$r_{II2} = f_i D$$

Let

$$\gamma = \frac{D \cos \alpha}{d_m} \quad (2.27)$$

Then,

$$\begin{aligned} \rho_{I1} &= \rho_{I2} = \frac{2}{D} \\ \rho_{II1} &= \frac{2}{D} \left(\frac{\gamma}{1 - \gamma} \right) \\ \rho_{II2} &= -\frac{1}{f_i D} \\ \Sigma \rho_i &= \frac{4}{D} - \frac{1}{f_i D} + \frac{2}{D} \left(\frac{\gamma}{1 - \gamma} \right) = \frac{1}{D} \left(4 - \frac{1}{f_i} + \frac{2\gamma}{1 - \gamma} \right) \end{aligned} \quad (2.28)$$

$$F(\rho)_i = \frac{\frac{2}{D} \left(\frac{\gamma}{1 - \gamma} \right) - \left(-\frac{1}{f_i D} \right)}{\Sigma \rho_i} = \frac{\frac{1}{f_i} + \frac{2\gamma}{1 - \gamma}}{4 - \frac{1}{f_i} + \frac{2\gamma}{1 - \gamma}} \quad (2.29)$$

For the ball–outer raceway contact, $\rho_{I1} = \rho_{I2} = 2/D$ as above; however,

$$r_{II1} = \frac{1}{2} \left(\frac{d_m}{\cos \alpha} + D \right)$$

$$r_{II2} = f_o D$$

Therefore,

$$\begin{aligned}\rho_{\text{II1}} &= -\frac{2}{D} \left(\frac{\gamma}{1 + \gamma} \right) \\ \rho_{\text{II2}} &= -\frac{1}{f_o D} \\ \Sigma \rho_o &= \frac{1}{D} \left(4 - \frac{1}{f_o} - \frac{2\gamma}{1 + \gamma} \right)\end{aligned}\quad (2.30)$$

$$F(\rho)_o = \frac{\frac{1}{f_o} - \frac{2\gamma}{1 + \gamma}}{4 - \frac{1}{f_o} - \frac{2\gamma}{1 + \gamma}} \quad (2.31)$$

$F(\rho)$ is always a number between 0 and 1, and typically in the range of 0.9 for ball bearings. Large magnitudes of f_i and f_o cause subsequently smaller values of $F(\rho)$.

See Example 2.5 and Example 2.6.

2.3 SPHERICAL ROLLER BEARINGS

2.3.1 PITCH DIAMETER AND DIAMETRAL PLAY

Equation 2.1 may also be used for spherical roller bearings to estimate the pitch diameter. Radial internal clearance, also called diametral play, as illustrated in Figure 2.9, is given by the following equation:

$$S_d = 2[r_o - (r_i + D)] \quad (2.32)$$

where r_i and r_o are the raceway contour radii. The diametral play S_d can be measured with a feeler gage. Table CD2.2 and Table CD2.3 from Ref. [1] give standard values of radial internal clearance (diametral play) under no load.

2.3.2 CONTACT ANGLE AND FREE ENDPLAY

Radial spherical roller bearings are normally assembled with free diametral play and hence exhibit free endplay P_e . From Figure 2.9, it can be seen that

$$r_o \cos \beta = \left(r_o - \frac{S_d}{2} \right) \cos \alpha \quad (2.33)$$

or

$$\beta = \cos^{-1} \left[\left(1 - \frac{S_d}{2r_o} \right) \cos \alpha \right] \quad (2.34)$$

Therefore, it can be determined that

$$P_e = 2r_o (\sin \beta - \sin \alpha) + S_d \sin \alpha \quad (2.35)$$

See Example 2.7.

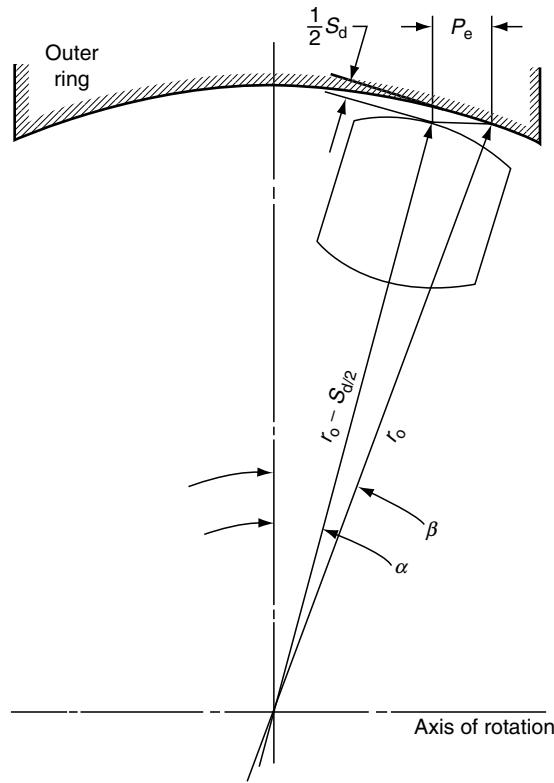


FIGURE 2.9 Schematic diagram of spherical roller bearing showing nominal contact angle α , dimetral play S_d , and endplay P_e .

2.3.3 OSCULATION

The term osculation also applies to spherical roller bearings in that, as illustrated in Figure 2.9 and Figure 2.10, the rollers and raceways have curvatures in the direction transverse to rolling. In this case, osculation is defined as follows:

$$\Phi = \frac{R}{r} \quad (2.36)$$

where R is the roller contour radius.

See Example 2.8.

2.3.4 CURVATURE

For spherical roller bearings with point contact between rollers and raceways, the equations for curvature sums and differences are as follows (see Figure 2.10):

$$\Sigma\rho_i = \frac{2}{D} + \frac{1}{R} + \frac{2\gamma}{D(1-\gamma)} - \frac{1}{r_i} = \frac{1}{D} \left[\frac{2}{1-\gamma} + D \left(\frac{1}{R} - \frac{1}{r_i} \right) \right] \quad (2.37)$$

$$F(\rho)_i = \frac{\frac{2}{D} - \frac{1}{R} + \frac{2\gamma}{D(1-\gamma)} - \left(-\frac{1}{r_i} \right)}{\Sigma\rho_i} = \frac{\frac{2}{1-\gamma} - D \left(\frac{1}{R} - \frac{1}{r_i} \right)}{\frac{2}{1-\gamma} + D \left(\frac{1}{R} - \frac{1}{r_i} \right)} \quad (2.38)$$

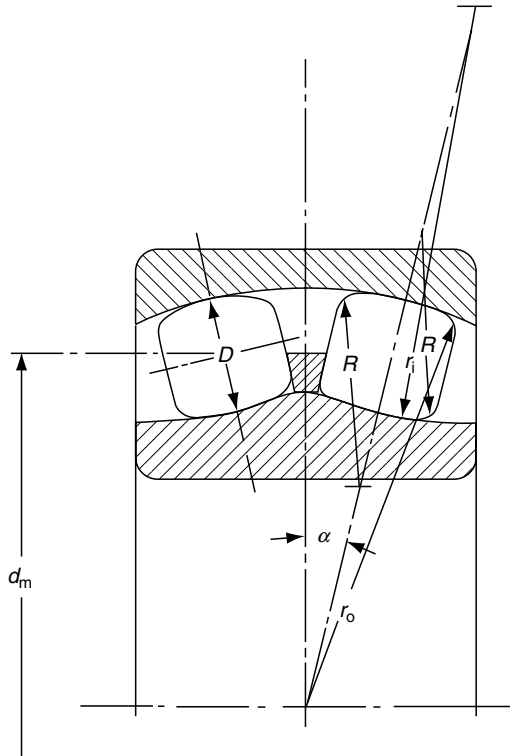


FIGURE 2.10 Spherical roller bearing geometry.

$$\Sigma \rho_o = \frac{2}{D} + \frac{1}{R} - \frac{2\gamma}{D(1+\gamma)} - \frac{1}{r_o} = \frac{1}{D} \left[\frac{2}{1+\gamma} + D \left(\frac{1}{R} - \frac{1}{r_o} \right) \right] \quad (2.39)$$

$$F(\rho)_o = \frac{\frac{2}{D} - \frac{1}{R} - \frac{2\gamma}{D(1+\gamma)} - \left(-\frac{1}{r_o} \right)}{\Sigma \rho_o} = \frac{\frac{2}{1+\gamma} - D \left(\frac{1}{R} - \frac{1}{r_o} \right)}{\frac{2}{1+\gamma} + D \left(\frac{1}{R} - \frac{1}{r_o} \right)} \quad (2.40)$$

where the curvature difference approaches unity.

2.4 RADIAL CYLINDRICAL ROLLER BEARINGS

2.4.1 PITCH DIAMETER, DIAMETRAL CLEARANCE, AND ENDPLAY

Equation 2.1 through Equation 2.3 are valid for radial cylindrical roller bearings as well as ball bearings. Table CD2.4, from Ref. [1], gives standard values of internal clearance for radial cylindrical roller bearings.

See Example 2.10.

Figure 2.11 illustrates a roller in a radial cylindrical roller bearing having two roller guide flanges on both the inner and outer rings. In this case, the roller is shown in contact with both the inner and outer raceways, which would occur in the bearing load zone when a simple radial loading is applied to the bearing. It is to be noted that clearance exists in the axial direction between the roller ends and the roller guide flanges.

It can be seen from Figure 2.11 that the bearing experiences an endplay defined by

$$P_e = 2(l_f - l_t) \quad (2.41)$$

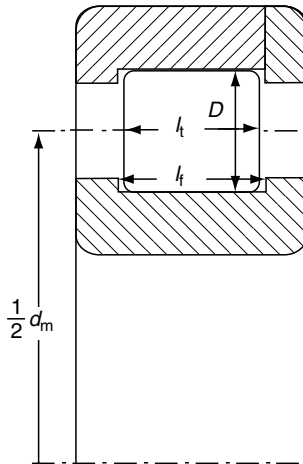


FIGURE 2.11 Schematic drawing of a radial cylindrical roller bearing having two integral roller guide flanges on the inner ring and one integral and one separable guide flange on the outer ring.

where l_f is the distance between the guide flanges of a ring and l_t is the total length of the roller. As mentioned in Chapter 1 and discussed in later chapters, radial cylindrical roller bearings with two roller guide flanges on both the inner and outer rings can support small amounts of applied thrust load in addition to the applied radial load. The bearing endplay influences the number of radially loaded rollers that will be used in supporting the thrust load. The endplay also influences the degree of roller skewing that can occur during bearing operations.

2.4.2 CURVATURE

Most cylindrical roller bearings employ crowned rollers to avoid the stress-increasing effects of edge-loading. This is discussed both in [Chapter 6](#) of this volume and in Chapter 1 of the Second Volume of this handbook. For these rollers, even if fully crowned as illustrated in Figure 1.38a, the contour or crown radius R is very large. Moreover, even if the raceways are crowned, $R = r_i = r_o \Rightarrow \infty$. Therefore, considering [Equation 2.37](#) and [Equation 2.39](#), which describe the curvature sums for the inner and outer raceway contacts, respectively, the difference of the reciprocals of these radii is essentially nil, and

$$\Sigma\rho_i = \frac{1}{D} \left[\frac{2}{1 - \gamma} \right] \quad (2.42)$$

$$\Sigma\rho_o = \frac{1}{D} \left[\frac{2}{1 + \gamma} \right] \quad (2.43)$$

Examining [Equation 2.38](#) and [Equation 2.40](#), it can be seen that $F(\rho)_i = F(\rho)_o = 1$.

2.5 TAPERED ROLLER BEARINGS

2.5.1 PITCH DIAMETER

The nomenclature associated with tapered roller bearings is different from that for other types of roller bearings. For example, as indicated in [Figure 2.12](#), the bearing inner ring is called the cone and the outer ring the cup. It can be seen that the operation of the bearing is associated with a pitch cone; [Equation 2.1](#) can be used to describe the mean diameter of that cone. For

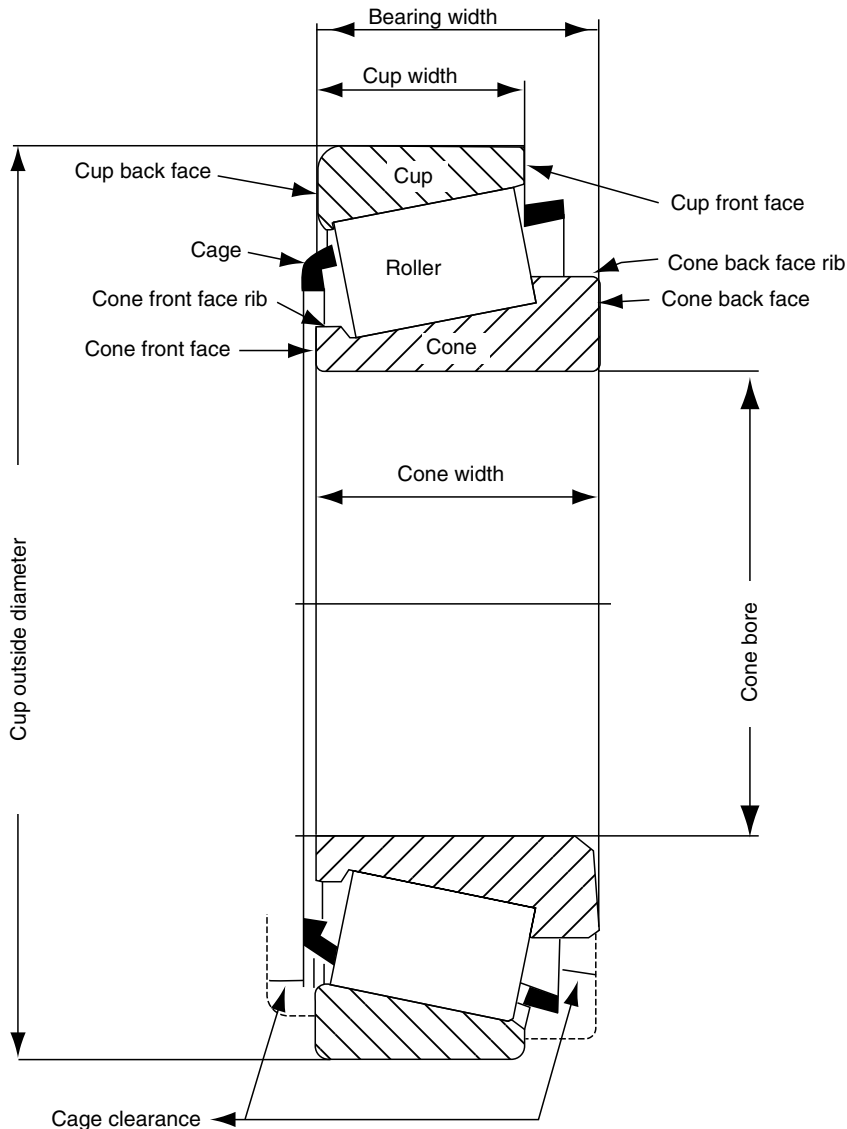


FIGURE 2.12 Schematic drawing of tapered roller bearing indicating nomenclature.

many calculations, this mean cone diameter will be used as the bearing pitch diameter d_m . Figure 2.13 indicates dimensions and angles necessary for the performance analysis of tapered roller bearings. From Figure 2.13, it can be seen that α_i , the inner raceway–roller contact angle $= \frac{1}{2}$ (cone-included angle); α_o , the outer raceway–roller contact angle $= \frac{1}{2}$ (cup-included angle); α_f , the roller large end-flange contact angle $= \frac{1}{2}$ (cone back face rib angle); and α_R is the roller-included angle. D_{\max} is the large-end diameter of the roller and D_{\min} is the small-end diameter of the roller, which has the end-to-end length l_t .

2.5.2 ENDPLAY

Tapered roller bearings are usually mounted in pairs. In general, the clearance is removed so that a line-to-line fit is achieved under no load. It is possible for a bearing set to support a

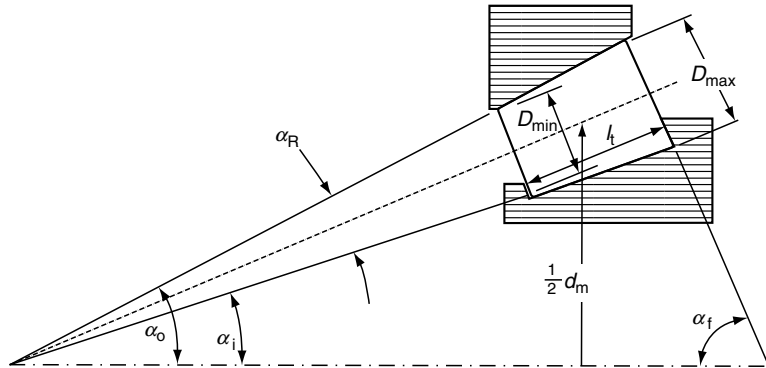


FIGURE 2.13 Internal dimensions for tapered roller bearing performance analysis.

substantially applied radial loading; however, a small amount of endplay is set at room temperature mounting to achieve the desired distribution of load among the tapered rollers under higher-temperature operating conditions. The endplay in tapered roller bearings is therefore associated with the bearing pair.

2.5.3 CURVATURE

From Figure 2.13, it is seen that the outer raceway contact angle is greater than the inner raceway contact angle. Therefore, considering Equation 2.37 and Equation 2.39, the curvature sums for the inner and outer raceway contacts are given by

$$\Sigma \rho_i = \frac{1}{D_m} \left[\frac{2}{1 - \gamma_i} \right] \quad (2.44)$$

$$\Sigma \rho_o = \frac{1}{D_m} \left[\frac{2}{1 + \gamma_o} \right] \quad (2.45)$$

where

$$D_m = \frac{1}{2}(D_{\max} + D_{\min}) \quad (2.46)$$

$$\gamma_i = \frac{D_m \cos \alpha_i}{d_m} \quad (2.47)$$

$$\gamma_o = \frac{D_m \cos \alpha_o}{d_m} \quad (2.48)$$

These equations give approximate values in the respective calculations of curvature sums because the mean radius of the roller lies in a plane slightly angled to that in which the raceway rolling radius lies.

As for cylindrical roller bearings, $F(\rho)_i = F(\rho)_o = 1$.

2.6 CLOSURE

The relationships developed in this chapter are based only on the macroshapes of the rolling components of the bearing. When a load is applied to the bearing, these contours may be

somewhat altered; however, undeformed geometry must be used to determine the distorted shape.

Numerical examples developed in this chapter were, out of necessity, very simple in format. The quantity of these simple examples is justified as the results from the calculations will subsequently be used as starting points in more complex numerical examples involving stresses, deflections, friction torques, and fatigue lives.

REFERENCES

1. American National Standards Institute (ANSI/ABMA) Std. 20-1996, Radial bearings of ball, cylindrical roller, and spherical roller types, metric design (September 6, 1996).
2. Jones, A., *Analysis of Stresses and Deflections*, vol. 1, New Departure Division, General Motors Corp., Bristol, CT, 1946, p. 12.

3 Interference Fitting and Clearance

LIST OF SYMBOLS

Symbol	Description	Units
d	Basic bore diameter	mm (in.)
d_i	Bearing inner raceway diameter	mm (in.)
d_o	Bearing outer raceway diameter	mm (in.)
D	Basic outside diameter	mm (in.)
D	Common diameter	mm (in.)
D_h	Basic housing bore	mm (in.)
D_1	Outside ring O.D.	mm (in.)
D_2	Inside ring I.D.	mm (in.)
D_s	Basic shaft diameter	mm (in.)
E	Modulus of elasticity	MPa (psi)
I	Interference	mm (in.)
L	Length	mm (in.)
P_d	Bearing clearance	mm (in.)
p	Pressure	MPa (psi)
R	Ring radius	mm (in.)
R_i	Inside radius of ring	mm (in.)
R_o	Outside radius of ring	mm (in.)
u	Radial deflection	mm (in.)
Δ_h	Clearance reduction due to press-fitting of bearing in housing	mm (in.)
Δ_s	Clearance reduction due to press-fitting of bearing on shaft	mm (in.)
Δ_t	Clearance increase due to thermal expansion	mm (in.)
T	Temperature	°C (°F)
ε_r	Strain in radial direction	mm/mm (in./in.)
ε_t	Strain in tangential direction	mm/mm (in./in.)
Γ	Coefficient of linear expansion	mm/mm/°C (in./in./°F)
ξ	Poisson's ratio	
σ_r	Normal stress in radial direction	MPa (psi)
σ_t	Normal stress in tangential direction	MPa (psi)

3.1 GENERAL

Ball and roller bearings are usually mounted on shafts or in housings with interference fits. This is done to prevent fretting corrosion that could be produced by relative movement between the bearing inner-ring bore and the shaft O.D. or the bearing outer-ring O.D. and the housing bore. The interference fit of the bearing inner ring with the shaft is usually accomplished by pressing the former member over the latter. In some cases, however, the inner ring is heated to a controlled temperature in an oven or in an oil bath. Then, the inner ring is slipped over the shaft and allowed to cool, thus accomplishing a shrink fit.

Press- or shrink-fitting of the inner ring on the shaft causes the inner ring to expand slightly. Similarly, press-fitting of the outer ring in the housing causes the former member to shrink slightly. Thus, the bearing's diametral clearance tends to decrease. Large amounts of interference in the fitting practice can cause the bearing clearance to vanish and even produce negative clearance or interference in the bearing.

Thermal conditions of bearing operations can also affect the diametral clearance. The heat generated by friction causes internal temperatures to rise. This in turn causes the expansion of the shaft, housing, and bearing components. Depending on the shaft and housing materials and on the magnitude of thermal gradients across the bearing and these supporting structures, clearance can tend to increase or decrease. It is also apparent that the thermal environment in which a bearing operates may have a significant effect on clearance.

In [Chapter 2](#), it was demonstrated that clearance significantly affects ball bearing contact angle. Subsequently, the effects of clearance on bearing internal load distribution and life will be investigated. It is therefore clear that the mechanics of bearing fitting practice is an important part of this book.

3.2 INDUSTRIAL, NATIONAL, AND INTERNATIONAL STANDARDS

3.2.1 METHOD OF ESTABLISHMENT AND SCOPE

Standards defining recommended practices for ball and roller bearing usage were first developed in the United States by the Anti-Friction Bearing Manufacturers' Association (AFBMA), which has now become the American Bearing Manufacturers' Association (ABMA). ABMA continues the process of revising the current standards and proposing and preparing new standards as deemed necessary by its bearing industry member companies. For the most recent information on or to obtain ABMA standards, the ABMA web site (www.abma-dc.org) can be consulted. ABMA-generated standards are subsequently proposed to the American National Standards Institute (ANSI) as United States national standards. ANSI has a committee dedicated to rolling bearing standards activities; this committee consists of representatives from bearing user organizations such as major industrial manufacturers and the United States government. Other countries have national standards organizations similar to ANSI, for example, DIN in Germany and JNS in Japan. Currently, 67 documents, some of them having metric and English unit system parts, have been published as ANSI/ABMA standards.

Any national standard may subsequently be proposed to the International Organization for Standardization (ISO), and after extended negotiation be published as an "International Standard" with an identifying number. Various bearing, shaft, and housing tolerance data in this chapter are excerpted from the American National Standards.

3.2.2 TOLERANCES FOR PRESS-FITTING OF BEARING RINGS ON SHAFTS AND IN HOUSINGS

ANSI/ABMA [1] defines the recommended practice in fitting bearing inner rings to shafts and outer rings in housings. These fits are recommended in terms of light, normal, and heavy

loading as defined in Figure 3.1. Each shaft-bearing fit tolerance range is designated by a lower case letter followed by a number, for example, g6, h5, and so on up to the tightest fit r7. Similarly, each tolerance range symbol for housing-bearing fit consists of an upper case letter followed by a number, for example, G7, H7, and so on up to the tightest fit P7. [Figure 3.2](#) graphically illustrates the range of each fit designation. Table CD3.1 gives the ANSI/ABMA recommended practice for fitting rings on shafts. Table CD3.2 shows the shaft-diameter tolerance limits corresponding to the recommended fit. Table CD3.3 and Table CD3.4 yield similar data for fitting of bearing O.D.s in housing bores.

ANSI/ABMA [2–8] also provides standards for tolerance ranges on bearing bore and O.D. for various types of radial bearings. Several of these bearing types, for example, needle roller bearings and instrument ball bearings, exist in too many variations to include all of the appropriate tolerance tables herein. On the other hand, American National Standard (ANSI/ABMA) Std 18.2-1982 (R 1999) [8] covers a wide range of standard radial ball and roller bearings; Table CD3.6 through Table CD3.10 are from Ref. [8]. For radial ball, cylindrical, and spherical roller bearings, the tolerances are grouped in ABEC¹ or RBEC² classes 1, 3, 5, 7, and 9 according to the accuracy of manufacturing. The accuracy improves and tolerance ranges narrow as the class number increases. Table CD3.6 through Table CD3.10 provide the tolerances on bore and O.D. for radial roller bearings as well as for ball bearings. The ABEC and RBEC tolerance classes correspond in every respect to the precision classes endorsed by ISO. Table CD3.5 shows the correspondence between the ANSI/ABMA and ISO classi-

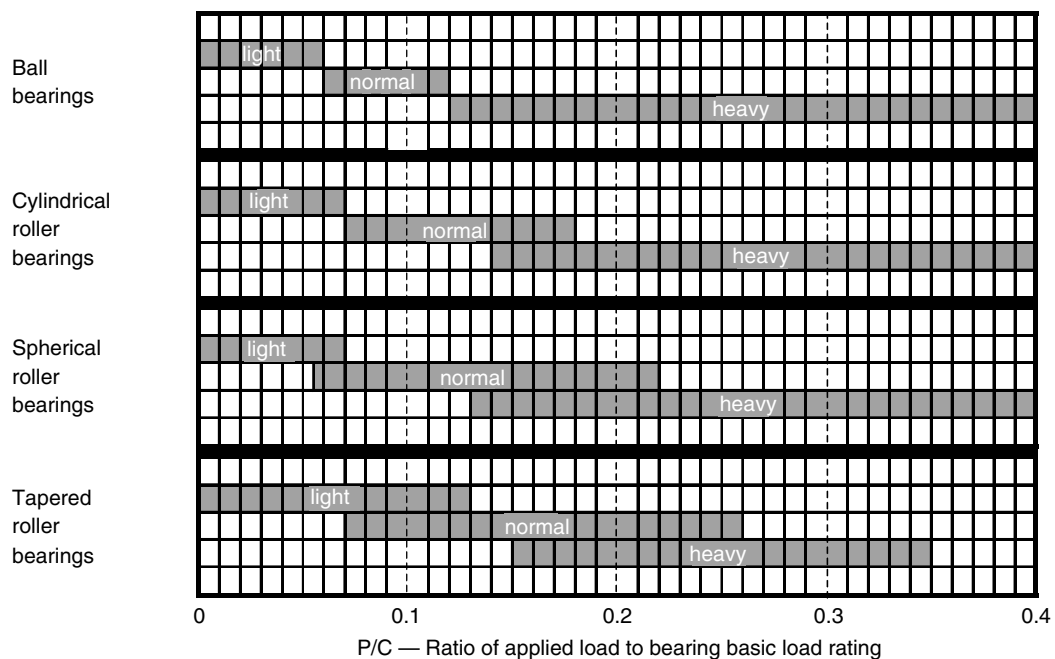


FIGURE 3.1 Classification of loading for ball, cylindrical roller, spherical roller, and tapered roller bearings used to determine required amount of press-fitting to prevent inner-ring rotation on the shaft “and/or” outer-ring rotation in the housing.

¹Annular Bearing Engineers’ Committee of ABMA.

²Roller Bearing Engineers’ Committee of ABMA.

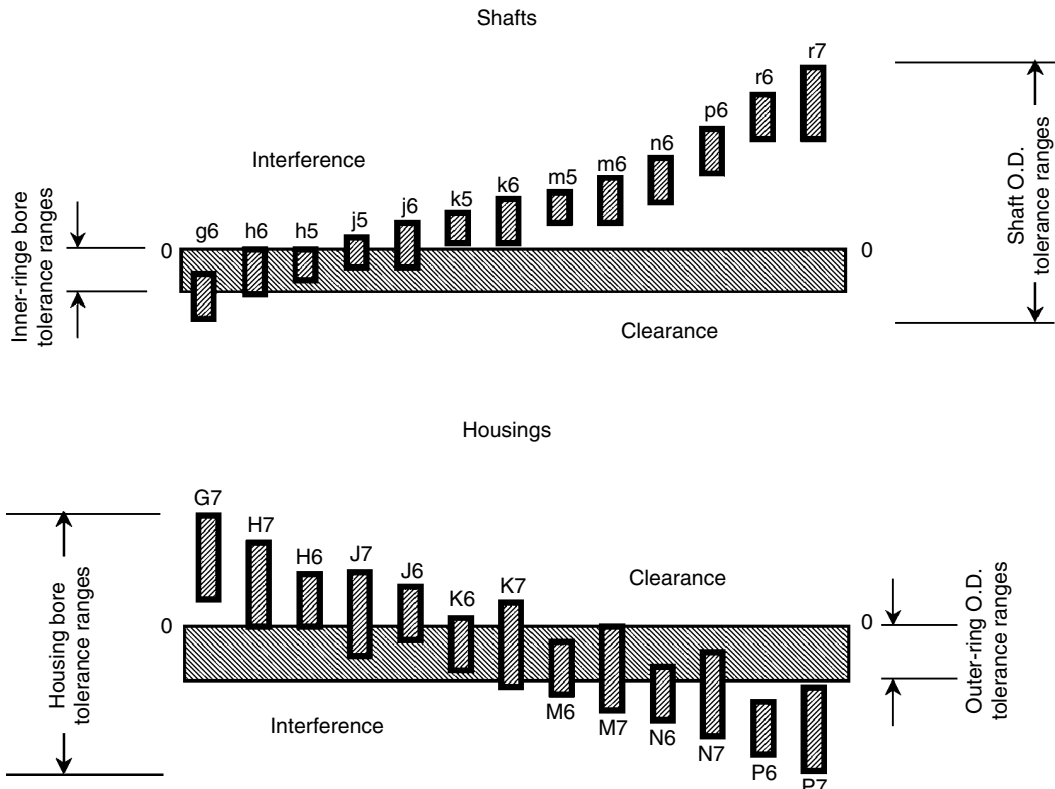


FIGURE 3.2 Graphical representation of bearing inner ring-shaft and bearing outer ring-housing standard fit classifications.

fications. It is further noted that inch tolerances given in Part II of Table CD3.6 through Table CD3.10 are calculated from primary metric tolerances given in Part I of those tables.

Opposed to the ball and radial bearings discussed here, which are primarily supplied as complete assemblies with equal inner- and outer-ring widths, tapered roller bearings are usually sold as independent cone (inner ring) and cup (outer ring) subassemblies of differing widths. With this combination of factors, different standards have evolved for the tapered roller bearing as opposed to the other radial bearing types [6,7]. Also, the tapered roller bearing was initially developed, and has extensive market penetration, in North America where the English system of measurement units is predominately used. This has led to the creation of two differing boundary plans for tapered roller bearings, one based on English (inch) and the other on metric dimensions, each with a different tolerance structure. The metric designs utilize a tolerance system similar to the other radial bearings, where the cone bore and cup outside diameter are allowed to deviate from the nominal dimension unilaterally in the negative direction. However, the inch designs utilize a tolerance system where the cone bore and cup outside diameter deviate unilaterally in the positive direction. Table CD3.11 through Table CD3.15 list the single-row metric design tapered roller bearing tolerance tables from Ref. [6] and Table CD3.16 through Table CD3.20 the single-row inch design tapered roller bearing tolerance tables from Ref. [7]. Note that the tapered roller bearing tolerances are grouped in classes 4, 2, 3, 0, and 00 for inch and K, N, C, B, and A for metric. Again, the metric tapered roller bearing tolerance classes correspond to the precision classes endorsed by ISO, as listed in Table CD3.5.

With a different tolerance structure on the tapered roller bearing bore and outside diameter, they also have different suggested fitting practices. The tapered roller bearing fitting

practice is listed in Table CD3.21 through Table 3.24 from [6] for metric bearings and Table CD3.25 through Table CD3.28 from [7] for inch bearings. Again, the definition of light, medium, and heavy load utilizes [Figure 3.1](#).

To define the range of interference or looseness in the mounting of an inner ring on a shaft or an outer ring in a housing, it is necessary to consider combinations of the shaft, housing, and bearing tolerances.

3.3 EFFECT OF INTERFERENCE FITTING ON CLEARANCE

The solution to the problem of the effect of interference fitting on clearance may be obtained by using elastic thick ring theory. Consider the ring in Figure 3.3 subjected to an internal pressure p per unit length. The ring has a bore radius R_i and an outside radius R_o . For the elemental area $R \cdot dR \cdot d\phi$, the summation of forces in the radial direction is zero for static equilibrium:

$$\sigma_r R d\phi + 2\sigma_t dR \sin \frac{d\phi}{2} - \left(\sigma_r + \frac{d\sigma_r}{dR} dR \right) (R + dR) d\phi = 0 \quad (3.1)$$

As $d\phi$ is small, $\sin(\frac{1}{2}d\phi) \approx \frac{1}{2}d\phi$ and, neglecting small quantities of higher order,

$$\sigma_t - \sigma_r - R \frac{d\sigma_r}{dR} = 0 \quad (3.2)$$

Corresponding to the stress in the radial direction, there is an elongation u and the unit strain in the radial direction is

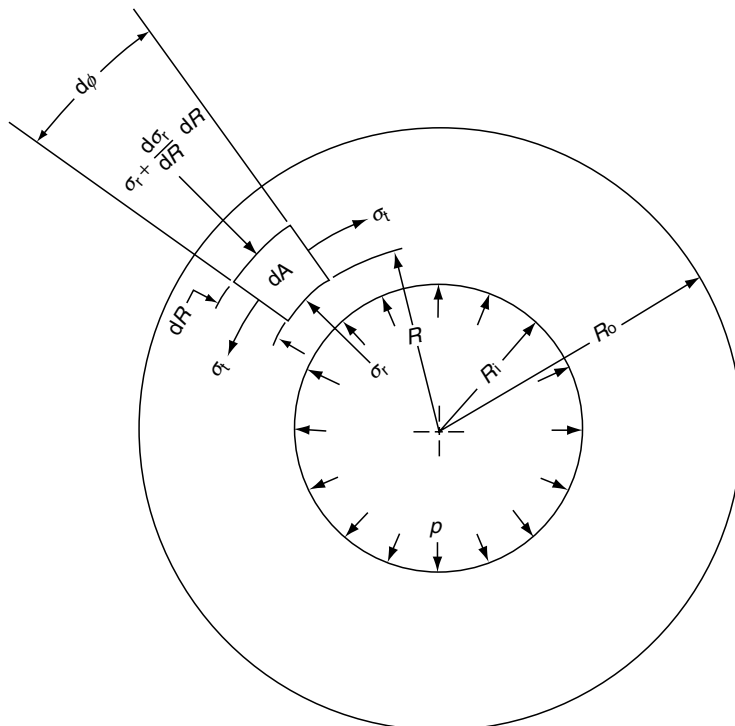


FIGURE 3.3 Thick ring loaded by internal pressure p .

$$\varepsilon_r = \frac{du}{dR} \quad (3.3)$$

In the circumferential direction, the unit strain is

$$\varepsilon_t = \frac{u}{R} \quad (3.4)$$

According to plane strain theory,

$$\varepsilon_r = \frac{1}{E} (\sigma_r - \xi \sigma_t) \quad (3.5)$$

$$\varepsilon_t = \frac{1}{E} (\sigma_t - \xi \sigma_r) \quad (3.6)$$

Combining Equation 3.3 through Equation 3.6 yields

$$\sigma_r = \frac{E}{1 - \xi^2} \left(\frac{du}{dR} + \xi \frac{u}{R} \right) \quad (3.7)$$

$$\sigma_t = \frac{E}{1 - \xi^2} \left(\frac{u}{R} + \xi \frac{du}{dR} \right) \quad (3.8)$$

Substituting Equation 3.7 and Equation 3.8 into [Equation 3.2](#) yields

$$\frac{d^2 u}{dR^2} + \frac{1}{R} \frac{du}{dR} - \frac{u}{R^2} = 0 \quad (3.9)$$

The general solution to Equation 3.9 is

$$u = c_1 R + c_2 R^{-1} \quad (3.10)$$

Substituting Equation 3.10 in Equation 3.7 and Equation 3.8 gives

$$\sigma_r = \frac{E}{1 - \xi^2} \left[c_1 (1 + \xi) - c_2 \frac{(1 - \xi)}{R^2} \right] \quad (3.11)$$

$$\sigma_t = \frac{E}{1 - \xi^2} \left[c_1 (1 + \xi) + c_2 \frac{(1 - \xi)}{R^2} \right] \quad (3.12)$$

At the boundaries, the pressure applied to the internal and external surfaces is directly equal to the radial stress in a compressive manner (i.e., $R = R_o$, $\sigma_r = -p_o$; $R = R_i$, $\sigma_r = -p_i$), and therefore,

$$c_1 = \frac{1 - \xi}{E} \left[\frac{R_i^2 p_i - R_o^2 p_o}{R_o^2 - R_i^2} \right] \quad (3.13)$$

$$c_2 = \frac{1 + \xi}{E} \left[\frac{R_i^2 R_o^2 (p_i - p_o)}{R_o^2 - R_i^2} \right] \quad (3.14)$$

Substituting [Equation 3.13](#) and [Equation 3.14](#) into [Equation 3.11](#) and [Equation 3.12](#) yields

$$\sigma_r = -p_i \left[\frac{(R_o/R)^2 - 1}{(R_o/R_i)^2 - 1} \right] - p_o \left[\frac{1 - (R_i/R)^2}{1 - (R_i/R_o)^2} \right] \quad (3.15)$$

$$\sigma_t = p_i \left[\frac{(R_o/R)^2 + 1}{(R_o/R_i)^2 - 1} \right] - p_o \left[\frac{1 + (R_i/R)^2}{1 - (R_i/R_o)^2} \right] \quad (3.16)$$

From [Equation 3.15](#), [Equation 3.16](#), and [Equation 3.5](#), the change in the radius u at any radial location R due to internal or external pressures p_i or p_o , respectively, is given by

$$u = \frac{R}{E} \left\{ p_i \left[\frac{(R_o/R)^2 + 1}{(R_o/R_i)^2 - 1} + \xi \frac{(R_o/R)^2 - 1}{(R_o/R_i)^2 - 1} \right] - p_o \left[\frac{1 + (R_i/R)^2}{1 - (R_i/R_o)^2} - \xi \frac{1 - (R_i/R)^2}{1 - (R_i/R_o)^2} \right] \right\} \quad (3.17)$$

[Equation 3.15](#) through [Equation 3.17](#) are the general equations for thick rings. Any condition of internal or external pressure can be considered independently by setting the other value of pressure to zero.

If a ring having elastic modulus E_1 , outside diameter D_1 , and bore D is mounted with a diametral interference I on a second ring having modulus E_2 , outside diameter D , and bore D_2 , then a common pressure p develops between the rings. The radial interference is the sum of the radial deflection of each ring due to pressure p . Hence, the diametral interference is given by

$$I = 2(u_1 + u_2) \quad (3.18)$$

In terms of the common diameter D , therefore,

$$I = pD \left\{ \frac{1}{E_1} \left[\frac{(D_1/D)^2 + 1}{(D_1/D)^2 - 1} + \xi_1 \right] + \frac{1}{E_2} \left[\frac{(D/D_2)^2 + 1}{(D/D_2)^2 - 1} + \xi_2 \right] \right\} \quad (3.19)$$

It can be seen that [Equation 3.19](#) can be used to determine p if I is known; thus,

$$p = \frac{I/D}{\frac{1}{E_1} \left[\frac{(D_1/D)^2 + 1}{(D_1/D)^2 - 1} + \xi_1 \right] + \frac{1}{E_2} \left[\frac{(D/D_2)^2 + 1}{(D/D_2)^2 - 1} - \xi_2 \right]} \quad (3.20)$$

If the external ring is a bearing inner ring of diameter D_1 and bore D_s as shown in [Figure 3.4](#), then the increase in D_1 due to press-fitting is

$$\Delta_s = \frac{2I(D_1/D_s)}{\left[(D_1/D_s)^2 - 1 \right] \left\{ \left[\frac{(D_1/D_s)^2 + 1}{(D_1/D_s)^2 - 1} + \xi_b \right] + \frac{E_b}{E_s} \left[\frac{(D_s/D_2)^2 + 1}{(D_s/D_2)^2 - 1} - \xi_s \right] \right\}} \quad (3.21)$$

If the bearing inner ring and shaft are both fabricated from the same material, then

$$\Delta_s = I \left(\frac{D_1}{D_s} \right) \left[\frac{(D_s/D_2)^2 - 1}{(D_1/D_2)^2 - 1} \right] \quad (3.22)$$

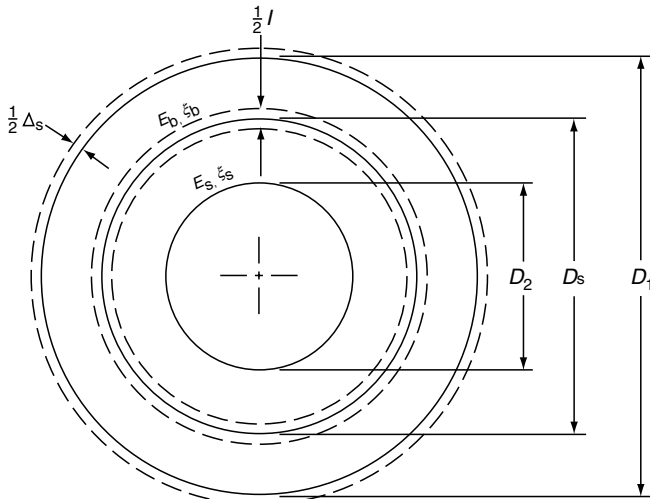


FIGURE 3.4 Schematic diagram of a bearing inner ring mounted on a shaft.

For a bearing inner ring mounted on a solid shaft of the same material, diameter D_2 is zero and

$$\Delta_s = I \left(\frac{D_s}{D_1} \right) \quad (3.23)$$

By a similar process, it is possible to determine the contraction of the bore of the internal ring of the assembly shown in Figure 3.5. Thus,

$$\Delta_h = \frac{2I(D_h/D_2)}{\left[(D_h/D_2)^2 - 1 \right] \left\{ \left[\frac{(D_h/D_2)^2 + 1}{(D_h/D_2)^2 - 1} + \xi_b \right] + \frac{E_b}{E_h} \left[\frac{(D_1/D_h)^2 + 1}{(D_1/D_h)^2 - 1} - \xi_h \right] \right\}} \quad (3.24)$$

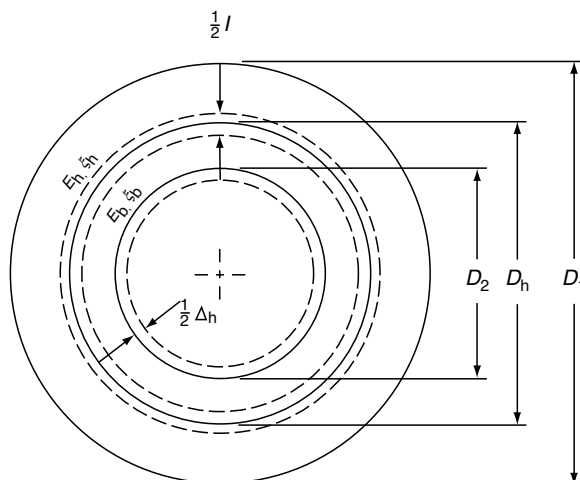


FIGURE 3.5 Schematic diagram of a bearing outer ring mounted in a housing.

For a bearing outer ring pressed into a housing of the same material,

$$\Delta_h = I \left(\frac{D_h}{D_2} \right) \left[\frac{(D_1/D_h)^2 - 1}{(D_1/D_2)^2 - 1} \right] \quad (3.25)$$

If the housing is large compared with the ring dimensions, diameter D_1 approaches infinity and

$$\Delta_h = I \left(\frac{D_2}{D_h} \right) \quad (3.26)$$

Considering a bearing having a clearance P_d before mounting, the change in clearance after mounting is given by

$$\Delta P_d = -\Delta_s - \Delta_h \quad (3.27)$$

The preceding equation takes no account of differential thermal expansions.

3.4 PRESS FORCE

As the pressure p between interfering surfaces is known, it is possible to estimate the amount of axial force necessary to accomplish or remove an interference fit. Because the area of shear is πDB , the axial force is given by

$$F_a = \mu \pi D B p \quad (3.28)$$

where μ is the coefficient of friction. According to Jones [9], the force required to press a steel ring on a solid steel shaft may be estimated by the following equation:

$$F_a = 47,100 BI \left[1 - \left(\frac{D_s}{D_1} \right)^2 \right] \quad (3.29)$$

This is based on a kinetic coefficient of friction $\mu = 0.15$. Similarly, the axial force required to press a steel bearing into a steel housing is given by

$$F_s = 47,100 BI \left[1 - \left(\frac{D_2}{D_h} \right)^2 \right] \quad (3.30)$$

3.5 DIFFERENTIAL EXPANSION

Rolling bearings are usually fabricated from hardened steel and are generally mounted with press-fits on steel shafts. In many applications, such as in aircraft, however, the bearing may be mounted in a housing of a dissimilar material. Bearings are usually mounted at room temperature; but they may operate at temperatures elevated ΔT above room temperature. The amount of temperature elevation may be determined by using the heat generation and heat transfer techniques indicated in later chapters. Under the influence of increased temperature, the material will expand linearly according to the following equation:

$$u = \Gamma L(T - T_a) \quad (3.31)$$

in which Γ is the coefficient of linear expansion in mm/mm/ $^{\circ}$ C and L is the characteristic length.

Consider a bearing outer ring of outside diameter d_o at temperatures $T_o - T_a$ above ambient, the increase in ring circumference is given approximately by

$$u_{toc} = \Gamma_b \pi d_o (T_o - T_a) \quad (3.32)$$

Therefore, the approximate increase in diameter is

$$u_{to} = \Gamma_b d_o (T_o - T_a) \quad (3.33)$$

The inner ring will undergo a similar expansion:

$$u_{ti} = \Gamma_b d_i (T_i - T_a) \quad (3.34)$$

Thus, the net diametral expansion of the fit is given by

$$\Delta_T = \Gamma_b [d_o (T_o - T_a) - d_i (T_i - T_a)] \quad (3.35)$$

When the housing is fabricated from a material other than steel, the interference I between the housing and the outer ring may either increase or decrease at elevated temperatures. Equation 3.36 gives the change in I with temperature:

$$\Delta I = (\Gamma_b - \Gamma_h) D_h (T_o - T_a) \quad (3.36)$$

where Γ_b and Γ_h are the coefficients of expansion of the bearing and housing, respectively. For dissimilar materials, the housing is most likely to expand more than the bearing, which tends to reduce the interference fit. Equation 3.27 therefore becomes

$$\Delta P_d = \Delta_T - \Delta_s - \Delta_h \quad (3.37)$$

If the shaft is not fabricated from the same material (usually steel) as the bearing, then a similar analysis applies.

3.6 EFFECT OF SURFACE FINISH

The interference I between a bore and an O.D. is somewhat less than the apparent dimensional value due to the smoothing of the minute peaks and valleys of the surface. The schedule of [Table 3.1](#) for reduction of I may be used.

It can be seen from Table 3.1 that for an accurately ground shaft mating with a similar bore, it may be expected that the reduction in the bore diameter would be 0.002 mm (0.00008 in.) and in the shaft possibly 0.0041 mm (0.00016 in.), or a total reduction in I of 0.0061 mm (0.00024 in.).

See Example 3.1 through Example 3.4.

3.7 CLOSURE

The important effect of bearing fitting practice on diametral clearance has been demonstrated for ball bearings with numerical examples. Because the ball bearing contact angle determines its

TABLE 3.1
Reduction in Interference Due to Surface Condition

Finish	Reduction	
	$\times 10^{-4}$ mm	$\times 10^{-6}$ in.
Accurately ground surface	20–51	8–20
Very smooth turned surface	61–142	24–56
Machine-reamed bores	102–239	40–94
Ordinary accurately turned surface	239–483	94–190

ability to carry thrust load and the contact angle is dependent on clearance, the analysis of the fit-up is important in many applications. The numerical examples herein were based on mean tolerance conditions. In many cases, however, it is necessary to examine the extremes of fit.

Although only the effect of fit-up on contact angle has been examined, it is not to be construed that this is the only effect of significance. Later, the sensitivity of other phases of a rolling bearing operation to clearance will be investigated.

The thermal conditions of operation have been shown to be of no less significance than the fit-up. In precision applications, the clearance must be evaluated under operating conditions.

Table CD3.6 through Table CD3.10 contain tolerance limits on radial and axial runout as well as the tolerance limits on mean diameters. Runout affects bearing performance in subtle ways such as through vibration as discussed in later chapters.

REFERENCES

1. American National Standards Institute, American National Standard (ANSI/ABMA) Std 7-1995 (R 2001), "Shaft and Housing Fits for Metric Ball and Roller Bearings (Except Tapered Roller Bearings) Conforming to Basic Boundary Plans" (October 27, 1995).
2. American National Standards Institute, American National Standard (ANSI/ABMA) Std 12.1-1992 (R 1998), "Instrument Ball Bearings Metric Design" (April 6, 1992).
3. American National Standards Institute, American National Standard (ANSI/ABMA) Std 12.2-1992 (R 1998), "Instrument Ball Bearings Inch Design" (April 6, 1992).
4. American National Standards Institute, American National Standard (ANSI/ABMA) Std 18.1-1982 (R 1999), "Needle Roller Bearings Radial Metric Design" (December 2, 1982).
5. American National Standards Institute, American National Standard (ANSI/ABMA) Std 18.2-1982 (R 1999), "Needle Roller Bearings Radial Inch Design" (May 14, 1982).
6. American National Standards Institute, American National Standard (ANSI/ABMA) Std 19.1-1987 (R 1999), "Tapered Roller Bearings Radial Metric Design" (October 19, 1987).
7. American National Standards Institute, American National Standard (ANSI/ABMA) Std 19.2-1994 (R 1999), "Tapered Roller Bearings Radial Inch Design" (May 12, 1994).
8. American National Standards Institute, American National Standard (ANSI/ABMA) Std 20-1996, "Radial Bearings of Ball, Cylindrical Roller, and Spherical Roller Types, Metric Design" (September 6, 1996).
9. Jones, A., *Analysis of Stresses and Deflections*, New Departure Division, General Motors Corp., Bristol, CT, 161–170, 1946.

4 Bearing Loads and Speeds

LIST OF SYMBOLS

Symbol	Description	Units
a	Distance to load point from right-hand bearing center	mm (in.)
e	Gear train value	
F	Bearing radial load	N (lb)
g	Gravitational constant	mm/s ² (in./s ²)
h	Thread pitch of worm at the pitch radius	mm (in.)
H	Power	W (hp)
l	Distance between bearing centers	mm (in.)
l	Length of connecting rod	mm (in.)
n	Speed	rpm
N	Number of teeth on gear	
P	Applied radial direction load	N (lb)
P_p	Force applied on piston pin	N (lb)
P_{il}	Inertial force due to reciprocating masses	N (lb)
P_{cl}	Centrifugal force acting on connecting rod bearing due to rotating masses	N (lb)
P_{cc}	Centrifugal force acting on crankshaft bearing due to rotating masses	N (lb)
r	Crank radius	mm (in.)
r_p	Gear pitch radius	mm (in.)
T	Applied moment load	N·mm (lb·in.)
w	Applied load per unit length	N/mm (lb/in.)
W_1	Weight of reciprocating parts	N (lb)
W_2	Weight of connecting rod including bearing assemblies	N (lb)
W_2'	Weight of reciprocating portion of connecting rod	N (lb)
W_2''	Weight of rotating portion of connecting rod	N (lb)
W_3	Weight of crank-pin and crank webs with balance weights	N (lb)
x	Distance along shaft	mm (in.)
Z	Number of threads on worm, teeth on worm wheel	
γ	Bevel gear cone angle	°, rad
λ	Lead angle of worm at the pitch radius	°, rad
ϕ	Gear pressure angle	°, rad
ψ	Gear helix angle	°, rad

4.1 GENERAL

The loading a rolling bearing supports is usually transmitted to the bearing through the shaft on which the bearing is mounted. Sometimes, however, the loading is transmitted through the housing that encompasses the bearing outer ring, for example, a wheel bearing. In either case, and in most applications, it is sufficient to consider the bearing as simply resisting the applied load and not as an integral part of the loaded system. This condition will be covered in this chapter together with a definition of the loads transferred to the shaft-bearing system by some common power transmission components.

4.2 CONCENTRATED RADIAL LOADING

4.2.1 BEARING LOADS

The most elementary rolling bearing-shaft assembly is shown in Figure 4.1 in which a concentrated load is supported between two bearings.

This load may be caused by a pulley, gear, piston and crank, electric motor, and so on. Generally, the shaft is relatively rigid, and the bearing misalignment due to shaft bending is negligible. Thus, the system is statically determinate; that is, the bearing reaction loads F may be determined from the equations of static equilibrium. Hence,

$$\Sigma F = 0 \quad (4.1)$$

$$F_1 + F_2 - P = 0 \quad (4.2)$$

$$\Sigma M = 0 \quad (4.3)$$

$$F_1 l - P(l - a) = 0 \quad (4.4)$$

Solving Equation 4.2 and Equation 4.4 simultaneously yields

$$F_1 = P\left(1 - \frac{a}{l}\right) \quad (4.5)$$

$$F_2 = P\frac{a}{l} \quad (4.6)$$

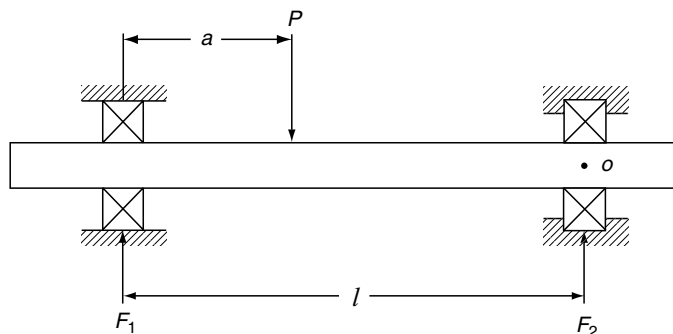


FIGURE 4.1 Two-bearing-shaft system.

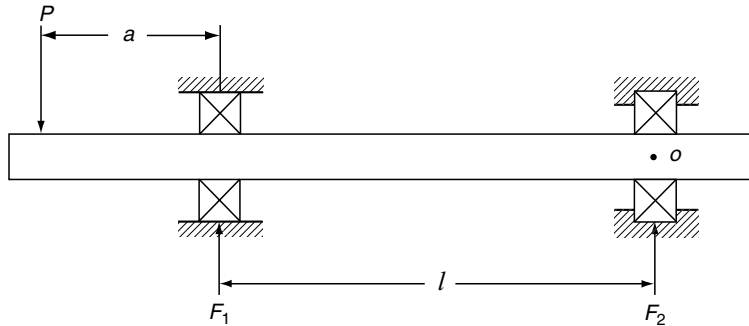


FIGURE 4.2 Two-bearing-shaft system, overhung load.

For an overhanging load as shown in Figure 4.2, [Equation 4.5](#) and [Equation 4.6](#) remain valid if the distances measured to the left of the left-hand bearing support are considered negative. [Equation 4.5](#) and [Equation 4.6](#) therefore become

$$F_1 = P \left(1 \mp \frac{a}{l} \right) \quad (4.7)$$

$$F_2 = \pm P \frac{a}{l} \quad (4.8)$$

If the number of loads P^k acts on the shaft as shown in Figure 4.3, the magnitude of the bearing reactions may be obtained by the principle of superposition. For these cases,

$$F_1 = \sum_{k=1}^{k=n} P^k \left(1 \mp \frac{a^k}{l} \right) \quad (4.9)$$

$$F_2 = \pm \sum_{k=1}^{k=n} P^k \frac{a^k}{l} \quad (4.10)$$

[Equation 4.9](#) and [Equation 4.10](#) are valid for loads applied in the same plane. If loading is applied in different planes, then the loads must be resolved into orthogonal components; for

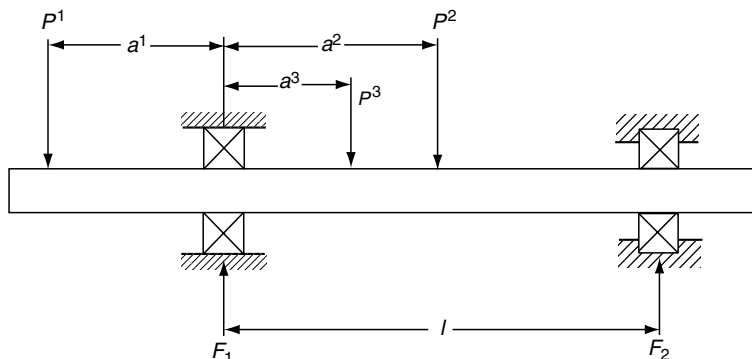


FIGURE 4.3 Two-bearing-shaft system, multiple loading.

example, P_y^k and P_z^k (assuming the shaft axis is aligned with the x -direction). Accordingly, the bearing radial reactions F_{1y} , F_{1z} , F_{2y} , and F_{2z} will be determined. Then,

$$F_1 = \left(F_{1y}^2 + F_{1z}^2 \right)^{1/2} \quad (4.11)$$

$$F_2 = \left(F_{2y}^2 + F_{2z}^2 \right)^{1/2} \quad (4.12)$$

4.2.2 GEAR LOADS

Among the most common machine elements used in combination with rolling bearings in power transmissions are involute form spur gears.

These gears are used to transmit power between parallel shafts. As shown by machine design texts (for example, Spotts and Shoup [1], Juvinall and Marshek [2], Hamrock et al. [3], and several others), load is transmitted normally to the flanks of the gear teeth at an angle ϕ to a tangent to the gear pitch circle at the point of contact. This normal load P can be resolved into a tangential load P_t and a separating or radial load P_r . Figure 4.4 illustrates the loads transmitted by spur gears at the gear pitch radius r_p . The tangential load P_t can be determined from the power relationship

$$H = \frac{2\pi n}{60} P_t r_p \quad (4.13)$$

The separating force is calculated using the following equation:

$$P_r = P_t \tan \phi \quad (4.14)$$

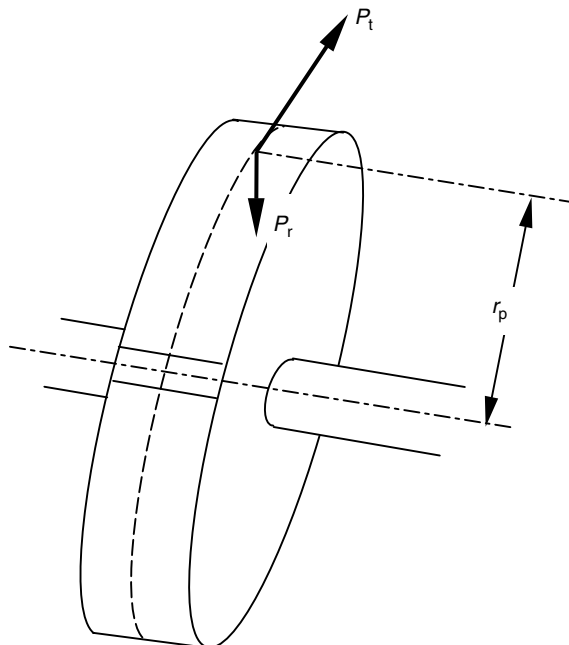


FIGURE 4.4 Loads transmitted by a spur gear.

[Equation 4.13](#) and [Equation 4.14](#) are also valid for herringbone gears, which also transmit power between parallel shafts. Such a gear is illustrated in Figure 4.5.

Loading of planet gears in planetary gear transmissions is illustrated in [Figure 4.6](#). It can be seen that the total radial load acting on the shaft is $2P_t$. Also, the separating loads are self-equilibrating; that is, they cancel each other. In Chapter 1 of the Second Volume of this handbook, the separating loads are shown to cause bearing outer-ring bending, affecting the distribution of loads among rollers.

4.2.3 BELT-AND-PULLEY AND CHAIN DRIVE LOADS

Belt-and-pulley arrangements also produce radial loading, as illustrated in [Figure 4.7](#). It can be seen from Figure 4.7 that the load applied to the pulley shaft is a function of the sum of the tension loads. Because of belt expansion and variation in the transmitted power, the belt is generally preloaded more than is theoretically necessary. The radial load on the shaft may be approximated by

$$P = f_1 f_2 P' \quad (4.15)$$

where P' is the theoretical pulley load. If the belt cross-section is very large, then

$$P \approx f_3 A \quad (4.16)$$

where A is the cross-sectional area. Values of f_1 , f_2 , and f_3 are given in [Table 4.1](#). In Table 4.1, the higher f_1 values are appropriate when the belt speed is low; the higher f_2 values should be used when the center distance is short and the operating conditions are not favorable.

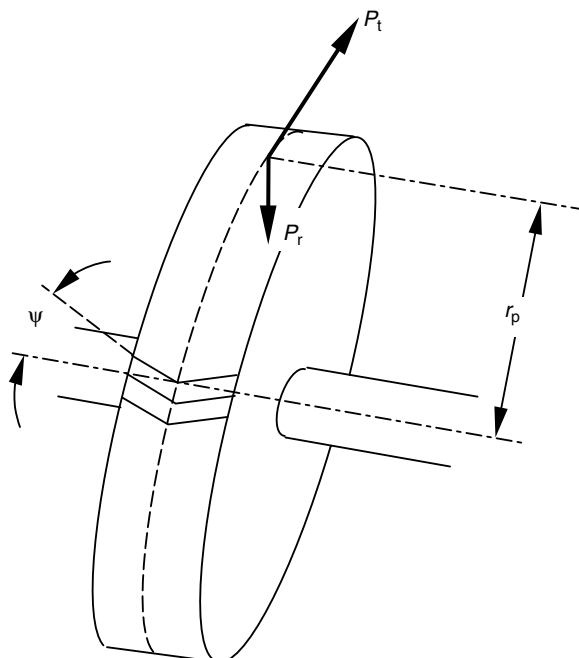


FIGURE 4.5 Loads transmitted by a herringbone gear; ψ is the helix angle.

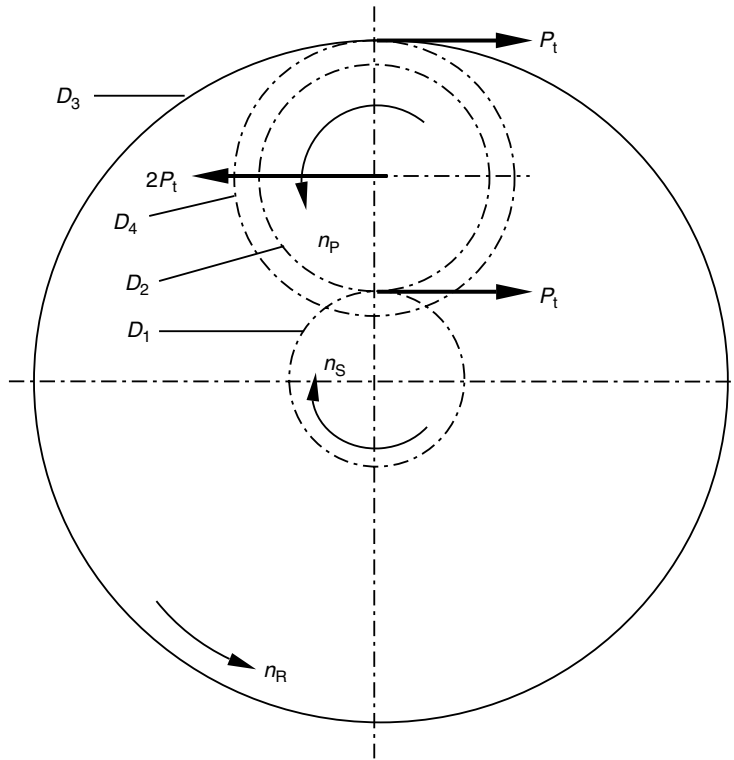


FIGURE 4.6 Planet gear loading.

4.2.4 FRICTION WHEEL DRIVES

Figure 4.8 schematically illustrates the loads in a friction wheel drive. In this case, a coefficient of friction must be determined as a function of the application. The combinations of materials and operating environments are too numerous for friction coefficient values to be included herein. It is suggested that a mechanical engineering handbook, for example, Avallone and Baumeister [4], be consulted.

4.2.5 DYNAMIC LOADING DUE TO AN ECCENTRIC ROTOR

In some applications, dynamic loading is generated due to the rotation of an eccentric mass. This is illustrated in Figure 4.9. The force P_d generated by the weight W located at distance e from the axis of rotation is given by

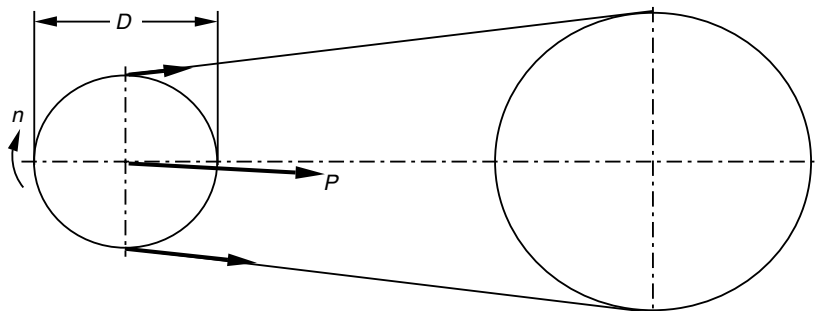


FIGURE 4.7 Belt-and-pulley arrangement.

TABLE 4.1
Factors for Belt and Chain Drive Calculations

Type of Drive	f_1	f_2	f_3
Flat leather belt with tension pulley	1.75–2.5	1.0–1.1	550
Flat leather belt without tension pulley			
Fabric belt, rubberized canvas belt, nylon belt	2.25–3.5	1.0–1.2	800
Balata belt			
V-belt	1.5–2.0	1.0–1.2	275
Steel belt	4.0–6.0	1.0–1.2	—
Chain	1	1.1–1.5	—

$$P_d = \frac{W}{g} e \omega^2 \quad (4.17)$$

where g is the gravitational acceleration and ω is the speed of rotation in rad/s. The force P_d is constant with regard to a rotating shaft angular position, and translates into a similar condition with regard to bearing loading. This condition must be considered in the evaluation of bearing fatigue life.

4.2.6 DYNAMIC LOADING DUE TO A CRANK-RECIPROCATING LOAD MECHANISM

Reciprocating mechanisms, such as pistons in internal combustion engines, air compressors, and axial pumps, may employ rolling bearings in several different locations. Each of these bearings experiences dynamic loading associated with the reciprocating motion. Figure 4.10 is a schematic representation of a crank mechanism. In Figure 4.10, three bearing locations are indicated: (1) crankshaft support bearings; (2) connecting rod-crank bearing; and (3) piston pin bearing. In this mechanism, usually 30–40% of the connecting rod is considered as reciprocating; therefore,

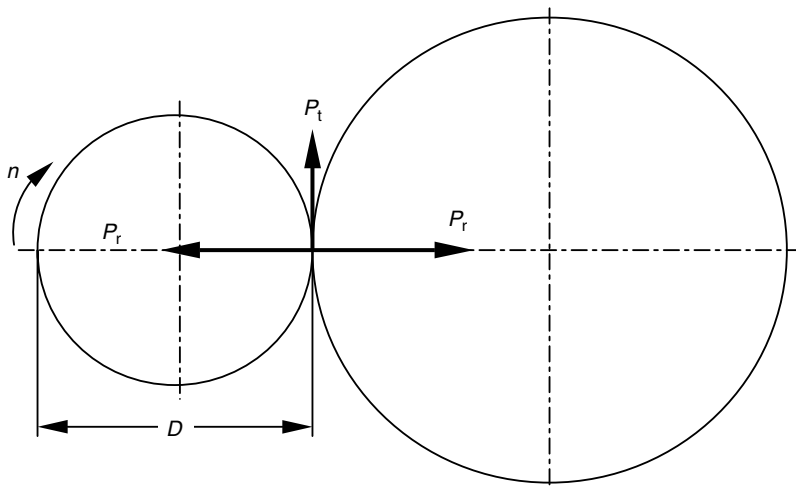


FIGURE 4.8 Schematic illustration of friction wheel loading.

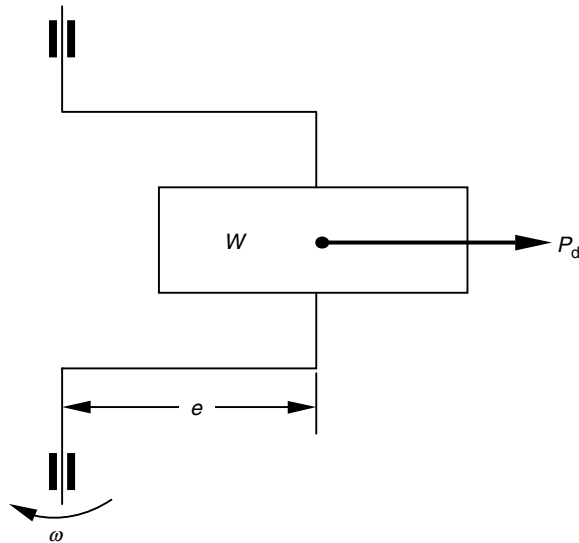


FIGURE 4.9 Rotor with eccentric mass.

$$W_{2'} = (0.3 - 0.4)W_2 \quad (4.18)$$

$$W_{2''} = (0.7 - 0.6)W_2 \quad (4.19)$$

All forces acting from left to right in Figure 4.10 are considered positive; they are negative when acting in the opposite direction. The reciprocating masses comprise the piston and piston pin and the reciprocating portion of the connecting rod assembly. Therefore, the inertial force due to reciprocating masses is

$$P_{il} = -(W_1 + W_{2'}) \frac{r\omega^2}{g} \left(\cos \alpha + \frac{r}{l} \cos(2\alpha) \right) \quad (4.20)$$

At top dead-center ($\alpha = 0^\circ$), P_{il} reaches a maximum of

$$P_{il} = -(W_1 + W_{2'}) \frac{r\omega^2}{g} \left(1 + \frac{r}{l} \right) \quad (4.21)$$

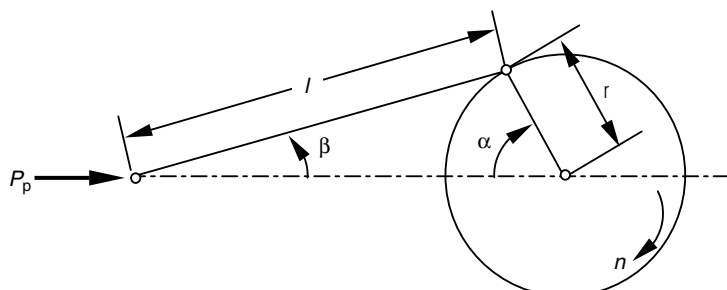


FIGURE 4.10 Schematic diagram of crank mechanism.

and at bottom dead-center ($\alpha = 180^\circ$)

$$P_{il} = + (W_1 + W_{2'}) \frac{r\omega^2}{g} \left(1 - \frac{r}{l} \right) \quad (4.22)$$

The centrifugal force acting on the large-end bearing of the connecting rod is given by

$$P_{cl} = W_{2''} \frac{r\omega^2}{g} \quad (4.23)$$

The centrifugal force transmitted to the crankshaft bearing is

$$P_{cc} = \left(W_{2''} \pm \frac{r_1}{r} W_3 \right) \frac{r\omega^2}{g} \quad (4.24)$$

In Equation 4.24, r_1 is the distance between the crankshaft axis and the center of gravity (CG) of weight W_3 ; the minus sign is used when the crank-pin and the CG are on opposite sides of the crankshaft axis.

The external force P_p and the inertial force P_{il} have a common line of action and may be combined such that the resultant is

$$P = P_p + P_{il} \quad (4.25)$$

4.3 CONCENTRATED RADIAL AND MOMENT LOADING

In some applications, only a single bearing is used to support the shaft as a cantilever subjected to load in the radial plane. As indicated in Figure 4.11, in this case the bearing must also support a moment or misaligning moment load. The equations for bearing radial and moment load are

$$F = \sum_{k=1}^{k=n} P^k \quad (4.26)$$

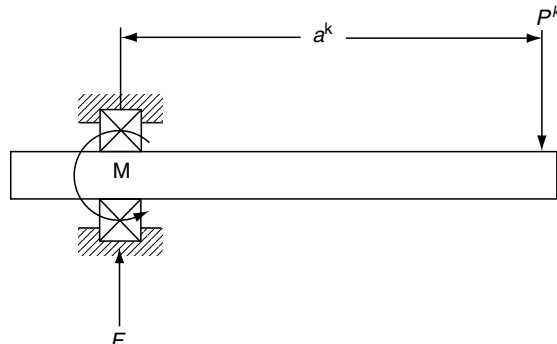


FIGURE 4.11 Single-bearing-shaft system.

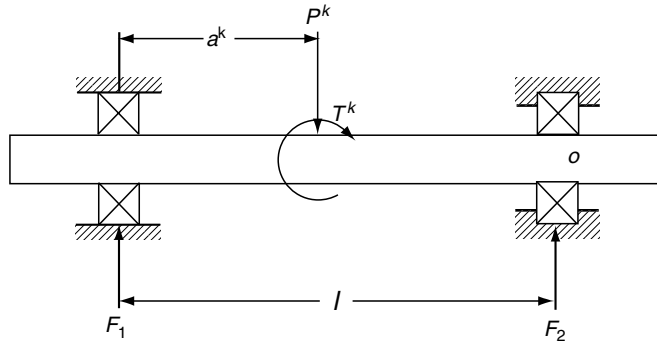


FIGURE 4.12 Two-bearing-shaft system with concentrated radial and moment loads.

$$M = \sum_{k=1}^{k=n} P^k a^k \quad (4.27)$$

In a power transmission system involving helical, bevel, spiral bevel, hypoid, or worm gearing, in addition to the radial loads, thrust loads are transmitted through the gears. These thrust loads occur at distances from the shaft axis and thereby create concentrated moments that act on the shaft. This is illustrated schematically in Figure 4.12. For these cases, the equations defining the radial loading of the bearings are

$$F_1 = \sum_{k=1}^{k=n} \left[P^k \left(1 \mp \frac{a^k}{l} \right) - \frac{T^k}{l} \right] \quad (4.28)$$

$$F_2 = \sum_{k=1}^{k=n} \left[P^k \frac{a^k}{l} + \frac{T^k}{l} \right] \quad (4.29)$$

4.3.1 HELICAL GEAR LOADS

Helical gears are also mostly used to transmit power between parallel shafts; the radial and axial loads transmitted are illustrated in Figure 4.13. As for spur gears, the tangential load component P_t is determined from Equation 4.12. The separating load is given by

$$P_r = P_t \frac{\tan \phi}{\cos \psi} \quad (4.30)$$

where ϕ is the pressure angle and ψ is the helix angle. The axial load component P_a is given by

$$P_a = P_t \tan \psi \quad (4.31)$$

Helical gears can also transmit power between crossed shafts. In this case, once P_t is determined using Equation 4.12, Equation 4.30 and Equation 4.31 can be used to determine P_{a1} , P_{r1} , P_{a2} , and P_{r2} for gears 1 and 2, which have helix angles ψ_1 and ψ_2 .

4.3.2 BEVEL GEAR LOADS

Bevel gears are used to transmit power between shafts whose axes of rotation intersect. Thus, the shaft axes lie in a common plane. As with helical gears, in bevel gears, radial and axial

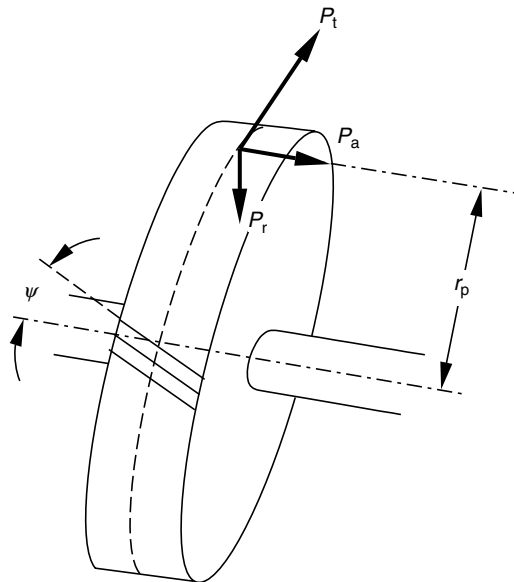


FIGURE 4.13 Loads transmitted by a helical gear.

loads are transmitted between the mating gear teeth. Because the axial load occurs at a distance r_p from the shaft axis, a concentrated moment $T = r_p \cdot P_a$ is created. Figure 4.14 shows the loads transmitted by a straight bevel gear. As for spur gears, the tangential load component P_t is determined from [Equation 4.12](#); however, a mean pitch radius of the teeth, for example, r_p , must be used. The radius to the pitch circle of the large end of the bevel gear is called the back cone radius r_b . Using the half-cone angle γ and the gear tooth flank length l_t , it can be determined that

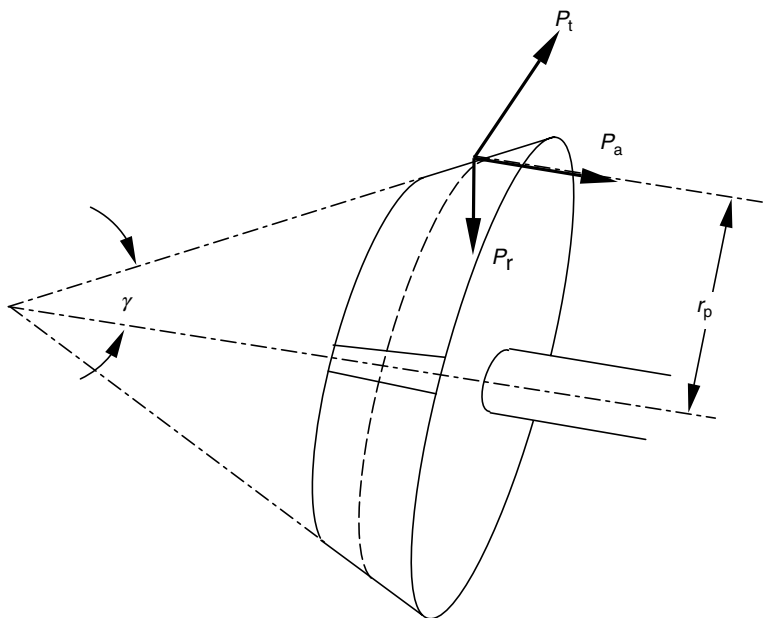


FIGURE 4.14 Loads transmitted by a straight bevel gear.

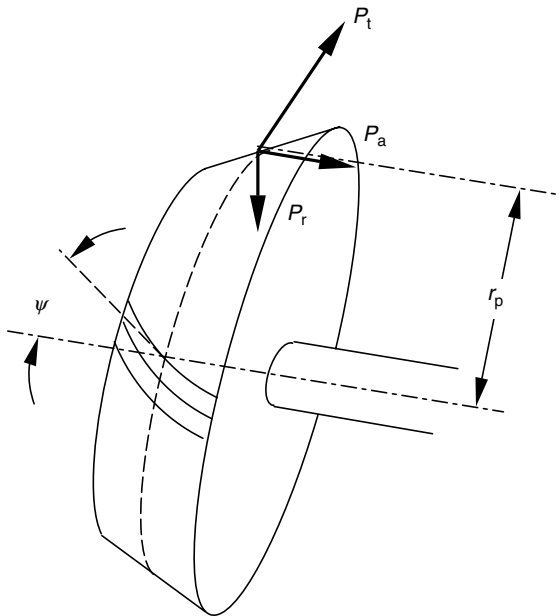


FIGURE 4.15 Loads transmitted by a spiral bevel gear.

$$r_p = r_b - \frac{l_t}{2} \sin \gamma \quad (4.32)$$

The separating (radial) and axial loads are given by the following equations

$$P_r = P_t \tan \phi \cos \gamma \quad (4.33)$$

$$P_a = P_t \tan \phi \sin \gamma \quad (4.34)$$

Spiral bevel gears, similar to helical gears, have a helix angle ψ as indicated in Figure 4.15. In this case, the axial and radial loads transmitted between the teeth are affected by the helix angle, the direction of the helix, and the direction of rotation of the gear. Furthermore, a distinction must be made between driving and driven gears. Considering the driving gear and the helix and rotational directions of Figure 4.16a, the gear forces transmitted are given by Equation 4.35 and Equation 4.36.

$$P_{a1} = \frac{P_t}{\cos \psi} (-\sin \psi \cos \gamma_1 + \tan \phi \sin \gamma_1) \quad (4.35)$$

$$P_{r1} = \frac{P_t}{\cos \psi} (\sin \psi \sin \gamma_1 + \tan \phi \cos \gamma_1) \quad (4.36)$$

where subscript 1 refers to the driving gear, and γ_1 is the half-cone-included angle. For the geometries and rotational directions described in Figure 4.16b. The following equations apply:



Right-hand helix (RH)
Clockwise rotation (CW) Left-hand helix (LH)
Counterclockwise rotation (CCW)

FIGURE 4.16a Helix direction and direction of rotation for individual driving spiral bevel gears.

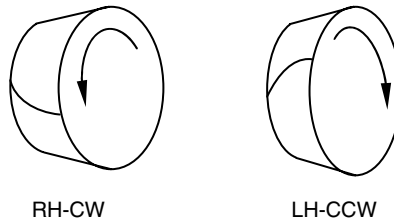


FIGURE 4.16b Helix direction and direction of rotation of individual driving spiral bevel gears.

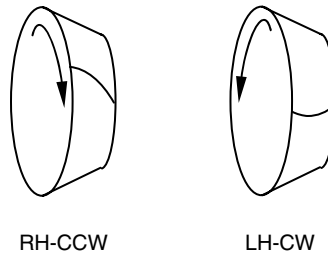


FIGURE 4.16c Helix direction and direction of rotation of individual driven spiral bevel gears.

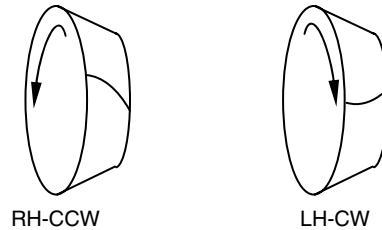


FIGURE 4.16d Helix direction and direction of rotation of individual driven spiral bevel gears.

$$P_{a1} = \frac{P_t}{\cos \psi} (\sin \psi \cos \gamma_1 + \tan \phi \sin \gamma_1) \quad (4.37)$$

$$P_{r1} = \frac{P_t}{\cos \psi} (-\sin \psi \sin \gamma_1 + \tan \phi \cos \gamma_1) \quad (4.38)$$

Considering the driven gear (subscript 2), and the geometries and rotational directions described in Figure 4.16c,

$$P_{a2} = \frac{P_t}{\cos \psi} (\sin \psi \cos \gamma_2 + \tan \phi \sin \gamma_2) \quad (4.39)$$

$$P_{r2} = \frac{P_t}{\cos \psi} (-\sin \psi \sin \gamma_2 + \tan \phi \cos \gamma_2) \quad (4.40)$$

whereas for the geometries and rotational directions described in Figure 4.16d, the following equations apply:

$$P_{a2} = \frac{P_t}{\cos \psi} (-\sin \psi \cos \gamma_2 + \tan \phi \sin \gamma_2) \quad (4.41)$$

$$P_{r2} = \frac{P_t}{\cos \psi} (\sin \psi \sin \gamma_2 + \tan \phi \cos \gamma_2) \quad (4.42)$$

4.3.3 HYPOID GEAR

Hypoid gears are used to transmit power between shafts whose axes of rotation do not intersect; that is, the shaft axes lie in different planes. Because of this arrangement, illustrated in Figure 4.17, a substantial amount of sliding occurs between contacting gear teeth, and the coefficient of sliding friction must be defined. For hypoid gears properly lubricated with a mineral or synthetic oil, the coefficient of friction $\mu \approx 0.1$ is representative. Similar to spiral bevel gears, the loading of the individual gears depends on the helix direction together with the direction of rotation. The equations for driving gear loads are given as functions of P , the resulting gear tooth load, which is defined by the following equation:

$$P = \frac{P_t}{\cos \phi \cos \psi_1 + \mu \sin \psi_1} \quad (4.43)$$

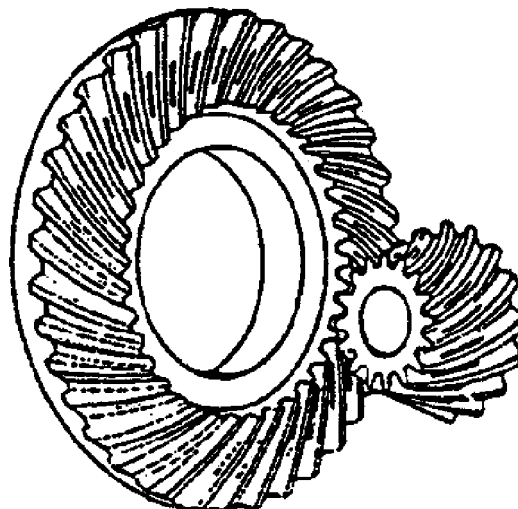


FIGURE 4.17 Hypoid gear mesh.

Considering the geometries and rotational conditions of [Figure 4.16a](#),

$$P_{a1} = P(-\cos \phi \sin \psi_1 \cos \gamma_1 + \sin \phi \sin \gamma_1 + \mu \cos \psi_1 \cos \gamma_1) \quad (4.44)$$

$$P_{r1} = P(\cos \phi \sin \psi_1 \sin \gamma_1 + \sin \phi \sin \gamma_1 - \mu \cos \psi_1 \sin \gamma_1) \quad (4.45)$$

whereas for the geometries and rotational conditions of [Figure 4.16b](#),

$$P_{a1} = P(\cos \phi \sin \psi_1 \cos \gamma_1 + \sin \phi \sin \gamma_1 - \mu \cos \psi_1 \cos \gamma_1) \quad (4.46)$$

$$P_{r1} = P(-\cos \phi \sin \psi_1 \sin \gamma_1 + \sin \phi \cos \gamma_1 + \mu \cos \psi_1 \sin \gamma_1) \quad (4.47)$$

The driven gear tooth loads are given by Equation 4.48 through Equation 4.51 for the geometries and rotational directions of [Figure 4.16c](#):

$$P_{a2} = P(\cos \phi \sin \psi_2 \cos \gamma_2 + \sin \phi \sin \gamma_2 - \mu \cos \psi_2 \cos \gamma_2) \quad (4.48)$$

$$P_{r2} = P(-\cos \phi \sin \psi_2 \sin \gamma_2 + \sin \phi \cos \gamma_2 + \mu \cos \psi_2 \sin \gamma_2) \quad (4.49)$$

whereas the geometries and rotational directions defined in [Figure 4.16d](#) are given by the following equations:

$$P_{a2} = P(-\cos \phi \sin \psi_2 \cos \gamma_2 + \sin \phi \sin \gamma_2 + \mu \cos \psi_2 \cos \gamma_2) \quad (4.50)$$

$$P_{r2} = P(\cos \phi \sin \psi_2 \sin \gamma_2 + \sin \phi \cos \gamma_2 - \mu \cos \psi_2 \sin \gamma_2) \quad (4.51)$$

4.3.4 WORM GEAR

Worm gearing, which may be regarded as a case of 90° crossed helical gears, is used to effect substantial reduction in speed within a single reduction set. Compared with hypoid gears, substantially more sliding occurs between the worm screw and the worm wheel teeth. [Figure 4.18](#) illustrates the loads transmitted in a worm gear drive. The lead angle λ of the worm thread at the pitch radius r_{pl} of the worm is defined in terms of the thread pitch h at that point and the friction coefficient by the following equation:

$$\tan \lambda = \frac{h}{2\mu r_{pl}} \quad (4.52)$$

Then, for the worm

$$P_{r1} = P_{t1} \frac{\sin \phi}{\cos \phi \sin \lambda + \mu \cos \lambda} \quad (4.53)$$

$$P_{a1} = P_{t1} \frac{\cos \phi - \mu \tan \lambda}{\mu + \cos \phi \tan \lambda} \quad (4.54)$$

For the worm wheel, the following relationships are true: $P_{t2} = P_{a1}$, $P_{r2} = P_{r1}$, and $P_{a2} = P_{t1}$.

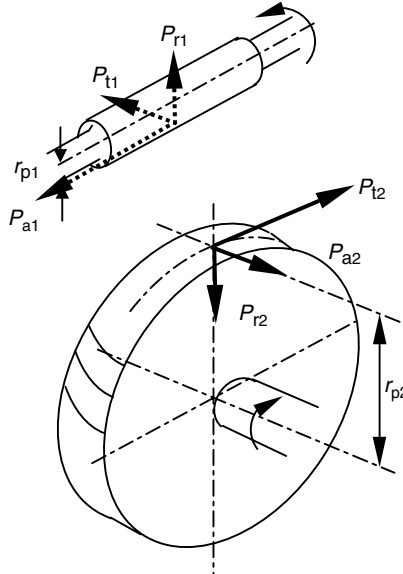


FIGURE 4.18 Schematic of tooth loading in a worm gear drive.

4.4 SHAFT SPEEDS

In some applications, only the input shaft speed is given; however, the performance of both input and output shaft bearings must be evaluated. In general, simple kinematic relationships relying on instant center concepts are used to determine the input–output speed relationship. Using the friction wheel shown in Figure 4.8, at the point of contact, the condition of no slippage is assumed, and therefore the surface velocity v of wheel 1 equals that of wheel 2. As $v = \omega r$,

$$\frac{\omega_2}{\omega_1} = \frac{n_2}{n_1} = \frac{r_1}{r_2} = \frac{D_1}{D_2} \quad (4.55)$$

The same relationship holds for pulleys and spur and helical gears.

For straight and helical bevel gears, the following equation applies:

$$\frac{n_2}{n_1} = \frac{r_{m1}}{r_{m2}} \quad (4.56)$$

where r_{m1} and r_{m2} are the mean pitch radii of gears 1 and 2, respectively. For hypoid gears,

$$\frac{n_2}{n_1} = \frac{r_{m1} \cos \psi_1}{r_{m2} \cos \psi_2} \quad (4.57)$$

For worm gearing,

$$\frac{n_2}{n_1} = \frac{Z_1}{Z_2} \quad (4.58)$$

where Z_1 is the number of threads on the worm and Z_2 is the number of teeth on the worm wheel.

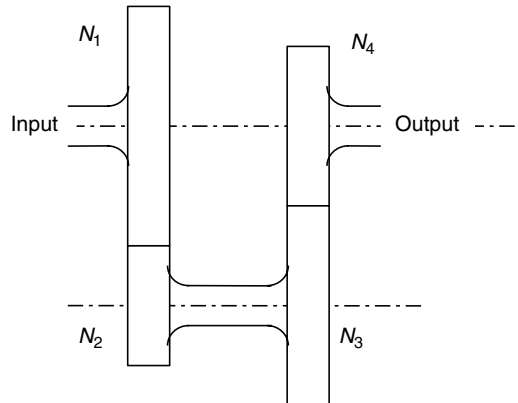


FIGURE 4.19 Simple four-gear train.

To achieve substantial speed reductions, gears are frequently combined in units called gear trains. Figure 4.19 illustrates a simple train composed of four gears. The train value is defined as the ratio of the output to input speeds; that is,

$$n_{\text{out}} = e n_{\text{in}} \quad (4.59)$$

It can be further demonstrated (see Ref. [1], etc.) that

$$e = \frac{r_{p1} \cdot r_{p3}}{r_{p2} \cdot r_{p4}} \quad (4.60)$$

More generally, for a train of several gears, the train value e is the ratio of the product of the pitch radii of the driving gears to the product of the pitch radii of the driven gears. (It is noted that the numbers of teeth can be substituted for the pitch radii.) Hence, the output shaft speed can be directly determined.

Planetary gear or epicyclic power transmissions are designed to achieve substantial speed reduction in a compact space. In its simplest form, the epicyclic transmission is shown schematically in Figure 4.20, in which R refers to the ring gear, P to the planet gear, and S to the sun gear. The sun gear is typically connected to the input shaft, and the output shaft is

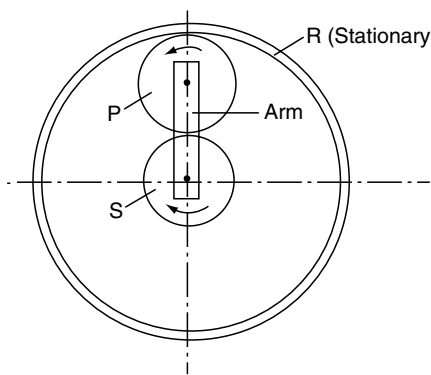


FIGURE 4.20 Schematic diagram of a simple epicyclic power transmission.

connected to the arm. In general, there are three or more planets; therefore, each planet gear shaft transmits one third or less of the input power. A single planet is shown in Figure 4.20 for the purpose of analysis of speeds. Using Figure 4.20, it can be seen that the speed of the sun gear relative to the arm is $n_{SA} = n_S - n_A$. Furthermore, the speed of the ring gear relative to the arm is $n_{RA} = n_R - n_A$. Therefore,

$$e = \frac{n_{RA}}{n_{SA}} = \frac{n_R - n_A}{n_S - n_A} \quad (4.61)$$

Now, by holding the arm stationary, allowing the ring gear to rotate as in a simple gear train, and applying Equation 4.60,

$$e = -\frac{r_{pS} \cdot r_{pP}}{r_{pP} \cdot r_{pR}} = -\frac{r_{pS}}{r_{pR}} \quad (4.62)$$

The minus sign in Equation 4.62 denotes that the ring gear (output) rotates in the opposite direction with regard to the sun gear (input). Using Equation 4.61 and Equation 4.62, setting $n_R = 0$ and rearranging yields the expression for the output shaft speed. Subsequently, the planet gear shaft speed can be determined:

$$n_A = n_S \left(\frac{1}{\frac{r_{pR}}{r_{pS}} + 1} \right) \quad (4.63)$$

Planetary gear transmission configurations are too numerous and varied to provide equations to calculate speeds for each case; however, the calculational method indicated herein is universally valid and may be applied.

4.5 DISTRIBUTED LOAD SYSTEMS

Sometimes the load is distributed over a portion of the shaft as in a rolling mill application. In general, this type of loading may be illustrated as in Figure 4.21. If the loading is irregular, then it may be considered as a series of loads P^k , each acting at its individual distance a^k from the left-hand bearing support. Equation 4.9 and Equation 4.10 may then be used to evaluate

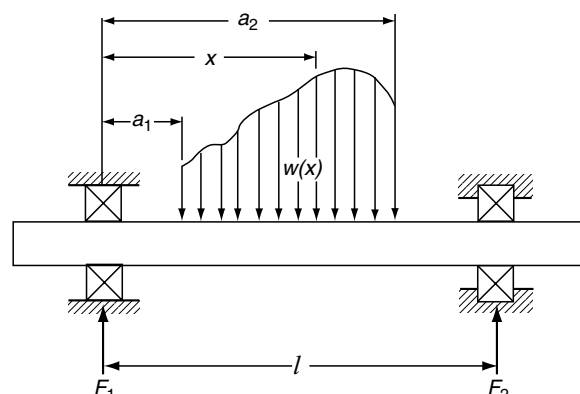


FIGURE 4.21 Simple two-bearing-shaft system, continuous loading.

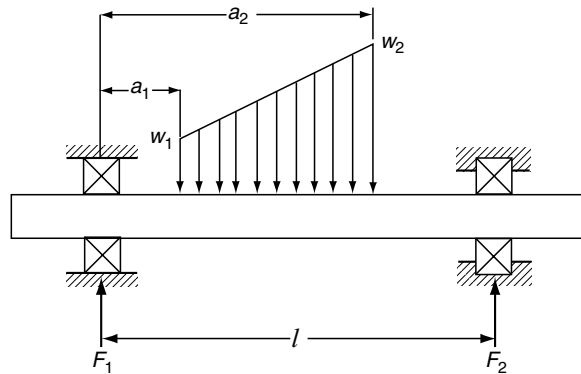


FIGURE 4.22 Simple two-bearing-shaft system, uniform continuous loading.

reactions F_1 and F_2 . For a distributed load for which the load per unit length w may be expressed by a continuous function, for example, $w = w_o \sin(x)$ or $w = w_o(1+bx)$, [Equation 4.9](#) and [Equation 4.10](#) become (see Figure 4.22)

$$F_1 = \int \left(1 + \frac{x}{l}\right) w \, dx \quad (4.64)$$

$$F_2 = \int w \frac{x}{l} \, dx \quad (4.65)$$

4.6 CLOSURE

In this chapter, methods and equations have been provided to calculate bearing loads in statically determinate shaft-bearing systems. These methods are adequate for performance analysis of ball and roller bearings in most applications. Also, methods and equations have been provided to estimate the loading transmitted through the shaft to its bearing supports resulting from various common power transmission, machine elements. Many applications are, however, more sophisticated than those covered in this chapter.

These may involve statically indeterminate systems, covered in the Second Volume of this handbook, and increased complexity of system loading, which can only be determined by detailed evaluation of the specific application.

REFERENCES

1. Spotts, M. and Shoup, T., *Design of Machine Elements*, 7th Ed., Prentice Hall, Englewood Cliffs, NJ, 1998.
2. Juvinall, R. and Marshek, K., *Fundamentals of Machine Component Design*, 2nd Ed., Wiley, New York, 1991.
3. Hamrock, B., Jacobson, B., and Schmid, S., *Fundamentals of Machine Elements*, McGraw-Hill, New York, 1999.
4. Avallone, E. and Baumeister, T., *Mark's Standard Handbook for Mechanical Engineers*, 9th Ed., McGraw-Hill, New York, 1987.

5 Ball and Roller Loads Due to Bearing Applied Loading

LIST OF SYMBOLS

Symbol	Description	Units
D	Ball or roller diameter	mm (in.)
d_m	Pitch diameter	mm (in.)
h	Span between cylindrical roller axial forces	mm (in.)
l	Roller length	mm (in.)
l_{eff}	Effective length of roller–raceway contact	mm (in.)
q	Roller–raceway load per unit length	N/mm (lb/in.)
Q	Ball or roller normal load	N (lb)
Q_r	Radial direction load on ball or roller	N (lb)
Q_a	Axial direction load on ball or roller	N (lb)
x	Coordinate direction distance	mm (in.)
α	Contact angle	°, rad
μ	Coefficient of friction	
ξ	Roller skewing angle	rad

Subscripts

a	Axial direction
f	Guide flange
i	Inner raceway
o	Outer raceway
r	Radial direction

5.1 GENERAL

The loads applied to ball and roller bearings are transmitted through the rolling elements from the inner ring to the outer ring or vice versa. The magnitude of the loading carried by the individual ball or roller depends on the internal geometry of the bearing and on the type of load applied to it. In addition to applied loading, rolling elements are subjected to inertial, that is dynamic, loading due to speed effects. Most calculations of ball and roller bearing performance, however, tend to consider only the applied loading when bearing operating speeds are nominal. The objective of this chapter is to define the rolling element loading under this condition, which might also be termed static loading.

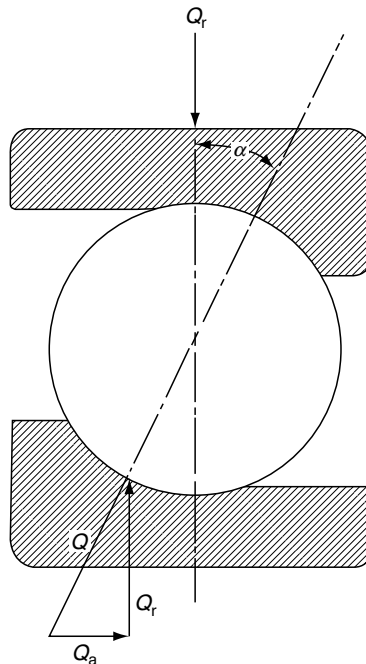


FIGURE 5.1 Radially loaded ball.

5.2 BALL–RACEWAY LOADING

A rolling element can support a normal load along the line of contact between the rolling element and the raceway (see Figure 5.1). If a radial load Q_r is applied to the ball in Figure 5.1, then the normal load supported by the ball is

$$Q = \frac{Q_r}{\cos \alpha} \quad (5.1)$$

Hence, a thrust load of magnitude

$$Q_a = Q \sin \alpha \quad (5.2)$$

or

$$Q_a = Q_r \tan \alpha \quad (5.3)$$

is induced in the assembly.

See Example 5.1 and Example 5.2.

5.3 SYMMETRICAL SPHERICAL ROLLER–RACEWAY LOADING

Equation 5.2 and Equation 5.3 are also valid for spherical roller bearings using symmetrical contour (barrel-shaped) rollers. For a double-row spherical roller bearing under an applied radial load, the induced roller thrust loads are self-equilibrating ([see Figure 5.2](#)).

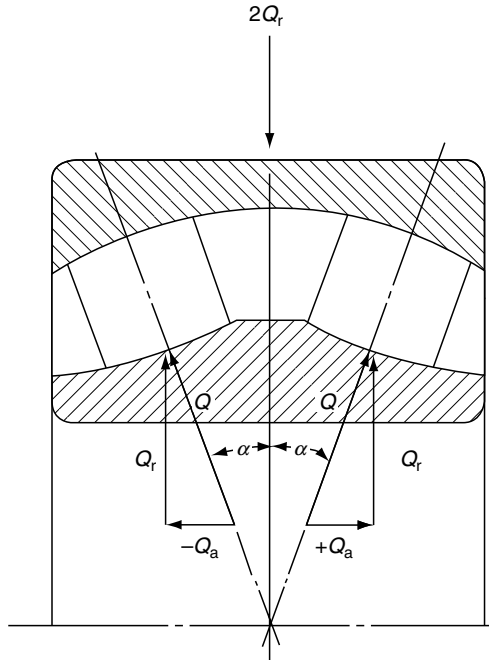


FIGURE 5.2 Radially loaded symmetrical rollers.

5.4 TAPERED AND ASYMMETRICAL Spherical ROLLER-RACEWAY AND ROLLER-FLANGE LOADING

Spherical roller bearings with asymmetrical contour rollers and tapered roller bearings usually have a fixed guide flange on the bearing inner ring. This flange, as shown in Figure 5.3, is subjected to loading through the roller ends. If a radial load Q_{ir} is applied to the assembly, the following loading occurs:

$$Q_i = \frac{Q_{ir}}{\cos \alpha_i} \quad (5.4)$$

$$Q_{ia} = Q_{ir} \tan \alpha_i \quad (5.5)$$

For static equilibrium, the sum of forces in any direction is equal to zero; therefore,

$$Q_{ir} - Q_{fr} - Q_{or} = 0 \quad (5.6)$$

$$Q_{ia} + Q_{fa} - Q_{oa} = 0 \quad (5.7)$$

or

$$Q_{ir} - Q_f \cos \alpha_f - Q_o \cos \alpha_o = 0 \quad (5.8)$$

$$Q_{ir} \tan \alpha_i + Q_f \sin \alpha_f - Q_o \sin \alpha_o = 0 \quad (5.9)$$

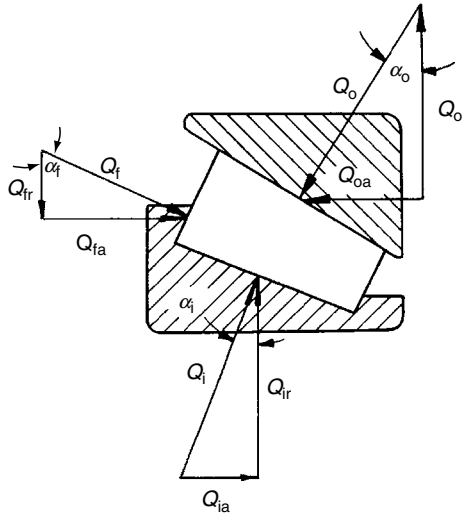


FIGURE 5.3 Radially loaded asymmetrical roller.

Solving Equation 5.8 and Equation 5.9 for Q_o and Q_f yields

$$Q_o = Q_{ir} \frac{(\sin \alpha_f + \tan \alpha_i \cos \alpha_f)}{\sin(\alpha_o + \alpha_f)} \quad (5.10)$$

$$Q_f = Q_{ir} \frac{(\sin \alpha_o - \tan \alpha_i \cos \alpha_f)}{\sin(\alpha_o + \alpha_f)} \quad (5.11)$$

The thrust load induced by the applied radial load is

$$Q_{oa} = Q_{ir} \frac{\sin \alpha_o}{\sin(\alpha_o + \alpha_f)} (\sin \alpha_f + \tan \alpha_i \cos \alpha_f) \quad (5.12)$$

Under an applied thrust load Q_{ia} , the following equations of load obtain, considering static equilibrium:

$$Q_o = Q_{ia} \frac{(\cos \alpha_f + \operatorname{ctn} \alpha_i \sin \alpha_f)}{\sin(\alpha_o + \alpha_f)} \quad (5.13)$$

$$Q_f = Q_{ia} \frac{(\operatorname{ctn} \alpha_i \sin \alpha_o - \cos \alpha_o)}{\sin(\alpha_o + \alpha_f)} \quad (5.14)$$

See Example 5.3.

5.5 CYLINDRICAL ROLLER–RACEWAY LOADING

5.5.1 RADIAL LOADING

As illustrated in Figure 5.4, a cylindrical roller under simple applied radial load carries the same radial load at both inner raceway–roller and outer raceway–roller contacts; that is, $Q_i = Q_o = Q$. In this case, the load is ideally considered to be distributed uniformly along l_{eff} ,

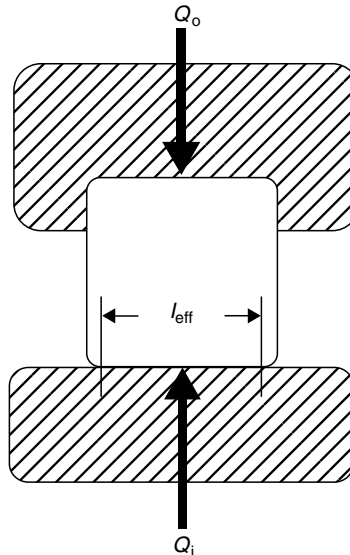


FIGURE 5.4 Cylindrical roller–raceway loading under simple applied radial load.

the effective length of the contact, as shown in Figure 5.5. The roller–raceway load per unit length $q = Q/l_{\text{eff}}$ at each raceway, or $Q = q \cdot l_{\text{eff}}$.

In Figure 5.4, the bearing outer ring has two roller guide flanges, and the inner ring has none. This means a thrust (axial) load will cause the bearing rings to separate. If, however, the inner ring is also equipped with a guide flange, as illustrated in Figure 1.37, the bearing can carry some axial load, provided it simultaneously supports a substantially larger radial load. Figure 5.6 illustrates the radial and axial loadings of a roller in such a bearing. To accommodate the axial load, the roller will tilt due to moment couple $Q_a h$ caused by the opposing axial loads. For a straight–raceway contact, this results in the nonuniform load distribution illustrated in Figure 5.6. It is apparent from this axial load distribution that rolling element–raceway contact load is

$$Q = \int_0^{l_{\text{eff}}} q dx \quad (5.15)$$

Designating the minimum load per unit length as q_0 and the maximum as q_i , it is apparent that $q_i > q$, the uniform load per unit length associated with the ideal loading. This results in increased contact stress and reduced endurance. This situation will be discussed in detail in Chapters 1 and 8 in the First VolumeI of this handbook. Because cylindrical rollers usually

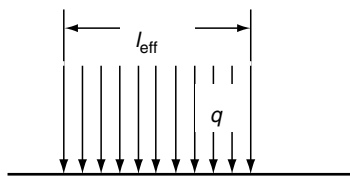


FIGURE 5.5 Uniform loading of cylindrical roller on inner raceway under applied radial load, ideal loading with straight profile rollers.

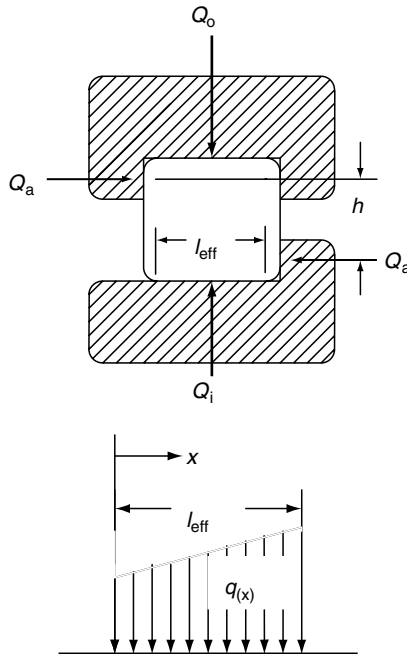


FIGURE 5.6 Loading of cylindrical roller on inner raceway under applied combined radial and axial loads, loading with straight profile rollers (no edge loading).

have a crowned profile as illustrated in Figure 1.38, the axial load distribution across the contact is generally less severe than that shown in Figure 5.6 (see Figure 5.7). Chapter 1 in the Second Volume of this handbook will investigate this condition in detail.

5.5.2 ROLLER SKEWING MOMENT

Because of the sliding motion between the roller ends and the ring flanges, friction occurs at these locations. Assuming each of these friction forces can be represented simply by a coefficient of friction μQ_a , a moment, is generated, that is, $\mu Q_a l$, in which l is the roller length from end-to-end (see Figure 5.8).

A detailed analysis of roller skewing is presented in [Chapter 3](#) the Second Volume of this handbook; however, it is important to note that the purpose of the guide flange is to minimize

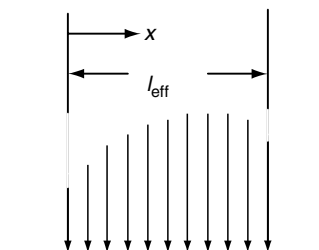


FIGURE 5.7 Loading of cylindrical roller on inner raceway under applied combined radial and axial loads, loading with crowned profile rollers.

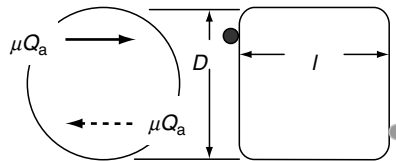


FIGURE 5.8 Schematic diagram of friction forces between roller ends and ring flanges. (The black dot represents a force vector passing into the page; the gray dot represents a force vector coming out of the page.)

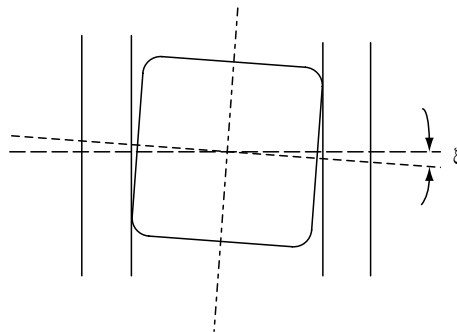


FIGURE 5.9 Roller skewing angle ξ limited by axial clearance between roller and guide flanges.

skewing by providing minimum clearance between the roller ends and ring flanges. This is illustrated in Figure 5.9.

5.6 CLOSURE

To analyze rolling bearing performance in an application, it is necessary to determine the load on individual balls or rollers. How well the balls or rollers accept the applied loads will determine the bearing endurance in most applications. For example, a light radial load applied to a 90° contact angle thrust bearing can cause the bearing to fail rapidly. Similarly, a thrust load applied to a 0° contact angle radial ball bearing is greatly magnified according to the final contact angle that obtains. In Chapter 7, the distribution of applied load among balls and rollers will be discussed. It will be shown that the manner in which each rolling element accepts its load will determine the loading of all others. In angular-contact ball bearings, the ball loading can affect ball and cage speeds significantly. This chapter is therefore fundamental even to a rudimentary analysis of a rolling bearing application.

6 Contact Stress and Deformation

LIST OF SYMBOLS

Symbol	Description	Units
a	Semimajor axis of the projected contact	mm (in.)
a^*	Dimensionless semimajor axis of contact ellipse	
b	Seminor axis of the projected contact ellipse	mm (in.)
b^*	Dimensionless semiminor axis of contact ellipse	
E	Modulus of elasticity	MPa (psi)
E	Complete elliptic integral of the second kind	
$E(\phi)$	Elliptic integral of the second kind	
F	Complete elliptic integral of the first kind	
$F(\phi)$	Elliptic integral of the first kind	
F	Force	N (lb)
G	Shear modulus of elasticity	MPa (psi)
l	Roller effective length	mm (in.)
Q	Normal force between rolling element and raceway	N (lb)
r	Radius of curvature	mm (in.)
S	Principal stress	MPa (psi)
u	Deflection in x direction	mm (in.)
U	Arbitrary function	
v	Deflection in y direction	mm (in.)
V	Arbitrary function	
w	Deflection in z direction	mm (in.)
x	Principal direction distance	mm (in.)
X	Dimensionless parameter	
y	Principal direction distance	mm (in.)
Y	Dimensionless parameter	
z	Principal direction distance	mm (in.)
z_1	Depth to maximum shear stress at $x=0, y=0$	mm (in.)
z_0	Depth to maximum reversing shear stress $y \neq 0, x=0$	mm (in.)
Z	Dimensionless parameter	
γ	Shear strain	
δ	Deformation	mm (in.)
δ^*	Dimensionless contact deformation	
ε	Linear strain	
ζ	z/b , roller tilting angle	°, rad
θ	Angle	rad

ϑ	Auxiliary angle	rad
κ	a/b	
λ	Parameter	
ξ	Poisson's ratio	
σ	Normal stress	MPa (psi)
τ	Shear stress	MPa (psi)
ν	Auxiliary angle	rad
ϕ	Auxiliary angle	rad or $^\circ$
$F(\rho)$	Curvature difference	
$\Sigma\rho$	Curvature sum	mm ⁻¹ (in. ⁻¹)

Subscripts

i	Inner raceway
o	Outer raceway
r	Radial direction
x	x Direction
y	y Direction
z	z Direction
yz	yz Plane
xz	xz Plane
I	Contact body I
II	Contact body II

6.1 GENERAL

Loads acting between the rolling elements and raceways in rolling bearings develop only small areas of contact between the mating members. Consequently, although the elemental loading may only be moderate, stresses induced on the surfaces of the rolling elements and raceways are usually large. It is not uncommon for rolling bearings to operate continuously with normal stresses exceeding 1,380 N/mm² (200,000 psi) compression on the rolling surfaces. In some applications and during endurance testing, normal stresses on rolling surfaces may exceed 3,449 N/mm² (500,000 psi) compression. As the effective area over which a load is supported rapidly increases with the depth below a rolling surface, the high compressive stress occurring at the surface does not permeate the entire rolling member. Therefore, bulk failure of rolling members is generally not a significant factor in rolling bearing design; however, destruction of the rolling surfaces is. This chapter is therefore concerned only with the determination of surface stresses and stresses occurring near the surface. Contact deformations are caused by contact stresses. Because of the rigid nature of the rolling members, these deformations are generally of a low order of magnitude, for example 0.025 mm (0.001 in.) or less in steel bearings. It is the purpose of this chapter to develop relationships permitting the determination of contact stresses and deformations in rolling bearings.

6.2 THEORY OF ELASTICITY

The classical solution for the local stress and deformation of two elastic bodies apparently contacting at a single point was established by Hertz [1] in 1896. Today, contact stresses are frequently called Hertzian or simply Hertz stresses in recognition of his accomplishment.

To develop the mathematics of contact stresses, one must have a firm foundation in the principles of mechanical elasticity. It is, however, not the purpose of this text to teach theory

of elasticity and therefore only a rudimentary discussion of that discipline is presented herein to demonstrate the complexity of contact stress problems. In this light, consider an infinitesimal cube of an isotropic homogeneous elastic material subjected to the stresses shown in Figure 6.1. Considering the stresses acting in the x direction and in the absence of body forces, static equilibrium requires that

$$\begin{aligned}\sigma_x \, dz \, dy + \tau_{xy} \, dx \, dz + \tau_{xz} \, dx \, dy - \left(\sigma_x + \frac{\partial \sigma_x}{\partial x} \, dx \right) dz \, dy \\ - \left(\tau_{xy} + \frac{\partial \tau_{xy}}{\partial y} \, dy \right) dx \, dz - \left(\tau_{xz} + \frac{\partial \tau_{xz}}{\partial z} \, dz \right) dx \, dy = 0\end{aligned}\quad (6.1)$$

Therefore,

$$\frac{\partial \sigma_x}{\partial x} + \frac{\partial \tau_{xy}}{\partial y} + \frac{\partial \tau_{xz}}{\partial z} = 0 \quad (6.2)$$

Similarly, for the y and z directions, respectively,

$$\frac{\partial \sigma_y}{\partial y} + \frac{\partial \tau_{xy}}{\partial x} + \frac{\partial \tau_{yz}}{\partial z} = 0 \quad (6.3)$$

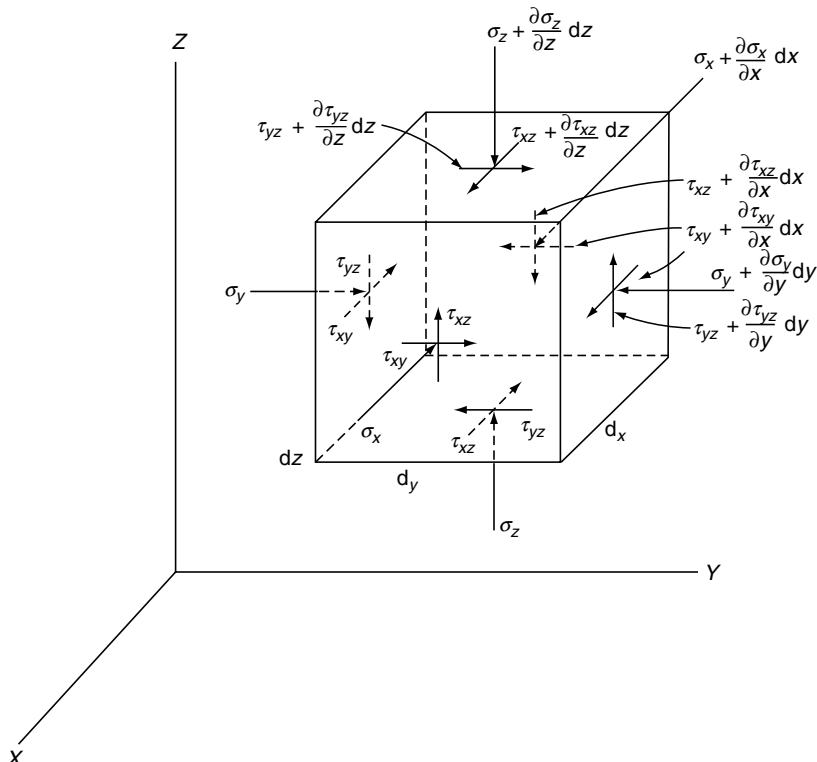


FIGURE 6.1 Stresses acting on an infinitesimal cube of material under load.

$$\frac{\partial \sigma_z}{\partial z} + \frac{\partial \tau_{xz}}{\partial x} + \frac{\partial \tau_{yz}}{\partial y} = 0 \quad (6.4)$$

[Equation 6.2](#) through [Equation 6.4](#) are the equations of equilibrium in Cartesian coordinates. Hooke's law for an elastic material states that within the proportional limit

$$\varepsilon = \frac{\sigma}{E} \quad (6.5)$$

where ε is the strain and E is the modulus of elasticity of the strained material. If u , v , and w are the deflections in the x , y , and z directions, respectively, then

$$\begin{aligned}\varepsilon_x &= \frac{\partial u}{\partial x} \\ \varepsilon_y &= \frac{\partial v}{\partial y} \\ \varepsilon_z &= \frac{\partial w}{\partial z}\end{aligned} \quad (6.6)$$

If instead of an elongation or compression, the sides of the cube undergo relative rotation such that the sides in the deformed conditions are no longer mutually perpendicular, then the rotational strains are given as

$$\begin{aligned}\gamma_{xy} &= \frac{\partial u}{\partial y} + \frac{\partial v}{\partial x} \\ \gamma_{xz} &= \frac{\partial u}{\partial z} + \frac{\partial w}{\partial x} \\ \gamma_{yz} &= \frac{\partial v}{\partial z} + \frac{\partial w}{\partial y}\end{aligned} \quad (6.7)$$

When a tensile stress σ_x is applied to two faces of a cube, then in addition to an extension in the x direction, a contraction is produced in the y and z directions as follows:

$$\begin{aligned}\varepsilon_x &= \frac{\sigma_x}{E} \\ \varepsilon_y &= -\frac{\xi \sigma_x}{E} \\ \varepsilon_z &= -\frac{\xi \sigma_x}{E}\end{aligned} \quad (6.8)$$

In [Equation 6.8](#), ξ is the Poisson's ratio; for steel $\xi \approx 0.3$.

Now, the total strain in each principal direction due to the action of normal stresses σ_x , σ_y , and σ_z is the total of the individual strains. Hence,

$$\begin{aligned}\varepsilon_x &= \frac{1}{E} [\sigma_x - \xi(\sigma_y + \sigma_z)] \\ \varepsilon_y &= \frac{1}{E} [\sigma_y - \xi(\sigma_x + \sigma_z)] \\ \varepsilon_z &= \frac{1}{E} [\sigma_z - \xi(\sigma_x + \sigma_y)]\end{aligned} \quad (6.9)$$

[Equations 6.9](#) were obtained by the method of superposition.

In accordance with Hooke's law, it can further be demonstrated that shear stress is related to shear strain as follows:

$$\begin{aligned}\gamma_{xy} &= \frac{\tau_{xy}}{G} \\ \gamma_{xz} &= \frac{\tau_{xz}}{G} \\ \gamma_{yz} &= \frac{\tau_{yz}}{G}\end{aligned}\quad (6.10)$$

where G is the modulus of elasticity in the shear and it is defined as

$$G = \frac{E}{2(1 + \xi)} \quad (6.11)$$

One further defines the volume expansion of the cube as follows:

$$\varepsilon = \varepsilon_x + \varepsilon_y + \varepsilon_z \quad (6.12)$$

Combining Equation 6.9, Equation 6.11, and Equation 6.12, one obtains for normal stresses

$$\begin{aligned}\sigma_x &= 2G\left(\frac{\partial u}{\partial x} + \frac{\xi}{1 - 2\xi}\varepsilon\right) \\ \sigma_y &= 2G\left(\frac{\partial v}{\partial y} + \frac{\xi}{1 - 2\xi}\varepsilon\right) \\ \sigma_z &= 2G\left(\frac{\partial w}{\partial z} + \frac{\xi}{1 - 2\xi}\varepsilon\right)\end{aligned}\quad (6.13)$$

Finally, a set of "compatibility" conditions can be developed by differentiation of the strain relationships, both linear and rotational, and substituting in the equilibrium [Equation 6.2](#) through [Equation 6.4](#):

$$\begin{aligned}\nabla^2 u + \frac{1}{1 - 2\xi} \frac{\partial \varepsilon}{\partial x} &= 0 \\ \nabla^2 v + \frac{1}{1 - 2\xi} \frac{\partial \varepsilon}{\partial y} &= 0 \\ \nabla^2 w + \frac{1}{1 - 2\xi} \frac{\partial \varepsilon}{\partial z} &= 0\end{aligned}\quad (6.14)$$

where

$$\nabla^2 = \frac{\partial^2}{\partial x^2} + \frac{\partial^2}{\partial y^2} + \frac{\partial^2}{\partial z^2} \quad (6.15)$$

Equations 6.14 represent a set of conditions that by using the known stresses acting on a body must be solved to determine the subsequent strains and internal stresses of that body. See Timoshenko and Goodier [2] for a detailed presentation.

6.3 SURFACE STRESSES AND DEFORMATIONS

Using polar coordinates rather than Cartesian ones, Boussinesq [3] in 1892 solved the simple radial distribution of stress within a semiinfinite solid as shown in Figure 6.2. With the boundary condition of a surface free of shear stress, the following solution was obtained for radial stress:

$$\sigma_r = -\frac{2F \cos \theta}{\pi r} \quad (6.16)$$

It is apparent from Equation 6.16 that as r approaches 0, σ_r becomes infinitely large. It is further apparent that this condition cannot exist without causing gross yielding or failure of the material at the surface.

Hertz reasoned that instead of a point or line contact, a small contact area must form, causing the load to be distributed over a surface, and thus alleviating the condition of infinite stress. In performing his analysis, he made the following assumptions:

1. The proportional limit of the material is not exceeded, that is, all deformation occurs in the elastic range.
2. Loading is perpendicular to the surface, that is, the effect of surface shear stresses is neglected.
3. The contact area dimensions are small compared with the radii of curvature of the bodies under load.
4. The radii of curvature of the contact areas are very large compared with the dimensions of these areas.

The solution of theoretical problems in elasticity is based on the assumption of a stress function or functions that fit the compatibility equations and the boundary conditions singly or in combination. For stress distribution in a semiinfinite elastic solid, Hertz introduced the assumptions:

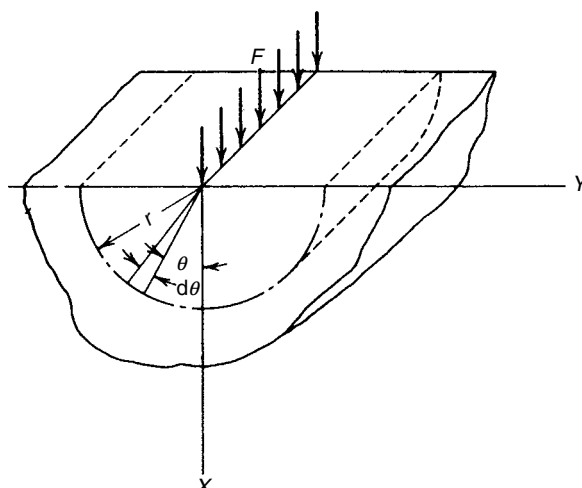


FIGURE 6.2 Model for Boussinesq analysis.

$$\begin{aligned} X &= \frac{x}{b} \\ Y &= \frac{y}{b} \\ Z &= \frac{z}{b} \end{aligned} \quad (6.17)$$

where b is an arbitrary fixed length and hence, X , Y , and Z are dimensionless parameters. Also,

$$\begin{aligned} \frac{u}{c} &= \frac{\partial U}{\partial X} - Z \frac{\partial V}{\partial X} \\ \frac{v}{c} &= \frac{\partial U}{\partial Y} - Z \frac{\partial V}{\partial Y} \\ \frac{w}{c} &= \frac{\partial U}{\partial Z} - Z \frac{\partial V}{\partial Z} + V \end{aligned} \quad (6.18)$$

where c is an arbitrary length such that the deformations u/c , v/c , and w/c are dimensionless. U and V are arbitrary functions of X and Y only such that

$$\begin{aligned} \nabla^2 U &= 0 \\ \nabla^2 V &= 0 \end{aligned} \quad (6.19)$$

Furthermore, b and c are related to U as follows:

$$\frac{b\varepsilon}{c} = -2 \frac{\partial^2 U}{\partial Z^2} \quad (6.20)$$

These assumptions, which are partly intuitive and partly based on experience, when combined with elasticity relationships ([Equation 6.7](#), [Equation 6.10](#), and [Equation 6.12](#) through [Equation 6.14](#)) yield the following expressions:

$$\begin{aligned} \frac{\sigma_x}{\sigma_0} &= Z \frac{\partial^2 V}{\partial X^2} - \frac{\partial^2 U}{\partial X^2} - 2 \frac{\partial V}{\partial Z} \\ \frac{\sigma_y}{\sigma_0} &= Z \frac{\partial^2 V}{\partial Y^2} - \frac{\partial^2 U}{\partial Y^2} - 2 \frac{\partial V}{\partial Z} \\ \frac{\sigma_z}{\sigma_0} &= Z \frac{\partial^2 V}{\partial Z^2} - \frac{\partial V}{\partial Z} \\ \frac{\tau_{xy}}{\sigma_0} &= Z \frac{\partial^2 V}{\partial X \partial Y} - \frac{\partial^2 U}{\partial X \partial Y} \\ \frac{\tau_{xz}}{\sigma_0} &= Z \frac{\partial^2 V}{\partial X \partial Z} \\ \frac{\tau_{yz}}{\sigma_0} &= \frac{\partial^2 V}{\partial Y \partial Z} \end{aligned} \quad (6.21)$$

where

$$\sigma_0 = (-2Gc)/b \quad \text{and} \quad U = (1 - 2\xi) \int_z^\infty V(X, Y, \xi) d\xi$$

From the preceding formulas, the stresses and deformations may be determined for a semiinfinite body limited by the xy plane on which $\tau_{xz} = \tau_{yz} = 0$ and σ_z is finite on the surface, that is, at $z = 0$.

Hertz's last assumption was that the shape of the deformed surface was that of an ellipsoid of revolution. The function V was expressed as follows:

$$V = \frac{1}{2} \int_{S_0}^{\infty} \frac{\left(1 - \frac{X^2}{\kappa^2 + S^2} - \frac{Y^2}{1 + S^2} - \frac{Z^2}{S^2}\right)}{\sqrt{(\kappa^2 + S^2)(1 + S^2)}} \kappa dS \quad (6.22)$$

where S_0 is the largest positive root of the equation

$$\frac{X^2}{\kappa^2 + S_0^2} + \frac{Y^2}{1 + S_0^2} + \frac{Z^2}{S_0^2} = 1 \quad (6.23)$$

and

$$\kappa = a/b \quad (6.24)$$

Here, a and b are the semimajor and semiminor axes of the projected elliptical area of contact. For an elliptical contact area, the stress at the geometrical center is

$$\sigma_0 = -\frac{3Q}{2\pi ab} \quad (6.25)$$

The arbitrary length c is defined by

$$c = \frac{3Q}{4\pi Ga} \quad (6.26)$$

Then, for the special case $\kappa = \infty$,

$$\sigma_0 = -\frac{2Q}{\pi b} \quad (6.27)$$

$$c = \frac{Q}{\pi G} \quad (6.28)$$

As the contact surface is assumed to be relatively small compared with the dimensions of the bodies, the distance between the bodies may be expressed as

$$z = \frac{x^2}{2r_x} + \frac{y^2}{2r_y} \quad (6.29)$$

where r_x and r_y are the principal radii of curvature.

Introducing the auxiliary quantity $F(\rho)$ as determined by Equation 2.26, this is found to be a function of the elliptical parameters a and b as follows:

$$F(\rho) = \frac{(\kappa^2 + 1)\mathbf{E} - 2\mathbf{F}}{(\kappa^2 - 1)\mathbf{E}} \quad (6.30)$$

where F and E are the complete elliptic integrals of the first and second kind, respectively,

$$F = \int_0^{\pi/2} \left[1 - \left(1 - \frac{1}{\kappa^2} \right) \sin^2 \phi \right]^{-1/2} d\phi \quad (6.31)$$

$$E = \int_0^{\pi/2} \left[1 - \left(1 - \frac{1}{\kappa^2} \right) \sin^2 \phi \right]^{1/2} d\phi \quad (6.32)$$

By assuming the values of the elliptical eccentricity parameter κ , it is possible to calculate corresponding values of $F(\rho)$ and thus create a table of κ vs. $F(\rho)$.

Brewer and Hamrock [4], using a least squares method of linear regression, obtained simplified approximations for κ , F , and E . These equations are:

$$\kappa \approx 1.0339 \left(\frac{R_y}{R_x} \right)^{0.636} \quad (6.33)$$

$$E \approx 1.0003 + \frac{0.5968}{\left(\frac{R_y}{R_x} \right)} \quad (6.34)$$

$$F \approx 1.5277 + 0.6023 \ln \left(\frac{R_y}{R_x} \right) \quad (6.35)$$

For $1 \leq \kappa \leq 10$, the errors in the calculation of κ are less than 3%, errors on E are essentially nil except at $\kappa = 1$ and vicinity where they are less than 2%, and errors on F are essentially nil except at $\kappa = 1$ and vicinity, where they are less than 2.6%. The directional equivalent radii R are defined by

$$R_x^{-1} = \rho_{xI} + \rho_{xII} \quad (6.36)$$

$$R_y^{-1} = \rho_{yI} + \rho_{yII} \quad (6.37)$$

where subscript x refers to the direction of the major axis of the contact and y refers to the minor axis direction.

Recall that $F(\rho)$ is a function of curvature of contacting bodies:

$$F(\rho) = \frac{(\rho_{II} - \rho_{I2}) + (\rho_{III} - \rho_{II2})}{\Sigma \rho} \quad (2.26)$$

It was further determined that

$$a = a^* \left[\frac{3Q}{2\Sigma\rho} \left(\frac{(1 - \xi_I^2)}{E_I} + \frac{(1 - \xi_{II}^2)}{E_{II}} \right) \right]^{1/3} \quad (6.38)$$

$$= 0.0236a^* \left(\frac{Q}{\Sigma\rho} \right)^{1/3} \quad (\text{for steel bodies}) \quad (6.39)$$

$$b = b^* \left[\frac{3Q}{2\Sigma\rho} \left(\frac{(1 - \xi_I^2)}{E_I} + \frac{(1 - \xi_{II}^2)}{E_{II}} \right) \right]^{1/3} \quad (6.40)$$

$$= 0.0236b^* \left(\frac{Q}{\Sigma\rho} \right)^{1/3} \quad (\text{for steel bodies}) \quad (6.41)$$

$$\delta = \delta^* \left[\frac{3Q}{2\Sigma\rho} \left(\frac{(1 - \xi_{\text{I}}^2)}{E_{\text{I}}} + \frac{(1 - \xi_{\text{II}}^2)}{E_{\text{II}}} \right) \right]^{2/3} \frac{\Sigma\rho}{2} \quad (6.42)$$

$$= 2.79 \times 10^{-4} \delta^* Q^{2/3} \Sigma\rho^{1/3} \quad (\text{for steel bodies}) \quad (6.43)$$

where δ is the relative approach of remote points in the contacting bodies and

$$a^* = \left(\frac{2\kappa^2 E}{\pi} \right)^{1/3} \quad (6.44)$$

$$b^* = \left(\frac{2E}{\pi\kappa} \right)^{1/3} \quad (6.45)$$

$$\delta^* = \frac{2F}{\pi} \left(\frac{\pi}{2\kappa^2 E} \right)^{1/3} \quad (6.46)$$

Values of the dimensionless quantities a^* , b^* , and δ^* as functions of $F(\rho)$ are given in Table 6.1. The values of Table 6.1 are also plotted in [Figure 6.3](#) through [Figure 6.5](#).

TABLE 6.1
Dimensionless Contact Parameters

$F(\rho)$	a^*	b^*	δ^*
0	1	1	1
0.1075	1.0760	0.9318	0.9974
0.3204	1.2623	0.8114	0.9761
0.4795	1.4556	0.7278	0.9429
0.5916	1.6440	0.6687	0.9077
0.6716	1.8258	0.6245	0.8733
0.7332	2.011	0.5881	0.8394
0.7948	2.265	0.5480	0.7961
0.83495	2.494	0.5186	0.7602
0.87366	2.800	0.4863	0.7169
0.90999	3.233	0.4499	0.6636
0.93657	3.738	0.4166	0.6112
0.95738	4.395	0.3830	0.5551
0.97290	5.267	0.3490	0.4960
0.983797	6.448	0.3150	0.4352
0.990902	8.062	0.2814	0.3745
0.995112	10.222	0.2497	0.3176
0.997300	12.789	0.2232	0.2705
0.9981847	14.839	0.2072	0.2427
0.9989156	17.974	0.18822	0.2106
0.9994785	23.55	0.16442	0.17167
0.9998527	37.38	0.13050	0.11995
1	∞	0	0

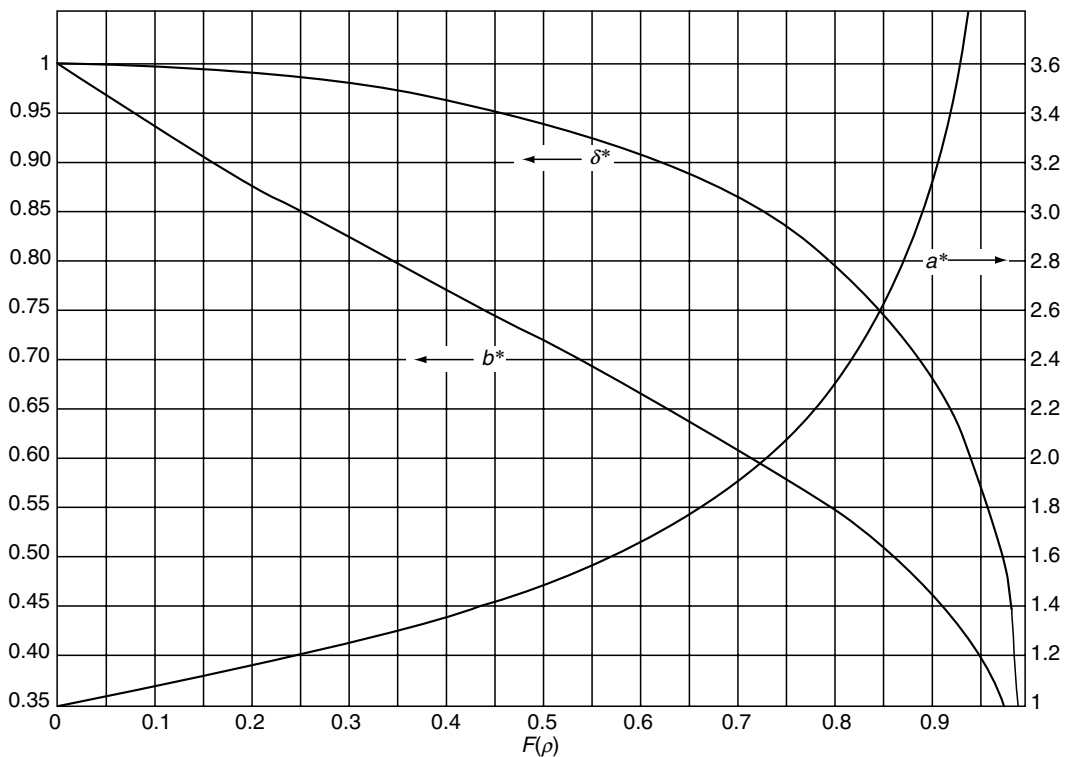


FIGURE 6.3 a^* , b^* , and δ^* vs. $F(\rho)$.

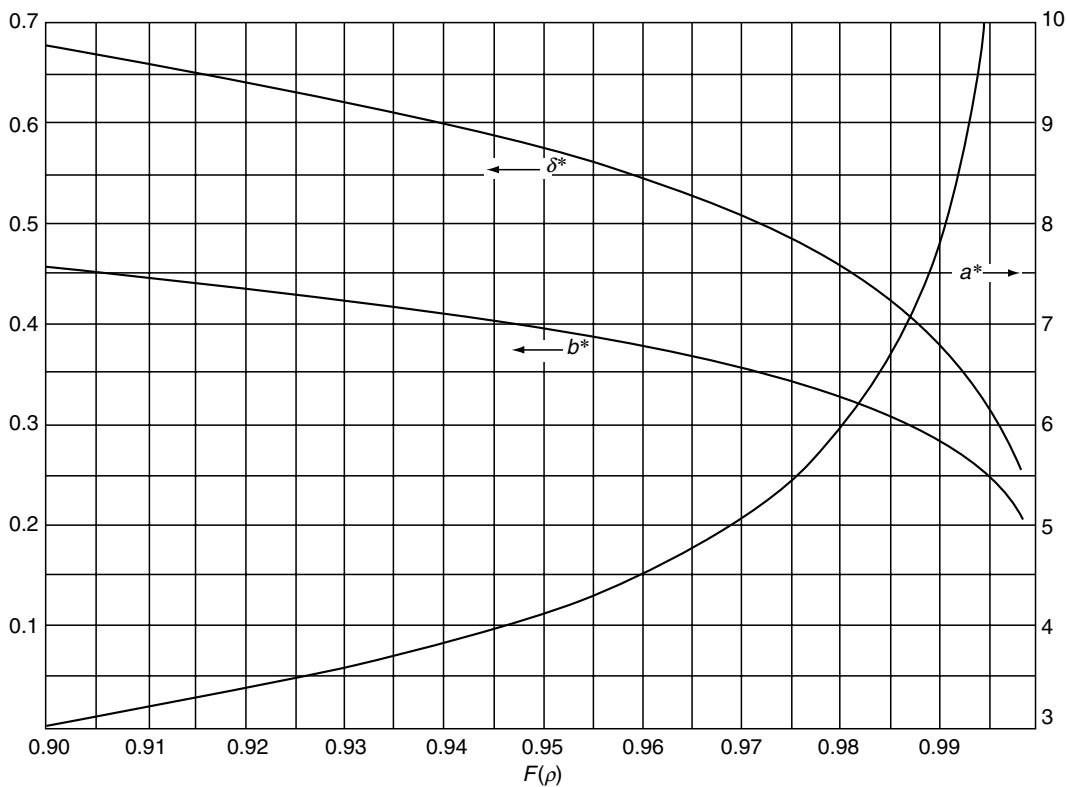


FIGURE 6.4 a^* , b^* , and δ^* vs. $F(\rho)$.

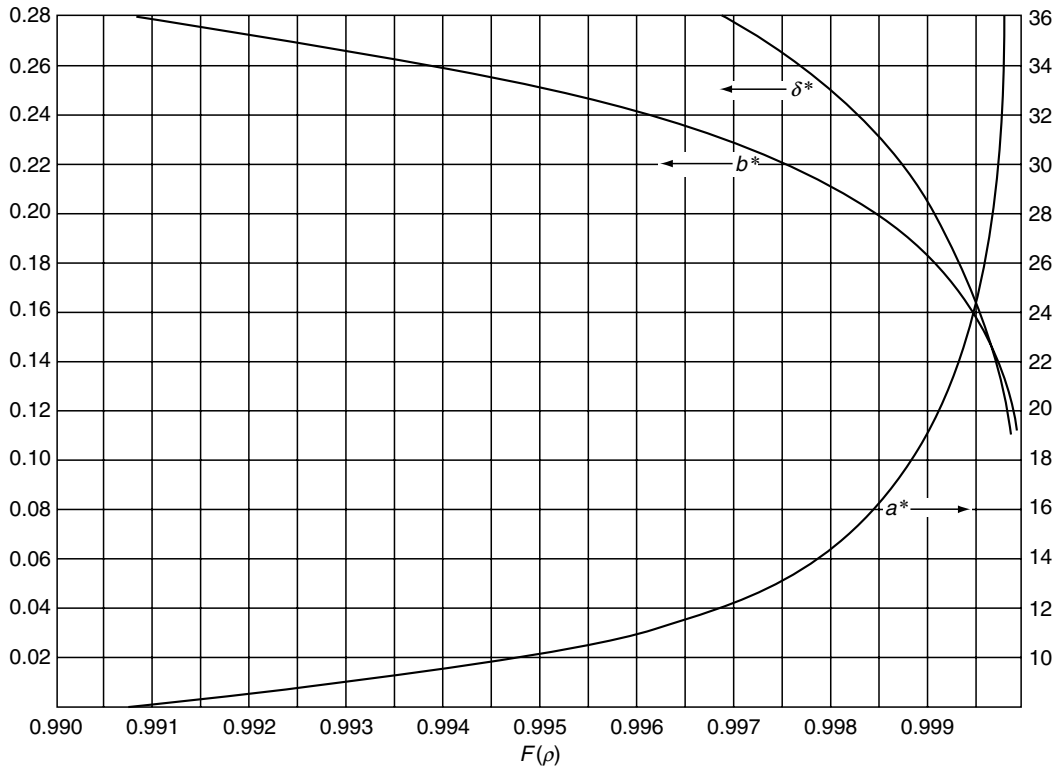


FIGURE 6.5 a^* , b^* , and δ^* vs. $F(\rho)$.

For an elliptical contact area, the maximum compressive stress occurs at the geometrical center. The magnitude of this stress is

$$\sigma_{\max} = \frac{3Q}{2\pi ab} \quad (6.47)$$

The normal stress at other points within the contact area is given by Equation 6.48 in accordance with Figure 6.6:

$$\sigma = \frac{3Q}{2\pi ab} \left[1 - \left(\frac{x}{a} \right)^2 - \left(\frac{y}{b} \right)^2 \right]^{1/2} \quad (6.48)$$

Equation 6.30 through Equation 6.43 of surface stress and deformation apply to point contacts.

See Example 6.1.

For ideal line contact to exist, the length of body I must equal that of body II. Then, κ approaches infinity and the stress distribution in the contact area degenerates to a semicylindrical form as shown in Figure 6.7. For this condition,

$$\sigma_{\max} = \frac{2Q}{\pi lb} \quad (6.49)$$

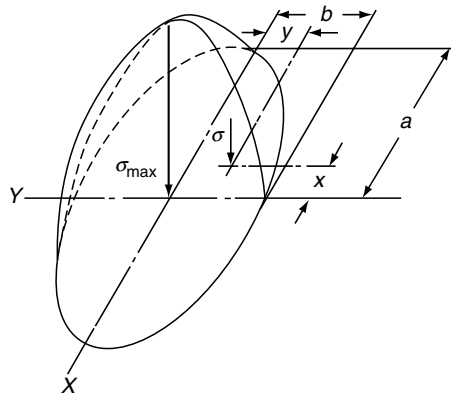


FIGURE 6.6 Ellipsoidal surface compressive stress distribution of point contact.

$$\sigma = \frac{2Q}{\pi lb} \left[1 - \left(\frac{y}{b} \right)^2 \right]^{1/2} \quad (6.50)$$

$$b = \left[\frac{4Q}{\pi l \Sigma \rho} \left(\frac{(1 - \xi_I^2)}{E_I} + \frac{(1 - \xi_{II}^2)}{E_{II}} \right) \right]^{1/2} \quad (6.51)$$

For steel roller bearings, the semiwidth of the contact surface may be approximated by

$$b = 3.35 \times 10^{-3} \left(\frac{Q}{l \Sigma \rho} \right)^{1/2} \quad (6.52)$$

The contact deformation for a line contact condition was determined by Lundberg and Sjövall [5] to be

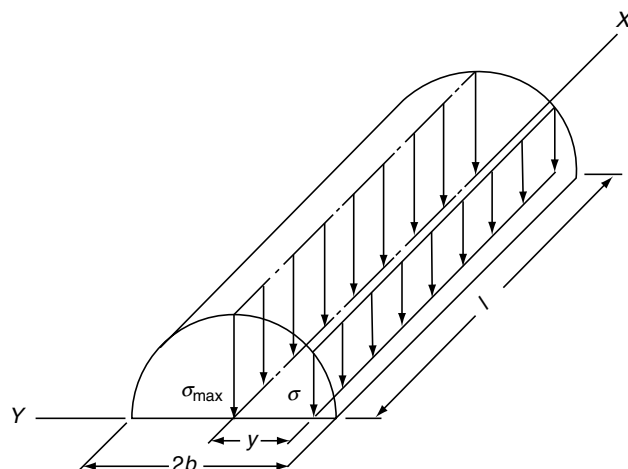


FIGURE 6.7 Semicylindrical surface compressive stress distribution of ideal line contact.

$$\delta = \frac{2Q(1-\xi^2)}{\pi El} \ln \left[\frac{\pi El^2}{Q(1-\xi^2)(1 \mp \gamma)} \right] \quad (6.53)$$

Equation 6.53 pertains to an ideal line contact. In practice, rollers are crowned as illustrated in [Figure 6.26b](#) through [Figure 6.26d](#). Based on laboratory testing of crowned rollers loaded against raceways, Palmgren [6] developed Equation 6.54 for contact deformation:

$$\delta = 3.84 \times 10^{-5} \frac{Q^{0.9}}{l^{0.8}} \quad (6.54)$$

In addition to Hertz [1] and Lundberg and Sjövall [5], Thomas and Hoersch [7] analyzed stresses and deformations associated with concentrated contacts. These references provide more complete information on the solution of the elasticity problems associated with concentrated contacts.

See Example 6.2.

6.4 SUBSURFACE STRESSES

Hertz's analysis pertained only to surface stresses caused by a concentrated force applied perpendicular to the surface. Experimental evidence indicates that the failure of rolling bearings in surface fatigue caused by this load emanates from points below the stressed surface. Therefore, it is of interest to determine the magnitude of the subsurface stresses. As the fatigue failure of the surfaces in rolling contact is a statistical phenomenon dependent on the volume of material stressed ([see Chapter 11](#)), the depths at which significant stresses occur below the surface are also of interest.

Again, considering only stresses caused by a concentrated force applied normal to the surface, Jones [8], using the method of Thomas and Hoersch [7], gives the following equations to calculate the principal stresses S_x , S_y , and S_z occurring along the Z axis at any depth below the contact surface.

As the surface stress is maximum at the Z axis, the principal stresses must attain maximum values there ([see Figure 6.8](#)):

$$\begin{aligned} S_x &= \lambda(\Omega_x + \xi\Omega'_x) \\ S_y &= \lambda(\Omega_y + \xi\Omega'_y) \\ S_z &= -\frac{1}{2}\lambda\left(\frac{1}{\nu} - \nu\right) \end{aligned} \quad (6.55)$$

where

$$\lambda = \frac{b\Sigma\rho}{\left(\kappa - \frac{1}{\kappa}\right)\mathbb{E}\left(\frac{1-\xi_L^2}{E_I} + \frac{1-\xi_{II}^2}{E_{II}}\right)} \quad (6.56)$$

$$\nu = \left(\frac{1+\zeta^2}{\kappa^2+\zeta^2}\right)^{1/2} \quad (6.57)$$

$$\zeta = \frac{z}{b} \quad (6.58)$$

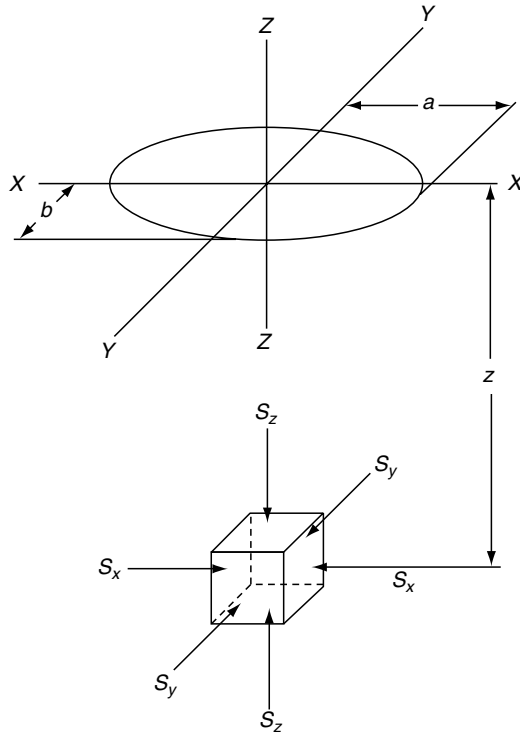


FIGURE 6.8 Principal stresses occurring on element on Z axis below contact surface.

$$\Omega_x = -\frac{1}{2}(1-\nu) + \zeta[\mathbf{F}(\phi) - \mathbf{E}(\phi)] \quad (6.59)$$

$$\Omega'_x = 1 - \kappa^2\nu + \zeta[\kappa^2\mathbf{E}(\phi) - \mathbf{F}(\phi)] \quad (6.60)$$

$$\Omega_y = \frac{1}{2}\left(1 + \frac{1}{\nu}\right) - \kappa^2\nu + \zeta[\kappa^2\mathbf{E}(\phi) - \mathbf{F}(\phi)] \quad (6.61)$$

$$\Omega'_y = -1 + \nu + \zeta[\mathbf{F}(\phi) - \mathbf{E}(\phi)] \quad (6.62)$$

$$\mathbf{F}(\phi) = \int_0^\phi \left[1 - \left(1 - \frac{1}{\kappa^2} \right) \sin^2 \phi \right]^{-1/2} d\phi \quad (6.63)$$

$$\mathbf{E}(\phi) = \int_0^\phi \left[1 - \left(1 - \frac{1}{\kappa^2} \right) \sin^2 \phi \right]^{1/2} d\phi \quad (6.64)$$

The principal stresses indicated by these equations are graphically illustrated in [Figure 6.9](#) through [Figure 6.11](#).

Since each of the maximum principal stresses can be determined, it is further possible to evaluate the maximum shear stress on the z axis below the contact surface. By Mohr's circle (see Ref. [2]), the maximum shear stress is found to be

$$\tau_{yz} = \frac{1}{2}(S_z - S_y) \quad (6.65)$$

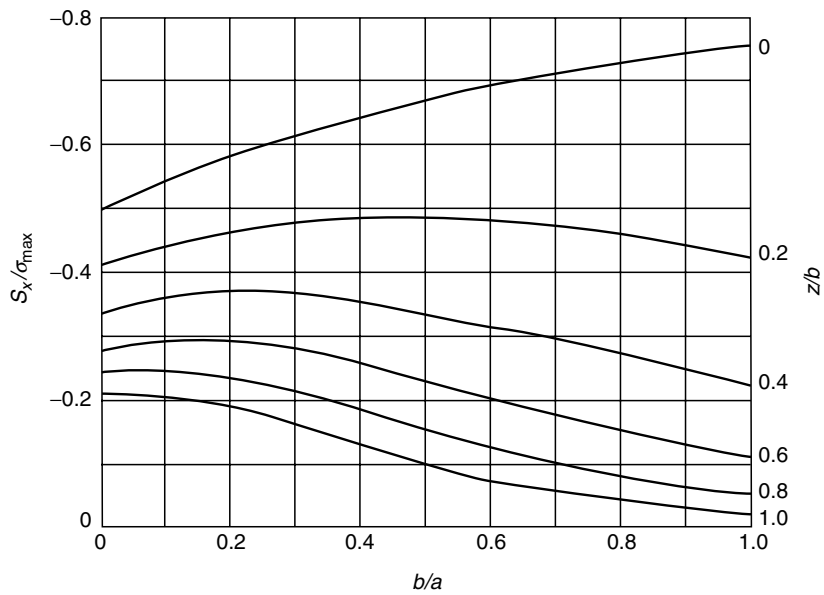


FIGURE 6.9 S_x / σ_{\max} vs. b/a and z/b .

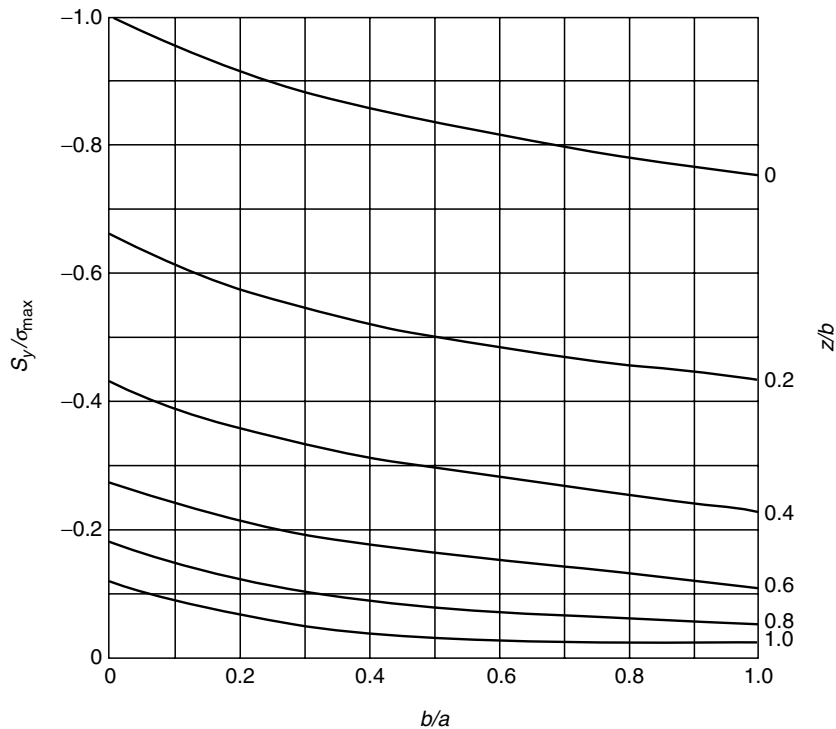


FIGURE 6.10 S_y / σ_{\max} vs. b/a and z/b .

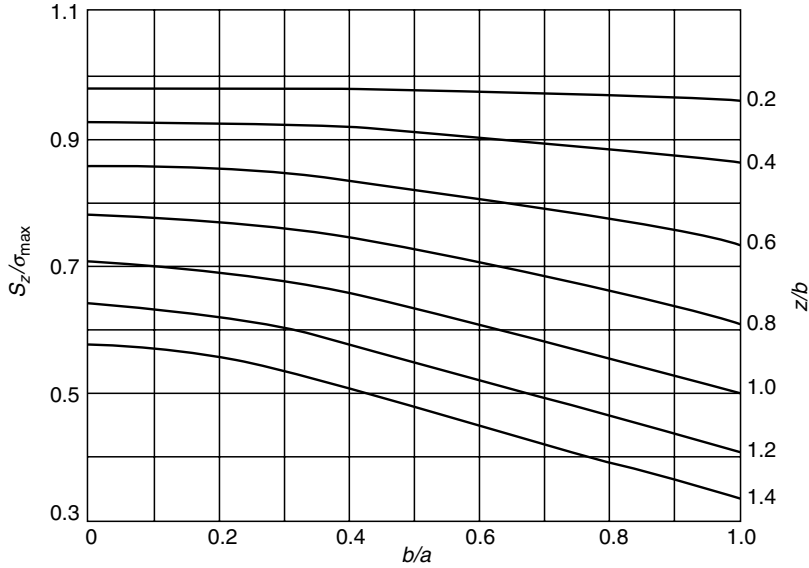


FIGURE 6.11 S_z/σ_{\max} vs. b/a and z/b .

As shown in Figure 6.12, the maximum shear stress occurs at various depths z , below the surface, being at $0.467b$ for simple point contact and $0.786b$ for line contact.

During the passage of a loaded rolling element over a point on the raceway surface, the maximum shear stress on the z axis varies between 0 and τ_{\max} . If the element rolls in the direction of the y axis, then the shear stresses occurring in the yz plane below the contact surface assume values from negative to positive for values of y less than and greater than zero, respectively. Thus, the maximum variation of shear stress in the yz plane at any point for a given depth is $2\tau_{yz}$.

Palmgren and Lundberg [9] show that

$$\tau_{yz} = \frac{3Q}{2\pi} \times \frac{\cos^2 \phi \sin \phi \sin \vartheta}{a^2 \tan^2 \vartheta + b^2 \cos^2 \phi} \quad (6.66)$$

wherein

$$y = (b^2 + a^2 \tan^2 \vartheta)^{1/2} \sin \phi \quad (6.67)$$

$$z = a \tan \vartheta \cos \phi \quad (6.68)$$

Here, ϑ and ϕ are auxiliary angles such that

$$\frac{\partial \tau_{yz}}{\partial \phi} = \frac{\partial \tau_{yz}}{\partial \vartheta} = 0$$

which defines the amplitude τ_0 of the shear stress. Further, ϑ and ϕ are related as follows:

$$\begin{aligned} \tan^2 \phi &= t \\ \tan^2 \vartheta &= t - 1 \end{aligned} \quad (6.69)$$

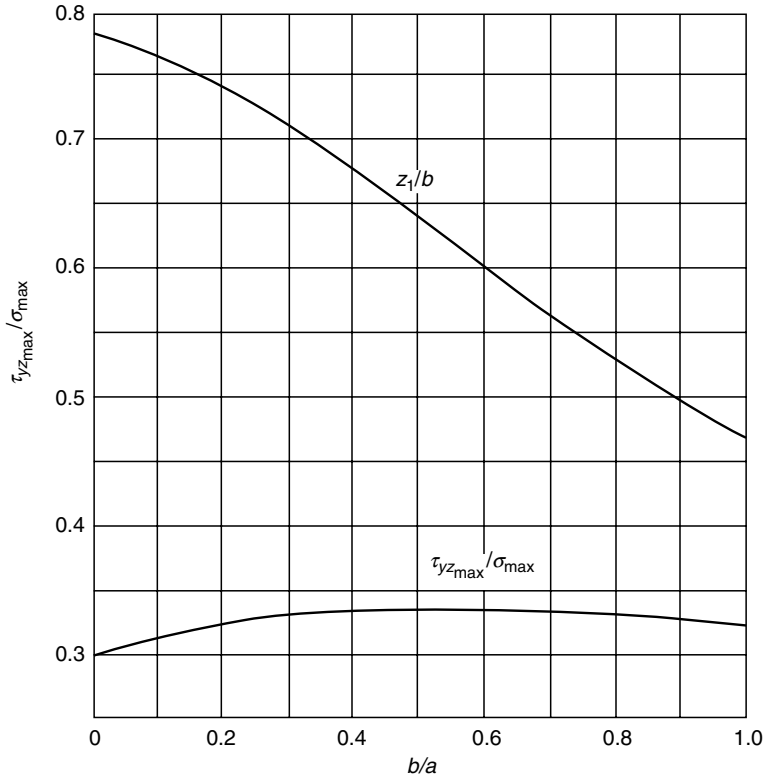


FIGURE 6.12 $\tau_{yz_{\max}}/\sigma_{\max}$ and z_1/b vs. b/a .

where t is an auxiliary parameter such that

$$\frac{b}{a} = [(t^2 - 1)(2t - 1)]^{1/2} \quad (6.70)$$

Solving Equation 6.66 through Equation 6.70 simultaneously, it is shown in [Chapter 5](#), Ref. [8] that

$$\frac{2\tau_0}{\sigma_{\max}} = \frac{(2t - 1)^{1/2}}{t(t + 1)} \quad (6.71)$$

and

$$\zeta = \frac{1}{(t + 1)(2t - 1)^{1/2}} \quad (6.72)$$

[Figure 6.13](#) shows the resulting distribution of shear stress at depth z_0 in the direction of rolling for $b/a = 0$, that is, a line contact.

[Figure 6.14](#) shows the shear stress amplitude of Equation 6.71 as a function of b/a . Also shown is the depth below the surface at which this shear stress occurs. As the shear stress amplitude indicated in Figure 6.14 is greater than that in Figure 6.12, Palmgren and Lundberg

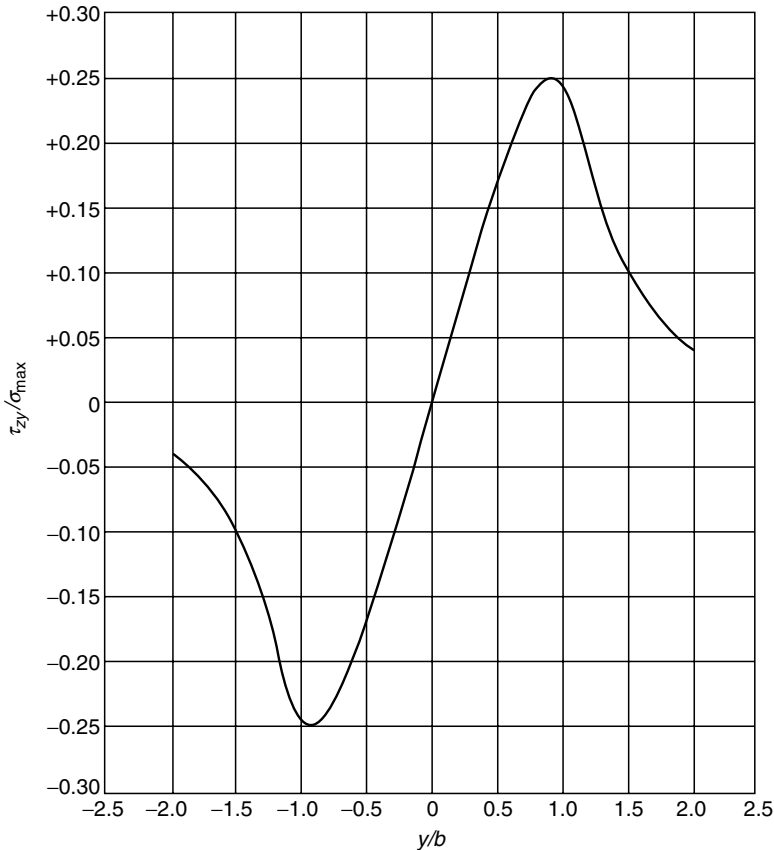


FIGURE 6.13 τ_{zy}/σ_{\max} vs. y/b for $b/a=0$ and $z=z_0$ (concentrated normal load).

[9] assumed this shear stress (called the maximum orthogonal shear stress) to be significant in causing fatigue failure of the surfaces in rolling contact. As can be seen from Figure 6.14, for a typical rolling bearing point contact of $b/a=0.1$, the depth below the surface at which this stress occurs is approximately $0.49b$. Moreover, as seen in Figure 6.13, this stress occurs at any instant near the extremities of the contact ellipse with regard to the direction of motion, that is, at $y=\pm 0.9b$.

Metallurgical research [10] based on plastic alterations detected in subsurface material by transmission electron microscopic investigation gives indications that the subsurface depth at which significant amounts of material alteration occur is approximately $0.75b$. Assuming that such plastic alteration is the forerunner of material failure, it would appear that the maximum shear stress of Figure 6.12 may be worthy of consideration as the significant stress causing failure. Figure 6.15 and Figure 6.16, obtained from Ref. [10], are photomicrographs showing the subsurface changes caused by constant rolling on the surface.

Many researchers consider the von Mises–Hencky distortion energy theory [11] and the scalar von Mises stress a better criterion for rolling contact failure. The latter stress is given by

$$\begin{aligned}\sigma_{VM} = & \frac{1}{\sqrt{2}} [(\sigma_x - \sigma_y)^2 + (\sigma_y - \sigma_z)^2 \\ & + (\sigma_z - \sigma_x)^2 + 6(\tau_{xy}^2 + \tau_{yz}^2 + \tau_{zx}^2)]^{1/2}\end{aligned}\quad (6.73)$$

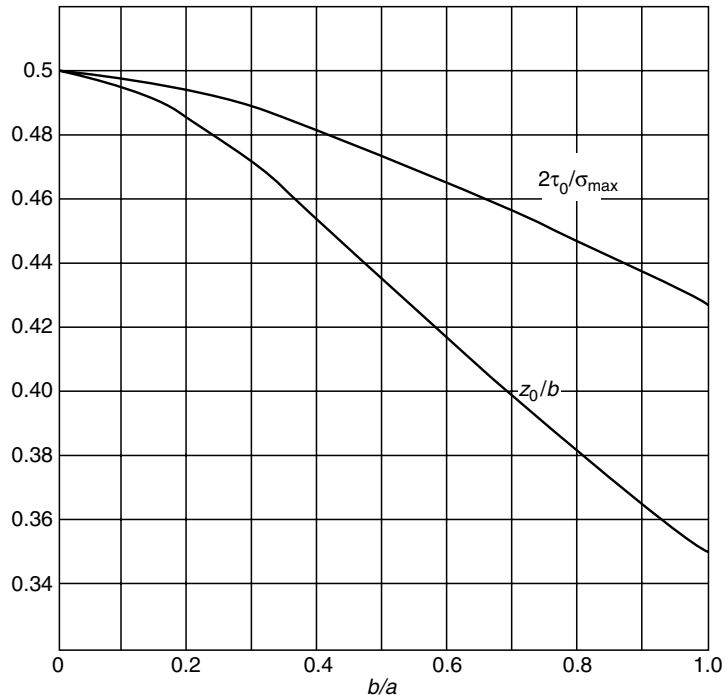


FIGURE 6.14 $2\tau_0/\sigma_{\max}$ and z_0/b vs. b/a (concentrated normal load).

As compared with the maximum orthogonal shear stress τ_0 , which occurs at depth z_0 approximately equal to $0.5b$, and at y approximately equal to $\pm 0.9b$ in the rolling direction, $\sigma_{VM,\max}$ occurs at z between $0.7b$ and $0.8b$ and at $y=0$.

Octahedral shear stress, a vector quantity favored by some researchers, is directly proportional to σ_{VM} :

$$\tau_{oct} = \frac{\sqrt{2}}{3} \sigma_{VM} \quad (6.74)$$

[Figure 6.17](#) compares the magnitudes of τ_0 , maximum shear stress, and τ_{oct} vs. depth.

See [Example 6.3](#).

6.5 EFFECT OF SURFACE SHEAR STRESS

In the determination of contact deformation vs. load, only the concentrated load applied normal to the surface need be considered for most applications. Moreover, in most rolling bearing applications, lubrication is at least adequate, and the sliding friction between rolling elements and raceways is negligible. This means that the shear stresses acting on the rolling elements and raceway surfaces in contact, that is, the elliptical areas of contact, are negligible compared with normal stresses.

For the determination of bearing endurance with regard to fatigue of the contacting rolling surfaces, the surface shear stress cannot be neglected and in many cases is the most significant factor in determining the endurance of a rolling bearing in a given application. Methods of calculation of the surface shear stresses (traction stresses) are discussed in [Chapter 5](#) of the

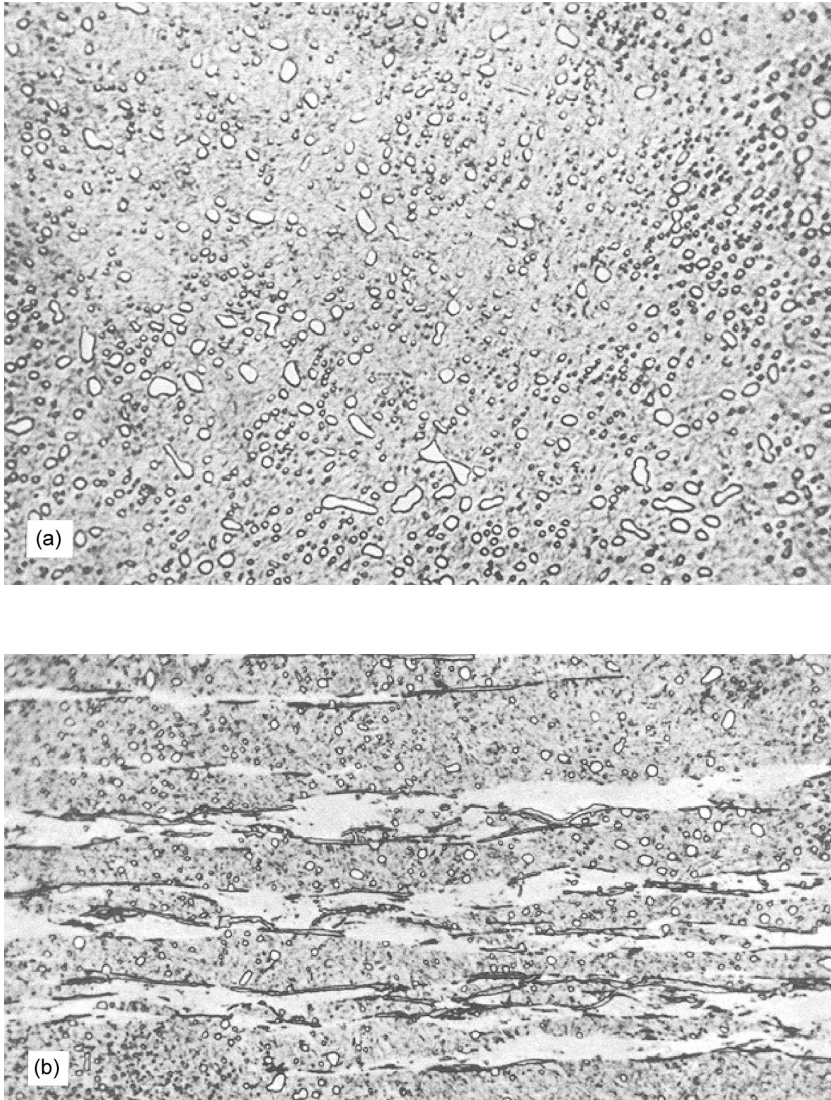


FIGURE 6.15 Subsurface metallurgical structure (1300 times magnification after picral etch) showing change due to repeated rolling under load. (a) Normal structure; (b) stress-cycled structure—white deformation bands and lenticular carbide formations are visible.

companion volume of this handbook. The means for determining the effect on the subsurface stresses of the combination of normal and tangential (traction) stresses applied at the surface are extremely complex, requiring the use of digital computation. Among others, Zwirlein and Schlicht [10] have calculated subsurface stress fields based on assumed ratios of surface shear stress to applied normal stress. Zwirlein and Schlicht [10] assume that the von Mises stress is most significant with regard to fatigue failure and give an illustration of this stress in [Figure 6.18](#).

[Figure 6.19](#), also from Ref. [10], shows the depths at which the various stresses occur. Figure 6.19 shows that as the ratio of surface shear to normal stress increases, the maximum von Mises stress moves closer to the surface. At a ratio of $\tau/\sigma = 0.3$, the maximum von Mises stress occurs at the surface. Various other investigators have found that if a shear stress is

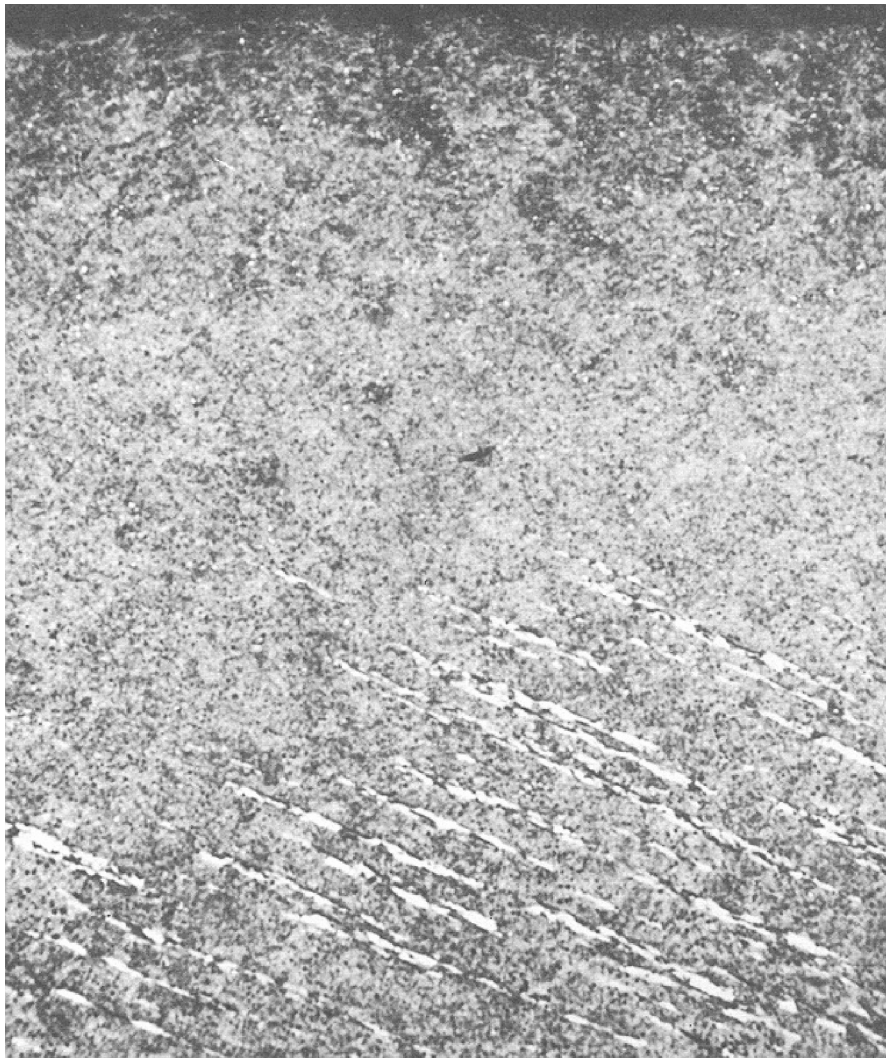


FIGURE 6.16 Subsurface structure (300 times magnification after picral etch) showing orientation of carbides to direction of rolling. Carbides are thought to be weak locations at which fatigue failure is initiated.

applied at the contact surface in addition to the normal stress, the maximum shear stress tends to increase, and it is located closer to the surface (see Refs. [11–15]). Indications of the effect of higher-order surfaces on the contact stress solution are given in Refs. [16–18]. The references cited above are intended not to be extensive, but to give only a representation of the field of knowledge.

The foregoing discussion pertained to the subsurface stress field caused by a concentrated normal load applied in combination with a uniform surface shear stress. The ratio of surface shear stress to normal stress is also called the coefficient of friction (see Chapter 5 of the Second Volume of this handbook). Because of infinitesimally small irregularities in the basic surface geometries of the rolling contact bodies, neither uniform normal stress fields as shown in Figure 6.6 and Figure 6.7 nor a uniform shear stress field are likely to occur in practice.

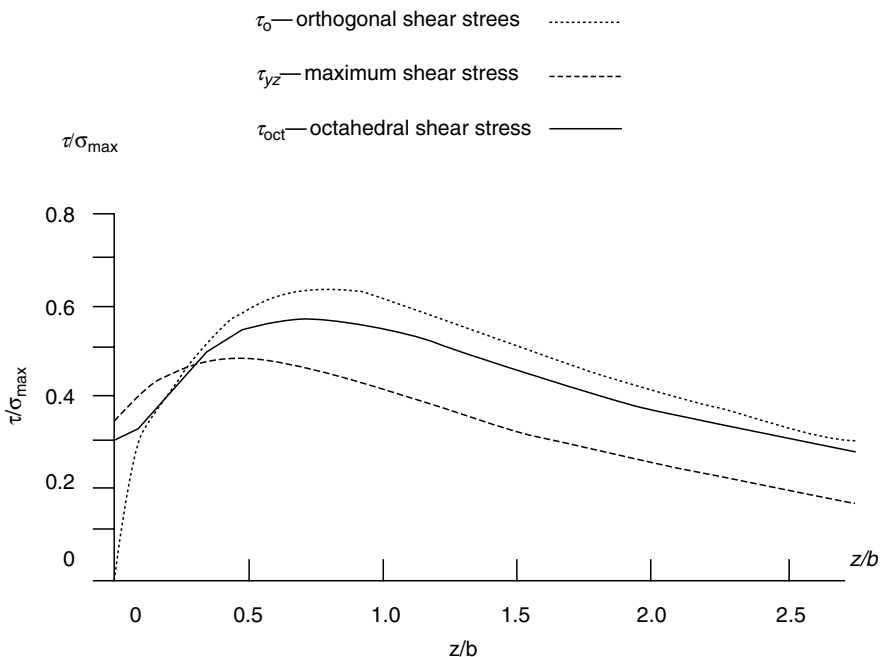


FIGURE 6.17 Comparison of shear stresses at depths beneath the contact surface ($x = y = 0$).

Sayles et al. [19] use the model shown in [Figure 6.20](#) in developing an elastic conformity factory.

Kalker [20] developed a mathematical model to calculate the subsurface stress distribution associated with an arbitrary distribution of shear and normal stresses over a surface in concentrated contact. Ahmadi et al. [21] developed a patch method that can be applied to determine the subsurface stresses for any concentrated contact surface subjected to arbitrarily distributed shear stresses. Using superposition, this method combined with that of Thomas and Hoersch [7], for example, for Hertzian surface loading, can be applied to determine the subsurface stress distributions occurring in rolling element–raceway contacts. Harris and Yu [22], applying this method of analysis, determined that the range of maximum orthogonal shear stress, i.e., $2\tau_0$, is not altered by the addition of surface shear stresses to the Hertzian stresses. [Figure 6.21](#) illustrates this condition.

As the Lundberg–Palmgren fatigue life theory [9] is based on maximum orthogonal shear stress as the fatigue failure-initiating stress, the adequacy of using that method to predict rolling bearing fatigue endurance is subject to question. Conversely, for a simple Hertzian loading, i.e., $f=0$, the maximum octahedral shear stress $\tau_{oct,\max}$ occurs directly under the center of the contact. [Figure 6.22](#) further shows that the magnitude of $\tau_{oct,\max}$ and the depth at which it occurs are substantially influenced by surface shear stress.

The question of which stress should be used for fatigue failure life prediction will be revisited in [Chapter 11](#) and [Chapter 8](#) of the Second Volume of this handbook.

6.6 TYPES OF CONTACTS

Basically, two hypothetical types of contact can be defined under conditions of *zero load*. These are

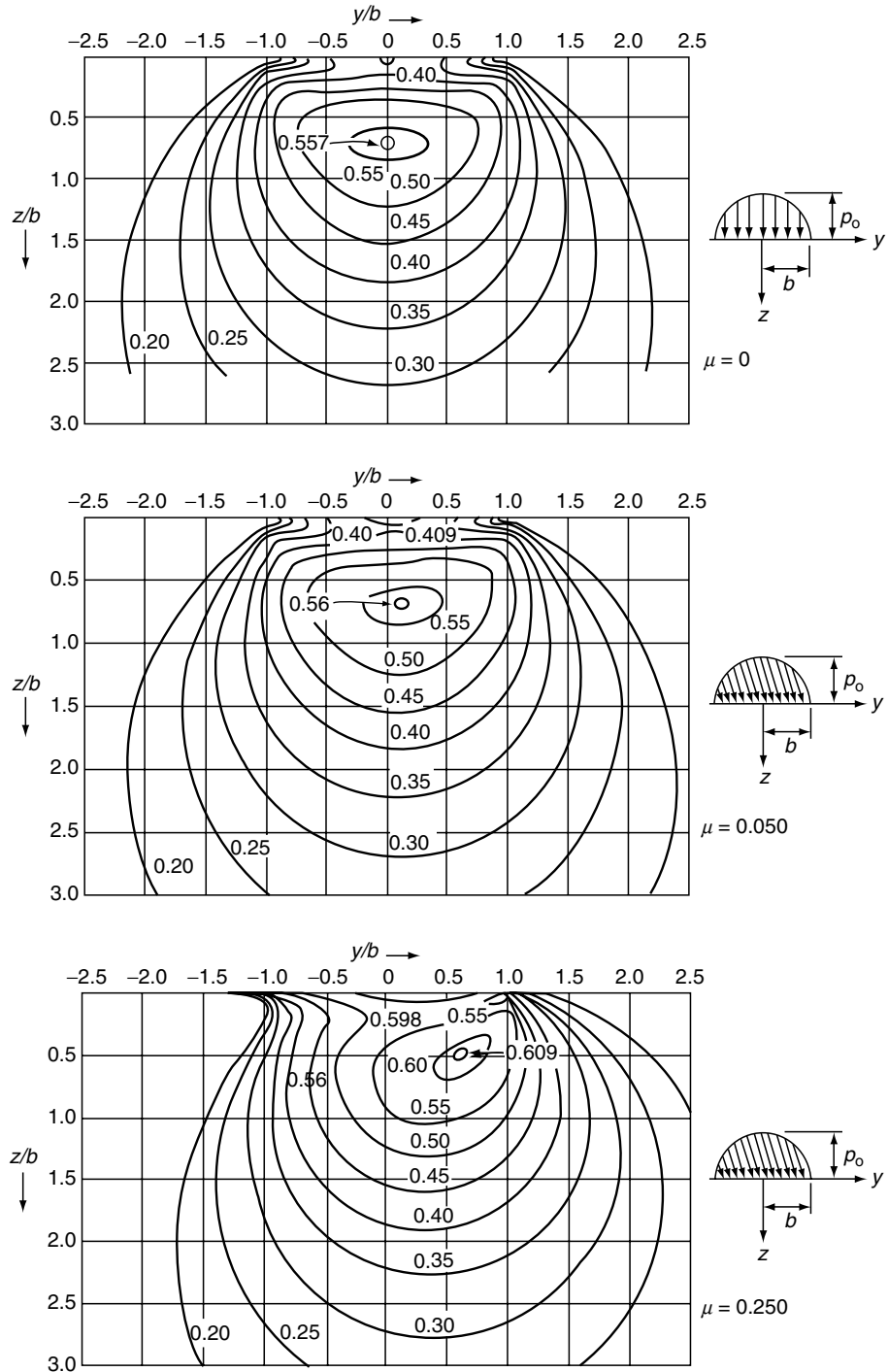


FIGURE 6.18 Lines of equal von Mises stress/normal applied stress for various surface shear stresses τ/σ . (From Zwirlein, O. and Schlicht, H., Werkstoffanstrengung bei Wälzbeanspruchung-Einfluss von Reibung und Eigenspannungen, *Z. Werkstofftech.*, 11, 1–14, 1980.)

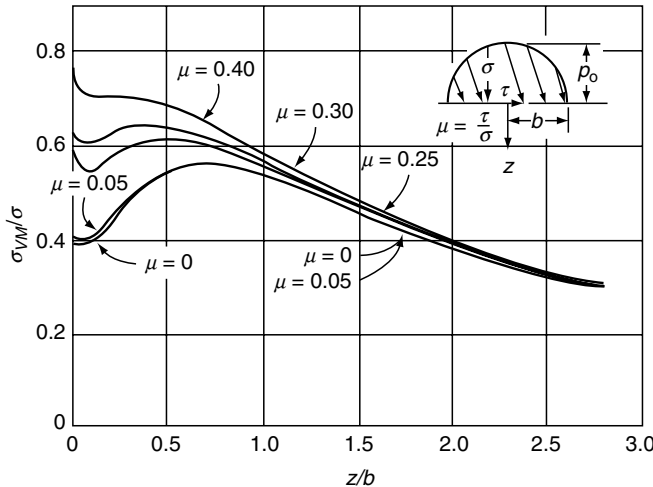


FIGURE 6.19 Material stressing (σ_{VM}/σ) vs. depth for different amounts of surface shear stress (τ/σ). (From Zwirlein, O. and Schlicht, H., Werkstoffanstrengung bei Wälzbeanspruchung-Einfluss von Reibung und Eigenspannungen, Z. Werkstofftech., 11, 1–14, 1980.)

1. Point contact, that is, two surfaces touch at a single point
2. Line contact, that is, two surfaces touch along a straight or curved line of zero width

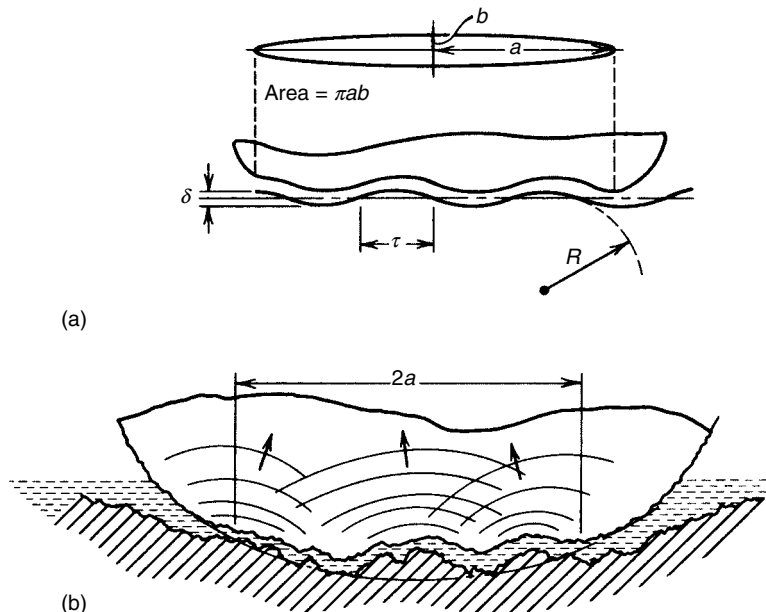


FIGURE 6.20 Models for less-than-ideal elastic conformity. (a) Hertzian contact model used in developing elastic conformity parameter. (b) Elastic conformity envisaged with real roughness would be preferential to certain asperity wavelengths. For convenience, the figure shows only one compliant rolling element, whereas in practice if materials of similar modulus were employed the deformation would be shared.

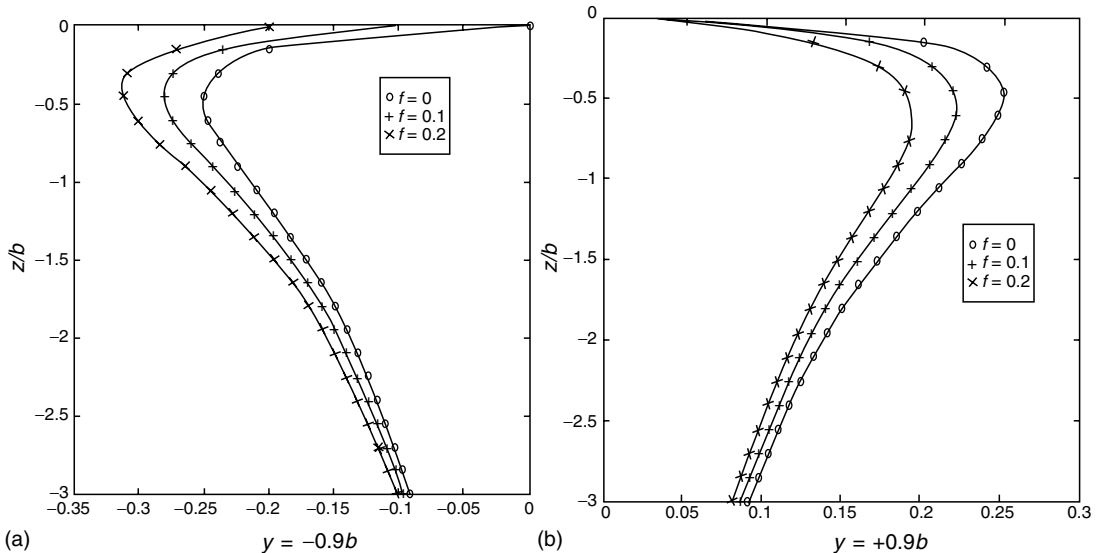


FIGURE 6.21 Orthogonal shear stress τ_{yz}/σ_{\max} (abscissa) vs. depth z/b at contact area location $x=0$ for friction coefficients $f=0, 0.1, 0.2$.

Obviously, after a load is applied to the contacting bodies the point expands to an ellipse and the line to a rectangle in ideal line contact, that is, the bodies have equal length. Figure 6.23 illustrates the surface compressive stress distribution that occurs in each case.

When a roller of finite length contacts a raceway of greater length, the axial stress distribution along the roller is altered, as that in Figure 6.23. Since the material in the raceway is in tension at the roller ends because of depression of the raceway outside of the roller ends, the roller end compressive stress tends to be higher than that in the center of contact. Figure 6.24 demonstrates this condition of edge loading.

To counteract this condition, cylindrical rollers (or the raceways) may be crowned as shown in Figure 1.38. The stress distribution is thereby made more uniform depending on the applied load. If the applied load is increased significantly, edge loading will occur once again.

Palmgren and Lundberg [9] have defined a condition of modified line contact for roller–raceway contact. Thus, when the major axis ($2a$) of the contact ellipse is greater than the

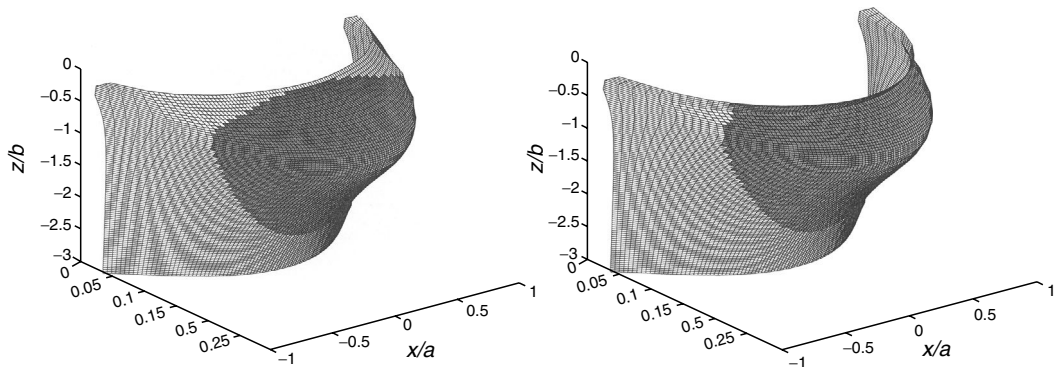


FIGURE 6.22 Octahedral shear stress τ_{oct}/σ_{\max} (y direction) vs. depth z/b and location x/a .

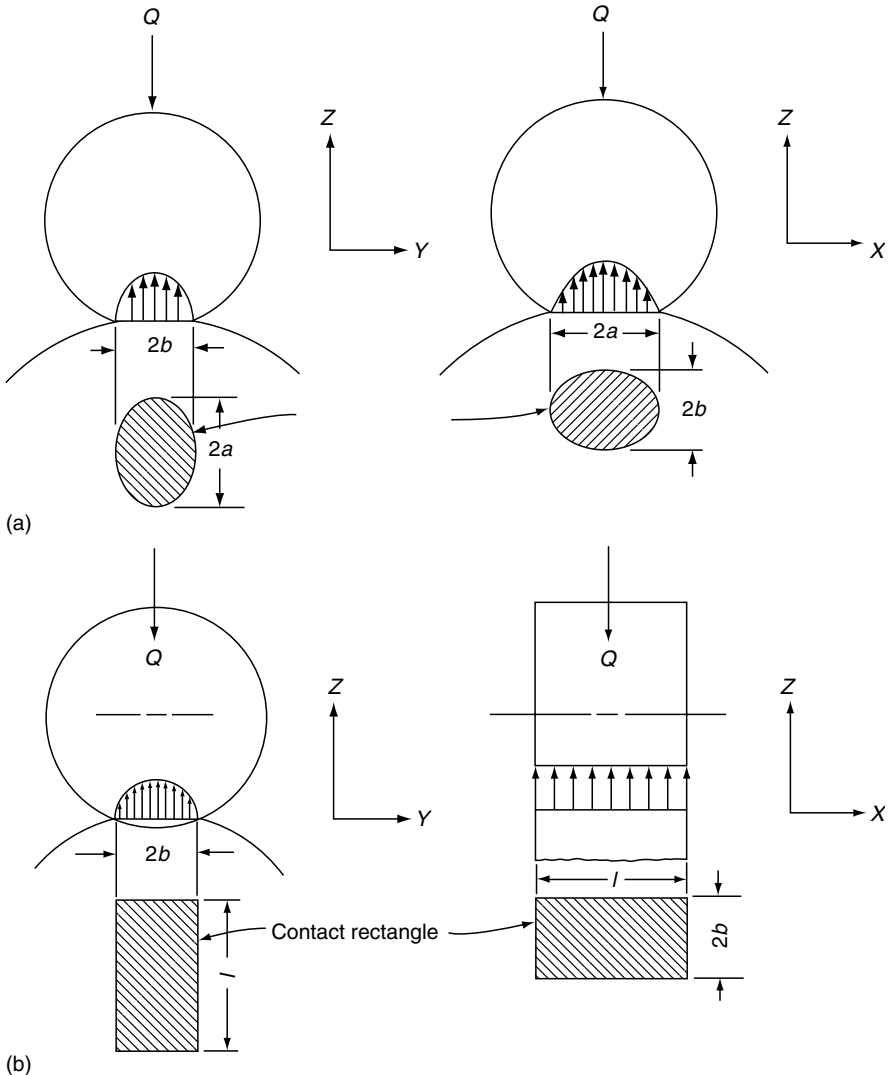


FIGURE 6.23 Surface compressive stress distribution. (a) Point contact; (b) ideal line contact.

effective roller length l but less than $1.5l$, a modified line contact is said to exist. If $2a < l$, then point contact exists; if $2a > 1.5l$, then line contact exists with attendant edge loading. This condition may be ascertained approximately by the methods presented in [Section 6.3](#), using the roller crown radius for R in [Equation 2.37](#) through [Equation 2.40](#).

The analysis of the contact stress and deformation presented in this section is based on the existence of an elliptical area of contact, except for the ideal roller under load, which has a rectangular contact. As it is desirable to preclude edge loading and attendant high stress concentrations, roller bearing applications should be examined carefully according to the modified line contact criterion. Where that criterion is exceeded, redesign of roller and raceway curvatures may be necessitated.

Rigorous mathematical and numerical methods have been developed to calculate the distribution and magnitude of surface stresses in any “line” contact situation, that is, including the effects of crowning of rollers, raceways, and combinations thereof as in [Section 1.6](#) of the

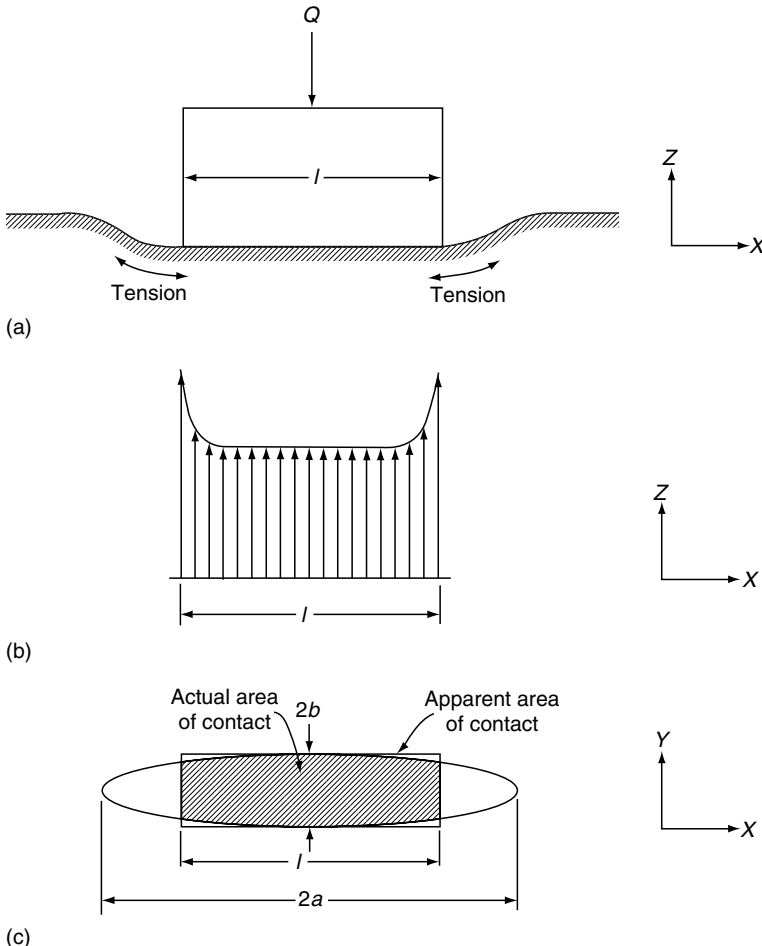


FIGURE 6.24 Line contact: (a) roller contacting a surface of infinite length; (b) roller–raceway compressive stress distribution; (c) contact ellipse.

Second Volume of this handbook, or see Refs. [23,24]. Additionally, finite element methods (FEMs) have been employed [25] to perform the same analysis. In all cases, digital computation is required to solve even a single contact situation. In a given roller bearing application, many contacts must be calculated. [Figure 6.25](#) shows the result of an FEM analysis of a heavily loaded typical spherical roller on a raceway. Note the slight “dogbone” shape of the contact surface. Note also the slight pressure increase where the roller crown blends into the roller end geometry.

See Examples 6.4 and 6.5

The circular crown shown in Figure 1.38a resulted from the theory of Hertz [1], whereas the cylindrical and crowned profiles of Figure 1.38b resulted from the work of Lundberg and Sjövall [5]. As illustrated in [Figure 6.26](#), each of these surface profiles, while minimizing edge stresses, has its drawbacks. Under light loads, a circular crowned profile does not enjoy full use of the roller length, somewhat negating the use of rollers in lieu of balls to carry heavier loads with longer endurance ([see Chapter 11](#)). Under heavier loads, while edge stresses are

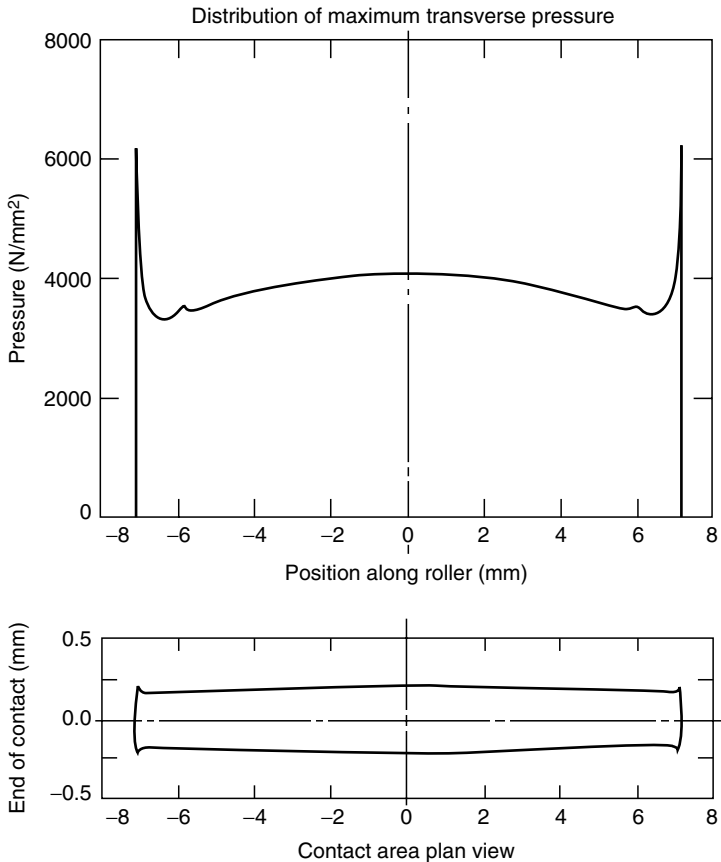


FIGURE 6.25 Heavy edge-loaded roller bearing contact (example of non-Hertzian contact).

avoided for most applications, the contact stress in the center of the contact can greatly exceed that in a straight profile contact, again resulting in substantially reduced endurance characteristics.

Under light loads, the partially crowned roller of Figure 1.38b as illustrated in Figure 6.26c experiences less contact stress than does a fully crowned roller under the same loading. Under heavy loading, the partially crowned roller also tends to outlast the fully crowned roller because of lower stress in the center of the contact; however, unless careful attention is paid to blending of the intersections of the “flat” (straight portion of the profiles) and the crown, stress concentrations can occur at the intersections with substantial reduction in endurance (see Chapter 11). When the roller axis is tilted relative to the bearing axis, both the fully crowned and partially crowned profiles tend to generate less edge stress under a given load as compared with the straight profile.

After many years of investigation and with the assistance of mathematical tools such as finite difference and FEMs as practiced using computers, a “logarithmic” profile was developed [26], yielding a substantially optimized stress distribution under most conditions of loading (see Figure 6.26d). The profile is so named because it can be expressed mathematically as a special logarithmic function. Under all loading conditions, the logarithmic profile uses more of the roller length than either the fully crowned or partially crowned roller

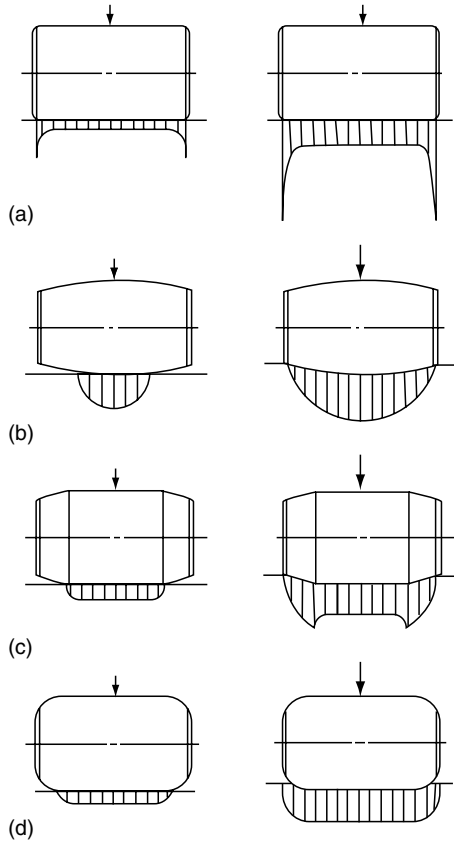


FIGURE 6.26 Roller–raceway contact load vs. length and applied load: a comparison of straight, fully crowned, and logarithmic profiles.

profiles. Under misalignment, edge loading tends to be avoided under all but exceptionally heavy loads. Under specific loading (Q/lD) from 20 to 100 MP_a (2900 to 14500 psi), Figure 6.27, taken from Ref. [26], illustrates the contact stress distributions attendant on the various surface profiles discussed herein. Figure 6.28, also from Ref. [26], compares the surface and subsurface stress characteristics for the various surface profiles.

6.7 ROLLER END–FLANGE CONTACT STRESS

The contact stresses between flange and roller ends may be estimated from the contact stress and deformation relationships previously presented. The roller ends are usually flat with corner radii blending into the crowned portion of the roller profile. The flange may also be a portion of a flat surface. This is the usual design in cylindrical roller bearings. When it is required to have the rollers carry thrust loads between the roller ends and the flange, sometimes the flange surface is designed as a portion of a cone. In this case, the roller corners contact the flange. The angle between the flange and a radial plane is called the layback angle. Alternatively, the roller end may be designed as a portion of a sphere that contacts the flange. The latter arrangement, that is a sphere-end roller contacting an angled flange, is conducive to improved lubrication while sacrificing some flange–roller guidance capability. In this case, some skewing control may have to be provided by the cage.

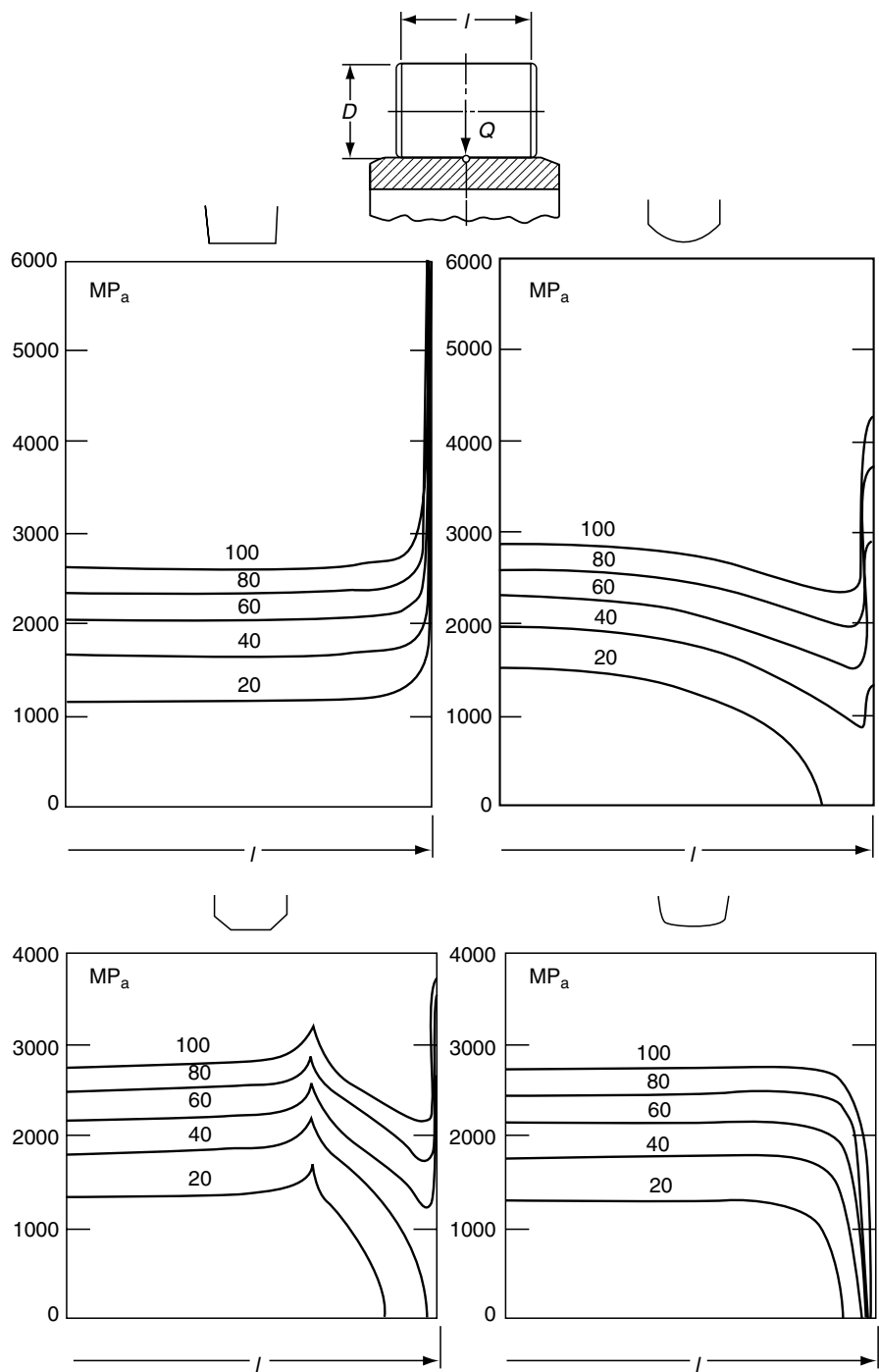


FIGURE 6.27 Compressive stress vs. length and specific roller load (Q/D) for various roller (or raceway) profiles. (From Reusner, H., *Ball Bearing J.*, 230, SKF, June 1987. With permission.)

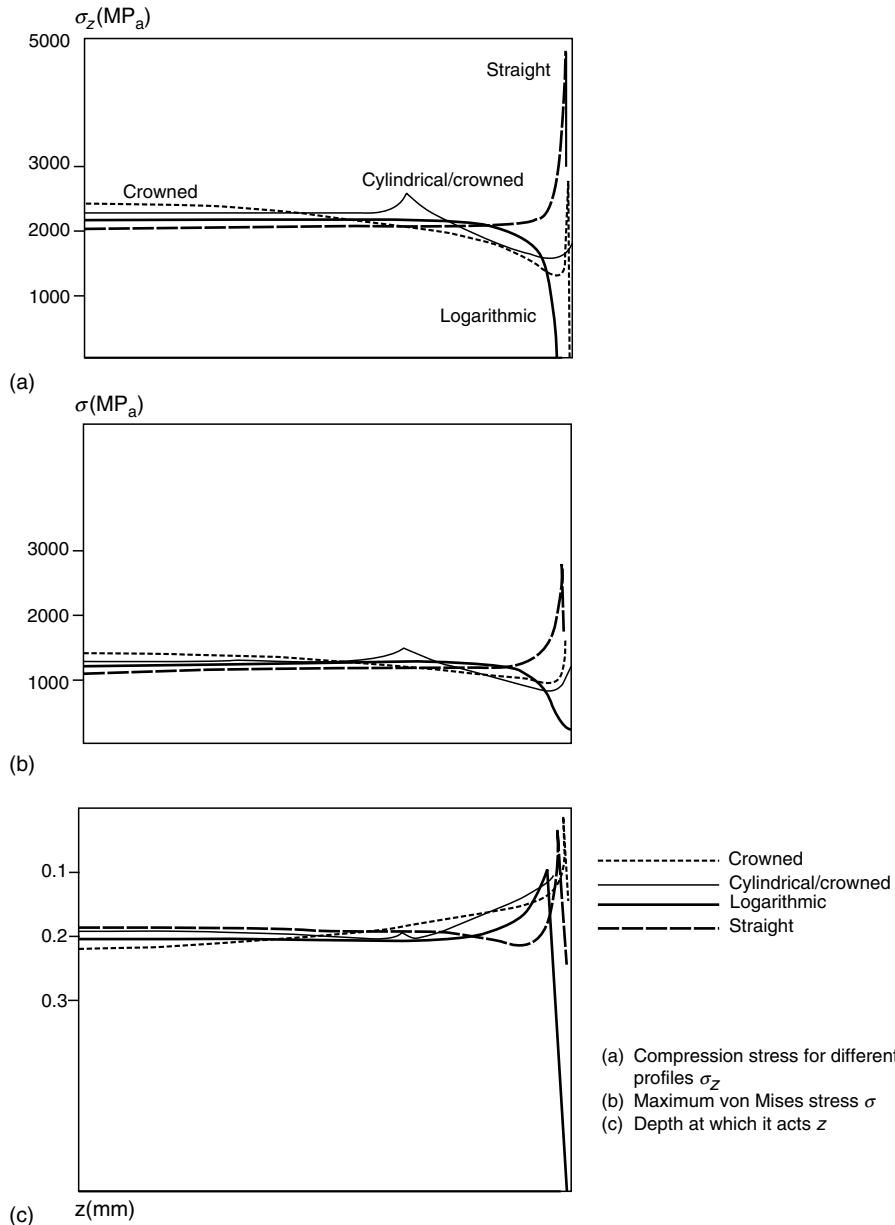


FIGURE 6.28 Comparison of surface compressive stress σ_z , maximum von Mises stress σ_{VM} , and depth z to the maximum von Mises stress for various roller (or raceway) profiles. (From Reusner, H., *Ball Bearing J.*, 230, SKF, June 1987. With permission.)

For the case of rollers having spherical shape ends and angled flange geometry, the individual contact may be modeled as a sphere contacting a cylinder. For the purpose of calculation, the sphere radius is set equal to the roller sphere end radius, and the cylinder radius can be approximated by the radius of curvature of the conical flange at the theoretical point of contact. By knowing the elastic contact load, roller-flange material properties, and contact geometries, the contact stress and deflection can be calculated. This approach is only approximate, because the roller end and flange do not meet the Hertzian half-space assumption. Also, the radius of

curvature on the conical flange is not a constant but will vary across the contact width. This method applies only to contacts that are fully confined to the spherical roller end and the conical portion of the flange. It is possible that improper geometry or excessive skewing could cause the elastic contact ellipse to be truncated by the flange edge, undercut, or roller corner radius. Such a situation is not properly modeled by Hertz stress theory and should be avoided in design because high edge stresses and poor lubrication can result.

The case of a flat-end roller and angled flange contact is less amenable to simple contact stress evaluation. The nature of the contact surface on the roller, which is at or near the intersection of the corner radius and end flat, is difficult to model adequately. The notion of an effective roller radius based on an assumed blend radius between roller corner and end flat is suitable for approximate calculations. A more precise contact stress distribution can be obtained by using FEM stress analysis technique if necessary.

6.8 CLOSURE

The information presented in this chapter is sufficient to make a determination of the contact stress level and elastic deformations occurring in a statically loaded rolling bearing. The model of a statically loaded bearing is somewhat distorted by the surface tangential stresses induced by rolling and lubricant actions. However, under the effects of moderate to heavy loading, the contact stresses calculated herein are sufficiently accurate for the rotating bearing as well as the bearing at rest. The same is true with regard to the effect of edge stresses on roller load distribution and hence deformation. These stresses subtend a rather small area and therefore do not influence the overall elastic load-deformation characteristic. In any event, from the simplified analytical methods presented in this chapter, a level of loading can be calculated against which to check other bearings at the same or different loads. The methods for calculation of elastic contact deformation are also sufficiently accurate, and these can be used to compare rolling bearing stiffness against the stiffness of other bearing types.

REFERENCES

1. Hertz, H., On the contact of rigid elastic solids and on hardness, in *Miscellaneous Papers*, MacMillan, London, 163–183, 1896.
2. Timoshenko, S. and Goodier, J., *Theory of Elasticity*, 3rd ed., McGraw-Hill, New York, 1970.
3. Boussinesq, J., *Compt. Rend.*, 114, 1465, 1892.
4. Brewe, D. and Hamrock, B., Simplified solution for elliptical-contact deformation between two elastic solids, *ASME Trans. J. Lub. Tech.*, 101(2), 231–239, 1977.
5. Lundberg, G. and Sjövall, H., *Stress and Deformation in Elastic Contacts*, Pub. 4, Institute of Theory of Elasticity and Strength of Materials, Chalmers Inst. Tech., Gothenburg, 1958.
6. Palmgren, A., *Ball and Roller Bearing Engineering*, 3rd ed., Burbank, Philadelphia, 1959.
7. Thomas, H. and Hoersch, V., Stresses due to the pressure of one elastic solid upon another, *Univ. Illinois Bull.*, 212, July 15, 1930.
8. Jones, A., *Analysis of Stresses and Deflections*, New Departure Engineering Data, Bristol, CT, 12–22, 1946.
9. Palmgren, A. and Lundberg, G., Dynamic capacity of rolling bearings, *Acta Polytech. Mech. Eng. Ser. 1*, R.S.A.E.E., No. 3, 7, 1947.
10. Zwirlein, O. and Schlicht, H., Werkstoffanstrengung bei Wälzbeanspruchung-Einfluss von Reibung und Eigenspannungen, *Z. Werkstofftech.*, 11, 1–14, 1980.
11. Johnson, K., The effects of an oscillating tangential force at the interface between elastic bodies in contact, Ph.D. Thesis, University of Manchester, 1954.
12. Smith, J. and Liu, C., Stresses due to tangential and normal loads on an elastic solid with application to some contact stress problems, ASME Paper 52-A-13, December 1952.

13. Radzimovsky, E., Stress distribution and strength condition of two rolling cylinders pressed together, *Univ. Illinois Eng. Experiment Station Bull.*, Series 408, February 1953.
14. Liu, C., Stress and deformations due to tangential and normal loads on an elastic solid with application to contact stress, Ph.D. Thesis, University of Illinois, June 1950.
15. Bryant, M. and Keer, L., Rough contact between elastically and geometrically identical curved bodies, *ASME Trans., J. Appl. Mech.*, 49, 345–352, June 1982.
16. Cattaneo, C., A theory of second order elastic contact, *Univ. Roma Rend. Mat. Appl.*, 6, 505–512, 1947.
17. Loo, T., A second approximation solution on the elastic contact problem, *Sci. Sinica*, 7, 1235–1246, 1958.
18. Deresiewicz, H., A note on second order Hertz contact, *ASME Trans. J. Appl. Mech.*, 28, 141–142, March 1961.
19. Sayles, R. et al., Elastic conformity in Hertzian contacts, *Tribol. Intl.*, 14, 315–322, 1981.
20. Kalker, J., Numerical calculation of the elastic field in a half-space due to an arbitrary load distributed over a bounded region of the surface, SKF Eng. and Res. Center Report NL82D002, Appendix, June 1982.
21. Ahmadi, N. et al., The interior stress field caused by tangential loading of a rectangular patch on an elastic half space, ASME Paper 86-Trib-15, October 1986.
22. Harris, T. and Yu, W.-K., Lundberg–Palmgren fatigue theory: considerations of failure stress and stressed volume, *ASME Trans. J. Tribol.*, 121, 85–90, January 1999.
23. Kunert, K., Spannungsverteilung im Halbraum bei Elliptischer Flächenpressungsverteilung über einer Rechteckigen Druckfläche, *Fortsch. Geb. Ingenieurwes.*, 27(6), 165–174, 1961.
24. Reusner, H., Druckflächenbelastung und Overflächenverschiebung in Wälzkontakt von Rotationskörpern, Dissertation, Schweinfurt, Germany, 1977.
25. Fredriksson, B., Three-dimensional roller–raceway contact stress analysis, Advanced Engineering Corp. Report, Linköping, Sweden, 1980.
26. Reusner, H., The logarithmic roller profile—the key to superior performance of cylindrical and taper roller bearings, *Ball Bearing J.*, 230, SKF, June 1987.

7 Distributions of Internal Loading in Statically Loaded Bearings

LIST OF SYMBOLS

Symbol	Description	Units
A	Distance between raceway groove curvature centers	mm (in.)
B	$f_i + f_o - 1$, total curvature	
D	Ball or roller diameter	mm (in.)
d_m	Bearing pitch diameter	mm (in.)
e	Eccentricity of loading	mm (in.)
E	Modulus of elasticity	MPa (psi)
f	r/D	
F	Applied load	N (lb)
i	Number of rows of rolling elements	
J_a	Axial load integral	
J_r	Radial load integral	
J_m	Moment load integral	
K	Load-deflection factor; axial load-deflection factor	N/mm ⁿ (lb/in. ⁿ)
l	Roller length	mm (in.)
L	Distance between rows	mm (in.)
M	Moment	
$N \cdot mm$ (lb · in.)		
M	Moment applied to bearing	N · mm (lb · in.)
n	Load-deflection exponent	
P_d	Diametral clearance	mm (in.)
Q	Ball- or roller-raceway normal load	N (lb)
r	Raceway groove curvature radius	mm (in.)
Z	Number of rolling elements	
α	Mounted contact angle	rad, °
α°	Free contact angle	rad, °
γ	$(D \cos \alpha)/d_m$	
δ	Deflection or contact deformation	mm (in.)
δ_1	Distance between inner and outer rings	mm (in.)
Δ	Contact deformation due to ideal normal loading	mm (in.)
$\Delta\psi$	Angular spacing between rolling elements	rad, °
ε	Load distribution factor	
$\Sigma\rho$	Curvature sum	mm ⁻¹ (in. ⁻¹)

ψ	Azimuth angle	rad, °
Subscripts		
a	Axial direction	
i	Inner raceway	
j	Rolling element position	
l	Line contact	
m	Raceway	
M	Moment loading	
n	Direction collinear with normal load	
o	Outer raceway	
p	Point contact	
r	Radial direction	
R	Rolling element	
1, 2	Bearing row	
ψ	Angular locationer	

7.1 GENERAL

It is possible to determine how the bearing load is distributed among the balls or rollers from a knowledge of how each ball or roller in a bearing carries load (as determined in [Chapter 5](#)). To do this it is first necessary to develop load-deflection relationships for rolling elements contacting raceways. By using [Chapter 2](#) and [Chapter 6](#), these load-deflection relationships can be developed for any type of rolling element contacting any type of raceway. Hence, the material presented in this chapter is completely dependent on the previous chapters, and a quick review might be advantageous at this point.

Most rolling bearing applications involve steady-state rotation of either the inner or outer raceway; sometimes both raceways rotate. In most applications, however, the speeds of rotation are usually not so great as to cause ball or roller inertial forces of sufficient magnitude to significantly affect the distribution of applied load among the rolling elements. Moreover, in most applications the frictional forces and moments acting on the rolling elements also do not significantly influence this load distribution. Therefore, in determining the distribution of rolling element loads, it is usually satisfactory to ignore these effects in most applications. Furthermore, before the general use of digital computation, relatively simple and effective means were developed to assist in the analyses of these load distributions. In this chapter, load distributions in statically loaded ball and roller bearings will be investigated using these simple and effective methods of analysis.

7.2 LOAD-DEFLECTION RELATIONSHIPS

From Equation 6.42, it can be seen that for a given ball-raceway contact (point loading),

$$\delta \sim Q^{2/3} \quad (7.1)$$

Inverting Equation 7.1 and expressing it in equation format yields

$$Q = K_p \delta^{3/2} \quad (7.2)$$

Similarly, for a given roller-raceway contact (line contact),

$$Q = K_l \delta^{10/9} \quad (7.3)$$

In general then,

$$Q = K\delta^n \quad (7.4)$$

where $n = 3/2$ ($= 1.5$) for ball bearings and $n = 10/9$ (≈ 1.11) for roller bearings.

The total normal approach between two raceways under the load separated by a rolling element is the sum of the approaches between the rolling element and each raceway. Hence,

$$\delta_n = \delta_i + \delta_o \quad (7.5)$$

Therefore,

$$K_n = \left[\frac{1}{(1/K_i)^{1/n} + (1/K_o)^{1/n}} \right]^n \quad (7.6)$$

and

$$Q = K_n \delta^n \quad (7.7)$$

For a steel ball–steel raceway contact,

$$K_p = 2.15 \times 10^5 \Sigma \rho^{-1/2} (\delta^*)^{-3/2} \quad (7.8)$$

Similarly, for steel roller–steel raceway contact,

$$K_1 = 8.06 \times 10^4 l^{8/9} \quad (7.9)$$

7.3 BEARINGS UNDER RADIAL LOAD

For a rigidly supported bearing subjected to a radial load, the radial deflection at any rolling element angular position is given by

$$\delta_\psi = \delta_r \cos \psi - \frac{1}{2} P_d \quad (7.10)$$

where δ_r is the ring radial shift, occurring at $\psi = 0$ and P_d is the diametral clearance. Figure 7.1 illustrates a radial bearing with clearance. Equation 7.10 may be rearranged in terms of maximum deformation as follows:

$$\delta_\psi = \delta_{\max} \left[1 - \frac{1}{2\varepsilon} (1 - \cos \psi) \right] \quad (7.11)$$

where

$$\varepsilon = \frac{1}{2} \left(1 - \frac{P_d}{2\delta_r} \right) \quad (7.12)$$

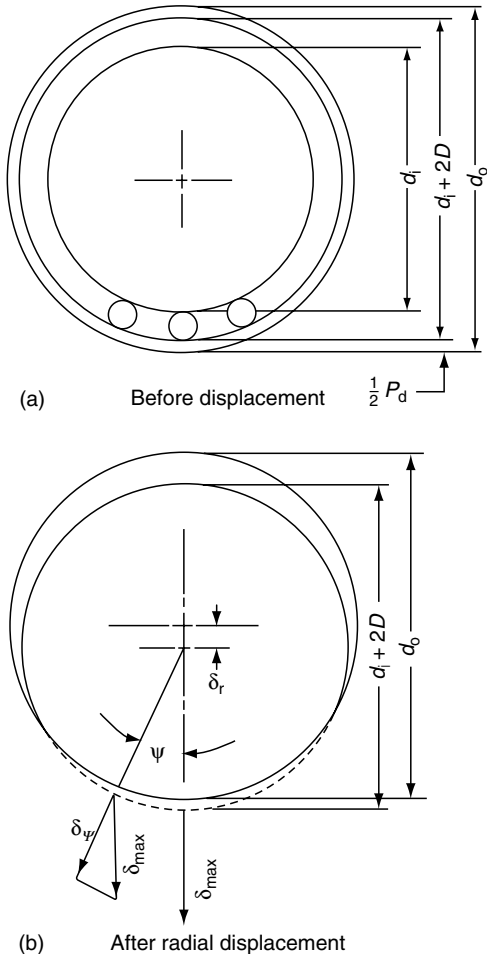


FIGURE 7.1 Bearing ring displacement.

From [Equation 7.12](#), the angular extent of the load zone is determined by the diametral clearance such that

$$\psi_l = \cos^{-1} \left(\frac{P_d}{2\delta_r} \right) \quad (7.13)$$

For zero clearance, $\psi_l = 90^\circ$.

From [Equation 7.4](#),

$$\frac{Q_\psi}{Q_{\max}} = \left(\frac{\delta_\psi}{\delta_{\max}} \right)^n \quad (7.14)$$

Therefore, from [Equation 7.11](#) and [Equation 7.14](#),

$$Q_\psi = Q_{\max} \left[1 - \frac{1}{2\varepsilon} (1 - \cos \psi) \right]^n \quad (7.15)$$

For static equilibrium, the applied radial load must equal the sum of the vertical components of the rolling element loads:

$$F_r = \sum_{\psi=0}^{\psi=\pm\psi_l} Q_\psi \cos \psi \quad (7.16)$$

or

$$F_r = Q_{\max} \sum_{\psi=0}^{\psi=\pm\psi_l} \left[1 - \frac{1}{2\varepsilon} (1 - \cos \psi) \right]^n \cos \psi \quad (7.17)$$

Equation 7.17 can also be written in integral form:

$$F_r = ZQ_{\max} \times \frac{1}{2\pi} \int_{-\psi_l}^{+\psi_l} \left[1 - \frac{1}{2\varepsilon} (1 - \cos \psi) \right]^n \cos \psi \, d\psi \quad (7.18)$$

or

$$F_r = ZQ_{\max} J_r(\varepsilon) \quad (7.19)$$

where

$$J_r(\varepsilon) = \frac{1}{2\pi} \int_{-\psi_l}^{+\psi_l} \left[1 - \frac{1}{2\varepsilon} (1 - \cos \psi) \right]^n \cos \psi \, d\psi \quad (7.20)$$

The radial integral $J_r(\varepsilon)$ of Equation 7.20 has been evaluated numerically for various values of ε . This is given in Table 7.1.

From [Equation 7.7](#),

$$Q_{\max} = K_n \delta_{\psi=0}^n = K_n (\delta_r - \frac{1}{2} P_d)^n \quad (7.21)$$

Therefore,

$$F_r = ZK_n (\delta_r - \frac{1}{2} P_d)^n J_r(\varepsilon) \quad (7.22)$$

TABLE 7.1
Load Distribution Integral $J_r(\varepsilon)$

ε	Point Contact	Line Contact	ε	Point Contact	Line Contact
0	1/Z	1/Z	0.8	0.2559	0.2658
0.1	0.1156	0.1268	0.9	0.2576	0.2628
0.2	0.1590	0.1737	1.0	0.2546	0.2523
0.3	0.1892	0.2055	1.25	0.2289	0.2078
0.4	0.2117	0.2286	1.67	0.1871	0.1589
0.5	0.2288	0.2453	2.5	0.1339	0.1075
0.6	0.2416	0.2568	5.0	0.0711	0.0544
0.7	0.2505	0.2636	∞	0	0

For a given bearing with a given clearance under a given load, [Equation 7.22](#) may be solved by trial and error. A value of δ_r is first assumed, and ε is calculated from [Equation 7.12](#). This yields $J_r(\varepsilon)$ from [Table 7.1](#). If [Equation 7.22](#) does not then balance, the process is repeated. [Figure 7.2](#) also gives values of J_r vs. ε .

[Figure 7.3](#) shows radial load distribution for values of ε : (1) corresponding to zero clearance ($\varepsilon = 0.5$), (2) positive clearance ($0 < \varepsilon < 0.5$), and (3) negative clearance or interference ($0.5 < \varepsilon < 1$). Here, ε may be considered the ratio of the load zone projected on a bearing diameter compared with the diameter.

For ball bearings having zero clearance and subjected to a simple radial load, [Stribeck \[1\]](#) determined that

$$Q_{\max} = \frac{4.37F_r}{Z \cos \alpha} \quad (7.23)$$

Accounting for nominal diametral clearance in the bearing, one may use the following approximation:

$$Q_{\max} = \frac{5F_r}{Z \cos \alpha} \quad (7.24)$$

For radial roller bearings having zero internal radial clearance and subjected to a simple radial load, it can also be determined that

$$Q_{\max} = \frac{4.08F_r}{Z \cos \alpha} \quad (7.25)$$

[Equation 7.24](#) is also a valid approximation for radial roller bearings having nominal radial clearance. For bearings supporting light loads, however, [Equation 7.24](#) is not adequate to determine the maximum rolling element load and should not be used in that situation.

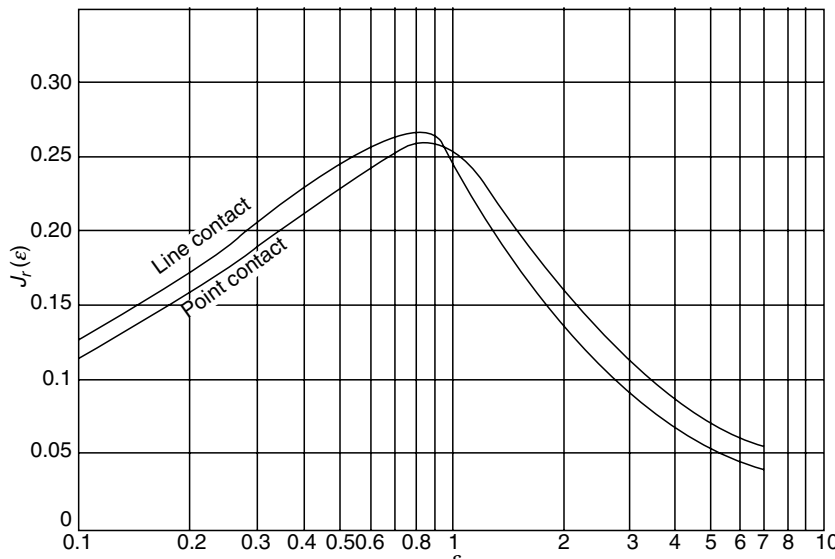


FIGURE 7.2 $J_r(\varepsilon)$ vs. ε for radial bearings.

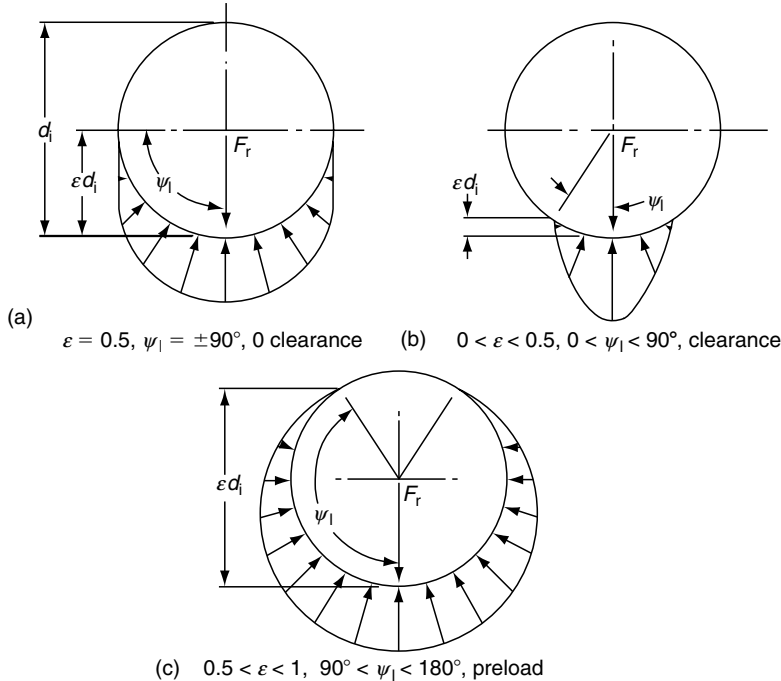


FIGURE 7.3 Rolling element load distribution for different amounts of clearance.

See Examples 7.1–7.4.

7.4 BEARINGS UNDER THRUST LOAD

7.4.1 CENTRIC THRUST LOAD

Thrust ball and roller bearings subjected to a centric thrust load have the load distributed equally among the rolling elements. Hence,

$$Q = \frac{F_a}{Z \sin \alpha} \quad (7.26)$$

In Equation 7.26, α is the contact angle that occurs in the loaded bearing. For thrust ball bearings whose contact angles are nominally less than 90° , the contact angle in the loaded bearing is greater than the initial contact angle α° that occurs in the nonloaded bearings. The phenomenon is discussed in detail in the next sections.

7.4.2 ANGULAR-CONTACT BALL BEARINGS

In the absence of centrifugal loading, the contact angles at inner and outer raceways are identical; however, they are greater than those in the unloaded condition. In the unloaded condition, the contact angle is defined by

$$\cos \alpha^\circ = 1 - \frac{P_d}{2BD} \quad (7.27)$$

where P_d is the mounted diametral clearance. A thrust load F_a applied to the inner ring as shown in Figure 7.4 causes an axial deflection δ_a . This axial deflection is a component of a normal deflection along the line of contact such that from Figure 7.4,

$$\delta_n = BD \left(\frac{\cos \alpha^\circ}{\cos \alpha} - 1 \right) \quad (7.28)$$

As $Q = K_n \delta_n^{1.5}$,

$$Q = K_n (BD)^{1.5} \left(\frac{\cos \alpha^\circ}{\cos \alpha} - 1 \right)^{1.5} \quad (7.29)$$

Substitution of Equation 7.26 into Equation 7.29 yields

$$\frac{F_a}{ZK_n(BD)^{1.5}} = \sin \alpha \left(\frac{\cos \alpha^\circ}{\cos \alpha} - 1 \right)^{1.5} \quad (7.30)$$

Since K_n is a function of the final contact angle α , Equation 7.30 must be solved by trial and error to yield an exact solution for α . Jones [2], however, defines an axial deflection constant K as follows:

$$K = \frac{B}{g(+\gamma) + g(-\gamma)} \quad (7.31)$$

where $\gamma = (D \cos \alpha) / d_m$, $g(+\gamma)$ refers to the inner raceway, and $g(-\gamma)$ refers to the outer raceway. Jones [2] further indicates that the sum of $g(+\gamma)$ and $g(-\gamma)$ remains virtually

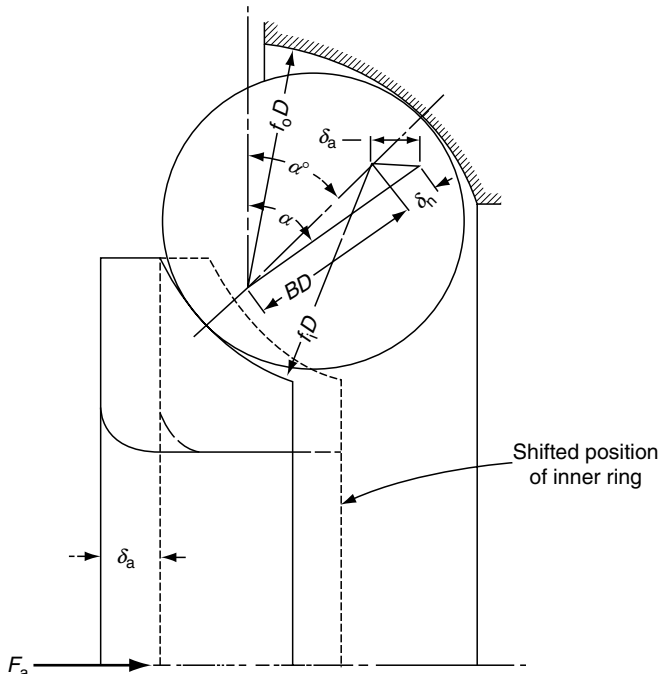


FIGURE 7.4 Angular-contact ball bearing under thrust load.

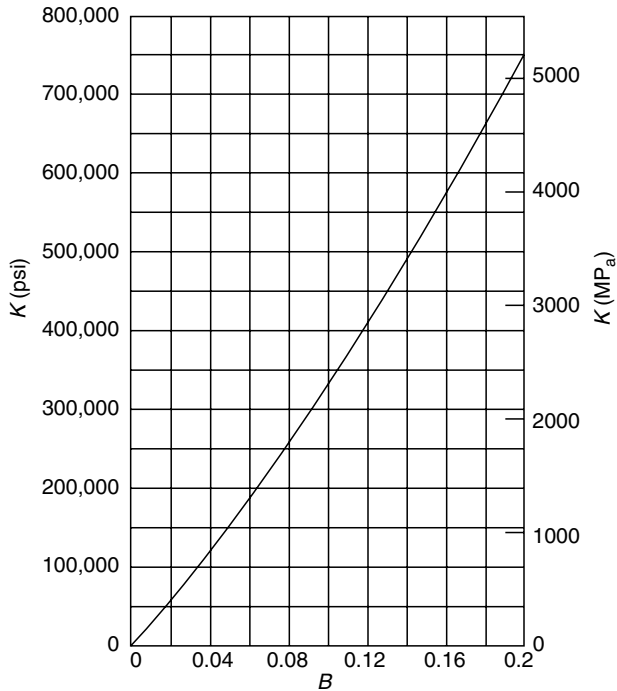


FIGURE 7.5 Axial deflection constant K vs. total curvature B for ball bearings ($B = f_o + f_i - 1$, $f = r/D$ [2]).

constant for all contact angles dependent only on total curvature B . The axial deflection constant K is related to K_n as follows:

$$K_n = \frac{KD^{0.5}}{B^{1.5}} \quad (7.32)$$

Hence,

$$\frac{F_a}{ZD^2K} = \sin \alpha \left(\frac{\cos \alpha^\circ}{\cos \alpha} - 1 \right)^{1.5} \quad (7.33)$$

Taking K from Figure 7.5, Equation 7.33 may be solved numerically by the Newton–Raphson method. The equation to be satisfied iteratively is

$$\alpha' = \alpha + \frac{\frac{F_a}{ZD^2K} - \sin \alpha \left(\frac{\cos \alpha^\circ}{\cos \alpha} - 1 \right)^{1.5}}{\cos \alpha \left(\frac{\cos \alpha^\circ}{\cos \alpha} - 1 \right)^{1.5} + 1.5 \tan^2 \alpha \left(\frac{\cos \alpha^\circ}{\cos \alpha} - 1 \right)^{0.5} \cos \alpha^\circ} \quad (7.34)$$

Equation 7.34 is satisfied when $\alpha' - \alpha$ is essentially zero.

The axial deflection δ_a corresponding to δ_n may also be determined from Figure 7.6 as follows:

$$\delta_a = (BD + \delta_n) \sin \alpha - BD \sin \alpha^\circ \quad (7.35)$$

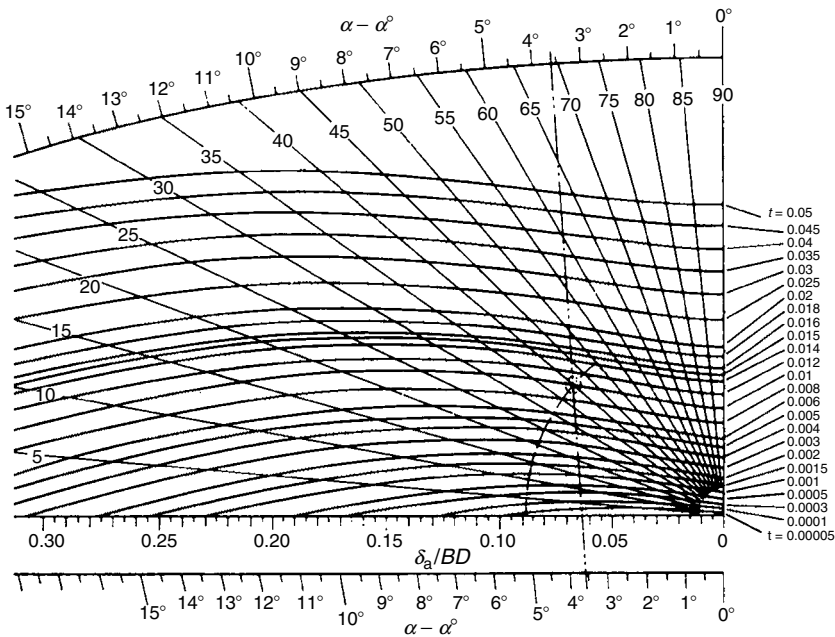


FIGURE 7.6 δ_a/BD and $\alpha = \alpha^\circ$ vs. $t = F_a/ZD^2K$ and α° .

Substituting δ_n from Equation 7.28 yields

$$\delta_a = \frac{BD \sin(\alpha - \alpha^\circ)}{\cos \alpha} \quad (7.36)$$

Figure 7.6 presents a series of curves for the rapid calculation of the change in contact angle ($\alpha - \alpha^\circ$), and axial deflection as functions of initial contact angle and $t = F_a/ZD^2K$.

See Example 7.5.

7.4.3 ECCENTRIC THRUST LOAD

7.4.3.1 Single-Direction Bearings

Figure 7.7 illustrates a single-row thrust bearing subjected to an eccentric thrust load. If we take $\psi = 0$ as the position of the maximum loaded rolling element, then

$$\delta_\psi = \delta_a + \frac{1}{2}\theta d_m \cos \psi \quad (7.37)$$

Also,

$$\delta_{\max} = \delta_a + \frac{1}{2}\theta d_m \quad (7.38)$$

From Equation 7.37 and Equation 7.38, one may develop the familiar relationship

$$\delta_\psi = \delta_{\max} \left[1 - \frac{1}{2\varepsilon} (1 - \cos \psi) \right] \quad (7.39)$$

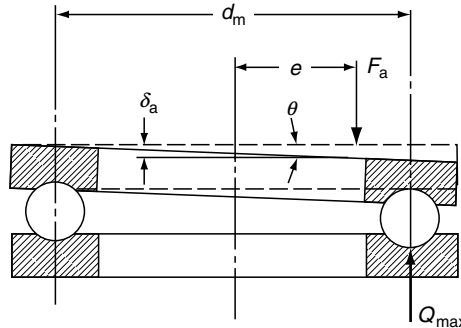


FIGURE 7.7 90° ball thrust bearing under an eccentric load.

where

$$\varepsilon = \frac{1}{2} \left(1 + \frac{2\delta_a}{\theta d_m} \right) \quad (7.40)$$

The extent of the zone of loading is defined by

$$\psi_\ell = \cos^{-1} \left(\frac{-2\delta_a}{\theta d_m} \right) \quad (7.41)$$

As before,

$$Q_\psi = Q_{\max} \left[1 - \frac{1}{2\varepsilon} (1 - \cos \psi) \right]^n \quad (7.42)$$

Static equilibrium requires that

$$F_a = \sum_{\psi=0}^{\psi=\pm\pi} Q_\psi \sin \alpha \quad (7.43)$$

$$M = eF_a = \sum_{\psi=0}^{\psi=\pm\pi} \frac{1}{2} Q_\psi d_m \sin \alpha \cos \psi \quad (7.44)$$

Equation 7.43 and Equation 7.44 may also be written in terms of thrust and moment integrals as follows:

$$F_a = ZQ_{\max}J_a(\varepsilon) \sin \alpha \quad (7.45)$$

where

$$J_a(\varepsilon) = \frac{1}{2\varepsilon} \int_{-\psi_\ell}^{+\psi_\ell} \left[1 - \frac{1}{2\varepsilon} (1 - \cos \psi) \right]^n d\psi \quad (7.46)$$

$$M = eF_a = \frac{1}{2} ZQ_{\max}d_m J_m(\varepsilon) \sin \alpha \quad (7.47)$$

where

$$J_m(\varepsilon) = \frac{1}{2\pi} \int_{-\psi_l}^{+\psi_l} \left[1 - \frac{1}{2\varepsilon} (1 - \cos \psi) \right]^n \cos \psi d\psi \quad (7.48)$$

Table 7.2, as shown by Rumbarger [3], gives values of $J_a(\varepsilon)$ and $J_m(\varepsilon)$ as functions of $2e/d_m$. [Figure 7.8](#) and [Figure 7.9](#) yield identical data in graphical format. [Figure 7.10](#) demonstrates a typical distribution of load in a 90° thrust bearing subjected to eccentric load.

7.4.3.2 Double-Direction Bearings

The following relationships are valid for a two-row double-direction thrust bearing:

$$\delta_{a1} = -\delta_{a2} \quad (7.49)$$

$$\theta_1 = \theta_2 \quad (7.50)$$

It can also be shown that

$$\varepsilon_1 + \varepsilon_2 = 1 \quad (7.51)$$

and

$$\frac{\delta_{\max_2}}{\delta_{\max_1}} = \frac{\varepsilon_2}{\varepsilon_1} \quad (7.52)$$

TABLE 7.2
 $J_a(\varepsilon)$ and $J_m(\varepsilon)$ for Single-Row Thrust Bearings

ε	Point Contact			Line Contact		
	$\frac{2e}{d_m}$	$J_m(\varepsilon)$	$J_a(\varepsilon)$	$\frac{2e}{d_m}$	$J_m(\varepsilon)$	$J_a(\varepsilon)$
0	1.0000	1/Z	1/Z	1.0000	1/Z	1/Z
0.1	0.9663	0.1156	0.1196	0.9613	0.1268	0.1319
0.2	0.9318	0.159	0.1707	0.9215	0.1737	0.1885
0.3	0.8964	0.1892	0.2110	0.8805	0.2055	0.2334
0.4	0.8601	0.2117	0.2462	0.8380	0.2286	0.2728
0.5	0.8225	0.2288	0.2782	0.7939	0.2453	0.3090
0.6	0.7835	0.2416	0.3084	0.7488	0.2568	0.3433
0.7	0.7427	0.2505	0.3374	0.6999	0.2636	0.3766
0.8	0.6995	0.2559	0.3658	0.6486	0.2658	0.4098
0.9	0.6529	0.2576	0.3945	0.5920	0.2628	0.4439
1.0	0.6000	0.2546	0.4244	0.5238	0.2523	0.4817
1.25	0.4338	0.2289	0.5044	0.3598	0.2078	0.5775
1.67	0.3088	0.1871	0.6060	0.2340	0.1589	0.6790
2.5	0.1850	0.1339	0.7240	0.1372	0.1075	0.7837
5.0	0.0831	0.0711	0.8558	0.0611	0.0544	0.8909
∞	0	0	1.0000	0	0	1.0000

Source: Rumbarger, J., Thrust bearing with eccentric loads, *Mach. Des.* February 15, 1962.

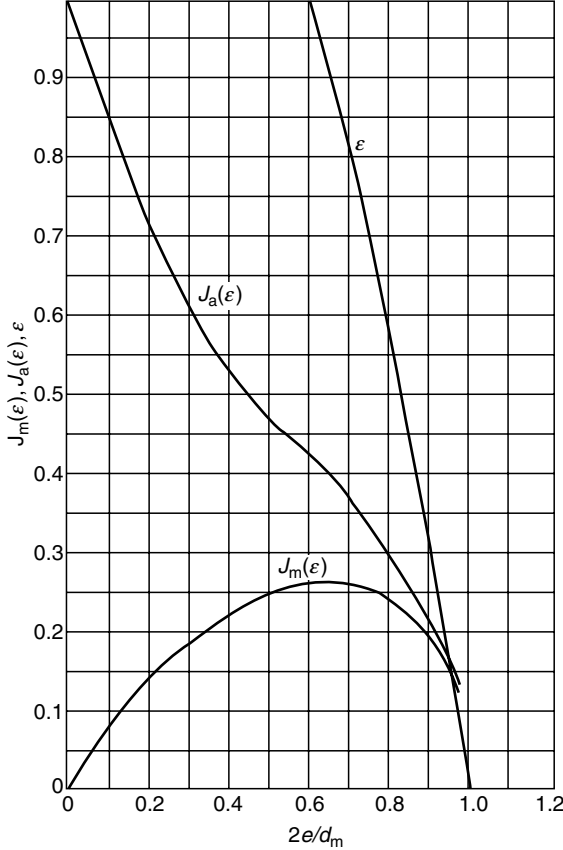


FIGURE 7.8 $J_m(\varepsilon)$, $J_a(\varepsilon)$, ε vs. $2e/d_m$ for point-contact thrust bearings.

Considering Equation 7.4, Equation 7.52 becomes

$$\frac{Q_{\max_2}}{Q_{\max_1}} = \left(\frac{\varepsilon_2}{\varepsilon_1}\right)^n \quad (7.53)$$

In Equation 7.53, $n = 1.5$ for ball bearings and $n = 1.11$ for roller bearings. From conditions of equilibrium one may conclude that

$$F_a = F_{a1} - F_{a2} = ZQ_{\max_1}J_a \sin \alpha \quad (7.54)$$

where

$$J_a = J_a(\varepsilon_1) - \frac{Q_{\max_2}}{Q_{\max_1}} J_a(\varepsilon_2) \quad (7.55)$$

$$M = M_1 + M_2 = \frac{1}{2}ZQ_{\max_1}d_mJ_m \sin \alpha \quad (7.56)$$

where

$$J_m = J_m(\varepsilon_1) + \frac{Q_{\max_2}}{Q_{\max_1}} J_m(\varepsilon_2) \quad (7.57)$$

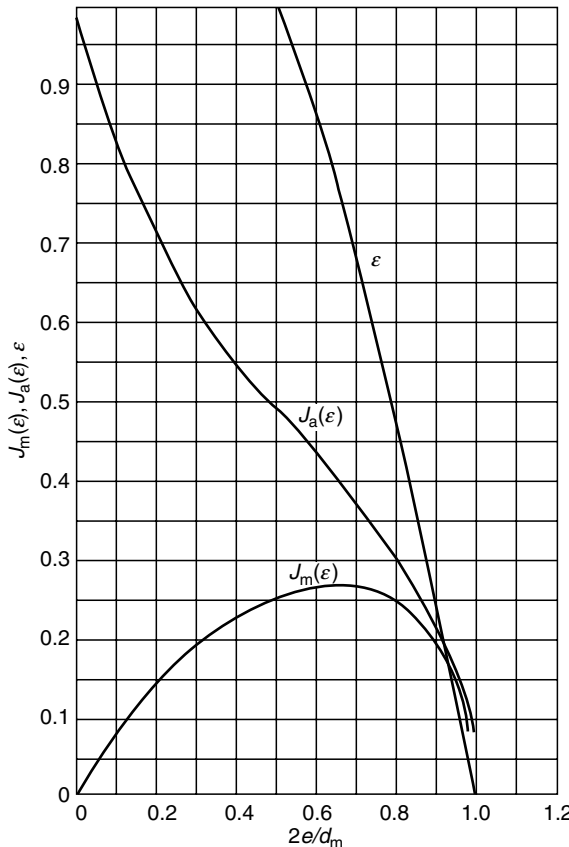


FIGURE 7.9 $J_m(\varepsilon)$, $J_a(\varepsilon)$, ε vs. $2e/d_m$ for line-contact thrust bearings.

Table 7.3 gives values of J_a and J_m as functions of $2e/d_m$ for two-row bearings. Figure 7.11 and Figure 7.12 give the same data in graphical format.

7.5 BEARINGS UNDER COMBINED RADIAL AND THRUST LOAD

7.5.1 SINGLE-ROW BEARINGS

If a rolling bearing without diametral clearance is subjected simultaneously to a radial load in the central plane of the rollers and a centric thrust load, then the inner and outer rings of the

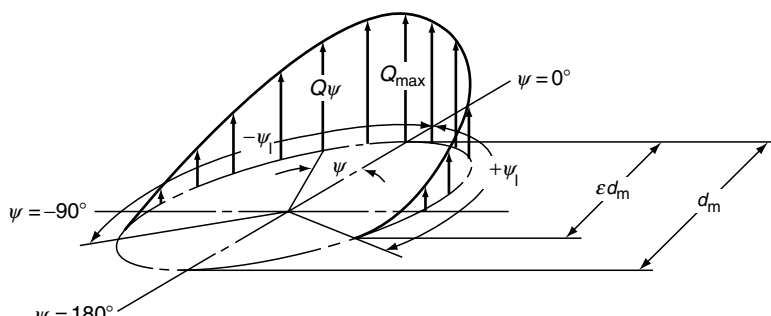


FIGURE 7.10 Load distribution in a 90° thrust bearing under eccentric load.

TABLE 7.3
 J_a and J_m for Two-Row Thrust Bearings

Point Contact						Line Contact			
ε_1	ε_2	$\frac{2e}{d_m}$	J_m	J_a	$\frac{Q_{\max_2}}{Q_{\max_1}}$	$\frac{2e}{d_m}$	J_m	J_a	$\frac{Q_{\max_2}}{Q_{\max_1}}$
0.50	0.50	∞	0.4577	0	1.000	∞	0.4906	0	1.000
0.51	0.49	25.72	0.4476	0.0174	0.941	28.50	0.4818	0.0169	0.955
0.60	0.40	2.046	0.3568	0.1744	0.544	2.389	0.4031	0.1687	0.640
0.70	0.30	1.092	0.3036	0.2782	0.281	1.210	0.3445	0.2847	0.394
0.80	0.20	0.800	0.2758	0.3445	0.125	0.823	0.3036	0.3688	0.218
0.90	0.10	0.671	0.2618	0.3900	0.037	0.634	0.2741	0.4321	0.089
1.0	0	0.600	0.2546	0.4244	0	0.524	0.2523	0.4817	0
1.25	0	0.434	0.2289	0.5044	0	0.360	0.2078	0.5775	0
1.67	0	0.309	0.1871	0.6060	0	0.234	0.1589	0.6790	0
2.5	0	0.185	0.1339	0.7240	0	0.137	0.1075	0.7837	0
5.0	0	0.083	0.0711	0.8558	0	0.061	0.0544	0.8909	0
∞	0	0	0	1.0000	0	0	0	1.0000	0

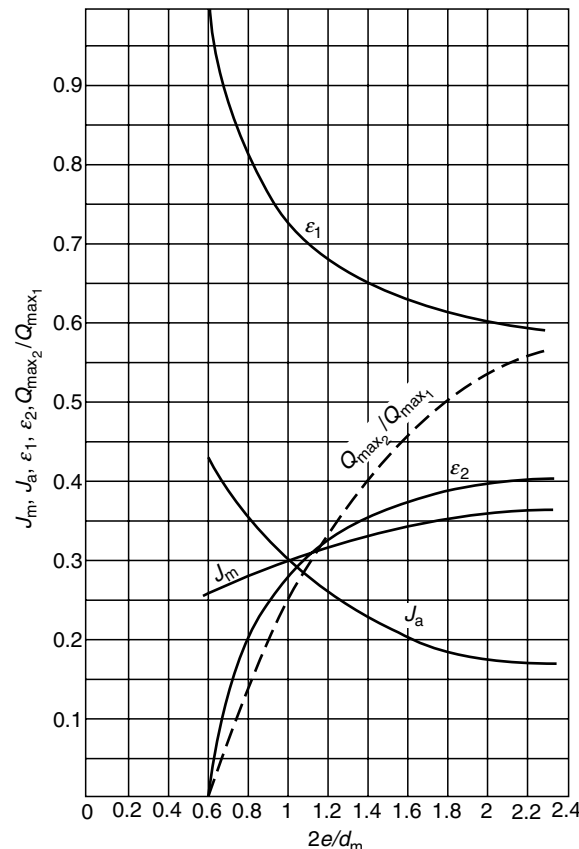


FIGURE 7.11 J_m , J_a , ε_1 , ε_2 , Q_{\max_2}/Q_{\max_1} vs. $2e/d_m$ for double-row point-contact thrust bearings.

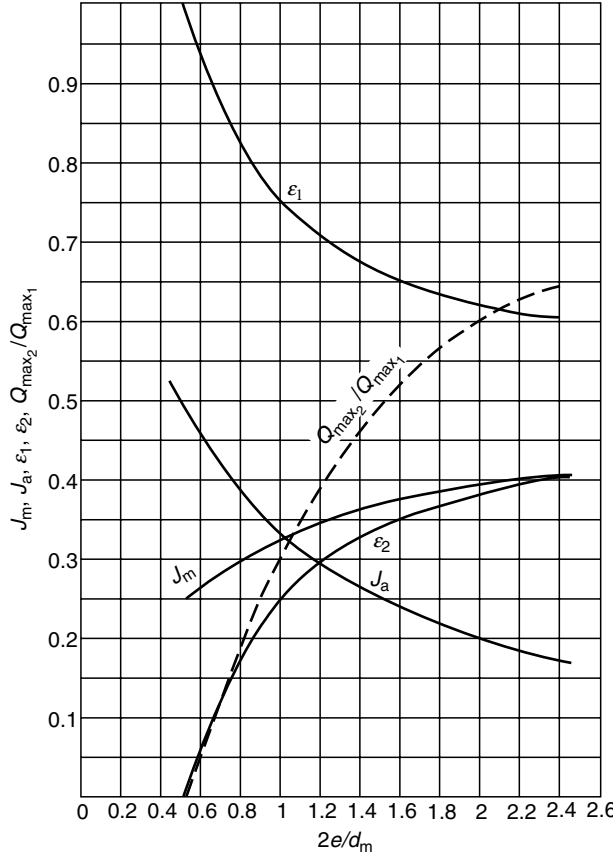


FIGURE 7.12 J_m , J_a , ε_1 , ε_2 , $Q_{\text{max}_2}/Q_{\text{max}_1}$ vs. $2e/d_m$ for double-row line-contact thrust bearings.

bearing will remain parallel and will be relatively displaced by a distance δ_a in the axial direction and δ_r in the radial direction. At any regular position ψ measured from the most heavily loaded rolling element, the approach of the rings is

$$\delta_\psi = \delta_a \sin \alpha + \delta_r \cos \alpha \cos \psi \quad (7.58)$$

Figure 7.13 illustrates this condition. At $\psi = 0$, maximum deflection occurs and is given by

$$\delta_{\text{max}} = \delta_a \sin \alpha + \delta_r \cos \alpha \quad (7.59)$$

Combining Equation 7.58 and Equation 7.59 yields

$$\delta_\psi = \delta_{\text{max}} \left[1 - \frac{1}{2\varepsilon} (1 - \cos \psi) \right] \quad (7.60)$$

This expression is identical in form to [Equation 7.11](#); however,

$$\varepsilon = \frac{1}{2} \left(1 + \frac{\delta_a \tan \alpha}{\delta_r} \right) \quad (7.61)$$

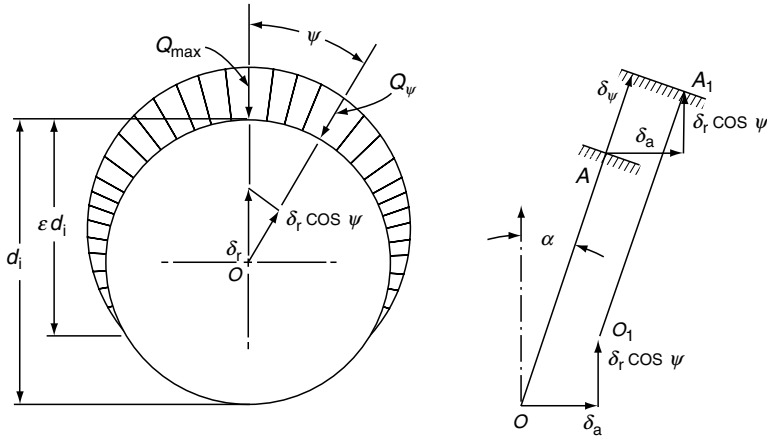


FIGURE 7.13 Rolling bearing displacements due to combined radial and axial loadings.

It should also be apparent that

$$Q_\psi = Q_{\max} \left[1 - \frac{1}{2\varepsilon} (1 - \cos \psi) \right]^n \quad (7.62)$$

As in [Equation 7.4](#), $n = 1.5$ for ball bearings and $n = 1.11$ for roller bearings.

For static equilibrium to exist, the summation of rolling element forces in each direction must equal the applied load in that direction:

$$F_r = \sum_{\psi=-\psi_\ell}^{\psi=+\psi_\ell} Q_\psi \cos \alpha \cos \psi \quad (7.63)$$

$$F_a = \sum_{\psi=-\psi_\ell}^{\psi=+\psi_\ell} Q_\psi \sin \alpha \quad (7.64)$$

where the limiting angle is defined by

$$\psi_\ell = \cos^{-1} \left(-\frac{\delta_a \tan \alpha}{\delta_r} \right) \quad (7.65)$$

[Equation 7.63](#) and [Equation 7.64](#) may be rewritten in terms of a radial integral and thrust integral, respectively:

$$F_r = Z Q_{\max} J_r(\varepsilon) \cos \alpha \quad (7.66)$$

where

$$J_r(\varepsilon) = \frac{1}{2\pi} \int_{-\psi_\ell}^{+\psi_\ell} \left[1 - \frac{1}{2\varepsilon} (1 - \cos \psi) \right]^n \cos \psi \, d\psi \quad (7.67)$$

TABLE 7.4
 $J_r(\varepsilon)$ and $J_a(\varepsilon)$ for Single-Row Bearings

ε	Point Contact			Line Contact		
	$\frac{F_r \tan \alpha}{F_a}$	$J_r(\varepsilon)$	$J_a(\varepsilon)$	$\frac{F_r \tan \alpha}{F_a}$	$J_r(\varepsilon)$	$J_a(\varepsilon)$
0	1	1/Z	1/Z	1	1/Z	1/Z
0.2	0.9318	0.1590	0.1707	0.9215	0.1737	0.1885
0.3	0.8964	0.1892	0.2110	0.8805	0.2055	0.2334
0.4	0.8601	0.2117	0.2462	0.8380	0.2286	0.2728
0.5	0.8225	0.2288	0.2782	0.7939	0.2453	0.3090
0.6	0.7835	0.2416	0.3084	0.7480	0.2568	0.3433
0.7	0.7427	0.2505	0.3374	0.6999	0.2636	0.3766
0.8	0.6995	0.2559	0.3658	0.6486	0.2658	0.4098
0.9	0.6529	0.2576	0.3945	0.5920	0.2628	0.4439
1	0.6000	0.2546	0.4244	0.5238	0.2523	0.4817
1.25	0.4338	0.2289	0.5044	0.3598	0.2078	0.5775
1.67	0.3088	0.1871	0.6060	0.2340	0.1589	0.6790
2.5	0.1850	0.1339	0.7240	0.1372	0.1075	0.7837
5	0.0831	0.0711	0.8558	0.0611	0.0544	0.8909
∞	0	0	1	0	0	1

and

$$F_a = Z Q_{\max} J_a(\varepsilon) \sin \alpha \quad (7.68)$$

where

$$J_a(\varepsilon) = \frac{1}{2\pi} \int_{-\psi_l}^{+\psi_l} \left[1 - \frac{1}{2\varepsilon} (1 - \cos \psi) \right]^n d\psi \quad (7.69)$$

The integrals of Equation 7.67 and Equation 7.69 were introduced by Sjoväll [4]. Table 7.4 gives values of these integrals for point and line contact as functions of $F_r \tan \alpha / F_a$.

Note that the contact angle α is assumed identical for all loaded balls or rollers. Thus, the values of the integrals are approximate; however, they are sufficiently accurate for most calculations. Using these integrals,

$$Q_{\max} = \frac{F_r}{J_r(\varepsilon) Z \sin \alpha} \quad (7.70)$$

or

$$Q_{\max} = \frac{F_a}{J_a(\varepsilon) Z \sin \alpha} \quad (7.71)$$

Figure 7.14 and Figure 7.15 also give values of J_r , J_a , and ε vs. $F_r \tan \alpha / F_a$ for point and line contacts, respectively.

See Example 7.7.

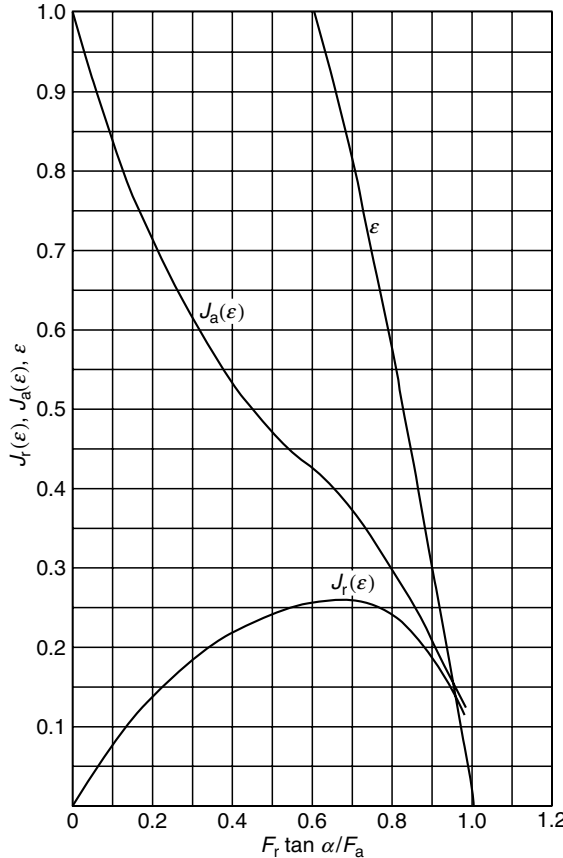


FIGURE 7.14 $J_r(\varepsilon)$, $J_a(\varepsilon)$, ε vs. $F_r \tan \alpha / F_a$ for point-contact bearings.

7.5.2 DOUBLE-ROW BEARINGS

Let the indices 1 and 2 designate the rows of a two-row bearing having zero diametral clearance. Then,

$$\delta_{r1} = \delta_{r2} = \delta_r \quad (7.72)$$

$$\delta_{a1} = -\delta_{a2} \quad (7.73)$$

Substituting these conditions into Equation 7.59 and Equation 7.60 yields

$$\frac{\delta_{\max_2}}{\delta_{\max_1}} = \frac{\varepsilon_2}{\varepsilon_1} \quad (7.74)$$

$$\varepsilon_1 + \varepsilon_2 = 1 \quad (7.75)$$

Equation 7.75 pertains only if both rows are loaded. If only one row is loaded, then

$$\varepsilon_1 \geq 1, \quad \varepsilon_2 = 0 \quad (7.76)$$

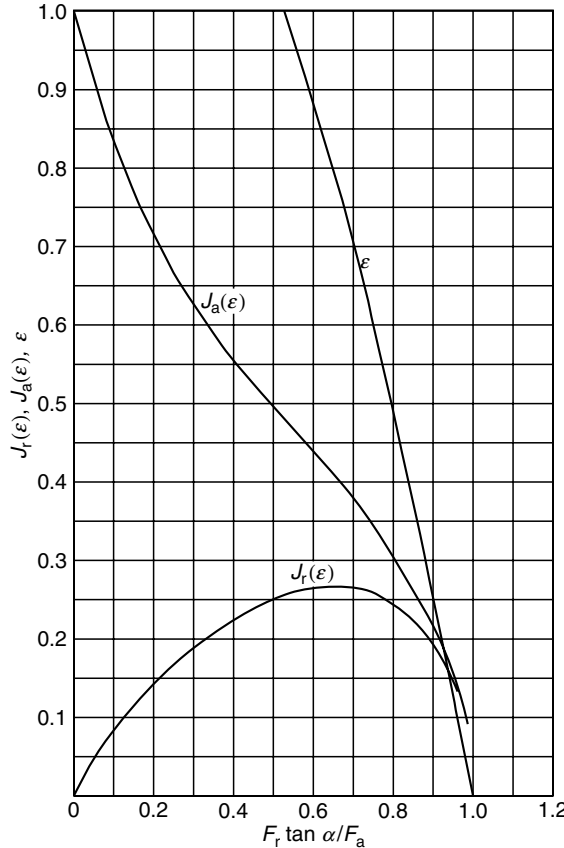


FIGURE 7.15 $J_r(\varepsilon)$, $J_a(\varepsilon)$, ε vs. $F_r \tan \alpha / F_a$ for line-contact bearings.

It is further clear from [Equation 7.4](#) that

$$\frac{Q_{\max_2}}{Q_{\max_1}} = \left(\frac{\varepsilon_2}{\varepsilon_1} \right)^n \quad (7.77)$$

The laws of static equilibrium dictate that

$$F_r = F_{r1} + F_{r2} \quad (7.78)$$

$$F_a = F_{a1} + F_{a2} \quad (7.79)$$

As before,

$$F_r = Z Q_{\max_1} J_r \cos \alpha \quad (7.80)$$

$$F_a = Z Q_{\max_1} J_a \sin \alpha \quad (7.81)$$

where

$$J_r = J_r(\varepsilon_1) + \frac{Q_{\max_2}}{Q_{\max_1}} J_r(\varepsilon_2) \quad (7.82)$$

TABLE 7.5
 J_a and J_r for Double-Row Bearings

Point Contact						Line Contact					
ε_1	ε_2	$\frac{F_r \tan \alpha}{F_a}$	J_r	J_a	$\frac{Q_{\max_2}}{Q_{\max_1}}$	$\frac{F_{r2}}{F_{r1}}$	$\frac{F_r \tan \alpha}{F_a}$	J_r	J_a	$\frac{Q_{\max_2}}{Q_{\max_1}}$	$\frac{F_{r2}}{F_{r1}}$
0.5	0.5	∞	0.4577	0	1	1	∞	0.4906	0	1	1
0.6	0.4	2.046	0.3568	0.1744	0.544	0.477	2.389	0.4031	0.1687	0.640	0.570
0.7	0.3	1.092	0.3036	0.2782	0.281	0.212	1.210	0.3445	0.2847	0.394	0.306
0.8	0.2	0.8005	0.2758	0.3445	0.125	0.078	0.8232	0.3036	0.3688	0.218	0.142
0.9	0.1	0.6713	0.2618	0.3900	0.037	0.017	0.6343	0.2741	0.4321	0.089	0.043
1.0	0	0.6000	0.2546	0.4244	0	0	0.5238	0.2523	0.4817	0	0

$$J_a = J_a(\varepsilon_1) + \frac{Q_{\max_2}}{Q_{\max_1}} J_a(\varepsilon_2) \quad (7.83)$$

Table 7.5 gives values of J_r and J_a as functions of $F_r \tan \alpha / F_a$. Figure 7.16 and Figure 7.17 give the same data in graphical format for point and line contact, respectively.

See Example 7.8.

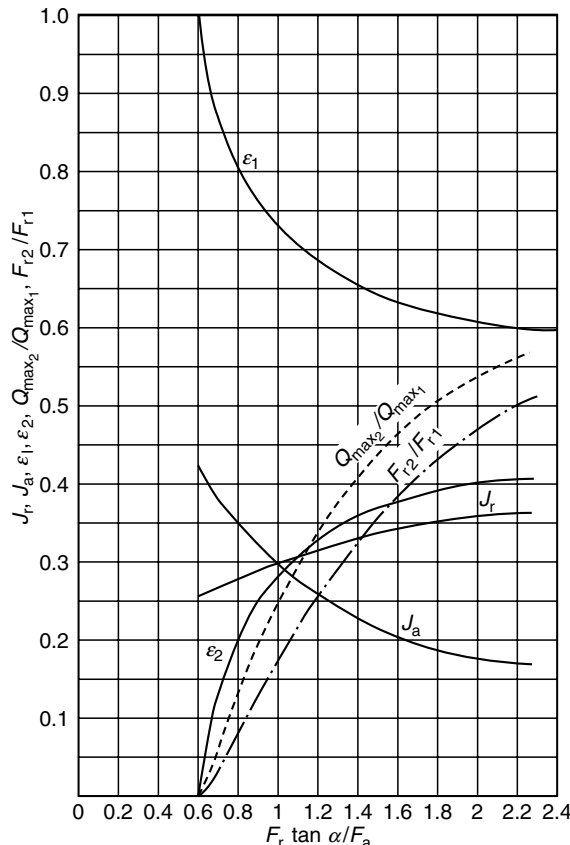


FIGURE 7.16 J_r , J_a , ε_1 , ε_2 , Q_{\max_2}/Q_{\max_1} , F_{r2}/F_{r1} vs. $F_r \tan \alpha / F_a$ for double-row point-contact bearings.

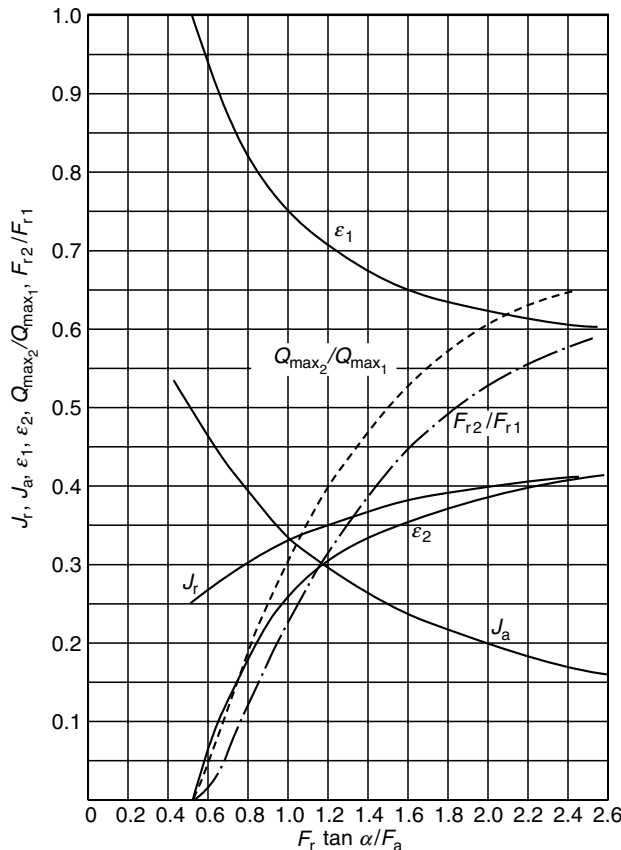


FIGURE 7.17 J_r , J_a , ϵ_1 , ϵ_2 , Q_{\max_2}/Q_{\max_1} , F_{r2}/F_{r1} vs. $F_r \tan \alpha / F_a$ for double-row line-contact bearings.

7.6 CLOSURE

The methods to calculate the distribution of load among the balls and rollers of rolling bearings shown in this chapter can be used in bearing applications where rotational speeds are slow to moderate. Under these speed conditions, effects of rolling element centrifugal forces and gyroscopic moments are negligible. At high rotational speeds, these body forces become significant, tending to alter contact angles and internal clearance and can affect the internal load distribution to a great extent.

In the foregoing discussion, relatively simple calculation techniques were used to determine the internal load distribution. Together with the tabular and graphical data provided, hand calculation devices may be employed to achieve the calculated results. In subsequent chapters in the Second Volume of this handbook, to evaluate the effects of loading in three or five degrees of freedom in ball and roller bearings, the effects of misalignment and thrust loading in roller bearings, and nonrigid bearing rings, digital computation must be used. Nevertheless, for many applications the relatively simple methods demonstrated in this chapter may be used effectively.

It has been demonstrated in this chapter that bearing radial and axial deflections are functions of the internal load distribution. Further, since the contact stresses in a bearing depend on the load, maximum contact stress in a bearing is also a function of load distribution. Consequently, bearing fatigue life, which is governed by stress level, is significantly affected by the rolling element load distribution.

REFERENCES

1. Stribeck, R., Ball bearings for various loads, *Trans. ASME* 29, 420–463, 1907.
2. Jones, A., *Analysis of Stresses and Deflections*, New Departure Engineering Data, Bristol, CT, 1946.
3. Rumbarger, J., Thrust bearing with eccentric loads, *Mach. Des.* (February 15, 1962).
4. Sjoväll, H., The load distribution within ball and roller bearings under given external radial and axial load, *Teknisk Tidskrift, Mek.*, h.9, 1933.

8 Bearing Deflection and Preloading

LIST OF SYMBOLS

Symbol	Description	Units
a	Semimajor axis of the projected contact ellipse	mm (in.)
b	Semiminor axis of the projected contact ellipse	mm (in.)
d_1	Land diameter	mm (in.)
D	Ball or roller diameter	mm (in.)
F	Applied force	N (lb)
$J_r (\varepsilon)$	Radial load integral	N/mm^x (lb/in. ^x)
K	Load-deflection constant	$\text{N} \cdot \text{mm}$ (in. lb)
l	Roller effective length	mm (in.)
M	Moment load	
Q	Rolling element load	N (lb)
Z	Number of rolling elements per row	
α	Contact angle	rad, °
γ	$D \cos \alpha / d_m$	
δ	Deflection or contact deformation	mm (in.)
δ'	Deflection rate	mm/N (in./lb)
ε	Projection of radial load zone on bearing pitch diameter	
θ	Angle of land	rad, °
σ_{\max}	Maximum contact stress	MPa (psi)
$\Sigma\rho$	Curvature sum	$\text{mm}^{-1} (\text{in.}^{-1})$
Φ	Angle	rad, °

Subscripts

a	Axial direction
i	Inner raceway
n	Direction collinear with rolling element load
o	Outer raceway
p	Preload condition
r	Radial direction
R	Ball or roller
1	Bearing 1
2	Bearing 2

8.1 GENERAL

In Chapter 6, methods for calculating the elastic contact deformations between a ball and a raceway and between a roller and a raceway were demonstrated. For bearings with rigidly supported rings, the elastic deflection of a bearing as a unit depends on the maximum elastic contact deformation in the direction of the applied load or in the direction of interest to the application designer. Because the maximum elastic contact deformation depends on the rolling element loads, it is necessary to analyze the load distribution occurring within the bearing before determination of the bearing deflection. Chapter 7 demonstrated methods for evaluating the load distribution among the rolling elements for bearings with rigidly supported rings subjected to a relatively simple statically applied loading. In these methods, the variables δ_r and δ_a , the principal bearing deflections, were utilized. These deflections may be critical in determining system stability, dynamic loading on other components, and accuracy of system operation in many applications and are discussed in this chapter.

8.2 DEFLECTIONS OF BEARINGS WITH RIGIDLY SUPPORTED RINGS

Using the methods of Chapter 7, it is possible to calculate the maximum rolling element load Q_{\max} due to a simple applied radial load, axial load, or combined radial and axial loads. In lieu of a more rigorous approach to the determination of bearing deflections, Palmgren [1] provided a series of formulas to calculate the bearing deflection for specific conditions of applied loading. For slow and moderate speed, deep-groove, and angular-contact ball bearings subject to a radial load that causes only radial deflection, that is $\delta_a = 0$,

$$\delta_r = 4.36 \times 10^{-4} \frac{Q_{\max}^{2/3}}{D^{1/3} \cos \alpha} \quad (8.1)$$

For self-aligning ball bearings,

$$\delta_r = 6.98 \times 10^{-4} \frac{Q_{\max}^{2/3}}{D^{1/3} \cos \alpha} \quad (8.2)$$

For slow and moderate speed radial roller bearings with point contact at one raceway and line contact at the other,

$$\delta_r = 1.81 \times 10^{-4} \frac{Q_{\max}^{3/4}}{l^{1/2} \cos \alpha} \quad (8.3)$$

For radial roller bearings with line contact at each raceway,

$$\delta_r = 7.68 \times 10^{-5} \frac{Q_{\max}^{0.9}}{l^{0.8} \cos \alpha} \quad (8.4)$$

To these given values, we must add the appropriate radial clearance and any deflection due to a nonrigid housing.

The axial deflection under pure axial load, that is, $\delta_r = 0$, for angular-contact ball bearings is given by

$$\delta_a = 4.36 \times 10^{-4} \frac{Q_{\max}^{2/3}}{D^{1/3} \sin \alpha} \quad (8.5)$$

For self-aligning ball bearings,

$$\delta_a = 6.98 \times 10^{-4} \frac{Q_{\max}^{2/3}}{D^{1/3} \sin \alpha} \quad (8.6)$$

For thrust ball bearings,

$$\delta_a = 5.24 \times 10^{-4} \frac{Q_{\max}^{2/3}}{D^{1/3} \sin \alpha} \quad (8.7)$$

For radial ball bearings subjected to axial load, the contact angle α must be determined before using [Equation 8.5](#). For roller bearings with point contact at one raceway and line contact at the other,

$$\delta_a = 1.81 \times 10^{-4} \frac{Q_{\max}^{3/4}}{l^{1/2} \sin \alpha} \quad (8.8)$$

For roller bearings with line contact at each raceway,

$$\delta_a = 7.68 \times 10^{-5} \frac{Q_{\max}^{0.9}}{l^{0.8} \sin \alpha} \quad (8.9)$$

See Examples 8.1 and 8.2.

8.3 PRELOADING

8.3.1 AXIAL PRELOADING

A typical curve of ball bearing deflection vs. load is shown in Figure 8.1. It can be seen from Figure 8.1 that as the load is increased uniformly, the rate of deflection increase declines. Hence, it would be advantageous with regard to minimizing bearing deflection under load to operate above the knee of the load-deflection curve. This condition can be realized by axially preloading angular-contact ball bearings. This is usually done, as shown in [Figure 8.2](#), by grinding the stock from opposing end faces of the bearings and then locking the bearings

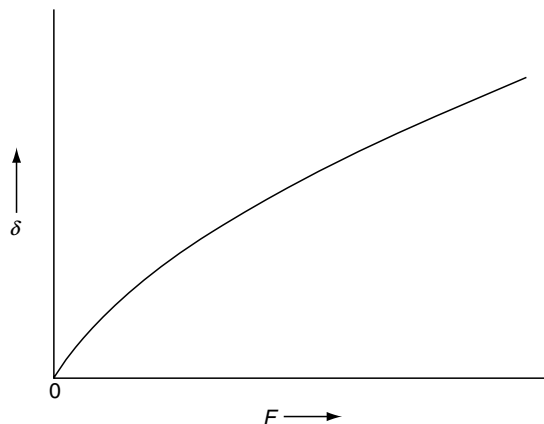


FIGURE 8.1 Deflection vs. load characteristic for ball bearings.

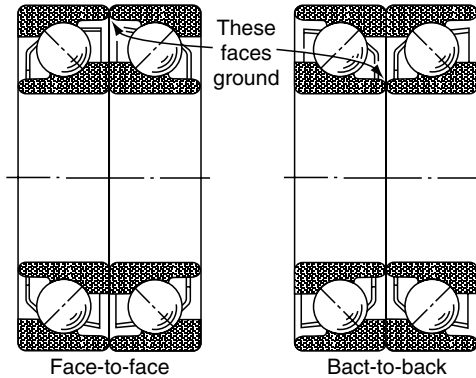


FIGURE 8.2 Duplex sets of angular-contact ball bearings.

together on the shaft. Figure 8.3 shows preloaded bearing sets before and after the bearings are axially locked together. Figure 8.4 illustrates, graphically, the improvement in load-deflection characteristics obtained by preloading ball bearings.

Suppose that two identical angular-contact ball bearings are placed back-to-back or face-to-face on a shaft as shown in Figure 8.5 and drawn together by a locking device. Each bearing experiences an axial deflection δ_p due to preload F_p . The shaft is thereafter subjected to thrust load F_a , as shown in Figure 8.5, and because of the thrust load, the bearing combination undergoes an axial deflection δ_a . In this situation, the total axial deflection at bearing 1 is

$$\delta_1 = \delta_p + \delta_a \quad (8.10)$$

and at bearing 2,

$$\delta_2 = \begin{cases} \delta_p - \delta_a & \delta > \delta_a \\ 0 & \delta_p \leq \delta_a \end{cases} \quad (8.11)$$

The total load in the bearings is equal to the applied thrust load:

$$F_a = F_1 - F_2 \quad (8.12)$$

For the purpose of this analysis, consider only the centric thrust load applied to the bearing; therefore, from Equation 7.33,

$$\frac{F_a}{ZD^2K} = \sin \alpha_1 \left(\frac{\cos \alpha^\circ}{\cos \alpha_1} - 1 \right)^{1.5} - \sin \alpha_2 \left(\frac{\cos \alpha^\circ}{\cos \alpha_2} - 1 \right)^{1.5} \quad (8.13)$$

Combining Equation 8.10 and Equation 8.11 yields

$$\delta_1 + \delta_2 = 2\delta_p \quad (8.14)$$

Substitution of Equation 8.10 for δ_1 and Equation 8.11 for δ_2 in Equation 7.36 gives

$$\frac{\sin(\alpha_1 - \alpha^\circ)}{\cos \alpha_1} + \frac{\sin(\alpha_2 - \alpha^\circ)}{\cos \alpha_2} = \frac{2\delta_p}{BD} \quad (8.15)$$

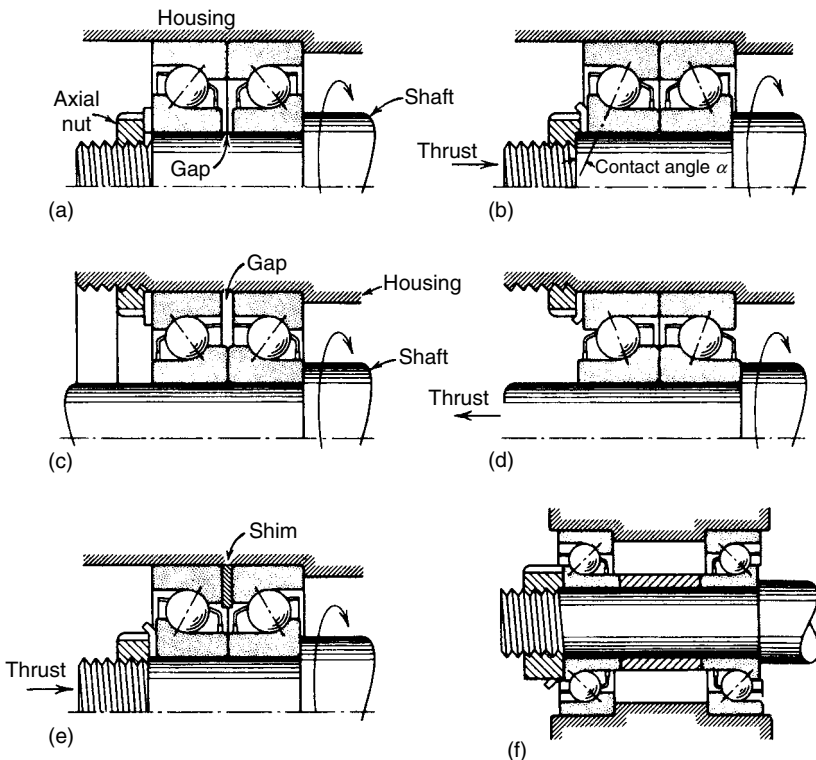


FIGURE 8.3 (a) Duplex set with back-to-back angular-contact ball bearings before axial preloading. The inner-ring faces are ground to provide a specific axial gap. (b) Same unit as in (a) after tightening axial nut to remove gap. The contact angles have increased. (c) Face-to-face angular-contact duplex set before preloading. In this case it is the outer-ring faces that are ground to provide the required gap. (d) Same set as in (c) after tightening the axial nut. The convergent contact angles increase under preloading. (e) Shim between two standard-width bearings avoids need for grinding the faces of the outer rings. (f) Precision spacers in between automatically provide proper preload by making the inner spacer slightly shorter than the outer.

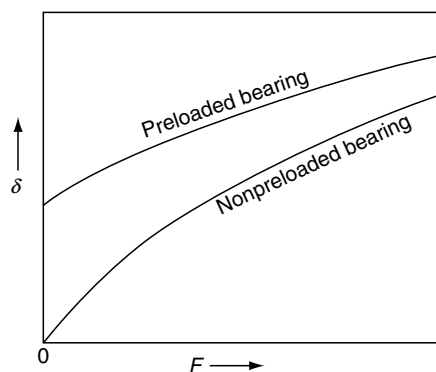


FIGURE 8.4 Deflection vs. load characteristics for ball bearings. As the load increases, the rate of increase of deflection decreases; therefore, preloading (top line) tends to reduce the bearing deflection under additional loading.

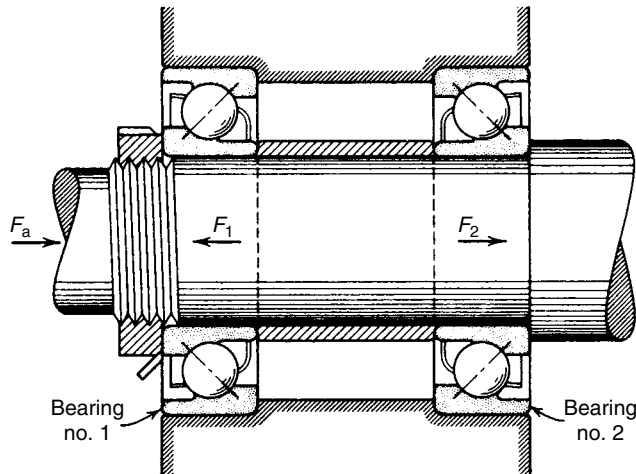


FIGURE 8.5 Preloaded set of duplex bearings subjected to F_a , an external thrust load. The computation for the resulting deflection is complicated by the fact that the preload at bearing 1 is increased by load F_a while the preload at bearing 2 is decreased.

Equation 8.13 and Equation 8.15 may now be solved for α_1 and α_2 . Subsequent substitution of α_1 and α_2 into Equation 7.36 yields values of α_1 and α_2 . The data pertaining to the selected preload F_p may be obtained from the following equations:

$$\frac{F_p}{ZD^2K} = \sin \alpha_p \left(\frac{\cos \alpha^\circ}{\cos \alpha_p} - 1 \right)^{1.5} \quad (8.16)$$

$$\delta_p = \frac{BD \sin(\alpha_p - \alpha^\circ)}{\cos \alpha_p} \quad (8.17)$$

Figure 8.6 shows a typical plot of bearing deflection δ_a vs. load. Note that deflection is everywhere less than that for a nonpreloaded bearing up to the load at which preload is removed. Thereafter, the unit acts as a single bearing under thrust load and assumes the same load-deflection characteristics as those given by the single-bearing curve. The point at which bearing 2 loses load may be determined graphically by inverting the single-bearing load-deflection curve about the preload point. This is shown in Figure 8.6.

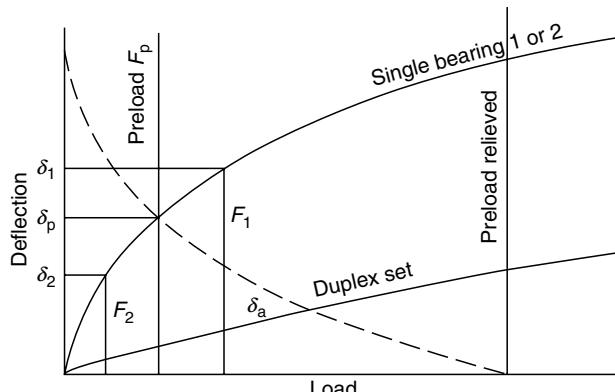


FIGURE 8.6 Deflection vs. load for a preloaded duplex set of ball bearings.

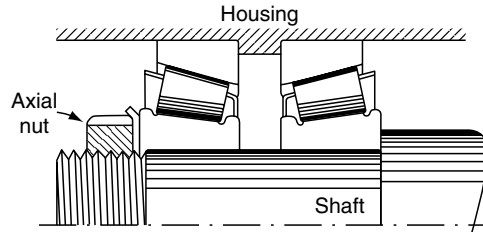


FIGURE 8.7 Lightly preloaded tapered roller bearings.

As roller bearing deflection is almost linear with respect to load, there is not much advantage to be gained by axially preloading tapered or spherical roller bearings; hence, this is not a universal practice as it is for ball bearings. Figure 8.7, however, shows tapered roller bearings axially locked together in a light preload arrangement.

See Example 8.3.

If it is desirable to preload ball bearings that are not identical, [Equation 8.13](#) and [Equation 8.15](#) become

$$F = Z_1 D_1^2 K_1 \sin \alpha_1 \left(\frac{\cos \alpha_1^\circ}{\cos \alpha_2} - 1 \right)^{1.5} - Z_2 D_2^2 K_2 \sin \alpha_2 \left(\frac{\cos \alpha_2^\circ}{\cos \alpha_1} - 1 \right)^{1.5} \quad (8.18)$$

$$\frac{B_1 D_1 \sin(\alpha_1 - \alpha_1^\circ)}{\cos \alpha_1} + \frac{B_2 D_2 \sin(\alpha_2 - \alpha_2^\circ)}{\cos \alpha_2} = 2\delta_p \quad (8.19)$$

[Equation 8.18](#) and [Equation 8.19](#) must be solved simultaneously for α_1 and α_2 . As before, [Equation 7.36](#) yields the corresponding values of δ .

To reduce axial deflection still further, more than two bearings can be locked together axially as shown in Figure 8.8. The disadvantages of this system are increased space, weight, and cost. More data on axial preloading are given in Ref. [2].

8.3.2 RADIAL PRELOADING

Radial preloading of rolling bearings is not usually used to eliminate initial large magnitude deflection as in axial preload. Instead, its purpose is generally to obtain a greater number of rolling elements under load and thus reduce the maximum rolling element load. It is also used to prevent skidding. Methods used to calculate maximum radial rolling element load are given in [Chapter 7](#). Figure 8.9 shows various methods to radially preload roller bearings.

See Example 8.4.

8.3.3 PRELOADING TO ACHIEVE ISOELASTICITY

It is sometimes desirable that the axial and radial yield rates of the bearing and its supporting structures be as nearly identical as possible. In other words, a load in either the axial or radial direction should cause identical deflections (ideally). This necessity for isoelasticity in the ball bearings came with the development of the highly accurate, low drift inertial gyroscopes for navigational systems, and for missile and space guidance systems. Such inertial gyroscopes usually have a single degree of freedom tilt axis and are extremely sensitive to error moments about this axis.

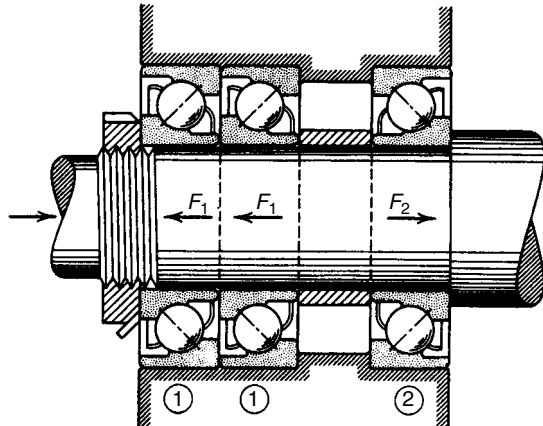


FIGURE 8.8 Triplex set of angular-contact bearings, two mounted in tandem and one opposed. This arrangement provides an even higher axial stiffness and longer bearing life than with a duplex set, but requires more space.

Consider a gyroscope in which the spin axis (Figure 8.10) is coincident with the x -axis. The tilt axis is perpendicular to the paper at the Origin O , and the center of gravity of the spin mass is acted on by a disturbing force F in the xz -plane and directed at an oblique angle ϕ to the x -axis; this force will tend to displace the spin mass center of gravity from O to O' . If, as shown in Figure 8.10, the displacements in the directions of the x - and z -axes are not equal, the force F will create an error moment about the tilt axis.

In terms of the axial and radial yield rates of the bearings, the error moment M is

$$M = \frac{1}{2} F^2 (\delta'_z - \delta'_x) \sin 2\phi \quad (8.20)$$

where the bearing yield rates δ'_z and δ'_x are in deflection per unit of force.

To minimize M and subsequent drift, δ'_z must be as nearly equal to δ'_x as possible—a requirement for pinpoint navigation or guidance. Also, from Figure 8.10 it can be noted that improving the rigidity of the bearing, that is, decreasing δ'_z and δ'_x collectively, reduces the magnitude of the minimal error moments achieved through isoelasticity.

In most radial ball bearings, the radial rate is usually smaller than the axial rate. This is best overcome by increasing the bearing contact angle, which reduces the axial yield rate and increases the radial yield rate. One-to-one ratios can be obtained by using bearings with contact angles that are 30° or higher.

At these high angles, the sensitivity of the axial-to-radial yield rate ratio to the amount of preload is quite small. It is, however, necessary to preload the bearings to maintain the desired contact angles.

8.4 LIMITING BALL BEARING THRUST LOAD

8.4.1 GENERAL CONSIDERATIONS

Most radial ball bearings can accommodate a thrust load and function properly provided the contact stress thereby induced is not excessively high or the ball does not override the land. The latter condition results in severe stress concentration and attendant rapid fatigue failure of the bearing. It may, therefore, be necessary to ascertain for a given bearing the maximum

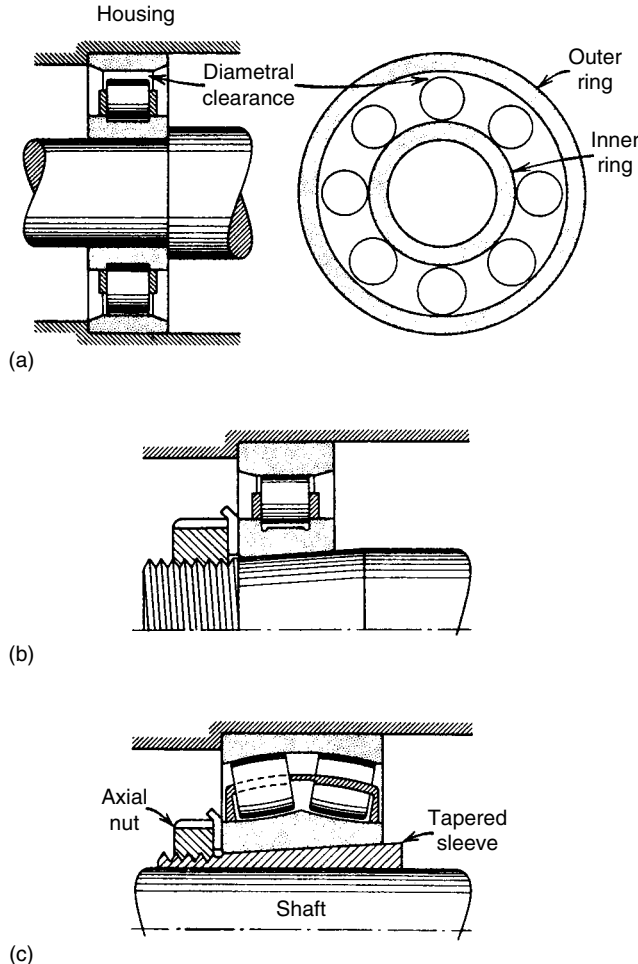


FIGURE 8.9 (a) Diametral (radial) clearance found in most off-the-shelf rolling bearings. One object of preloading is to remove this clearance during assembly. (b) Cylindrical roller bearing mounted on tapered shaft, to expand inner ring. Such bearings are usually made with a taper on the inner surface of $\frac{1}{12}$ mm/mm. (c) Spherical roller bearing mounted on tapered sleeve to expand the inner ring.

thrust load that the bearing can sustain and still function under. The situation in which the balls override the land will be examined first.

8.4.2 THRUST LOAD CAUSING BALL TO OVERRIDE LAND

Figure 8.11 shows an angular-contact bearing under thrust in which the balls are riding at an extreme angular location without the ring lands cutting into the balls.

From Figure 8.11 it can be seen that the thrust load, which causes the major axis of the contact ellipse to just reach the land of the bearing, is the maximum permissible load that the bearing can accommodate without overriding the corresponding land. Both the inner and outer ring lands must be considered. Also, from Figure 8.11 it can be determined that the angle θ_o describing the juncture of the outer ring land with the outer raceway is equal to $\alpha + \phi$ in which α is the raceway contact angle under the load necessary to cause the major axis of the contact ellipse, that is, $2a_o$, to extend to θ_o and ϕ is one half of the angle subtended by the chord $2a$. The angle θ_o is given approximately by

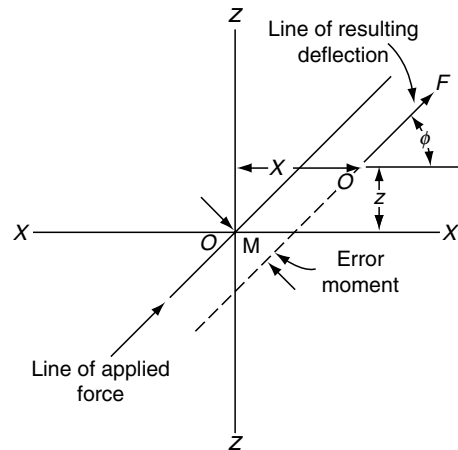


FIGURE 8.10 Effect of disturbing force F on the center of gravity of spring mass. It is frequently desirable to obtain isoelasticity in bearings in which the displacement in any direction is in line with the disturbing force.

$$\theta_o = \cos^{-1} \left(1 - \frac{d_o - d_{lo}}{D} \right) \quad (8.21)$$

As the contact deformation is small, r'_o to the midpoint of the chord $2a_o$ is approximately equal to $D/2$; therefore, $\sin \phi \approx 2a_o/D$ or

$$\sin(\theta_o - \alpha) = \frac{2a_o}{D} \quad (8.22)$$

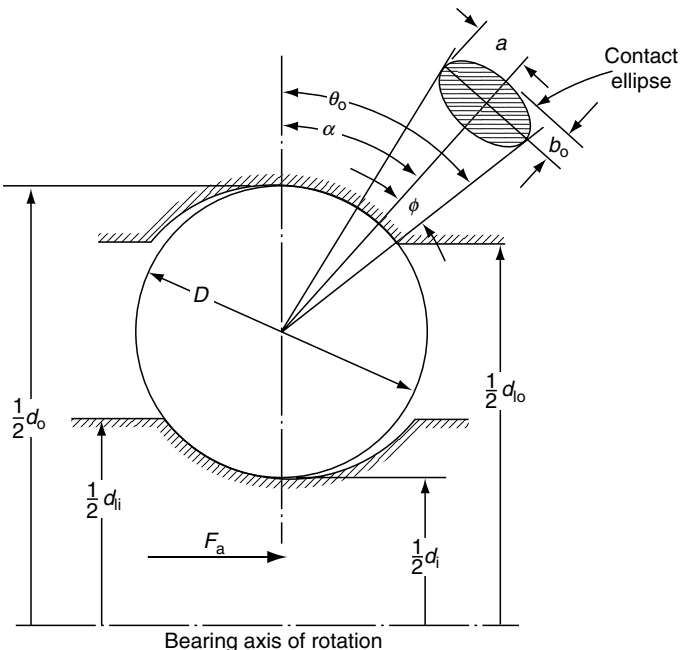


FIGURE 8.11 Ball-raceway contact under limiting thrust load.

For steel balls contacting steel raceways, the semimajor axis of the contact ellipse is given by

$$a_o = 0.0236 a_o^* \left(\frac{Q}{\Sigma \rho_o} \right)^{1/3} \quad (6.39)$$

where $\Sigma \rho_o$ is given by

$$\Sigma \rho_o = \frac{1}{D} \left(4 - \frac{1}{f_o} - \frac{2\gamma}{1 + \gamma} \right) \quad (2.30)$$

and a_o^* is a function of $F(\rho)_o$ defined by

$$F(\rho)_o = \frac{\frac{1}{f_o} - \frac{2\gamma}{(1 + \gamma)}}{4 - \frac{1}{f_o} - \frac{2\gamma}{(1 + \gamma)}} \quad (2.31)$$

$$\gamma = \frac{D \cos \alpha}{d_m} \quad (2.27)$$

According to Equation 7.26 for a thrust-loaded ball bearing,

$$Q = \frac{F_a}{Z \sin \alpha} \quad (7.26)$$

Combining Equation 6.39, Equation 2.30, [Equation 8.22](#), and Equation 7.26, one obtains

$$F_{ao} = Z \sin \alpha \Sigma \rho_o \left[\frac{D \sin(\theta_o - \alpha)}{0.0472 a_o^*} \right]^3 \quad (8.23)$$

In [Chapter 7](#), Equation 7.33 was developed, defining the resultant contact angle α in terms of thrust load and mounted contact angle

$$\frac{F_a}{Z D^2 K} = \sin \alpha \left(\frac{\cos \alpha^\circ}{\cos \alpha} - 1 \right)^{1.5} \quad (7.33)$$

where K is Jones' axial deflection constant, obtainable from Figure 7.5. Combining Equation 7.33 with Equation 8.23 yields the following relationship:

$$\sin(\theta_o - \alpha) = 0.0472 \frac{a_o^* K^{1/3} \left(\frac{\cos \alpha^\circ}{\cos \alpha} - 1 \right)^{0.5}}{(D \Sigma \rho_o)^{1/3}} \quad (8.24)$$

This equation may be solved iteratively for α using numerical methods.

Having calculated α , it is then possible to determine the limiting thrust load F_{ao} for the ball overriding the outer land from Equation 7.33.

Similarly for the inner raceway

$$\sin(\theta_i - \alpha) = 0.0472 \frac{a_i^* K^{1/3} \left(\frac{\cos \alpha^\circ}{\cos \alpha} - 1 \right)^{0.5}}{(D \Sigma \rho_i)^{1/3}} \quad (8.25)$$

$$\theta_i = \cos^{-1} \left(\frac{d_{ii} - d_i}{D} \right) \quad (8.26)$$

and $\Sigma\rho_i$ and $F(\rho)_i$ are determined from Equation 2.28 and Equation 2.29, respectively.

8.4.3 THRUST LOAD CAUSING EXCESSIVE CONTACT STRESS

It is possible that before overriding of either land an excessive contact stress may occur at the inner raceway contact (or outer raceway contact for a self-aligning ball bearing). The maximum contact stress due to ball load Q is

$$\sigma_{\max} = \frac{3Q}{2\pi ab} \quad (6.47)$$

where

$$b = 0.0236b_i^* \left(\frac{Q}{\Sigma\rho_i} \right)^{1/3} \quad (6.41)$$

A combination of Equation 6.41, Equation 6.39, Equation 6.47, and Equation 7.33 yields

$$\left(\frac{\cos \alpha^\circ}{\cos \alpha} - 1 \right)^{1/3} = \frac{1.166 \times 10^{-3} a_i^* b_i^* \sigma_{\max}}{(D^2 K)^{1/3} (\Sigma\rho_i)^{2/3}} \quad (8.27)$$

Assuming a value of maximum permissible contact stress σ_{\max} permits a numerical solution for α ; thereafter, the limiting F_a may be calculated from Equation 7.33. Present-day practice uses $\sigma_{\max} = 2069 \text{ N/mm}^2$ (300,000 psi) as a practical limit for steel ball bearings. If the balls do not override the lands, however, it is not uncommon to allow stresses to exceed $3,449 \text{ N/m}^2$ (500,000 psi) for short time periods.

8.5 CLOSURE

In many engineering applications, bearing deflection must be known to establish the dynamic stability of the rotor system. This consideration is important in high-speed systems such as aircraft gas turbines. The bearing radial deflection in this case can contribute to the system eccentricity. In other applications, such as inertial gyroscopes, radiotelescopes, and machine tools, minimization of bearing deflection under load is required to achieve system accuracy or accuracy of manufacturing. That the bearing deflection is a function of bearing internal design, dimensions, clearance, speeds, and load distribution has been indicated in the previous chapters. However, for applications in which speeds are slow and extreme accuracy is not required, the simplified equations presented in this chapter are sufficient to estimate bearing deflection.

To minimize deflection, axial or radial preloading may be employed. Care must be exercised, however, not to excessively preload rolling bearings since this can cause increased friction torque, resulting in bearing overheating and reduction in endurance.

REFERENCES

1. Palmgren, A., *Ball and Roller Bearing Engineering*, 3rd ed., Burbank, Philadelphia, 49–51, 1959.
2. Harris, T., How to compute the effects of preloaded bearings, *Prod. Eng.*, 84–93, July 19, 1965.

9 Permanent Deformation and Bearing Static Capacity

LIST OF SYMBOLS

Symbol	Description	Units
C_s	Basic static load rating	N (lb)
d_m	Pitch diameter	mm (in.)
D	Ball or roller diameter	mm (in.)
F	Load	N (lb)
f	r/D	
FS	Factor of safety	
HV	Vickers hardness	
i	Number of rows	
l	Roller effective length	mm (in.)
P_d	Radial clearance	mm (in.)
Q	Rolling element load	N (lb)
r	Groove curvature radius	mm (in.)
R	Roller contour radius	mm (in.)
X_s	Radial load factor	
Y_s	Axial load factor	
Z	Number of rolling elements per row	◦
α	Contact angle	
γ	$D \cos \alpha / d_m$	
δ_s	Permanent deformation	mm (in.)
η	Hardness reduction factor	
ρ	Curvature	mm^{-1} (in.^{-1})
σ	Yield or limit stress	MPa (psi)
φ_s	Load rating factor	

Subscript

a	Axial direction
i	Inner raceway
ip	Incipient plastic flow of material
o	Outer raceway
r	Radial direction
s	Static loading

9.1 GENERAL

Many structural materials exhibit a strain limit under load beyond which full recovery of the original elemental dimensions is not possible when the load is removed. Bearing steel loaded in compression behaves in a similar manner. Thus, when a loaded ball is pressed on a bearing raceway, an indentation may remain in the raceway and the ball may exhibit a flat spot after the load is removed. These permanent deformations, if they are sufficiently large, can cause excessive vibration and possibly stress concentrations of considerable magnitude.

9.2 CALCULATION OF PERMANENT DEFORMATION

In practice, permanent deformations of small magnitude occur even under light loads. Figure 9.1, from Ref. [1], shows a very large magnification of the contacting rolling element surfaces in a typical ball bearing both in the direction of rolling motion and transverse to that direction. Figure 9.2, also from Ref. [1], shows an isometric view of a ground surface having spatial properties similar to honed and lapped raceway surfaces. Noting the occurrence of peaks and valleys even with a finely finished surface, it is apparent that before distributing a load between the rolling element and raceway over the entire contact area, thus giving an average compressive stress $\sigma = Q/A$, the load is distributed only over the smaller area of contacting peaks, giving a much larger stress than σ . Thus, it is probable that the compressive yield strength is exceeded locally and both surfaces are somewhat flattened and polished in operation. According to Palmgren [2], this flattening has little effect on the bearing operation because of the extremely small magnitude of deformation. It may be detected by a slight change in reflection of light from the surface.

It was shown in Chapter 6 that the relative approach of two solid steel bodies loaded elastically in point contact is given by

$$\delta = 2.79 \times 10^{-4} \delta^* Q^{2/3} \sum_{\rho}^{1/3} \quad (6.43)$$

where δ^* is a constant depending on the shapes of the contacting surfaces. As the load between the surfaces is increased, the deformation gradually departs from that depicted in Equation 6.43 and becomes larger for any given load (see Figure 9.3). The point of departure

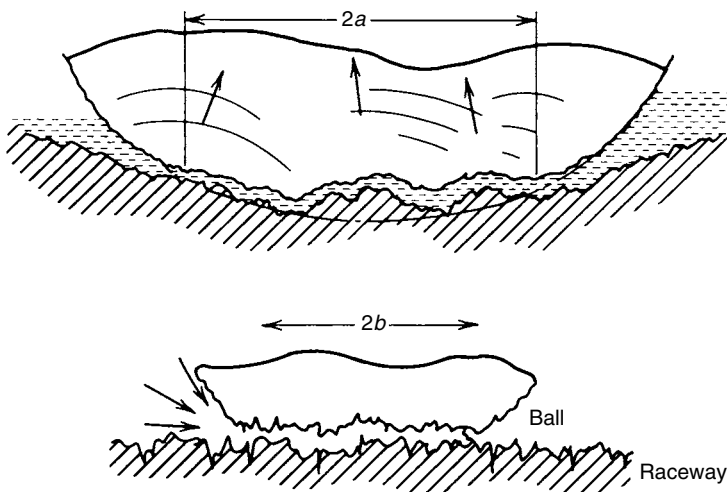


FIGURE 9.1 Ball and raceway contacting surfaces (greatly magnified). (From Sayles, R. and Poon, S., Surface topography and rolling element vibration, *Precis. Eng.*, 137–144, 1981.)

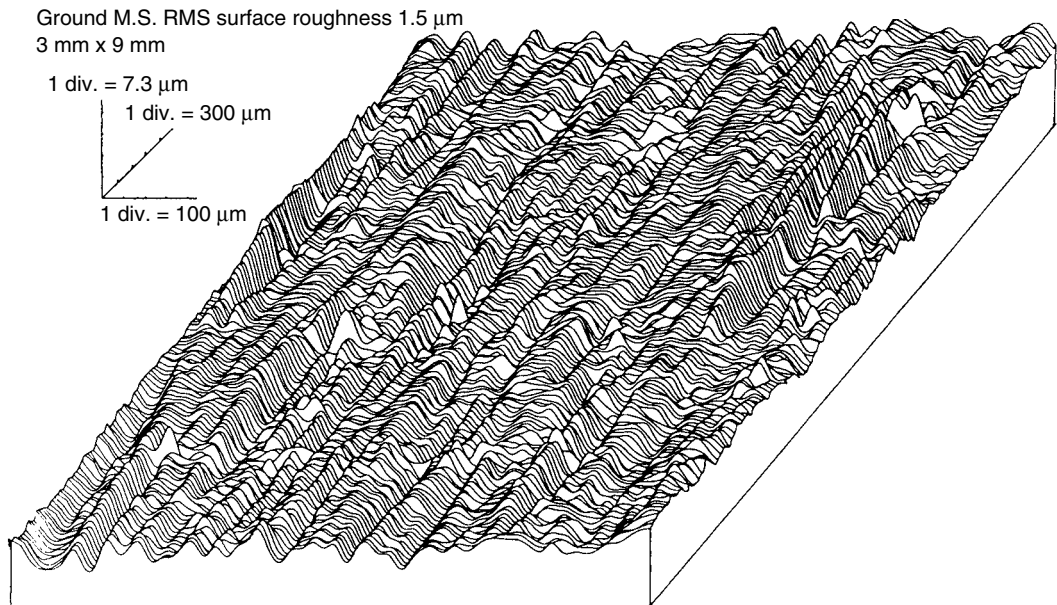


FIGURE 9.2 Isometric view of a typical honed and lapped surface. (From Sayles, R. and Poon, S., Surface topography and rolling element vibration, *Precis. Eng.*, 137–144, 1981.

is the bulk compressive yield strength. On the basis of empirical data for bearing quality steel hardened between 63.5 and 65.5 Rockwell C, Palmgren [2] developed the following formula to describe permanent deformation point contact:

$$\delta_s = 1.3 \times 10^{-7} \frac{Q^2}{D} (\rho_{I1} + \rho_{II1})(\rho_{I2} + \rho_{II2}) \quad (9.1)$$

where ρ_{I1} is the curvature of body I in plane 1, and so on. For ball–raceway contact, Equation 9.1 is

$$\delta_s = 5.25 \times 10^{-7} \frac{Q^2}{D^3} \left[1 \pm \frac{\gamma}{(1 \mp \gamma)} \right] \left(1 - \frac{1}{2f} \right) \quad (9.2)$$

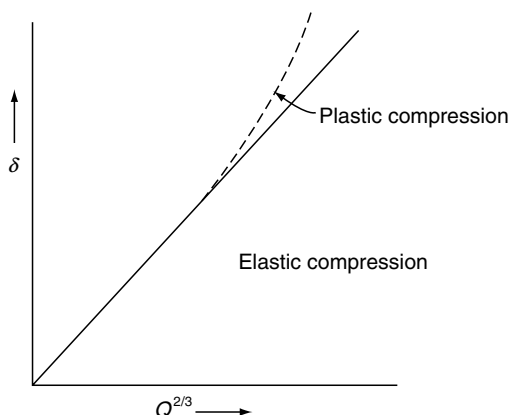


FIGURE 9.3 Deflection vs. load in point contact.

where the upper signs refer to the inner raceway contact and the lower signs refer to the outer raceway contact. For roller–raceway point contact, the following equation obtains:

$$\delta_s = 2.52 \times 10^{-7} \left(\frac{Q}{D} \right)^2 \left[1 \pm \frac{\gamma}{(1 \mp \gamma)} \right] \left(\frac{1}{R} - \frac{1}{r} \right) \quad (9.3)$$

where R is the roller contour radius and r is the groove radius. The foregoing formulas are valid for permanent deformation in the vicinity of the compressive elastic limit (yield point) of the steel.

See Example 9.1.

For line contact between roller and raceway, the following formula may be used to ascertain permanent deformation with the same restrictions as earlier:

$$\delta_s = \frac{6.03 \times 10^{-11}}{D^2} \left[\frac{Q}{l} \left(\frac{1}{1 \mp \gamma} \right)^{1/2} \right]^2 \quad (9.4)$$

According to Lundberg et al. [3], the deformation predicted by Equation 9.4 occurs at the ends of a line contact when the raceway length tends to exceed the roller effective length. The corresponding deformation in the center of the contact is $\delta_s/6.2$ according to Ref. [3]. Palmgren [2] stated that of the total permanent deformation, approximately two thirds occur in the ring and one third in the rolling element.

Palmgren's data were based on indentation tests carried out in the 1940s, and the data were dependent on the measurement devices available then. Later, some of these tests were repeated using modern measurement devices. The following conclusions were reached:

1. The amount of total permanent indentation occurring due to an applied load Q between a ball and a raceway appears to be less than that given in [Equation 9.1](#).
2. The amount of permanent deformation that occurs in the ball surface is virtually equal to that occurring in the raceway, when balls have not been work hardened.

Accordingly, it can be stated that permanent deformations calculated according to Equation 9.1 through Equation 9.4 will tend to be greater than will actually occur in modern ball and roller bearings of good quality steel and with relatively smooth surface finishes.

9.3 STATIC LOAD RATING OF BEARINGS

As indicated earlier, some degree of permanent deformation is unavoidable in loaded rolling bearings. Moreover, experience has demonstrated that rolling bearings do not generally fracture under normal operating loads. Further, experience has shown that permanent deformations have little effect on the operation of the bearing if the magnitude at any given contact point is limited to a maximum of $0.0001D$. If the deformations become much larger, the cavities formed in the raceways cause the bearing to vibrate and become noisier, although bearing friction does not appear to increase significantly. The bearing operation is usually not impaired in any other manner; however, indentations together with conditions of marginal lubrication can lead to surface-initiated fatigue.

The basic static load rating of a rolling bearing is defined as the load applied to a nonrotating bearing that will result in a permanent deformation of $0.0001D$ at the weaker of the inner or outer raceway contacts occurring at the position of the maximum loaded rolling element. In other words, in [Equation 9.2](#) through [Equation 9.4](#), $\delta_s/D = 0.0001$ at

$Q = Q_{\max}$. This concept of an allowable amount of permanent deformation consistent with smooth minimal vibration and noise operation of a rolling bearing continues to be the basis of the ISO standard [4] and ANSI standards [5,6]. In the latest revision of the ISO standard [4], it is stated that contact stresses at the center of contact at the maximum loaded rolling elements as shown in Table 9.1 yield permanent deformations of $0.0001D$ for the bearing types indicated. The ANSI standards [5,6] use the same criteria.

For most radial ball bearing and roller bearing applications, the maximum loaded rolling element load according to [Chapter 7](#) may be approximated by

$$Q_{\max} = \frac{5F_r}{iZ \cos \alpha} \quad (7.24)$$

where i is the number of rows of rolling elements. Setting $F_r = C_s$ yields

$$C_s = 0.2iZQ_{\max} \cos \alpha \quad (9.5)$$

Considering the stress criterion, Equation 6.25, Equation 6.34, and Equation 6.36 may be used to determine Q_{\max} corresponding to 4,200 MPa (609,000 psi) for standard radial ball bearings. Substituting for Q_{\max} in Equation 9.5 yields the equation

$$C_s = \frac{23.8iZD^2(a_i^*b_i^*)^3 \cos \alpha}{\left[4 - \frac{1}{f_i} + \left(\frac{2\gamma}{1-\gamma}\right)\right]^2} \quad (9.6)$$

if the maximum stress occurs at the inner raceway and

$$C_s = \frac{23.8iZD^2(a_o^*b_o^*)^3 \cos \alpha}{\left[4 - \frac{1}{f_o} - \left(\frac{2\gamma}{1+\gamma}\right)\right]^2} \quad (9.7)$$

if the maximum stress occurs at the outer raceway. Reference [4] reduces these equations to

$$C_s = \varphi_s iZD^2 \cos \alpha \quad (9.8)$$

where values of φ_s are given in Table CD9.1 for standard ball bearings.

The corresponding formula for radial roller bearings as taken from Ref. [4] is

$$C_s = 44(1 - \gamma)iZD \cos \alpha \quad (9.9)$$

TABLE 9.1
Contact Stress That Causes $0.0001D$ Permanent Deformation

Bearing Type	Contact Stress	
	MPa	psi
Self-aligning ball bearing	4,600	667,000
Other ball bearings	4,200	609,000
Roller bearings	4,000	580,000

For thrust bearings,

$$Q_{\max} = \frac{F_a}{iZ \sin \alpha} \quad (7.26)$$

Setting $F_a = C_{sa}$ yields

$$C_{sa} = iZ Q_{\max} \sin \alpha \quad (9.10)$$

Correspondingly, the standard stress criterion formula is

$$C_{sa} = \varphi_s Z D^2 \sin \alpha \quad (9.11)$$

where φ_s is given in [Table CD9.1](#).

For thrust roller bearings with line contact,

$$C_{sa} = 220 (1 - \gamma) Z ID \sin \alpha \quad (9.12)$$

When the hardness of the surfaces is less than the specified lower limit of validity, a correction factor may be applied directly to the basic static capacity such that

$$C'_s = \eta_s C_s \quad (9.13)$$

where

$$\eta_s = \eta_1 \left(\frac{HV}{800} \right)^2 \leq 1 \quad (9.14)$$

and HV is the Vickers hardness. A graph of Vickers hardness versus Rockwell C hardness is shown in [Figure 9.4](#).

Equation 9.14 was developed empirically by SKF. The values of η_1 depend on the type of contact and are given in [Table 9.2](#). η_s has a maximum value of unity.

9.4 STATIC EQUIVALENT LOAD

To compare the load on a nonrotating bearing with the basic static capacity, it is necessary to determine the static equivalent load, that is, the pure radial or pure thrust load—whichever is appropriate—that would cause the same total permanent deformation at the most heavily loaded contact as the applied combined load. A theoretical calculation of this load may be made in accordance with the methods of [Chapter 7](#).

In lieu of the more rigorous approach, for bearings subjected to combined radial and thrust loads, the static equivalent load may be calculated as follows:

$$F_s = X_s F_r + Y_s F_a \quad (9.15)$$

If F_r is greater than F_s as calculated in Equation 9.15, use F_s equal to F_r . [Table 9.3](#), taken from Ref. [5], gives values of X_s and Y_s for radial ball bearings.

Data in Table 9.3 pertain to bearings having a groove curvature not greater than 53% of the ball diameter. Double-row bearings are presumed to be symmetrical. Face-to-face and

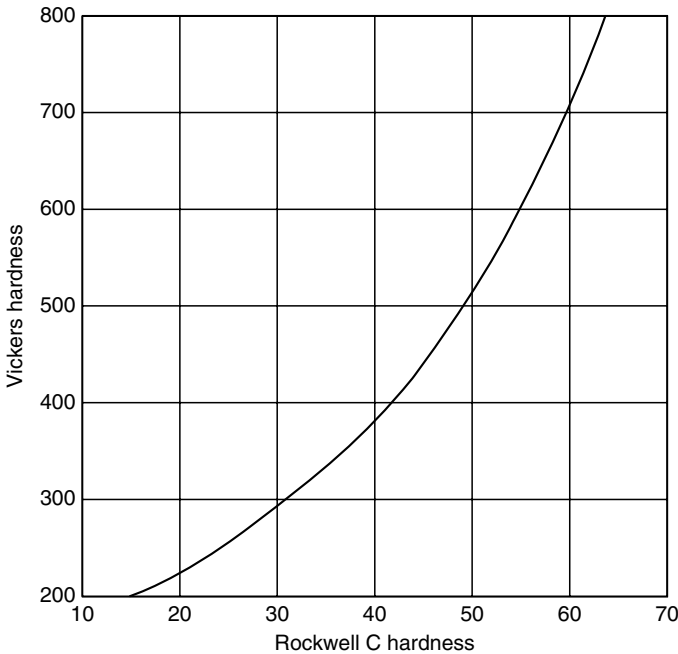


FIGURE 9.4 Vickers hardness vs. Rockwell C hardness.

back-to-back mounted angular-contact ball bearings are similar to double-row bearings; tandem mounted bearings are similar to single bearings.

For radial roller bearings, the values of Table 9.4, taken from Ref. [6], apply.

For thrust bearings, the static equivalent load is given by

$$F_{\text{sa}} = F_a + 2.3 F_r \tan \alpha \quad (9.16)$$

When F_r is greater than $0.44F_a \operatorname{ctn} \alpha$, the accuracy of Equation 9.16 diminishes and the theoretical approach according to [Chapter 7](#) is warranted.

9.5 FRACTURE OF BEARING COMPONENTS

It is generally considered that the load that will fracture bearing rolling elements or raceways is greater than $8C_s$ (see Ref. [2]).

TABLE 9.2
Values of η_1

η_1	Type of Contact
1	Ball on plane (self-aligning ball bearings)
1.5	Ball on groove
2	Roller on roller (radial roller bearings)
2.5	Roller on plane

TABLE 9.3
Values of X_s and Y_s for Radial Ball Bearings

Bearing Type	Single-Row Bearings		Double-Row Bearings	
	X_s	Y_s^b	X_s	Y_s^b
Radial-contact groove ball bearing ^{a,c}	0.6	0.5	0.6	0.5
Angular-contact groove ball bearings				
$\alpha = 15^\circ$	0.5	0.47	1	0.94
$\alpha = 20^\circ$	0.5	0.42	1	0.84
$\alpha = 25^\circ$	0.5	0.38	1	0.76
$\alpha = 30^\circ$	0.5	0.33	1	0.66
$\alpha = 35^\circ$	0.5	0.29	1	0.58
$\alpha = 40^\circ$	0.5	0.26	1	0.52
Self-aligning ball bearings	0.5	0.22 ctn α	1	0.44 ctn α

^a P_o is always $\geq F_r$.

^bValues of Y_o for intermediate contact angles are obtained by linear interpolation.

^cPermissible maximum value of F_a/C_o depends on the bearing design (groove depth and internal clearance).

Source: American National Standard, *ANSI/AFBMA Std 9-1990*, load ratings and fatigue life for ball bearings.

9.6 PERMISSIBLE STATIC LOAD

It is known that the maximum load on a rotating bearing may be permitted to exceed the basic load rating, provided this load acts continuously through several revolutions of bearing rotation. In this manner, the permanent deformations that occur are uniformly distributed over the raceways and rolling elements, and the bearing retains satisfactory operation. If, on the other hand, the load is of short duration, unevenly distributed deformations may develop even when the bearing is rotating at the instant when shock occurs. For this situation, it is necessary to use a bearing whose basic static load rating exceeds the maximum applied load. When the load is of longer duration, the basic static load rating may be exceeded without impairing the operation of the bearing.

According to the type of bearing service, a factor of safety may be applied to the basic load rating. Therefore, the allowable load is given by

$$F_s = \frac{C_s}{FS} \quad (9.17)$$

TABLE 9.4
Values of X_s and Y_s for Radial Roller Bearings^a

Bearing Type	Single-Row Bearings ^b			Double-Row Bearings	
	X_s	Y_s	X_s	Y_s	
Self-aligning and tapered roller bearings, $\alpha \neq 0^\circ$	0.5	0.22 ctn α	1	0.44 ctn α	

^aThe ability of radial roller bearings with $\alpha = 0^\circ$ to support axial loads varies considerably with bearing design and execution. The bearing user should therefore consult the bearing manufacturer for recommendations regarding the evaluation of equivalent load in cases where bearings with $\alpha = 0^\circ$ are subjected to axial loads.

^b F_s is always $\geq F_r$. The elastic equivalent radial load for radial roller bearings with $\alpha = 0^\circ$, and subjected to radial load only is $F_s = F_r$.

Source: American National Standard, *ANSI/AFBMA Std 11-1990*, load ratings and fatigue life for roller bearings.

TABLE 9.5
Factor of Safety for Static Loading

Factor of Safety (<i>FS</i>)	Service
≥ 0.5	Smooth shock-free operation
≥ 1	Ordinary service
≥ 2	Sudden shocks and high requirements for smooth running

Table 9.5 gives satisfactory values of *FS* for various types of services.

See Example 9.2.

9.7 CLOSURE

Smoothness of operation is an important consideration in modern ball and roller bearings. Interruptions in the rolling path such as those caused by permanent deformations result in increased friction, noise, and vibration. Chapter 14 discusses the noise and vibration phenomenon in substantial detail. In this chapter, the discussion centered on bearing static load ratings, which, if not exceeded while the bearing was not rotating, would preclude permanent deformations of significant magnitude. The ratings were based on a maximum allowable permanent deformation of $0.0001D$. Subsequently, it was determined that for various types of ball and roller bearings, this deformation could be related to a value of rolling element–raceway contact stress. In accordance with this stress, basic static load ratings are developed for each rolling bearing type and size.

Generally, a load of magnitude equal to the basic static load rating cannot be continuously applied to the bearing with the expectation of obtaining satisfactory endurance characteristics. Rather, the basic static load rating is based on a sudden overload or, at most, one of short duration compared with the normal loading during a continuous operation. Exceptions to this rule are bearings that undergo infrequent operations of short durations, for example, bearings on doors of missile silos or dam gate bearings. For these and simpler applications, the bearing design may be based on basic static load rating rather than on endurance of fatigue. Whereas the current static load ratings are based on damage during nonrotation, during operation under heavy load and slow speed, rolling contact, components experience significant microstructural alterations. Because of the relatively slow speeds of rotation and infrequent operation, neither vibration nor surface fatigue may be as significant in such applications as excessive plastic flow of subsurface material. The bearings could thus be sized to eliminate or minimize such plastic flow and ultimately bearing failure.

REFERENCES

1. Sayles, R. and Poon, S., Surface topography and rolling element vibration, *Precis. Eng.*, 137–144, 1981.
2. Palmgren, A., *Ball and Roller Bearing Engineering*, 3rd ed., Burbank, Philadelphia, 1959.
3. Lundberg, G., Palmgren, A., and Bratt, E., Statiska Bärörmagan hos Kullager och Rullager, *Kullagertidningen*, 3, 1943.
4. International Standard ISO 76, Rolling bearings—static load ratings, 1989.
5. American National Standard, *ANSI/AFBMA Std 9-1990*, Load ratings and fatigue life for ball bearings.
6. American National Standard, *ANSI/AFBMA Std 11-1990*, Load ratings and fatigue life for roller bearings.

10 Kinematic Speeds, Friction Torque, and Power Loss

LIST OF SYMBOLS

Symbol	Description	Units
A	Area	mm ² (in. ²)
B	Bearing width	mm (in.)
C_s	Bearing basic static load rating	N (lb)
d_m	Bearing pitch diameter	mm (in.)
d	Bearing bore diameter	mm (in.)
d_1	Thrust bearing shaft washer outside diameter	mm (in.)
D	Ball or roller diameter	mm (in.)
D	Bearing outside diameter	mm (in.)
D_1	Thrust bearing housing washer inside diameter	mm (in.)
F_s	Bearing static equivalent load	N (lb)
H	Frictional power loss	W (Btu/hr)
l	length of needle roller	mm
M	Bearing friction torque (total)	N×mm (in. × lb)
M_f	Bearing friction torque due to roller end-flange load	N×mm (in. × lb)
M_l	Bearing friction torque due to load	N×mm (in. × lb)
M_v	Bearing friction torque due to lubrication	N×mm (in. × lb)
n	Rotational speed	rpm
q	Heat flow/unit area	W/mm ² (Btu/hr-in. ²)
r	Raceway radius	mm (in.)
T	Thrust bearing thickness	mm (in.)
v	Surface velocity	mm/sec (in./sec)
Z	Number of rolling elements	
α	Contact angle	rad, °
γ	$D \cos \alpha / d_m$	
ν_o	Lubricant kinematic viscosity	centistokes
ω	Rotational speed	rad/sec
Subscripts		
i	Inner ring or raceway	
m	Cage motion or orbital motion of rolling element	
o	Outer ring or raceway	
θ	Thermal reference speed condition	
R	Rolling Element	

10.1 GENERAL

Ball and roller bearings are used to support various kinds of loads while permitting rotational and translatory motions of a shaft or slider. In this book, treatment has been restricted to shaft or outer-ring rotation or oscillation.

Unlike hydrodynamic or hydrostatic bearings, motions occurring in rolling bearings are not restricted to simple movements. For instance, in a rolling bearing mounted on a shaft that rotates at n rpm, the rolling elements orbit the bearing axis at a speed of n_m rpm, and they simultaneously revolve about their own axes at speeds of n_R rpm. In most applications, particularly those operating at relatively slow shaft or outer-ring speeds, these internal speeds can be calculated with sufficient accuracy using simple kinematical relationships; that is, the balls or rollers are assumed to roll on the raceways without sliding. This condition will be considered in this chapter.

Resisting the rotary motion of the bearing is a friction torque that, in conjunction with shaft or outer-ring speed, can be used to estimate bearing power loss. On the basis of laboratory testing of rolling bearings, empirical equations have been developed to enable the estimation of this friction torque in applications where speeds are relatively slow, that is, where inertial forces and contact friction forces are not significantly influenced by contact deformations and speed. These empirical equations are presented in this chapter.

10.2 CAGE SPEED

In the case of slow-speed rotation or an applied load of large magnitude, rolling bearings can be analyzed while neglecting dynamic effects. This slow-speed behavior is called kinematical behavior.

As a general case, it will be initially assumed that both inner and outer rings rotate in a bearing having a common contact angle α as indicated in Figure 10.1. For rotation about an axis,

$$v = \omega r \quad (10.1)$$

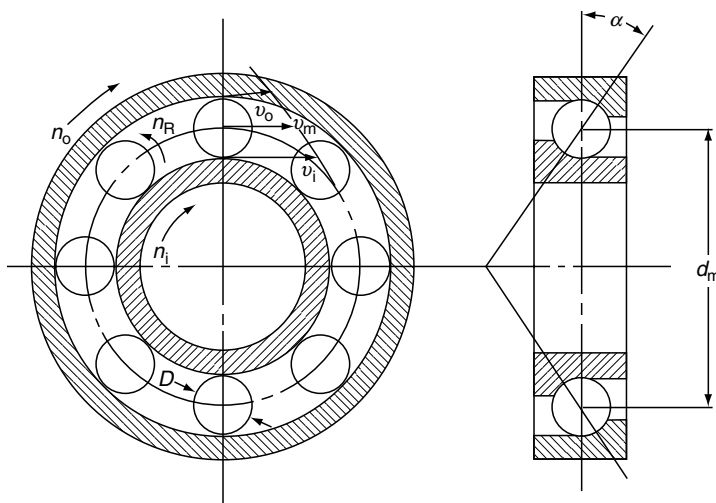


FIGURE 10.1 Rolling speeds and velocities in a bearing.

where ω is in radians per second.

Consequently,

$$v_i = \frac{1}{2} \omega_i (d_m - D \cos \alpha) = \frac{1}{2} \omega_i d_m (1 - \gamma) \quad (10.2)$$

Similarly,

$$v_o = \frac{1}{2} \omega_o d_m (1 + \gamma) \quad (10.3)$$

As

$$\omega = \frac{2\pi n}{60} \quad (10.4)$$

where n is in rpm, therefore,

$$v_i = \frac{\pi n_i d_m}{60} (1 - \gamma) \quad (10.5)$$

$$v_o = \frac{\pi n_o d_m}{60} (1 + \gamma) \quad (10.6)$$

If there is no gross slip at the rolling element–raceway contact, then the velocity of the cage and rolling element set is the mean of the inner and outer raceway velocities. Hence,

$$v_m = \frac{1}{2} (v_i + v_o) \quad (10.7)$$

Substituting Equation 10.5 and Equation 10.6 into Equation 10.7 yields

$$v_m = \frac{\pi d_m}{120} [n_i(1 - \gamma) + n_o(1 + \gamma)] \quad (10.8)$$

As

$$v_m = \frac{1}{2} \omega_m d_m = \frac{\pi d_m n_m}{60}$$

therefore,

$$n_m = \frac{1}{2} [n_i(1 - \gamma) + n_o(1 + \gamma)] \quad (10.9)$$

10.3 ROLLING ELEMENT SPEED

The rotational speed of the cage relative to the inner raceway is

$$n_{mi} = n_m - n_i \quad (10.10)$$

Assuming no gross slip at the inner raceway–ball contact, the velocity of the ball is identical to that of the raceway at the point of contact. Hence,

$$\frac{1}{2} \omega_m d_m (1 - \gamma) = \frac{1}{2} \omega_R D \quad (10.11)$$

Therefore, since n is proportional to ω and by substituting n_{mi} as in [Equation 10.10](#)

$$n_R = (n_m - n_i) \frac{d_m}{D} (1 - \gamma) \quad (10.12)$$

Substituting [Equation 10.9](#) for n_m yields

$$n_R = \frac{d_m}{2D} (1 - \gamma)(1 + \gamma)(n_o - n_i) \quad (10.13)$$

Considering only inner-ring rotation, [Equation 10.9](#) and [Equation 10.13](#) become

$$n_m = \frac{n_i}{2} (1 - \gamma) \quad (10.14)$$

$$n_R = \frac{d_m n_i}{2D} (1 - \gamma^2) \quad (10.15)$$

For a thrust bearing having a contact angle of 90° , $\cos \alpha = 0$, therefore,

$$n_m = \frac{1}{2} (n_i + n_o) \quad (10.16)$$

$$n_R = \frac{d_m}{2D} (n_o - n_i) \quad (10.17)$$

See Example 10.1.

10.4 ROLLING BEARING FRICTION

Friction due to rolling of nonlubricated surfaces over each other is considerably less than that encountered by sliding the same surfaces over each other. Notwithstanding the fact that the motions of the contacting elements in rolling bearings are more complex than indicated by pure rolling, rolling bearings exhibit much less friction than most fluid-film or sleeve bearings of comparable size, speed, and load-carrying ability. A notable exception to this generalization is the hydrostatic gas bearing; however, such a bearing is not self-acting, as is a rolling bearing, and it requires a complex and expensive gas supply system.

Friction of any magnitude retards motion and results in energy loss. In an operating rolling bearing, friction causes temperature increase and may be measured as a motion-resisting torque. It will be shown in a later chapter that, even considering the name rolling bearing, the principal causes of friction in moderately-to-heavily loaded ball and roller bearings are sliding motions in the deformed rolling element-raceway contacts. In addition, in tapered roller bearings, the major source of friction is the sliding motion between the roller ends and the large end flange on the inner ring or cone. In cylindrical roller bearings, the sliding between the roller ends and roller guide flanges on the inner, outer, or both rings is a major source of friction. Rolling bearings with cages experience sliding between the rolling elements and cage pockets; if the cage is piloted on the inner or outer ring, sliding friction occurs between the cage rail and the piloting surface.

In all of the above conditions, the amount of friction occurring depends considerably on the type of lubricant used. Moreover, in fluid-lubricated rolling bearings, the lubricant

occupies a portion of the free space within the bearing boundaries and resists the passage of the orbiting balls or rollers. This frictional resistance is a function of the lubricant properties, the amount of lubricant in the free space, and the orbital speed of the rolling elements. In the Second Volume of this handbook, it will be demonstrated that this friction component influences the rolling element speeds.

10.5 ROLLING BEARING FRICTION TORQUE

10.5.1 BALL BEARINGS

Exclusive of a mathematical approach to analyze and calculate bearing friction torque, Palmgren [1] empirically evaluated bearing friction torque through laboratory testing of bearings of various types and sizes. These tests were conducted under loads ranging from light to heavy, at slow-to-moderate shaft speeds, and using a variety of lubricants and lubrication techniques. In evaluating the test results, Palmgren [1] separated the measured friction torque into a component due to applied load and a component due to the viscous property of the lubricant type, the amount of the lubricant employed, and bearing speed. Actually, as suggested in [Section 10.4](#), even the friction torque component due to applied load is heavily dependent on the mechanical properties of the lubricant in the rolling element-raceway contacts. For the purposes of the simplified analytical methods that follow, however, it is sufficient to attribute this friction torque component to applied loading. Within the constraints of a slow-to-moderate-speed bearing operation, Palmgren's empirical equations for friction torque of rolling bearings can be very useful. This is particularly true, for example, when providing comparison between rolling bearings and fluid-film bearings.

10.5.1.1 Torque Due to Applied Load

Palmgren [1] gave the following equation to describe this torque:

$$M_1 = f_1 F_\beta d_m \quad (10.18)$$

where f_1 is a factor depending on the bearing design and relative bearing load:

$$f_1 = z \left(\frac{F_s}{C_s} \right)^y \quad (10.19)$$

where F_s is the static equivalent load and C_s is the basic static load rating. These terms were explained in [Chapter 9](#). [Table 10.1](#) gives appropriate values of z and y . Values of C_s are generally given in manufacturers' catalogs along with data to enable calculation of F_s .

F_β in Equation 10.18 depends on the magnitude and direction of the applied load. It may be expressed in equation form as follows for radial ball bearings:

$$F_\beta = 0.9F_a \cot \alpha - 0.1F_r \quad \text{or} \quad F_\beta = F_r \quad (10.20)$$

Of Equations 10.20, the one yielding the larger value of F_β is used. For deep-groove ball bearings having a nominal contact angle 0° , the first equation can be approximated by

$$F_\beta = 3F_a - 0.1F_r \quad (10.21)$$

For thrust ball bearings, $F_\beta = F_a$.

TABLE 10.1
Values of z and y

Ball Bearing Type	Nominal Contact Angle (°)	z	y
Radial deep-groove	0	0.0004–0.0006 ^a	0.55
Angular-contact	30–40	0.001	0.33
Thrust	90	0.0008	0.33
Double-row, self-aligning	10	0.0003	0.40

^aLower values pertain to light series bearings; higher values to heavy series bearings.

10.5.1.2 Torque Due to Lubricant Viscous Friction

For bearings that operate at moderate speeds, Palmgren [1] established the following empirical equations to estimate bearing friction torque caused by orbiting rolling elements as they plow through the viscous lubricant that occupies the free space within the bearing boundaries:

$$M_v = 10^{-7} f_o (\nu_o n)^{2/3} d_m^3 \quad \nu_o n \geq 2000 \quad (10.22)$$

$$M_v = 160 \times 10^{-7} f_o d_m^3 \quad \nu_o n < 2000 \quad (10.23)$$

where ν_o is given in centistokes and n in revolutions per minute. In Equation 10.22 and Equation 10.23, f_o is a factor depending on the type of bearing and the method of lubrication. Table 10.2 as updated with data in Ref. [2] gives values of f_o for various types of ball bearings subjected to different conditions of lubrication. Equation 10.22 and Equation 10.23 are valid for oils having a specific gravity of approximately 0.9. Palmgren [1] gave a more complete formula for oils of different densities. For grease-lubricated bearings, ν_o refers to the oil within the grease, and the equation is valid shortly after the addition of the lubricant.

10.5.1.3 Total Friction Torque

A reasonable estimate of the friction torque of a given rolling bearing under moderate load and speed conditions is the sum of the load friction torque and viscous friction torque, that is,

$$M = M_l + M_v \quad (10.24)$$

As M_l and M_v are based on empirical formulas, the effect of rolling element–cage pocket sliding is included.

TABLE 10.2
Values of f_o vs. Ball Bearing Type and Lubrication Method

Ball Bearing Type	Grease	Oil Mist	Oil Bath	Oil Bath (Vertical Shaft) or Oil Jet
Deep-groove ball ^a	0.7–2 ^b	1	2	4
Self-aligning ball ^c	1.5–2 ^b	0.7–1 ^b	1.5–2 ^b	3–4 ^b
Thrust ball	5.5	0.8	1.5	3
Angular-contact ball ^a	2	1.7	3.3	6.6

^aUse $2 \cdot f_o$ for paired bearings or double-row bearings.

^bLower values pertain to light series bearings; higher values to heavy series bearings.

^cDouble row bearings only.

TABLE 10.3
 f_1 for Cylindrical Roller Bearings

Roller Bearing Type	f_1
Radial cylindrical with cage	0.0002–0.0004 ^a
Radial cylindrical, full complement	0.00055
Thrust cylindrical	0.0015

^aLower values pertain to light series bearings; higher values pertain to heavy series bearing.

See Example 10.2.

10.5.2 CYLINDRICAL ROLLER BEARINGS

10.5.2.1 Torque Due to Applied Load

Equation 10.18 also applies to cylindrical roller bearings; the values of f_1 may be obtained from Table 10.3.

In Equation 10.18 for radial roller bearings,

$$F_\beta = 0.8F_a \cot \alpha \quad \text{or} \quad F_\beta = F_r \quad (10.25)$$

Again, the larger value of F_β is used. For thrust cylindrical roller bearings, $F_\beta = F_a$.

10.5.2.2 Torque Due to Lubricant Viscous Friction

Equation 10.22 and Equation 10.23 also apply to cylindrical roller bearings; values of f_o from Ref. [2] are given in Table 10.4.

10.5.2.3 Torque Due to Roller End–Ring Flange Sliding Friction

Radial cylindrical roller bearings with flanges on both inner and outer rings can carry thrust loads in addition to the normal loads. In this case, the rollers are loaded against one flange on each ring. The bearing friction torque due to the roller end motions against properly designed and manufactured flanges is given by

TABLE 10.4
Values of f_o vs. Cylindrical Roller Bearing Type and Lubrication

Bearing Type	Type of Lubrication			
	Grease	Oil Mist	Oil Bath	Oil Bath (Vertical Shaft) or Oil Jet
Cylindrical roller with cage ^a	0.6–1 ^b	1.5–2.8 ^b	2.2–4 ^b	2.2–4 ^{b,c}
Cylindrical roller full complement ^a	5–10 ^b	—	5–10 ^b	—
Thrust cylindrical roller	9	—	3.5	8

^bLower values are for light series bearings; higher values for heavy series bearings.

^cFor oil bath lubrication and vertical shaft application use $2 \cdot f_o$.

TABLE 10.5
Values of f_f for Radial Cylindrical Roller Bearings

Bearing Type	Grease Lubrication	Oil Lubrication
With cage, optimum design	0.003	0.002
With cage, other designs	0.009	0.006
Full complement, single-row	0.006	0.003
Full complement, double-row	0.015	0.009

$$M_f = f_f F_a d_m \quad (10.26)$$

When $F_a/F_r \leq 0.4$, and the lubricant is sufficiently viscous, values of f_f are given in Table 10.5.

10.5.2.4 Total Friction Torque

A reasonable estimate of the friction torque of a given rolling bearing under moderate load and speed conditions is the sum of the load friction torque, viscous friction torque, and roller end-flange friction torque, if any; that is,

$$M = M_l + M_v + M_f \quad (10.27)$$

Since M_l and M_v are based on empirical formulas, the effect of rolling element–cage pocket sliding is included.

See Example 10.3.

10.5.3 SPHERICAL ROLLER BEARINGS

10.5.3.1 Torque Due to Applied Load

For modern design double-row, radial spherical roller bearings, SKF used the formula:

$$M_l = f_l F^a d^b \quad (10.28)$$

In Equation 10.28, the constants f_l and exponents a and b depend on the specific bearing series. Table 10.6 gives values of f_l , a , and b as provided in the SKF catalog [2]. As the internal

TABLE 10.6
Values of f_l , a , and b for Spherical Roller Bearings

Bearing Dimension Series	f_l	a	b
13	0.00022	1.35	0.2
22	0.00015	1.35	0.3
23	0.00065	1.35	0.1
30	0.001	1.5	-0.3
31	0.00035	1.5	-0.1
32	0.00045	1.5	-0.1
39	0.00025	1.5	-0.1
40	0.0008	1.5	-0.2
41	0.001	1.5	-0.2

TABLE 10.7
Values of f_1 , a , and b for Thrust Spherical Roller Bearings

Bearing Series	f_1	a	b
292	0.0003	1	1
293	0.0004	1	1
294	0.0005	1	1

design of these bearings is specific to SKF during the time period covered by the catalog, application of [Equation 10.28](#) using data of [Table 10.6](#) is substantially limited to the bearings listed in Ref. [2].¹ Even if other manufacturers employ similar raceway and roller designs for similar bearing series, variations in surface finish, cage design, etc. will cause variations in the friction torque due to load. Therefore, [Equation 10.28](#) accompanied by [Table 10.6](#) is provided herein to permit preliminary comparative calculations of bearing friction torque.

For thrust spherical roller bearings, [Table 10.7](#) gives values of f_1 , a , and b . For thrust roller bearings, $F = F_a$.

10.5.3.2 Torque Due to Lubricant Viscous Friction

[Equation 10.22](#) and [Equation 10.23](#) also apply to spherical roller bearings; values of f_o from Ref. [2] are given in [Table 10.8](#).

10.5.3.3 Total Friction Torque

[Equation 10.24](#) may be used for spherical roller bearings also.

Values of bearing load torque as calculated from [Equation 10.18](#) and bearing viscous lubricant friction torque as calculated using [Equation 10.22](#) and [Equation 10.23](#) appear to be reasonably accurate for bearings operating under reasonable loads and relatively slow-speed conditions. Harris [4] used these data successfully in the thermal evaluation of a submarine propeller shaft radial and thrust bearing assembly.

10.5.4 NEEDLE ROLLER BEARINGS

Needle roller bearings are slightly different in their design and operation from the ball, cylindrical, and spherical roller bearings discussed earlier. The typical roller length is at least three to four times larger than the diameter. Longer rollers lead to more sliding at the roller ends with small amounts of roller–raceway misalignment or skewing that is typically not significant in other bearing types. This is especially true for thrust needle roller bearings, where the raceway surface velocity is dependent on the contact diameter, while the roller surface velocity is constant along its length, necessitating a sliding motion at the ends of the roller–raceway contacts. Also, needle bearings are frequently mounted directly in contact with the shaft or housing manufactured by the bearing user. This results in surface roughness and textures slightly different from those found on the raceways fabricated onto bearing rings by bearing manufacturers. Both of these situations cause different friction conditions to exist in the operation of needle roller bearings as compared with other bearing types.

¹SKF has since published a new and updated version of their general catalog [3]. In this catalog, the friction torque calculation method has been modified. Nevertheless, [Equation 10.28](#) together with [Table 10.6](#) should provide adequate representation for the bearings noted.

TABLE 10.8
Values of f_0 vs. Spherical Roller Bearing Type and Lubrication

Spherical Roller Bearing Type	Type of Lubrication			
	Grease	Oil Mist	Oil Bath	Oil Bath (Vertical Shaft) or Oil Jet
Double-row radial	3.5–7 ^b	1.7–3.5 ^b	3.5–7 ^b	7–14 ^b
Thrust	—	—	2.5–5 ^b	5–10 ^b

^bLower values are for light series bearings; higher values for heavy series bearings.

Later chapters will cover direct methods for estimating contact friction and hence bearing running friction torque; however, empirical friction torque equations for radial and thrust needle bearings developed by Chiu and Myers [5] will be presented here. Following the work of Trippett [6], Chiu and Myers put forth the following equation for radial, caged needle roller bearings:

$$M = d_m (4.5 \times 10^{-7} \nu_o^{0.3} n^{0.6} + 0.12 F_r^{0.41}) \quad (10.29)$$

Chiu and Myers testing also showed that full complement radial needle roller bearings operate at 1.5 to 2 times the torque determined using Equation 10.29. Similarly, the running friction torque of thrust needle roller bearings is given by

$$M = 4.5 \times 10^{-7} \nu_o^{0.3} n^{0.6} d_m + 0.016 F_a l \quad (10.30)$$

The dependence of running friction torque for thrust needle roller bearings on the contact length of the roller–raceway in Equation 10.30 is apparent. This is directly related to the sliding at the roller ends as discussed earlier, and was evident in Chiu and Myers testing.

Equation 10.29 and Equation 10.30 both pertain to a bearing operating with circulating oil lubrication, as such was used in the test effort. For grease lubrication, the viscosity of the base oil can be used to estimate the running torque shortly after regreasing and after the initial transient torque related to the rollers pushing the grease out of the cavity has subsided. Finally, the torque due to oil bath lubrication can also be estimated from Equation 10.29 and Equation 10.30, as the tests from Trippett [6] found significantly more influence of the bearing torque on lubricant supply temperature, which controls the oil viscosity, than on the flow rate.

See Example 10.4 and Example 10.5.

10.5.5 TAPERED ROLLER BEARINGS

Tapered roller bearings are different from other bearing types in that they operate with a sliding motion at the roller end–large end rib contact. Witte [7] empirically studied the running friction torque of tapered roller bearings, which resulted in Equation 10.31 and Equation 10.32 for radial and thrust loaded bearings, respectively.

$$M = 3.35 \times 10^{-8} G(n\nu_o)^{1/2} \left(f_t \frac{F_r}{K} \right)^{1/3} \quad (10.31)$$

$$M = 3.35 \times 10^{-8} G(n\nu_o)^{1/2} F_a^{1/3} \quad (10.32)$$

Similar to the viscous torque equations, [Equation 10.22](#) and [Equation 10.23](#), [Equation 10.31](#) and [Equation 10.32](#) are valid for oils having a specific gravity of approximately 0.9. Witte discusses how to deal with oils having differing values of specific gravity. The geometry factor G is based on the internal dimensions of the bearing and is determined by

$$G = d_m^{1/2} D^{1/6} (Z \cdot l)^{2/3} (\sin \alpha)^{-1/3} \quad (10.33)$$

The radial load factor f_t in [Equation 10.31](#) is taken from [Figure 10.2](#).

As Witte's [7] work was empirically based, the ring large end rib–roller end friction is taken into account for a typical range of operating conditions. These conditions are defined as

$$\begin{aligned} F_r/C_r \quad \text{or} \quad F_a/C_a &\leq 0.519 \\ n\nu_o &\geq 2700 \end{aligned} \quad (10.34)$$

Ensuring that these conditions are maintained will prevent the roller end–rib friction from becoming significant, which would lead to an underestimation of bearing running torque.

Witte and Hill [8] further discuss the effects of roller end–rib friction on the bearing torque using [Equation 10.31](#) and [Equation 10.32](#) when the limiting conditions of [Equation 10.34](#) are not maintained.

Witte used both oil bath lubrication and circulating oil lubrication systems in the development of [Equation 10.31](#) and [Equation 10.32](#). With both conditions, Witte also found a minimum effect of the torque on the type of lubrication system; however, a more significant effect was found with lubricant viscosity. In most likelihood, the drag of the rollers plowing through the lubricant is more dependent on lubricant viscosity than on the amount of lubricant within the bearing cavity. For grease lubrication, the viscosity of the base oil can be used for estimates of the running torque.

See Example 10.6 and Example 10.7.

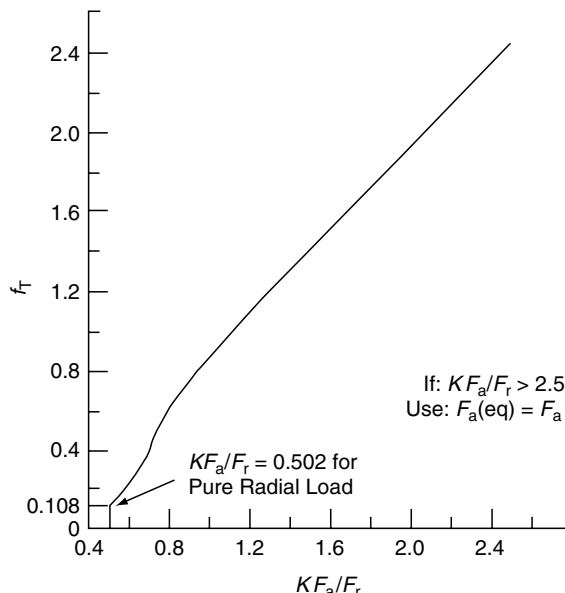


FIGURE 10.2 Values of f_t for radial loaded tapered roller bearings.

10.5.6 HIGH-SPEED EFFECTS

For high-speed ball and roller bearings in which rolling element centrifugal forces and gyroscopic moments become significant, the friction due to sliding motions tends to increase significantly, and the equations provided in this chapter will tend to underestimate the amount of friction. Analytical methods to calculate friction in high-speed ball and roller bearings are detailed in the Second Volume of this handbook.

10.6 BEARING POWER LOSS

From simple physics, power equals force times velocity or torque times speed. Therefore, the power loss due to bearing friction may be calculated from the following relationship:

$$H = 0.001M \cdot \omega \quad (10.35)$$

where H is in watts, M is in $\text{N} \times \text{mm}$ (milli-joules), and ω is in rad/sec. Using bearing speed n in rpm, [Equation 10.34](#) becomes

$$H = 1.047 \times 10^{-4}M \cdot n \quad (10.36)$$

10.7 THERMAL SPEED RATINGS

ISO [9] defines the maximum speed for a given set of reference operating conditions using the torque equations set forth by Palmgren [1] and discussed in the earlier sections. Equating the bearing power loss to an amount of heat flow from the bearing results in the following energy balance:

$$\frac{\pi \cdot n_\theta}{30 \times 10^3} \left[10^{-7} f_{o\theta} (\nu_{o\theta} n_\theta)^{2/3} d_m^3 + f_{t\theta} F_\theta d_m \right] = q_\theta A_\theta \quad (10.37)$$

Using [Equation 10.37](#), the reference viscosity $\nu_{o\theta}$ is specified as 12 cSt for radial bearings and 24 cSt for thrust bearings, and the reference radial load F_θ as 5% and 2% of the static load rating for radial and thrust bearings, respectively. Also, the heat emitting surface areas are defined as

$$A_\theta = \begin{cases} \frac{\pi \cdot B(D+d)}{\pi \cdot T(D+d)} & \text{radial bearings (except tapered roller)} \\ \frac{\pi}{2} (D^2 - d^2) & \text{tapered roller bearings} \\ \frac{\pi}{4} (D^2 + d_1^2 - D_1^2 - d^2) & \text{thrust cylindrical roller bearings} \\ & \text{thrust spherical roller bearings} \end{cases} \quad (10.38)$$

For radial bearings:

$$q_\theta = 0.016 \left(\frac{A_\theta}{50,000} \right)^{-0.34} \quad (q_\theta \geq 0.016) \quad (10.39)$$

For thrust bearings:

$$q_\theta = 0.020 \left(\frac{A_\theta}{50,000} \right)^{-0.34} \quad (q_\theta \geq 0.020) \quad (10.40)$$

The reference coefficients for load- and viscous-dependent torque are defined in Table CD10.1. Using [Equation 10.38](#), [Equation 10.39](#) with [Equation 10.37](#) defines a nonlinear equation for the thermal reference speed rating, which can be calculated using an iterative technique such as the Newton–Raphson method.

Thermal speed ratings are valuable for initial selections of bearing type for a given application. As the actual operating conditions for an application can be very different from those used to define the reference conditions, the actual speed limitations for an application may be greatly different from those defined by ISO. For example, the ISO speed rating does not include the heat dissipated from the system due to circulating oil or forced air cooling of a bearing housing. Other conditions such as heavier load or higher viscosities than specified might result in lower speed capabilities than the speed rating indicates. As such, care needs to be used, and the friction power generation by the application should be considered with regard to the actual heat dissipation conditions associated with the bearing system. A discussion on the operating temperatures of rolling element bearings can be found in [Chapter 7](#) of the Second Volume of this handbook.

10.8 CLOSURE

In the first part of the 20th century, ball and roller bearings were called antifriction bearings to emphasize the small amount of frictional power consumed during their operation. Comparison of the friction power losses associated with hydrodynamic fluid-film bearings or simple sleeve bearings in the same application amply demonstrates this fact.

In this chapter, in which only relatively slow-speed and moderate load rolling bearing applications are considered, a simple rolling motion and associated kinematical relationships were used to determine rolling element and cage speeds. For similar operating conditions, empirical equations were introduced to enable the estimation of bearing friction torque and bearing power loss. While these calculation methods suffice in the analysis of many bearing applications, in the Second Volume of this handbook, methods are developed that permit more accurate calculation of internal speeds, contact friction, and heat generation rates under operating conditions involving heavy loads, misalignment, high speeds, and high temperatures, to cite some principal departures from more common applications.

REFERENCES

1. Palmgren, A., *Ball and Roller Bearing Engineering*, 3rd ed., Burbank, Philadelphia, 34–41, 1959.
2. SKF, General Catalog 4000, US, 2nd ed., 1997.
3. SKF, General Catalog 4000, 2004.
4. Harris, T., Prediction of temperature in a rolling contact bearing assembly, *Lub. Eng.*, 145–150, April 1964.
5. Chiu, Y. and Myers, M., A rational approach for determining permissible speed for needle roller bearings, SAE Tech. Paper No. 982030, September 1998.
6. Trippett, R., Ball and needle bearing friction correlations under radial load conditions, SAE Tech. Paper No. 851512, September 1985.
7. Witte, D., Operating torque of tapered roller bearings, *ASLE Trans.*, 16(1), 61–67, 1973.
8. Witte, D. and Hill, H., Tapered roller bearing torque characteristics with emphasis on rib-roller end contact, SAE Tech. Paper No. 871984, October 1987.
9. International Organization for Standards, International Standard (ISO) Std. 15312:2003, Rolling bearings—thermal speed ratings—calculations and coefficients, December 1, 2003.

11 Fatigue Life: Basic Theory and Rating Standards

LIST OF SYMBOLS

Symbol	Description	Units
A	Material factor for ball bearings, constant	
a	Semimajor axis of projected contact ellipse	mm (in.)
a^*	Dimensionless semimajor axis	
B	Material factor for roller bearings with line contact	
b	Semiminor axis of projected contact ellipse	mm (in.)
b^*	Dimensionless semiminor axis	
b_m	Rating factor for contemporary material	
C	Basic dynamic capacity of a bearing raceway or entire bearing	N (lb)
c	Exponent on τ_0	
d	Diameter	mm (in.)
d_m	Pitch diameter	mm (in.)
D	Ball or roller diameter	mm (in.)
E	Modulus of elasticity	MPa (psi)
e	Weibull slope	
F	Probability of failure	
F_r	Applied radial load	N (lb)
F_a	Applied axial load	N (lb)
F_e	Equivalent applied load	N (lb)
f	r/D	
f_m	Material factor	
g_c	Factor combining the basic dynamic capacities of the separate bearing raceways	
h	Exponent on z_0	
i	Number of rows	
J_1	Factor relating mean load on a rotating raceway to Q_{\max}	
J_2	Factor relating mean load on a nonrotating raceway to Q_{\max}	
J_r	Radial load integral	
J_a	Axial load integral	
K	Constant	
L	Fatigue life	
L_{10}	Fatigue life that 90% of a group of bearings will endure	revolutions $\times 10^6$
L_{50}	Fatigue life that 50% of a group of bearings will endure	revolutions $\times 10^6$

l	Effective roller length	mm (in.)
L	Length of rolling path	mm (in.)
N	Number of revolutions	
n	Rotational speed	rpm
N	Number of bearings in a group	
n_{mi}	Orbital speed of rolling elements relative to inner raceway	rpm
Q	Ball or roller load	N (lb)
Q_c	Basic dynamic capacity of a raceway contact	N (lb)
Q_e	Equivalent rolling element load	N (lb)
R	Roller contour radius	mm (in.)
r	Raceway groove radius	mm (in.)
S	Probability of survival	
T	τ_0/σ_{max}	
u	Number of stress cycles per revolution	
V	Volume under stress	mm ³ (in. ³)
V	Rotation factor	
v	$J_2(0.5)/J_1(0.5)$	
X	Radial load factor	
Y	Axial load factor	
Z	Number of rolling elements per row	
z_0	Depth of maximum orthogonal shear stress	mm (in.)
α	Contact angle	rad, [°]
γ	$D \cos \alpha/d_m$	
ε	Factor describing load distribution	
ζ	z_0/b	
η	Capacity reduction factor	
λ	Reduction factor to account for edge loading and nonuniform stress distribution on the rolling elements	
ν	Reduction factor used in conjunction with a load-life exponent $n = 10/3$	
σ	Normal stress	MPa (psi)
τ_0	Maximum orthogonal subsurface shear stress	MPa (psi)
ψ	Position angle of rolling element	rad, [°]
ψ_1	Limiting position angle	rad, [°]
ω_s	Spinning speed	rad/sec
ω_{roll}	Rolling speed	rad/sec
$\Sigma\rho$	Curvature sum	mm ⁻¹ (in. ⁻¹)
$F(\rho)$	Curvature difference	

Subscripts

a	Axial direction
c	Single contact
e	Equivalent load
i	Inner raceway
j	Rolling element location
l	Line contact
μ	Rotating raceway
ν	Nonrotating raceway
o	Outer raceway
r	Radial direction
s	Probability of survival S

R	Rolling element
I	Body
II	Body

11.1 GENERAL

If a rolling bearing in service is properly lubricated, properly mounted and aligned, kept free of abrasives, moisture, and corrosive reagents, and not overloaded, then all causes of damage and failure are eliminated except material fatigue. Through the first eight decades of the 20th century, industry-accepted theory asserted that no rolling bearing could give unlimited service because of the probability of fatigue of the surfaces in rolling contact. As indicated in [Chapter 6](#), the stresses repeatedly acting on these surfaces are extremely high compared with other stresses acting on engineering component structures. In the design of such components, the material endurance limit is consistently used. This is a cyclically applied, reversing stress level, which if not exceeded during the component operation, the component will not fail due to structural fatigue. Basic rolling bearing fatigue theory has not included the concept of an endurance limit. In the second volume of this hand book, this concept is discussed and developed. In this chapter, however, only the basic concept of rolling contact fatigue and its association with bearing load and life ratings will be explored for the following reasons:

1. Load and life rating standard methods of calculation currently in active universal use have their foundation in the basic theory.
2. Use of the basic theory in the calculation of bearing lives tends to generate conservative estimates.
3. Understanding of the basic theory is a necessary foundation for the development and use of the more accurate and modern theory, including, but not limited to, the use of an endurance limit stress.

11.2 ROLLING CONTACT FATIGUE

11.2.1 MATERIAL MICROSTRUCTURE BEFORE BEARING OPERATION

For rolling bearings manufactured from AISI 52100 steel, before operation that includes over-rolling of the bearing raceways by the rolling elements, the microstructure of the material appears as shown in [Figure 11.1](#). This was the material used in the manufacture of the rings, balls, and rollers of all of the bearings endurance-tested by Lundberg and Palmgren [1] to establish the basic method for the calculation of rolling bearing dynamic load ratings and fatigue life. The microstructure consists primarily of plate martensite [2] with 5–8 vol.% of $(\text{Fe,Cr})_3\text{C}$ type carbides [3] and up to 20 vol.% retained austenite, depending on austenitizing and tempering conditions. Tempered hardness is generally 58–64 on the Rockwell C scale. The lower values of the retained austenite content and hardness are associated with higher tempering temperatures.

11.2.2 ALTERATION OF THE MICROSTRUCTURE CAUSED BY OVER-ROLLING

Marked alteration of the near-surface microstructure of endurance-tested bearing inner rings has been reported since 1946, for example, [4–6]. The alterations are illustrated by differences in the nital acid etching response of the microstructure in the region just beneath the raceway surface ([see Figure 11.2](#)) and are most heavily concentrated at a depth corresponding to the maximum shear stress associated with the Hertzian stress field of the rolling element–raceway contact. From Figure 6.12 it can be determined that this depth is about $0.76b$; where b is the semiminor axis of the contact ellipse in a typical ball bearing application. See Ref. [7,8].

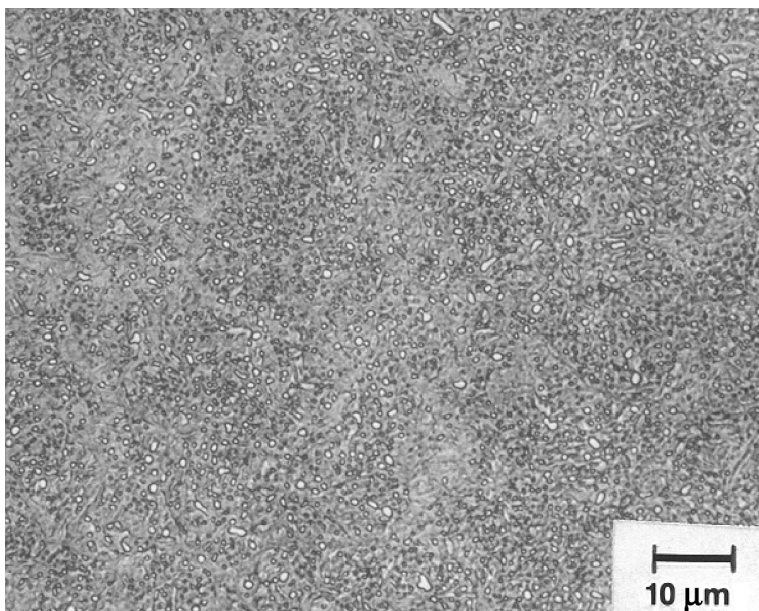


FIGURE 11.1 Microstructure of hardened and tempered AISI 52100 steel.

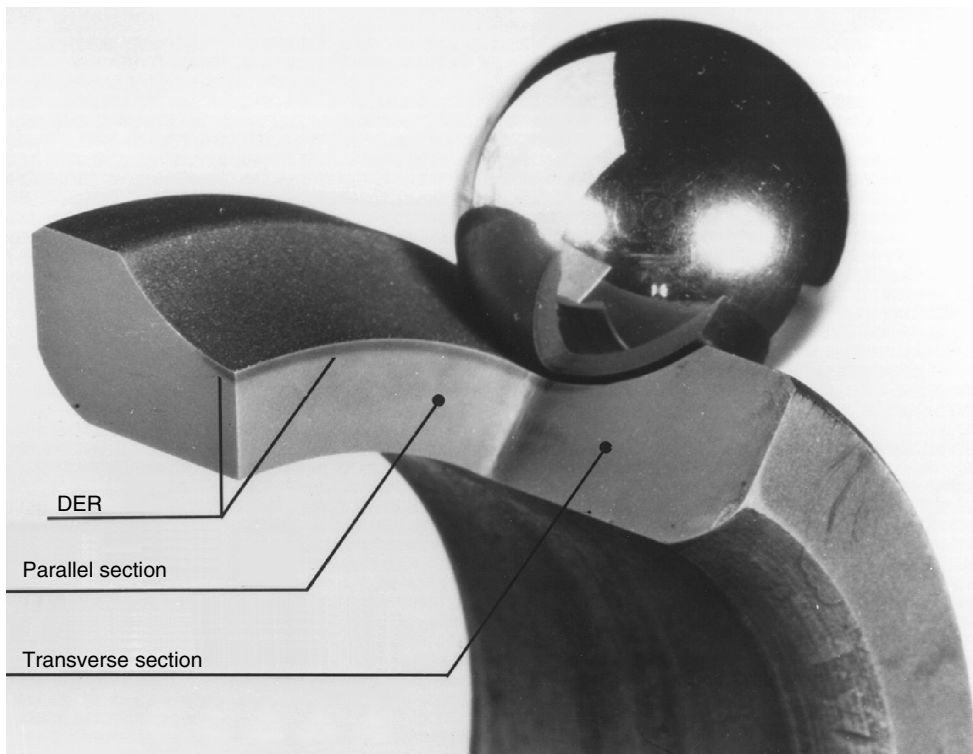


FIGURE 11.2 Orientation of viewing sections and location of region of microstructural alterations in a 309 deep-groove ball bearing inner ring. (From Swahn, H., Becker, P., and Vingsbo, O., Martensite decay during rolling contact fatigue in ball bearings, *Metallurgical Trans. A*, 7A, 1099–1110, August 1976. With permission.)

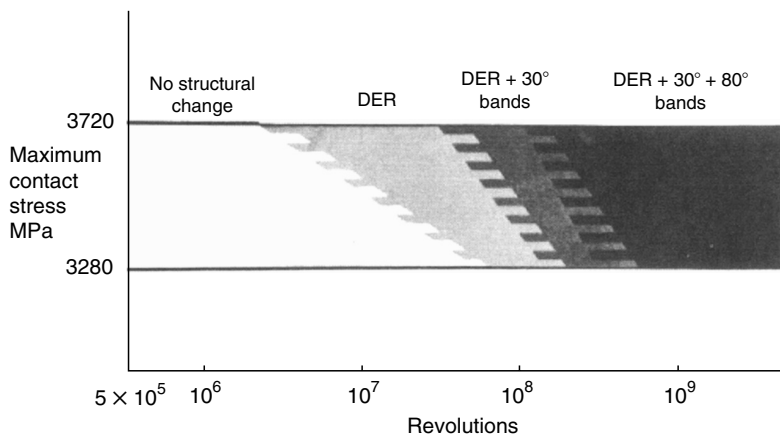


FIGURE 11.3 Microstructural alterations as a function of stress level and number of inner-ring revolutions. (From Swahn, H., Becker, P., and Vingsbo, O., Martensite decay during rolling contact fatigue in ball bearings, *Metallurgical Trans. A*, 7A, 1099–1110, August 1976. With permission.)

Swahn et al. [9] and Lund [10] described three aspects of microstructural alterations: the dark-etching region (DER), DER + 30° bands, and DER + 30° bands + 80° bands. Swahn et al. [9] also chronologically characterized the three regions as shown in Figure 11.3. Optical micrographs of the microstructural alterations, in parallel sections, are shown in Figure 11.4.

The first alteration is the formation of the DER. This consists of a ferritic phase containing a nonhomogeneously distributed excess carbon content (equivalent to that of the initial

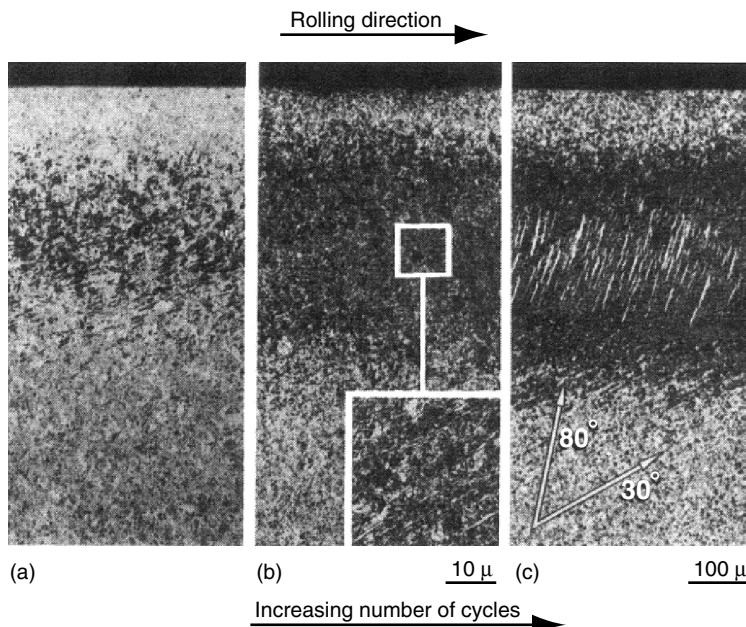


FIGURE 11.4 Optical micrographs of structural changes in 309 deep-groove ball bearing inner rings (parallel section). (a) DER in early stage. (b) Fully developed DER and 30° bands. (c) DER, 30° bands and 80° bands. (From Swahn, H., Becker, P., and Vingsbo, O., Martensite decay during rolling contact fatigue in ball bearings, *Metallurgical Trans. A*, 7A, 1099–1110, August 1976. With permission.)

martensite) mixed with residual parent martensite. Swahn et al. [9] determined that a stress-induced process of martensitic decay occurs. The second aspect of altered microstructure is the formation of white-etching, disk-shaped regions of ferrite, about 0.1–0.5 μm (40–200 $\mu\text{in.}$) thick and inclined approximately 30° to the raceway circumferential tangent. These regions are sandwiched between carbide-rich layers. The third feature is a second set of white-etching bands, considerably larger than the 30° bands, and inclined 80° to the raceway tangent in parallel sections. These disk-shaped regions are about 10 μm (400 $\mu\text{in.}$) thick and consisting of severely plastically deformed ferrite.

11.2.3 FATIGUE CRACKING AND RACEWAY SPALLING CAUSED BY OVER-ROLLING

Rolling contact fatigue is manifested as a flaking off of material particles from the surfaces of the raceways and rolling elements. For well-lubricated, properly manufactured bearings, this flaking usually commences as a crack below the surface. This crack propagates to the surface, eventually forming a spall (pit) in the load-carrying surface. Figure 11.5 is a photograph of a fatigue crack in the material below a bearing raceway, and [Figure 11.6](#) is a photograph of a typical fatigue failure in a ball bearing raceway.

Actually, Figure 11.5, while illustrating a subsurface crack, also illustrates a “butterfly.” This is a manifestation of the microstructural alteration found in bearing rolling contact components that have experienced substantially heavy loading. It is called a butterfly because of wing-like emanations from a body composed of a nonmetallic inclusion. After nitric acid etching of the surface of the sectioned component, the butterfly wings appear white in contrast to the surrounding matrix of martensite. As shown in [Figure 11.7](#) the wings and crack are oriented at an angle of 40–45° to the raceway track in a direction determined by the direction

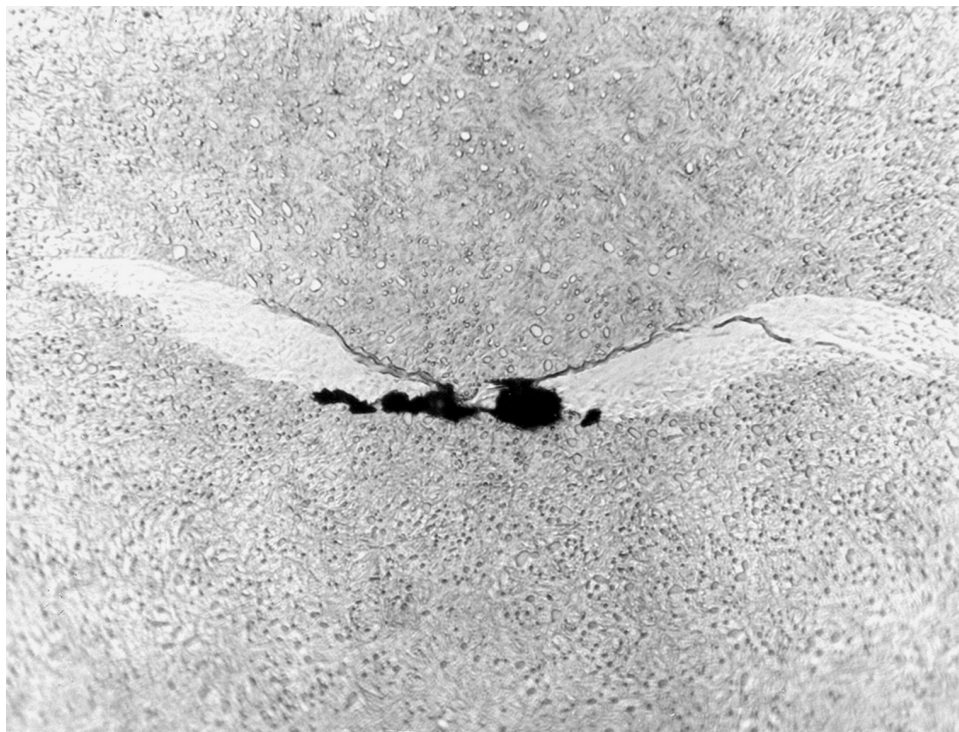


FIGURE 11.5 Fatigue crack in the subsurface of a ball bearing raceway.

of the friction force acting on the surface. According to Littmann and Widner [4], wing development depends on the stress level and the number of stress cycles. A comprehensive characterization of the microstructural features of butterfly wings by Becker [11] concluded that they consist of a dispersion of ultrafine grained ferrite and carbide, very similar in nature and formation mode to the 30° and 80° white-etching bands described earlier. Further, according to both Littmann and Widner [4] and Becker [11], the wings are probably initiated by preexisting cracks associated with nonmetallic inclusion bodies. Subsequent crack and wing growth proceed together. White-etching bands and butterflies are manifestations of high-stress, high-cycle, rolling contact. While it has been difficult to positively identify them as failure-initiating characteristics, Nélias [12] indicates that fatigue failure does not seem to occur in their absence.

11.2.4 FATIGUE FAILURE-INITIATING STRESS AND DEPTH

In their development of the basic theory of rolling bearing fatigue failure, Lundberg and Palmgren [1] postulated that fatigue cracking commences at weak points below the surface of the raceway material (steel). Hence, changing the metallurgical structure and homogeneity of the steel can significantly affect the fatigue characteristics of a bearing, all other factors remaining the same. Weak points do not include macroscopic slag inclusions; these result in imperfect steel for bearing fabrication and hence premature bearing fatigue failure. Rather, microscopic inclusions and metallurgical dislocations, undetectable except by laboratory methods, are possibly the weak points in question.

Lundberg and Palmgren [1] further postulated that it is the range of the maximum orthogonal shear stress τ_0 , that is, $2\tau_0$ that initiates the crack. According to Figure 6.14, the depth below the raceway surface at which τ_0 occurs is approximately $0.49b$ for typical ball bearings. As indicated above, the microstructural alterations associated with the butterflies and fatigue cracking tend to occur at a depth 50% greater than τ_0 , that is, $0.76b$. Also, the approximately 45° orientation of the butterflies with the raceway surface is consistent with the orientation of the maximum shear stress. Nevertheless, the Lundberg–Palmgren theory and subsequent development of the standard load and life rating formulas are based on the maximum orthogonal shear stress τ_0 and the depth at which it occurs.

11.3 FATIGUE LIFE DISPERSION

If a population of apparently identical rolling bearings is subjected to identical load, speed, lubrication, and environmental conditions, the individual bearings do not achieve the same fatigue life. Instead, the bearings fail according to a dispersion such as that presented in [Figure 11.8](#). Figure 11.8 indicates the number of revolutions a bearing may accomplish with 100% probability of survival; that is, $S = 1$, in fatigue is zero. Alternatively, the probability of any bearing in the population having infinite endurance is zero. For this model, fatigue is assumed to occur when the spall is observed on a load-carrying surface. It is apparent assuming crack initiation in the subsurface, owing to the time required for a crack to propagate from the subsurface depth of initiation to the surface, that a practical fatigue life of zero is not possible. In general, the time for crack propagation is much smaller than the time to initiation. Therefore, assuming subsurface crack initiation, it is also safe to assume the time at which spalling is observed as the bearing fatigue life.

Because a life dispersion occurs, bearing manufacturers have chosen to use one or two points (or both) on the curve to define bearing endurance. These are

1. L_{10} the fatigue life that 90% of the bearing population will endure.
2. L_{50} the median fatigue life; that is, the life that 50% of the bearing population will endure.

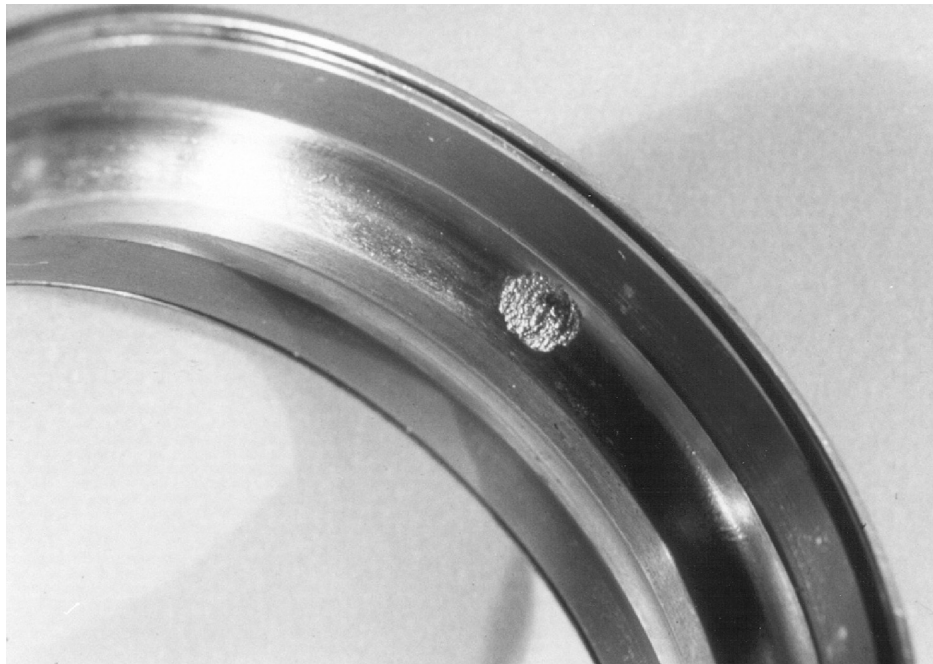


FIGURE 11.6 Fatigue spall in ball bearing raceway surface.

In Figure 11.8, $L_{50} = 5L_{10}$ approximately. This relationship is based on fatigue endurance data for all types of bearings tested and is a good rule of thumb when more exact information is unavailable.

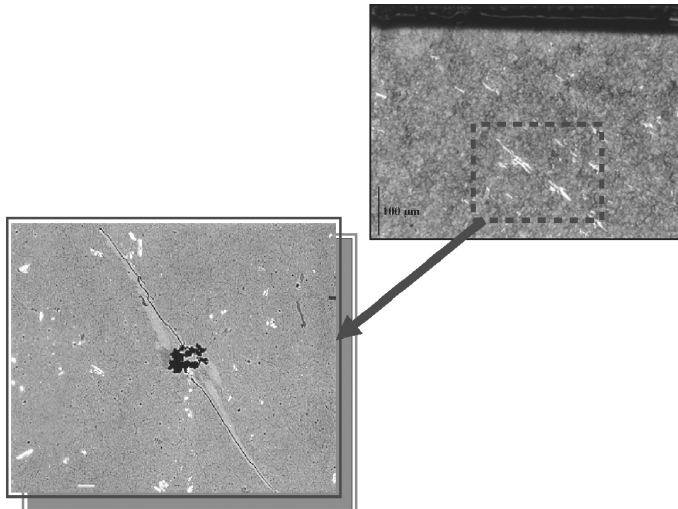


FIGURE 11.7 Subsurface “butterfly” in M50 steel ring, shown at 45° orientation to the rolling contact surface. The surface friction force is directed to the left. (From Nélias, D., Contribution a L'étude des Roulements, Dossier d'Habilitation a Diriger des Recherches, Laboratoire de Mécanique des Contacts, UMR-CNRS-INSA de Lyon No. 5514, December 16, 1999. With permission.)

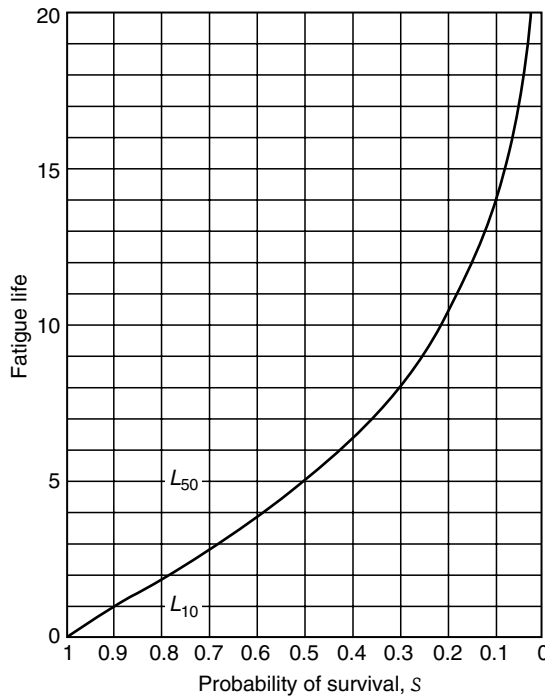


FIGURE 11.8 Rolling bearing fatigue life distribution.

The probability of survival S is described as follows:

$$S = \frac{N_s}{N} \quad (11.1)$$

where N_s is the number of bearings that have successively endured L_s revolutions of operation and N is the total number of bearings under test. Thus, if 100 bearings are tested and 12 bearings have failed in fatigue at L_{12} revolutions, the probability of survival of the remaining bearings is $S = 0.88$. Conversely, a probability of failure may be defined as follows:

$$\mathcal{F} = 1 - S \quad (11.2)$$

Bearing manufacturers almost universally refer to a “rating life” as a measure of the fatigue endurance of a given bearing operation under given load conditions. This rating life is the estimated L_{10} fatigue life of a large population of such bearings operating under the specified loading.

In fact, it is not possible to ascribe a given fatigue life to a solitary bearing application. One may however refer to the reliability of the bearing. Thus, if for a given application using a given bearing, a bearing manufacturer estimates a rating life, the manufacturer is, in effect, stating that the bearing will survive the rating life (L_{10} revolutions) with 90% reliability. Reliability is therefore synonymous with probability of survival. Fatigue life is generally stated in millions of revolutions. As an alternative, it may be, and frequently is, given in hours of successful operation at a given speed.

An interesting aspect of bearing fatigue is the life of multirow bearings. As an example of this effect, [Figure 11.9](#) shows the actual endurance data of a group of single-row bearings superimposed on the dispersion curve of Figure 11.8. Now, consider that the test bearings are

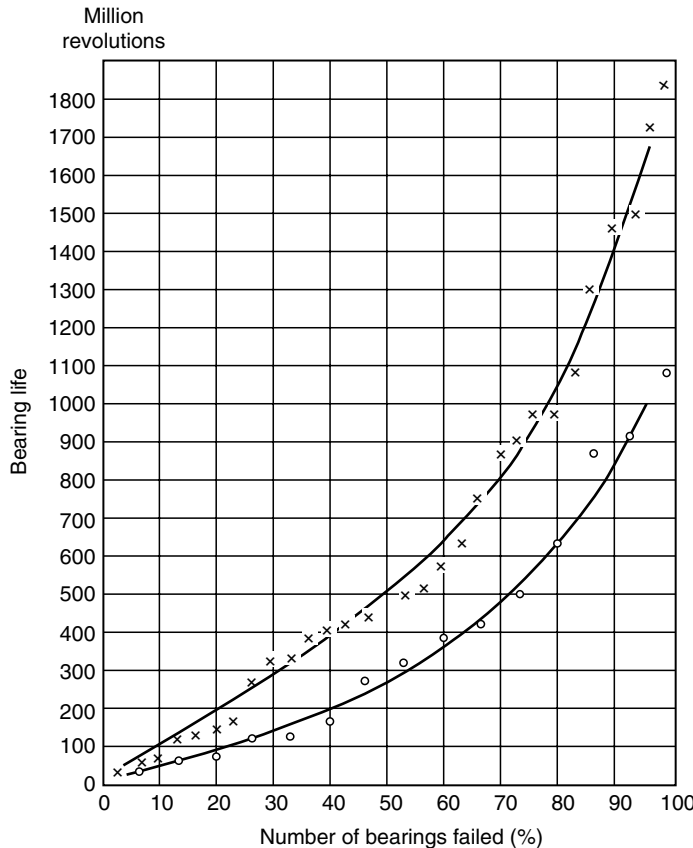


FIGURE 11.9 Fatigue life comparison of a single-row bearing to a two-row bearing. A group of single-row bearings programmed for fatigue testing was numbered by random selection, No. 1–30, inclusive. The resultant lives, plotted individually, give the upper curve. The lower curve results if bearing Nos. 1 and 2, Nos. 3 and 4, Nos. 5 and 6, and so on were considered two-row bearings and the shorter life of the two plotted as the life of a two-row bearing.

randomly grouped in pairs. The fatigue life of each pair is evidently the least life of the pair if one considers that a pair is essentially a double-row bearing. Note from Figure 11.9 that the life dispersion curve of the paired bearings falls below that of the single bearings. Thus, the life of a double-row bearing subjected to the same specified loading as a single-row of identical design is less than the life of a single-row bearing. Hence, in the fatigue of rolling bearings, the product law of probability [13] is in effect.

When one considers the postulated cause of surface fatigue, the physical truth of this rule becomes apparent. If fatigue failure is, indeed, a function of the number of weak points in a highly stressed region, then as the region increases in volume, the number of weak points increases and the probability of failure increases although the specific loading is unaltered. This phenomenon is further explained by Weibull [14,15].

11.4 WEIBULL DISTRIBUTION

In a statistical approach to the static failure of brittle engineering materials, Weibull [15] determined that the ultimate strength of a material cannot be expressed by a single numerical

value and that a statistical distribution was required for this purpose. The application of the calculus of probability led to the fundamental law of the Weibull theory:

$$\ln(1 - \mathcal{F}) = \int_{\mathcal{V}} n(\sigma) \, d\mathcal{V} \quad (11.3)$$

Equation 11.3 describes the probability of rupture \mathcal{F} due to a given distribution of stress σ over volume V where $n(\sigma)$ is a material characteristic. Weibull's principal contribution is the determination that structural failure is a function of the volume under stress. The theory is based on the assumption that the initial crack leads to a break. In the fatigue of rolling bearings, experience has demonstrated that many cracks are formed below the surface that do not propagate to the surface. Thus, Weibull's theory is not directly applicable to rolling bearings. Lundberg and Palmgren [1] theorized that consideration ought to be given to the fact that the probability of the occurrence of a fatigue break should be a function of the depth z_0 below the load-carrying surface at which the most severe shear stress occurs. The Weibull theory and rolling bearing statistical methods are discussed in greater detail in the second volume of this hand book.

According to Lundberg and Palmgren [1], let $\Gamma(n)$ be a function that describes the condition of a material at depth z after n loadings. Therefore, $d\Gamma(n)$ is the change in that condition after a small number of dn subsequent loadings. The probability that a crack will occur in the volume element \mathcal{V} at depth z for that change in condition is given by

$$\mathcal{F}(n) = g[\Gamma(n)] \, d\Gamma(n) \Delta \mathcal{V} \quad (11.4)$$

Thus, the probability of failure is assumed to be proportional to the condition of the stressed material, the change in the condition of the stressed material, and the stressed volume. The magnitude of the stressed volume is evidently a measure of the number of weak points under stress.

In accordance with Equation 11.4, $S(n) = 1 - \mathcal{F}(n)$ is the probability that the material will endure at least n cycles of loading. The probability that the material will survive at least $n + dn$ loadings is the product of the probabilities that it will survive n load cycles and that the material will endure the change in condition $d\Gamma(n)$. In equation format, that is

$$\Delta S(n + dn) = \Delta S(n) \{1 - g[\Gamma(n)] \, d\Gamma(n) \Delta \mathcal{V}\} \quad (11.5)$$

Rearranging Equation 11.5 and taking the limit as dn approaches zero yields

$$\frac{1}{S(n)} \frac{d\Delta S(n)}{dn} = -g[\Gamma(n)] \frac{d\Gamma(n)}{dn} \Delta \mathcal{V} \quad (11.6)$$

Integrating Equation 11.6 between 0 and N and recognizing that $\Delta S(0) = 1$ gives

$$\ln \frac{1}{\Delta S} = \Delta \mathcal{V} \int_0^N g[\Gamma(n)] \frac{d\Gamma(n)}{dn} \, dn \quad (11.7)$$

or

$$\ln \frac{1}{\Delta S(N)} = G[\Gamma(n)] \Delta \mathcal{V} \quad (11.8)$$

By the product law of probability, it is known that the probability $S(N)$ the entire volume \mathcal{V} will endure is

$$S(N) = \Delta_1 S(N) \times \Delta_2 S(N) \cdots \quad (11.9)$$

Combining [Equation 11.8](#) and [Equation 11.9](#) and taking the limit as dn approaches zero yields

$$\ln \frac{1}{S(n)} = \int_{\mathcal{V}} G[\Gamma(n)] d\mathcal{V} \quad (11.10)$$

[Equation 11.10](#) is similar in form to Weibull's function [Equation 11.3](#) except that $G[\Gamma(n)]$ includes the effect of depth z on failure. Alternatively, [Equation 11.10](#) could be written as follows:

$$\ln \frac{1}{S} = f(\tau_0, N, z_0) \mathcal{V} \quad (11.11)$$

where τ_0 is the maximum orthogonal shear stress, z_0 is the depth below the load-carrying surface at which this shear stress occurs, and N is the number of stress cycles survived with probability S . It can be seen here that τ_0 and z_0 could be replaced by another stress-depth relationship.

Lundberg and Palmgren [1] empirically determined the following relationship, which they felt adequately matched their test results:

$$f(\tau_0, N, z_0) \sim \tau_0^c N^e z_0^{-h} \quad (11.12)$$

Furthermore, an assumption was made that the stressed volume was effectively bounded by the width $2a$ of the contact ellipse, the depth z_0 , and the length \mathcal{L} of the path, that is,

$$\mathcal{V} \sim az_0 \mathcal{L} \quad (11.13)$$

Substituting [Equation 11.12](#) and [Equation 11.13](#) into [Equation 11.11](#) gives

$$\ln \frac{1}{S} \sim \tau_0^c z_0^{1-h} a \mathcal{L} N^e \quad (11.14)$$

At present, it is known that a lubricant film fully separates the rolling elements from the raceways in an accurately manufactured bearing that is properly lubricated. In this situation, the surface shear stress in a rolling contact is generally negligible. Considering the operating conditions and the bearings used by Lundberg and Palmgren in the 1940s to develop their theory, it is probable that surface shear stresses of magnitudes greater than zero occurred in the rolling element-raceway contacts. It has been shown by many researchers that, if a surface shear stress occurs in addition to the normal stress, the depth at which the maximum subsurface shear stress occurs will be closer to the surface than z_0 . Hence, the use of z_0 in [Equation 11.12](#) through [Equation 11.14](#) must be questioned considering the Lundberg-Palmgren test bearings and probable test conditions. Moreover, if z_0 is in question, then the use of a in the stressed volume relationship must be reconsidered.

If the number of stress cycles N equals uL , where u is the number of stress cycles per revolution and L is the life in revolutions, then

$$\ln \frac{1}{S} \sim \tau_0^c z_0^{1-h} a L u^e L^e \quad (11.15)$$

More simply, for a given bearing under a given load,

$$\ln \frac{1}{S} = A L_s^e \quad (11.16)$$

or

$$\ln \ln \frac{1}{S} = e \ln L_s + \ln A \quad (11.17)$$

Equation 11.17 defines what is called a Weibull distribution of rolling bearing fatigue life. The exponent e is called the Weibull slope.

It has been found experimentally that between the L_7 and L_{60} lives of the bearing life distribution, the Weibull distribution fits the test data extremely well (see Ref. [16]). From Equation 11.17, it can be seen that $\ln \ln 1/S$ vs. $\ln L$ plots as a straight line. Figure 11.10 shows a Weibull plot of bearing test data. It should be evident from the earlier discussion and Figure 11.10 that the Weibull slope e is a measure of bearing fatigue life dispersion. From Equation 11.17, it can be determined that the Weibull slope for a given test group is given by

$$e = \frac{\ln \frac{\ln(1/S_1)}{\ln(1/S_2)}}{\ln \frac{L_1}{L_2}} \quad (11.18)$$

where (L_1, S_1) and (L_2, S_2) are any two points on the best straight line passing through the test data. This best straight line may be accurately determined from a given set of endurance test data by using methods of extreme value statistics as described by Lieblein [17]. According to Lundberg and Palmgren [1,18], $e = 10/9$ for ball bearings and $e = 9/8$ for roller bearings. These values are based on actual bearing endurance data from bearings fabricated from

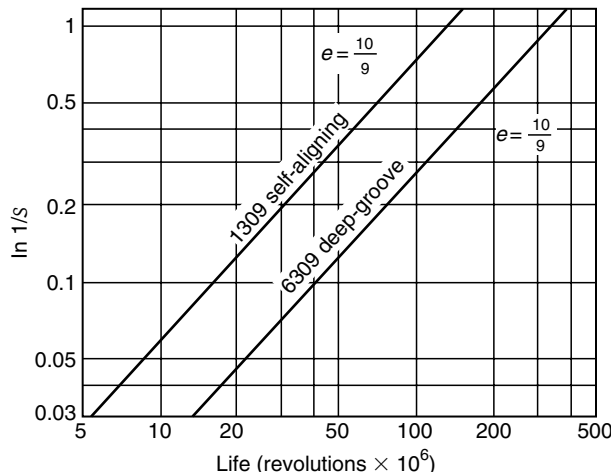


FIGURE 11.10 Typical Weibull plot for the ball bearings. (From Lundberg, G. and Palmgren, A., Dynamic capacity of rolling bearings, *Acta Polytech. Mech. Eng.*, Ser. 1, No. 3, 7, Royal Swedish Acad. Eng., 1947. Reprinted with permission.)

through-hardened AISI 52100 steel. Palmgren [19] states that for commonly used bearing steels, e is in the range 1.1–1.5. For modern, ultraclean, vacuum-remelted steels, values of e in the range 0.7–3.5 have been found. The lower value of e indicates greater dispersion of fatigue life.

At $L = L_{10}$, $S = 0.9$. Setting these values in [Equation 11.17](#) gives

$$\ln \frac{1}{0.9} = e \ln L_{10} + \ln A \quad (11.19)$$

Eliminating A between [Equation 11.17](#) and [Equation 11.19](#) yields

$$\ln \frac{1}{S} = \left(\frac{L_s}{L_{10}} \right)^e \ln \frac{1}{0.9} \quad (11.20)$$

or

$$\ln \frac{1}{S} = 0.1053 \left(\frac{L_s}{L_{10}} \right)^e \quad (11.21)$$

[Equation 11.21](#) enables the estimation of L_s , the bearing fatigue life at reliability S (probability of survival), once the Weibull slope e and “rating life” have been determined for a given application. The equation is valid between $S = 0.93$ and $S = 0.40$ —a range that is useful for most bearing applications.

See [Example 11.1](#) through [Example 11.3](#).

11.5 DYNAMIC CAPACITY AND LIFE OF A ROLLING CONTACT

In [Equation 6.71](#) it was established that at point contact

$$\frac{2\tau_0}{\sigma_{\max}} = \frac{(2t - 1)^{1/3}}{t(t + 1)} \quad (6.71)$$

More simply,

$$\tau_0 = T\sigma_{\max} \quad (11.22)$$

where T is a function of the contact surface dimensions, that is, b/a (see [Figure 6.14](#)). From [Equation 6.47](#), the maximum compressive stress within the contact ellipse is

$$\sigma_{\max} = \frac{3Q}{2\pi ab} \quad (6.47)$$

Furthermore, from [Equation 6.38](#) and [Equation 6.40](#), a and b are

$$a = a^* \left(\frac{3Q}{E_0 \Sigma \rho} \right)^{1/3} \quad (6.38)$$

$$b = b^* \left(\frac{3Q}{E_0 \Sigma \rho} \right)^{1/3} \quad (6.40)$$

where

$$E_0 = \left\{ \frac{1}{2} \left[\frac{(1 - \xi_{\text{I}}^2)}{E_{\text{I}}} + \frac{(1 - \xi_{\text{II}}^2)}{E_{\text{II}}} \right] \right\}^{-1} \quad (11.23)$$

By Equation 6.58

$$z_0 = \zeta b$$

where ζ is a function of b/a as per Equation 6.72 and Equation 6.14.

Substituting Equation 6.47 and Equation 6.40 in Equation 11.15 yields

$$\ln \frac{1}{S} \sim \frac{T^c a \mathcal{L}}{(\zeta b)^{h-1}} \left(\frac{Q}{ab} \right)^c u^e L^e \quad (11.24)$$

Letting d equal the raceway diameter, then $\mathcal{L} = \pi d$ and

$$\ln \frac{1}{S} \sim \frac{T^c u^e L^e d}{\zeta^{h-1}} \left(\frac{1}{b} \right)^{c+h-1} \left(\frac{1}{a} \right)^{c-1} Q^c \quad (11.25)$$

Rearranging Equation 11.25

$$\ln \frac{1}{S} \sim \frac{T^c u^e L^e d}{\zeta^{h-1}} \left(\frac{Q}{ab^2} \right)^{(c+h-1)/2} \left(\frac{1}{a} \right)^{(c-h-1)/2} Q^{(c-h+1)/2} \quad (11.26)$$

From Equation 6.38 and Equation 6.40,

$$\frac{Q}{ab^2} = \frac{E_0 \Sigma \rho}{3a^*(b^*)^2} \quad (11.27)$$

Creating the identity

$$D^{(c+h-1)/2} D^{(c-h-1)/2} \left(\frac{1}{D^2} \right)^{(c-h+1)/2} D^{2-h} = 1 \quad (11.28)$$

and substituting Equation 11.27 and Equation 11.28 into Equation 11.26 yields

$$\ln \frac{1}{S} \sim \frac{T^c}{\zeta^{h-1}} \left[\frac{E_0 D \Sigma \rho}{3a^*(b^*)^2} \right]^{(c+h-1)/2} \left(\frac{D}{a} \right)^{(c-h-1)/2} \left(\frac{Q}{D^2} \right)^{(c-h+1)/2} d D^{2-h} u^e L^e \quad (11.29)$$

Substituting Equation 6.38 for the semimajor axis a in point contact in Equation 11.29:

$$\ln \frac{1}{S} \sim \frac{T^c}{\zeta^{h-1}} \left[\frac{E_0 D \Sigma \rho}{3a^*(b^*)^2} \right]^{(c+h-1)/2} \left[\frac{D}{a^*} \left(\frac{E_0 \Sigma \rho}{3Q} \right)^{1/3} \right]^{(c-h-1)/2} \left(\frac{Q}{D^2} \right)^{(c-h+1)/2} d D^{2-h} u^e L^e \quad (11.30)$$

Rearranging Equation 11.30 gives

$$\ln \frac{1}{S} \sim \frac{T^c d D^{2-h} u^e L^e}{\zeta^{h-1} (a^*)^{c-1} (b^*)^{c+h-1}} \left(\frac{E_0 D \Sigma \rho}{3} \right)^{(2c+h-2)/3} \left(\frac{Q}{D^2} \right)^{(c-h+2)/3} \quad (11.31)$$

Equation 11.31 can be further rearranged. Recognizing that the probability of survival S is a constant for any given bearing application,

$$\left(\frac{Q}{D^2} \right)^{(c-h+2)/3} L^e \sim \left[\frac{T^c d D^{2-h} u^e}{\zeta^{h-1} (a^*)^{c-1} (b^*)^{c+h-1}} \left(\frac{E_0 D \Sigma \rho}{3} \right)^{(2c+h-2)/3} \right]^{-1} \quad (11.32)$$

Letting $T = T_1$ and $\zeta = \zeta_1$ when $b/a = 1$, then

$$\left(\frac{Q}{D^2} \right)^{(c-h+2)/3} L^e \sim \left[\left(\frac{T}{T_1} \right)^c \left(\frac{\zeta_1}{\zeta} \right)^{h-1} \frac{(D \Sigma \rho)^{(2c+h-2)/3}}{(a^*)^{c-1} (b^*)^{c+h-1}} \frac{d}{D} u^e \right]^{-1} D^{-(3-h)} \quad (11.33)$$

Further rearrangement yields

$$Q L^{(3e)/(c-h+2)} = A_1 \Phi D^{(2c+h-5)/(c-h+2)} \quad (11.34)$$

where A_1 is a material constant and

$$\Phi = \left[\left(\frac{T}{T_1} \right)^c \left(\frac{\zeta_1}{\zeta} \right)^{h-1} \frac{(D \Sigma \rho)^{(2c+h-2)/3}}{(a^*)^{c-1} (b^*)^{c+h-1}} \frac{d}{D} u^e \right]^{-3/(c-h+2)} \quad (11.35)$$

For a given probability of survival, the basic dynamic capacity of a rolling element–raceway contact is defined as the load that the contact will endure for one million revolutions of a bearing ring. Hence, Q_c , the basic dynamic capacity of a contact is

$$Q_c = A_1 \Phi D^{(2c+h-5)/(c-h+2)} \quad (11.36)$$

For a bearing of given dimension, by equating Equation 11.34 with Equation 11.36, one obtains

$$Q L^{(3e)/(c-h+2)} = Q_c \quad (11.37)$$

or

$$L = \left(\frac{Q_c}{Q} \right)^{(c-h+2)/(3e)} \quad (11.38)$$

Thus, for an applied load Q and a basic dynamic capacity Q_c (of a contact), the fatigue life in millions of revolutions may be calculated.

Endurance tests of ball bearings [1] have shown the load–life exponent to be very close to 3. Figure 11.11 is a typical plot of fatigue life vs. load for ball bearings. The adequacy of the value of 3 was substantiated through statistical analysis by the U.S. National Bureau of Standards [20]. Equation 11.38 thereby becomes

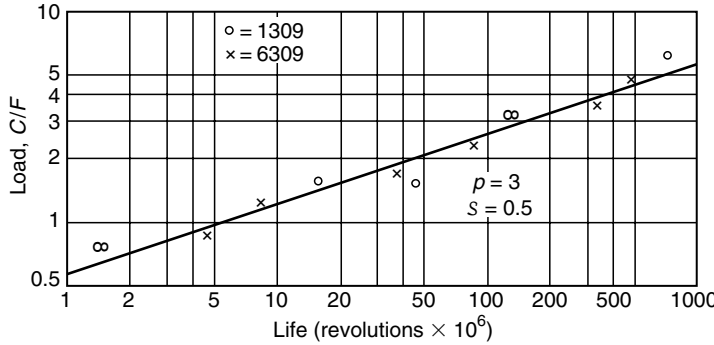


FIGURE 11.11 Load vs. life for ball bearings. (From Lundberg, G. and Palmgren, A., Dynamic capacity of rolling bearings, *Acta Polytech. Mech. Eng.*, Ser. 1, No. 3, 7, Royal Swedish Acad. Eng., 1947. Reprinted with permission.)

$$L = \left(\frac{Q_c}{Q} \right)^3 \quad (11.39)$$

This equation is also accurate for roller bearings having point contact.

As $e = 10/9$ for point contact,

$$c - h = 8 \quad (11.40)$$

Evaluating the endurance test data of approximately 1500 bearings, Lundberg and Palmgren [1] determined that $c = 31/3$ and $h = 7/3$. Substituting the values for c and h in [Equation 11.35](#) and [Equation 11.36](#), respectively, gives

$$\Phi = \left(\frac{T_1}{T} \right)^{3.1} \left(\frac{\zeta}{\zeta_1} \right)^{0.4} \frac{(a^*)^{2.8} (b^*)^{3.5}}{(D \Sigma \rho)^{2.1}} \left(\frac{D}{d} \right)^{0.3} u^{-1/3} \quad (11.41)$$

$$Q_c = A_1 \Phi D^{1.8} \quad (11.42)$$

Recall that for a roller–raceway point contact in a roller bearing

$$F(\rho) = \frac{\frac{2}{D} - \frac{1}{R} \pm \frac{2\gamma}{D(1 \mp \gamma)} + \frac{1}{r}}{\Sigma \rho} \quad (2.38, 2.40)$$

Therefore,

$$\frac{D}{2} \Sigma \rho F(\rho) = 1 - \frac{D}{2R} \pm \frac{\gamma}{1 \mp \gamma} + \frac{D}{2r} \quad (11.43)$$

Also, from [Equation 2.37](#),

$$\frac{D}{2} \Sigma \rho = 1 + \frac{D}{2R} \pm \frac{\gamma}{1 \mp \gamma} - \frac{D}{2r} \quad (11.44)$$

Adding [Equation 11.43](#) and [Equation 11.44](#) gives

$$[1 + F(\rho)] \frac{D}{2} \Sigma \rho = \frac{2}{1 \mp \gamma} \quad (11.45)$$

Subtracting [Equation 11.43](#) from [Equation 11.44](#) yields

$$[1 - F(\rho)] \frac{D}{2} \Sigma \rho = D \left(\frac{1}{R} - \frac{1}{r} \right) \quad (11.46)$$

From [Equation 11.45](#),

$$D \Sigma \rho = \frac{4}{[1 + F(\rho)](1 \mp \gamma)} \quad (11.47)$$

At this point in the analysis, define Ω as follows:

$$\Omega = \frac{1 - F(\rho)}{1 + F(\rho)} = \frac{D}{2R} \frac{r - R}{r} (1 \mp \gamma) \quad (11.48)$$

Let

$$\Omega_1 = [1 + F(\rho)]^{2.1} \left(\frac{T}{T_1} \right)^{3.1} \left(\frac{\zeta_1}{\zeta} \right)^{0.4} (a^*)^{2.8} (b^*)^{3.5} \quad (11.49)$$

Also, recognize that d in [Equation 11.41](#) is given by

$$d = d_m (1 \mp \gamma) \quad (11.50)$$

Therefore, substituting [Equation 11.49](#) and [Equation 11.50](#) into [Equation 11.41](#) yields

$$\Phi = \frac{\Omega_1}{[1 + F(\rho)]^{2.1}} \frac{1}{(D \times \Sigma \rho)^{2.1}} \left[\frac{D}{d_m (1 \mp \gamma)} \right]^{0.3} u^{-1/3} \quad (11.51)$$

Lundberg and Palmgren [1] determined that within the range corresponding to ball and roller bearings, Ω_1 very nearly is given by

$$\Omega_1 = 1.3 \Omega^{-0.41} \quad (11.52)$$

[Figure 11.12](#), from Ref. [1], establishes the validity of this assumption. Substituting [Equation 11.52](#) and [Equation 11.47](#) into [Equation 11.51](#) gives

$$\Phi = 0.0706 \left(\frac{2R}{D} \frac{r}{r - R} \right)^{0.41} (1 \mp \gamma)^{1.39} \left(\frac{D}{d_m} \right)^{0.3} u^{-1/3} \quad (11.53)$$

The number of stress cycles u per revolution is the number of rolling elements that pass a given point (under load) on the raceway of one ring while the other ring has turned through

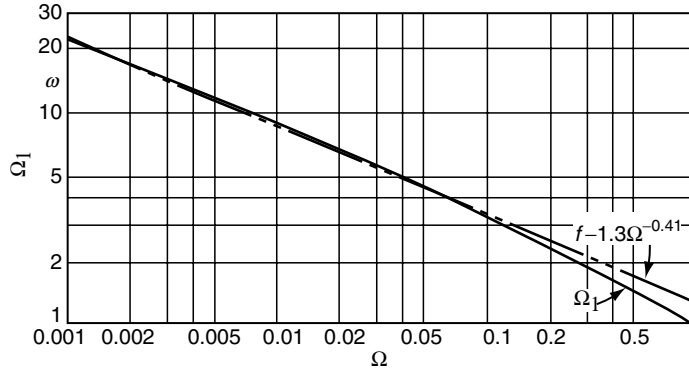


FIGURE 11.12 Ω_1 vs. Ω for point-contact ball and roller bearings. (From Lundberg, G. and Palmgren, A., Dynamic capacity of rolling bearings, *Acta Polytech. Mech. Eng.*, Ser. 1, No. 3, 7, Royal Swedish Acad. Eng., 1947. Reprinted with permission.)

one complete revolution. Hence, from [Chapter 10](#) the number of rolling elements passing a point on the inner ring per unit time is

$$u_i = Z \frac{n_{mi}}{n} = 0.5Z(1 + \gamma) \quad (11.54)$$

For the outer ring,

$$u_o = 0.5Z(1 - \gamma) \quad (11.55)$$

or

$$u = 0.5Z(1 \pm \gamma) \quad (11.56)$$

where the upper sign refers to the inner ring and the lower sign refers to the outer ring.

Substitution of Equation 11.56 in [Equation 11.53](#) gives

$$\Phi = 0.089 \left(\frac{2R}{D} \frac{r}{r-R} \right)^{0.41} \frac{(1 \mp \gamma)^{1.39}}{(1 \pm \gamma)^{1/3}} \left(\frac{D}{d_m} \right)^{0.3} Z^{-1/3} \quad (11.57)$$

Combining Equation 11.57 with [Equation 11.42](#) yields an equation for Q_c , the basic dynamic capacity of a point contact, in terms of the bearing design parameters:

$$Q_c = A \left(\frac{2R}{D} \frac{r}{r-R} \right)^{0.41} \frac{(1 \mp \gamma)^{1.39}}{(1 \pm \gamma)^{1/3}} \left(\frac{\gamma}{\cos \alpha} \right)^{0.3} D^{1.8} Z^{-1/3} \quad (11.58)$$

Test data of Lundberg and Palmgren [1] resulted in an average value $A = 98.1 \text{ mm} \cdot \text{N}$ (7450 in. lb) for bearings fabricated from 52100 steel through-hardened to Rockwell C = 61.7–64.5. This value strictly pertains to the steel quality and manufacturing accuracies achievable at that time, that is, up to approximately 1960. Subsequent improvements in

steel-making and manufacturing processes have resulted in significant increases in this ball bearing material factor. This situation will be discussed in greater detail later in this chapter.

11.5.1 LINE CONTACT

Equation 11.29 is equally valid for line contact. It can be shown for line contact that as b/a approaches zero, $(a^*)(b^*)^2$ approaches the limit $2/\pi$. Therefore, the following expression can be written for line contact:

$$\ln \frac{1}{S} \sim \frac{T^c}{\zeta^{h-1}} \left(\frac{\pi E_0 D \Sigma \rho}{6} \right)^{(c+h-1)/2} \left(\frac{4D}{3l} \right)^{(c-h-1)/2} \left(\frac{Q}{D^2} \right)^{(c-h+1)/2} dD^{2-h} u^e L^e \quad (11.59)$$

In a manner similar to that used for point contact, it can be developed that

$$Q_c = B_1 \Psi D^{(c+h-3)/(c-h+1)} l^{(c-h-1)/(c-h+1)} \quad (11.60)$$

where

$$B_1 = \left(\frac{3}{4} \right)^{(c-h-1)/(c-h+1)} \left(\frac{\pi}{2} \right)^{-(c+h-1)/(c-h+1)} \left(\frac{T_1}{T_0} \right)^{(2c)/(c-h+1)} \times \left(\frac{\zeta_0}{\zeta_1} \right)^{2(h-1)/(c-h+1)} \left(\frac{E_0}{3} \right)^{(c-h-1)/[3(c-h+1)]} A^{(2c-2h+4)/(3c-3h+3)} \quad (11.61)$$

$$\Psi = \left[(D \Sigma \rho)^{(c+h-1)/2} \frac{d}{D} u^e \right]^{-2/(c-h+1)} \quad (11.62)$$

It can be further established that

$$\Psi = 0.513 \frac{(1 \mp \gamma)^{29/27}}{(1 \pm \gamma)^{1/4}} \left(\frac{D}{d_m} \right)^{2/9} Z^{-1/4} \quad (11.63)$$

and

$$Q_c = B \frac{(1 \mp \gamma)^{29/27}}{(1 \pm \gamma)^{1/4}} \left(\frac{\gamma}{\cos \alpha} \right)^{2/9} D^{29/27} l^{7/9} Z^{-1/4} \quad (11.64)$$

where $B = 552 \text{ mm} \cdot \text{N}$ (49,500 in. · lb) for bearings fabricated from through-hardened 52100 steel. As for ball bearings, the material factor for roller bearings has undergone substantial increase since the investigations of Lundberg and Palmgren. This situation will be covered in greater detail later in this chapter.

For line contact, it was determined that

$$L = \left(\frac{Q_c}{Q} \right)^4 \quad (11.65)$$

and further, from Lundberg and Palmgren [18], that

$$\frac{c - h + 1}{2e} = 4 \quad (11.66)$$

Because $e = 9/8$ for line contact, from [Equation 11.66](#),

$$c - h = 8$$

which is identical for point contact, establishing that c and h are material constants.

Some roller bearings have fully crowned rollers such that edge loading does not occur under the probable maximum loads, that is, modified line contact occurs under such loads. Under lighter loading, however, point contact occurs. For such a condition, [Equation 11.64](#) should yield the same capacity value as [Equation 11.58](#). Unfortunately, this is a deficiency in the original Lundberg–Palmgren theory owing to the calculation tools then available. This situation can be rectified for the sake of continuity by utilizing the exponent $\frac{20}{81}$ in lieu of $\frac{1}{4}$ (and $-\frac{20}{81}$ in lieu of $-\frac{1}{4}$) in [Equation 11.64](#). Also, the value of constant B becomes 488 mm · N (43,800 in · lb) for roller bearings fabricated from through-hardened 52100 steel. Again, this material factor strictly pertains to the roller bearings of the Lundberg–Palmgren era.

11.6 FATIGUE LIFE OF A ROLLING BEARING

11.6.1 POINT-CONTACT RADIAL BEARINGS

According to the foregoing analysis, the fatigue life of a rolling element–raceway point contact subjected to normal load Q may be estimated by

$$L = \left(\frac{Q_c}{Q} \right)^3 \quad (11.39)$$

where L is in millions of revolutions and

$$Q_c = 98.1 \left(\frac{2R}{D} \frac{r}{r-R} \right)^{0.41} \frac{(1 \mp \gamma)^{1.39}}{(1 \pm \gamma)^{1/3}} \left(\frac{\gamma}{\cos \alpha} \right)^{0.3} D^{1.8} Z^{-1/3} \quad (11.58)$$

For ball bearings, this equation becomes

$$Q_c = 98.1 * \left(\frac{2f}{2f-1} \right)^{0.41} \frac{(1 \mp \gamma)^{1.39}}{(1 \pm \gamma)^{1/3}} \left(\frac{\gamma}{\cos \alpha} \right)^{0.3} D^{1.8} Z^{-1/3} \quad (11.67)$$

where the upper signs refer to the inner raceway contact and the lower signs refer to the outer raceway contact. As stress is usually higher at the inner raceway contact than at the outer raceway contact, failure generally occurs on the inner raceway first. This is not necessarily true for self-aligning ball bearings for which stress is high on the outer raceway, which is a portion of a sphere.

A rolling bearing consists of a plurality of contacts. For instance, a point on the inner raceway of a bearing with inner-ring rotation may experience a load cycle as shown in [Figure 11.13](#). Although the maximum load and hence maximum stress are significant in

*Palmgren recommended reducing this constant to 93.2 (7080) for single-row ball bearings and to 88.2 (6700) for double-row, deep-groove ball bearings to account for inaccuracies in raceway groove form owing to the manufacturing processes at that time. Subsequent improvements in the steel quality and in the manufacturing accuracies have seen the material factor increase significantly for groove-type bearings. This increase is accommodated by a factor b_m that augments the above-indicated material factors; this is discussed in detail later in this chapter.

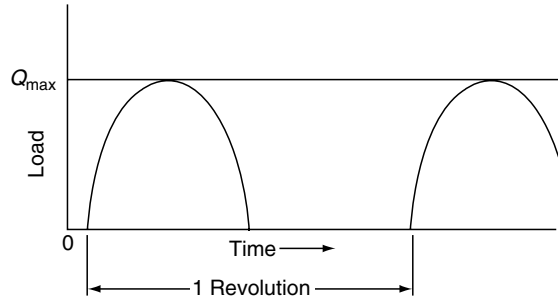


FIGURE 11.13 Typical load cycle for a point on the inner raceway of a radial bearing.

causing failure, the statistical nature of fatigue failure requires that the load history be considered. Lundberg and Palmgren [1] determined empirically that a cubic mean load fits the test data very well for point contact. Hence, for a ring which rotates relative to a load,

$$Q_{e\mu} = \left(\frac{1}{Z} \sum_{j=1}^{j=z} Q_j^3 \right)^{1/3} \quad (11.68)$$

In the terms of the angular disposition of the rolling element,

$$Q_{e\mu} = \left(\frac{1}{2\pi} \int_0^{2\pi} Q_\psi^3 d\psi \right)^{1/3} \quad (11.69)$$

The fatigue life of a rotating raceway is therefore calculated as follows:

$$L_\mu = \left(\frac{Q_{c\mu}}{Q_{e\mu}} \right)^3 \quad (11.70)$$

Each point on a raceway that is stationary relative to the applied load is subjected to a virtually constant stress amplitude. Only the space between rolling elements causes the amplitude to fluctuate with time. From [Equation 11.31](#) it can be determined that the probability of survival of any given contact point on the nonrotating raceway is given by

$$\ln \frac{1}{S_{v_j}} \sim Q_j^{(c-h+2)/3} L_j^e \quad (11.71)$$

According to the product law of probability, the probability of failure of the ring is the product of the probability of failure of the individual parts; hence, as $3e = (c - h + 2)/3$,

$$\ln \frac{1}{S} \sim L^e \int_0^{2\pi} Q_\psi^{3e} d\psi = L^e Q_{e\nu}^{3e} \quad (11.72)$$

where $Q_{e\nu}$ is defined as follows:

$$Q_{e\nu} = \left(\frac{1}{2\pi} \int_0^{2\pi} Q_\psi^{3e} d\psi \right)^{1/3e} = \left(\frac{1}{2\pi} \int_0^{2\pi} Q_\psi^{10/3} d\psi \right)^{0.3} \quad (11.73)$$

In discrete numerical format, Equation 11.73 becomes

$$Q_{e\nu} = \left(\frac{1}{Z} \sum_{j=1}^{j=z} Q_j^{10/3} \right)^{0.3} \quad (11.74)$$

From Equation 11.74 and [Equation 11.39](#), the fatigue life of a nonrotating ring may be calculated by

$$L_\nu = \left(\frac{Q_{c\nu}}{Q_{e\nu}} \right)^3 \quad (11.75)$$

To determine the life of an entire bearing, the lives of the rotating and nonrotating (inner and outer or vice versa) raceways must be statistically combined according to the product law. The probability of survival of the rotating raceway is given by

$$\ln \frac{1}{S_\mu} = K_\mu L_\mu^e \quad (11.76)$$

Similarly, for the nonrotating raceway,

$$\ln \frac{1}{S_\nu} = K_\nu L_\nu^e \quad (11.77)$$

and for the entire bearing,

$$\ln \frac{1}{S} = (K_\mu + K_\nu) L^e \quad (11.78)$$

As $S_\mu = S_\nu = S$, the combination of Equation 11.76 through Equation 11.78 yields

$$L = (L_\mu^{-e} + L_\nu^{-e})^{-1/e} \quad (11.79)$$

As $e = 10/9$ for point contact, Equation 11.79 becomes

$$L = (L_\mu^{-10/9} + L_\nu^{-10/9})^{-0.9} \quad (11.80)$$

On the basis of the preceding development, it is possible to calculate a rolling bearing fatigue life in point contact if the normal load is known at each rolling element position. These data may be calculated by methods established in [Chapter 7](#).

It is seen that the bearing lives determined according to the methods given here are based on subsurface-initiated fatigue failure of the raceways. Ball failure was not considered apparently because it was not frequently observed in the Lundberg–Palmgren fatigue endurance test data. It was rationalized that, because a ball could change rotational axes readily, the entire ball

surface was subjected to stress, spreading the stress cycles over greater volume consequently reducing the probability of ball fatigue failure before raceway fatigue failure. It has subsequently been observed by some researchers that each ball tends to seek a single axis of rotation, irrespective of original orientation before the bearing operation. This tends to negate the Lundberg–Palmgren assumption. It is perhaps correct to assume that Lundberg and Palmgren did not observe significant numbers of ball fatigue failures because during their era the ability to manufacture accurate geometry balls of good metallurgical properties exceeded that for the corresponding raceways. The ability to accurately manufacture raceways of good quality steel has consistently improved since that era. For many modern ball bearings, the incidence of ball fatigue failure in lieu of raceway fatigue failure is frequently observed. While the accuracy of ball manufacture has also improved, the gap between raceway and ball fatigue failures has narrowed significantly.

See Example 11.4.

In lieu of the foregoing rigorous approach to the calculation of bearing fatigue life, an approximate method was developed by Lundberg and Palmgren [1] for bearings having rigidly supported rings and operating at moderate speeds. It was developed in [Chapter 7](#) that

$$Q_\psi = Q_{\max} \left[1 - \frac{1}{2\varepsilon(1 - \cos \psi)} \right]^n \quad (7.15)$$

and $n = 1.5$ for point contact. This equation may be substituted into [Equation 11.69](#) for $Q_{e\mu}$ to yield

$$Q_{e\mu} = Q_{\max} \left\{ \frac{1}{2\pi} \int_{-\psi_1}^{+\psi_1} \left[1 - \frac{1}{2\varepsilon(1 - \cos \psi)} \right]^{4.5} d\psi \right\}^{1/3} \quad (11.81)$$

or

$$Q_{e\mu} = Q_{\max} J_1 \quad (11.82)$$

Similarly, for the nonrotating ring,

$$Q_{e\nu} = Q_{\max} \left\{ \frac{1}{2\pi} \int_{-\psi_1}^{+\psi_1} \left[1 - \frac{1}{2\varepsilon(1 - \cos \psi)} \right]^5 d\psi \right\}^{0.3} \quad (11.83)$$

or

$$Q_{e\nu} = Q_{\max} J_2 \quad (11.84)$$

[Table 11.1](#) gives values of J_1 and J_2 for point contact and various values for ε .

Again referring to Chapter 7, Equation 7.66 states for a radial bearing:

$$F_r = ZQ_{\max} J_r \cos \alpha \quad (7.66)$$

Setting $F_r = C_\mu$, the basic dynamic capacity of the rotating ring (relative to the applied load), and substituting for Q_{\max} according to [Equation 11.82](#) gives

$$C_\mu = Q_{e\mu} Z \cos \alpha \frac{J_r}{J_1} \quad (11.85)$$

TABLE 11.1
 J_1 and J_2 for Point Contact

Single-Row Bearings			Double-Row Bearings			
ε	J_1	J_2	ε_{I}	ε_{II}	J_1	J_2
0	0	0				
0.1	0.4275	0.4608	0.5	0.5	0.6925	0.7233
0.2	0.4806	0.5100	0.6	0.4	0.5983	0.6231
0.3	0.5150	0.5427	0.7	0.3	0.5986	0.6215
0.4	0.5411	0.5673	0.8	0.2	0.6105	0.6331
0.5	0.5625	0.5875	0.9	0.1	0.6248	0.6453
0.6	0.5808	0.6045	1.0	0	0.6372	0.6566
0.7	0.5970	0.6196				
0.8	0.6104	0.6330				
0.9	0.6248	0.6453				
1.0	0.6372	0.6566				
1.24	0.6652	0.6821				
1.67	0.7064	0.7190				
2.5	0.7707	0.7777				
5	0.8675	0.8693				
∞	1	1				

Basic dynamic capacity is defined here as that radial load for which 90% of a group of apparently identical bearing rings will survive for one million revolutions. Table 7.1 and Table 7.4 give values of J_r .

Similarly, for the nonrotating ring,

$$C_\nu = Q_{c\nu} Z \cos \alpha \frac{J_r}{J_2} \quad (11.86)$$

At $\varepsilon = 0.5$, which is a nominal value for radial rolling bearings,

$$C_\mu = 0.407 Q_{c\mu} Z \cos \alpha \quad (11.87)$$

$$C_\nu = 0.389 Q_{c\nu} Z \cos \alpha \quad (11.88)$$

Again, the product law of probability is introduced to relate the bearing fatigue life of the components. From [Equation 11.31](#), it can be established that

$$\ln \frac{1}{S_\mu} = K_\mu F^{3e} = K_\mu C_\mu^{10/3} \quad (11.89)$$

Similarly,

$$\ln \frac{1}{S_\nu} = K_\nu C_\nu^{10/3} \quad (11.90)$$

$$\ln \frac{1}{S} = (K_\mu + K_\nu) C^{10/3} \quad (11.91)$$

Combining [Equation 11.89](#) through [Equation 11.91](#) determines

$$C = (C_\mu^{-10/3} + C_\nu^{-10/3})^{-0.3} \quad (11.92)$$

where C is the basic dynamic capacity of the bearing. Rearrangement of [Equation 11.91](#) gives

$$C = C_\mu \left[1 + \left(\frac{C_\mu}{C_\nu} \right)^{10/3} \right]^{-0.3} = g_c C_\mu \quad (11.93)$$

A similar approach may be taken toward calculation of the effect of a plurality of rows of rolling elements. Consider that a bearing with point contact has two identical rows of rolling elements, with each row loaded identically. Then, for each row the basic dynamic capacity is C_1 and the basic dynamic capacity of the bearing is C . From [Equation 11.93](#),

$$C = 2C_1(1+1)^{-0.3} = 2^{0.7}C_1 = 1.625C_1$$

Hence, a two-row bearing does not have twice the basic dynamic capacity of a single-row bearing because of the statistical nature of fatigue failure.

In general, for a bearing with point contact having a plurality of rows i of rolling elements,

$$C = i^{0.7} C_k \quad (11.94)$$

where C_k is the basic dynamic capacity of one row. [Equation 11.85](#) and [Equation 11.86](#) can now be rewritten as follows:

$$C_\mu = Q_{c\mu} i^{0.7} Z \cos \alpha \frac{J_r}{J_1} \quad (11.95)$$

or

$$C_\mu = 0.407 Q_{c\mu} i^{0.7} Z \cos \alpha \quad (\varepsilon = 0.5) \quad (11.96)$$

$$C_\nu = Q_{c\nu} i^{0.7} Z \cos \alpha \frac{J_r}{J_2} \quad (11.97)$$

$$C_\nu = 0.389 Q_{c\nu} i^{0.7} Z \cos \alpha \quad (\varepsilon = 0.5) \quad (11.98)$$

Substitution of Q_c from [Equation 11.58](#) into [Equation 11.95](#) gives the following expression for basic dynamic capacity of a rotating ring:

$$C_\mu = 98.1 \left(\frac{2R}{D} \frac{r}{r-R} \right)^{0.41} \frac{(1 \mp \gamma)^{1.39}}{(1 \pm \gamma)^{1/3}} \gamma^{0.3} (i \cos \alpha)^{0.7} Z^{2/3} D^{1.8} \frac{J_r}{J_1} \quad (11.99)$$

$$C_\mu = 39.9 \left(\frac{2R}{D} \frac{r}{r-R} \right)^{0.41} \frac{(1 \mp \gamma)^{1.39}}{(1 \pm \gamma)^{1/3}} \gamma^{0.3} (i \cos \alpha)^{0.7} Z^{2/3} D^{1.8} \quad (\varepsilon = 0.5) \quad (11.100)$$

For the nonrotating ring,

$$C_\nu = 98.1 \left(\frac{2R}{D} \frac{r}{r-R} \right)^{0.41} \frac{(1 \mp \gamma)^{1.39}}{(1 \pm \gamma)^{1/3}} \gamma^{0.3} (i \cos \alpha)^{0.7} Z^{2/3} D^{1.8} \frac{J_r}{J_2} \quad (11.101)$$

$$C_v = 38.2 \left(\frac{2R}{D} \frac{r}{r-R} \right)^{0.41} \frac{(1 \mp \gamma)^{1.39}}{(1 \pm \gamma)^{1/3}} \gamma^{0.3} (i \cos \alpha)^{0.7} Z^{2/3} D^{1.8} \quad (\varepsilon = 0.5) \quad (11.102)$$

According to [Equation 11.93](#), the basic dynamic capacity of the bearing assembly is as follows for $\varepsilon = 0.5$:

$$C = f_c (i \cos \alpha)^{0.7} Z^{2/3} D^{1.8^*} \quad (11.103)$$

where

$$f_c = 39.9 \left\{ 1 + \left[1.04 \left(\frac{1 \mp \gamma}{1 \pm \gamma} \right)^{1.72} \left(\frac{r_\mu}{r_\nu} \times \frac{(2r_\nu - D)}{(2r_\mu - D)} \right)^{0.41} \right]^{10/3} \right\}^{-0.3} \times \frac{\gamma^{0.3} (1 \mp \gamma)^{1.39}}{(1 \pm \gamma)^{1/3}} \left(\frac{2r_\mu}{2r_\mu - D} \right)^{0.41} \quad (11.104)$$

Generally, it is the inner raceway that rotates relative to the load and therefore

$$f_c = 39.9 \left\{ 1 + \left[1.04 \left(\frac{1 - \gamma}{1 + \gamma} \right)^{1.72} \left(\frac{r_i}{r_o} \times \frac{r_o - D}{r_i - D} \right)^{0.41} \right]^{10/3} \right\}^{-0.3} \times \frac{\gamma^{0.3} (1 - \gamma)^{1.39}}{(1 + \gamma)^{1/3}} \left(\frac{2r_i}{2r_i - D} \right)^{0.41} \quad (11.105)$$

For ball bearings, [Equation 11.105](#) becomes

$$f_c = 39.9^* \left\{ 1 + \left[1.04 \left(\frac{1 - \gamma}{1 + \gamma} \right)^{1.72} \left(\frac{f_i}{f_o} \times \frac{(2f_o - 1)}{(2f_i - 1)} \right)^{0.41} \right]^{10/3} \right\}^{-0.3} \times \frac{\gamma^{0.3} (1 - \gamma)^{1.39}}{(1 + \gamma)^{1/3}} \left(\frac{2f_i}{2f_i - 1} \right)^{0.41} \quad (11.106)$$

[Equation 11.103](#) in conjunction with [Equation 11.106](#) is generally considered valid for ball bearings whose rings and balls are fabricated from AISI 52100 steel heat-treated at least to Rockwell C 58 hardness throughout. If the hardness of the bearing steel is less than Rockwell C 58, a reduction in the bearing basic dynamic capacity according to the following formula may be used:

$$C' = C \left(\frac{RC}{58} \right)^{3.6} \quad (11.107)$$

where RC is the Rockwell C scale hardness.

*According to Palmgren [19] this factor can be as low as 37.9 (2880) for single-row ball bearings and 35.9 (2730) for double-row deep-groove ball bearings to account for manufacturing inaccuracies.

By using [Equation 11.103](#) and [Equation 11.106](#), the basic dynamic capacity* of a radially loaded bearing may be calculated. The pertinent L_{10} fatigue life formula is given below:

$$L = \left(\frac{C}{F_e} \right)^3 \quad (11.108)$$

where F_e is an equivalent radial load that will cause the same L_{10} fatigue life as the applied load.

From [Equation 7.66](#) it can be seen that

$$Q_{\max} = \frac{F_r}{Z \cos \alpha J_r} \quad (7.66)$$

where F_r is an applied radial load and Q_{\max} is the maximum rolling element load. For a rotating ring, from [Equation 11.22](#) $Q_{e\mu} = Q_{\max} J_1$; therefore,

$$Q_{e\mu} = \frac{F}{Z \cos \alpha} \times \frac{J_1}{J_r} \quad (11.109)$$

where $Q_{e\mu}$ is the mean equivalent rolling element load in a combined loading defined by J_r . At $\varepsilon = 0.5$ (see [Chapter 7](#), and [Equation 11.82](#) and [Equation 11.84](#)), loading is ideal and purely radial; therefore,

$$Q_{e\mu} = \frac{F_{e\mu}}{Z \cos \alpha} \times \frac{J_1(0.5)}{J_r(0.5)} \quad (11.110)$$

where $F_{e\mu}$ is the equivalent radial load.

Similarly, for a nonrotating ring,

$$Q_{e\nu} = \frac{F_{e\nu}}{Z \cos \alpha} \times \frac{J_2(0.5)}{J_r(0.5)} \quad (11.111)$$

The fatigue life of the rotating ring may be described by

$$\ln \frac{1}{S_\mu} = \left(\frac{F_{e\mu}}{C_\mu} \right)^{3.33} L_\mu^{1.11} \ln \frac{1}{0.9} \quad (11.112)$$

(see [Equation 11.20](#), and [Equation 11.89](#) through [Equation 11.91](#)). Similarly, for the non-rotating ring,

$$\ln \frac{1}{S_\nu} = \left(\frac{F_{e\nu}}{C_\nu} \right)^{3.33} L_\nu^{1.11} \ln \frac{1}{0.9} \quad (11.113)$$

For the bearing,

$$\ln \frac{1}{S} = \left(\frac{F_e}{C} \right)^{3.33} L^{1.11} \ln \frac{1}{0.9} \quad (11.114)$$

*The term basic dynamic capacity was created by Lundberg and Palmgren [1]. ANSI [21,22] uses the term basic load rating and ISO [23] uses basic dynamic load rating. These terms are interchangeable.

Combining [Equation 11.112](#) through [Equation 11.114](#) yields

$$\left(\frac{F_e}{C}\right)^{3.33} = \left(\frac{F_{e\mu}}{C_\mu}\right)^{3.33} + \left(\frac{F_{e\nu}}{C_\nu}\right)^{3.33} \quad (11.115)$$

[Equation 11.109](#) and [Equation 11.110](#) gives

$$F_{e\mu} = \frac{J_r(0.5)J_1}{J_1(0.5)J_r} \quad (11.116)$$

Similarly,

$$F_{e\nu} = \frac{J_r(0.5)J_2}{J_2(0.5)J_r} \quad (11.117)$$

Substituting for $F_{e\mu}$ and $F_{e\nu}$ in [Equation 11.115](#) yields the following expression for equivalent radial load:

$$F_e = \left[\left(\frac{C}{C_\mu} \times \frac{J_r(0.5)}{J_1(0.5)} \times \frac{J_1}{J_r} \right)^{3.33} + \left(\frac{C}{C_\nu} \times \frac{J_r(0.5)}{J_2(0.5)} \times \frac{J_2}{J_r} \right)^{3.33} \right]^{0.3} F_r \quad (11.118)$$

In terms of an axial load F_a applied to a radial bearing:

$$Q_{\max} = \frac{F_a}{Z \sin \alpha J_a} \quad (11.119)$$

(see [Chapter 7](#) for evaluation of J_a).

In a manner similar to that developed for a radial load F_r ,

$$Q_{e\mu} = \frac{F_a}{Z \sin \alpha} \times \frac{J_1}{J_a} \quad (11.120)$$

$$Q_{e\nu} = \frac{F_a}{Z \sin \alpha} \times \frac{J_2}{J_a} \quad (11.121)$$

Combining [Equation 11.110](#) and [Equation 11.120](#) yields

$$F_{e\mu} = \left[\frac{J_r(0.5)}{J_1(0.5)} \times \frac{J_1}{J_a} \tan \alpha \right] F_a \quad (11.122)$$

Similarly, from [Equation 11.111](#) and [Equation 11.121](#),

$$F_{e\nu} = \left[\frac{J_r(0.5)}{J_2(0.5)} \times \frac{J_2}{J_a} \tan \alpha \right] F_a \quad (11.123)$$

Substituting [Equation 11.122](#) and [Equation 11.123](#) for $F_{e\mu}$ and $F_{e\nu}$, respectively, in [Equation 11.115](#) gives

$$F_e = \left\{ \left[\frac{C}{C_\mu} \times \frac{J_1}{J_1(0.5)} \right]^{3.33} + \left[\frac{C}{C_\nu} \times \frac{J_2}{J_2(0.5)} \right]^{3.33} \right\}^{0.3} \frac{J_r(0.5)}{J_a \tan \alpha} F_a \quad (11.124)$$

In Equation 11.118 and Equation 11.124, for inner ring rotation, that is, with load stationary relative to the outer ring, $C_\mu = C_i$ and $C_\nu = C_o$. For pure radial displacement of the bearing rings ($\varepsilon = 0.5$); therefore,

$$F_e = \left[\left(\frac{C}{C_i} \right)^{3.33} + \left(\frac{C}{C_o} \right)^{3.33} \right]^{0.3} F_r \quad (11.125)$$

For outer-ring rotation, that is, with the inner ring stationary relative to load, $C_\mu = \nu C_o$ and $C_\nu = C_i/\nu$, where $\nu = J_2(0.5)/J_1(0.5)$. For this case in pure radial load,

$$F_e = VF_r \quad (11.126)$$

where

$$V = \left[\left(\frac{C}{\nu C_o} \right)^{3.33} + \left(\frac{\nu C}{C_i} \right)^{3.33} \right]^{0.3} \quad (11.127)$$

The factor V , which is a rotation factor, can be rearranged as follows

$$V = \nu \left[\frac{1 + \left(\frac{C_i}{\nu^2 C_o} \right)^{3.33}}{1 + \left(\frac{C_i}{C_o} \right)^{3.33}} \right]^{0.3} \quad (11.128)$$

When C_i/C_o approaches 0, then $V = \nu = 1.04$ for point contact. In the other extreme, when C_i/C_o becomes infinitely large, $V = 1/\nu = 0.962$ for point contact. Figure 11.14 shows the variation of V with C_i/C_o for outer-ring rotation. For most applications, $V = 1$ is sufficiently accurate.

Both ANSI [21] and ISO [23] neglect the rotation factor and simply recommend the following equation for an equivalent radial load:

$$F_e = XF_r + YF_a \quad (11.129)$$

Values of X and Y are given in Table 11.2 for radial ball bearings.

11.6.2 POINT-CONTACT THRUST BEARINGS

For a bearing loaded in pure thrust every rolling element is loaded equally as follows:

$$Q = \frac{F_a}{Z \sin \alpha} \quad (7.26)$$

For both the rotating and stationary raceways, the mean equivalent rolling element load is simply Q as defined by Equation 7.26. Setting $F_a = C_a$, therefore,

$$C_{a\mu} = Q_{c\mu} Z \sin \alpha \quad (11.130)$$

$$C_{a\nu} = Q_{c\nu} Z \sin \alpha \quad (11.131)$$

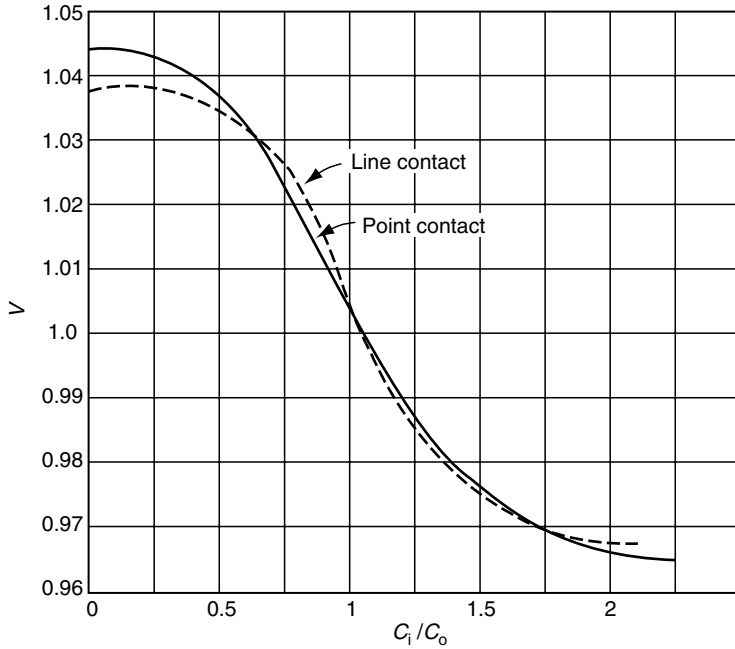


FIGURE 11.14 Rotation factor V vs. C_i/C_o .

Hence, by Equation 11.58,

$$C_{a\mu} = 98.1 \left[\frac{2R}{D} \frac{r_\mu}{(r_\mu - R)} \right]^{0.41} \frac{(1 \mp \gamma)^{1.39}}{(1 \pm \gamma)^{0.33}} \gamma^{0.3} (\cos \alpha)^{0.7} Z^{0.67} \tan \alpha D^{1.8} \quad (11.132)$$

$$C_{a\nu} = 98.1 \left[\frac{2R}{D} \frac{r_\nu}{(r_\nu - R)} \right]^{0.41} \frac{(1 \mp \gamma)^{1.39}}{(1 \pm \gamma)^{0.33}} \gamma^{0.3} (\cos \alpha)^{0.7} Z^{0.67} \tan \alpha D^{1.8} \quad (11.133)$$

In Equation 11.132 and Equation 11.133 the upper signs refer to an inner raceway and the lower signs to an outer raceway. The basic dynamic capacity of an entire thrust bearing assembly is given by

$$C_a = 98.1 \left\{ 1 + \left[\left(\frac{1 \mp \gamma}{1 \pm \gamma} \right)^{1.72} \left(\frac{r_\mu}{r_\nu} \times \frac{2r_\nu - D}{2r_\mu - D} \right)^{0.41} \right]^{3.33} \right\}^{-0.3} \times \left(\frac{2r_\mu}{2r_\mu - D} \right)^{0.41} \frac{\gamma^{0.3} (1 \mp \gamma)^{1.39}}{(1 \pm \gamma)^{0.33}} (\cos \alpha)^{0.7} \tan \alpha Z^{0.67} D^{1.8} \quad (11.134)$$

For ball bearings with inner-ring rotation, Equation 11.134 becomes

$$C_a = 98.1 \left\{ 1 + \left[\left(\frac{1 - \gamma}{1 + \gamma} \right)^{1.72} \left(\frac{f_i}{f_o} \times \frac{2f_o - 1}{2f_i - 1} \right)^{0.41} \right]^{3.33} \right\}^{-0.3} \times \left(\frac{2f_i}{2f_i - 1} \right)^{0.41} \frac{\gamma^{0.3} (1 - \gamma)^{1.39}}{(1 + \gamma)^{0.33}} (\cos \alpha)^{0.7} \tan \alpha Z^{0.67} D^{1.8} \quad (11.135)$$

TABLE 11.2
Values of X and Y for Radial Ball Bearings

Bearing Type				Single-Row Bearings		Double-Row Bearings			$\frac{F_a}{F_r} > e$	
	$\frac{F_a}{iZD^2}$			$\frac{F_a}{F_r} > e$		$\frac{F_a}{F_r} < e$				
	$\frac{F_a}{C_o}$	Units (N · mm)	Units (lb · in.)	X	Y	X	Y	X	Y	
Radial-contact groove ball bearings	0.014	0.172	25		2.30				2.30	0.19
	0.028	0.345	50		1.99				1.99	0.22
	0.056	0.689	100		1.71				1.71	0.26
	0.084	1.03	150		1.56				1.55	0.28
	0.11	1.38	200	0.56	1.45	1	0	0.56	1.45	0.30
	0.17	2.07	300		1.31				1.31	0.34
	0.28	3.45	500		1.15				1.15	0.38
	0.42	5.17	750		1.04				1.04	0.42
	0.56	6.89	1000		1.00				1.00	0.44
Angular-contact ball bearings with contact angle	0.014	0.172	25	For this type, use the X , Y , and e values applicable to single-row radial-contact bearings		2.78			3.74	0.23
	0.028	0.345	50		3.23	0.26			2.78	0.30
	0.056	0.689	100			2.07			2.52	0.34
	0.085	1.03	150		1	1.87	0.78			
	0.11	1.38	200			1.75		2.36	0.36	
5°	0.17	2.07	300			1.58		2.13	0.40	
	0.28	3.45	500			1.39		1.87	0.45	
	0.42	5.17	750			1.26		1.69	0.50	
	0.56	6.89	1000			1.21		1.63	0.52	
	0.014	0.172	25		1.88	2.18		3.06	0.29	
10°	0.029	0.345	50		1.71	1.98		2.78	0.32	
	0.057	0.689	100		1.52	1.76		2.47	0.36	
	0.086	1.03	150		1.41	1.63		2.20	0.38	

	0.11	1.38	200	0.46	1.34	1	1.55	0.75	2.18	0.40
	0.29	2.07	300		1.23		1.42		2.00	0.44
	0.43	3.45	500		1.10		1.27		1.79	0.49
	0.57	5.17	750		1.01		1.17		1.64	0.54
		6.89	1000		1.00		1.16		1.63	0.54
15°	0.015	0.172	25		1.47		1.65		2.39	0.38
	0.029	0.345	50		1.40		1.57		2.28	0.40
	0.058	0.689	100		1.30		1.46	0.72	2.11	0.43
	0.087	1.03	150		1.23		1.38		2.00	0.46
	0.12	1.38	200	0.44	1.19	1	1.34		1.93	0.47
	0.17	2.07	300		1.12		1.26		1.82	0.50
	0.29	3.45	500		1.02		1.14		1.66	0.55
	0.44	5.17	750		1.00		1.12		1.63	0.56
	0.58	6.89	1000		1.00		1.12		1.63	0.56
20°				0.43	1.00	1	1.09	0.70	1.63	0.57
25°				0.41	0.87	1	0.92	0.67	1.41	0.68
30°				0.39	0.76	1	0.78	0.63	1.24	0.80
35°				0.37	0.66	1	0.66	0.60	1.07	0.95
40°				0.35	0.57	1	0.55	0.57	0.98	1.14
Self-aligning ball bearings				0.40	0.4 ctn α	1	0.42 ctn α	0.65	0.65 ctn α	1.5 tan α

^aTwo similar single-row angular-contact ball bearings mounted face-to-face or back-to-back are considered as one double-row angular-contact bearings.

^bValues of X , Y , and e for a load or contact angle other than that shown are obtained by linear interpolation.

^cValues of X , Y , and e do not apply to filling slot bearings for applications in which ball–raceway contact areas project substantially into the filling slot under load.

^dFor single-row bearings when $F_a/F_r \neq e$, use $X=1$, $Y=0$.

Lundberg and Palmgren [1] recommended a reduction in the material constant to accommodate inaccuracies in manufacturing that cause unequal internal load distributions. Hence, Equation 11.135 becomes

$$C_a = 88.2^*(1 - 0.33 \sin \alpha) \\ \times \left\{ 1 + \left[\left(\frac{1-\gamma}{1+\gamma} \right)^{1.72} \left(\frac{f_i}{f_o} \times \left(\frac{2f_o - 1}{2f_i - 1} \right)^{0.41} \right]^{3.33} \right\}^{-0.3} \times \left(\frac{2f_i}{2f_i - 1} \right)^{0.41} \\ \times \frac{\gamma^{0.3} (1-\gamma)^{1.39}}{(1+\gamma)^{0.33}} (\cos \alpha)^{0.7} \tan \alpha Z^{0.67} D^{1.8} \quad (11.136)$$

In Equation 11.136 as recommended by Palmgren [19], the term $(1 - 0.33 \sin \alpha)$ accounts for reduction in C_a caused by added friction due to spinning (presumably). The following is the formula for basic dynamic thrust capacity:

$$C_a = f_c (i \cos \alpha)^{0.7} \tan \alpha Z^{2/3} D^{1.8\dagger} \quad (11.137)$$

for which it is apparent that (approximately)

$$f_c = 88.2 (1 - 0.33 \sin \alpha) \\ \times \left\{ 1 + \left[\left(\frac{1-\gamma}{1+\gamma} \right)^{1.72} \times \left(\frac{f_i}{f_o} \times \frac{2f_o - 1}{2f_i - 1} \right)^{0.41} \right]^{3.33} \right\}^{-0.3} \\ \times \frac{\gamma^{0.3} (1-\gamma)^{1.39}}{(1+\gamma)^{0.33}} \left(\frac{2f_i}{2f_i - 1} \right)^{0.41} \quad (11.138)$$

For thrust bearings with a 90° contact angle,

$$C_a = f_c Z^{2/3} D^{1.8} \quad (11.139)$$

where (approximately)

$$f_c = 59.1 \left[1 + \left(\frac{f_i}{f_o} \times \frac{2f_o - 1}{2f_i - 1} \right)^{1.36} \right]^{-0.3} \gamma^{0.3} \left(\frac{2f_i}{2f_i - 1} \right)^{0.41} \quad (11.140)$$

For thrust bearings having i rows of balls in which Z_k is the number of rolling elements per row and C_{ak} is the basic dynamic capacity per row, the basic dynamic capacity C_a of the bearing may be determined as follows:

$$C_a = \sum_{k=1}^{k=i} Z_k \left[\sum_{k=1}^{k=i} \left(\frac{Z_k}{C_{ak}} \right)^{3.33} \right]^{-0.3} \quad (11.141)$$

*This value can be as high as 93.2 (7080) for angular-contact ball bearings.

†ANSI [21] recommends using D raised to the 1.4 power in lieu of 1.8 for bearings having balls of diameter greater than 25.4 mm (1 in.).

As for radial bearings, the L_{10} life of a thrust bearing is given by

$$L = \left(\frac{C_a}{F_{ea}} \right)^3 \quad (11.142)$$

where F_{ea} is the equivalent axial load. As before,

$$F_{ea} = X F_r + Y F_a$$

X and Y as recommended by ANSI are given in Table 11.3.

See Example 11.5.

11.6.3 LINE-CONTACT RADIAL BEARINGS

The L_{10} fatigue life of a roller–raceway line contact subjected to normal load Q may be estimated by

$$L = \left(\frac{Q_c}{Q} \right)^4 \quad (11.65)$$

where L is in millions of revolutions and

$$Q_c = 552 \frac{(1 \mp \gamma)^{29/27}}{(1 \pm \gamma)^{1/4}} \left(\frac{\gamma}{\cos \alpha} \right)^{2/9} D^{29/27} l^{7/9} Z^{-1/4} \quad (11.64)$$

The upper signs refer to an inner raceway contact and the lower signs refer to an outer raceway contact.

To account for stress concentrations due to edge loading of rollers and noncentered roller loads, Lundberg and Palmgren [18] introduced a reduction factor λ such that

$$Q_c = 552\lambda \frac{(1 \mp \gamma)^{29/27}}{(1 \pm \gamma)^{1/4}} \left(\frac{\gamma}{\cos \alpha} \right)^{2/9} D^{29/27} l^{7/9} Z^{-1/4} \quad (11.143)$$

TABLE 11.3
X and Y Factors for Ball Thrust Bearings

Bearing Type	Single-Direction Bearings		Double-Direction Bearings ^a		
	X	Y	X	Y	X
Thrust ball bearings with contact angle ^b					
$\alpha = 45^\circ$	0.66	1	1.18	0.59	0.66
$\alpha = 60^\circ$	0.92	1	1.90	0.54	0.92
$\alpha = 75^\circ$	1.66	1	3.89	0.52	1.66
					e

^aDouble-direction bearings are presumed to be symmetrical.

^bFor $\alpha = 90^\circ$: $F_r = 0$ and $Y = 1$.

On the basis of their test results, the schedule of Table 11.4 for λ_i and λ_o was developed. The variation in λ for line contact is probably due to the method of roller guiding; for example, in some bearings rollers are guided by flanges that are integral with a bearing ring, other bearings employ roller guiding cages.

In lieu of a cubic mean roller load for a raceway contact, a quartic mean will be used such that

$$Q_{e\mu} = \left(\frac{1}{Z} \sum_{j=1}^{j=Z} Q_j^4 \right)^{1/4} = \left(\frac{1}{2\pi} \int_0^{2\pi} Q_\psi^4 d\psi \right)^{1/4} \quad (11.144)$$

The difference between a cubic mean load and a quartic mean load is substantially negligible. The fatigue life of the rotating raceway is

$$L_\mu = \left(\frac{Q_{c\mu}}{Q_{e\mu}} \right)^4 \quad (11.145)$$

As with point-contact bearings, the equivalent loading of a nonrotating raceway is given by

$$Q_{e\nu} = \left(\frac{1}{Z} \sum_{j=1}^{j=Z} Q_j^4 \right)^{1/4e} = \left(\frac{1}{2\pi} \int_0^{2\pi} Q_\psi^{4.5} d\psi \right)^{1/4.5} \quad (11.146)$$

The life of the stationary raceway is

$$L_\nu = \left(\frac{Q_{c\nu}}{Q_{e\nu}} \right)^4 \quad (11.147)$$

As with point-contact bearings, the life of a roller bearing having line contact is calculated from

$$L = (L_\mu^{-9/8} + L_\nu^{-9/8})^{-8/9} \quad (11.148)$$

Thus, if each roller load has been determined by the methods in [Chapter 7](#), the fatigue life of the bearing may be estimated by using Equation 11.144 and Equation 11.148.

See Example 11.6.

To simplify the rigorous method of calculating bearing fatigue life just outlined, an approximate method was developed by Lundberg and Palmgren [1,18] for roller bearings having rigid rings and moderate speeds. In a manner similar to point-contact bearings,

$$Q_{e\mu} = Q_{\max} J_1 \quad (11.149)$$

TABLE 11.4
Values of λ_i and λ_o

Contact	Inner Raceway	Outer Raceway
Line contact	0.41–0.56	0.38–0.6
Modified line contact	0.6–0.8	0.6–0.8

$$J_1 = \left\{ \frac{1}{2\pi} \int_{-\psi_1}^{+\psi_1} \left[1 - \frac{1}{2\varepsilon} (1 - \cos \psi) \right]^{4.4} d\psi \right\}^{1/4} \quad (11.150)$$

$$Q_{e\nu} = Q_{\max} J_2 \quad (11.151)$$

$$J_2 = \left\{ \frac{1}{2\pi} \int_{-\psi_1}^{+\psi_1} \left[1 - \frac{1}{2\varepsilon} (1 - \cos \psi) \right]^{4.95} d\psi \right\}^{2/9} \quad (11.152)$$

Table 11.5 gives values of J_1 and J_2 as functions of ε .

As for point-contact bearings, Equation 7.66, [Equation 11.85](#), and [Equation 11.86](#) are equally valid for radial roller bearings in line contact. Therefore, at $\varepsilon=0.5$,

$$C_\mu = 0.377 i^{7/9} Q_\mu Z \cos \alpha \quad (11.153)$$

$$C_\nu = 0.363 i^{7/9} Q_\nu Z \cos \alpha \quad (11.154)$$

According to the product law of probability,

$$C = C_\mu \left[1 + \left(\frac{C_\mu}{C_\nu} \right)^{9/2} \right]^{2/9} = g_c C_\mu \quad (11.155)$$

The reduction factor λ according to edge loading may be applied to the entire bearing assembly. For line contact at one raceway and point contact at the other, $\lambda=0.54$ if a symmetrical pressure distribution similar to that shown in Figure 6.23b is attained along

TABLE 11.5
 J_1 and J_2 for Line Contact

ε	Single Row		Double Row			
	J_1	J_2	ε_I	ε_{II}	J_1	J_2
0	0	0				
0.1	0.5287	0.5633	0.5	0.5	0.7577	0.7867
0.2	0.5772	0.6073	0.6	0.4	0.6807	0.7044
0.3	0.6079	0.6359	0.7	0.3	0.6806	0.7032
0.4	0.6309	0.6571	0.8	0.2	0.6907	0.7127
0.5	0.6495	0.6744	0.9	0.1	0.7028	0.7229
0.6	0.6653	0.6888				
0.7	0.6792	0.7015				
0.8	0.6906	0.7127				
0.9	0.7028	0.7229				
1	0.7132	0.7323				
1.25	0.7366	0.7532				
1.67	0.7705	0.7832				
2.5	0.8216	0.8301				
5	0.8989	0.9014				
∞	1	1				

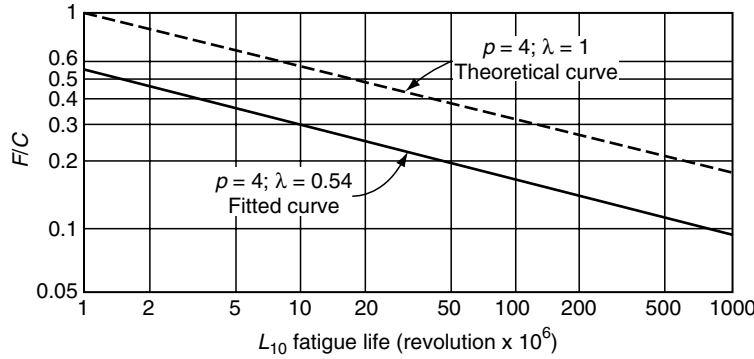


FIGURE 11.15 L_{10} vs. F/C for roller bearing. Test points are for an SKF 21309 spherical roller bearing. (From Lundberg, G. and Palmgren, A., Dynamic capacity of roller bearings, *Acta Polytech. Mech. Eng.*, Ser. 2, No. 4, 96, Royal Swedish Acad. Eng., 1952.)

the roller length. Figure 11.15, taken from Ref. [18], shows the result of the fit obtained to the test data while using $\lambda = 0.54$. Table 11.6 is a schedule for λ for bearing assemblies.

Using the reduction factor λ , the resulting expression for basic dynamic capacity of a radial roller bearing is

$$C = 207\lambda \left\{ 1 + \left[1.04 \left(\frac{1 \mp \gamma}{1 \pm \gamma} \right)^{143/108} \right]^{9/2} \right\}^{-2/9} \frac{\gamma^{2/9} (1 \mp \gamma)^{29/27}}{(1 \pm \gamma)^{1/4}} \times (il \cos \alpha)^{7/9} Z^{3/4} D^{29/27} \quad (11.156)$$

In most bearing applications, the inner raceway rotates and

$$C = 207\lambda \left\{ 1 + \left[1.04 \left(\frac{1 - \gamma}{1 + \gamma} \right)^{143/108} \right]^{9/2} \right\}^{-2/9} \frac{\gamma^{2/9} (1 - \gamma)^{29/27}}{(1 + \gamma)^{1/4}} \times (il \cos \alpha)^{7/9} Z^{3/4} D^{29/27} \quad (11.157)$$

As for point-contact bearings, an equivalent radial load can be developed and

$$F_e = \left\{ \left[\frac{C}{C_i} \times \frac{J_r(0.5)J_1}{J_1(0.5)J_r} \right]^{9/2} + \left[\frac{CJ_r(0.5)J_2}{C_o J_2(0.5)J_r} \right]^{9/2} \right\}^{2/9} F_r + \left\{ \left[\frac{CJ_1}{C_i J_1(0.5)} \right]^{9/2} + \left[\frac{CJ_2}{C_o J_2(0.5)} \right]^{9/2} \right\}^{2/9} \frac{J_r(0.5)}{J_a \tan \alpha} F_a \quad (11.158)$$

TABLE 11.6
Reduction Factor λ

Contact Condition	λ Range
Line contact at both raceways	0.4–0.5
Line contact at one raceway	
Point contact at other raceway	0.5–0.6
Modified line contact	0.6–0.8

TABLE 11.7
X and Y for Radial Roller Bearings

	$F_a/F_r \leq 1.5 \tan \alpha$		$F_a/F_r > 1.5 \tan \alpha$	
	X	Y	X	Y
Single-row bearing	1	0	0.4	0.4 $\operatorname{ctn} \alpha$
Double-row bearing	1	0.45 $\operatorname{ctn} \alpha$	0.67	0.67 $\operatorname{ctn} \alpha$

The rotation factor V is given by

$$V = \nu \left[\frac{1 + \left(\frac{C_i}{\nu^2 C_o} \right)^{9/2}}{1 + \left(\frac{C_i}{C_o} \right)^{9/2}} \right]^{2/9} \quad (11.159)$$

where $\nu = J_2(0.5)/J_1(0.5)$. Figure 11.14 shows the variation of V with C_i/C_o for both point and line contacts.

ANSI [22] gives the same formula for equivalent radial load for radial roller bearings as for radial ball bearings. (Rotation factor V is once again neglected.):

$$F_e = X F_r + Y F_a \quad (11.129)$$

X and Y for spherical self-aligning and tapered roller bearings are given in Table 11.7.

The life of a roller bearing in line contact is given by

$$L = \left(\frac{C}{F_e} \right)^4 \quad (11.160)$$

11.6.4 LINE-CONTACT THRUST BEARINGS

For thrust bearings, Lundberg and Palmgren [18] introduced the reduction factor η , in addition to λ , to account for variations in raceway groove dimensions, which may cause a roller from experiencing the theoretical uniform loading:

$$Q = \frac{F_a}{Z \sin \alpha} \quad (7.26)$$

According to [18], for thrust roller bearings,

$$\eta = 1 - 0.15 \sin \alpha \quad (11.161)$$

Considering the capacity reductions due to λ and η , for thrust roller bearings in line contact, the following equations may be used for thrust bearings in which $\alpha \neq 90^\circ$:

$$C_{ak} = 552 \lambda \eta \gamma^{2/9} \frac{(1 \mp \gamma)^{29/27}}{(1 \pm \gamma)^{1/4}} (l \cos \alpha)^{7/9} \tan \alpha Z^{3/4} D^{29/27} \quad (11.162)$$

In [Equation 11.162](#) the upper signs refer to the inner raceway, that is, $k = i$; the lower signs refer to the outer raceway, that is, $k = o$.

For thrust roller bearings in which $\alpha = 90^\circ$,

$$C_{ai} = C_{ao} = 469\lambda \gamma^{2/9} l^{7/9} D^{29/27} Z^{3/4} \quad (11.163)$$

[Equation 11.162](#) and [Equation 11.163](#) may be substituted into [Equation 11.155](#) to obtain the basic dynamic capacity of a bearing row in thrust loading. [Equation 11.164](#) may be used to determine the basic dynamic capacity in thrust loading for a thrust roller bearing having i rows and Z_i rollers in each row:

$$C_a = \sum_{k=1}^{k=i} Z_k \left[\sum_{k=1}^{k=i} \left(\frac{Z_k}{C_{ak}} \right)^{9/2} \right]^{-2/9} \quad (11.164)$$

The fatigue life of a thrust roller bearing can be calculated by the following equation:

$$L = \left(\frac{C_a}{F_{ea}} \right)^4 \quad (11.165)$$

According to ANSI [22], the equivalent thrust load may be estimated by

$$F_{ea} = XF_r + YF_a \quad (11.166)$$

Table 11.8 gives values of X and Y .

11.6.5 RADIAL ROLLER BEARINGS WITH POINT AND LINE CONTACT

If a roller bearing contains rollers and raceways having straight profiles, then line contact obtains at each contact and the formulations of the preceding two sections are valid. If, however, the rollers have a curved profile (crowned; see [Figure 1.38](#)) of smaller radius than one or both of the conforming raceway profiles or if one or both raceways have a convex profile and the rollers have straight profiles, then depending on the angular position of a roller and its roller load, one of the contact conditions in [Table 11.9](#) will occur.

Of the contact conditions in [Table 11.9](#), the optimum roller bearing design for any given application is generally achieved when the most heavily loaded roller is in modified line contact. As stated in [Chapter 6](#), this condition produces the most nearly uniform stress distribution along the roller profile, and edge loading is precluded. It is also stated in Chapter 6 that a logarithmic profile roller can produce an even better load distribution over a wider

TABLE 11.8
 X and Y for Thrust Roller Bearings

Bearing Type	Contact Angle	Loading	X	Y
Single direction	$\alpha < 90^\circ$	$F_a/F_r \leq 1.5 \tan \alpha$	0	1
	$\alpha = 90^\circ$	$F_r = 0$	0	1
	$\alpha > 90^\circ$	$F_a/F_r > 1.5 \tan \alpha$	$\tan \alpha$	1
Double direction	$\alpha < 90^\circ$	$F_a/F_r \leq 1.5 \tan \alpha$	$1.5 \tan \alpha$	0.67
	$\alpha > 90^\circ$	$F_a/F_r > 1.5 \tan \alpha$	$\tan \alpha$	1

TABLE 11.9
Roller–Raceway Contact

Condition	Inner Raceway	a_i^a	Outer Raceway	a_o^b	Load
1	Line	$2a_i > 1.5l$	Line	$2a_o > 1.5l$	Heavy
2	Line	$2a_i > 1.5l$	Point	$2a_o < l$	Moderate
3	Point	$2a_i < l$	Line	$2a_o > 1.5l$	Moderate
4	Modified line	$l \leq 2a_i \leq 1.5l$	Modified line	$l \leq 2a_o \leq 1.5l$	Moderate
5	Point	$2a_i < l$	Point	$2a_o < l$	Light

^a a_i is the semimajor axis of inner raceway contact ellipse.

^b a_o is the semimajor axis of outer raceway contact ellipse.

range of loading; however, this roller profile tends to be special. The more usual profile is that of the partially crowned roller. It should be apparent that the optimum crown radii or osculations necessary to obtain modified line contact can only be evaluated for a given bearing after the loading has been established. Series of bearings, however, are often optimized by basing the crown radii or osculations on an estimated load, for example, $0.5C$ or $0.25C$, where C is the basic dynamic capacity. Depending on the applied loads, bearings in such a series may operate anywhere from point to line contact at the most heavily loaded roller.

Because it is desirable to use one rating method for a given roller bearing, and because in any given roller bearing application it is possible to have combinations of line and point contact, Lundberg and Palmgren [18] estimated that the fatigue life should be calculated from

$$L = \left(\frac{C}{F_e} \right)^{10/3} \quad (11.167)$$

Note that $10/3$ lies between the exponents 3 and 4. In equation

$$C = \nu C_1 \quad (11.168)$$

C_1 is the basic dynamic capacity in line contact as calculated by [Equation 11.157](#) or [Equation 11.163](#).

If both inner and outer raceway contacts are line contacts and $\lambda = 0.45$ to account for edge loading and nonuniform stress distribution, curve 1 of [Figure 11.16](#) shows the variation of load with life by using [Equation 11.160](#) and the fourth power slope. Assuming $\nu = 1.36$ and using [Equation 11.167](#), curve 2 illustrates the approximation to curve 1. The shaded area shows the error which occurs when using the approximation. Points *A* on [Figure 11.16](#) represent 5% error.

If outer and inner raceway contacts are point contacts for loads arbitrarily less than $0.21C$ ($L = 100$ million revolutions), then for $\lambda = 0.65$ curve 1 of [Figure 11.17](#) shows the load–life variation of the bearing. Note that the inverse slope of the curve decreases from 4 to 3 at $L = 100$ million revolutions. Curve 2 of [Figure 11.17](#) shows the fit obtained while using [Equation 11.167](#) and $\nu = 1.20$.

Lastly, if one raceway contact is line contact and the other is point contact, curve 1 of [Figure 11.18](#) shows load–life variation for $\lambda = 0.54$. Transformation from point to line contact is arbitrarily assumed to occur at $L = 100$ million revolutions. Curve 2 of [Figure 11.18](#) shows the fit obtained while using [Equation 11.167](#) and $\nu = 1.26$.

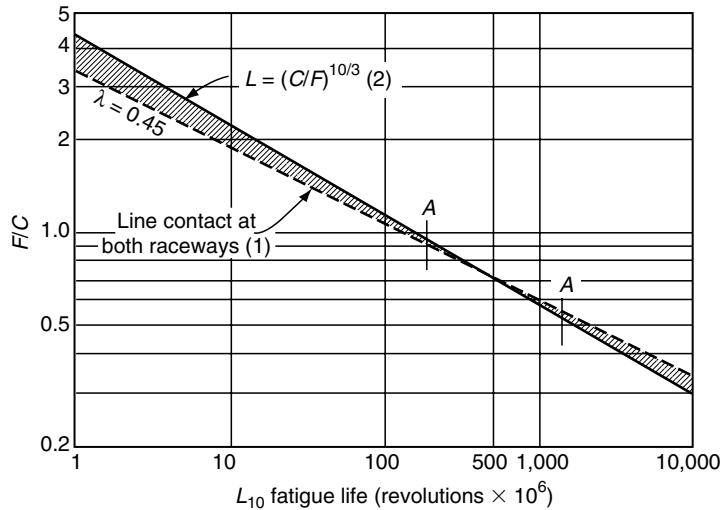


FIGURE 11.16 L_{10} vs. F/C for line contact at both raceways.

In Figure 11.16, using [equation 11.167](#), fatigue lives between 150 and 1,500 million revolutions have a calculation error less than 5%. Similarly, in Figure 11.17, lives between 15 and 2,000 million revolutions have less than 5% calculation error, and in [Figure 11.18](#), lives between 40 and 10,000 million revolutions have less than 5% calculation error. As the foregoing ranges represent probable regions of roller bearing operation, Lundberg and Palmgren [18] considered that Equation 11.167 was a satisfactory approximation by which to estimate the fatigue life of roller bearings.

Accordingly, the data in [Table 11.10](#) were developed. [Equation 11.156](#) becomes

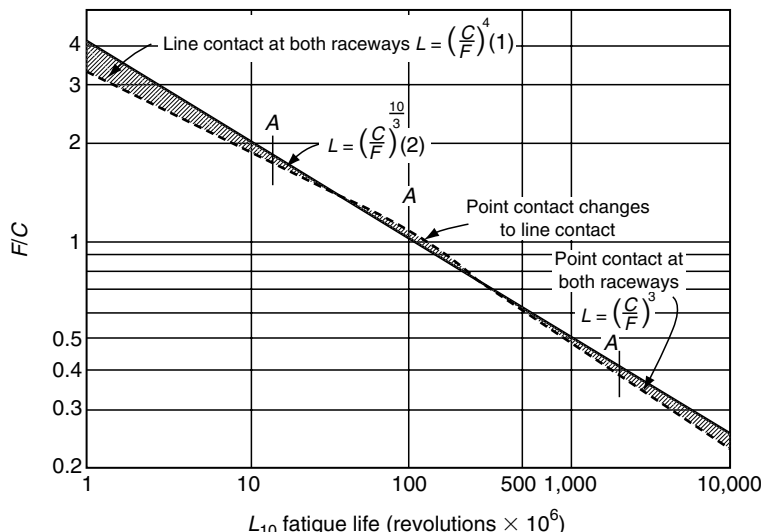


FIGURE 11.17 L_{10} vs. F/C for point or line contact at both raceways.

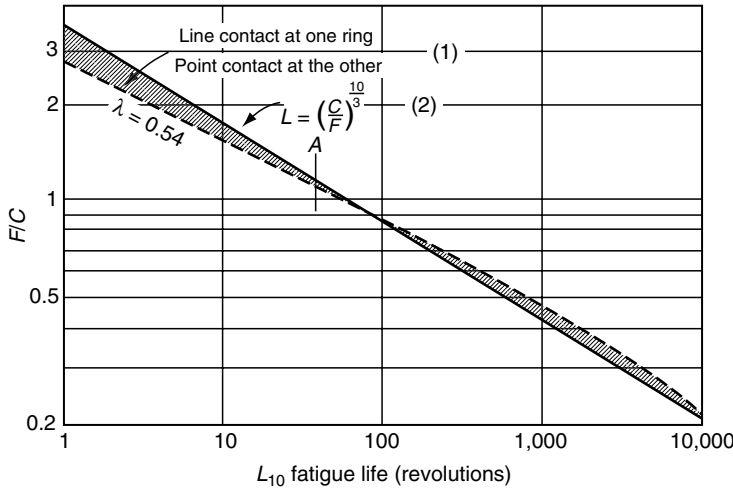


FIGURE 11.18 L_{10} vs. F/C for combination of line and point contact. (From Voskamp, A., Material response to rolling contact loading, *ASME Trans., J. Tribol.*, 107, 359–366, 1985. Reprinted with permission.)

$$C = 207\lambda\nu \left\{ 1 + \left[1.04 \left(\frac{1 \mp \gamma}{1 \pm \gamma} \right)^{143/108} \right]^{9/2} \right\}^{-2/9} \times \frac{\gamma^{2/9} (1 \mp \gamma)^{29/27}}{(1 \pm \gamma)^{1/4}} \times (il \cos \alpha)^{7/9} Z^{3/4} D^{29/27} \quad (11.169)$$

11.6.6 THRUST ROLLER BEARING WITH POINT AND LINE CONTACT

For thrust roller bearings operating with a combination point and line contact at the raceways, [Equation 11.162](#) and [Equation 11.163](#) become

$$C_{ak} = 552\lambda\eta\nu\gamma^{2/9} \frac{(1 \mp \gamma)^{29/27}}{(1 \pm \gamma)^{1/4}} (l \cos \alpha)^{7/9} \tan \alpha Z^{3/4} D^{29/27} \quad \alpha \neq 90^\circ \quad (11.170)$$

$$C_{ai} = C_{ao} = 469\lambda\nu\gamma^{2/9} l^{7/9} Z^{3/4} D^{29/27} \quad \alpha = 90^\circ \quad (11.171)$$

TABLE 11.10
 ν and λ for Roller Bearings

Condition	λ	ν	$\lambda\nu$
Modified line contact in cylindrical roller bearings	0.61	1.36	0.83
Modified line contact in spherical and tapered roller bearings	0.57	1.36	0.78
Combination line and point contact (inner and outer raceways)	0.54	1.26	0.68
Line contact	0.45	1.36	0.61

11.7 LOAD RATING STANDARDS

To provide bearing users with means to compare the ball and roller bearings produced and sold by bearing manufacturers around the world, standards for rating bearings according to load-carrying capability were developed. These standards are based on the work of Lundberg and Palmgren [1,18]. As indicated in previous sections of this chapter, the empirical equations developed in those references are strictly valid for bearings manufactured from AISI 52100 steel through-hardened to a minimum of Rockwell C 58. Moreover, the equations are based on the 52100 steel, which existed at the time of Lundberg and Palmgren's endurance testing. Considerable reduction in the amounts of fatigue life-reducing impurities has been achieved together with improved homogeneity using vacuum processing. Such cleaner and more homogeneous 52100 steel produces rolling bearings with much greater resistance to rolling contact fatigue. Additionally, improved means for forming and finishing the rolling contact surfaces also result in greater fatigue resistance. Therefore, the ANSI and ISO load rating standards [21–23] respectively employ a b_m factor directly in the equations for basic dynamic radial load rating* and basic dynamic axial load rating* to accommodate these improvements. For example, [Equation 11.103](#) for radial ball bearings becomes:

$$C = b_m f_c (i \cos \alpha)^{0.7} Z^{2/3} D^{1.8\dagger} \quad (11.172)$$

ISO [23] gives values of the factor b_m , which may be applied to the formulas for basic dynamic capacity for each of the various executions of ball and roller as deemed appropriate. Table 11.11 summarizes these b_m values.

TABLE 11.11
Rating Factor for Contemporary Bearing Factor

Bearing Type	b_m Rating Factor
Radial ball (except filling slot and self-aligning types)	1.3
Angular-contact ball	1.3
Filling slot ball	1.1
Thrust ball	1.1
Radial spherical roller	1.15
Radial cylindrical roller	1.1
Radial tapered roller	1.1
Radial needle roller with machined rings	1.1
Drawn cup needle roller	1.0
Thrust tapered roller	1.1
Thrust spherical roller	1.15
Thrust cylindrical roller	1.0
Thrust needle roller	1.0

*The terms basic load rating, basic dynamic radial load rating (or basic dynamic axial load rating), and basic dynamic capacity may be used interchangeably. The last term was created by Lundberg and Palmgren [1].

†ANSI [18.10] recommends using D raised to the 1.4 power in lieu of 1.8 for bearings having balls of diameter greater than 25.4 mm (1 in.). In this case, for metric units calculation of basic load rating, f_{cm} values must be multiplied by 3.647; that is, $f_{cm} = 3.647 \times f_{cm}$ (tabular value).

Ball and roller bearings are also manufactured from through-hardening steels other than 52100, for example, tool steels such as M50 and stainless steels such as 440C. Tapered roller bearings, in particular, and other roller bearings are manufactured from surface-hardened steels such as SAE 8620 and 9310 among many others. Strictly speaking, the basic load rating standards as described in this chapter do not apply to such bearings. Because of the demand to accommodate and rate such bearings, the basic load rating standards have been modified. This development along with other life-modifying effects is discussed in the Second Volume of this handbook.

The ANSI load rating standards [10,12] have incorporated the b_m factors into f_{cm} factors, which are simply $f_{cm} = b_m \times f_c$. Table CD11.1 and Table CD11.2 give the f_{cm} values to be used in the standard basic load rating Equation 11.173 for radial ball bearings:

$$C = f_{cm}(i \cos \alpha)^{0.7} Z^{2/3} D^{1.8^*} \quad (11.173)$$

Similarly, for thrust ball bearings, Table CD11.3 and Table CD11.4 give the f_{cm} values to be used in the standard basic load rating Equation 11.174 and Equation 11.175:

$$C_a = f_{cm}(\cos \alpha)^{0.7} \tan \alpha Z^{2/3} D^{1.8^*} \quad \alpha \neq 90^\circ \quad (11.174)$$

$$C_a = f_{cm} Z^{2/3} D^{1.8^*} \quad \alpha = 90^\circ \quad (11.175)$$

For radial roller bearings, Table CD11.5 and Table CD11.6 provide f_{cm} values for use in the standard basic load rating Equation 11.176:

$$C = f_{cm}(il \cos \alpha)^{7/9} Z^{3/4} D^{29/27} \quad (11.176)$$

And for thrust roller bearings of various executions, Table CD11.7 through Table CD11.12 give f_{cm} values to be used in the standard basic load rating Equation 11.177 and Equation 11.178:

$$C_a = f_{cm}(l \cos \alpha)^{7/9} \tan \alpha Z^{3/4} D^{29/27} \quad \alpha \neq 90^\circ \quad (11.177)$$

$$C_a = f_{cm} l^{7/9} Z^{3/4} D^{29/27} \quad \alpha = 90^\circ \quad (11.178)$$

With regard to the use of the standard load rating equations and tabular data on f_{cm} , X , and Y factors to estimate rolling bearing fatigue life endurance, certain limitations should be observed:

1. Load ratings pertain only to bearings fabricated from properly hardened, good quality steel.
2. Rating life calculations assume that the bearing inner and outer rings are rigidly supported.

*ANSI [21] recommends using D raised to the 1.4 power in lieu of 1.8 for bearings having balls of diameter greater than 25.4 mm (1 in.).

3. Rating life calculations assume that the bearing inner and outer ring axes are properly aligned.
4. Rating life calculations assume that the bearing has only a nominal internal clearance during operation.
5. With regard to ball bearings, the raceway groove radii must fall within $0.52 \leq f \leq 0.53$ ($f = \text{groove radius} \div D$).
6. With regard to roller bearings, the load ratings pertain only to bearings manufactured to achieve optimized contact. This involves good roller guidance by flanges or cage as well as optimum roller and raceway profiles.
7. For both ball and roller bearings, no stress concentrations may occur due to loading conditions. In a ball bearing, this condition can be caused if the applied thrust load is sufficient to cause the balls to override the land edges.

See Example 11.7 through Example 11.9.

11.8 EFFECT OF VARIABLE LOADING ON FATIGUE LIFE

Many applications do not involve invariant applied loading; rather, they undergo a defined load vs. time cycle. To analyze these applications, use is made of the Palmgren–Miner rule, which is defined by Equation 11.179:

$$\sum_{i=1}^{i=n} \frac{N_i}{L_i} = 1 \quad (11.179)$$

This equation refers to a set of bearing operating conditions n , each individual condition designated i , each condition having a potential fatigue life L_i revolutions, and the bearing operating only for N_i revolutions where $N_i < L_i$.

To determine the life of a rolling bearing subjected to a time-variant load, it is necessary to determine a mean effective bearing load such that

$$L = \left(\frac{C}{F_m} \right)^p \quad (11.180)$$

where $p = 3$ for point-contact bearings, and $p = 4$ for line-contact bearings. Actually, there is little difference in F_m calculated for $p = 3$ as compared with F_m calculated for $p = 4$; therefore, a cubic mean effective load is frequently used for roller bearings with little error.

Consider a bearing subjected to a load F_1 for N_1 revolutions and F_2 for N_2 revolutions. The calculated fatigue lives for these loads are

$$L_1 = \left(\frac{C}{F_1} \right)^p \quad (11.181)$$

$$L_2 = \left(\frac{C}{F_2} \right)^p \quad (11.182)$$

Substituting Equation 11.181 and Equation 11.182 into Equation 11.179 yields

$$\frac{F_1^p N_1}{C^p} + \frac{F_2^p N_2}{C^p} = 1 \quad (11.183)$$

Dividing the total bearing fatigue life by L , and substituting for L according to Equation 11.180 yields

$$\frac{F_1^p N_1}{L} + \frac{F_2^p N_2}{L} = F_m^p \quad (11.184)$$

Hence,

$$F_m = \left(\frac{F_1^p N_1 + F_2^p N_2}{L} \right)^{1/p} \quad (11.185)$$

It is apparent that $L = N_1 + N_2$. Thus, in general for k loads each operating for N_k revolutions, the mean effective load is given by

$$F_m = \left(\frac{\sum F_k^p N_k}{N} \right)^{1/p} \quad (11.186)$$

where N is the total number of revolutions in one load cycle. In integral format, Equation 11.186 becomes

$$F_m = \left(\frac{1}{N} \int_0^N F^p dN \right)^{1/p} \quad (11.187)$$

For a cyclic load of period τ ,

$$F_m = \left(\frac{1}{\tau} \int_0^\tau F_t^p dt \right)^{1/p} \quad (11.188)$$

where F_t is a defined function of time.

See Example 11.10.

Some special cases of fluctuating load can now be defined. Palmgren [19] states that for a bearing load that varies nearly linearly between F_{\min} and F_{\max} as shown in Figure 11.19, the following approximation is valid:

$$F_m = \frac{1}{3} F_{\min} + \frac{2}{3} F_{\max} \quad (11.189)$$

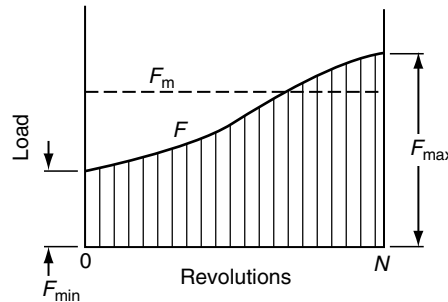


FIGURE 11.19 Load vs. time, nearly linear.

If the load variation is truly linear, then

$$F_m = F_{\min} + \left(\frac{F_{\max} - F_{\min}}{\tau} \right) \times t \quad (11.190)$$

and

$$F_m = F_{\min} \left\{ \int_0^1 \left[1 + \left(\frac{F_{\max}}{F_{\min}} - 1 \right) z \right]^p dz \right\}^{1/p} \quad (11.191)$$

where z is a dummy variable.

A bearing load may be composed of a steady load F_1 upon which a sinusoidally varying load of amplitude F_3 is superimposed as shown in Figure 11.20.

In this case,

$$F_t = F_1 - F_3 \cos \omega t \quad (11.192)$$

where ω is the circular frequency in radians per second. Thus,

$$F_m = F_1 \left[\frac{1}{\tau} \int_0^\tau \left(1 + \frac{F_3}{F_1 \cos \omega t} \right)^p dt \right]^{1/p} \quad (11.193)$$

A more general case of loading is that of a steady load F_1 , a rotating load F_2 , and a sinusoidally varying load of amplitude F_3 (in phase with F_1) simultaneously applied to a rolling bearing. Figure 11.21 demonstrates this form of loading. The maximum bearing load occurs when F_1 , F_2 , and F_3 assume the same line of action. Steady loads F_1 are caused by the weight of machine elements on a shaft and also by their imposed loading such as gear or belt loads. Rotating loads F_2 are caused by unbalance in spinning mechanisms, either intentional or not. Sinusoidal loads F_3 are caused by inertial forces of reciprocating machinery. For this general loading, one may simply state that

$$F_m = \phi_m (F_1 + F_2 + F_3) \quad (11.194)$$

where

$$\phi_m = \frac{\left\{ \frac{1}{2\pi} \int_0^{2\pi} \left\{ [F_1 + (F_2 + F_3) \cos \psi]^2 + (F_2 \sin \psi)^2 \right\}^{p/2} d\psi \right\}^{1/p}}{F_1 + F_2 + F_3} \quad (11.195)$$

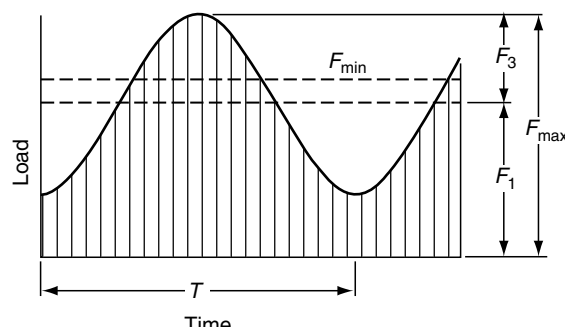


FIGURE 11.20 Sinusoidal load F_3 superimposed on a steady load F_1 .

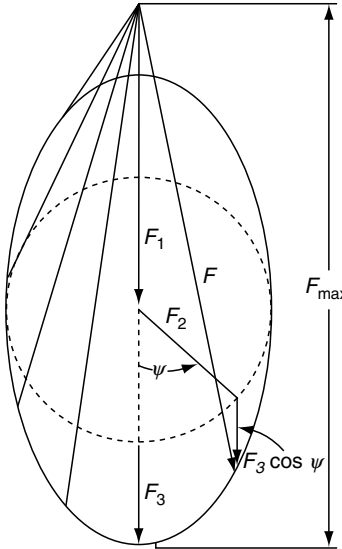


FIGURE 11.21 Load vector diagram for generalizing bearing loading consisting of steady load F_1 , rotating load F_2 , and sinusoidal load F_3 in phase with F_1 .

SKF has developed a series of curves depicting this relationship in terms of the relative magnitudes of F_1 , F_2 , and F_3 . Figure 11.22a applies to point contact, that is, $p=3$, and Figure 11.22b applies to line contact, $p=4$. Note that when $F_2=0$, the loading of Figure 11.23 occurs. Thus, the lowest curves of Figure 11.22 refer to that loading situation. If F_1 and F_2 are individually absent, that is, for the sinusoidal bearing loading demonstrated in Figure 11.23, then according to Figure 11.22, $\phi_m=0.75$ for point contact and $\phi_m=0.79$ for line contact.

Figure 11.24 demonstrates a bearing loading in which F_3 , the sinusoidal load, acts 90° out-of-phase to the steady load F_1 . Figure 11.25a and Figure 11.25b yield values of ϕ_m for this type of loading for point and line contact, respectively. When steady load F_1 is absent and maximum F_3 occurs 90° out-of-phase with F_2 , then Figure 11.26 illustrates the bearing loading with time, and Figure 11.27 gives values of ϕ_m for point and line contact.

11.9 FATIGUE LIFE OF OSCILLATING BEARINGS

Oscillating bearings do not turn through complete revolutions. If one refers to the frequency of oscillation as n cycles per minute, then an oscillating bearing operating at frequency n will have a longer fatigue life than the same bearing rotating at n rpm under the same load. This is due to a lesser mean equivalent load per rolling element. One oscillation (cycle) refers to the motion of the bearing from one extreme position to the other, and return. The time to traverse the angular amplitude ϕ of oscillation starting from 0° position is one fourth of a cycle, or $\tau/4$, where τ is the period of the oscillation.

To determine the fatigue life of an oscillating bearing, the applied load may be converted to an equivalent load for a rotating bearing, thus accounting for the decreased number of stress cycles. For a given bearing design having a given fatigue life, Equation 11.31 yields the following relationship for point contact:

$$Q^{(c-h+2)/3} u^e = G \quad (11.196)$$

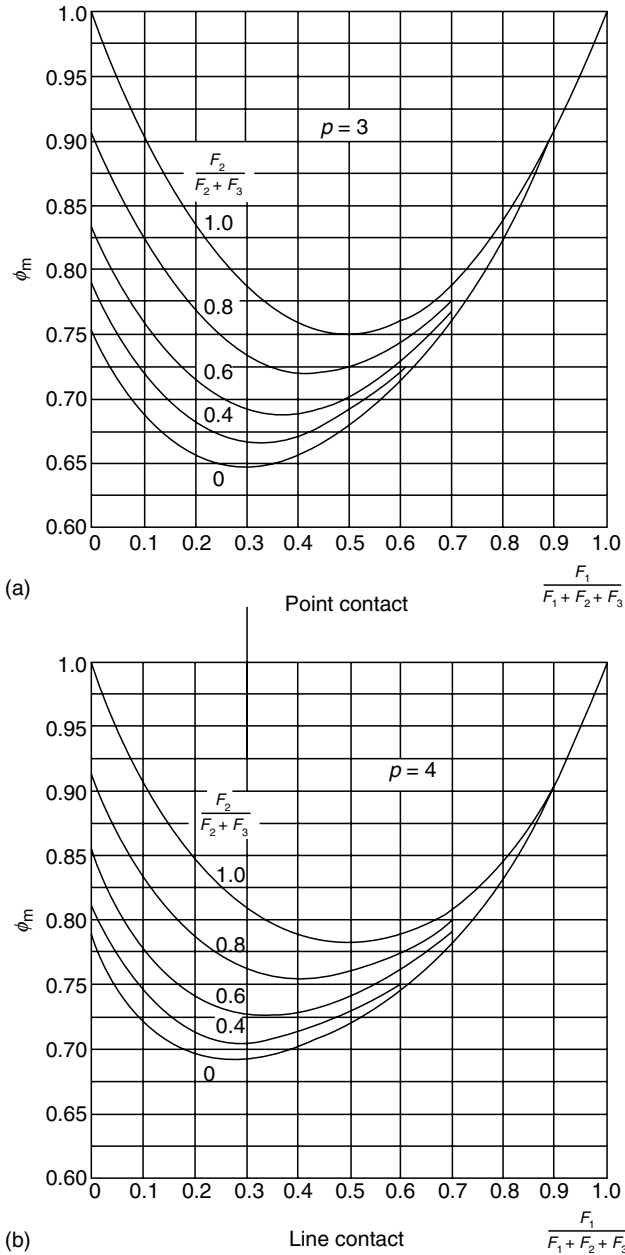


FIGURE 11.22 ϕ_m vs. $F_1/(F_1 + F_2 + F_3)$ for the generalized loading in [Figure 11.21](#).

where G is a constant, u is the number of stress cycles per revolution, and e is the Weibull slope. It was shown in [Equation 11.37](#) and [Equation 11.38](#) that

$$\frac{c - h + 2}{3e} = 3 = p \quad (11.197)$$

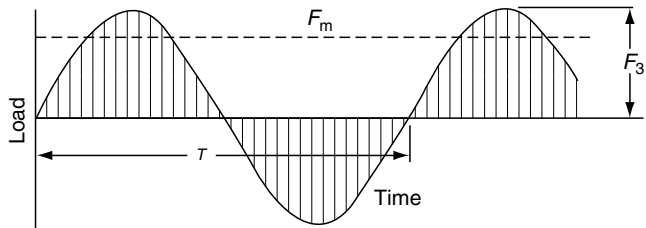


FIGURE 11.23 Sinusoidal bearing load.

Therefore,

$$Q^P u = G \quad (11.198)$$

Using the subscript RE for the equivalent rotating bearing, osc for an oscillating bearing, and R for a rotating bearing, from Equation 11.198,

$$Q_{\text{RE}} = \left(\frac{u_{\text{osc}}}{u_R} \right)^{1/p} Q_{\text{osc}} \quad (11.199)$$

The length of arc stressed during one complete revolution of a rotating bearing is $2\pi r$, where r is the raceway radius. The length of arc stressed during one complete oscillation is $4\phi r$, where ϕ is the amplitude of oscillation in radians. It is apparent that

$$\frac{u_R}{u_{\text{osc}}} = \frac{\pi}{2\phi} \quad (11.200)$$

Thus,

$$Q_{\text{RE}} = \left(\frac{2\phi}{\pi} \right)^{1/p} Q_{\text{osc}} \quad (11.201)$$

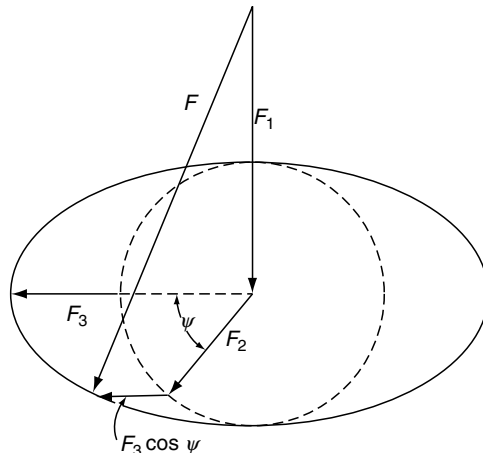
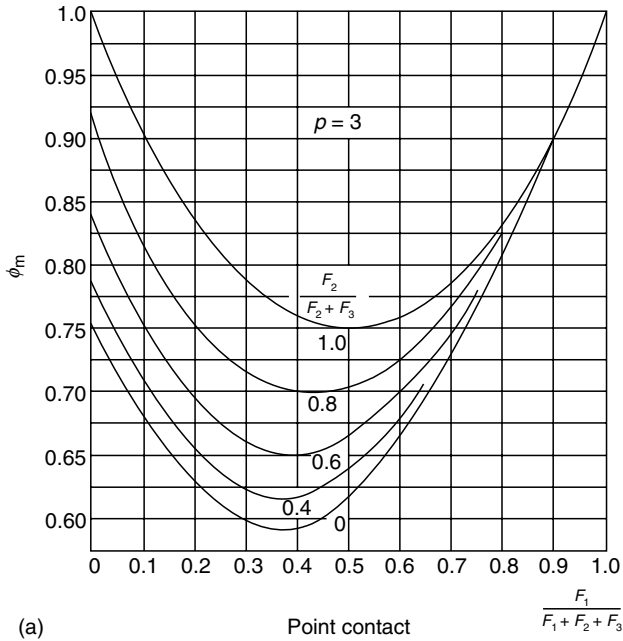
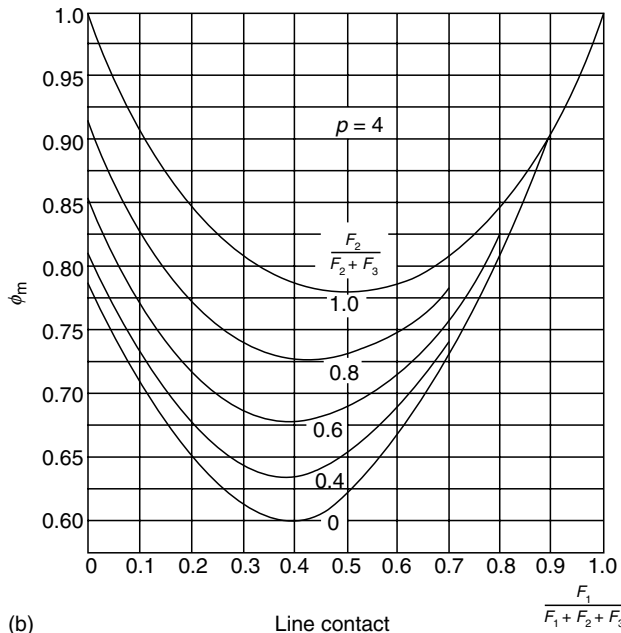


FIGURE 11.24 Load vector diagram for generalized bearing loading consisting of steady load F_1 , rotating load F_2 , and sinusoidal load F_3 , 90° out-of-phase with F_1 .



(a)

Point contact



(b)

Line contact

FIGURE 11.25 ϕ_m vs. $F_1/(F_1 + F_2 + F_3)$ for the generalized loading of [Figure 11.24](#).

In this example, Q is the load of a contact yielding a fatigue life of L million revolutions. Therefore, for an oscillating bearing,

$$L = \left(\frac{C}{F_{RE}} \right)^p \quad (11.202)$$

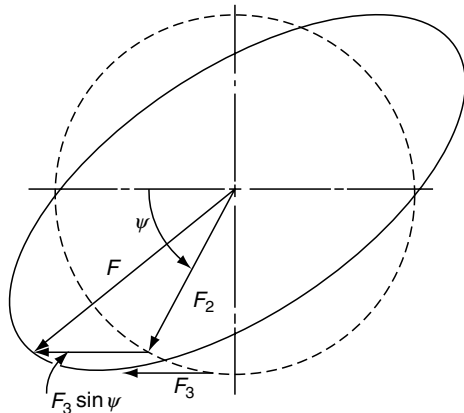


FIGURE 11.26 Load vector diagram for bearing loading consisting of a rotating load F_2 and a sinusoidal load F_3 . Maximum F_3 occurs 90° out-of-phase with F_2 .

where

$$F_{RE} = \left(\frac{2\phi}{\pi}\right)^{1/p} \text{ or } F_{RE} = \left(\frac{\phi}{90}\right)^{1/p} F \quad (11.203)$$

for oscillation angle in radians and degrees, respectively.

Houpert [24] refined this method for bearings subjected to combined radial and thrust load (F_r and F_a), the load zone defined by

$$\varepsilon = \frac{1}{2} \left(1 + \frac{\delta_a \tan \alpha}{\delta_r} \right) \quad (7.61)$$

Also, from Table 7.4, the value of ε for a given application can be found directly as a function of $(F_r \tan \alpha)/F_a$. He applied the Palmgren–Miner rule to modify the lives of the raceways,

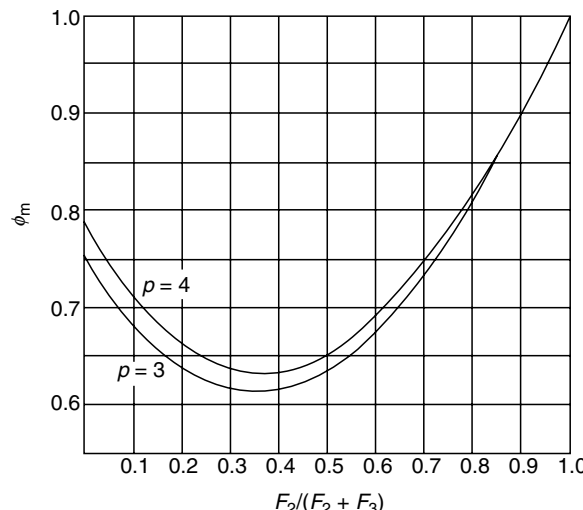


FIGURE 11.27 ϕ_m vs. $F_2/(F_2 + F_3)$ for the loading in Figure 11.26.

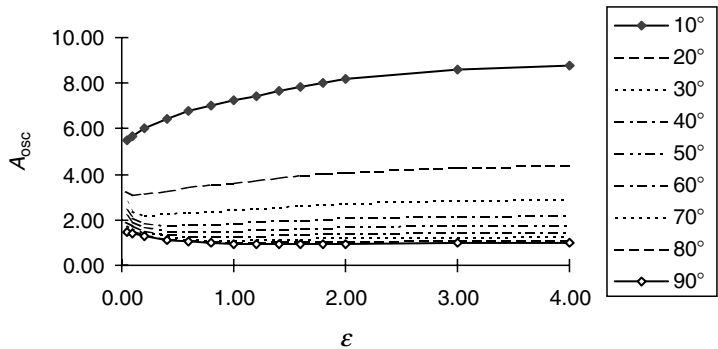


FIGURE 11.28 A_{osc} vs. load zone extent and 10–90° oscillation angles.

more accurately accounting for the number of stress cycles experienced by each sector. Accordingly, an oscillation-life factor A_{osc} was developed such that

$$L = A_{osc} \left(\frac{C}{F} \right)^P \quad (11.204)$$

Figure 11.28 and Figure 11.29 give A_{osc} vs. extent of load zone for various oscillation angles.

The Houpert [24] method tends to yield more accurate results than the simpler method described in [Equation 11.202](#) and [Equation 11.203](#). When the extent of the load zone is such that $\epsilon > 1$, however, the simpler method generally will provide sufficiently accurate results.

When $\phi/90 < 1/Z$, where Z is the number of rolling elements per row, then a strong possibility exists that indentation of the raceways will occur. In this situation, surface fatigue may not be a valid criterion of failure in view of the vibration that may obtain. Furthermore, it is possible that lubrication may be inadequate, resulting in surface wear and excessive heat generation.

11.10 RELIABILITY AND FATIGUE LIFE

Based on the analysis of endurance test data pertaining to more than 2500 bearings, Tallian [16] confirmed that a Weibull distribution fits the test data in the most used cumulative failure

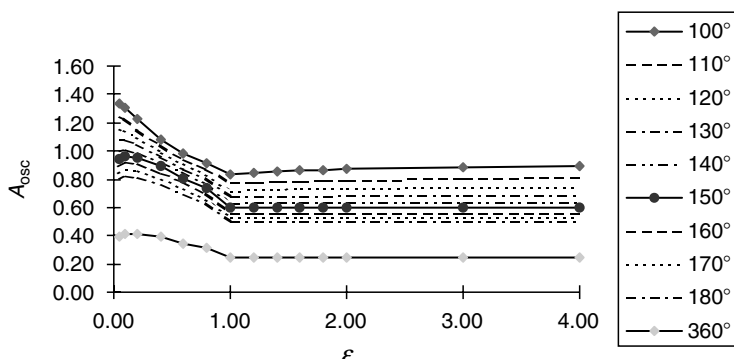


FIGURE 11.29 A_{osc} vs. load zone extent and 100–360° oscillation angles.

probability region, that is, $0.07 \leq F \leq 0.60$. Everywhere outside of this region, fatigue life is greater than that predicted by a Weibull distribution.

Generally, bearing users are not concerned about fatigue lives in excess of L_{50} , the median life; therefore, the upper failure region is not of interest here. Rolling bearing users are, however, extremely interested in the region $0 \leq F \leq 0.10$. In fact, a reliability better than 99% is not an uncommon requirement. Some automobile manufacturers are now providing 10 year—167,000 km (100,000 miles) warranties on power transmission components including bearings and hence require bearings of greater reliability. Considering the availability of high-quality, modern bearing steels, it is possible to manufacture bearings with increased fatigue life. It may therefore be necessary to specify the fatigue of a given rolling bearing application in terms of L_1 , L_5 , and so on, instead of L_{10} .

Figure 11.30, from Ref. [16], shows the deviation from the Weibull distribution for probability of failure F less than 10%. Note that below approximately a standardized bearing life of 0.004, that is, below $\gamma = (L/L_{50})^e \ln 2 = 0.004$ there is apparently no decrease in fatigue life. Figure 11.31, which is a similar plot shown by Harris [25] on semilogarithmic coordinates, demonstrates more dramatically the significance of Tallian's research. It is apparent that "no-failure" fatigue life may be predicted with an attendant reliability of 100% ($S = 1.0$, $F = 0$). According to Tallian [16], the no-failure fatigue life may be approximated by

$$L_{NF} \cong 0.05L_{10} \quad (11.205)$$

Tallian [16] reasoned that bearing fatigue life may be separated into two discrete phases:

1. The time between commencement of rotation and initiation of the crack below the surface, that is, L_a .
2. The time necessary for the crack to propagate to the surface, that is, L_b .

Hence, the fatigue life measured represents the sum of the two durations:

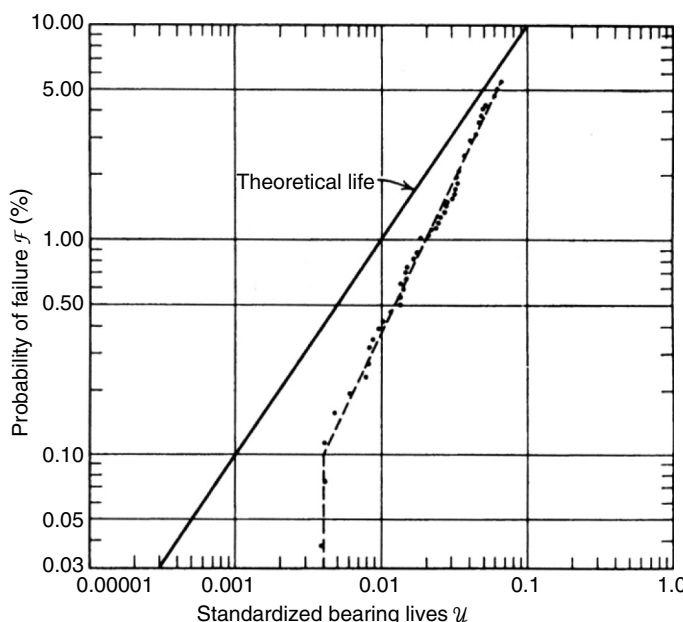


FIGURE 11.30 Life distribution in the early failure region. (From Tallian, T., Weibull distribution of rolling contact fatigue life and deviations there from, *ASLE Trans.*, 5(1), April 1962.)

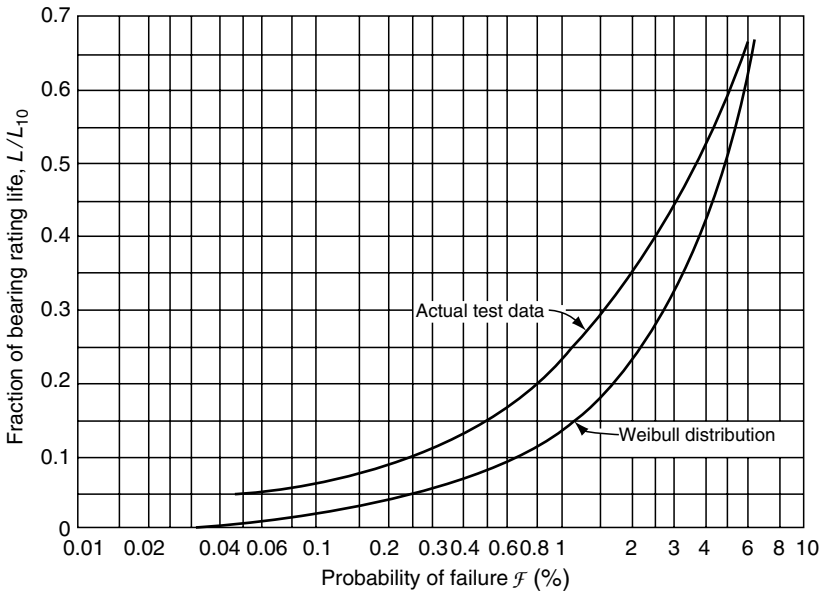


FIGURE 11.31 Fraction L_{10} life vs. probability of failure.

$$L = L_a + L_b \quad (11.206)$$

L_b may be called an excess life since L_a is the fatigue life predicted by Weibull theory. If a crack is initiated when rotation has just commenced, L_b is very much greater than L_a and L is not a valid Weibull life measurement. If a crack is initiated a considerable time after rotation has started, then L_b is insignificant compared with L_a and L is a reasonably accurate Weibull life estimator. Thus, the deviation of early failures from the Weibull distribution was explained. In equation format, one may determine the fatigue life at reliabilities other than $S = 0.9$ as follows:

$$\frac{L}{L_{10}} = \left(\frac{\ln \frac{1}{S} + \gamma_e}{\ln \frac{1}{0.9}} \right)^{1/e} \quad (11.207)$$

where γ_e is the standardized excess life. Tallian [16] gives the schedule for γ_e presented in Table 11.12.

Increase in reliability may be assigned to a given bearing by reduction in its basic dynamic capacity. Harris [25] developed Figure 11.32, which determines the reduction in basic dynamic capacity required to achieve a reliability higher than 90%.

See Example 11.11 and Example 11.12.

TABLE 11.12
Excess Standardized Life γ_e

Probability of Survival (%)	Standardized Theoretical Life	Standardized Life
$S \geq 99.9$	$\gamma \leq 0.001$	$\gamma + \gamma_e = 0.004$
$99.9 \geq S \geq 95$	$0.001 < \gamma < 0.05$	$\ln(\gamma + \gamma_e) = 0.690 \ln(0.328 \gamma)$
$95 > S > 40$	$0.05 < \gamma < 0.6$	$\gamma_e = 0.013$

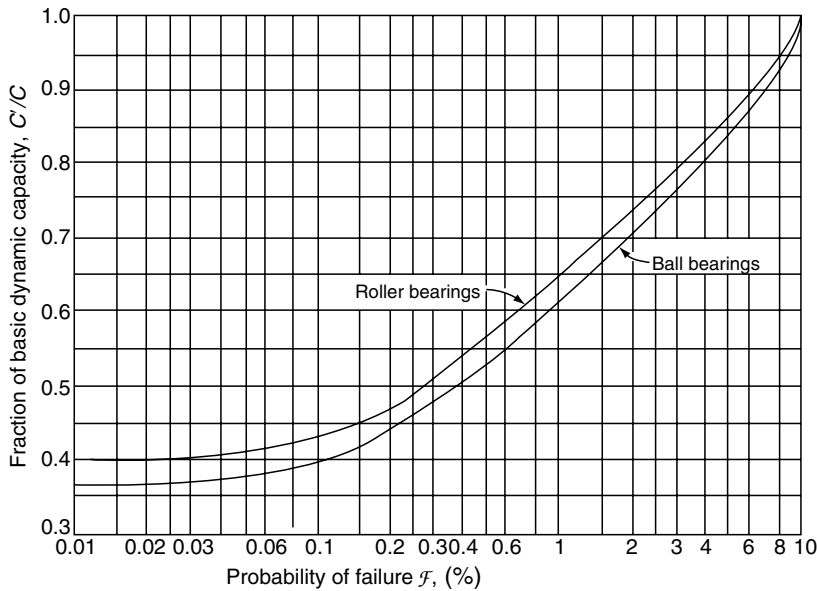


FIGURE 11.32 Reduction in basic dynamic capacity required for increased reliability. (From Harris, T., Predicting bearing reliability, *Mach. Des.*, 129–132, January 3, 1963.)

11.11 CLOSURE

The rolling bearing industry was among the first to use fatigue life as a design criterion. As a result, the space-age term “reliability,” synonymous with “probability of survival,” is familiar to rolling bearing manufacturers and users. The concepts of L_{10} or rating life and L_{50} or median life are used as measures of bearing performance. By means of national (ANSI, DIN, JIS, etc.) and international (ISO) load rating standards, the rolling bearing industry established relatively uncomplicated methods to evaluate rating life. These standards can be applied to compare the adequacy of diverse bearing types from different manufacturers for use in most engineering applications.

The load rating standards may be used to evaluate performance of bearings in the majority of bearing applications. These applications involve the following parameters:

- Relatively slow operating speeds such that ball or roller inertial forces are not significant compared with applied forces.
- Bearing inner ring accurately mounted on a rigid shaft; bearing outer ring accurately mounted in a rigid housing.
- Sufficient lubrication to prevent overheating.
- Bearings subjected to simple radial or axial loading or a proper combination of these.

Also, the standards pertain to bearings manufactured from 52100 steel through-hardened to a minimum Rockwell C 58. Notwithstanding this criterion, the load and life rating standards are routinely applied to bearings manufactured from case-hardened steels.

This chapter concludes the material that may be considered as expanded bearing catalog data and information. It provides a basis for understanding the material presented in bearing catalogs and also for the material that follows in the remainder of the text. That information is concerned with bearing applications that do not lie within the simple application conditions. For example:

- Bearing operating speeds are such that ball or roller centrifugal forces and gyroscopic moments influence bearing internal load distribution.
- Friction forces and moments influence rolling element loading and component endurance.
- Internal temperatures and their effects on bearing internal load distribution, friction, lubricant endurance, and bearing endurance must be considered.
- Misalignment of bearing rings influences bearing endurance.
- Bearing rings are mounted in flexible supports that influence bearing internal load distribution.
- Bearing rings and rolling elements are manufactured from materials other than 52100 steel. For such materials, increased endurance strength and residual stresses resulting from heat processing and material finishing can significantly affect bearing endurance.

The means to conduct the analyses required to evaluate bearing performance in applications involving such extraordinary conditions are discussed in the Second Volume of this handbook.

REFERENCES

1. Lundberg, G. and Palmgren, A., Dynamic capacity of rolling bearings, *Acta Polytech. Mech. Eng.*, Ser. 1, No. 3, 7, Royal Swedish Acad. Eng., 1947.
2. Van den Sanden, J., Martensite morphology of low alloy commercial steels, *Pract. Metallogr.*, 17, 238–248, 1980.
3. Rescalvo, J., Fracture and fatigue crack growth in 52100, M50 and 18-4-1 bearing steels, Ph.D. thesis, Department of Materials Science and Engineering, Massachusetts Institute of Technology, June 1979.
4. Littmann, W. and Widner, R., Propagation of contact fatigue from surface and subsurface origins, *J. Basic Eng.*, 88, 624–636, 1966.
5. Uhrus, L., *Clean Steel*, Iron and Steel Institute, London, 104–109, 1963.
6. Martin, T., Borgese, S., and Eberhardt, A., Microstructural alterations of rolling bearing steel undergoing cyclic stressing, ASME Preprint 65-WA/CF-4, Winter Annual Meeting, Chicago, November 1965.
7. Tallian, T., On competing failure modes in rolling contact, *ASLE Trans.*, 10, 418–439, 1967.
8. Voskamp, A., Material response to rolling contact loading, *ASME Trans., J. Tribol.*, 107, 359–366, 1985.
9. Swahn, H., Becker, P., and Vingsbo, O., Martensite decay during rolling contact fatigue in ball bearings, *Metallurgical Trans. A*, 7A, 1099–1110, August 1976.
10. Lund, T., *Jernkontorets Ann.*, 153, 337, 1969.
11. Becker, P., Microstructural changes around non-metallic inclusions caused by rolling-contact fatigue of ball bearing steels, *Metals Technol.*, 234–243, June 1981.
12. Nélias, D., Contribution a L'étude des Roulements, Dossier d'Habilitation a Diriger des Recherches, Laboratoire de Mécanique des Contacts, UMR-CNRS-INSA de Lyon No. 5514, December 16, 1999.
13. Hoel, P., *Introduction to Mathematical Statistics*, 2nd Ed., Wiley, New York, 1954.
14. Weibull, W., A statistical representation of fatigue failure in solids, *Acta Polytech. Mech. Eng.*, Ser. 1, No. 9, 49, Royal Swedish Acad. Eng., 1949.
15. Weibull, W., A statistical theory of the strength of materials, *Proceedings of the Royal Swedish Institute for Engineering Research*, No. 151, Stockholm, 1939.
16. Tallian, T., Weibull distribution of rolling contact fatigue life and deviations there from, *ASLE Trans.*, 5(1), April 1962.
17. Lieblein, J., A new method of analyzing extreme-value data, Technical Note 3053, NACA, January 1954.
18. Lundberg, G. and Palmgren, A., Dynamic capacity of roller bearings, *Acta Polytech. Mech. Eng.*, Ser. 2, No. 4, 96, Royal Swedish Acad. Eng., 1952.

19. Palmgren, A., *Ball and Roller Bearing Engineering*, 3rd Ed., Burbank, Philadelphia, 1959.
20. Lieblein, J. and Zelen, M., Statistical investigation of fatigue life of ball bearings, *National Bureau of Standards*, Report No. 3996, March 28, 1955.
21. American National Standards Institute, American National Standard (ANSI/ABMA) Std. 9-1990, Load ratings and fatigue life for ball bearings, July 17, 1990.
22. American National Standards Institute, American National Standard (ANSI/ABMA) Std. 11-1990, Load ratings and fatigue life for roller bearings, July 17, 1990.
23. International Organization for Standards, International Standard ISO 281Amendment 2, Rolling bearings-dynamic load ratings and rating life, February 15, 2000.
24. Houpert, L., Bearing life calculation in oscillatory applications, *Tribol. Trans.*, 1(42), 136–143, 1999.
25. Harris, T., Predicting bearing reliability, *Mach. Des.*, 129–132, January 3, 1963.

12 Lubricants and Lubrication Techniques

12.1 GENERAL

The primary function of a lubricant is to prevent wear of the rolling and sliding contacts of a bearing through hydrodynamic, elastohydrodynamic (EHL), or boundary lubrication; however, there are many other vital functions, such as:

- Minimizing the frictional power loss of the bearing
- Acting as a heat transfer medium to remove heat from the bearing, or redistributing the heat energy within the bearing to minimize differential thermal expansions
- Protecting the precision surfaces of the bearing components from corrosion
- Removing wear debris from the roller contact paths
- Minimizing the amount of extraneous dirt entering the roller contact paths
- Providing a damping medium for cage dynamic motions

No single lubricant or class of lubricants can satisfy all the requirements for bearing operating conditions, from cryogenic to ultrahigh temperatures, from very slow to ultrahigh speeds, and from benign to highly reactive operating environments. As for most engineering tasks, a compromise is generally exercised between performance and economic constraints. The economic constraints involve not only the cost of the lubricant and the method of application, but also its impact on the life cycle cost of the mechanical system.

Cost and performance decisions are frequently complicated because many other components of a mechanical system also need lubrication or cooling, and they might dominate the selection process. For example, an automotive gearbox typically comprises gears, a ring synchronizer, rolling bearings of several types operating in very different load and speed regimes, plain bearings, clutches, and splines.

12.2 TYPES OF LUBRICANTS

12.2.1 SELECTION OF LUBRICANT TYPE

The selection of a lubricant type for a bearing application is based on several considerations, for example:

- Operating temperature
- Operating environment
- Mechanical properties
- Chemical properties
- Transport properties

- Retention in the bearing
- Accessibility for periodic maintenance
- Cost

To provide the necessary performance for a given rolling bearing application, lubricants may be provided in liquid, grease, or solid form.

12.2.2 LIQUID LUBRICANTS

Liquid lubricants are most commonly mineral oils, that is, fluids produced from petroleum-based stocks. Chemically, they have a wide range of molecular constituents and molecular chain lengths, giving rise to a large variation in flow properties and chemical performances. They are generally enhanced with additives to improve both mechanical and chemical performances. Generally, mineral oils provide good performance characteristics at relatively inexpensive costs.

Synthetic hydrocarbon fluids are manufactured from petroleum-based materials with both narrowly limited and specifically chosen molecular compounds to provide favorable properties for lubrication purposes. Synthetic fluids with unique properties can, however, be manufactured from nonpetroleum-based stocks. These include polyglycols, phosphate esters, dibasic acid esters, silicone fluids, silicate esters, and fluorinated ethers.

12.2.3 GREASES

A grease consists of an oil that is physically retained in a thickener by capillary action. The thickener is generally a soap or another material composed of very long, twisted or contorted molecules that both physically interlock and have a large surface area to retain the oil. The grease behaves as a soft solid, capable of bleeding oil at controlled rates to meet the consumption demands of the bearing.

12.2.4 POLYMERIC LUBRICANTS

Polymeric lubricants are similar to greases; however, the oil-retaining matrix in the former is a sponge that holds its physical shape and location in the bearing. The oil content can be made higher than in a grease, and a greater quantity can be installed in the free space within the bearing envelope. The greater oil quantity tends to provide longer bearing life before the oil is depleted by oxidation, evaporation, or leakage.

12.2.5 SOLID LUBRICANTS

Solid lubricants are used when extreme operating environments such as very high temperature, very high pressure, or hard vacuum preclude the use of liquid lubricants or greases. As compared with the hydrodynamic fluid film forming capability of liquid lubricants and greases, solid lubricants perform as boundary lubricants, consisting of thin layers of lower shear strength than the bearing materials. The use of solid lubricants results in higher bearing friction, higher bearing temperatures, and wear if they are not replenished appropriately.

12.3 LIQUID LUBRICANTS

12.3.1 TYPES OF LIQUID LUBRICANTS

12.3.1.1 Mineral Oil

This is a generic term referring to fluids produced from petroleum. Chemically, these fluids consist of paraffinic, naphthenic, and aromatic groups combined into many molecules.

Elementally, the composition of petroleum oils is quite constant: 83–87% carbon, 11–14% hydrogen; the remainder are trace quantities of sulfur, nitrogen, and oxygen. The molecular makeup of the fluid is very complex and depends on its source. The crude petroleum may consist of gasoline and light solvents, or it may consist of heavy asphalts. Distillation, refining, and blending techniques allow the production of a wide range of oil types from a given crude stock; however, some crude stocks are more desirable for lubricant formulation.

Mineral lubricants are usually paraffinic oils and are rated using the American Petroleum Institute's (API) three-group designations. The designations are based on the (1) ability of the manufacturing process to create or separate the desired lubricant molecule from the crude stock with minimal amounts of other molecules and (2) the resulting lubricant's viscosity index (VI). As the group designation increases from I to III, the quality of the lubricant increases, or the amount of nondesired molecules remaining after processing decreases. This increases the VI as lower or higher molecular weight paraffinic oils are not present, causing larger variations with temperature. API Group I and Group II oils have VIs in the range of 80–119, and Group III lubricants have VIs greater than 120.

API Group III lubricants, though petroleum-based oils, are processed using molecular synthesis, and are often grouped with synthetic hydrocarbons. Their typical VI ranges are similar to those of synthetic hydrocarbons (polyalphaolefin or API Group IV).

12.3.1.2 Synthetic Oils

There are many different synthetic lubricants tailored to specific types of applications. Because they are synthesized products, the particular compounds present can be both narrowly limited and specifically formulated. This allows the production of a lubricant with the most favorable properties for the lubrication purposes; however, the process is typically more expensive than the processing of mineral crude stocks.

The most common types of synthetic oils are synthetic hydrocarbons, which include poly-alphaolefins; however, there are several other types of synthesized lubricants such as esters, silicones, phenyl ether, and perfluoroalkyl ether. [Table 12.1](#) lists a few synthetic lubricants with typical properties and common applications. Nonhydrocarbon synthetic lubricants generally have advantages in very particular operating conditions with significant tradeoffs. For instance, the high-temperature lubricants developed for military applications usually have much shorter useful lives than their commercial, lower-temperature counterparts. Also, phosphate esters are fire resistant; however, they have very low VI and hydrolytic stability.

12.3.1.3 Environmentally Acceptable Oils

Concerns for the environment have led to the development of more environmentally acceptable lubricants. Biodegradability and low ecotoxicity are required for these lubricants, and many countries now have specific requirements for branding lubricants as environmentally friendly. Initially, two-cycle engine marine and forest applications were targeted for use of biodegradable lubricants. This use has now been extended to include hydraulic fluids, engine oils in general, and greases.

Biodegradability and low ecotoxicity of a lubricant depend on the base stock. Biodegradable fluids include vegetable oils, synthetic esters, polyalkylene glycols, and some polyalphaolefins. The susceptibility of a substance to be biodegraded by microorganisms is a measure of its biodegradability. Biodegradability can be partial, resulting in the loss of some specific process such as splitting an ester linkage (primary biodegradation), or complete, resulting in the total breakdown of the substance into simple compounds such as carbon dioxide and water (ultimate biodegradation). There is currently no standard method accepted for assessing an environmentally acceptable lubricant, and several methods are in use worldwide.

TABLE 12.1
Typical Properties of Lubricant Base Stocks^a

	Density (g/cm ³)	Viscosity (40°C cSt)	Viscosity Index	Flash Point (°C)	Pour Point (°C)	Oxidation			Thermal Stability	Application Range
						Volatility	Resistance	Lubricity		
<i>Mineral Oils</i>										
Paraffinic	0.881	95	100	210	-7	5	5	5	5	Standard lubricants either as oil or grease base
Naphthenic	0.894	70	65	180	-18	5	5	5	5	
Mixed based	0.884	80	99	218	12	5	5	5	5	
High VI	0.831	33	242	127	-40	5	5	5	5	
<i>Synthetic hydrocarbons</i>										
Polyalphaolefin	0.853	32	135	227	-54	4	4	5	4	
<i>Esters</i>										
Dibasic	0.945	14	152	232	<-60	3-5	3-7	3-6	4-7	Jet turbine lubricants, hydraulic fluids, heat transfer products. Used as bases
Polyol	0.971	60	132	275	-54	3	5	5	5	for low-volatility, low-viscosity grease.
Tricresyl phosphate	1.160	37	-65	235	-23	3	3	3	7	Phosphate esters fire resistant
Polyglycol ether	0.984	36	150	210	-46	3-5	7	4	5	
Silicate	0.909	6.5	150	188	<-60	3	7	6	4	
<i>Silicones</i>										
Dimethyl	0.968	100	400	300	<-60	1	1	7	1-5	High-temperature/low-volatility applications either as oil or grease base.
Phenyl methyl	0.990	75	350	260	<-60	1	1	7	1-5	Lightly loaded bearings. Excellent thermal stability
Chlorophenyl	1.050	55	160	288	<-60	1	1	7	1-5	
Perfluoromethyl	1.230	44	158	>300	<-60	1	1	7	1-5	
<i>Phenyl ether</i>										
Low viscosity	1.180	75	-20	263	9.5	1	1-3	5-7	1	
High viscosity	1.210	355	-74	343	4.4	1	1-3	5-7	1	
Perfluoroalkyl ether	1.910	320	138	-	-32	3-7	1	5-7	1-3	Extreme temperature fluid. Used in very low-volatility applications

^aFor volatility, oxidation resistance, lubricity, and thermal stability, a rating of 5 is taken as characteristic of highly refined mineral oil. Numbers <5 reflect superior performance; numbers >5 reflect inferior performance to mineral oil with respect to lubrication properties.

12.3.2 BASE STOCK LUBRICANT

Typical liquid lubricants are composed of approximately 90–99% base stock lubricant; the remainder are additives. The selection of the base stock lubricant is thus critical, as it comprises the single largest portion of the lubricant. Selection is usually intended to optimize the properties of the lubricant for the bearing operating conditions.

12.3.3 PROPERTIES OF BASE LIQUID LUBRICANTS

12.3.3.1 Viscosity

The viscosity of the lubricant is a measure of its resistance to flow when operated on by a shear stress. It is typically measured kinematically according to the American Society for Testing and Materials (ASTM) specification D-455. The viscosity is probably the single most important factor for the selection of the lubricant as it is critical to the formation of a sufficient lubricating film. The viscosity increases exponentially with pressure as shown in Figure 12.1; however, it decreases exponentially with temperature as shown in Figure 12.2. As such, it is important to consider the entire range of operating conditions for the system. As calculation of the lubricant film magnitude is covered extensively in Chapter 4 of the Second Volume of this handbook, it will not be discussed in detail in this chapter. Figure 12.3, from [1], does, however, allow for a quick estimation of the minimum viscosity to form the required lubricant film for operation of good quality rolling bearings.

12.3.3.2 Viscosity Index

The VI is an arbitrary number indicating the effect of temperature on the kinematic viscosity for a fluid. The higher the VI is for an oil, the smaller the viscosity change will be with

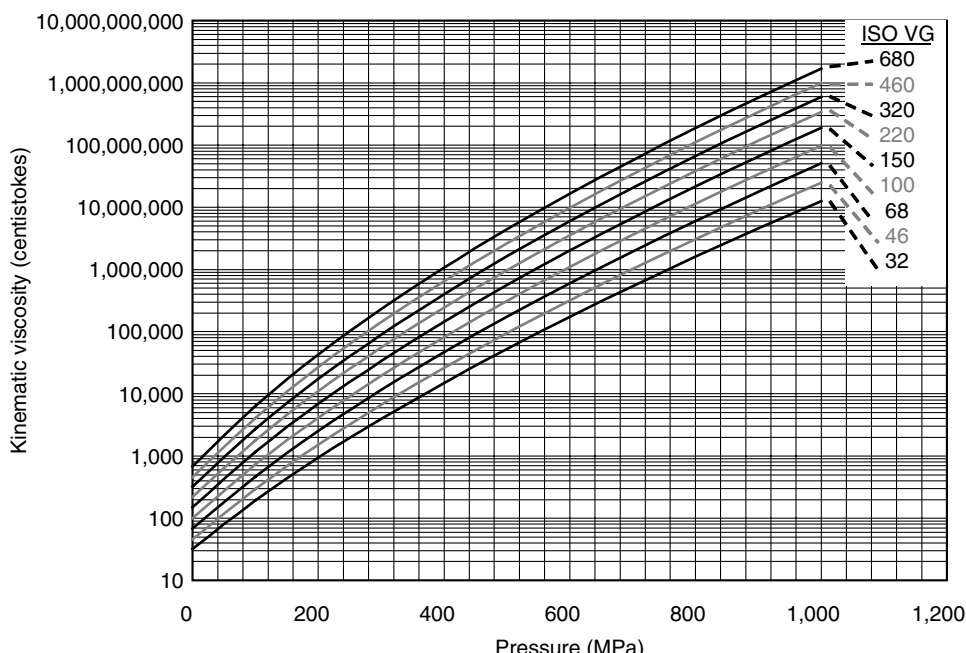


FIGURE 12.1 Variation of lubricant viscosity with pressure for various mineral oils.

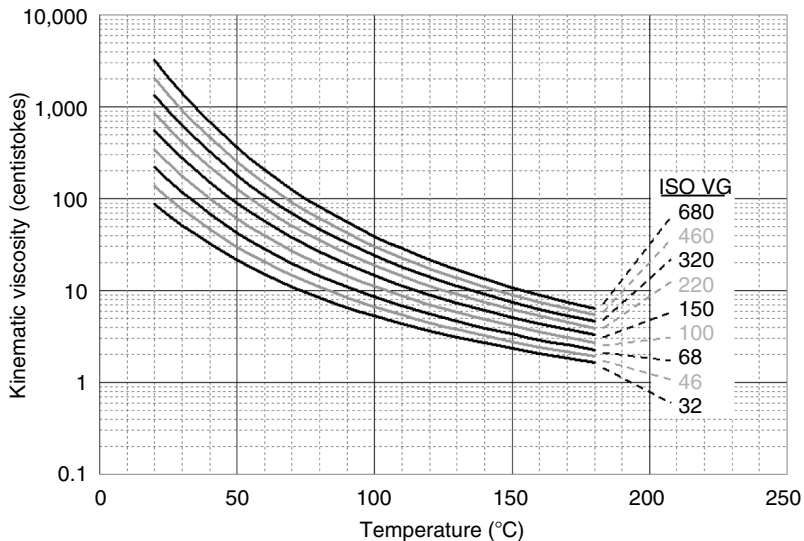


FIGURE 12.2 Variation of lubricant viscosity with temperature for various mineral oils (at atmospheric pressure).

temperature. The method for calculating VI from measured viscosities is described in ASTM specification D-567.

12.3.3.3 Pour Point

The pour point relates to the lowest temperature at which the lubricant will pour or flow. The pour point is measured under the conditions in ASTM specification D-97. The pour point together with measured low-temperature viscosities gives an indication of the low-temperature serviceability of an oil.

12.3.3.4 Flash Point

According to ASTM specification D-566, the flash point is the lowest temperature at which the lubricant will give off inflammable vapor by evaporation.

12.3.3.5 Evaporation Loss

The method for determining evaporative loss is described in ASTM specification D-972. The sample in an evaporation cell is placed in a bath maintained at the desired test temperature (usually 99–149°C [210–300°F]). Heated air is passed over the cell surface for 22 h. The evaporation loss is calculated from the sample weight loss.

Table 12.1 is a listing of typical properties for various lubricant base stocks.

12.3.4 LUBRICANT ADDITIVE

12.3.4.1 Purpose

While the base stock of a liquid lubricant provides the bulk properties such as viscosity and density, which directly influence its hydrodynamic performance, chemical additives are frequently employed to increase the longevity of operation of the lubricant and the bearing. This is especially true in applications involving extremes of temperature, pressure, and environment.

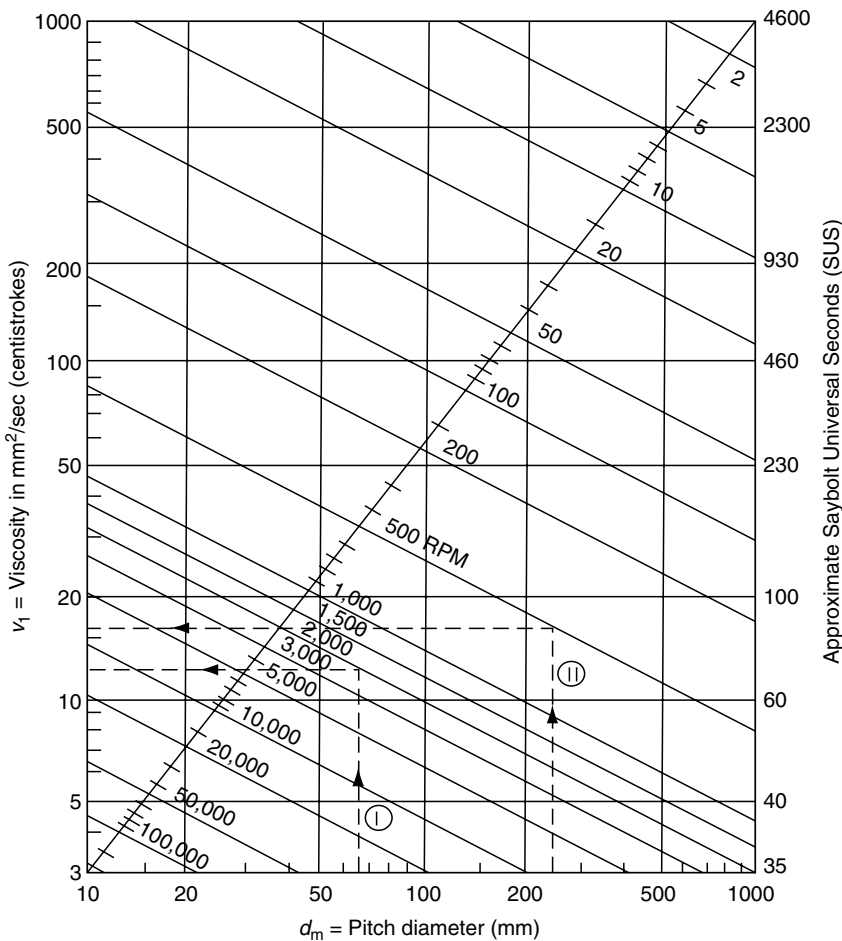


FIGURE 12.3 Minimum required lubricant kinematic viscosity (ν_1) vs. bearing pitch diameter (d_m) and speed. (From SKF, *General Catalog 4000 US*, 2nd Ed., 1997–2001. With permission.)

12.3.4.2 VI Improvers

VI properties are usually related to the type of base oil selected; however, polymeric additives can be used to increase the VI. These long chain polymers are commonly used with multigrade mineral, engine oils (e.g. SAE 10W-30) to obtain sufficient VI for high- and low-temperature operations. However, it has been shown that the polymers only enhance VI under minimal shear stresses and at high shear stresses, similar to those in rolling bearings, they elongate and do not restrict the flow to increase viscosity. Also, under high shear conditions, the polymers break down faster than the lubricant, thus acting as the limiting factor in the lubricant lifespan.

12.3.4.3 Extreme Pressure/Antiwear

To increase the boundary lubrication capabilities of the lubricant to lower friction and prevent scuffing and scoring wear, it is common to add extreme pressure/antiwear (EP/AW) compounds to the lubricant. EP additives are generally made from sulfur or phosphorus, and they chemically interact with the surface to create a lubricous sacrificial layer on the surface. Conversely, AW additives are long chain polar molecules of fatty oils, acids, or esters, which

create lubricious adsorbed layers on the surface. These additives are almost universally beneficial for industrial gears; however, they can be beneficial or detrimental to the bearings operating among them [2]. The effect on bearing fatigue appears to be application dependent based on chemical makeup, and cannot be quantified analytically at this time. Therefore, testing must be accomplished to understand this effect if necessary.

12.3.4.4 Other Additives

Listed above are the two most important lubricant additives for rolling bearings; however, there are many other additives of importance to the overall system. A few of the other main additive groups are pour point depressants, antifoaming agents, oxidation inhibitors, corrosion inhibitors, detergents, dispersants, and demulsifiers. The functions of these additives are somewhat intuitive and will not be discussed further.

12.4 GREASE

12.4.1 How GREASE LUBRICATION FUNCTIONS

Grease provides lubricant by bleeding, that is, when the moving parts of a bearing come into contact with grease, a small quantity of oil contained within the grease will adhere to the bearing surfaces. The oil is gradually degraded by oxidation or lost by evaporation, centrifugal force, and so on; in time the oil in the grease near the bearing will be depleted.

Differing viewpoints exist concerning the exact mechanism of grease operation. Until recently, grease was considered as merely a sponge holding oil near the working contacts. As these contacts consumed oil by way of evaporation and oxidation, a replenishment flow maintained equilibrium as long as the supply lasted. Research using optical EHL and micro-flow lubrication assessment techniques has shown that the thickener phase plays rather complex roles in both the development of a separating film between the surfaces and in the modulation of the replenishing flows. How the thickener controls oil outflow, reabsorbs fluid thrown from the contacts, and acts as a trap for debris are little understood at this time. The mechanism is not steady state; rather, it is characterized by a series of identifiable events.

12.4.2 ADVANTAGES OF GREASE LUBRICATION

As compared with lubrication with liquids, grease lubrication offers the following advantages:

- Maintenance is reduced because there is no oil level to maintain. New lubricant needs to be added less frequently.
- Lubricant in proper quantity is confined to the housing. Design of enclosures can therefore be simplified.
- Freedom from lubricant leakage can be accomplished, avoiding contamination of products in food, textile, and chemical industries.
- Efficiency of labyrinth “seals” is improved, and better sealing is offered for the bearing in general.
- Bearing friction torque and temperature rise are generally more favorable.

12.4.3 TYPES OF GREASES

12.4.3.1 General

Thickener composition is critical to grease performance, particularly, with respect to temperature capability, water-resistance, and oil-bleeding characteristics. Thickeners are divided

into two broad classes: soaps and nonsoaps. Soaps refer to a compound of a fatty acid and a metal. Common metals for soaps include aluminum, barium, calcium, lithium, and sodium. The great majority of commercial greases are soap type, with lithium as the most widely used.

12.4.3.2 Lithium Soap Greases

Lithium soaps are divided into two types: 12-hydroxystearate and complex. The latter material is derived from organic acid components and permits higher-temperature performance. The upper operating temperature limit of the usual lithium-based grease is approximately 110°C (230°F). For a lithium complex-based grease, the upper temperature limit is extended to 140°C (284°F). Conversely, the lower operating temperature limits are –30°C (–22°F) and –20°C (–4°F), respectively. High-quality lithium soap greases of both types have excellent service histories in rolling bearings and have been used extensively in sealed- and greased-for-life applications. Lithium-based products have found acceptance in multipurpose greases and have no serious deficiencies except in severe temperature or loading extremes.

12.4.3.3 Calcium Soap Greases

The oldest of the metallic soap types, calcium-based grease, has undergone several important technical changes. In the first formulations, substantial water (0.5–1.5%) was needed to stabilize the finished product. Loss of water destroys grease consistency; as such, the upper temperature operating limiting of the grease is only 60°C (140°F). (Correspondingly, the lower operating temperature is only –10°C [14°F].) Regardless of temperature, evaporation of water occurs, requiring frequent relubrication of the bearing. Alternatively, the ability of the grease to entrain water is of some advantage; such greases have been widely used in food-processing plants, water pumps, and wet applications in general. Today, this type of formulation has been made obsolete by newer products with better temperature performance.

The latest development in calcium soap greases is the calcium complex-based grease. Herein, the soap is modified by adding an acetate, and a substantially different product results having upper and lower temperature limits of 130°C (266°F) and –20°C (–4°F), respectively. The performance of these greases in rolling bearings is sometimes less than optimal. Although high-temperature and EP characteristics have been exhibited, there are some problems with excessive grease thickening in use, causing an eventual loss of lubrication to the bearing.

12.4.3.4 Sodium Soap Greases

Sodium soap greases were developed to provide an increase in the limited temperature capability of early calcium soap greases. An inherent problem with this thickener is poor water-washout resistance; however, small amounts of water are emulsified into the grease pack, which helps to protect the metal surface from rusting. The upper operating temperature limit for such greases is only 80°C (176°F); the lower operating temperature limit is –30°C (–22°F). Sodium soap greases have been superseded by more water-resistant products in applications such as electric motors and front wheel bearings. Sodium complex-base greases have subsequently been developed having upper and lower operating temperature limits of 140°C (284°F) and –20°C (–4°F), respectively.

12.4.3.5 Aluminum Complex Greases

Aluminum stearate greases are seldom used in rolling bearings, but aluminum complex-base greases are used more often. Greases formed from the complex soap perform favorably in water-resistance tests; however, the upper operating temperature limit is somewhat low at 110°C (230°F) compared with other types of high-quality greases. The lower operating

temperature limit is satisfactory at -30°C (-22°F). These greases find use in rolling mills and food-processing plants.

12.4.3.6 Nonsoap-Base Greases

Organic thickeners, including ureas, amides, and dyes, are used to provide higher-temperature capability than is available with metallic soap thickeners. Improved oxidation stability over metallic soaps occurs because these materials do not catalyze base oil oxidation. Dropping points for greases of these types are generally above 260°C (500°F) with generally good low-temperature properties (see later). The most popular of these thickeners is polyurea, which is extensively used in high-temperature ball bearing applications for electric motors. The recommended upper operating temperature limit for polyurea-base grease is 140°C (284°F); the lower temperature limit is -30°C (-22°F).

12.4.3.7 Inorganic Thickeners for Grease

These include various clays such as bentonite. Greases made from clay base do not have a melting point, so the service temperature depends on the oxidation and thermal resistance of the base oil. These greases find use in special military and aerospace applications requiring very high-temperature performance for short intervals, for example, greater than 170°C (338°F). On the other hand, the recommended upper temperature limit for continuous operation is only 130°C (266°F); the lower temperature limit is -30°C (-22°F).

12.4.3.8 Combining Greases

Mixing greases of differing thickeners and base oils can produce an incompatibility and loss of lubrication with eventual bearing failure. When differing thickeners are mixed, for example, soap and nonsoap or different soap types, substantial changes in consistency can result, leading to the grease too stiff to lubricate properly or too fluid to remain in the bearing cavity. Mixing greases of differing base oils, for example, petroleum and silicone oils, can produce a two-component fluid phase that will not provide a continuous lubrication medium. Early failures can be expected under these conditions. The best practice to follow is to not mix lubricants, but rather purge bearing cavities and supply lines with a new lubricant until the previous grease cannot be detected before starting bearing operation.

12.4.4 GREASE PROPERTIES

12.4.4.1 Properties of Retained Oil

The oil contained within the grease has all of the properties defined for liquid lubricants, particularly those defined for the base stock lubricant. Additionally, greases have other properties as listed herein.

12.4.4.2 Dropping Point

Dropping point is the temperature at which a grease becomes a liquid; it is sometimes referred to as the melting point. The pertinent test is performed according to ASTM specification D-566.

12.4.4.3 Low-Temperature Torque

Low-temperature torque is the extent to which a low-temperature grease retards the rotation of a slow-speed ball bearing when subject to subzero temperatures.

12.4.4.4 Oil Separation

This is the tendency of the oil to separate from the thickener during storage in both conventional and crated containers. The test for separation is described in ASTM specification D-1742. In the test, the sample is determined by supporting on a 74- μm sieve subjected to 0.0017 MPa (0.25 psi) air pressure for 24 h at 25°C (77°F). Any oil seepage drains into a beaker and is weighed.

12.4.4.5 Penetration

The penetration is determined at 25°C (77°F) by releasing a cone assembly from a penetrometer and allowing the cone to drop into the grease for 5 sec. The greater the penetration, the softer is the grease. Worked penetrations are determined immediately after working the sample for 60 strokes in a standard grease worker. Prolonged penetrations are performed after 100,000 strokes in a standard grease worker. A common grease characteristic is described by the National Lubricating Grease Institute (NLGI) grade assigned, as shown in Table 12.2. Most rolling bearing applications employ a grease that has NLGI grade 1, 2, or 3.

12.5 SOLID LUBRICANTS

Solid lubricants can survive temperatures well above the decomposition temperatures of oils. They can also be used in chemically reactive environments. The disadvantages of solid lubricants are:

- High coefficient of friction
- Inability to act as a coolant
- Finite wear life
- Difficult replenishment
- Little damping control for vibration instabilities of rolling elements and cages

Many common solid lubricants such as graphite and molybdenum disulfide (MoS_2) are layered lattice compounds that shear easily along preferred planes of their structures. MoS_2 has weak van der Waals forces between sulfur bonds, giving the material a characteristic relatively low coefficient of friction. It oxidizes in air at approximately 399°C (750°F); the oxides can be abrasive.

TABLE 12.2
NLGI Penetration Grades

NLGI Grades	Penetration (60 Strokes)
000	445–475
00	400–430
0	355–385
1	310–340
2	265–295
3	220–250
4	175–205
5	130–160
6	85–115

The low friction associated with graphite depends on intercalation with gases, liquids, or other substances. For example, the presence of absorbed water in graphite imparts good lubricating qualities. Thus, pure graphite has deficiencies as a lubricant except when used in an environment containing contaminants such as gases and water vapor. With proper additives, graphite can be effective to 649°C (1200°F).

Tungsten disulfide (WS_2) is similar to MoS_2 in that it is a type of layered lattice solid lubricant. It does not need absorbable vapors to develop low-shear-strength characteristics.

Other solid lubricating materials are solid at bulk temperatures of the bearing, but melt from frictional heating at points of local contact, giving rise to a low-shear-strength film. This melting may be very localized and of very short duration. Soft oxides such as lead monoxide (PbO) are relatively nonabrasive and have relatively low friction coefficients, especially at high temperatures where their shear strengths are reduced. At these temperatures, deformation occurs by plastic flow rather than by brittle fracture. Metal oxides can form a glaze on the surface. This glaze can decrease or increase friction, depending on the viscosity of the glaze within the contact region. Stable fluorides such as lithium fluoride (LiF_2), calcium fluoride (CaF_2), and barium fluoride (BaF_2) also lubricate well at high temperatures, and over a broader range than lead oxides.

12.6 LUBRICANT DELIVERY SYSTEMS

12.6.1 OIL BATH/SPLASH OIL

Decisions in connection with the selection of lubricants must parallel decisions in connection with the supply of the lubricant to the bearing for maintaining conditions that will prevent rapid deterioration of the lubricant and bearing. An oil sump applicable to horizontal, inclined, and vertical axis arrangements provides a small pool of oil contained in contact with the bearing, as shown in Figure 12.4.

The liquid level in the stationary condition is arranged to just reach the lower portion of the rolling elements. Experience has shown that higher levels lead to excessive lubricant churning and resultant excessive temperature. This churning in turn can cause premature lubricant oxidation and subsequent bearing failure. Lower liquid levels threaten oil starvation at operating speeds where windage can redistribute the oil and cut off communication with the working surfaces. Maintenance of proper oil level is thus very important and the provision of a sight glass is recommended.

Oil bath systems are used at low-to-moderate speeds where grease is ruled out by short relubrication intervals, hot environments, or where purging of grease could cause problems. Heat dissipation is somewhat better than for a greased bearing due to fluid circulation,

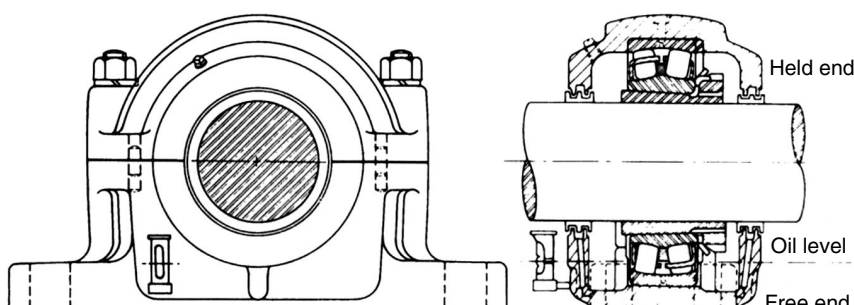


FIGURE 12.4 Pillow block with oil sump.

offering improved performance under conditions of heavy load where contact friction losses are greater than the lubricant churning losses. This method is often used when conditions warrant a specially formulated oil, not available in a grease. A cooling coil is sometimes used to extend the applicable temperature range of the oil bath. This usually takes the form of a water-circulating loop or, in some applications, the fitting of one or more heat pipes.

Wick-feed and oil-ring methods of raising oil from a sump to feed the bearing are not generally used with rolling bearings, but occasionally, shaft motion is used to drive a viscous pump for oil elevation, thus reducing the sensitivity of the system to oil level. A disk dipping into the sump drags oil up a narrow groove in the housing to a scraper blade or stop that deflects the oil to a drilled passage leading to the bearing. A major limitation of all sump systems is the lack of filtration or debris entrapment. Fitting a magnetic drain plug is advantageous for controlling ferrous particles, but otherwise sump systems are only suitable for clean conditions.

12.6.2 CIRCULATING OIL

As the speeds and loads on a bearing are increased, the need for deliberate means of cooling also increases. The simple use of a reservoir and a pump to supply a lubricant flow increases the heat dissipation capabilities significantly. Pressure feed permits the introduction of appropriate heat exchange arrangements. Not only can excess heat be removed, but also heat can be added to assure flow under extremely cold start-ups. Some systems are equipped with thermostatically controlled valves to keep the oil in an optimum viscosity range.

Another equally important point is that a circulating system can be fitted with a filtration system to remove the inevitable wear particles and extraneous debris. The mechanisms of debris-induced wear and the effects of even microscale indentations on the EHL process and the consequent reductions in fatigue life are discussed in the Second Volume of this handbook. Finer filtration is introduced to existing circulating systems with beneficial effects; however, increased pressure drops, space, weight, cost, and reliability have to be considered.

Circulating systems are used exclusively in critical high-performance applications, of which the main shaft support bearings of an aircraft gas turbine engine constitute prime examples. Subjected to heavy thrusts at near limiting speeds, the angular-contact ball bearings generate considerable frictional heat. This heat must be removed effectively together with leakage heat conducted to the bearing cavity from the surrounding engine components.

Heavily loaded bearings running at moderate speeds can be supplied with oil jets aimed at the rolling elements. At higher speeds, bearing windage deflects the jets, and lubrication and cooling become ineffective. This problem can be avoided by routing the oil to pickup scoops on the shaft with centrifugal force taking the oil via drilled passages to the inner ring, as shown in [Figure 12.5](#). Much of the flow passes through axial slots in the bore of the inner ring, removing heat as it does so. Only a small portion of the lubricant is metered to the rolling contacts through grooves between the inner-ring halves. Separate drilled holes may be used to supply the cage lands.

Adequate space should be provided on both sides of the bearing to facilitate lubricant drainage. Often, space is at a premium, so a system of baffles can be substituted to shield the lubricant from the windage, permitting it to be scavenged without severe churning. When the lubricant pump is activated at the same time as the main machinery, these baffles act as a dam and retain a small pool of lubricant in the bottom of the bearing to provide lubrication at start-up until the circulating flow becomes established.

Hydrocarbon-based fluids are satisfactory for circulating lubricant systems operating at temperatures of about 274°C (525°F). Hydrocarbon oxidation starts at room temperature; oxidation becomes significant at 175°C (347°F). Incipient thermal decomposition starts at

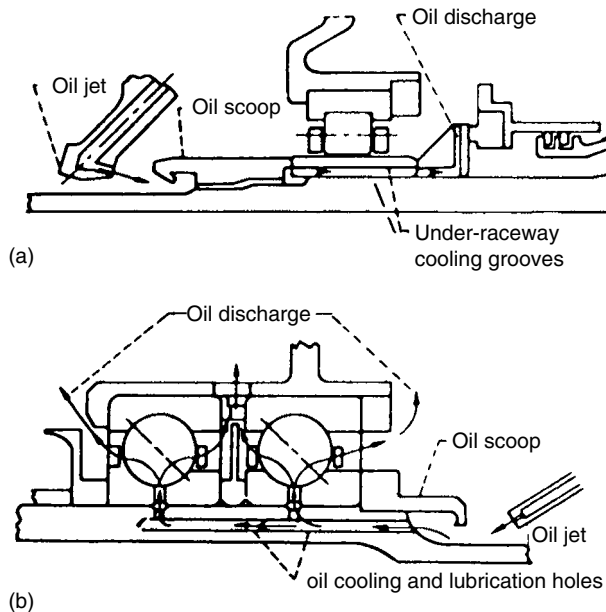


FIGURE 12.5 Under-raceway lubricating systems for mainshaft bearings in an aircraft gas turbine engine. (a) Cylindrical roller bearing. (b) Ball bearing.

about 300°C (572°F), and becomes a significant problem at about 449°C (840°F). Use of an inert cover gas to exclude oxygen can extend the working range to the latter limit. Beyond 449°C (840°F), fluorocarbon-based fluids are serviceable, but conspicuously lack the lubrication properties of the hydrocarbon-based fluids, and have superior oxidation stability. Up to this time, they have not been able to reach the temperature limits inherent in the tool steels used in aircraft gas turbine bearing applications.

12.6.3 AIR–OIL/OIL MIST

A separate class of lubrication arrangements can be used when minimal bearing friction is essential at moderate-to-high speeds and where loads are sufficiently low, so that heat removal is not a major concern. The lubricant is delivered to the bearing as a fine spray or an air-entrained mist in just sufficient quantities to maintain the necessary lubricant films in the contacts. Lubricant churning is virtually eliminated, and the volume of lubricant is so small that it can be discarded after a single passage through the bearing. Scavenging, cooling, and storage facilities are unnecessary. The one-time exposure to high shear stresses and temperatures relaxes the oxidation and the stability requirements of the fluid to some extent. The necessity for satisfactory air quality in the workplace requires that the exhaust droplets be reclassified and lubricant collected before discharge. It has also been shown that the spray does not need to be continuous. Trace injection of minute quantities of lubricant at intervals of up to 1 h is sufficient to keep precision spindle assemblies running at friction torque levels unobtainable by any other method.

12.6.4 GREASE

Grease may be considered as a lubricant delivery system, which is employed in the majority of rolling bearing applications. Grease lubrication is, however, generally restricted to relatively slower-speed applications owing to reduced capability for frictional heat dissipation as compared with that of oil. Hence, limiting speeds as shown in bearing catalogs are less for

grease lubrication than for oil lubrication. Moreover, care must be exercised when charging a bearing with grease. Too much grease will cause a rapid temperature rise and potential bearing seizure. Therefore, while the bearing free space may be filled with grease, the surrounding space in the housing in general should only be partially (30–50%) filled. For very slow-speed operations, to provide maximum corrosion protection, the housing may be completely filled.

If the service life of the grease used to lubricate the bearing is less than the expected bearing life, the bearing needs to be relubricated before lubricant deterioration. Relubrication intervals are dependent on bearing type, size, speed, operating temperature, grease type, and the ambient conditions associated with the application. As operating conditions become more severe, particularly in terms of frictional heat generation and operating temperature, the bearing must be relubricated more frequently. Some manufacturers specify relubrication intervals for their catalog bearings [1]. Such recommendations, given in the form of charts, are specific to the manufacturer's bearing internal designs and are generally based on good quality, lithium soap-based grease operating at temperatures not exceeding 70°C (158°F). Because relubrication intervals depend on specific internal design features of bearings such as rolling element proportions, working surface finishes, and cage configurations, they are different for each manufacturer even for basic bearing sizes. Therefore, no such charts are given in this text; they may be found in manufacturers' catalogs. It should be noted that often with smaller bearings, the relubrication intervals are longer than their fatigue life, and the bearings are often greased and sealed for the life of the bearing.

Even though relubrication charts are not included, a few universal factors relating operation to grease life are. For every 15°C (28°F) above 70°C (158°F), relubrication intervals must be halved. Bearings operating at temperatures lower than 70°C (158°F) tend to require relubrication less often; however, the lower operating temperature limit of the grease may not be exceeded (−30°C [−22°F] for a lithium-based grease). Also, bearings operating on vertical shafts need to be relubricated approximately twice as often as bearings on horizontal shafts. (Relubrication interval charts are generally based on the latter application.) If the relubrication interval is greater than 6 months, then all of the used grease should be purged from the bearing arrangement and replaced with new grease. If the relubrication interval is less than 6 months, periodic charges of grease can be applied based on the manufacturer's guidelines. This 6-month limit is considered a rough guideline. Finally, where there is a definite risk of contamination, the recommended relubrication intervals should be reduced. This also applies to applications in which the grease is required to seal against moisture.

12.6.5 POLYMERIC LUBRICANT

Similar to grease, a polymeric lubricant may be considered as a lubricant delivery system. Lubrication functions are provided only by the oil that has bled from the sponge. The ultrahigh molecular weight polyethylene pack retaining the lubricant is temperature limited to about 100°C (212°F), precluding its use in many rolling bearing applications. Some higher temperature materials, such as polymethylpentene, form excellent porous structures for lubricant retention, but are relatively expensive and suffer from excessive shrinkage.

Figure 12.6 shows bearings filled with a polymeric lubricant. Successful application has been achieved where a bearing must operate under severe acceleration conditions such as those occurring in planetary transmissions. The rotational speed of the bearing about its own axis may be moderate, but the centrifuging action due to the planetary motion is strong enough to throw conventional greases out of the bearing despite the presence of seals. When polymeric-lubricated bearings are substituted, life improvements of two orders of magnitude are not uncommon. Such situations occur in cable-making, tire-cord winding, and textile mill applications.



FIGURE 12.6 Polymeric-lubricated rolling bearings.

Another major market for polymeric lubricants is food processing. Food machinery must be cleaned frequently, often daily, using steam, caustic, or sulfamic acid solutions. These degreasing fluids tend to remove lubricant from the bearings, and it is standard practice to follow every cleaning procedure with a relubrication sequence. Polymeric lubricants have proven to be highly resistant to washout by such cleansing methods, hence the need for regreasing is reduced. The reservoir effect of polymeric lubricants has been exploited to a degree in bearings normally lubricated by a circulating oil system where there can be a delay in the oil reaching a critical location. The same effect has been used to provide a backup in case the oil supply system should fail.

The high occupancy ratio of the void space by the polymer minimizes the opportunity for the bearing to “breathe” as temperatures change. Corrosion due to internal moisture condensation is therefore reduced. As all ferrous surfaces are very close to the pack, conditions are optimum for using vapor phase corrosion-control additives in the formulations.

Despite these advantages, polymeric lubricants have some specific drawbacks. There tends to be considerable physical contact between the pack and the moving surfaces of the bearing. This leads to increased frictional torque, which produces more heat in the bearing. In conjunction with the thermal insulating properties of the polymer and its inherently limited temperature tolerance, the speed capability is reduced. Moreover, compared with grease, the solid polymer is relatively incapable of entrapping wear debris and dirt particles.

12.7 SEALS

12.7.1 FUNCTION OF SEALS

Once the general method of lubricating a bearing has been determined, the question of a suitable sealing method frequently needs to be addressed. A seal has two basic tasks: keeping

the lubricant in and keeping contaminants out of the bearing system. This separation must be accomplished between surfaces in relative motion, usually a shaft or bearing inner ring and a housing. Accommodating the relative motion is even more difficult due to the eccentricities and run-outs of the surfaces, bearing clearance, misalignments, and deflections. The selection of a seal design depends on the type of lubrication system employed and the type and amount of contaminants that must be kept out. Other considerations in the decision must include speed, friction, wear, ease of replacement, and economics. Bearings run under a great variety of conditions, so it is necessary to judge which seal type will be sufficiently effective in each particular circumstance.

12.7.2 TYPES OF SEALS

12.7.2.1 Labyrinth Seals

Labyrinth seals, as shown in Figure 12.7, consist of an intricate series of narrow passages that protect well against dirt intrusion. This type is suitable for use in pillow blocks or other assemblies where the outer stationary structure is separable. The inner part is free to float on the shaft so that it can position itself relative to the fixed sections. The mechanism of sealing is complex, as it is associated with turbulent flow fluid mechanics. It is reasonably effective with liquids, greases, and gases, provided that there is no continuous static head across the assembly.

It is normal practice to add grease to the labyrinth, making the gaps even smaller than can be achieved mechanically due to tolerance stack-ups. Dirt has virtually no chance of penetrating such a system without becoming ensnared in the grease. A further advantage accrues at regreasing. Spent lubricant can purge readily through the labyrinth and flush the trapped debris within it.

The relatively moving parts are separated by a finite gap, so wear, in the absence of large bridging particles of dirt, is essentially nonexistent. Likewise, frictional losses are extremely

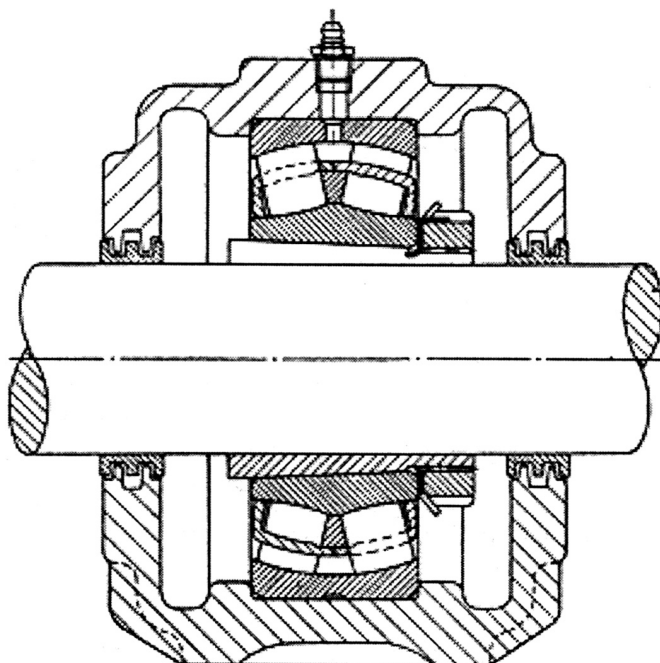


FIGURE 12.7 Bearing housing with labyrinth seals.

low. The number of convolutions of the labyrinth passage can be increased with the severity of the dirt exclusion requirements. Separate flingers and trash guards or cutters may be added on the outboard side to deal with wet or fibrous contaminants that could damage or penetrate the labyrinth. Figure 12.8 shows a ball bearing with an integral labyrinth seal and outboard flinger ring.

12.7.2.2 Shields

As [Figure 12.9](#) shows, a shield takes up very little axial space and can usually be accommodated within the standard boundary dimensions of the bearing. The near knife edge standing just clear of the ring land is, in effect, a single-stage labyrinth seal. Effective enough to keep all but the most fluid greases in the bearing, the shield can be considered as a modest dirt excluder, suitable for use in most workplace environments. Under harsher conditions, it must be backed up with extra guards. Special greases or acceptance of leakage and reduced lubricant life are necessary when shielded bearings are used in vertical axis applications. The absence of contact friction permits these bearings to be used at the highest speed allowed by the bearing and lubricant system.

12.7.2.3 Elastomeric Lip Seals

The narrow gap between a shield and an inner-ring groove or chamfer can be closed by a carefully designed section of elastomer (nitrile rubber for general purpose). [Figure 12.10](#)

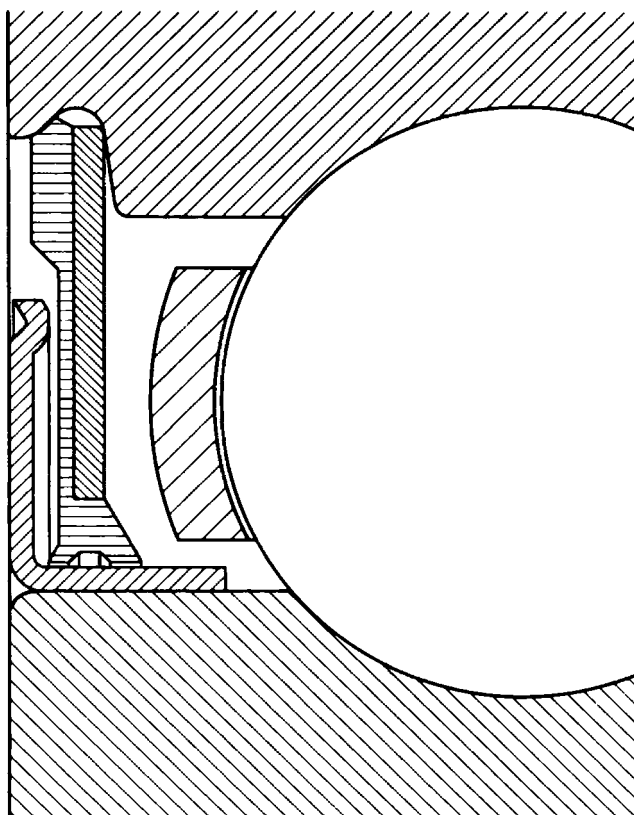


FIGURE 12.8 Deep-groove ball bearing assembly with integral labyrinth seal and flinger ring.

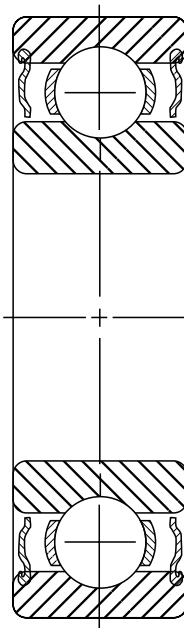


FIGURE 12.9 Radial ball bearing with double shields.

illustrates a typical configuration. The flexible material makes rubbing contact with the ring and establishes a barrier to the outward flow of lubricant or the ingress of contaminants. When the bearing is in motion, the elastomer slides over the metal surface, and a frictional drag is produced, which even for a well-designed seal is generally greater than the frictional torque of the bearing. Often more important is the seal breakaway torque, which can be several times the running torque. Considerable research has been devoted to finding both elastomers and seal designs that achieve a suitable balance between sealing efficiency, lip or ring wear, and frictional torque.

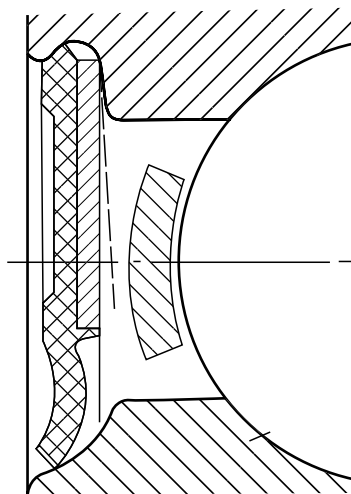


FIGURE 12.10 Radial ball bearing with integral single-lip seal.

The lip of the seal must bear on the ring with sufficient pressure to follow the relative motions of the surface as discussed earlier. This pressure is achieved by a slight interference fit producing a dilation of the seal. The spring rate of the lip governs the speed at which the lip can respond to the running errors without any gap formation through which the fluid can pass.

At first glance, even though a lubricant is present, no hydrodynamic lift would be expected on the lip because of the axial symmetry. Recent work has established, both theoretically and experimentally, that a very thin, stable dynamic fluid persists over much of the operating regime. The mechanism of sealing is a complex one involving the elastomeric lip, the counterface, and the grease, or at least the oil phase of the grease. As such, the lip seal requires the presence of lubricant, for if it is allowed to run dry, wear and failure are usually rapid. The grease charge of a bearing must be positioned to wet the seals on assembly. In most cases, the grease volume is sufficient to require a period of working when the bearing first operates. This is followed by channeling, and the formation of grease packs against the inside surface of the seals.

The primary task of the single-lip seal is to contain grease. It can exclude moderate dust as found in typical home or commercial atmospheres, and it finds a great many suitable applications. Some dusts, such as those from wood sanders or lint accumulating on the bearings in textile machinery, have the ability to wick considerable amounts of oil through the lip film, which shortens bearing life. In these situations and where there is heavy exposure to dirt, particularly water-borne dirt, such as in automotive uses, additional protection in the form of dust lips and flingers should be provided. Figure 12.11 shows an example of a double-lip seal.

12.7.2.4 Garter Seals

Similar in many respects to the lip seal, the garter seal uses a hoop spring or garter to apply an essentially constant inward pressure on the lip. As shown in [Figure 12.12](#), the arrangement

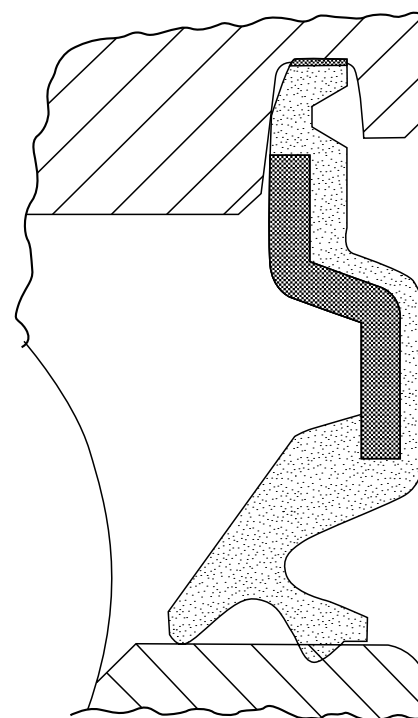


FIGURE 12.11 Double-lip seal. Inside lip is for fluid retention; outside lip is for dust exclusion.

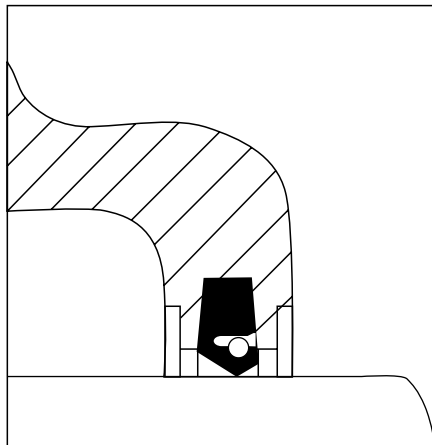


FIGURE 12.12 Garter seal cross-section showing retaining spring.

requires more axial space than is available in a bearing of standard envelope dimensions. Either extrawide rings must be used or the seal must be fitted as a separate entity in the assembly.

The spring-induced pressure gives a very positive sealing effect and is used to contain oil rather than grease for two reasons: (1) oil can be thrown or pumped by an operating bearing with considerable velocity, sufficient to cause leakage through a lip seal; and (2) the lip itself requires a generous supply of oil for lubrication and removal of friction heat. Relieved of the need to provide the closing force, the elastomer section can be designed to hinge freely so that relatively large amplitudes of shaft eccentricity can be accommodated. The strictly radial nature of the spring force precludes the use of anything other than a cylindrical counterface surface. Axial floating of the shaft is therefore accommodated well.

The design lends itself to molding, and the inclusion of specially designed film generating textures to be formed on the lip face. Figure 12.13 shows an example of a helical rib pattern intended not only to enhance the oil film thickness, but also to act as a screw pump to minimize leakage.

12.8 CLOSURE

Following the design and manufacture of a rolling element bearing, the technology associated with creating and maintaining the environment of the bearing during its operation is the single most important factor connected with its performance and life. This environment is

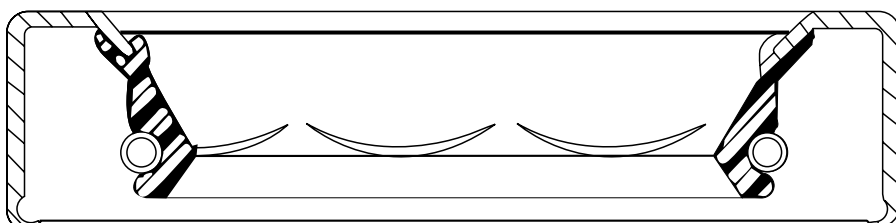


FIGURE 12.13 Radial seal with “quarter moon” projections molded on the lip to develop a hydrodynamic lubricant film during operation.

intimately associated with the lubricant selected, its means of application, and the method of sealing. In this chapter, a brief overview has been given to each of these important considerations. No attempt has been made to provide an exhaustive study of lubricant types, means of lubrication, or means of sealing. It remains for the reader to explore each of these topics to the depth required by the individual application.

REFERENCES

1. SKF, *General Catalog 4000US*, 2nd Ed., 1997–2001.
2. Nixon, H. and Zantopulos, H., Lubricant additives—friend or foe... what the equipment design engineer needs to know, *Lub. Eng.*, 51(10), 815, 1995.

13 Structural Materials of Bearings

13.1 GENERAL

The functional performance and endurance of a dimensionally perfect bearing with ideal internal geometries and surfaces, correct mounting, and preferential operating conditions are significantly influenced by the characteristics of its materials. The major criteria to be considered for the satisfactory performance of bearings include material selection and processing with resultant physical properties. This chapter contains brief descriptions of various bearing steel analyses, melting practices, manufacturing process variables, and the influence of these factors on the physical and metallurgical properties with respect to bearing performance. It also contains discussions concerning metallic and nonmetallic materials used for tribological coatings, cages, seals, and shields.

13.2 ROLLING BEARING STEELS

13.2.1 TYPES OF STEELS FOR ROLLING COMPONENTS

Rolling bearing steels are selected primarily on the basis of hardenability, fatigue strength, wear resistance, and toughness. The American Iron and Steel Institute (AISI) 52100 steel, an alloy machinable in its annealed condition and exhibiting high hardness in the heat-treated state, was introduced around 1900 and is still the most-used steel for ball bearings and for many roller bearing applications. For large bearing sizes, particularly with respect to cross-sectional thickness, modifications to this basic analysis incorporating silicon, manganese, and molybdenum were introduced. Carburizing steel came into being when the tapered roller bearing was introduced. Over the years, more demanding product requirements promoted the introduction of high-speed steels and stainless steels for high-temperature operating conditions and corrosion resistance.

13.2.2 THROUGH-HARDENING STEELS

The largest tonnage of bearing steels currently produced is the category of through-hardening steels. [Table 13.1](#) lists common grade designations and respective chemical compositions of this family of alloys.

Through-hardening steels are classified as hypereutectoid-type steels when containing greater than 0.8% carbon by weight and essentially containing less than 5% by weight of total alloying elements. Assuming satisfactory material availability, the bearing producer selects the appropriate grade of steel, based on bearing size, geometry, dimensional characteristics, specific product performance requirements, manufacturing methods, and associated costs.

TABLE 13.1
Chemical Composition of Through-Hardening Bearing Steels

Grade ^a	Composition (%)				
	C	Mn	Si	Cr	Mo
ASTM ^b -A295 (52100)	min.	0.98	0.25	0.15	1.30
ISO ^c Grade 1, 683/XVII	max.	1.10	0.45	0.35	1.60
ASTM-A295 (51100)	min.	0.98	0.25	0.15	0.90
DIN ^d 105 Cr4	max.	1.10	0.45	0.35	1.15
ASTM-A295 (50100)	min.	0.98	0.25	0.15	0.40
DIN 105 Cr2	max.	1.10	0.45	0.35	0.60
ASTM-A295 (5195)	min.	0.90	0.75	0.15	0.70
	max.	1.03	1.00	0.35	0.90
ASTM-A295 (K19526)	min.	0.89	0.50	0.15	0.40
	max.	1.01	0.80	0.35	0.60
ASTM-A295 (1570)	min.	0.65	0.80	0.15	—
	max.	0.75	1.10	0.35	—
ASTM-A295 (1560)	min.	0.56	0.75	0.15	0.70
	max.	0.64	1.00	0.35	0.90
ASTM-A485 grade 1	min.	0.95	0.95	0.45	0.90
ISO Grade 2, 683/XVII	max.	1.05	1.25	0.75	1.20
ASTM-A485 grade 2	min.	0.85	1.40	0.50	1.40
	max.	1.00	1.70	0.80	1.80
ASTM-A485 grade 3	min.	0.95	0.65	0.15	1.10
	max.	1.10	0.90	0.35	1.50
ASTM-A485 grade 4	min.	0.95	1.05	0.15	1.10
	max.	1.10	1.35	0.35	1.50
DIN 100 CrMo6	min.	0.92	0.25	0.25	1.65
ISO Grade 4, 683/XVII	max.	1.02	0.40	0.40	1.95
					0.40

^aPhosphorus and sulfur limitation for each alloy is 0.025% maximum (each element).

^bAmerican Society for Testing and Materials [1].

^cInternational Organization for Standards.

^dDeutsches Institut für Normung e.V.

13.2.3 CASE-HARDENING STEELS

These steels are classified as hypoeutectoid steels; their carbon content is generally below 0.80%. Carburizing steels are alloyed with nickel, chromium, molybdenum, and manganese to increase hardenability. Higher-hardenability grades are used in applications requiring bearing ring components of heavier cross-sections. Carbon is diffused into the surface layer of the machined components to approximately 0.65–1.10% during the heat treatment operation to achieve surface hardness comparable to that attained with through-hardened grades of steel. Table 13.2 outlines the grade designations and corresponding chemical compositions of the common carburizing steels.

13.2.4 STEELS FOR SPECIAL BEARINGS

The demand for good bearing performance under hostile operating conditions has consistently increased. The aerospace industry, in particular, requires products capable of

TABLE 13.2
Chemical Composition of Carburizing Bearing Steels

Grade ^a	Composition (%)					
	C	Mn	Si	Ni	Cr	Mo
SAE ^b 4118	min.	0.18	0.70	0.15	—	0.40
	max.	0.23	0.90	0.35	—	0.60
SAE 8620, ISO 12 DIN 20 NiCrMo2	min.	0.18	0.70	0.15	0.40	0.40
	max.	0.23	0.90	0.35	0.70	0.60
SAE 5120 AFNOR ^c 18C3	min.	0.17	0.70	0.15	—	0.70
	max.	0.22	0.90	0.35	—	0.90
SAE 4720, ISO 13	min.	0.17	0.50	0.15	0.90	0.35
	max.	0.22	0.70	0.35	1.20	0.55
SAE 4620	min.	0.17	0.45	0.15	1.65	—
	max.	0.22	0.65	0.35	2.00	—
SAE 4320, ISO 14	min.	0.17	0.45	0.15	1.65	0.40
	max.	0.22	0.65	0.35	2.00	0.60
SAE E9310	min.	0.08	0.45	0.15	3.00	1.00
	max.	0.13	0.65	0.35	3.50	1.40
SAE E3310	min.	0.08	0.45	0.15	3.25	1.40
	max.	0.13	0.60	0.35	3.75	1.75
KRUPP	min.	0.10	0.45	0.15	3.75	1.35
	max.	0.15	0.65	0.35	4.25	1.75

^aGrades are listed in ASTM-A534 [2]; phosphorus and sulfur limitation for each alloy is 0.025% maximum (each element).

^bSociety of Automotive Engineers.

^cFrench Standard.

operating at increasingly higher speeds, heavier loads, and with high reliability. Other challenging applications include performing in corrosive atmospheres, at cryogenic temperatures, and in hard vacuum. To achieve satisfactory bearing operation in the critical applications associated with these conditions, it is necessary to minimize the adverse effects on fatigue life due to undesirable nonmetallic inclusions. This requires substantial changes in steel-melting practice. Vacuum induction-melted, vacuum arc-remelted (VIMVAR) alloy steels such as M50 and BG42 were developed to provide the required high reliability in resistance to fatigue. M50-NiL [2–4] was developed as a high-temperature operation, carburizing steel to provide through-cracking resistance for very high-speed bearing inner rings. Also used with limited success has been Cronidur 30 [5,6], a steel rich in nitrogen and chromium, which had been introduced to satisfy the requirements for high-temperature operations with both high-reliability fatigue resistance and corrosion resistance at low temperatures; however, the corrosion resistance at high temperatures has been the limiting factor. Furthermore, in many aircraft power transmissions, to minimize weight and space, inner raceways of bearings are made integral with a one-piece gear-shaft component. Thus, the steel used must satisfy the fatigue-resistance requirements for the gear as well as the shaft and supporting bearings; pyrowear 675 carburizing steel is frequently employed in such applications. Table 13.3 lists the chemical compositions of several special bearing steels.

TABLE 13.3
Chemical Composition of Special Bearing Steels

Grade	Typical Composition (%)								
	C	Mn	Si	Cr	Ni	V	Mo	W	N
M50	0.80	0.25	0.25	4.00	0.10	1.00	4.25	—	—
BG-42	1.15	0.50	0.30	14.50	—	1.20	4.00	—	—
440-C	1.10	1.00	1.00	17.00	—	—	0.75	—	—
CBS-600	0.20	0.60	1.00	1.45	—	—	1.00	—	—
CBS-1000	0.15	3.00	0.50	1.05	3.00	0.35	4.50	—	—
VASCO X-2	0.22	0.30	0.90	5.00	—	0.45	1.40	—	—
M50-NiL ^a	0.15	0.15	0.18	4.00	3.50	1.00	4.00	1.35	—
Pyrowear 675 ^a	0.07	0.65	0.40	13.00	2.60	0.60	1.80	—	—
EX-53	0.10	0.37	0.98	1.05	—	0.12	0.94	2.13	—
Cronidur 30	0.31	—	0.55	15.20	—	—	1.02	—	0.38

^aM50-NiL and Pyrowear 675 are surface-hardening steels.

13.3 STEEL MANUFACTURE

13.3.1 MELTING METHODS

Since the 1960s, the electric arc furnace has been used to melt high-quality bearing steels. During the oxidizing period in the furnace cycle, impurities such as phosphorus and some sulfur are removed from the steel. Further refining removes dissolved oxides and other impurities that might negatively affect the steel's performance. Unfortunately, this furnace practice by itself does not remove undesirable gases absorbed by the molten steel during melting and entrapped during solidification. Although vacuum ladle degassing was patented in 1943 [7], it was not until the 1960s through 1970s that cost-effective vacuum degassing production facilities were used to principally remove oxygen and hydrogen, and to further improve material quality. These processes provide bearing steels with the good machinability, hardenability, and homogeneity required for manufacturing economy and good product performance.

The advent of high-performance, aircraft gas turbine engines and the corresponding demand for premium-quality bearing steels led to the development of sophisticated induction and consumable electrode vacuum melting techniques. Electroslag remelting capability was developed in concert with these two vacuum processes. These special melting techniques have significantly influenced the development of higher-alloy tool steels for elevated temperature- and corrosion-resistant bearing applications.

13.3.2 RAW MATERIALS

The demand on the steel industry to provide higher-quality alloy steels promoted the development of the cold charge in the basic material-lined, electric arc furnace. These furnaces let higher- and lower-grade alloy scraps be mixed with plain carbon scrap; economical operation and product quality are achieved through proper selection and weight control of these materials. Knowing the exact chemistry of the scrap charge reduces the consumption of more costly alloys that are added to the melt and minimizes the introduction of undesirable tramp alloying elements. The abundance of certain trace metallic elements, occurring unintentionally in AISI 52100 steel, has shown a negative correlation to the fatigue life in ball bearings [8].

13.3.3 BASIC ELECTRIC FURNACE PROCESS

The basic electric arc furnace (Figure 13.1) [9] is circular, lined with heat-resistant bricks, and contains three electrodes in a removable roof. The charge is blended to provide efficient melting, the electrodes are lowered, and the arcing begins. A layer of complex slag that covers the molten surface layer and absorbs impurities from the steel is produced. During this oxidizing period, a carbon boil occurs, which produces gases from the molten bath. This complex slag is then treated with a reducing slag to decrease the oxygen levels.

Because the molten metal in the refining cycle is less active than in the oxidizing cycle, furnaces may be equipped with inductive stirrers. These stirrers generate a magnetic field that imparts a circulatory motion to the molten bath, enhancing both temperature control and homogeneity of chemical composition throughout the melt. When the chemical composition of the molten steel has been adjusted to the desired range and the proper pouring temperature has been reached, the steel heat is tapped or removed from the furnace. Material not to be vacuum treated is then ready for teeming into ingot molds.

13.3.4 VACUUM DEGASSING OF STEEL

The quality of the material produced in the basic electric arc furnace process can be improved through vacuum degassing by various methods, including ladle degassing [10], stream degassing [11], Dortmund–Hörder processes, and Ruhrstahl–Heraeus processes [12]. In conjunction with these refining practices, inert gas shrouding may be incorporated with both bottom pouring and uphill teeming. These methods economically reduce undesirable gases and remove nonmetallic inclusions from the molten steel.

13.3.5 LADLE FURNACE

Ladle metallurgy of molten steel is conducted in a ladle furnace outside the normal constraints of the initial electric arc melting furnace. The ladle furnace is equipped with

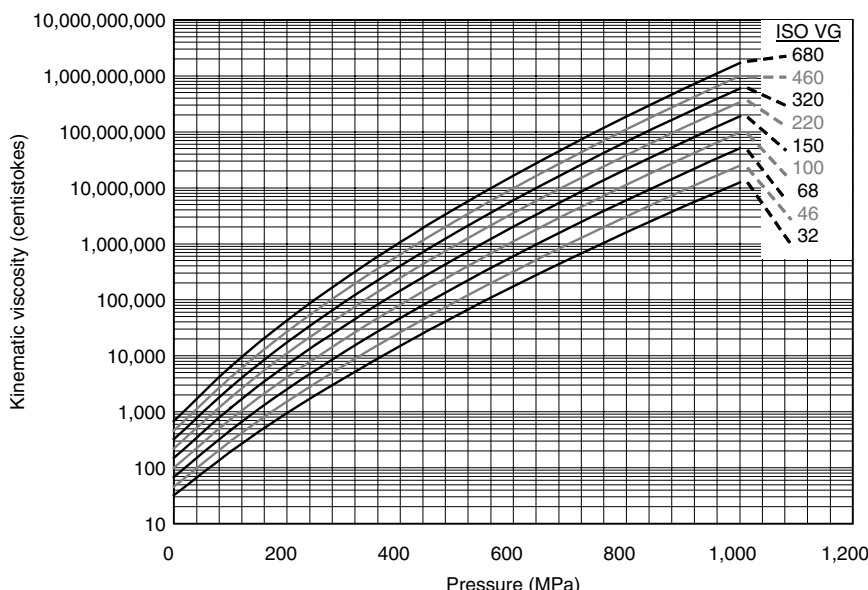


FIGURE 13.1 Basic electric arc furnace.

independent electrodes for both temperature control and electromagnetic stirrers for bath circulation. Therefore, there is no need to superheat steel in the electric arc furnace to compensate for subsequent temperature drops experienced in standard ladle degassing practices as previously mentioned.

Lance injection permits powdered alloys to be inserted deep into the ladle. Argon is used as a carrier gas for these powders; the resulting bubble action helps disperse particles uniformly throughout the molten bath. Lance injection combined with wire feeding provides inclusion shape control, reduction of sulfur content, and improvement of fluidity, chemical homogeneity, and overall microcleanliness.

Ladle furnace technology permits very rapid meltdown of scrap in the electric arc furnace and improved refining capability in a subsequent ladle furnace operation. This system generates improved product quality with a correspondingly improved economy in steel melting.

13.3.6 METHODS FOR PRODUCING ULTRAHIGH-PURITY STEEL

13.3.6.1 Vacuum Induction Melting

Yet more sophisticated steel-melting processes were introduced during the 1960s for producing ultrahigh-purity steels, also called *clean* bearing steels, which are essentially free from deleterious nonmetallic-type inclusions.

In vacuum induction melting, selected scrap material containing few impurities and comparable in chemical composition to the alloy-grade melt is charged into a small electrical induction furnace. The furnace (Figure 13.2) [13] is encapsulated in a large vacuum chamber containing sealed hoppers strategically located for adding the required alloys.

Outgassing of the melt occurs early in a very rapid meltdown and refining period. After the melting cycle, furnace tilting and pouring of the molten metal into ingot molds takes place. The molds are automatically manipulated into and out of the pouring position while still within the vacuum-sealed chamber. This vacuum induction melting process was among the first vacuum induction melting furnace processing methods employed in manufacturing premium aircraft quality bearing steels. One of the primary functions today is to provide electrodes for use in producing ultrahigh-purity, vacuum arc-remelted steels.

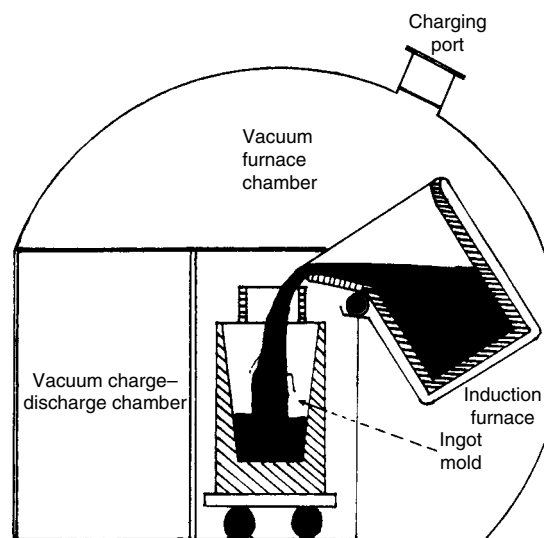


FIGURE 13.2 Schematic view of induction vacuum melting furnace.

13.3.6.2 Vacuum Arc Remelting

Vacuum technology for bearing steel alloy production, as described in [Section 13.3.4](#) and [Section 13.3.6.1](#), provided a way to reduce the gas content and nonmetallic inclusions in steel. Steel electrodes, melted in furnaces using vacuum technology, can be remelted by still more sophisticated techniques, such as the consumable electrode vacuum melt practices, to provide materials for bearings requiring the utmost reliability. This process, illustrated in Figure 13.3, involves inserting an electrode of the desired chemical composition into a water-cooled, copper mold in which a vacuum is created.

An electrical arc is struck between the bottom face of the electrode and a base plate of the same alloy composition. As the electrode is consumed under extremely high vacuum conditions, it is automatically lowered and the voltage is controlled to maintain constant melting parameters. Because the solidification pattern is controlled, the remelted product is essentially free from center porosity and ingot segregation. The product has improved mechanical properties, particularly in the transverse direction. Aircraft bearing material specifications for critical applications specify the VIMVAR steel-melting practice.

13.3.6.3 Electroslag Refining

The electroslag refining (ESR) process is very similar to that of the consumable electrode vacuum melting process except that a liquid slag bath positioned at the base of the electrode provides the electrical resistance required for melting. The slag bath is either introduced into the furnace chamber in the molten state or is provided as a powder slag that will quickly melt on striking an arc between the electrode and the base plate. Refinement of the molten steel occurs as steel droplets pass through the slag bath. Control of slag composition permits the

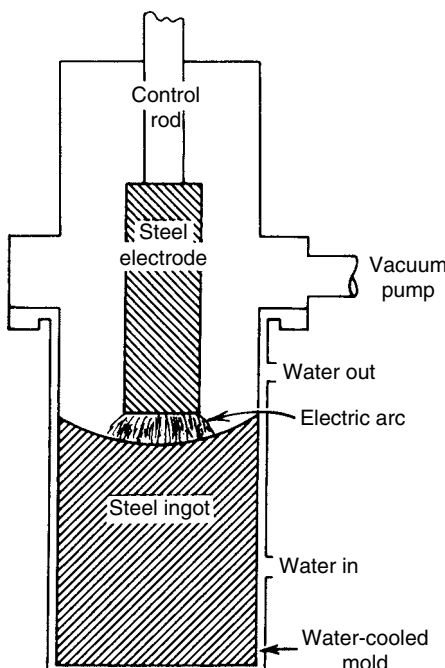


FIGURE 13.3 Vacuum-arc remelting furnace.

removal of sulfur and oxygen, and undesirable impurities. The resulting ingot solidification pattern reduces porosity, minimizes segregation, and provides for improved physical properties in the transverse and longitudinal directions.

13.3.7 STEEL PRODUCTS

Rolling bearings cover a broad spectrum of sizes with ring components varying in both cross-sectional configurations and material grades. Balls or rollers vary in size and shape to accommodate their mating ring components. Generally, these components are manufactured from forgings, tubing, bar stock, or wire. From the steel producer, the bearing manufacturer orders the raw material with the form and condition best suited for the selected method of processing and that will result in effective bearing performance and meet customer requirements.

Regardless of the melting practice employed, the resulting ingots are stripped from the molds, homogenized in soaking pits, rolled into blooms or billets, and subsequently conditioned to remove surface defects. Billets are reheated and hot-worked into bars, tubes, forgings, or rolled rings. Additional cold-working operations convert the hot-rolled tubes and bars into cold-reduced tubes, bars, and cold-drawn wires. As an ingot passes back and forth between the rolls on a blooming mill, its cast structure is broken up and refined. Continued hot-working operations elongate and break up nonmetallic inclusions and alloy segregation. Hot mechanical working operations also permit the plastic deformation of the material into the desired shape or form. The subsequent cold-working of material results in induced stresses and improved machinability. Cold-working also produces changes in the mechanical properties, with improved surface finishes, and reduced tolerances. Dimensional tolerances and eccentricities of cold-worked tubes are far superior to those of hot-rolled tubes.

Most mill product forms require thermal treatment at the mill before or after final finishing so that the forms are ready for machining or forming. The thermal treatment may include annealing, normalizing, or stress relieving. The product is then straightened, if necessary, inspected, and readied for transport.

13.3.8 STEEL METALLURGICAL CHARACTERISTICS

13.3.8.1 Cleanliness

Steel quality with respect to nonmetallic inclusions depends on the initial raw material charge, selection of the melting furnace type and practice, and control of the entire process, including teeming and conditioning of the ingot molds. Exogenous inclusions result from erosion or breakdown of furnace refractory material or from other dirt particles outside the melt that are entrapped during tapping and teeming. Indigenous inclusions are products of deoxidation occurring within the melt. Inclusions less than 0.5 mm (0.020 in.) are considered microinclusions; larger ones are considered macroinclusions. Nonmetallic inclusions are classified by their composition and morphology as sulfides, aluminates, silicates, and oxides. Occasionally, nitrides are included in rating steel cleanliness.

Nonmetallic inclusions are generally detrimental to rolling contact fatigue life. Furthermore, hard, brittle-type inclusions, based on their size, shape, and distribution, are more detrimental than soft deformable-type particles such as sulfides. Sulfides act beneficially by encapsulating harder, nonmetallic particles and forming a cocoon or cushion around them so that they do not become points of stress concentration under cyclic loading. Sulfide inclusions can also enhance machinability by performing as a lubricant. Because aluminates and silicates have sharp corners and are very brittle, they can act as stress raisers and initiate early fatigue

failures. Globular oxides are inclusions formed with elements such as calcium; these particles are very brittle and are considered to be most detrimental to machinability and rolling contact fatigue life.

Since approximately 1960, consistent efforts have been made to improve the quality of bearing steels, particularly its cleanliness. During the 1960s and 1970s, it was not uncommon for bearing steels to have high oxygen contents; for example, 35 parts per million (ppm) and substantial amounts of macroinclusions. During the 1970s, the acid open hearth furnace was introduced, which improved cleanliness; that is, oxygen content in the form of oxides was reduced to 20 ppm, and macroinclusions over a period of time were reduced to virtually nil. By 1982, vacuum degassing processes lowered the oxygen content to 10 ppm while maintaining a low level of macroinclusions. As shown in Figure 13.4, the decrease in oxygen content from 35 to 10 ppm afforded at least a tenfold improvement in bearing fatigue life. However, as indicated in Figure 13.5, as oxygen content decreased below 20 ppm, the effect of lowering oxygen further was less pronounced and significantly more scatter was present in the fatigue performance of the steels. During the 1980s and 1990s, ultrasonic techniques [14] were used to study the quantity, shape, and size of microinclusions relative to bearing fatigue performance, as indicated in Figure 13.6. This allowed for further improvements in the process and process controls, such as teeming temperatures, bottom pouring, shrouding, and ladle stirring to further eliminate microinclusions and their effects on fatigue performance.

Many methods have been devised for detecting or quantitatively defining nonmetallic inclusions [16]. One of the most popular methods involves microscopic examination at 100 \times magnification of polished specimens of a predetermined size from specific ingot locations and comparing the worst field observed against standard photographs weighted on a numbered evaluation system [12]. Other commonly cited tests include fracture, magnaflux step-down (AMS 2300/AMS 2301), and visual rating–counting indications on machined bar surfaces to determine material quality with respect to nonmetallic inclusion content.

With respect to detection of nonmetallic inclusions, premium-quality aircraft bearing steel is automatically checked on a 100% bar product basis by employing both eddy current and ultrasonic test procedures.

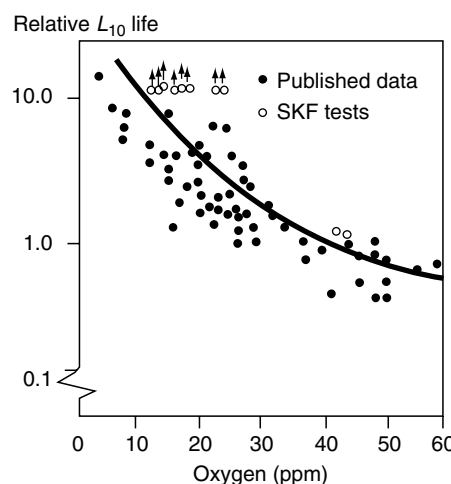


FIGURE 13.4 Fatigue life of AISI 52100 steel ball bearings vs oxygen content. (From Åkesson, J. and Lund, T., SKF rolling bearing steels—properties and processes, *Ball Bearing J.*, 217, 32–44, 1983. With permission.)

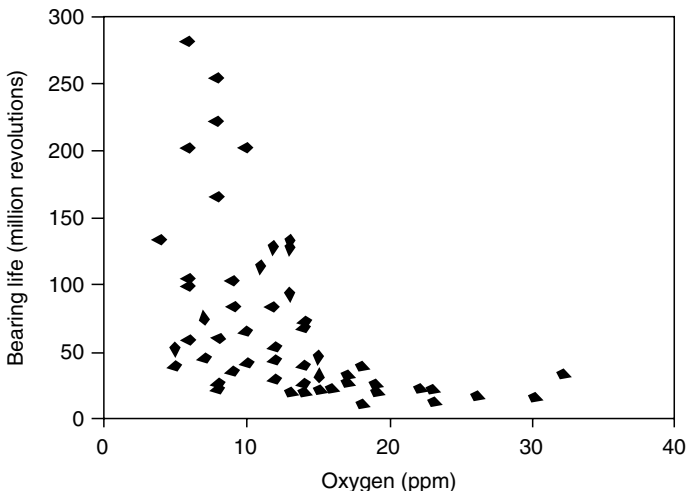


FIGURE 13.5 Fatigue life of carburized tapered roller bearings vs. oxygen content. (From Eckel, J., et al., Clean engineered steels—progress at the end of the twentieth century, in *Advances in the Production and Use of Steel with Improved Internal Cleanliness*, J. Mahoney (Ed.), ASTM STP 1361, 1999. With permission.)

13.3.8.2 Segregation

The nonuniform solidification rate of molten steel within an ingot mold might lead to the segregation of alloying constituents. Because of the rapid freezing rate occurring in the mold-ingot interface, the outermost portion or shell will solidify first and form columnar crystals. At the centermost portion of the ingot, which cools at a much slower rate, the grains are

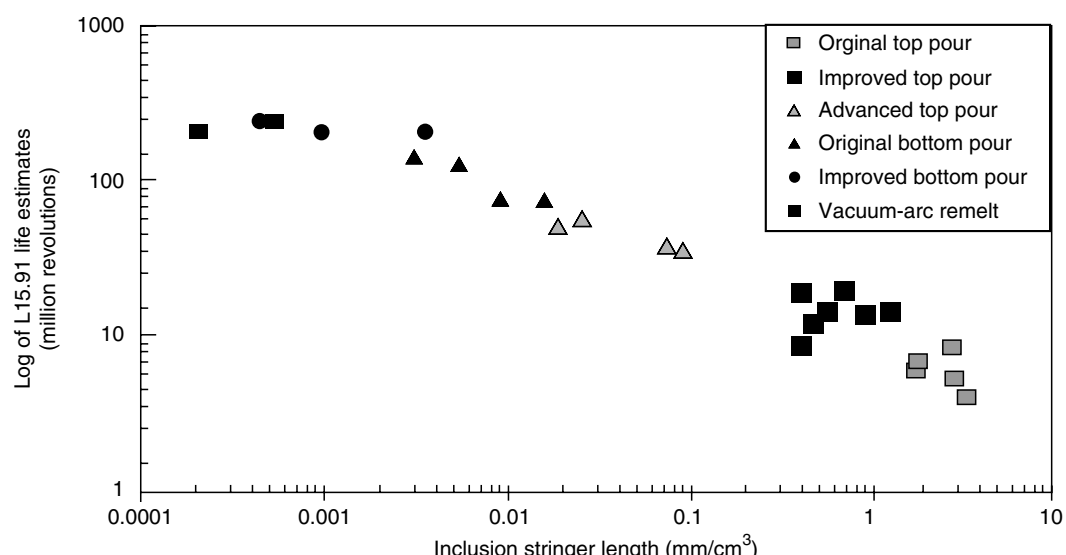


FIGURE 13.6 Fatigue life of carburized tapered roller bearings vs. ultrasonic inclusion stringer length. (From Eckel, J., et al., Clean engineered steels—progress at the end of the twentieth century, in *Advances in the Production and Use of Steel with Improved Internal Cleanliness*, J. Mahoney (Ed.), ASTM STP 1361, 1999. With permission.)

equiaxed. Because solidification is not spontaneous throughout the ingot, the molten metal that freezes last will also become richer in alloying elements such as manganese, phosphorus, and sulfur, because the elements have inherently lower melting points.

Segregation is only slightly improved by thermal treatment and hot-working. Precautions must be taken in the melting and pouring practices, such as incorporating special molds designed to control the rate of freezing and thereby to prevent or minimize segregation during solidification.

Macroetching of properly prepared billet or bar slices, employing dilute, hot hydrochloric acid solution, which preferentially attacks these numerous alloying constituents, is used to reveal material segregation.

13.3.8.3 Structure

Both macroscopic and microscopic methods of inspection are used to evaluate steel structure. Discs cut from the ends of bars or billets for macroscopic examination are prepared according to industry standards, acid etched, and examined with the unaided eye or under magnification generally not exceeding $10\times$. Although numerous etching reagents are available, the generally recommended and accepted solution is hot, dilute hydrochloric (muriatic) acid.

In addition to the detection of alloy segregates, material may be microstructurally evaluated for other objectionable characteristics such as pipe porosity, blow holes, decarburization, excessive inclusions, cracks, and banding. The aerospace industry uses hot acid etching and forging inspection to ensure conformance of grain flow patterns to a previously type-tested product.

Microscopic examination of steel involves a more detailed study of the structure at magnifications generally between $100\times$ and $1000\times$. Numerous reagents are available to help identify and rate specific microconstituents. The steel producers' manufacturing processes, incorporating thermal cycles, influence the resulting microstructure of the finished mill product. Because microstructures are a reflection of material physical properties, microstructural ratings are contained with specifications or purchase order agreements. Bars and tubes that are fed into automatic single or multiple spindle machines for turning into ring components must be in a soft annealed condition. Carbides should be uniform in size and well distributed throughout a ferrite matrix. Tool life may be expected to increase as the sizes of the spheroidal carbides increase. Conversely, presence of lamellar carbide will adversely affect machinability and tool life.

When choosing the optimum microstructure for maximum machinability of low-carbon, carburizing steel, a blocky microstructure of ferrite and pearlite should be selected. A very soft annealed structure in these low-carbon grades, such as AISI 8620, is appropriate for cold-forming operations, but is considered gummy and unsatisfactory in machining operations. Each material grade in its finished mill product form must exhibit the proper microstructure and hardness so that it can be economically converted to its designated configuration.

13.4 EFFECTS OF PROCESSING METHODS ON STEEL COMPONENTS

Many of the mechanical properties of finished bearing components are developed by manufacturing methods that dictate the form and condition for raw material. Generally, raw material is produced by either hot- or cold-reduction processes and furnished as tubing, bars, wires, and forgings. Cold-reduction for producing bars, tubing, balls, and rollers of AISI 52100 will lower both the austenite transformation temperature during heating for hardening and the martensite start (MS) temperature on cooling [17]. The resulting fracture grain size of a ring produced from a cold-reduced tube will be finer than that of an identical

ring from a hot-rolled annealed tube. Although the volume change for the hot-rolled and cold-reduced components is the same, the ring from the cold-reduced tube will have a smaller diameter after heat treatment.

Bars and tubes are elongated during manufacture and display directional properties; that is, the mechanical properties are different in the longitudinal direction compared with the transverse direction. Forging the bar into ring components provides a more homogeneous product. Ring rolling might provide beneficial grain flow conforming to the rolling contact surface. Bearing endurance tests demonstrate that the end grain is detrimental to rolling contact fatigue life [18].

Raw material intended for machining operations before heat treatment should be received in a readily machinable condition. The material should have sufficient stock to render an “as-machined” component free from carburization, decarburization, and other surface defects.

13.5 HEAT TREATMENT OF STEEL

13.5.1 BASIC PRINCIPLES

Heat treatment of bearing steel components necessitates heating and cooling under controlled atmospheric conditions to impart the desired material characteristics and properties such as hardness, a diffused high carbon surface layer, high fracture toughness or ductility, high tensile strength, improved machinability, proper grain size, or reduced stress state. The specific thermal cycles that produce these material characteristics are annealing, normalizing, hardening, carburizing, tempering, and stress relieving. Selective thermal cycles provide distinctive microstructures such as bainite, martensite, austenite, ferrite, and pearlite.

Iron and carbon are the basic constituents in bearing steels along with specific amounts of manganese, silicon, or other alloying elements such as chromium, nickel, molybdenum, vanadium, and tungsten. Bearing steels have a distribution of carbon content from 0.08% minimum (AISI 3310) to 1.10% maximum (AISI 52100). Beginning with ingot solidification, bearing steels take on a crystalline structure. These crystals are composed of atoms located at fixed locations within a unit cell. Spacings remain constant at fixed temperatures. Although there are 14 different space lattice types, bearing metallurgy is primarily concerned with three types: body-centered cubic (bcc), face-centered cubic (fcc), and body-centered tetragonal (bct). [See Figure 13.7](#).

These types of three-dimensional cells have different physical and mechanical properties because of differences in atomic spacings; they also have a different solubility for atoms of other alloying elements. An atom of one or more such alloying elements residing in the high-carbon bearing steel may be substituted for an iron atom. Elements with very small atomic radius, such as carbon, which is about one eighth the size of iron, can be placed in the interstitial spaces in the lattice.

Pure iron has a bcc structure at room temperature and an fcc structure within a specific elevated temperature range. The temperature on heating or cooling, at which the atoms shift from one unit-cell type to another, is called the transformation temperature. These alterations can be observed in the time-temperature cooling curve for iron.

Pure iron has a bcc below 912°C (1673°F) and an fcc above this temperature. When carbon is added to iron, the transformation temperature is lowered and extended over a broader temperature range. Because bearing steels rarely exceed 1.1% carbon and their heat treatments do not exceed a metal temperature of 1302°C (2375°F) (for T-1(C-0.70, Cr-4.00, W-1.00, V-18.00)), only a section of the iron–carbon phase diagram ([Figure 13.8](#)) will be required for further discussion.

Carbon is dissolvable in molten iron, and it is this action occurring in solid solution that enables the alteration of the mechanical properties of steel. High-carbon–chromium bearing

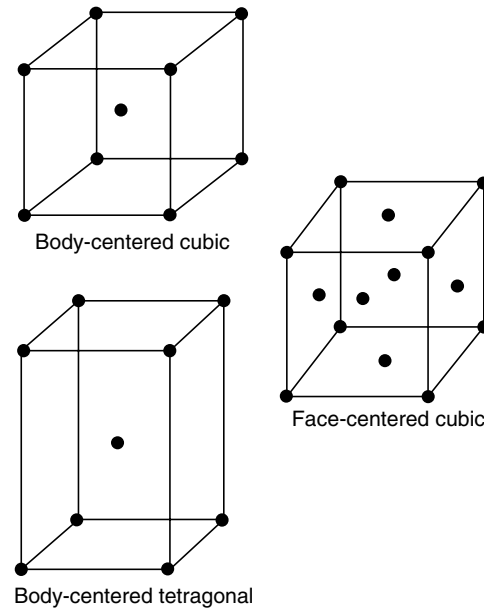


FIGURE 13.7 Crystal structures of steel.

steels, as received from the steel producer, are generally in a soft, spheroidized annealed condition suitable for machining. The microstructure consists of spheroidal carbide particles in a ferritic matrix. This mixture of ferrite and carbide that exists at room temperature transforms to austenite at approximately 727°C (1340°F). The austenite is capable of dissolving far larger quantities of carbon than that contained within the ferrite. By altering the cooling rate from the austenitizing temperature, the distribution of the resulting ferrite and carbide can be modified, thus giving a wide variation in the resulting material properties.

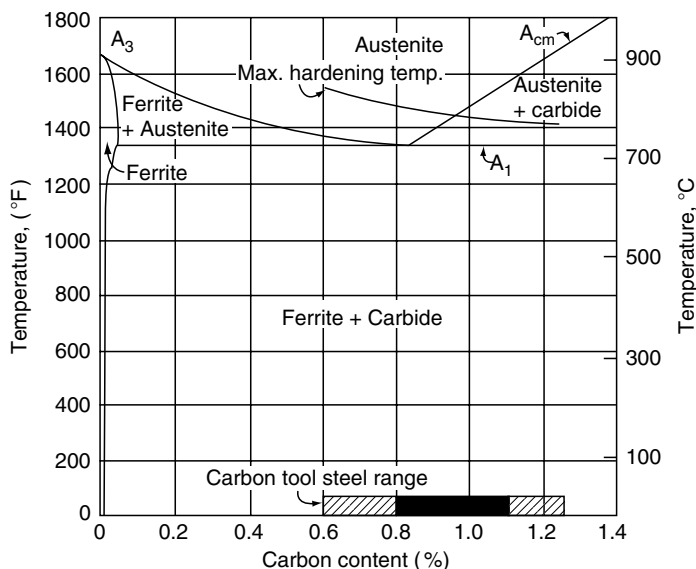


FIGURE 13.8 Section of the iron–carbon phase diagram.

On the basis of carbon content, steel can be put into three categories: eutectoid, hypoeutectoid, and hypereutectoid. Eutectoid steels are those containing 0.8% carbon, which on heating above 727°C (1340°F) become 100% austenite. This composition on cooling from the austenitic range to approximately 727°C (1340°F) simultaneously forms ferrite and cementite. This product is termed pearlite, and it will revert to austenite if it is reheated to slightly above 727°C (1340°F).

Hypoeutectoid steels are those containing less than 0.80% carbon. The iron–carbon diagram indicates that for a 0.40% carbon steel, approximately 843°C (1550°F) is required to dissolve all the carbon into the austenite. Under conditions of slow cooling, ferrite separates from the austenite until the mixture reaches 727°C (1340°F). At this point, the remaining austenite, containing 0.80% carbon, transforms into pearlite; the resulting microstructure is a mixture of ferrite and pearlite. The pearlite will dissolve into a solid solution when it is reheated to approximately 727°C (1340°F). At temperatures above 727°C (1340°F) the ferrite will dissolve into austenite.

The iron–carbon diagram indicates the existing phases when very slow heating and cooling rates are enacted.

13.5.2 TIME-TEMPERATURE TRANSFORMATION CURVE

The time–temperature transformation(TTT) diagram is an isothermal transformation diagram. Steel transforms when cooled rapidly from the austenitizing temperature to a lower temperature than the minimum at which the austenite is stable. Diagrams for various grades of steel at specific austenitizing temperatures have been developed to depict the time required for the austenite to begin to transform and to be completely transformed at any constant temperature studied. [Figure 13.9](#) [19] shows an isothermal TTT diagram for a typical high-carbon steel (AISI 52100). The shape and the position of the curves change with increased alloy content, grain size of the austenite, and austenitizing temperature. [Figure 13.10](#) [20] depicts the TTT diagram for a typical alloy steel (AISI 4337).

13.5.3 CONTINUOUS COOLING TRANSFORMATION CURVES

An eutectoid steel, on slow cooling, will transform to pearlite at approximately 727°C (1340°F). If the same steel specimen is quenched into a liquid medium controlled at a temperature just below 727°C (1340°F), a coarse pearlite structure will result. As the temperature of the holding medium is lowered, however, the diffusion of carbon atoms is decreased, and the lattice spacing of ferrite and cementite is reduced, thus producing a pearlitic microstructure. These microstructures indicate that the formation of pearlite is a nucleation and growth process. At still lower temperatures, carbon atoms move more slowly, and the resulting transformation product is bainite, which consists of ferrite needles containing a fine dispersion of cementite. Under still further cooling, the transformation product martensite is formed, which consists of a very fine needle-like structure. Martensite forms athermally involving a shear mechanism in the microstructure; it is not a product of isothermal transformation. The quenching must be done very rapidly into a medium such as molten salt or oil at a controlled temperature to prevent the austenite from converting to a soft transformation product such as pearlite.

The TTT diagrams reveal the microstructures that form at a single constant temperature; however, steel heat treatment uses rapid cooling, and transformation occurs over a range of temperatures. Continuous cooling transformation (CCT) curves have been developed to explain the resulting transformations. [Figure 13.11](#) is a cooling transformation diagram for AISI 52100 steel.

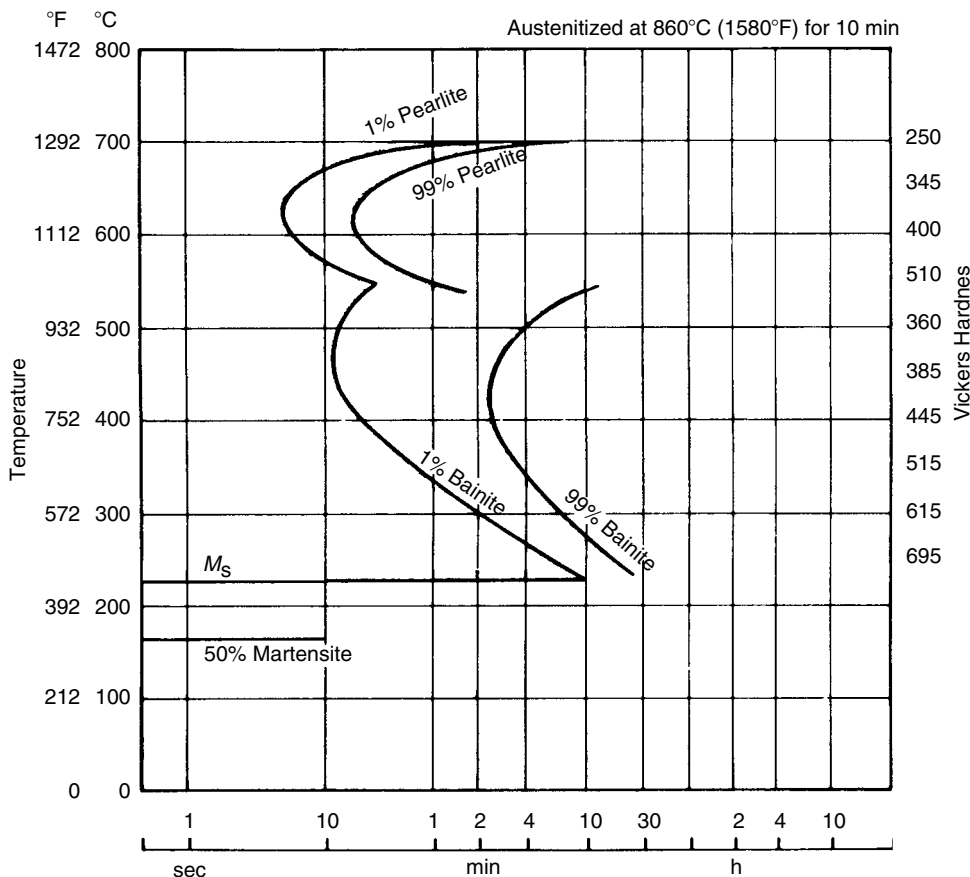


FIGURE 13.9 Time-temperature transformation diagram for AISI 52100 steel. (From SKF Steel, *The Black Book*, Vol. 194, 1984. With permission.)

An AISI 52100 steel Jominy test bar 25.4 mm (1 in.) in diameter by 76.2 or 101.6 mm (3 or 4 in.) long may be used to explain the value of the CCT diagram. The piece is austenitized at 843°C (1550°F) and, while held vertically, is sprayed with a stream of water on the lower end face. The cooling rate then varies from the quenched surface to the extreme opposite end, which cools much slower. Microstructures can then be correlated with various cooling rates occurring along the length of the bar.

13.5.4 HARDENABILITY

Hardness is resistance to penetration, and hardenability pertains to the depth of hardness achievable in an alloy. The alloying elements in the steel, as witnessed by the movement of the isothermal transformation curves to the right on the TTT diagram, permit additional cooling time from the austenitizing temperature to the point of martensite transformation. This positive effect of alloy addition to steel readily explains the need for the numerous modifications of the basic AISI 52100 for varying section thicknesses of the bearing components.

Hardenability is also influenced by the effect of grain size and the degree of hot-working. The hardenability of coarse-grained steel is much greater than that of fine-grained steel. Hot-working of material into progressively smaller bar sizes correspondingly reduces the hardenability spread found in ingots and blooms by reducing the segregation of carbon

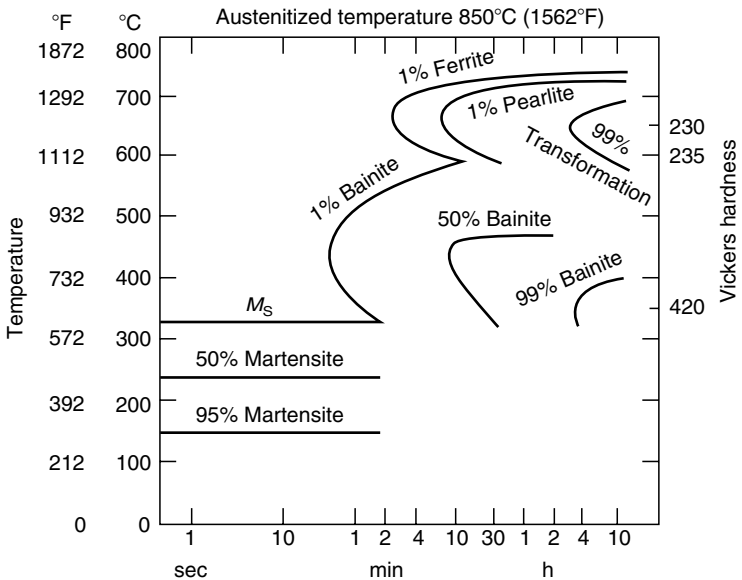


FIGURE 13.10 Time–temperature transformation diagram for AISI 4337 steel. (From SKF Steel, *The Black Book*, Vol. 151, 1984. With permission.)

and other alloying elements normally experienced during ingot solidification. Higher austenitizing temperatures and longer soaking times at temperatures that promote grain coarsening also enhance hardenability by permitting more carbon to go into solid solution.

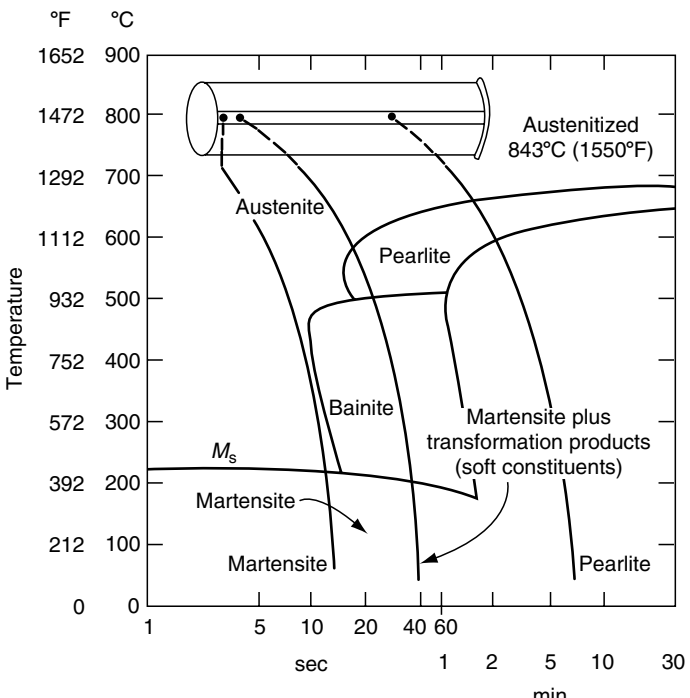


FIGURE 13.11 CCT diagram for AISI 52100 steel.

Because hardenability is a measure of the depth of hardness achieved under perfect heat treatment parameters, it is possible to quench bar products varying in diameter and to measure the resulting cross-sectional hardness patterns to determine hardenability. Grossman [21] defined the ideal critical size of a bar processed in this manner to be one in which the core hardens in an ideal quench to 50% martensite and fully to 100% martensite at the surface. An ideal quench is one in which the surface of the treated test specimen instantaneously reaches the quench medium temperature. Quenching identical specimens in media of less severity reduces the extent of hardening. Under these conditions, Grossman defined the smaller bar diameter that hardened to 50% martensite in the core as the “actual critical diameter.” This variance led to the development of severity quench curves (H-values) relating to both the ideal critical diameter and the actual critical diameter.

The Jominy end-quench hardenability test is standardized [22] with respect to the specimen geometry, apparatus, water temperature, and flow rate such that all results can be rated on a comparison basis. The hardness ratings at 1.6 mm (0.0625-in.) intervals when plotted against specimen length provide a curve indicative of the hardenability of an alloy. End-quench hardenability data normally incorporate both the maximum and minimum hardenability limits anticipated under specific heat treatment parameters [23].

13.5.5 HARDENING METHODS

Heat treatment practices used for bearing components are either through-hardenning or surface hardening. Heat treatments for the through-hardenning martensitic grades are substantially comparable in that they necessitate heating (to an austenitizing temperature), quenching, washing, and tempering. Time-temperature parameters, primarily based on weight and cross-sectional thickness of the part that is processed, have been established for the various through-hardenning bearing alloys.

Ring components, particularly of large diameter and thin section thickness, require elaborate means of handling to minimize physical damage. In furnace construction, precautions are taken to avoid mass loading and excessive weight, which could adversely influence the geometry of the parts during heating or quenching.

Furnace manufacturers generally use natural gas or electricity as their heat source for equipment. Arrangements for protective atmospheres are normally provided to minimize carburization or decarburization of the high-carbon-chromium steel parts during processing. Furnaces of comparable construction and processing capability are also selected for the heat treatment of carburizing grades of steel except that the atmosphere is controlled to provide the carbon potential necessary for carbon to diffuse into the steel.

Precise, uniform furnace temperatures are maintained and controlled, providing exact reproducibility of processing cycles. Adequate quenching facilities are provided for salt, oils, water, or synthetic-type quenchants. Temperature control, agitation, and fixtures are used independently or in combination to reduce distortion in the heat-treated components.

Induction heating, often using synthetic-type quenchants, can be used for automated heat treatment of special bearing components. This can be a selective-type heat treatment in which only the rolling contact surface is hardened.

After hardening, the parts are washed to remove all quenchant residue before tempering. Tempering furnaces are generally electric or gas-fired. Parts may be either batch loaded or automatically transported through these units.

Many types of furnaces are used to process bearing components: for example, roller hearths, rotary drums, rotary hearths, shaker hearths, batch and pit types, conveyor belt and cast link types, and pusher trays. In addition, automated salt lines using

programmable hoists are in operation for steels requiring austenitizing temperatures of 802–1302°C (1475–2375°F).

13.5.6 THROUGH-HARDENING, HIGH-CARBON–CHROMIUM BEARING STEELS

13.5.6.1 General Treatment

The high hardness and high strength required for through-hardening bearing steels are achieved by first austenitizing at a temperature sufficiently high to provide carbon solution and then cooling sufficiently fast into the bainite or martensite temperature ranges to avoid the formation of undesirable soft constituents. Heat treatment of these steels generally involves temperatures of approximately 802–871°C (1475–1600°F), uniform soaking and quenching into a medium of salt, water, or synthetic oil, controlled between approximately 27°C and 230°C (80°F and 445°F). The resulting “as-quenched” hardness range for martensite-hardened components is normally Rockwell C (R_C) 63–67; for bainite-hardened components, R_C 57–62. Although bainite-hardened components do not require subsequent thermal treatment, martensite-hardened components are tempered.

13.5.6.2 Martensite

The MS temperature is lowered as the austenitizing temperature and the time at temperature are increased, permitting more carbon to go into solid solution. Correspondingly, the tendency exists for more austenite to be retained during the martensite transformation. The morphology of the resultant martensite also depends on the dissolved carbon content: high amounts of dissolved carbon are associated with plate martensite formation, and low amounts promote a tendency to form lath martensite.

High austenitizing temperatures also have the tendency to coarsen the material grain size. This condition is evident both visually and under low-power magnification of fracture surfaces. Properly heat-treated, high-carbon–chromium grades of steel show a fine, silk-like appearance on fracture faces.

After quenching, components are washed and tempered to relieve stresses and improve toughness. Tempering at temperatures at or slightly above the MS point will also transform the retained austenite to bainite. The penalty for tempering at higher temperatures is the loss of hardness, which can adversely affect the load-carrying capacity and endurance of the bearing component. Components of lower hardness are also more prone to handling and functional surface damage than their harder counterparts.

13.5.6.3 Marquenching

Quenching into a low-temperature medium (49–82°C [120–180°F]) can produce thermal shock and nonuniform phase transformation stresses. Components with nonuniform cross-sections or sharp corners can warp or fracture. Transformation stresses may be reduced by quenching the part into a hot-oil or hot-salt medium controlled at a temperature between 177°C and 218°C (350°F and 425°F), the uppermost portion of the martensite transformation range. Temperature equalization throughout the cross-section of the component permits uniform phase transformation to progress during subsequent air cooling to room temperature. Although the as-quenched hardness is normally R_C 63–65, tempering cycles for marquenched parts are similar to those used in straight martensite hardening.

13.5.6.4 Bainite

Bainite hardening is an austempering-type heat treatment in which the component is quenched from the austenitizing temperature to a temperature slightly above the MS

temperature, which is the lower bainite transformation zone. Molten salt baths between 220 and 230°C (425 and 450°F) are normally used for this type of heat treatment. Water can be added to the quench bath to achieve the critical quench rate, thus avoiding the formation of undesirable soft constituents. Bainite-hardening grades of steel are again selected on the basis of component cross-sectional area. The higher the hardenability, the greater is the permissible cross-sectional area or thickness of a given component. As the alloy content increases, the nose and knee of the transformation curve are pushed further to the right, which lengthens the time for bainite transformation to begin.

These alloys normally require 4 hours or more for complete transformation to bainite. Hardness values of R_C 57–63 are achieved in components processed in this manner; subsequent tempering is not required. Quenching into molten salts and holding at these temperatures significantly reduce stresses induced due to thermal shock and phase transformation.

Bainite hardening produces components with small compressive surface stresses, in contrast to martensite hardening, which produces small tensile stresses in the as-quenched surface layers. A bainite microstructure is coarser, with a more feathery needle than that produced in straight martensite hardening.

13.5.7 SURFACE HARDENING

13.5.7.1 Methods

Surface hardening is done by altering the chemical composition of the base material—for example, by carburizing or carbonitriding—or by selectively heat treating the surface layer of a given high-carbon bearing steel component. Induction-hardening and flame-hardening are used to fabricate production bearings. Laser beam and electron beam processes are also possible, depending on the hardness depth required.

Surface hardening of bearing steels produces well-defined depths of high surface hardness and wear characteristics as well as residual compressive stresses in the surface layer. These compressive stresses generally tend to enhance rolling contact fatigue resistance. The surface layer is supported by a softer and tougher core, which tends to retard crack propagation.

13.5.7.2 Carburizing

The carburizing source or medium (gas, liquid, or solid) supplies carbon for absorption and diffusion into the steel. The same precautions followed for through-hardening furnace operations are followed in carburizing to minimize handling damage, to reduce part distortion, and to provide process economy. The normal carburizing temperature range is 899–982°C (1650–1800°F), with the carbon diffusion rate increasing with temperature. Therefore, it is easier to control narrow case depth ranges at the lower carburizing temperatures.

Based on the alloy steel that is processed, time, temperature, and atmospheric composition determine the resulting carbon gradient. The resulting carbon content affects the hardness, the amount of retained austenite, and the microstructure of the carburized case. The hardness profile and compressive residual stress field depend on the carbon profile.

Although the practice of quenching directly from the carburizing furnace is used to heat-treat bearing components, it is a general practice to reharden carburized components to develop both case and core properties and, at the same time, to employ fixture-quenching devices to reduce part distortion.

Based on the grade of steel that is carburized, the carbon potential or the furnace atmosphere must be adjusted so that large carbides or a carbide network are not formed. Alloying elements such as chromium, which lower the eutectoid carbon content, are most likely to form globular carbides. Carbon can be further precipitated to the grain boundaries if

the steel is then slowly cooled before quenching. These grain boundary carbides and the carbide network can reduce mechanical properties.

Choosing the bearing material not only involves proper surface hardness and microstructure, but it also must incorporate the core properties to prevent case crushing. Resistance to case crushing is generally provided by increasing the subsurface strength. Therefore, a material with a section thickness and hardenability that will provide a core hardness of R_C 30–45 is selected. Carburizing grades should be fine grained to minimize sensitivity to grain growth at high carburizing temperatures.

Direct quenching from the carburizing furnace has the advantage that a case microstructure can be obtained free of soft constituents, such as bainite, while using a leaner alloy steel. This heat treatment practice offers less part distortion than is experienced in reheating and quenching, particularly if the temperature is lowered to 816–843°C (1500–1550°F) before quenching. Adversely, this practice can produce parts with too much retained austenite and possible microcracking. The excess austenite in the case could permit plastic deformation of components under heavy loads; microcracking could provide initiation points for fatigue. Microcracking can be minimized by keeping the carbon content in the as-carburized component lower than the eutectoid level. Reheating at the lower austenitizing temperature and quenching tend to reduce microcracking.

Gas carburizing is common to the roller bearing industry because the gas flow rates and carbon potential of the atmosphere may be accurately controlled. Gases present in furnace atmospheres include carbon dioxide, carbon monoxide, water vapor, methane, nitrogen, and hydrogen.

Over a period of time at a predetermined temperature, the specified case depth is established. This effective case depth (ECD) is generally defined as the perpendicular distance from the surface to the farthest point where the hardness drops to R_C 50. Normal ECDs for bearing components range between 0.5 and 5 mm (0.020–0.200 in.), with a surface carbon content between 0.75% and 1.00%.

Carburized components are tempered after quenching to increase their toughness. Cold-treating might be introduced to transform the retained austenite to martensite. Additional tempering is then required.

13.5.7.3 Carbonitriding

Carbonitriding is a modified gas-carburization process. Because of the health hazards and ecological problems in disposing of cyanide salts, the preferred method is to use a gaseous atmosphere. At an elevated temperature, an atmosphere is generated that has a given carbon potential to which ammonia is added. Nitrogen and carbon are diffused into the steel forming the hard, wear-resistant case. Because these hard carbonitrided cases are generally shallow in nature, ranging from approximately 0.07 to 0.75 mm (0.003 to 0.030 in.), produced at furnace temperatures ranging from 788 to 843°C (1450 to 1550°F), the case–core interface is easily differentiated. These same beneficial shallow case characteristics can also be achieved in components requiring excessively heavy case depths. In this instance, the parts are generally carburized to the heavy case depths and then reheated in a carbonitriding atmosphere.

Ammonia added to the carburizing atmosphere dissociates to form nascent nitrogen at the work surface. The combination of carbon and nitrogen adsorbed into the surface layer of the steel lowers the critical cooling rate of the steel; that is, the hardenability of the steel is significantly increased by the nitrogen. This characteristic permits lower-cost materials, such as AISI 1010 and 1020, to be processed to the desired high hardness by oil quenching and thus minimizing distortion during heat treatment.

As all parameters are constant, the carbonitrided component will result in a more uniform case depth than that produced by carburizing. Because nitrogen lowers the transformation temperature, carbonitrided components have more retained austenite than carburized components of the same carbon content. These high levels of austenite may be reduced by increasing the carbonitriding temperature, controlling the surface concentrations to approximately 0.70–0.85% carbon, keeping the ammonia content at a minimum during processing and introducing a diffusion cycle before quenching.

The presence of nitrogen in the carbonitrided case also enhances resistance to tempering. Carbonitrided components are tempered in the 190–205°C (375–400°F) range to increase the toughness and to maintain a minimum hardness of R_C 58.

13.5.7.4 Induction Heating

Induction heating is a means for rapidly bringing the surface layer of a high-carbon–low-alloy bearing steel component into the austenitic temperature range, from which it can be quenched directly to martensite. Induction heating is accomplished by passing an alternating current through a work coil or inductor. A concentrated magnetic field is then induced within the coil. This magnetic field will in turn induce an electrical potential in a part placed within the coil. As a part represents a closed circuit, the induced potential establishes an electrical current within the part. Heating of the part is then the result of the material's resistance to the flow of induced current.

Power generating equipment is selected according to frequency requirements. Motor generators have historically been used to provide medium frequency ranges from 1 to 10 kHz and to provide deep, hardened surface layers. These units are currently replaced by solid-state inverters using silicon-control-rectifier (SCR) switching devices. Radio frequency generators provide frequencies ranging from 100 to 500 kHz for very shallow case depth requirements.

The chief factors influencing the success of the induction-heating operation are frequency selection, power density, heating time, and coupling distance:

- Frequency selection: the size of the part and the depth of heating desired dictate the frequency requirement.
- Power density: the watts available per mm^2 of inductor surface influence the depth to which a part can be surface hardened.
- Heating time: the heating time required to bring the part to temperature is a critical factor with respect to overheating and the resulting case depth.
- Coupling distance: the coupling distance is defined as the distance between the coil and the part surface.

Quenching of induction-hardened components is generally accomplished by either a spray or immersion method. Spray quenching involves a pressure deposition of the quenchant onto the component by a series of holes machined into the inductor or by a separate quench ring. The immersion method necessitates dropping the part out of the inductor into an agitated quench bath. The required physical and metallurgical properties in high-carbon–chromium bearing steel can be achieved by using a synthetic quenchant in lieu of water or oil. Concentrations may be adjusted to provide maximum quenchability while minimizing the tendency for cracking.

All surface-hardened components require tempering after quenching. Although the case depth may be similar to those achieved by carburizing, a steeper hardness gradient exists in the case–core transition zone.

Properly induction-hardened AISI 52100 steel bearing components will generally achieve hardness values of R_C 65–67 as quenched. If the part before heat treatment is in the annealed condition, the microstructure of the as-hardened surface zone will consist of fine spheroidal carbide and a matrix of untempered martensite. When it is examined for fractures, a fine grain size can be seen.

13.5.7.5 Flame-Hardening

Flame-hardening is used primarily in the heat treatment of rings of high-carbon–low-alloy steel components, generally more than 1 m (approximately 3 ft) in diameter. A combustible gas is mixed with oxygen to fire a cluster of burners directed to selectively heat the ring component as it rotates at a fixed rate through the impinging flame. The depth of the heat-affected zone is a function of the dwell time of the part at the heat source. The rotating part, on reaching the proper austenitic temperature, is water quenched. The core material, in the unaffected heat zone, remains in the annealed condition. Subsequent tempering is mandatory to relieve stresses and increase the ductility of the as-quenched component.

Flame-hardening is not a capital-intensive process from an equipment standpoint. It is very versatile for selective hardening and rapidly adaptable for changing ring sizes with varying cross-sectional configurations and thicknesses.

The progressive zone heating method means an overlap will occur after 360° is completed. The resulting over-tempering effect in the heat sink zone will result in a spot of lower hardness. Precautions must be taken to minimize the thermal and transformation stresses at the overlap point to prevent cracking.

13.5.8 THERMAL TREATMENT FOR STRUCTURAL STABILITY

A knowledge of size and shape changes in rolling bearing components occurring in heat treatment is critical to subsequent manufacturing operations and to the component's functional suitability. Basic high-carbon–low-alloy steel with a bcc structure expands rapidly (Figure 13.12) as it is heated to approximately 727°C (1340°F). At this critical temperature,

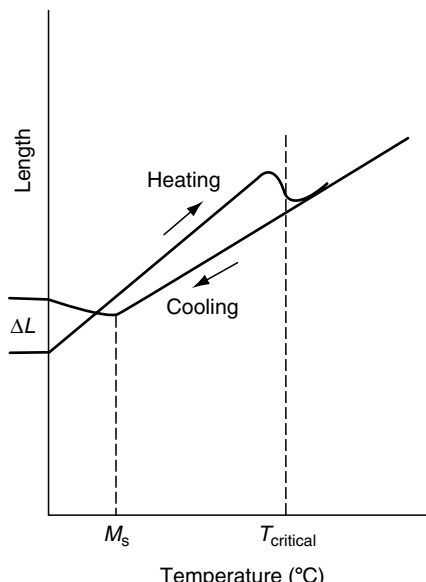


FIGURE 13.12 Volume changes during heating and quenching (hardening) of high-carbon bearing steel.

the material undergoes phase transformation to an fcc structure (i.e. austenite), resulting in component shrinkage. The specific volume of austenite is less than that of ferrite. If the material is heated to still higher temperatures within the austenite range, it continues to increase in volume. Conversely, when rapidly cooled, the material shrinks to the martensite transformation temperature. The martensite, formed as the part continues to contract while cooling to room temperature, has a bct structure. The resulting increase in volume, due to this transformation occurring at such low temperatures, stresses the material. Because it is virtually impossible in production heat treatment to complete the transformation from the austenitic (fcc) structure to the untempered martensite (bct), varying amounts of austenite, depending on the severity of the quench, are retained in the as-quenched microstructure. Components must be thermally treated to reduce the residual stresses and to provide the required structural stability.

Dimensional changes occurring in bearing steels essentially depend on the precipitation of fine carbide from martensite and decomposition or transformation of retained austenite. Because changes can also be induced during bearing operation, due to the temperature or stress environment, the manufacturer must select the appropriate heat treatment to provide the required stability. Tempering of high-carbon-chromium steels generally occurs in the range 66–260°C (150–500°F). At these temperatures, fine carbide is precipitated, and the tempered martensite remains essentially bct with some shrinkage. Tempering in the range 205–288°C (400–550°F) results in a time-temperature-dependent decomposition of the retained austenite to bainite and a volume increase. Loss of hardness at high temperatures is prevented by tempering below 260°C (500°F).

The annealed microstructures of high-speed steels, providing maximum machinability, contain numerous hard metallic carbides, such as tungsten, molybdenum, vanadium, or chromium, imbedded in a soft ferritic matrix. Unlike the high-carbon-chromium steels, temperatures far above the critical temperature must be attained to dissolve the desired amount of these hard carbide particles. Carbide precipitation is avoided by rapidly cooling the steel from the austenitizing temperature into the martensite transformation temperature range. After further cooling to room temperature, the structure normally contains 20–30% retained austenite. Heating to temperatures required for tempering high-carbon-chromium steel produces only slight tempering of the martensite. Between 427 and 593°C (800 and 1100°F), “secondary hardening” occurs; that is, the austenite is conditioned and subsequently transforms to martensite on cooling back through the MS temperature transformation range. Multiple tempering at these high temperatures is required to complete the transformation of austenite to martensite and to precipitate very fine alloy carbides, which are responsible for the secondary hardening phenomenon and which provide for the high-temperature hardness retention characteristic of high-speed steels.

Subzero treatments are often used after the initial quench or intermittently between tempering cycles to complete austenite-to-martensite transformation on cooling. However, because cold treatment sets up high internal stresses in the as-quenched components, it is generally recommended that cold treatment be practiced only after the first tempering cycle.

Corrosion-resistant steels, for example, AISI 440C and BG42 (AMS 5749), are generally heat-treated incorporating deep freezing immediately after rapid cooling from the austenitizing temperature. AISI 440C may be subsequently multiple tempered at approximately 149°C (300°F) or 316°C (600°F), depending on the product hardness requirements. Because of its alloy composition, BG42 is heat-treated according to standard practices for high-speed steels; that is, multiple tempering at 524°C (975°F) incorporating refrigeration cycles.

Retained austenite, present in the case microstructure of case-carburized steels, is a relatively soft constituent providing some tolerance for stress concentrations arising from inclusions, handling damage, and surface roughness. Case properties are preserved by

generally tempering bearing components from 135 to 196°C (285°F to 385°F). The core is stable at normal bearing operating temperatures.

13.5.9 MECHANICAL PROPERTIES AFFECTED BY HEAT TREATMENT

13.5.9.1 Elasticity

The elastic properties of rolling bearing steels are not significantly affected by heat treatment. Hence, the modulus of elasticity at normal temperatures is 202 GPa (29.3×10^6 psi) for both through-hardened and case-hardened steels.

The limit of elastic behavior, that is, the stress under maximum uniaxial loading giving insignificant plastic deformation or permanent set, is described for rolling bearing steels by a 0.2% offset yield strength (0.2% remaining plastic strain). Figure 13.13 illustrates that strength properties tend to decline as the transformation temperature increases for a given rolling bearing steel composition.

13.5.9.2 Ultimate Strength

Ultimate strength is the stress at which the sample breaks in the uniaxial test described before; it is significantly affected by heat treatment. For through-hardened AISI 52100, the ultimate strength for martensitic steel generally lies between 2900 and 3500 MPa (420 and 510 ksi). For the best case-hardened bearing steels, for example, AISI 8620, the ultimate strength approximates 2600 MP_a (380 ksi).

13.5.9.3 Fatigue Strength

Fatigue strength is determined in a cyclic push-pull or reversed bending test as the maximum stress that can be endured with no failure before accumulating 10 million cycles. These data

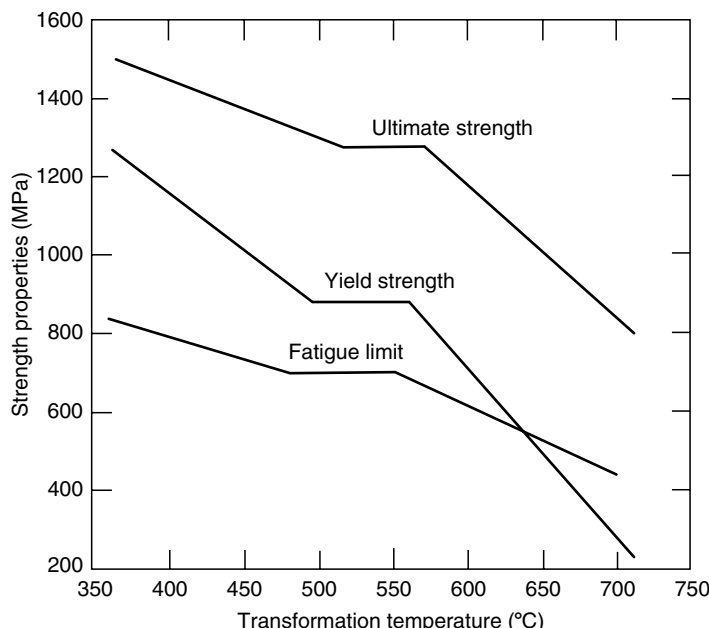


FIGURE 13.13 Properties of a 0.8% C steel vs. transformation temperature.

depend strongly on heat treatment, surface finish and treatment, test conditions, and so on. Accordingly, it is difficult to generalize and no numerical values are given herein. It is best to test the individual steel.

13.5.9.4 Toughness

Two test methods are used to determine the toughness of bearing steels: the fracture toughness test and the impact test. In the first, a plain stress value K_{IC} is measured in $\text{MP}_a \text{m}^{1/2}$; this is the stress related to the defect size that can be tolerated without incipient structural failure. For martensitic AISI 52100, K_{IC} falls between 15 and 22, depending on the heat treatment. A slight increase in K_{IC} occurs as temperature increases. Case-hardening steel tends to have a greater fracture toughness than through-hardening steel. A K_{IC} value of 60 is not uncommon for surface-hardened steel.

The second test—the impact of a hammer blow of defined energy on a sample—measures the energy absorbed in breaking the sample. For martensite-hardened AISI 52100, this is only 4.5 J (3.3 ft-lb) compared with 172 J (127 ft-lb) for the soft annealed material.

13.5.9.5 Hardness

The manner in which carbon is distributed in steel dictates the resulting hardness and mechanical properties. Although carbon makes by far the greatest contribution to hardness, increasing the alloy content also increases hardness.

Hardness, a material's resistance to penetration, and hence wear, can be measured by static or dynamic methods. Static testing involves applying a load through a penetrator of defined geometry. Depending on the type of hardness tester employed, either the depth of penetration or the size of the indentation becomes the measurement of the material hardness. See Figure 13.14.

Dynamic testing involves bouncing a diamond-tipped hammer from a specific height onto the surface of the test specimen. The resultant rebound height is a measure of material hardness. The scleroscope is the only piece of equipment based on the dynamic test principle.

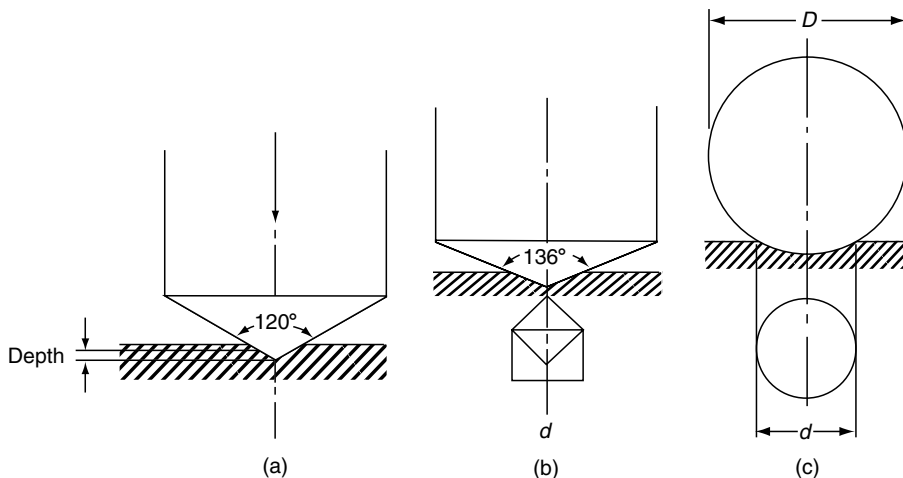


FIGURE 13.14 Hardness tests. (a) Rockwell R_C ; indentation body: diamond cone, load 150 kgf (including 10 kgf preload), indentation depth for R_C 63: 74 μm , hardness testing range: R_C 20–67. (b) Vickers; indentation body: diamond pyramid 136°, indentation depth: $1/\sqrt{d}$ —for V 782 $\approx R_C$: 22 μm , hardness testing range: up to V 2000. (c) Brinell; indentation body: hardened steel ball (D), hard metal ball (d), indentation depth: $1/5d$, Hardness testing range: up to 400 B (~42.5 R_C), up to 600 B (~57 R_C).

13.5.9.6 Residual Stress

Stresses induced in a component through fabrication or thermal treatments are totally eliminated on uniform heating and soaking in the austenite temperature range. Quenching of the component can once again generate tremendous internal stresses in the part. Through-hardening of the martensitic high-carbon steels may produce surface tensile stresses that can produce part distortion or even cracking. Surface-hardening heat treatments, including carburizing, carbonitriding, induction, or flame-hardening, generally produce parts showing surface compressive stresses. Regardless of the heating method selected for austenitizing, subsequent thermal cycles with or without subzero treatment can appreciably alter the established stress state in the as-quenched parts.

The stresses induced in a through-hardened component during quenching are principally the results of temperature variations and nonuniform phase transformations. Bearing rings, essentially thin hoops of varying cross-section thicknesses, are prone to both size and shape changes. Fixture quenching, employed to retain the components' as-machined dimensional characteristics, may hamper quench medium flow and induce additional nonuniform stress distribution in the part because of mechanical restraints that do not adapt to size or shape changes. The machined undercuts, grooves, filling slots, oil holes, and flanges having sharp corners, and recesses provide additional focal points for stress concentration.

The high-carbon-chromium bearing steels under recommended austenitizing temperatures have an MS temperature range of approximately 204–232°C (400–450°F). Increasing the carbon content and various alloying elements in this family of steels will tend to depress the MS temperature. Coarse-grained materials will also have a lower MS point than fine-grained materials of the same chemistry. Therefore, austenitizing at very high temperatures will reduce the MS point into the range where the material is less able to adjust plastically. The higher the austenitizing temperatures, the higher the thermal gradients occurring in the parts during quenching. Subzero treatments that permit the austenite-to-martensite transformation to be further completed could cause high stress levels, which can crack the parts. Bainitic heat treatment or martempering will appreciably reduce transformation stresses during quenching.

It is standard practice in the rolling bearing industry to cool martensite-hardened parts to room temperature from the quenching bath, wash the parts, and subject them to a tempering cycle. A low-tempering temperature for a long time is equivalent to a high temperature for a short time from the standpoint of reducing the residual component stresses. This sequence of operation may be interrupted by a subzero treatment following the washing operation to permit the completion of the austenite-to-martensite transformation. Parts processed in this manner are very prone to cracking because of the resulting high residual stress state. These parts must be tempered as soon as they are warmed to room temperature.

Surface-hardening heat treatments, by a diffusion process altering the composition of the material or by the rapid heating of a selected surface area of a homogeneous steel, are developed and controlled to provide surface compressive stresses with normal counterbalancing tensile stresses in the core. Induction surface hardening of an appropriate material to the proper case depth results in the maximum compressive stress located at the case–core transition zone. The magnitude of this compressive stress in a surface-hardened high-carbon steel alloy will normally be less than that produced in a carburized part at its point of maximum compressive stress, which is at the approximate midpoint of the total case depth. This point corresponds to the carbon content of approximately 0.50%.

Tempering of as-quenched, surface-hardened components with or without the support of subzero treatment will generally reduce the retained austenite level and modestly alter the level of compressive stresses.

13.6 MATERIALS FOR SPECIAL BEARINGS

For most rolling bearing applications, the through-hardening steel AISI 52100 and case-hardening steels described in [Table 13.2](#) are sufficient to provide good performance characteristics such as fatigue and wear resistance, appropriate fracture toughness, and consistently reliable mechanical properties. The advent of the aircraft piston engine, however, created the demand for long-lived endurance at higher operating temperatures. This demand was met by using the tool steels M1, M2, M10, and T1. These steels lost their prominence in the 1950s with the introduction of vacuum-melted M50 to meet the needs of aircraft gas turbine engine bearings. In many applications, particularly instrument ball bearings, corrosion resistance became important and this requirement was met by using AISI 440C and BG42 stainless steels generally at the sacrifice of fatigue endurance when compared with bearings fabricated from AISI 52100. Because of light applied loading, however, fatigue endurance is not a major consideration in such applications. The chemical composition of some of the foregoing steels are given in [Table 13.3](#).

The exploration of space and the continuing development of the aircraft gas turbine engine provided the demand for yet increased development of exotic materials. Examples are sapphire for balls, precipitation-hardening stainless steels, and nickel-based superalloys. Additionally, the nuclear power industry created the need for cobalt alloys such as L605, Stellite-3, and Stellite-6. Powder metal-forming techniques have now provided the means to create steels of differential properties; for example, extremely hard, corrosion-resistant surfaces combined with tough, high-strength substrates.

The requirement for aircraft gas turbine engine mainshaft ball and roller bearings to operate at ever-increasing speeds initiated the search for a relatively high-temperature capability, fracture-tough steel. Because of the bearing ring hoop stresses caused by ring centrifugal stresses and rolling element centrifugal forces at high speeds, fatigue spalls under such conditions can lead to fracture of rings fabricated from through-hardening steels such as M50. Thus, the operating speeds of aircraft gas turbine engines were limited to approximately 2.4 million dN (bearing bore in mm \times shaft speed in rpm). With the development of M50-NiL, a case-hardening derivative of M50 whose chemical composition is shown in Table 13.3, this limitation has been overcome.

The need for bearings to operate at ultrahigh temperatures has triggered the development of cemented carbides and ceramics as rolling bearing materials. Materials such as titanium carbide, tungsten carbide, silicon carbide, sialon, and particularly, silicon nitride have been developed. At elevated temperatures, these materials retain hardness, have corrosion resistance, and provide some unique properties, some of which are advantageous, such as low specific gravity for silicon nitride. Conversely, other properties of these materials, such as extremely high elastic modulus and low thermal coefficient of expansion for silicon nitride as compared with steel, create significant bearing design problems that must be overcome if these materials are to succeed for use in rolling bearing structure components, particularly rings. Ceramic materials such as silicon nitride, as illustrated in [Figure 13.16](#), commence life as powders that after a series of processes, principal among which is hot-isostatic pressing, are transformed into highly engineered bearing components.

[Table 13.4](#), excerpted from Pallini [24], gives significant mechanical properties and allowable operating temperatures for several of the materials described above. Considering the low

TABLE 13.4
Properties of Special Bearing Structural Materials

Material	Rockwell Hardness (room temp.)	Max. Useful Temperature °C (°F)	Specific Gravity	Elastic Modulus GPa (psi × 10 ⁶)	Poisson's Ratio	Coefficient of Thermal Expansion 10 ⁻⁶ /°C (10 ⁻⁶ /°F)
440C stainless steel		260 (500)	7.8	200 (29)	0.28	10.1 (100°C) (5.61)
M50 tool steel	62	320 (600)	7.6	190 (28)	0.28	12.3 (300°C) (6.83)
M2 tool steel	64	480 (900)	7.6	190 (28)	0.28	12.3 (300°C) (6.83)
T5 tool steel	66	560 (1050)	7.6	190 (28)	0.28	11.3 (6.28)
T15 tool steel	65	590 (1100)	8.8	190 (28)	0.28	11.9 (6.61)
Titanium carbide cermet	67	800 (1470)	8.2	390 (57)	0.23	10.47 (5.94)
Tungsten carbide	78	815 (1500)	14.0	533 (77.3)	0.24	5.9 (3.28)
Silicon nitride		1200 (2200)	3.2	310 (48)	0.26	2.9 (1.61)
Silicon carbide	78	1200 (2200)	3.2	410 (59)	0.25	5.0 (2.78)
Sialon 201	90	1300 (2372)	3.3	288 (42)	0.23	3.0 (1.67)

density and high elastic modulus of hot isostatically pressed (HIP) silicon nitride (Si_3N_4) as compared with steel, [Figure 3.15](#) through [Figure 3.17](#) in the companion volume of this handbook compare the performance parameters of a 218 angular-contact ball bearing that has HIP silicon nitride balls with those of the bearing having steel balls. It can be seen that, at high speeds, there is a tradeoff between reduced ball load and increased contact Hertz stress. [Figure 13.17](#) from Ref. [24] indicates the frictional properties of HIP silicon nitride when used with various types of lubricants. It is apparent that for sustained low-friction operations, bearings with HIP silicon nitride balls require oil lubrication. It is usual for standard ball bearings to have raceway groove curvature radii equal to $0.52\text{--}0.53D$, where D is the ball diameter. For applications using bearings with HIP silicon nitride balls, it is possible to reduce one or both of these radii to, for example $0.51\text{--}0.515D$, thereby decreasing Hertz stresses. Unfortunately, this action also causes an increase in contact friction; therefore, ball bearings using HIP silicon nitride balls may have their designs optimized for Hertz stress (and hence fatigue life) or friction. Considering the basically straight contour raceways, this option is not available for cylindrical or tapered roller bearings.

[Figure 13.17](#) further shows that irrespective of fluid or dry-film lubrication, the friction coefficient of HIP silicon nitride is dependent on the operating temperature and environment. It has been demonstrated, however, that when lubricant flow is interrupted, steel bearings

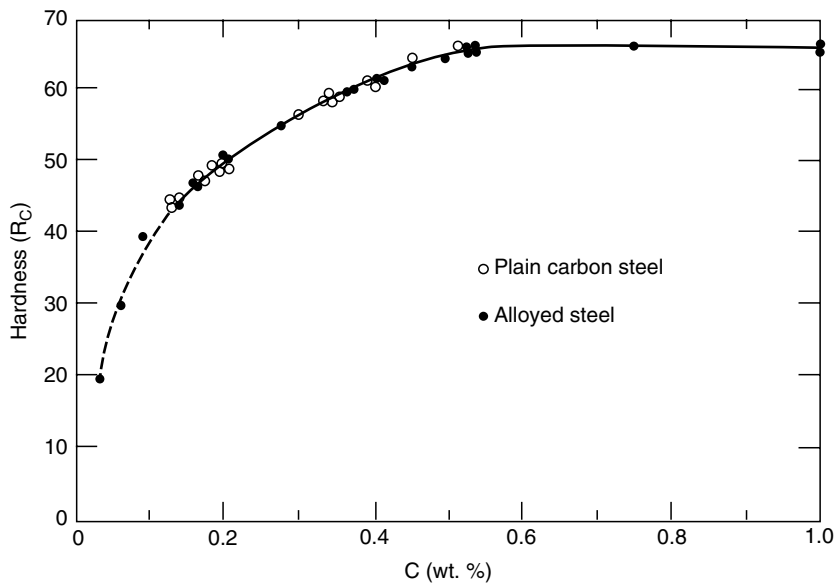


FIGURE 13.15 Maximum hardness vs. carbon content.



FIGURE 13.16 Bearing quality silicon nitride begins life as a powder before a series of processes transforms it into a highly engineered bearing component. (Photograph courtesy of SKF.)

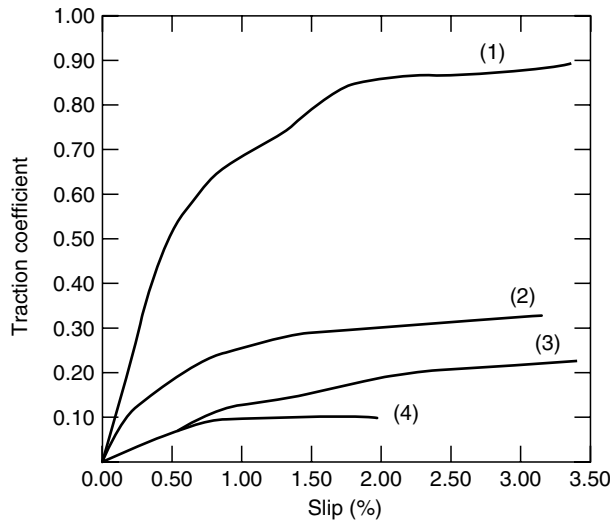


FIGURE 13.17 Traction coefficient vs percent slip in the contact between two bodies of hot-pressed silicon nitride. Contact stress is 2,068 MP_a (300,000 psi); nominal speed is 3,800 mm/sec (150 in./sec). (From Pallini, R., Turbine engine bearings for ultrahigh temperatures, *Ball Bearing J.*, SKF, 234, 12–15, July 1989. With permission.) Operating conditions: (1) 25°C (77°F)—dry contact; (2) 370°C (698°F)—graphite lubrication; (3) 538°C (1000°F)—graphite lubrication; (4) 25°C (77°F)—oil lubrication.

with HIP silicon nitride balls will sustain operation longer without seizure as compared with the same bearings with steel balls.

While the compressive strength of HIP silicon nitride is excellent, the tensile strength is only about 30% that of M50 steel. The fracture toughness is also only a small percentage of that of M50 steel, let alone M50-NiL steel. Furthermore, although in rolling contact under a heavy load the material tends to fail by surface fatigue and even tends to have longer fatigue life than steel, any disruption of the surface can lead to rapid crumbling of the surface under continued operation. Means for failure detection are therefore an important consideration in life-critical applications.

13.7 CAGE MATERIALS

13.7.1 MATERIAL TYPES

The generally stated function of the rolling bearing cage is to maintain the rolling elements at properly spaced intervals for assembly purposes. It is sometimes inferred that, in normal bearing operations, the cage is not necessary; that is, it is not a highly stressed component requiring the strength of the accompanying ring components. There are more exceptions to this statement than examples. For example, mainshaft and accessory aircraft gas turbine engine bearings require AISI 4340 steel (AMS 6414 or AMS 5415) cages supplied in the hardness range of RC 28–35. These cages are also silver plated (AMS 2410 or AMS 2412) to provide corrosion resistance and added lubricity. In many bearing applications, not only do the rolling elements contact the cage pockets, but the cages themselves are either inner ring or outer ring land “riding.”

Although cages are manufactured from many types of material, including aluminum, S-Monel, graphite, nylon, and cast iron, the major bearing product lines use brass or steel. In ball bearings principally, but also in some roller bearings, polymers are replacing these metals.

13.7.2 LOW-CARBON STEEL

Plain, low-carbon strip steel, suitable for cold-forming (0.1–0.23% C) is used in the bulk fabrication of pressed, two-piece, or finger-retention-type steel cages. Two-piece cages are joined by mechanical lock joints, rivets, or welds. The material has a tensile strength of 300–400 MP_a (44–58 ksi). The AISI 4340 machined cages previously mentioned for aircraft applications have approximately 0.4% C for increased strength. Additionally, low-carbon steel tubes and forgings are used to make cages for bearing applications that need unique features for lubrication or greater material strength. Many cages are surface hardened or phosphate coated to provide improved wear characteristics.

13.7.3 BRASS

Brass cages are generally manufactured from continuously cast rounds, centrifugally cast cylinders, sand castings, or sheet metal and plate. Because of high tensile strength, 300–380 MP_a (44–55 ksi), alpha brass has poor machinability, but is readily capable of deep drawing (ductility increasing with increasing zinc content up to 38%). It is used for cold-formed, one-piece cages. When zinc is increased from 38% to 46%, a mixture of alpha and beta phases is formed. The ultimate strength is higher with the higher amounts of zinc. Adding phosphorus or aluminum provides alloys that can be centrifugally cast, readily machined, drilled, or broached for making ball and roller bearing cages. Other nonferrous brass alloys may be centrifugally cast, but they are hot-worked by upsetting or ring rolling to meet specific product requirements. Cage blanks may also be produced by extruding the centrifugally cast billet.

13.7.4 BRONZE

Silicon–iron–bronze (Cu, 91.5%; Zn, 3.5%; Si, 3.25%; Mn, 1%; and Fe, 1.20%) is an alloy recommended for ball and roller bearing cages operating at temperatures up to 316°C (600°F). The as-cast billet material must be extensively hot-worked and extruded to promote optimum material properties.

13.7.5 POLYMERIC CAGE MATERIALS

13.7.5.1 Advantages and Disadvantages

The use of polymer, particularly nylon (polyamide) 6,6, as a cage material is widespread in many rolling bearing applications. Polymeric cages have the following advantages over metallic cages in both production and operation:

1. Processing of polymeric materials often allows one-step fabrication of complex designs, thus eliminating the machining operations necessary to produce a comparable metallic retainer and saving money.
2. Polymer cages tend to be free from the debris that accompanies the production of metallic cages. The increased cleanliness contributes to reduced bearing noise.
3. Polymers are more flexible than metals. This is advantageous in cage assembly and in bearing operation under some difficult loading conditions.
4. Favorable physical properties of polymeric materials lead to cage performance advantages in many applications; for example, low density (reduced cage weight), good chemical resistance, low friction and damping properties for low torque, and quiet running.

The primary disadvantage of polymer usage is the deterioration of initial properties of the material due to temperature, lubricant, and environmental exposure. Polymer deterioration

causes loss of strength and flexibility, which is important to the cage function during bearing operation. Bearing rotation causes centrifugal forces to act on the cage, which deform it radially. Misalignment of the inner and outer rings can cause large stresses on the cage during bearing operation. Hence, the loss of cage strength can lead to failure. Therefore, polymeric material candidates must be evaluated for the rate and degree of deterioration under conditions of extreme temperature, lubricant exposure, and other environmental factors.

13.7.5.2 Rolling Bearing Polymer Cages

Some examples of polymeric cage designs are shown in Figure 13.18. Properties of cage polymeric material are

- Low coefficient of thermal expansion
- Good physical property retention, especially strength and flexibility, throughout the temperature range of operation
- Compatibility with lubricants and environmental factors
- Development of suitable cage design to minimize friction and provide proper lubrication

This list indicates essential differences between polymeric and metallic cage materials. Lubricant compatibility is rarely a factor, and loss of physical properties does not occur within bearing operating temperatures with metals. Cage design depends on the specific polymer used in a more intimate fashion than when steel or brass is used.

The low density of the material, approximately 15% that of steel, results in a low cage mass. The centrifugal force induced by a phenolic cage is consequently only 15% of the force for a steel cage. At high speeds, centrifugal force causes a cage to spread radially. The low-density



FIGURE 13.18 Polymeric cage designs. (a) Snap cage for ball bearing (nylon-6,6).



(b)



(c)

FIGURE 13.18 (Continued) (b) Cage for cylindrical roller bearing (nylon-6,6). (c) Cage for high-angular-contact bearing (nylon-6,6).

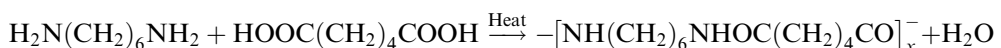


(d)

FIGURE 13.18 (Continued) (d) Phenolic cage for precision ball bearing.

cage therefore offers better dimensional stability at high speeds. Use of a phenolic resin, however, is limited to bearing applications that do not exceed temperatures of 100°C (248°F) peak. Another disadvantage with the phenolic resin is the necessity of machining operations to obtain the final shape. Other resins, discussed in the following paragraphs, can be injection molded into a final shape directly, thus reducing the process cost. Resins of this type, particularly nylon-6,6, have replaced phenolic in many rolling bearing applications.

The nylon-6,6 (polyamide 6,6) resin is the most widely used polymer for bearing cages. It provides a low material price, desirable physical properties, and low processing costs in one product. The material is constructed of aliphatic linkages connected by amide linkages to form a polymer of molecular weight between 25,000 and 40,000. Nylon-6,6 is synthesized from carbon hexamethylenediamine and adipic acid, both of which have six carbons, hence the 6,6 designation.



The material is semicrystalline and thermoplastic. It possesses many desirable properties for cage applications: strength, toughness, abrasion resistance, chemical resistance, and impact

resistance. The resin is somewhat hygroscopic (to 3%), and absorbed water causes dimensional changes that must be considered during cage design.

Product modifications containing additives are abundant for nylon-6,6. The variations provide improved physical properties, environmental inertness, and improved processing characteristics. Nylon-6,6 is thermoplastic, and hence it is an injection-moldable resin allowing direct production of complex cage shapes with obvious cost advantages. In general, resin compatibility with lubricants is very good. Cages formed from this resin exhibit a high degree of flexibility, which allows easy assembly and operation under misalignment of the inner and outer bearing rings. Glass fiber reinforcement is often used with the resin at levels of 25% fill. The glass fiber gives better retention of strength and toughness at high temperatures, but with loss of flexibility.

Rolling bearings selected from manufacturers' catalogs are designed to operate in wide varieties of applications. Therefore, the strength/toughness properties afforded to nylon-6,6 cages by glass-fiber reinforcement are required for bearing series employing such cage material. Figure 13.19, from Ref. [25], illustrates the endurance capability of 25% glass-fiber-filled nylon-6,6 as a function of the operating temperature. In Figure 13.19, the shaded band indicates the spread determined with various lubricants. The lower edge of the band is applicable to aggressive lubricants such as transmission oils (with extreme pressure (EP) additives), while the upper edge pertains to mild lubricants such as motor oils and normal greases. Table 13.5, from Ref. [25], indicates the strength, thermal, chemical, and structural properties of this material in the dry and conditioned states. The conditioned state is that in which some water has been adsorbed. By comparison of Figure 13.19 with Table 13.5, it can be seen that the permissible operating temperature of 120°C (250°F) corresponds to a probable endurance of approximately 5,000 to 10,000 hours depending on the lubricant type. This refers to continuous operation at 120°C (250°F); operation at lesser temperatures will extend satisfactory cage performance for greater duration.

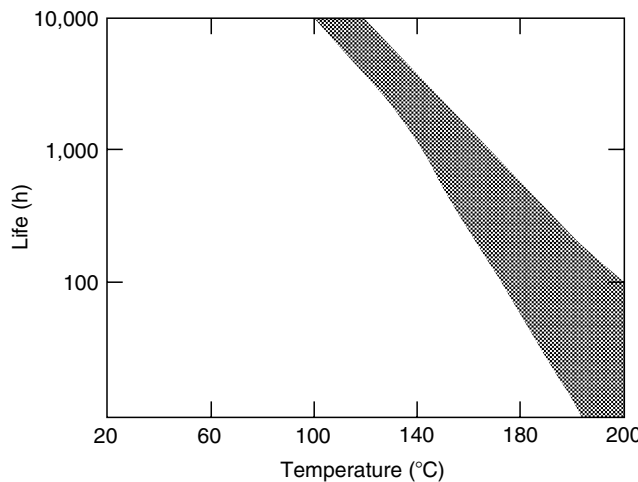


FIGURE 13.19 Life expectancy vs. operating temperature for nylon-6,6 with 25% glass-fiber fill. (From Lankamp, H., Materials for plastic cages in rolling bearings, *Ball Bearing J.*, SKF, 227, 14–18, August 1986. With permission.)

TABLE 13.5
Properties of Glass-Fiber Filled^a Thermoplastic Polymers for Cages

Property	PA ^b 6,6 dry	PA 6,6 Conditioned ^c	PES	PEEK
Tensile strength ^d	160	110	150	130
MPa (ksi)	(23.2)	(15.9)	(21.7)	(18.8)
Yield stress ^d	4	5	2.3	4.4
Bending strength ^d MPa (ksi)	270 (39.1)	230 (33.3)	210 (30.4)	240 (34.8)
Impact resistance ^d kJ/m ² (lb/in.)	30 (171)	50 (286)	30 (171)	30 (171)
Coefficient of thermal expansion $10^{-5}/^{\circ}\text{C}$ ($10^{-5}/^{\circ}\text{F}$)	2–3 (1.1–1.7)	2–3 (1.1–1.7)	2–6 (1.1–1.3)	2–3 (1.1–1.7)
Specific gravity	1.3	1.3	1.51	1.44
Operating temperature, max. °C (°F)	120 (248)	120 (248)	170 (338)	250 (482)
Operating temperature, min. °C (°F)	−60 (−76)	−60 (−76)	−100 (−148)	−70 (−94)
Resistance to grease	Good	Good	Satisfactory	Very good
Resistance to oil	Very good	Very good	Good	Very good

^aPA 6,6 has 25% glass-fiber fill;

PES and PEEK 20%.

^bNylon is a polyamide (PA).

^cConditioned refers to increased flexibility owing to absorption of a small amount of water.

^dStrength properties determined at 20°C (68°F).

Source: Lankamp, H., Materials for plastic cages in rolling bearings, *Ball Bearing J.*, SKF, 227, 14–18, August 1986.

13.7.6 HIGH-TEMPERATURE POLYMERS

A variety of high-temperature resins with and without glass-fiber fill have been evaluated for use as cage materials. Included in the list are polybutylene terephthalate (PBT), polyethylene terephthalate (PET), polyethersulfone (PES), polyamideimide (PAI), and polyetheretherketone (PEEK). Of these materials, only PES and PEEK have demonstrated sufficient promise as high-temperature bearing cage materials; these materials are discussed in further detail below.

PES is a high-temperature thermoplastic material with good strength, toughness, and impact behavior for cage applications. The resin consists of diaryl sulfone groups linked together by ether groups. The structure is wholly aromatic, providing the basis for excellent high-temperature properties. PES is thermoplastic, and so it can be processed using conventional molding equipment. This allows direct part production; that is, without subsequent machining or finishing. In lubricant-temperature exposure tests, the resin has performed well to 170°C (338°F). The material is suitable for applications using petroleum and silicon lubricants; however, there are some problems with polymer degradation after exposure to ester-based lubricants and greases. The properties of PES are also shown in Table 13.5; it can be seen that PES is not as strong as nylon-6,6. When it is desired to use a “snap-in”-type assembly of balls or rollers in a one-piece cage as illustrated in Figure 13.18, this somewhat lesser strength can result in crack formation during assembly of the bearing.

PEEK is a wholly aromatic thermoplastic that shows excellent physical properties to 250°C (482°F). It is particularly good for cage applications because of its abrasion resistance,

fatigue strength, and toughness. It is a crystalline material and can be injection molded. Lubricant compatibility tests show excellent performance to 200°C (392°F) and above. Tests also indicate antiwear performance equal to or better than nylon-6,6. [Table 13.5](#) compares the properties of PEEK with those of PES and nylon-6,6. The only known drawback to the extensive use of PEEK as a bearing cage material is cost. This currently restricts its use to specialized applications. See Ref. [26].

13.8 SEAL MATERIALS

13.8.1 FUNCTION, DESCRIPTION, AND ILLUSTRATION

To prevent lubricant loss and contamination ingress, manufacturers provide bearings with sealing. The effectiveness of the sealing has a critical effect on bearing endurance. When choosing a sealing arrangement for a bearing application, rotational speed at the sealing surface, seal friction and resultant temperature rise, type of lubricant, available volume, environmental contaminants, misalignment, and cost must all be considered.

A bearing can be protected by an integral seal consisting of an elastomeric ring with a metallic support ring, the elastomer riding on an inner-ring surface (see Figure 12.10), or by a stamped shield of mild steel staked into the outer ring and approaching the inner ring closely, but not in intimate contact with it (see Figure 12.9).

Shields cost less than seals and do not increase the torque for the bearing in operation; they are useful for excluding gross particulate contamination (150 µm). Often used with greased bearings, they are also used in bearings lubricated by liquids that must pass through the bearing. The seal configuration is more expensive because of the design and materials. Depending on seal lip design, it adds to bearing friction torque to a greater or lesser extent. Seals are used in greased bearings when moisture and all contamination must be excluded. They are also the best choice to minimize grease purging.

13.8.2 ELASTOMERIC SEAL MATERIALS

Because of the prevalence of elastomeric seals in rolling bearings, a variety of materials have been developed to meet the requirements of differing applications. Important properties of elastomeric seal materials include lubricant compatibility, high- and low-temperature performance, wear resistance, and frictional characteristics. [Table 13.6](#) summarizes the physical properties, and [Table 13.7](#) lists the general application guidelines.

In the following discussion of elastomer types, it is important to note that compounding variations starting with a particular elastomer type can lead to products of distinct properties. The general inputs to a formulated compound may be taken as follows:

- Elastomer—basic polymer that determines the ranges of final product properties.
- Curing agents, activators, accelerators—determine degree and rate of elastomeric vulcanization (cross-linking).
- Plasticizers improve flexibility characteristics and serve as processing aids.
- Antioxidants improve antifatigue and antioxidation properties of product.

Nitrile rubber represents the most widely used elastomer for bearing seals. This material, consisting of copolymers of butadiene and acrylonitrile, is also known as Buna N and NBR. Varying the ratio of butadiene to acrylonitrile has a major effect on the final product properties.

TABLE 13.6
Physical Properties of Seal Elastomers

Elastomer	Fluoroelastomers			Nitrile Rubber				Polyacrylate	Silicone
	Standard	Peroxide-Cured	Fluoro-Silicone	Standard	Heat Resistant	Hydro-Generated			
Material Designation (ASTM D1418)	FKM	FKM	FVMQ	NBR	NBR		ACM	VMQ, PVMQ	
Material Designation (ASTM D-2000/SAE J-200)	HK	HK	FK	BF, BG, BK, CH	CH, CK	DH, DK	DF, DH	FC, FE, GE	
<i>Mechanical properties</i>									
Hardness range (Durometer)	60–95	60–95	60–80	40–90	40–90	40–95	40–80	40–85	
Tensile strength	B	B	C	A	A	A	C	C	
Resilience (73°F)	C	C	C	B	B	B	C	C-A	
Tear strength	C	C	D	B	B	A	D	D	
Abrasion resistance	B	B	D	A	A	A	C	D	
Brittle point (°F)	–40	–40	–85	–40	–40	–30	–40	–90 to –180	
Adhesion to metal	C	C	D	A	A	A	BC	C	
<i>Electrical properties</i>	B	B	A	C	C	C	C	A	
<i>Resistance to</i>									
Gas permeability	A	A	D	B	B	B	B	D	
Ozone	A	A	A	D	D	A	A	A	
Weather	A	A	A	D	D	A	A	A	
Water	A	A	A	A	A	A	D	B	
Steam	B	A	C	C	C	B	NR	C	
Synthetic lubricants (diester)	A	A	A	B	B	B	D	NR	
Lubricating oils	A	A	A	A	A	A	A	C	
Aliphatic hydrocarbons	A	A	A	A	A	A	B	NR	
Aromatic hydrocarbons	A	A	A	B	B	B	D	NR	
Acids	A	A	B	B	B	B	D	C	
Bases	A	A	B	B	B	B	D	A	

A = excellent, B = good, C = fair, D = use with caution, NR = not recommended

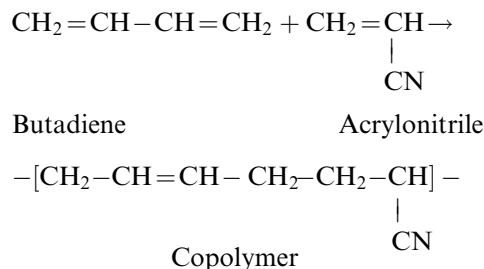
Source: From Delta Rubber Company, *Elastomer Selection Guide*. With permission.

TABLE 13.7
Application Guidelines for Seal Elastomers

Elastomer	Fluoroelastomers			Nitrile Rubber				Polyacrylate	Silicone
	Standard	Peroxide-Cured	Fluoro-Silicone	Standard	Heat Resistant	Hydro-Generated			
Material Designation (ASTM D1418)	FKM	FKM	FVMQ	NBR	NBR		ACM	VMQ, PVMQ	
Material Designation (ASTM D-2000/ SAE J-200)	HK	HK	FK	BF, BG, BK, CH	CH, CK	DH, DK	DF, DH	FC, FE, GE	
Temperature service range (°F)	-40 to 450	-40 to 450	-80 to 400	-40 to 225	-40 to 250	-40 to 300	40 to 325	-80 to 450	
Advantages	Excellent heat resistance	Excellent heat resistance	Good low-temp. flexibility	Low cost	Fair heat resistance	Good heat resistance	Moderate heat resistance	Excellent heat resistance	
	Excellent resistance to fluids and additives	Excellent resistance to fluids and additives	Good fluid resistance	Good mech. Strength	Good mech. strength	Good mech. strength	Good fluid resistance	Excellent low-temp. flexibility	
		Excellent steam resistance	Good heat resistance	Good fluid resistance	Good fluid resistance	Good fluid resistance	Resistance to EP additives		
Disadvantages	High cost	High cost	High cost	Limited heat resistance	Limited heat resistance	High cost	Poor mech. strength	Poor fluid resistance	
	Poor hot mech. strength	Poor hot mech. strength	Poor mech. strength	Attacked by EP additives	Attacked by EP additives		Poor abrasion	Poor mech. strength	
	Poor abrasion	Poor abrasion	Difficult to process					Poor water & steam resistance	
	Poor water, steam and amine resistance		Difficult to bond to						

Source: From Delta Rubber Company, *Elastomer Selection Guide*. With permission.

The general polymer reaction can be represented as



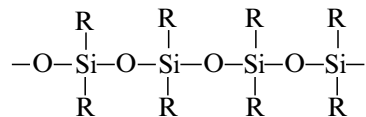
Nitrile rubbers are commercially available with a range of acrylonitrile contents from 20 to 50% and containing a variety of antioxidants. Particularly polymer selection will depend on lubricant low-temperature requirements and the thermal resistance required.

The nitrile rubber seal is used in many standard bearing application areas. Material cost is low compared with other elastomers. The material is injection-moldable, which allows one-step processing of complex lip shapes. Lubricant compatibility with petroleum-based lubricants is good for high acrylonitrile versions. This elastomer is suitable for applications to 100°C (212°F) and is therefore not indicated for high-temperature bearing applications.

Polyacrylic elastomers have been used in bearing applications. The acrylic polymer is generally based on ethyl acrylate or butyl acrylate, usually with an acrylonitrile comonomer present. As with nitrile rubbers, the higher the percentage of acrylonitrile present, the better the lubricant resistance. However, higher acrylonitrile levels degrade low-temperature properties of these rubbers. These materials are able to withstand operating temperatures up to 150°C (302°F) and, if properly formulated, show very good resistance to mineral oils and EP lubricant additives.

Negative features of this material are poor water resistance, substandard strength and wear resistance for most seal applications, and high cost. Although no longer used for high-temperature applications, it is still used when a low sealing force is required.

Silicon rubbers are used as seal materials in some high-temperature and food-containing bearing applications. Silicon rubbers have a backbone structure made up of silicon-oxygen linkages, which give excellent thermal resistance. A typical polymer is



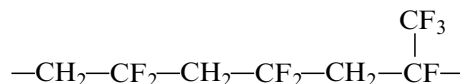
The silicon polymer is modified by introducing different side groups, R, into the structure in varying amounts. Typical organic substitutes are methyl, phenyl, and vinyl. If R = CH₃, the polymer is dimethylpolysiloxane.

Advantages of silicon rubber seal use are high-temperature performance to 180°C (356°F) and good low-temperature flexibility to -60°C (-76°F). The material is nontoxic and inert; hence it is chosen for food, beverage, and medical applications. It is stable with regard to the

effects of repeated high temperature. Its excellent low-temperature flexibility makes this elastomer useful for low-temperature applications where sealing is required.

Silicon rubbers are very expensive compared with nitrile rubbers. Lubricant resistance and mechanical strength are poor for most seal applications. On the whole, silicon elastomers have limited usefulness.

Fluoroelastomers have become increasingly popular as seal materials because of excellent high-temperature and lubricant-compatibility characteristics. Typical polymers of this class are the copolymers of vinylidene fluoride and hexafluoropropylene, which can be represented as



Materials of this general type have become common for bearing seal applications at temperatures exceeding 130°C (266°F). Suitably compounded fluoroelastomers show good wear resistance and water resistance for bearing seal applications. As would be expected, the material cost is very high compared with nitrile rubbers.

13.9 TRIBOLOGICAL COATINGS FOR BEARING COMPONENTS

13.9.1 COATINGS IN GENERAL

Several coatings exist to improve surface characteristics of bearing components without affecting gross properties of the bearing material. Within the realm of standard bearing applications, coatings are used to provide wear resistance, initial lubrication, sliding characteristics, and cosmetic improvements. In addition, bearings operating in extreme environments of temperature, wear, or corrosivity can be specially treated.

13.9.2 COATING DEPOSITION PROCESSES

13.9.2.1 General

Tribological coatings for rolling element bearings are mainly produced by gaseous or solution state processes. Gaseous state processes include chemical vapor deposition (CVD), physical vapor deposition (PVD), and ion implantation. Solution state processes include chemical solution and electrochemical deposition (electroplating). Molten and semimolten processes such as laser cladding and thermal spraying are less likely to be used for tribological purposes, but are many times used to rebuild bearing bores or to provide electrical isolation to the bearing. An excellent review of the processes used to deposit tribological coatings is provided by Holmberg and Matthews [28]; however, a quick introduction to the most common processes used on rolling element bearings follows.

13.9.2.2 Chemical Conversion Coatings

Chemical conversion coatings are created by submersion of the bearing components into a reagent in solution to chemically react with the surface, forming the desired compound. Common bearing coatings of this type include phosphate and black oxide.

Zinc and manganese phosphate coatings are applied by immersion in acidic solutions of their metal phosphates at temperature, producing a conversion coating integrally bonded

to the bearing surface. The coated surface is nonmetallic and nonconductive. The zinc phosphate process gives a finer structure, which may be preferred cosmetically, while the manganese phosphate yields a heavier structure that is preferred for aiding with lubricant retention, and as a sacrificial layer for surface break-in.

Black oxide is a generic term referring to the formation of a mixture of iron oxides on a steel surface. An advantage of the process is that no dimensional change results, so tolerances can be maintained after treatment. A common approach to obtaining this coating consists of treating a steel component in a highly oxidizing bath. Because the chemical process results in dissolution of surface iron, close process control is necessary to prevent objectionable surface damage. The black color is obtained from the presence of Fe_3O_4 . Typically, black oxide is utilized for providing a cosmetic uniformity in appearance to components, aiding in surface break-in by acting as a sacrificial layer, and for rust protection during extended storage.

13.9.2.3 Electroplating and Electroless Plating

The plating process involves the deposition of elements, usually metallic, in solution onto the desired surface of a bearing component. Electroplating involves the deposition of the metallic elements, typically in an aqueous solution, onto the bearing component acting as an electrode through the process of electrolysis. The most commonly used plated coatings for bearing applications are chrome (Cr), zinc–nickel alloys (Zn–Ni), silver (Ag), gold (Au), and lead (Pb).

The Cr and Zn–Ni alloys are often applied to bearing components for adding a level of corrosion resistance in applications that contain chemically active environments. For example, nodular thin dense chrome (TDC) plating is often used in the food industry where routine wash down of the equipment is necessary. Comprehensive testing of TDC on rolling contact bearings was performed by Rhoads et al. [29] and Johnson et al. [30] who found that while the TDC-coated bearings demonstrate improved corrosion resistance, they did not work well in increasing fatigue life or providing wear resistance. Similar results were found for Zn–Ni in steel rolling applications by Smitek et al. [31]; however, the Zn–Ni alloys are softer and wear away quicker than TDC, and are thus not as effective over the entire operating life of the bearing.

13.9.2.4 Chemical Vapor Deposition

In CVD, gases containing volatile compounds of the coating elements are introduced into the reaction chamber, and condensed onto the bearing component surfaces to form the coating. Typically, CVD processing needs temperatures of 850–1050°C (1562–1922°F). Although these temperatures will promote diffusion with the substrate, the processing temperatures exceed the tempering temperature of most bearing steels, and thus a heat treatment after coating is usually required. Postcoating heat treatment may cause dimensional distortion, and the requirement for additional processing diminishes the attractiveness of CVD coatings for bearing components.

The most commonly used CVD bearing coating is titanium carbide (TiC). TiC is applied using vaporized titanium tetrachloride, which is allowed to react with the steel substrate at high temperatures in the presence of hydrogen and methane gases.

13.9.2.5 Physical Vapor Deposition

In PVD, the coating material is atomized or vaporized from the solid state and then deposited onto the bearing component surfaces. Typically, this is accomplished with sputtering, which entails bombarding the surface with coating atoms, leading to a pseudodiffusion layer as the

momentum of the coating atoms causes embedding into the bearing steel matrix. The pseudodiffusion layer leads to the formation of high bond strengths. Also, as the coatings are vaporized or atomized from a solid state, and deposited onto the bearing surfaces, PVD allows for the creation of multilayered coatings and coatings with variable characteristics through their thickness. Another major advantage of PVD over CVD is that substrate temperatures below 550°C (1022°F) are used, thus postcoating heat treatment is not required.

Traditional PVD coatings on bearing surfaces utilize traditional tribological coating materials such as Au, Ag, Pb, molybdenum disulfide (MoS_2), and tungsten disulfide (WS_2). However, more recently, nanocrystalline (nc) metal carbides (MC) embedded into an amorphous hydrocarbon matrix (/aC:H), also known as diamond-like coatings (DLC), are used. With these DLCs, the most common MCs in bearing applications are TiC and tungsten carbide (WC).

13.9.3 SURFACE TREATMENTS FOR MITIGATION OF DAMAGE MECHANISMS ASSOCIATED WITH SEVERE OPERATING CONDITIONS

13.9.3.1 General

The endurance of rolling element bearings can be significantly reduced from the standard predicted life; for example, when operating under conditions of poor lubrication, in the presence of debris, or stationary while experiencing high-frequency oscillatory motion. For these damage mechanisms, tribological coatings have been successfully used to extend the time of useful operation. The sections below review well-established and newly realized applications in which tribological coatings have been used to enhance the performance of rolling element bearings. The damage mechanisms referenced within are detailed in [Chapter 10](#) of the Second Volume of this handbook.

13.9.3.2 Interruption or Lack of Lubricant Supply to the Bearing

Coatings such as Au, Ag, Pb, MoS_2 , and WS_2 are applied to bearing rolling elements, raceways, and cages for applications where lubrication is either inconsistent or nonexistent [32]. In these extreme conditions, the lack of separation between the mating surfaces leads to premature bearing damage from severe wear due to the interaction of the surfaces or thermal imbalance due to the increased friction.

As an example, Ag is routinely applied via a solution state process to cages for aircraft gas turbine engine mainshaft ball and roller bearing applications [33], where the bearing must be capable of sustaining operation for a short time after loss of lubricant, to allow safe landing in this life-critical application. Ag plating of the cage is used to not only function as a wear barrier between the cage and the rolling elements, but also as a solid lubricant via a transfer film on the balls and rollers. This approach has not been without problems. In some situations, ceramic and metallic debris particles become embedded in the Ag, transforming the cage into a high-speed grinding wheel from the viewpoint of the bearing. If enough material is removed from the bearing surfaces that guide the cage, the cage can become unbalanced and generate enormous amounts of frictional heating. This can result in thermal imbalance failure, and cause the bearing to cease rotation with catastrophic consequences to the turbine engine. To address this issue, Fisher et al. [34] have developed the approach of applying TiN coatings by PVD to the cage guiding surfaces of the bearing.

Other applications with boundary-lubricated, rolling bearings are rotating anode x-ray tubes used for biomedical and scientific pursuits. Here, tribological PVD coatings of Au, Ag, or Pb must function as solid lubricants as no other means of lubrication is possible.

13.9.3.3 False Brinelling

False brinelling is an adhesive wear mechanism that occurs between rolling elements and raceways when a nonrotating bearing is subjected to external vibration. As the bearing is not rotating, a protective oil film cannot form between the raceways and the rolling elements, resulting in metal-to-metal contact. The small, relative motions between these parts under these conditions cause wear, forming grooves on the raceways. False Brinelling typically occurs during transportation (usually by truck or rail), during storage if the storage area is subject to vibration, or can be a consequence of the machine design.

In the early 1980s, Boving et al. [35] developed a procedure for applying TiC coatings by CVD to 440C steel balls for gyroscope bearings that exhibit false Brinelling. The function of the TiC coating was to defeat the adhesive wear mechanism responsible for false Brinelling by eliminating the metal-to-metal contact. Today this practice is phased out in favor of using Si_3N_4 ceramic balls instead of steel balls.

As it is often not economically practical to use ceramic rollers in bearings, WC/aC:H PVD coatings have been applied to roller bodies for eliminating metal-to-metal contact, thus minimizing adhesive wear and false brinelling. Figure 13.20 shows the results of WC/aC:H-coated rollers in laboratory fretting tests, which shows that the WC/aC:H coating reduced the resulting wear groove depth from $1.85 \mu\text{m}$ (72.8×10^{-6} in.) to $0.68 \mu\text{m}$ (26.8×10^{-6} in.), respectively. It should be noted that the groove depth did not disappear entirely when using coated rollers, as the wear mechanism was changed from adhesion to an abrasive micro-polishing of the raceway. However, a significant prolongation of the useful bearing service life is obtained, which often allows for other damage mechanisms to be the ultimate limiting factors. Currently, WC/aC:H-coated rollers are used in off-highway truck transmission and tractors, rolling mill, and wind turbine applications to mitigate false brinelling damage.

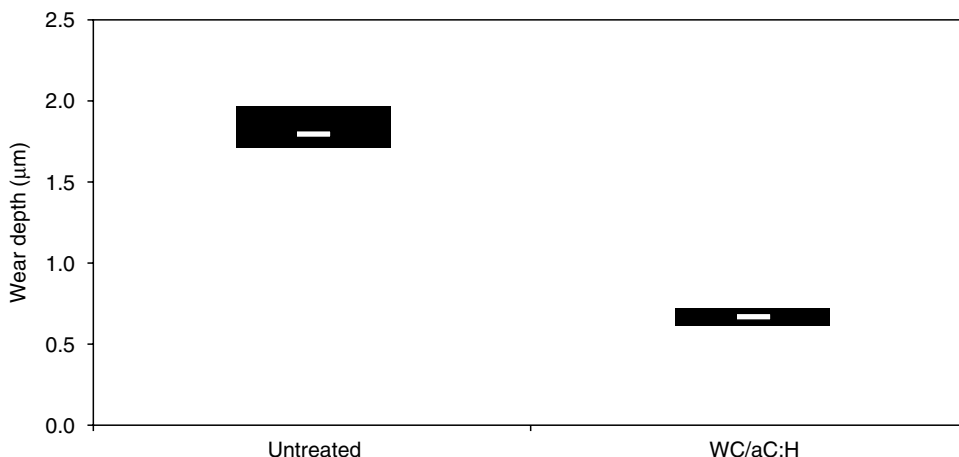


FIGURE 13.20 Tapered roller bearing false brinelling test of untreated steel and WC/aC:H-coated rollers showing the mean with bars of one standard deviation of the resulting groove depth. Twenty-five tests for each condition were conducted with a GL-4 gear oil oscillating under an $18,700 \text{ N}$ ($4,204 \text{ lb}$) axial load for 500,000 cycles.

13.9.3.4 Indentations Caused by Hard Particle Contaminants

Many times, bearings are exposed to debris contamination that is either generated by other components (gears for example) or enters the system through worn or failing seals. Depending on the size, type, and quantity of the debris particles, the life of a bearing can be severely compromised, as discussed in [Chapter 8](#) of the Second Volume of this handbook. The hard particle contamination causes plastic deformation of the raceways, which in turn raises the metal at the edges of the dent. A majority of the fatigue caused by hard particle indentation is due to the stress concentrations at the edge of the dent from this raised metal.

To minimize the stress concentrations, WC/aC:H is used due to its abrasive wear resistance and ability to micropolish counterface surfaces, as shown by Kotzalas [36] using ball-on-disk testing of WC/aC:H-coated balls on steel disks; see [Figure 13.21](#). Specifically, the abrasive wear resistance of WC/aC:H enables the coating to remain intact on the roller while preferentially removing the raised metal at the dent edges due to the increased contact pressures. [Figure 13.22](#), from Ref. [36], shows the appearance of debris-dented, spherical roller bearing raceways after testing with and without coated rollers, and the micropolishing that occurs. Doll et al. [37] found the life of case-carburized tapered roller bearings to increase by a factor of 4.46 when the rollers were coated with WC/aC:H compared with standard rollers when fatigue tested after denting with 25–53 μm (0.00098–0.00209 in.) hard steel powder. Kotzalas [36], in similar testing with larger debris particles of 90–110 μm (0.00354–0.00433 in.), found a factor of 1.41 increase in fatigue life for through-hardened AISI 52100 spherical roller bearings, which is not to the extent of that found by Doll et al. [37]. The difference in performance was most likely due to the combination of more severe contaminant damage due to larger debris particles, higher roller-raceway friction in spherical roller bearings, and the absence of compressive residual stresses in the through-hardened bearing steel.

Currently, bearings with WC/aC:H-coated rollers are used to minimize the effects of debris entering the gearboxes of off-highway vehicles and down-hole drilling heads where external contamination is inherently difficult to control.

13.9.3.5 Severe Wear (Galling or Smearing)

Smearing of rolling element bearings typically occurs under less than favorable lubrication conditions, where localized temperatures from high friction cause adhesion of the contacting surfaces and subsequent material transfer. In tapered roller bearings, this commonly occurs between the roller ends and the rib flange at high speeds, loads, and minimal lubricant conditions. Evans et al. [38] found PVD TiC/aC:H-coated roller ends to extend the time

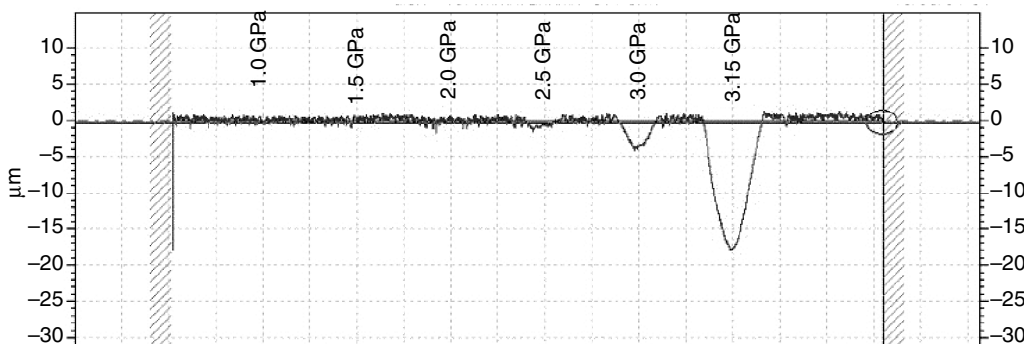


FIGURE 13.21 Steel disk wear marks after ball-on-disk testing with a WC/aC:H coated ball for 15 min in a 75W-90 oil with 10 m/s (32.8 ft/s) rolling and 5 m/s (16.4 ft/s) sliding speed.



(a)



(b)

FIGURE 13.22 Through-hardened AISI 52100 spherical roller bearings dented with 90–110 μm (0.00354–0.00433 in.) hard steel powder and endurance tested at 38.9% of the basic dynamic load rating with an ISO VG 68 mineral oil supplied at 37.8°C (100°F). Raceway of bearing with: (a) untreated steel, (b) WC/aC:H-coated rollers. (From Kotzalas, M., Debris signature analysisSM and engineered surfaces for increasing bearing debris resistance, *Proc. BMPTA Brdg. Seminar, Fatigue or Murder? Rolling Bearing Failures and How to Prevent Them*, Leicester, England, October 2004.

until scuffing occurs in thrust loaded tapered roller bearings. To ensure minimum lubrication conditions, the bearings were immersed in a solution containing 80% hexane and 20% GL-5 gear oil, and then the hexane was allowed to evaporate before testing commenced. Twenty-five bearings were tested in a vertical thrust test rig under an axial load of 4450 N (1000 lb) and 3000 rpm inner-ring speed. Testing continued on each bearing until the onset of rib–roller end smearing. The median time to the occurrence of smearing damage (L_{50}) was determined

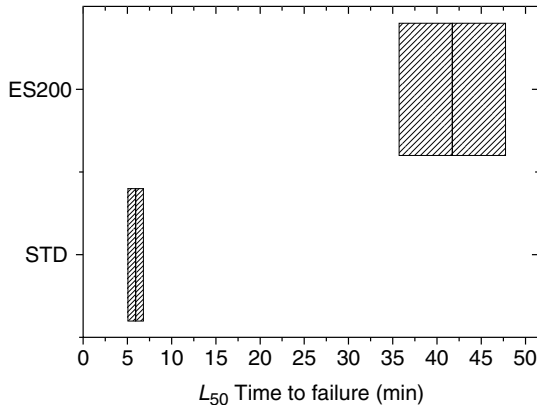


FIGURE 13.23 Rib–roller end scuffing test results with 90% confidence bands for bearings with standard (STD) and TiC/aC:H-coated (ES200) roller large ends. (Evans, R., et al., Nanocomposite tribological coatings for rolling element bearings, *Mat. Res. Soc. Symp.*, 750, 407–417, 2003. With permission.)

for both standard and coated roller ends using Weibull statistics, as discussed in Chapter 10 of the companion volume of this handbook, and shown in Figure 13.23. As can be seen, the time during which minimal lubrication conditions can be sustained before the occurrence of smearing damage can be extended up to seven times by adding TiC/aC:H coating to the roller ends. Similar results have been found for spherical roller bearings [39,40].

Because of the significant decrease in smearing damage available from the application of MC/aC:H coatings, several applications where this has been the limiting factor in bearing endurance are employing this surface treatment. These applications include aircraft landing wheel bearings, rolling mills, pinion bearings, wheel bearings, and paper machines.

13.9.3.6 Surface-Initiated Fatigue

Surface-initiated fatigue is generally associated with high stresses on the surface of bearing components that exceed the fatigue limit leading to crack formation. Owing to the micro-polishing effect of MC/aC:H coatings found on gears by Doll [41] and Anderson and Lev [42], a TiC/aC:H PVD coating was applied to the rollers of bearings operating with thin lubricant films. Doll and Osborne [43] endurance tested tapered roller bearings with untreated steel and TiC/aC:H-coated rollers in a SAE 10 oil. The lubricant input temperature was elevated to make the lubricant film parameter (Λ) (defined in Chapter 8 of the companion volume of this handbook) as the lubricant film thickness-to-composite surface roughness, approximately equal to 0.6. Figure 13.24 displays the results showing that TiC/aC:H coatings on the rollers doubled the life as compared with the untreated bearings. Further investigation of the tested bearings revealed a micropolishing mechanism of the TiC/aC:H coating as increasing surface fatigue life. Optical images (100 \times magnification) of outer raceways taken before and after testing are shown in Figure 13.25. Whereas features associated with the grinding of the raceway are evident in the before-testing image in Figure 13.25a and the image after testing with standard rollers in Figure 13.25b, most of those features are absent in the after-testing image in Figure 13.25c. Further, Doll and Osborne [43] found the root-mean-square (rms) surface roughness of the outer raceways to decrease from 0.11 μm (4.3×10^{-6} in.) when new, to 0.10 μm (3.9×10^{-6} in.) after tests with standard rollers, and 0.07 μm (2.8×10^{-6} in.) after tests with coated rollers. The micropolishing dynamically increased the Λ value, in turn increasing endurance.

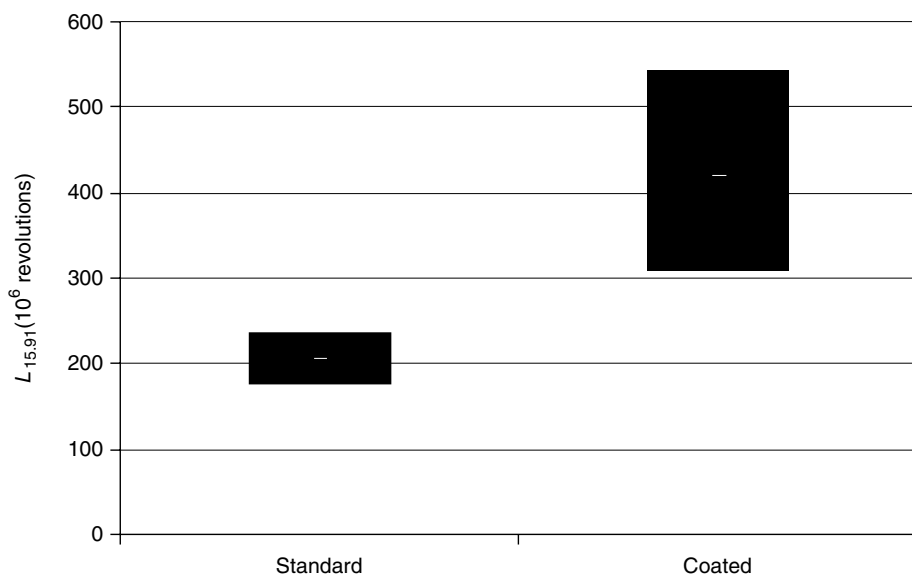


FIGURE 13.24 Endurance test results with 65% confidence bands for tapered roller bearings operating in thin lubricant films with (coated) and without (standard) TiC/aC:H-coated rollers.

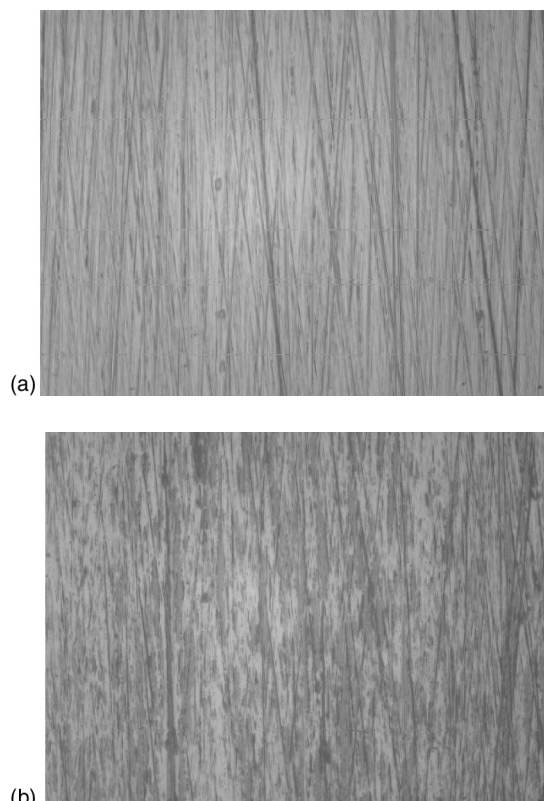


FIGURE 13.25 Optical images of outer raceways at 100 \times : (a) before testing, (b) after testing with standard rollers, and



FIGURE 13.25 (Continued) (c) after testing with WC/aC:H-coated rollers.

13.10 CLOSURE

An operating rolling bearing is a system containing rings, raceways, rolling elements, cage, lubricant, seals, and ring support. In general, ball and roller bearings selected from listings in manufacturers' catalogs must be able to satisfy broad ranges of operating conditions. Accordingly, the materials used must be universal in their applicability. Through-hardened AISI 52100 steel, nylon-6,6, lithium-based greases, and so on are among the materials that have met the test of universality for many years. Moreover, these materials as indicated in this chapter have undergone significant improvement, particularly in the past few decades.

For special applications involving extra-heavy applied loading, very high speeds, high temperatures, very low temperatures, severe ambient environment, and combinations of these, the bearing system materials must be carefully matched to each other to achieve the desired operational longevity. In an aircraft gas turbine engine mainshaft bearing for example, it is insufficient that the M50 or M50-NiL bearing rings provide long-term operating capability at engine operating temperatures and speeds; rather, the bearing cage materials and lubricant must also survive for the same operating period. Therefore, cages for such applications are generally fabricated from tough steel and are silver plated; nylon cages are precluded by the elevated operating temperatures and possibly by incompatibility with the lubricant. The upper limit of bearing operating temperature is established by the lubricant; in most cases this is a synthetic oil according to United States military specification Mil-L-23699 or Mil-L-7808.

An example of an extreme operating condition is the liquid oxygen (LOX) turbopump for the space shuttle main engine. In this application, the bearings must rotate at a very high speed (30,000 rpm) during lubrication by LOX. The LOX vaporizes in the confines of the bearing, and the bearing tends to burn up and wear notwithstanding the initial cryogenic temperature (-150°C [-302°F]) of the LOX. To achieve sufficient duration of satisfactory operation, the ball bearing cage has been fabricated from Armalon, a woven fiberglass reinforced PTFE material [44] that lubricates by transfer of PTFE film from the cage pockets to the balls. The bearing rings are fabricated from vacuum-melted AISI 440C stainless steel. The target duration for the bearing operation is only a few hours.

REFERENCES

1. American Society for Testing and Materials, Std A295-84, High Carbon Ball and Roller Bearing Steels; Std A485-79, "High Hardenability Bearing Steels."
2. American Society for Testing and Materials, Std A534-79, "Carburizing Steels for Anti-Friction Bearings."
3. Braza, J., Pearson, P., and Hannigan, C., The performance of 52100, M50 and M50-NiL steels in radial bearings, *SAE Technical Paper 932470*, September 1993.
4. Zaretsky, E., Bearing and gear steels for aerospace applications, *NASA Technical Memorandum 102529*, March 1990.
5. Trojahn, W., et al., Progress in bearing performance of advanced nitrogen alloyed stainless steel, in *Bearing Steels into the 21st Century*, J. Hoo (Ed.), ASTM STP 1327, 1997.
6. Böhmer, H.-J., Hirsch, T., and Streit, E., Rolling contact fatigue behavior of heat resistant bearing steels at high operational temperatures, in *Bearing Steels into the 21st Century*, J. Hoo (Ed.), ASTM STP 1327, 1997.
7. Finkl, C., Degassing—then and now, *Iron and Steelmaker*, 26–32, December 1981.
8. Morrison, T., et al., The effect of material variables on the fatigue life of AISI 52100 steel ball bearings, *ASLE Trans.*, 5, 347–364, 1962.
9. United States Steel Corp., *Making, Shaping, and Treating of Steel*, 9th Ed., 1971, p. 551.
10. United States Steel Corp., *Making, Shaping, and Treating of Steel*, 9th Ed., 1971, pp. 596–597.
11. United States Steel Corp., *Making, Shaping, and Treating of Steel*, 9th Ed., 1971, p. 594.
12. United States Steel Corp., *Making, Shaping, and Treating of Steel*, 9th Ed., 1971, p. 598.
13. United States Steel Corp., *Making, Shaping, and Treating of Steel*, 9th Ed., 1971, p. 580.
14. Eckel, J., et al., Clean engineered steels—progress at the end of the twentieth century, in *Advances in the Production and Use of Steel with Improved Internal Cleanliness*, J. Mahoney (Ed.), ASTM STP 1361, 1999.
15. Åkesson, J. and Lund, T., SKF rolling bearing steels—properties and processes, *Ball Bearing J.*, 217, 32–44, 1983.
16. American Society for Testing and Materials, Std E45-81, "Standard Practice for Determining the Inclusion Content of Steel."
17. Beswick, J., Effects of prior cold work on the martensite transformation in SAE 52100, *Metall. Trans. A*, 15A, 299–305, 1984.
18. Butler, R., Bear, H., and Carter, T., Effect of fiber orientation on ball failures under rolling contact, *NASA TN 3933*, 1975.
19. SKF Steel, *The Black Book*, Vol. 194, 1984.
20. SKF Steel, *The Black Book*, Vol. 151, 1984.
21. Grossman, M., *Principles of Heat Treatment*, American Society for Metals, 1962.
22. American Society for Testing and Materials, Std A255-67, "End-Quench Test for Hardenability of Steel" (1979).
23. American Society for Metals, *Atlas of Isothermal Transformation and Cooling Transformation Diagrams*, 1977.
24. Pallini, R., Turbine engine bearings for ultra-high temperatures, *Ball Bearing J.*, SKF, 234, 12–15, July 1989.
25. Lankamp, H., Materials for plastic cages in rolling bearings, *Ball Bearing J.*, SKF, 227, 14–18, August 1986.
26. Oleschewski, A., High temperature cage plastics, *Ball Bearing J.*, SKF, 228, 13–16, November 1986.
27. Delta Rubber Company, *Elastomer Selection Guide*.
28. Holmberg, K. and Matthews, A., *Coatings Tribology: Properties, Techniques, and Applications in Surface Engineering*, Elsevier, Amsterdam, 1994.
29. Rhoads, M., Shucktis, B., and Johnson, M., Thin dense chrome bearing insertion program, Report NTIS, AD-A330 677 (microfiche), GE Aircraft Engine, 1997.
30. Johnson, M., Laritz, J., and Rhoads, M., Thin dense chrome insertion program—Pyrowear 675 and Cronidur wear testing, Report NTIS AD-A361 451 (microfiche), GE Aircraft Engine, 1998.
31. Smitek, J., et al., Corrosion-resistant antifriction bearings, *AISI Steel Tech.*, 76, 12, 19–23, 1999.

32. Bhushan, B. and Gupta, B., *Handbook of Tribology: Materials, Coatings, and Surface Treatments*, McGraw-Hill, New York, 1991.
33. Brown, P., Bearing retainer material for modern jet engines, *ASLE Trans.*, 13(3), 225–239, 1970.
34. Fisher, K., et al., Rolling element bearing having wear resistant race land regions, US Pat. No. 5,165,804, 1992.
35. Boving, H., Hinterman, H., and Stehle, G., TiC-coated cemented carbide balls in gyro application ball bearings, *Lub. Eng.*, 39(4), 209–215, 1983.
36. Kotzalas, M., Debris signature analysisSM and engineered surfaces for increasing bearing debris resistance, *Proc. BMPTA Brg. Seminar, Fatigue or Murder? Rolling Bearing Failures and How to Prevent Them*, Leicester, England, October 2004.
37. Doll, G., Ribaudo, C., and Evans, R., Engineered surfaces for steel rolling element bearings and gears, Materials Science and Technology, MS and T 2004; volume 2: AIST/TMS Proceedings, 367–374, 2004.
38. Evans, R., et al., Nanocomposite tribological coatings for rolling element bearings, *Mat. Res. Soc. Symp. Proc.*, 750, 407–417, 2003.
39. Anon, Eliminating smearing in soft calender bearings, *Pulp Paper Canada*, 103(11), 10, 2002.
40. SKF Brochure, *NoWearTM, Less Than You Can Imagine*, Publ. No. 5047E, 2000.
41. Doll, G., Engineering gear surfaces, Presented at Balzers *Prec. Comp. Seminar*, Amherst, NY, October 21, 1999.
42. Anderson, N. and Lev, L., Coatings for automotive planetary gear sets, Presented at *ASME Des. Eng. Tech. Conf.*, Chicago, IL, September 2, 2003.
43. Doll, G. and Osborn, B., Engineering surfaces of precision steel components, Presented at *44th Soc. of Vac. Coaters Tech. Conf.*, Philadelphia, PA, April 21–26, 2001.
44. Maurer, R. and Wedeven, L., Material selection for space shuttle fuel pumps, *Ball Bearing J.*, SKF, 226, 2–9, April 1986.

14 Vibration, Noise, and Condition Monitoring

LIST OF SYMBOLS

Symbol	Description	Units
A	Peak displacement amplitude	mm (in.)
D	Rolling element diameter	mm (in.)
dB	Decibels relative logarithmic amplitude	
d_m	Pitch diameter	mm (in.)
F_B	Reaction force by bearing	N (lb)
f	Frequency	rps, Hz
g	Acceleration due to gravity	mm/sec ² (in./sec ²)
M	Mass	kg (lb-sec ² /in.)
n	Speed	rpm, rps
r	Radial deviation	mm (in.)
t	Time	sec
Z	Number of balls or rollers	
ω	Angular velocity	rad/sec
Subscripts		
c	Cage	
i	Inner ring, shaft of raceway	
o	Outer ring or raceway	
r	Rolling element	

14.1 GENERAL

This chapter provides a brief overview of bearing vibration. Where relevant, reference is also made to noise, sometimes resulting from excessive bearing vibration. A few common bearing applications in which noise and vibration are important are described.

Machine vibration or noise levels, whether excessive or not, are affected by bearings in three ways: as a structural element defining in part a machine's stiffness; as a generator of vibration by virtue of the way load distribution within the bearing varies cyclically; and as a vibration generator because of geometrical imperfections from manufacturing, installation or wear, and damage after continued use.

Detection of progressive bearing deterioration in operating machinery by vibration measurements has been in use for a long time and has become more economical and reliable in recent years. Some aspects of such machinery monitoring are considered.

14.2 VIBRATION- AND NOISE-SENSITIVE APPLICATIONS

14.2.1 SIGNIFICANCE OF VIBRATION AND NOISE

In many cases, objectionable airborne noise from a machine results from measurable vibration of machine components. Correlation between bearing noise and machine vibration measurements has been reported [1,2]. Therefore, with respect to rolling bearings, the terms "noise" and "vibration" usually denote similar and related phenomena. Regardless of which seems to be more important in a particular application, noise and vibration may both be used as indicators in machines that have quality problems with bearings, machine components, or assembly methods when they are new, and as the first indication of an approaching need for repair or replacement after running for extended periods of time.

14.2.2 NOISE-SENSITIVE APPLICATIONS

The application that has been the major driving force for reducing noise is that of small and medium electric motors, primarily utilizing deep-groove ball bearings. Figure 14.1 shows such an application. The outer ring of the bearing at the left end of the motor is free to move axially under controlled thrust load of a spring to remove axial clearance within the bearing. This allows for thermal expansion of the shaft and motor assembly without loss of preload while simultaneously preventing excessive bearing loads or distortion of motor components.

Quiet running characteristics of electric motors are required in office equipment and household appliances where noise may be an irritant. Noise is also a problem in building heating and air conditioning systems, where motor or fan support bearing noise can be transmitted and amplified through ductwork or air columns. Also included in this category are drive systems of elevators, using larger electric motors with deep-groove ball bearings and cylindrical roller bearings and spherical roller bearing in pillow blocks to support cable sheaves. Apart from irritation, excessive noise in the latter application might make passengers

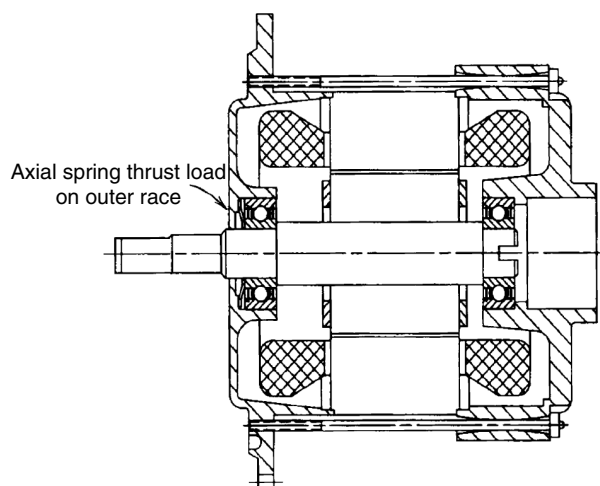


FIGURE 14.1 Schematic drawing of electric motor.

concerned. Automotive applications also requiring quiet running performance include alternators (deep-groove ball bearings and needle roller bearings), transmissions, differentials (tapered roller bearings), and fans.

Objectionable noise might be characterized by volume or sound level and pitch or frequency. Sound from a machine may be more irritating if a particular frequency is dominant. Possibly even more objectionable are intermittent or transient sounds that vary with time in either pitch or volume at regular or irregular intervals. Such effects might be more easily heard than measured, as common measuring methods may be acquiring data over time periods that are long compared with short-duration transient sounds or vibrations. In addition, transient sound or vibration is sometimes most significant when a machine is coming to operating speed or coasting down. Even in vacuum cleaners or dishwashers this effect is sometimes heard.

The U.S. Navy has made extensive demands on bearing manufacturers with respect to bearing vibration and noise reduction as well as boundary dimension and running accuracy tolerances [3]. This stems in part from the requirement to make submarines more difficult to detect by monitoring the sound transmitted through water. Coincidentally, improvement in reliability and reduced maintenance costs are achieved. Extensive research efforts on bearing vibration were sponsored by the U.S. Navy [4].

14.2.3 VIBRATION-SENSITIVE APPLICATIONS

Applications where bearing and machine vibration are more important than noise fall into two categories. In some cases, the machine must be capable of high running and positioning accuracies to function properly. In other cases, the major concerns are safety, if vibration causes catastrophic failure, and the economic impact of reduced machine utilization and increased repair cost if vibration foreshortens the life of components.

Not only is noise intrinsically less important than vibration in these categories, but it may also be incapable of indicating a significant problem. This would occur if the predominant frequency of high-amplitude vibration falls outside the audible range; for example, rotating imbalance in a machine running at 1800 rpm (30 Hz). In addition, abnormal noise might be undetectable because of ambient noise or because of normal noise from the process the machine performs.

Bearing applications where machine accuracy might be affected by vibration include machine tools. Grinding spindles often must be capable of producing components with size and two- or three-point roundness within a micrometer ($40 \mu\text{in.}$). Figure 14.2 shows a grinding wheel spindle using precision double-row, cylindrical roller bearings and a double-direction, angular-contact ball thrust bearing to achieve high radial and axial stiffness. The cylindrical roller bearings have tapered bores for accurately controlling preload. Precision angular-contact ball bearings in matched sets are also widely applied in spindles.

In addition to size control and roundness, precision spindles must be capable of producing even finer levels of geometrical accuracy such as relatively low levels of surface roughness and circumferential waviness amplitudes of much less than a micrometer ($40 \mu\text{in.}$). Vibration can contribute to excessive roughness or waviness and can also produce chatter, a more severe form of waviness that can cause permanent metallurgical damage to hardened steel parts.

Other machines in which vibration might prevent the required accuracy from being achieved include rolling mills for sheet steel, paper, and chemical films. Computer disk drives are a further example, requiring nonrepeatable bearing runout accuracy of no more than 0.25 to $0.50 \mu\text{m}$ (10–20 $\mu\text{in.}$) for the spindle and head combined. Similarly, gyroscope bearings require good dynamic running accuracy as well as very low torque levels.

Cases where the running accuracy is not as important as safety and machine reliability often involve machines that are producing or transmitting high horsepower, have massive rotating

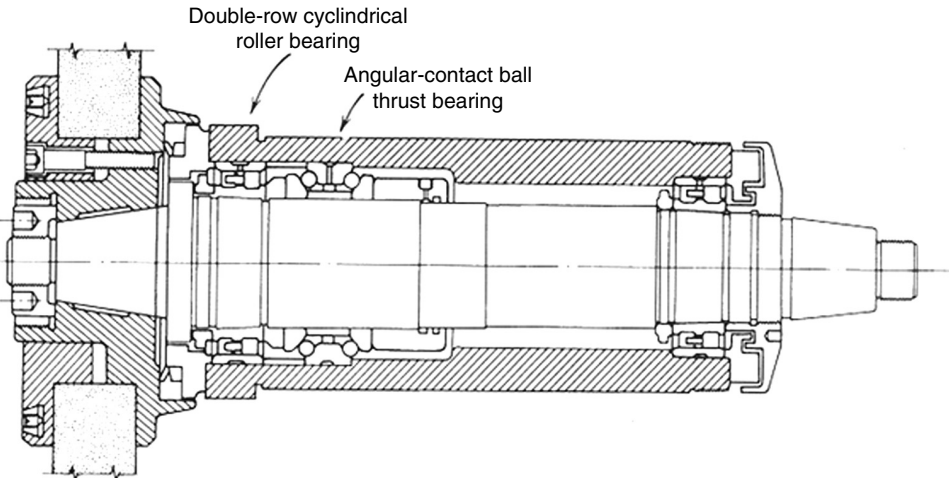


FIGURE 14.2 Grinding wheel spindle.

components, and are running at high speeds relative to the size of the equipment. Eccentric mass produces large and potentially destructive forces in these applications. Such equipments may operate at speeds above resonant frequencies; so large amplifications of vibration could occur as the equipments are run up to speed. Examples include compressors, pumps, and turbines.

For these applications, the dynamic characteristics associated with the entire rotational system are analyzed during the machine design phase using classical vibration [5–7] and rotor dynamic techniques [8–12]. Typically, the rotor dynamic analyses estimate the system critical speeds, synchronous response curves, and mode shapes as a function of the bearing stiffness. Using the methods in [Chapter 8](#), stiffness is calculated based on bearing type, contact angle, applied load, and operating diametral clearance (including preload). Also, in [Chapter 3](#) of the Second Volume of this handbook, the effects of centrifugal force and gyroscopic moment due to high operating speeds on the operating contact angle and ball–raceway and roller–raceway contact loads, and hence bearing stiffness, are detailed. Using these results as input, it is possible to model the dynamic response of a rotating system using methods described in great detail in many other texts; thus such methods are not presented herein.

Applications in this section are examples where machine noise or vibration is important. More demanding applications continually arise, requiring greater accuracy, higher speeds and loads, and improved reliability. Therefore, bearing manufacturers have continuously emphasized improvements of bearing quality with respect to noise and vibration through ongoing development of machines and methods for manufacturing and inspection.

14.3 THE ROLE OF BEARINGS IN MACHINE VIBRATION

14.3.1 BEARING EFFECTS ON MACHINE VIBRATION

Rolling bearings have three effects with respect to machine vibration. The first effect is as a structural element that acts as a spring and also adds mass to a system. As such, bearings define, in part, the vibration response of the system to external time-varying forces. The second and third effects occur because bearings act as excitation sources, producing time-varying forces that cause system vibration. In one case, this excitation is inherent in the design of rolling bearings and cannot be avoided. In the other case, these forces result from imperfections, which usually are avoidable.

14.3.2 STRUCTURAL ELEMENTS

Under sufficient applied load, the bearing is a stiff structural member of a machine. It is a spring whose deflection varies nonlinearly with force, in contrast to the usual linear spring characteristics assumed in dynamic models, such as the single degree-of-freedom spring-mass-damper model. As a first approximation, it may be adequate to estimate machine vibration response by considering the bearing as a linear spring. In this case, a bearing spring constant is determined by taking the slope of the force-deflection curve of the bearing at the normal operating load. The approximation may be insufficient in cases requiring precise knowledge of transient vibration response, particularly near machine resonant frequencies. In these cases, extensive mathematical modeling and experimental modal analysis are performed, both of which are beyond the objectives of this chapter. If it is sufficient to consider bearing stiffness as a constant, under a specific set of operating conditions, then this approximation can be derived from equations in [Chapter 8](#).

Bearing stiffness increases with increasing load, a characteristic referred to as a “hardening” spring. Larger nominal operating loads or built-in preload would result in smaller variations in dynamic bearing deflection when subjected to a particular dynamic load variation. Similarly, increased bearing stiffness raises the value of a resonant frequency associated with this spring, as a resonant frequency is inversely proportional to the square root of stiffness. Moreover, radial stiffness decreases with increasing contact angle, whereas the reverse is true for axial stiffness. Therefore, response to dynamic load variation will depend strongly on the direction of such loads relative to that of the nominal load that governs the contact angle.

As the bearing spring is nonlinear, it is evident that sinusoidal deviations from the nominal load will not cause sinusoidal bearing deflection. When the load is greatest, the increase to nominal bearing deflection will be less than the decrease from nominal bearing deflection when the load is at its lowest value. If large dynamic fluctuations in load are experienced, for example, in a radially loaded bearing, then it is possible for the load zone to alternate from the bottom to the top of the outer raceway. If the bearing has radial internal clearance, there is the possibility of essentially no loading at all on the outer raceway for brief instances. Such conditions could arise because of external loading or conditions within the bearing.

14.3.3 VARIABLE ELASTIC COMPLIANCE

The second effect of bearings on machine vibration occurs because bearings carry load with discrete elements whose angular position, with respect to the line of action of the load, continually changes with time. This mere change of position causes the inner and outer raceways to undergo periodic relative motion even if the bearing is geometrically perfect. Analysis of this motion is found in Ref. [4].

[Figure 14.3](#) shows a bearing containing eight balls, at two different times. In Figure 14.3a, ball 1 is located directly under the load; balls 1, 2, and 8 carry the load. In Figure 14.3b, balls 1 and 8 straddle the load symmetrically, and balls 1, 2, 7, and 8 carry the load. Obviously, the radial deflection is different in each situation. Assuming this is a 204 ball bearing with 7.938 mm (0.3125 in.) balls and an applied radial load of 4450 N (1000 lb), the estimated deflection for the condition in Figure 14.3a is 0.04232 mm (0.001702 in.) and for Figure 14.3b is 0.04353 mm (0.001714 in.). The position of the ball set in Figure 14.3a gives a stiffer bearing at that instant. The shaft and inner raceway have approached closer to the outer raceway in the time it takes for one half of the ball spacing to pass a point on the outer raceway to reach the position shown in Figure 14.3b. The shaft will return to its original position as ball 1 comes under the load line. This frequency of vibration is therefore equal to the cage rotational frequency multiplied by the number of balls; that is, the frequency of this vibration occurs at the frequency of balls passing the outer raceway.

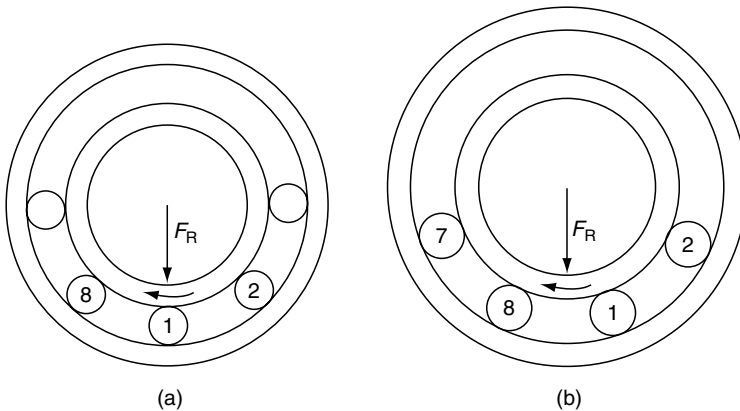


FIGURE 14.3 (a) Angular position of ball set, time = 0. (b) Angular position, time = $\frac{1}{2}[1/Z]$ (cage rotation frequency)].

Horizontal motion also occurs, at the same vibrational frequency, as the ball set assumes angular positions that are asymmetrical with respect to the load line. Both vertical and horizontal vibration amplitudes are nonsinusoidal as a result of the nonlinear deflection characteristics. The existence of this type of vibration, which occurs even with a geometrically perfect bearing, is one reason why bearing damage detection is best performed by monitoring frequencies other than the fundamental bearing frequencies.

See Example 14.1.

14.3.4 GEOMETRIC IMPERFECTIONS

14.3.4.1 General

The third effect that bearings have on machine vibration arises from geometrical imperfections. These imperfections are always present to varying degrees in manufactured components. Sayles and Poon [13] discuss three mechanisms by which imperfections in bearings cause vibration: waviness (Figure 14.4) and other form errors causing radial or axial motion of

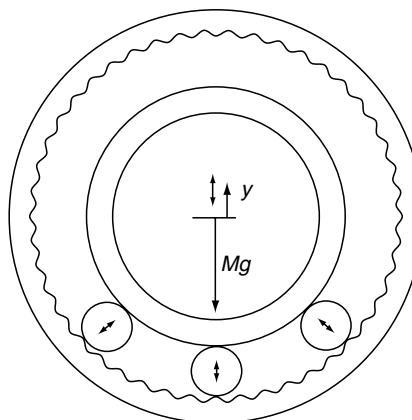


FIGURE 14.4 Vibration from raceway waviness. (Courtesy of Oceana Sensor Technologies, Virginia Beach, Virginia.)

raceways; microslip together with asperity collisions and entrained debris that break through the lubricant film; and shocks due to local elastic deformations caused by surface roughness peaks that do not break through the lubricant film. Of the three mechanisms, it can be seen that the first occurs on a scale larger in magnitude than the Hertzian contact zone, and thus the rolling element follows a general contour prescribed by these form errors. However, the last two geometric imperfections occur on a scale of equal or smaller magnitude than the Hertzian contact, with differing effects on the vibration characteristics of the bearing assembly.

Controlling component waviness and other types of errors from manufacturing, distortion, or damage occurring while the bearing is assembled to the machine is a high priority. The effect of such form errors on machine vibration or noise can be significant.

14.3.4.2 Microscale

In this case, the local elastic contacts are of approximately the same size or are smaller than the Hertzian contact areas. At any instant, there may be only a few such peaks in the Hertzian deformation zone, depending on the types of bearing component finishing processes employed, for example, honing and lapping. Elastic deformations of the type discussed occur rapidly, and the time separating one such contact from the next is brief. A major contribution to bearing vibration in the higher frequencies, for example, above 10,000 Hz, is thought to be the result of such deformations. Because of their impulsive nature, however, they are capable of exciting lower-frequency resonances.

14.3.4.3 Waviness and Other Form Errors

Typically, a part is said to be round in a specific cross section if there exists a point within that cross section from which all other points on the periphery are equidistant. The first-mentioned point is of course the center of the circle, and the cross section is a perfect circle as indicated in Figure 14.5a. If the cross section is not a perfect circle as in Figure 14.5b, it is said to be out-of-round with the “out-of-roundness” specified as the difference in distance of points on the periphery from the center. Thus, out-of-roundness in Figure 14.5b is $r_1 - r_2$. In addition to the basic profile in Figure 14.5b, an irregular profile similar to Figure 14.5c is usually present in manufactured machine elements, and this includes rolling bearing raceways and rolling elements. The irregular surface of Figure 14.5c is of substantial importance to bearing frictional performance and endurance; this will be discussed in [Chapter 5](#) and [Chapter 8](#) of the companion volume of this handbook. The lobed surface of Figure 14.5b is also significant, as it is a causative factor of bearing vibration. The important feature is called waviness, that is, the number of lobes per circumference.

For a tapered roller bearing mounted in an SKF VKL tester, shown schematically in [Figure 14.6](#), Yhland [14] examined the correspondence between waviness and the resulting

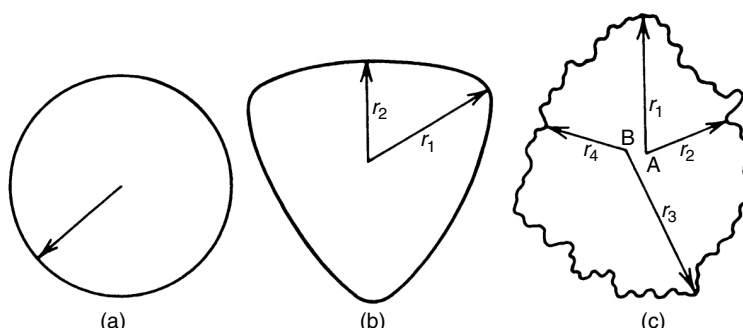


FIGURE 14.5 Illustrations of a round surface.

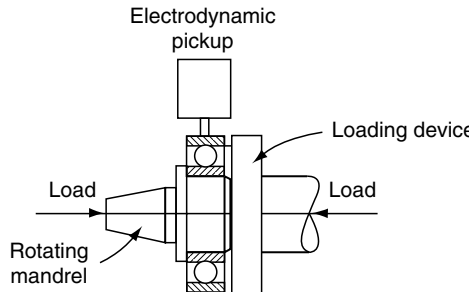


FIGURE 14.6 Schematic view of VKL vibration tester. (From Yhland, E., Waviness measurement—an instrument for quality control in rolling bearing industry, *Proc. Inst. Mech. Eng.*, 182, Pt. 3K, 438–445, 1967–1968.)

vibration spectrum. For a bearing with Z rolling elements, if p and q are integers equal to or greater than 1 and 0, respectively, then for vibrations in the radial direction measured at a point on the outside diameter of the bearing outer ring, the vibration circular frequencies as functions of inner ring, outer ring, and roller waviness are given in Table 14.1.

In Table 14.1, ω_i , ω_c , and ω_r are the inner ring, cage, and roller angular velocities, respectively. Rigid body vibrations are indicated when $p=1$; that is, the outer ring of the bearing moves as a rigid body. For $p > 1$, vibrations are of the flexural type with p equal to the number of outer circumference lobes of the outer-ring deflection curve. For a waviness spectrum obtained at an inner-ring speed of 900 rpm, for a bearing with accentuated inner-ring waviness, Yhland [14] obtained the vibration spectrum at 1800 rpm shown in Figure 14.7. Also shown in Figure 14.7 is the waviness measurement (Talyrond trace) of the inner ring; the tested tapered roller bearing contained very smooth rollers and outer ring.

See Example 14.2.

Waviness can occur in the machining process. A round bar or ring type element is compressed at the points of contact in a chuck, three jaw or five jaw, causing stresses in the part. The part is then turned or ground perfectly circular; however, when it is released from the chuck, the stresses are released, and the part becomes lobed. To minimize this problem, parts are often magnetically chucked instead of using jaws, but waviness still results from the dynamic action and accuracies associated with the machine tool spindle. Even with centerless grinding, waviness can result from irregularities in the original bar stock.

Waviness is typically associated with a more uniform type of form error. Figure 14.8 shows circumferential traces of two spherical roller bearing inner raceways. One raceway has a peak-to-valley amplitude of approximately 4 μm (0.00016 in.), the other approximately 9 μm (0.00036 in.); each has nine wave cycles per circumference. Other types of imperfections that are nonuniform can, however, result. One such cause can be machine malfunction, such as that shown in Figure 14.8, where the roller was released from the grinding station before

TABLE 14.1
Vibration Frequencies vs. Waviness

Component	Waviness of Orders	Vibration with Circular Frequencies
Inner ring	$k = qZ \pm p$	$qZ(\omega_i - \omega_c) \pm p\omega_i$
Outer ring	$k = qZ \pm p$	$qZ\omega_c$
Roller	k (even)	$k\omega_r \pm p\omega_c$

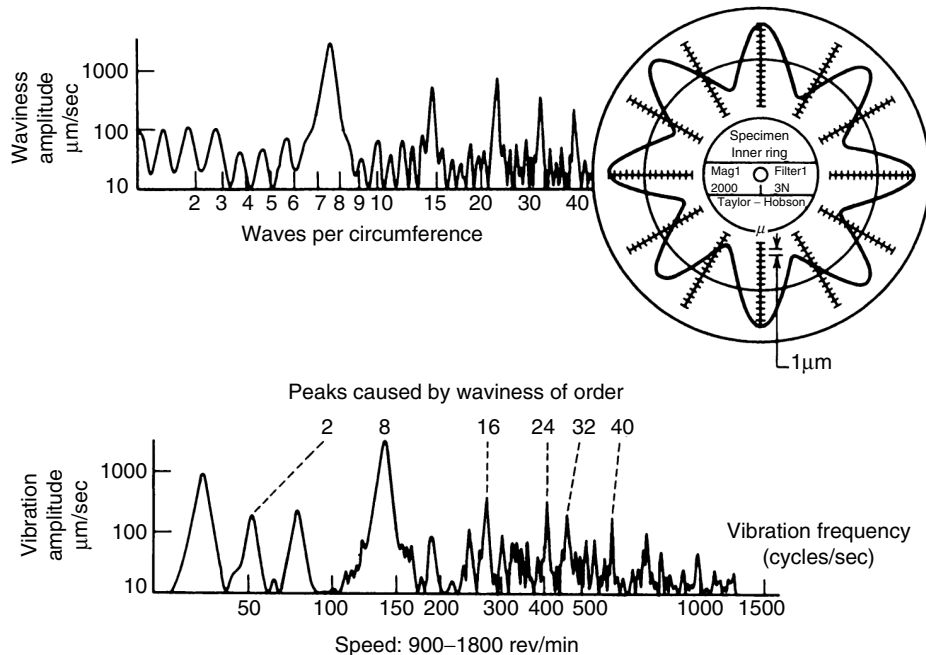


FIGURE 14.7 Waviness and vibration spectra from an inner ring with accentuated waviness. (From Yhland, E., Waviness measurement—an instrument for quality control in rolling bearing industry, *Proc. Inst. Mech. Eng.*, 182, Pt. 3K, 438–445, 1967–1968.)

the wheel was retracted. This led to a localized flat spot over approximately 5% of the circumference to a maximum depth of 18 μm (0.00072 in.).

More subtle defects can also occur. They may be characterized by much smaller deviations from true geometrical form than can be detected measuring two, three, or four diameters and require more detailed component inspection, such as waviness testing or vibration testing of assembled bearings. Figure 14.9 is an example of such a defect on a cylindrical roller with lower-amplitude and higher-frequency waviness than in the previous examples. The roller has over 100 waves with a peak-to-valley amplitude of less than 0.5 μm (20 μin .). This roller was part of a bearing installed in a large electric motor that emitted a periodic audible noise at a slow running speed. With a stopwatch, the repetition rate of the noise could be associated with the cage revolution, and subsequent rig testing traced the noise to this particular roller.

See Example 14.3 through Example 14.5.

14.3.5 WAVINESS MODEL

Figure 14.4 represents a bearing with waviness on the outer raceway. It is assumed that the bearing supports a mass and that the outer ring is rigidly supported by a housing. If no waviness is present on the surface of the bearing raceways, a force balance in the vertical direction is

$$F_B - Mg = 0 \quad (14.1)$$

If waviness is present, then for an approximation it will be assumed that the mass will move up and down as a rigid body, with reaction force produced in the bearing as a result of the acceleration of the mass. In this case, the force balance is

$$F_B + \Delta F_B - Mg = M\ddot{y} \quad (14.2)$$



FIGURE 14.8 Spherical roller bearing inner-ring waviness, machine setup error. Each radial division equals 1 μm .

For waviness that can be approximated as sinusoidal, the equations are

$$y = A \sin(2\pi ft) \quad (14.3)$$

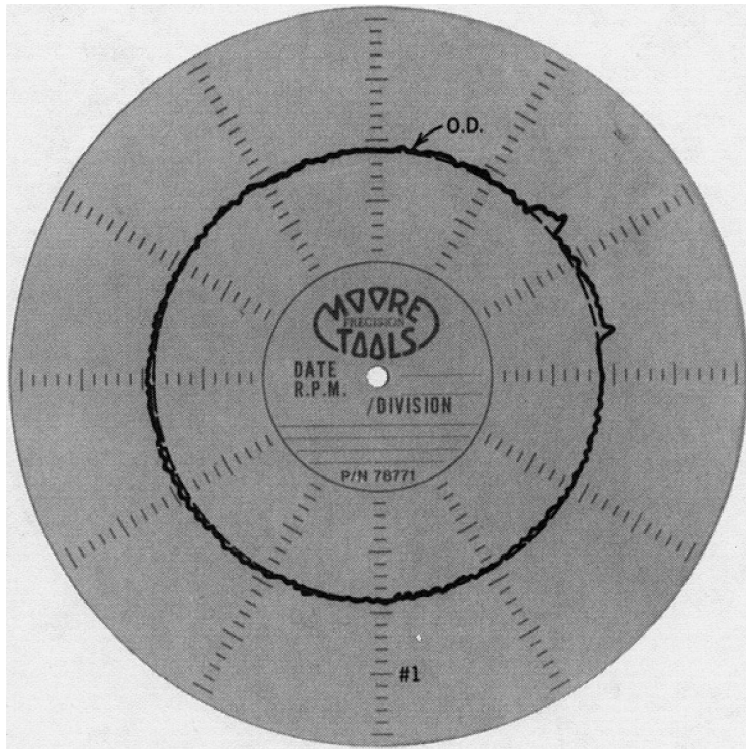


FIGURE 14.9 Low-amplitude, high-frequency waviness.

and

$$\ddot{y} = -A(2\pi f)^2 \sin(2\pi ft) \quad (14.4)$$

The frequency f is the rate at which balls pass over a complete wave cycle. The assumption of only vertical motion of the mass implies two conditions: (1) that the wave peaks are always in phase with balls and (2) that variation of the ball set angular position within the load zone has no influence on the direction of motion. For illustrative purposes, these simplifying assumptions will suffice to demonstrate the importance of relatively small form errors.

Combining [Equation 14.2](#) and [Equation 14.4](#) and rearranging,

$$F_B + \Delta F_B = Mg - MA(2\pi f)^2 \sin(2\pi ft) \quad (14.5)$$

For sufficient waviness amplitude and passage frequency, the right-hand side of the equation can vanish, in which case the bearing force (left-hand side of the equation) vanishes, or it can become negative, and in which case the bearing produces a negative force to restrain the motion of the mass. In this case, the load zone would alternate from the bottom to the top of the outer raceway. If the bearing has clearance, it could become unloaded in either direction at some instant. [Example 14.6](#) gives an estimate of the waviness amplitude that would cause this condition. However, bearing raceway waviness of this amplitude and frequency are in excess of acceptable levels. Although wavy components of this type rarely occur, they can occur due to improper manufacturing procedures or manufacturing machine malfunctions.

See Example 14.6.

14.4 MEASUREMENT OF NONROUNDNESS AND VIBRATION

14.4.1 WAVINESS TESTING

Component inspection for waviness has been performed for many years; see Refs. [14,15]. This inspection is used to assess the degree of radial deviations from a true circle on the circumference of a component. This is accomplished by rotating the component on a hydro-dynamically supported spindle and applying a contacting transducer perpendicular to the surface of the component, as shown in Figure 14.10. The transducer is a stylus that follows the radial deviations and produces a voltage output proportional to the displacement of the stylus or to instantaneous rate of change of the displacement of the stylus. For rate of displacement change stylus measurements, the signal from the transducer is proportional to velocity. This proportionality exists over a wide frequency range, such as 10,000 Hz, which allows reasonably high test speeds to be used.

The voltage signal from the transducer is amplified and converted from an analog-to-digital signal for input into a computer, along with a measurement of the spindle speed for the rate of displacement change stylus systems. Within the computer, the signal is usually bandpass filtered for determining the form error within a predetermined range of wavelengths (e.g., peak-to-valley deviation within 2 to 25 waves per revolution) or performing frequency spectrum analysis to determine the corresponding waviness amplitude at a given frequency (e.g., amplitude of waviness corresponding to 3 waves per revolution). The data can now be compared with specifications to determine the acceptance or rejection of the lot of components that are inspected and to provide information for corrective action on the manufacturing process.

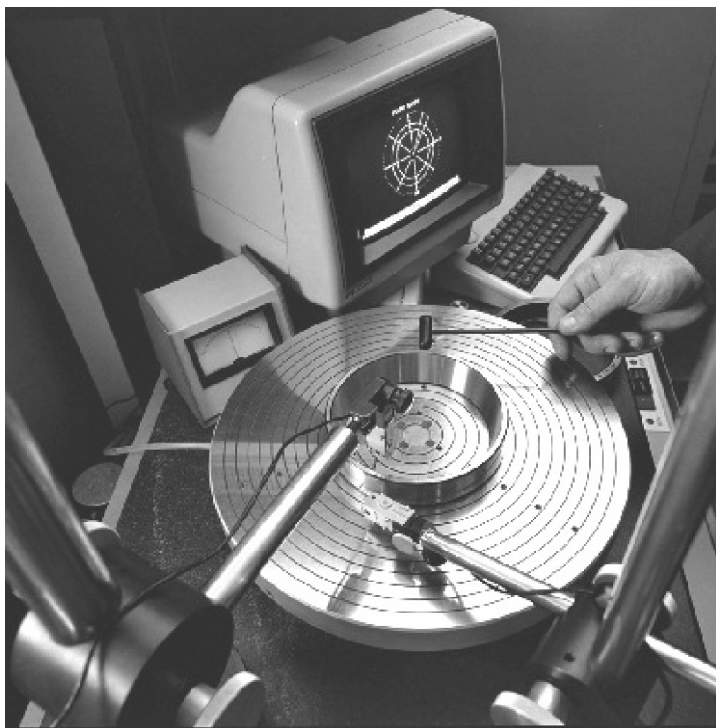


FIGURE 14.10 Bearing component waviness tester. (Courtesy of Timken Company.)

Some types of defects that can arise on components are very local in nature. Detection of these defects may not be feasible with waviness testing, which may only acquire circumferential data from one or two axial locations on the components being tested. Balls have numerous potential axes of rotation. Therefore, visual component inspection and vibration testing of assembled bearings provide more definitive assurance of final bearing quality.

See Example 14.7.

14.4.2 VIBRATION TESTING

Aside from defects not discovered in waviness testing, vibration testing of the assembly allows the detection of damage occurring during assembly, such as a binding or excessively loose cage, brinell damage to raceways or scuffing of balls and distortion of raceways from incorrect insertion of seals or shields with bearings tested after grease insertion.

Certain types of geometrical problems may also be detected in vibration testing. These include, for example, oversized rolling elements, improper cross-groove form on raceways, or groove runout to side faces of the raceways. In addition, testing can reveal contamination by dirt or inferior grease quality.

[Figure 14.11](#) shows a manually operated vibration testing apparatus of relatively small bearings, for example, up to 100 mm outside diameter. Similar equipment is used for larger diameter bearings and automatic versions are implemented on production lines. The main elements of the system are the test station and the vibration signal analysis instrument. The test station consists of a hydrodynamic spindle, an air cylinder for applying load to the bearing being tested, and an adjustable slide for positioning the velocity transducer. The spindle is belt driven by the motor mounted beneath the stand. A schematic representation of the system is shown in [Figure 14.12](#).

The inner raceway of the bearing mounts on a precision arbor fastened to the spindle, which rotates at 1800 rpm. A specified thrust load is applied to the side face of the nonrotating outer ring. The tip of the velocity transducer is lightly spring-loaded on the outer diameter of the outer ring. The loading tool (not shown) consists of a thin-walled steel ring molded into a neoprene annulus; the ring contacts the side face of the outer ring. The tool and load combinations are sufficiently compliant to allow radial motion of the outer ring to occur as balls roll over wavy surfaces or defects in the ball grooves. The voltage signal from the transducer is input to an amplifier, converted to a digital signal for input into a computer that bandpasses filters and displays the rms velocity values in each band. The three frequency bands used are 50–300, 300–1800, and 1800–10,000 Hz. Larger bearings are tested at slower rotational speeds (700 rpm) with correspondingly lower filter bands: 20–120, 120–700, and 700–4000 Hz. Using digital computers, other analytical methods are also available such as peak detection of asynchronous events, which would typically be filtered or would have minimal effect on the time-averaged results.

The basic testing technique has been successfully used by bearing manufacturers and customers for many years. Numerous refinements have been made during this time, and development work continues in the area of vibration measurement. Such efforts include investigations of alternative transducer design and system calibration procedures, different methods of applying load to the test bearings, increased application of statistical methods in setting product specifications and analyzing test results, and implementation of supplementary methods of signal analysis.

14.4.3 BEARING PASS FREQUENCIES

The calculation of the fundamental pass frequencies of rolling contact bearings is used to establish component waviness testing speeds and filter bands that coincide with vibration

measurement bands. In addition, knowledge of these frequencies is useful, though not always essential, in machinery condition monitoring. Derivation of equations for bearing component speeds was presented in [Chapter 10](#). The bearing pass frequencies are derived from those equations. Results are given here for the case of a stationary outer ring and rotating inner ring, as is used in typical bearing applications.

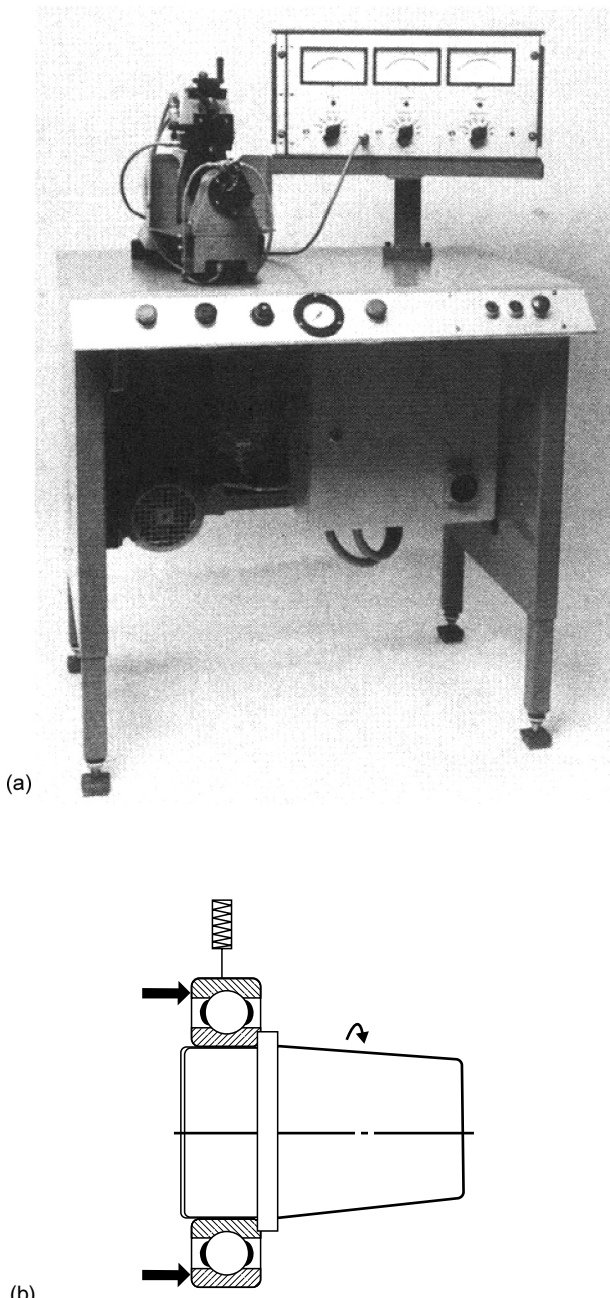


FIGURE 14.11 Bearing vibration tester: (a) test stand and (b) schematic of bearing loading and accelerometer on bearing outside diameter.

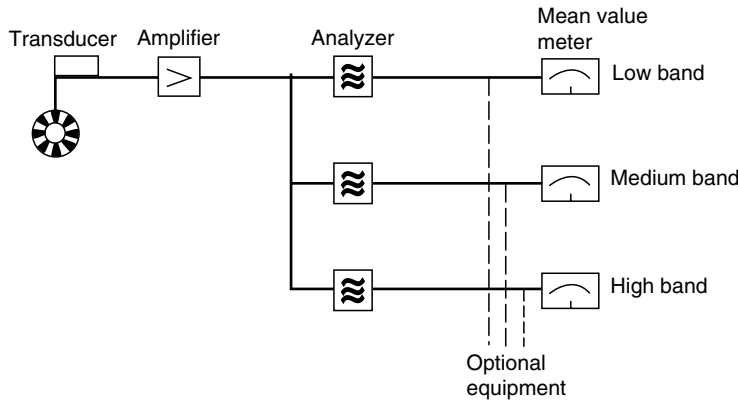


FIGURE 14.12 Schematic of bearing vibration measurements.

The rotational speed of the cage is

$$f_c = \frac{n_i}{2} \left(1 - \frac{D}{d_m} \cos \alpha \right) \quad (14.6)$$

The rotational speed of the inner ring relative to the cage is the rate at which a fixed point on the inner ring passes by a fixed point on the cage. This relative speed is

$$f_{ci} = \frac{n_i}{2} \left(1 + \frac{D}{d_m} \cos \alpha \right) \quad (14.7)$$

The rate at which rolling elements pass a point in the groove of the outer raceway (also called the rolling element-pass–outer raceway frequency or outer raceway defect frequency) is

$$f_{REpor} = Z f_c \quad (14.8)$$

The rate at which a point in the inner-ring groove passes rolling elements (also called the rolling element-pass–inner raceway frequency or inner raceway defect frequency) is

$$f_{REPir} = Z f_{ci} = Z(n_i - f_c) \quad (14.9)$$

The rate of rotation of a rolling element about its own axis is

$$f_R = \frac{n_i d_m}{2D} \left[1 - \left(\frac{D}{d_m} \cos \alpha \right)^2 \right] \quad (14.10)$$

A single defect on a ball or roller would contact both raceways in one ball or roller revolution so that the defect frequency is $2f_R$. In addition, the defect could contact one or both sides of the cage pocket; however, this usually will have little influence on vibration measured external to the bearing.

14.4.4 RELATION OF VIBRATION AND WAVINESS OR OTHER DEFECTS

Within the range of the vibration measurement frequency bands, the number of waves on a component that influences a particular band can be calculated. For outer raceway waviness,

any rolling element rolls over all the waves in the outer raceway in one cage revolution. Therefore, the rolling element passage frequency over an individual wave cycle on the outer raceway is $f_c \times$ number of waves per circumference. Consequently, dividing the filter frequencies by f_c determines the number of waves per circumference of the outer raceway producing vibration within a particular band. For rolling elements, the filter band frequencies are divided by f_R to determine the number of waves per circumference of a rolling element producing vibration within a band.

Similarly, for the inner raceway, the band frequencies are divided by f_{ci} . The lobes of low orders of inner raceway waviness, such as two- and three-point out-of-roundness, however, can cause flexure of the outer ring (two- or three-point lobing) and vibration at two or three times n_i , affecting readings at the low-frequency band.

Waviness testing procedures are established to correlate with average waviness ranges over a wide range of bearing sizes. In addition, the range of waviness measurements corresponds approximately to wavelengths of the size of the minor axis of the Hertzian contact ellipse in typical applications such as electric motors [14].

Defects other than waviness can also be detected through monitoring vibration. Some of these are difficult to detect with the conventional three-band inspection method, such as local defects on raceways or rolling elements, dirt, grease with improper constituents or properties, and cages with incorrect clearance or geometry. Some of these defect types may produce brief disturbances spaced widely apart in time, which, as a consequence, have only a small effect on the average measured vibration in the inspection bands through excitation of resonant frequencies of the outer ring. Their presence, however, is best determined through monitoring of the peak values that can vary with time in the case of rolling element or inner raceway defects.

See Example 14.8.

14.5 DETECTION OF FAILING BEARINGS IN MACHINES

Vibration analysis is one of the most common methods used to evaluate the conditions of bearings in an operating machine. Such measurements may be used for machines with bearings in new condition as well as for machines whose bearings are deteriorating and approaching the end of their useful lives. If a machine's vibration response to known excitation forces has been determined through techniques such as finite element analysis and modal analysis, then vibration measurements during service can define the dynamic characteristics of the forces acting on the machine.

Vibration data can also be used to infer forcing characteristics and the condition of machine components, including bearings. General methods for evaluating data include one or more of the following:

1. Comparison of data with guidelines developed empirically on similar types of equipment [16–18]
2. Comparison of data from similar or identical machines in service within the same factory
3. Trending of data from one machine over time
4. Evaluation of data in an absolute sense with no prior history. For example, by evaluating time signals or frequency spectra to associate vibration with specific machine components

Many machine problems can be traced to faults other than damaged bearings. If a moderately detailed vibration analysis capability is not available, however, bearings are often replaced unnecessarily.

The beginning of progressive bearing damage, which can be called incipient failure, is often characterized by a sizeable local defect on one of the components. When this occurs, subsequent rolling over the damage zone will produce repetitive shocks or short-duration impulses. It can be surmised that such impulses might appear, if they could be measured, as those in Figure 14.13a and b.

Figure 14.13a could represent, for example, the effect of successive rolling elements passing over a damaged area on the outer raceway. Similarly, Figure 14.13b might represent the effect of inner raceway damage interacting with several rolling elements in the load zone of a radially loaded bearing without preload. In this case, the damage enters the load zone once per revolution of the shaft. The location of the rolling elements with respect to the load zone will vary somewhat from one shaft revolution to the next. If a sensor were placed on the bearing housing to measure the resulting vibration from the series of impacts, it may show a response as in Figure 14.13c. This vibration corresponds to lightly damped oscillation of some system natural frequency greater than the repetition frequency of the train of impacts. It could, for example, be a resonant response as excited by harmonics that exist in the periodic nonsinusoidal forcing function. [Figure 14.14](#) shows the time history of an electrical signal representing a pulse train with a fundamental frequency of 160 Hz; [Figure 14.15](#) is the frequency spectrum of that signal. It contains all harmonics of the fundamental.

Impulsive occurrences in bearings, therefore, can cause system vibration at many frequencies that can be harmonically related. Forcing harmonics that are near-system resonant frequencies can cause significantly amplified vibration response compared with the vibration at nonresonant frequencies. In the early stage of failure, the impulse might have little effect on the amplitude of vibration at the fundamental bearing pass frequencies. In addition, significant normal machine vibration could occur at these lower frequencies, so a small change in

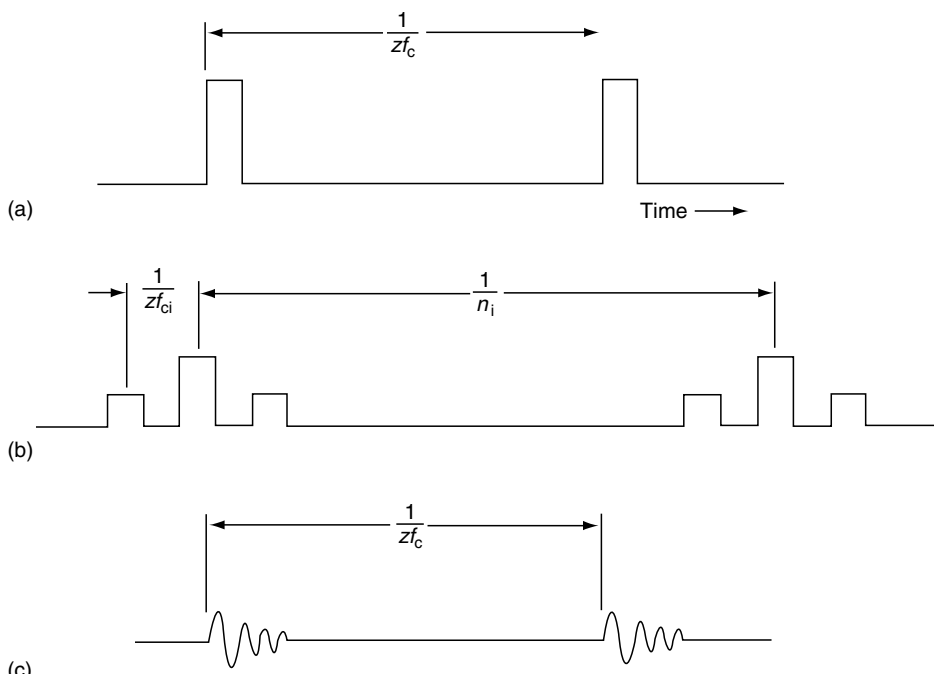


FIGURE 14.13 Impulse train. (a) Outer raceway damage. (b) Inner raceway damage. (c) Resonant vibration.

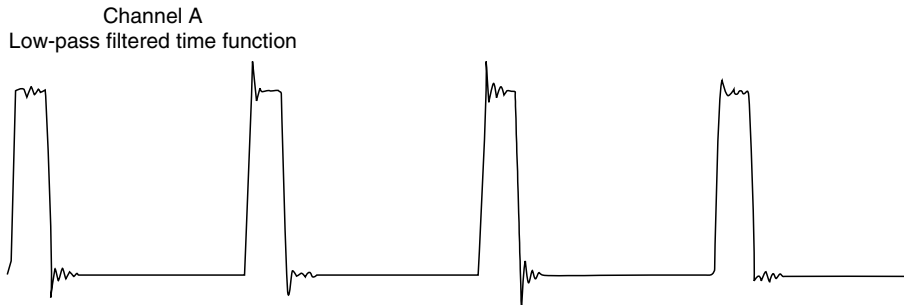


FIGURE 14.14 Periodic impulsive time domain.

vibration amplitude initially may be difficult to detect. Higher-order harmonics, with spacing related to specific component frequencies, however, might be detectable at higher frequencies if the sensor and mounting method provide sufficient response at the higher frequencies. Small accelerometers stud-mounted to electrically isolated nuts and glued to a surface on the machine work satisfactorily. Magnetic mount is faster but it requires a better surface and the frequency is lower.

See Example 14.9.

Aside from evaluation of vibration spectra to identify machine frequencies, data can be obtained or analyzed by other means to trend the onset of failure. Mathew and Alfredson [19] present a comprehensive evaluation of vibration parameters over the life of bearings run to advanced stages of damage progression or failure. Conditions under which bearings were tested include bearing components with initial damage, contained lubrication, overload conditions leading to cage collapse, and sudden loss of lubrication. Parameters that might be obtained with relatively low-cost instrumentation include peak acceleration, rms acceleration

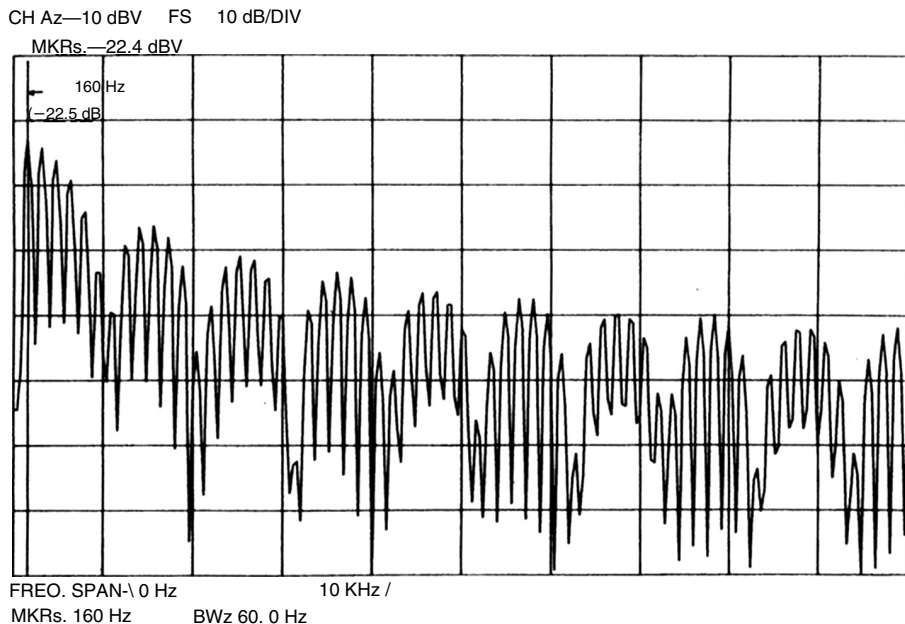


FIGURE 14.15 Frequency spectrum.

over a broad frequency band, and shock pulse data. The last evaluates vibration at a frequency corresponding to the resonant frequency of the accelerometer (32 Hz). Other parameters were calculated by performing arithmetic operations on two frequency spectra, one of which was usually the initial spectrum obtained when the tests were begun. The calculated parameters were trended. Statistical functions, including probability density, skewness, and kurtosis, were also evaluated. The results indicated that several parameters evaluated from frequency spectra were successful trend indicators, generally providing a 30-dB increase or more by the time a test run was completed. One such parameter is simply obtained by subtracting the initial spectrum from each new spectrum and computing the rms of the resulting spectrum. This value is then trended over the duration of the tests.

The shock pulse method was also reported to provide successful detection for all tests except the case of total lubrication loss. For the successful tests, the shock pulse values were estimated to have increased 40 dB. In the test with lubrication loss, seizure occurred in two hours. This suggests that lower-frequency vibration may be a better initial indicator than higher-frequency vibration unless the components have time to undergo sufficient gradual distress to be detectable in the high-frequency regime.

Another method studied for detecting rolling bearing fatigue is the sensing of acoustic emissions (AEs). AEs are transient elastic waves within a continuum due to the rapid release of strain energy. In a rolling bearing, this is caused by the normal transient strain energy associated with the deformation of the rolling element–raceway contacts, or by the dynamic interactions of the fatigue crack faces under the cyclic state of strain. As such, Yoshioka and Fujiwara [20] found that AE sensors were capable of detecting the onset of bearing fatigue damage before changes in the vibration signal, as AE can detect subsurface cracks before spalling occurs. However, AE signals attenuate rapidly, as they are associated with high frequencies. This makes the location of the sensor relative to the bearing more critical than vibration sensors, and typically the subsequent signal processing is more complex to isolate the defect from the background noise. As such, AE sensors are not as commonly used in industrial equipment as traditional vibration monitoring methods.

When oil lubrication systems are used, debris monitoring is also a common method for detecting bearing damage. Typically, debris monitoring is done offline by periodic sampling of the lubricant after it has traveled through the bearing, and before it is filtered for redelivery to the bearing. The debris is separated from the oil sample and the number, size, and shape of the particles are determined using an optical microscope. Further analysis is often conducted when the damage is suspected by utilizing energy dispersive x-rays, or similar techniques, to determine the chemical makeup of the particles. The information gathered can be compared with the attributes of debris particles from known damage and wear mechanisms [21,22] to assess the condition of the bearing.

Offline oil debris analysis has some benefits and drawbacks compared with vibration analysis. The major benefit is that it is not affected by the background noise and vibrations within the factory, and it does not directly depend on the machine operating conditions. Side benefits of offline oil debris analysis include the ability to quantify the contamination level to which the bearings are exposed; the latter has an influence on the bearing endurance as described in [Chapter 8](#) of the Second Volume of this handbook. Also, the condition of the oil can be assessed to determine when a change is necessary. The major drawback of this system is that the time and manpower necessary for oil sampling and particle analysis are often more than that associated with routine vibration monitoring. Also, the time differential between bearing damage and detection can be much longer than that for fixed machine-mount vibration sensors, which are able to monitor the machine condition in real time. Finally, oil debris analysis methods are not capable of detecting the exact location of the damaged bearing when multiple bearings are connected to the same lubricating system. Nor can they

detect the damaged component (rolling element, inner, or outer ring), or other undesirable machine operating conditions such as rotating unbalance, excessive shaft/housing misalignment, or bearing manufacturing quality problems.

Online oil debris analysis is also available through the use of particle counters that determine the number and size of debris leaving the bearing [23]. The benefit of online systems is that the monitoring of the oil occurs continuously, allowing real-time assessment of bearing damage, as can be accomplished with fixed machine-mount vibration sensors. However, the qualitative information from offline analysis, such as shape, chemistry, and comparison with wear particles from known mechanisms, is not available.

Most forms of damage preceding bearing catastrophic failure will result in progressive wear and roughening of component surfaces and irregular running geometry. Such irregularities may produce vibration that can clearly be identified with specific components, or they could produce vibration that shows amplitude that varies randomly in time and frequency content. The progressive wear generates particles that can be sized, counted, and further analyzed, allowing more qualitative assessments of the machine condition. All methods described above have specific benefits and drawbacks, and as such, it is often the case that multiple methods are employed together to best determine the bearing condition for minimizing unscheduled downtime and unnecessary bearing replacement.

14.6 CONDITION-BASED MAINTENANCE

In the earlier sections, it has been demonstrated that monitoring bearing vibrations and comparing the vibration signals against a baseline for satisfactory bearing operation may be used as a means to detect impending bearing failures. According to definitions of bearing failure discussed thus far—for example, initial spalling or pitting of rolling contact surfaces—the occurrence of abnormal signals may indicate that bearing failure has already occurred. On the other hand, the bearing, although running rough with increased friction, generally will continue to rotate after initial surface damage, permitting continued effective machinery use. Eventually, the rolling contact surfaces will be completely destroyed and the machinery will cease to function because of bearing seizure or excessive vibratory loading and component fracture. These last conditions represent potential catastrophe from the minimum standpoint of unscheduled machinery downtime and excessive cost, or worse, from the standpoint of loss of human life in life-critical applications. The latter would include, for example, air transport applications and applications that handle hazardous fluids. From the time at which excessive vibration signal is experienced to the time at which the machinery no longer functions represents a duration in which action may be taken to prevent catastrophic events.

Historically, many applications have relied on preventive maintenance to minimize unscheduled downtime due to bearing failure. Based on calculations of bearing endurance, either from fatigue of rolling contact surfaces or other wear phenomena, or based on past experience of bearing failures, periodic stoppages of machinery are scheduled, during which bearings are inspected and replaced. Frequently, inspection does not occur and rolling bearings are simply replaced. The problem with this procedure, in addition to the cost of taking equipment out of service and losing production and revenue, is that the bearings that had been in operation were most likely not prone to failure; however, they might be replaced with bearings that could fail. Once a rolling bearing has experienced sustained operation, it has passed the period in which birth defects cause early failures, and under proper mounting, applied load, speed, and lubrication conditions, it will continue to operate without failure. Thus, presuming proper operation, it is usually best to allow the bearing to run without interruption once an initial operating period has been successfully achieved.

Maintenance is considered the largest controllable cost in modern industry. Based on bearing condition monitoring, which provides operational information on impending failure, and prognostic knowledge of the duration of effective bearing performance, taking failure-prevention action after the first signals of impending bearing failure have been received, but before the occurrence of catastrophic events is a more cost-effective procedure than preventive maintenance; unnecessary machinery downtime is avoided. Of course, condition-monitoring sensors and techniques must be proven reliable, and life prognostication methods must be proven sufficiently accurate. This procedure is called condition-based maintenance (CBM).

CBM is a relatively new concept, and additional information is required for its effective implementation. The initial CBM consideration is that, more often than not, the actual load-speed-temperature operating conditions experienced by the bearing are significantly different from the design. Bearing types and sizes are selected based on a design duty cycle of the machinery. Therefore, at any instant, prediction of the remaining bearing life should be based on actual accumulated conditions of operation. In describing the Health Usage and Monitoring System (HUMS) technology under development for helicopter maintenance, Cronkhite [24] illustrated the potential increased endurance of helicopter mechanical components; see Figure 14.16. Design conditions tend to be conservative to assure reliable operation; the lower shaded area in Figure 14.16 indicates that the actual life will tend to exceed design life. Load-and speed-sensing equipments are readily available to enable the acquisition of such data. Miniature microcomputers are also available at reasonable cost to enable detailed evaluations of the acquired data. With regard to prediction of bearing life to the initial spall, the actual load-speed-temperature operation of the bearing must be accommodated in the analysis.

Instead of considering failure at the occurrence of the initial spall, the ability to detect incipient spalling becomes important. This knowledge would most likely indicate the additional time in which to take failure-prevention action. With the continued development of micro-sized pressure, temperature, and ultrasonic sensors, which can be embedded in close proximity to, or directly in, the bearing, it appears probable that effective means to sense incipient fatigue failure will eventually be available. Figure 14.17 shows a stress pin, a miniature pressure sensor, embedded in the outer ring of a tapered roller bearing. This

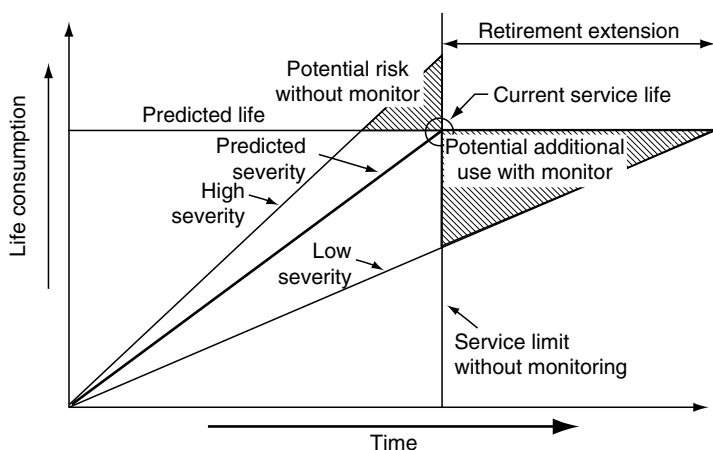


FIGURE 14.16 Component life consumption in actual service compared with design. Stress pins inserted into the cup of a tapered roller bearing: (a) locations to determine axial stress distribution; (b) circumferential locations to determine distribution of load among the rollers—showing wireless connection of analog/digital converter for transmission of signal. (Courtesy of Oceana Sensor Technologies, Virginia Beach, Virginia.)

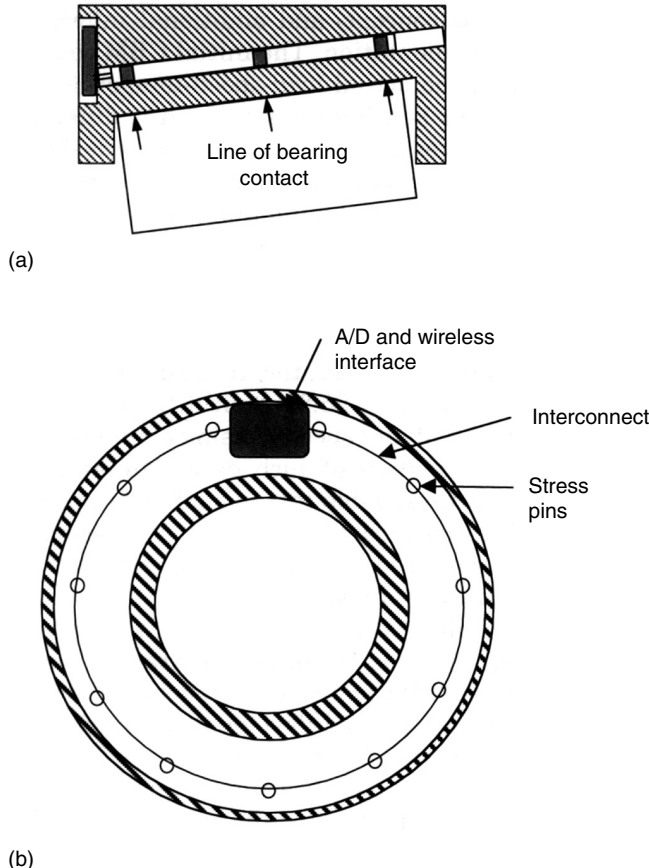
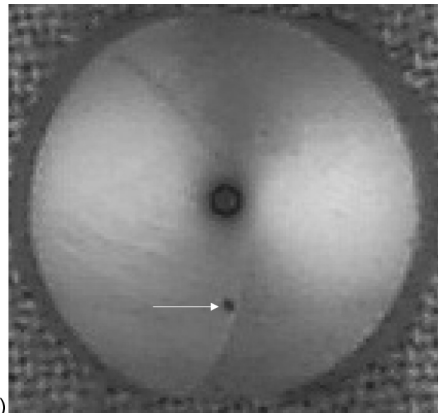


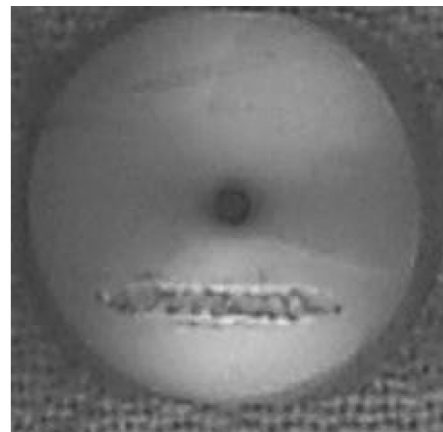
FIGURE 14.17 Stress pins inserted into the cup of a tapered roller bearing: (a) locations to determine axial stress distribution; (b) circumferential locations to determine distribution of load among the rollers—showing wireless connection of analog/digital converter for transmission of signal. (Courtesy of Oceana Sensor Technologies, Virginia Beach, Virginia.)

sensor does not impair bearing function, and may be used to determine whether bearing loading conforms to design. If bearing loading is substantially in excess of design, this is an indication of failure occurrence or incipient failure.

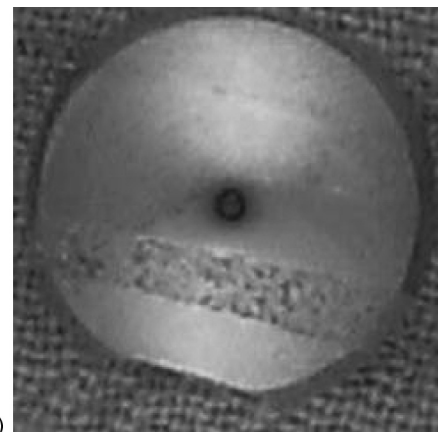
Additionally, since bearing operation will continue after the occurrence of the initial spall, algorithms to establish the time available for effective operation after this event can be developed. Kotzalas [25], using a ball/v-ring rig, progressed ball spalls past the initial surface flaking until the entire track was eventually destroyed. Figure 14.18 shows spall progression. Figure 14.19 illustrates the voltage signal from an accelerometer mounted on the test head. It can be seen that vibration loading remains rather low for more than 1.5 hours, even under the heavy load and high-speed operation of the test condition. Using a ball-disk test rig to measure the traction coefficient of the failed balls, Kotzalas [25] determined that an effective lubricant film was generated even in the presence of gross spalling, and it is presumed that this film was instrumental in assuring the continued operation of the test ball. The increase in vibration after 100 min points to the breakdown of the lubricant film, the metal-to-metal contact, the component temperature rise, and eventual seizure or fracture, depending on heat dissipation paths. Figure 14.20 shows the effect of increased load on the time from initial spalling to component failure. It can be seen that Hertz stress magnitude, and hence load



(a)



(b)



(c)

FIGURE 14.18 AISI 52100 steel, 22.22-mm (0.875 in.) diameter ball (a) showing initial spall after endurance testing at 45,000 rpm, 3,170 MPa (460,000 psi) maximum Hertz stress, and 71.1°C (160°F) lubricant supply temperature in a ball/v-ring test rig; (b) showing progression to 33% spalling over track; (c) showing progression to 100% spalling over track (From Kotzalas, M., Power transmission component failure and rolling contact fatigue progression, Ph.D. thesis in Mech. Eng., Pennsylvania State Univ., August 1999.)

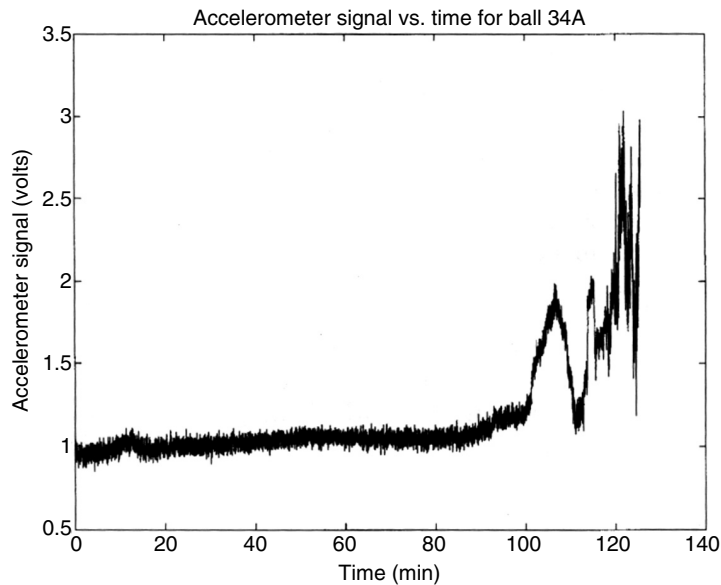


FIGURE 14.19 Accelerometer voltage signal for ball operating conditions in [Figure 14.18](#). (Courtesy of Oceana Sensor Technologies, Virginia Beach, Virginia.)

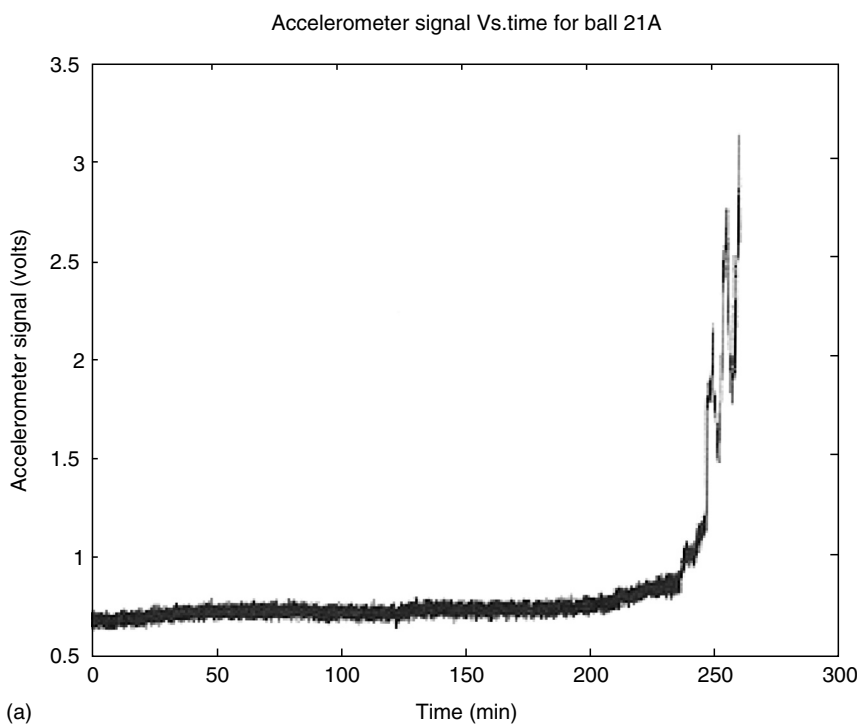


FIGURE 14.20 Accelerometer voltage signal for an AISI 52100 steel, 22.22-mm (0.875 in.) diameter ball, endurance tested at 45,000 rpm, and 37.8°C (100°F) lubricant supply temperature in a ball/v-ring test rig at (a) 3,170 MPa (460,000 psi) maximum Hertz stress.

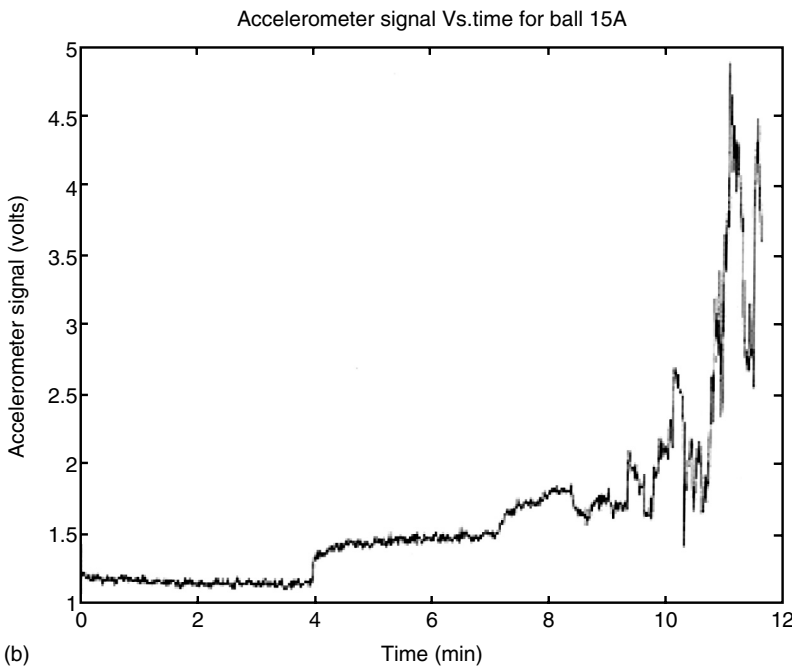


FIGURE 14.20 (Continued) (b) 3,860 MPa (560,000 psi) maximum Hertz stress.

magnitude, has a profound effect on the duration of spall progression. Moreover, comparing Figure 14.20a [37.8°C (100°F)] with [Figure 14.19](#) [71.1°C (160°F)], it may be determined that lubricant film thickness and heat dissipation rate have a significant effect on the rate of spall progression; the lower the temperature, the longer the duration of spall progression to component failure.

Kotzalas [25] also correlated the ball traction coefficient with the degree of spall progression, and the degree of spall progression with the accelerometer signal. Thus, it was possible to correlate friction with the accelerometer signal. Therefore, accelerometer signal, so correlated, might be used to indicate friction, which may be used in an on-board computer program to predict the remaining bearing life.

14.7 CLOSURE

This chapter provides an indication of how bearings can affect the vibration of machines, as a result of either inherent design characteristics or imperfections and deviations from ideal running geometry within the bearing. Such imperfections and geometric deviations can occur during bearing component manufacture, during assembly of a bearing into a machine, or from bearing deterioration during operation. Each can have a pronounced effect on machine vibration, either by altering stiffness properties or by acting as a source of forces to directly generate vibration.

It was also shown that detection of vibration frequencies and amplitudes is used as a means to determine the health of bearings in machinery. Using condition-monitoring, it is possible to detect bearing fatigue failure in machinery and to determine the location of the failed bearing. Recognizing that bearing function does not cease with the initial rolling component surface spall and using the prognostic methods associated with CBM techniques,

it is possible to estimate how long the machine may be expected to continue to function reasonably.

REFERENCES

1. Tallian, T. and Gustafsson, O., Progress in rolling bearing vibration research and control, ASLE Paper 64C-27, October 1964.
2. Scanlan, R., Noise in rolling-element bearings, ASME Paper 65-WA/MD-6, November 1965.
3. Military Specification Mil-B-17931D (Ships), Bearings, ball annular, for quiet operation, April 15, 1975.
4. Gustafsson, O. et al., Final report on the study of vibration characteristics of bearings, U.S. Navy Contract Nobs-78552, U.S. Navy Index No. NE 071 200, December 6, 1963.
5. DenHartog, J., *Mechanical Vibrations*, 4th ed., McGraw-Hill, New York, 1956.
6. Thomson, W., *Theory of Vibration with Applications*, 2nd ed., Prentice-Hall, Englewood Cliffs, NJ, 1972.
7. Vierck, R., *Vibration Analysis*, Harper & Row, New York, 1979.
8. Air Force Aero Propulsion Laboratory Report AFAPL-TR-65-45, Parts I-X, Rotor bearing dynamics design technology, June 1965.
9. Air Force Aero Propulsion Laboratory Report AFAPL-TR-78-6, Parts I-IV, Rotor bearing dynamics design technology, February 1978.
10. Jones, A. and McGrew, J., Rotor bearing dynamics design guide, Part II, ball bearings, AFFAPL-TR-78-6, Part II, February 1978.
11. Gunter, E., Dynamic stability of rotor-bearing systems, NASA SP-113, U.S. Government Printing Office, Washington, DC, 1966.
12. Rieger, N., Balancing of rigid and flexible rotors, The Shock and Vibration Information Center, Naval Research Laboratory, Washington, DC, 1986.
13. Sayles, R. and Poon, S., Surface topography and rolling element vibration, in *Precision Engineering*, IPC Business Press, 1981.
14. Yhland, E., Waviness measurement—an instrument for quality control in rolling bearing industry, *Proc. Inst. Mech. Eng.*, 182, Pt. 3K, 438–445, 1967–1968.
15. Gustafsson, O. and Rimrott, U., Measurement of surface waviness of rolling element bearing parts, SAE Paper 195C, June 1960.
16. Mitchell, J., *Machinery Analysis and Monitoring*, PennWell, Tulsa, Chap. 9 and 10, 1981.
17. International Organization for Standardization, Acoustics, vibration and shock, ISO Standards Handbook 4, 1980.
18. Norris, S., Suggested guidelines for forced vibration in machine tools for use in protective maintenance and analysis applications, in *Vibration Analysis to Improve Reliability and Reduce Failure*, ASME H00331, September 1985.
19. Mathew, J. and Alfredson, R., The condition monitoring of rolling element bearings using vibration analysis, ASME Paper 83-WA/NCA-1, November 1983.
20. Yochioka, T. and Fujiwara, T., New acoustic emission source locating system for the study of rolling contact fatigue, *Wear*, 81(1), 183–186, 1982.
21. Anderson, D., *Wear Particle Atlas*, Telus Inc., Peabody, MA, 1982.
22. Hunt, T., *Handbook of Wear Debris Analysis and Particle Detection in Liquids*, Elsevier Applied Science, London, 1993.
23. Goddard, K. and MacIsaac, B., Use of oil borne debris as a failure criterion for rolling element bearings, *Lubr. Eng.*, 51(6), 481–487, 1995.
24. Cronkhite, J., Practical applications of health and usage monitoring (HUMS) to helicopter rotor, engine, and drive systems, Paper presented at the American Helicopter Society 49th Annual Forum, St. Louis, MO, May 19–21, 1993.
25. Kotzalas, M., Power transmission component failure and rolling contact fatigue progression, Ph.D. thesis in Mech. Eng., Pennsylvania State Univ., August 1999.

Appendix

All equations in the text are written in metric or Standard International system units. In this appendix, Table A.1 gives factors for conversion of Standard International system units to English system units. Note that for the former, only millimeters are used for length and square millimeters for area. Furthermore, the basic unit of power used herein is the watt (as opposed to kilowatt). To be consistent with this, Table A.2 provides the appropriate English system unit constants for each equation in the text having SI unit constants.

TABLE A.1
Unit Conversion Factors^a

Unit	Standard International System	Conversion Factor	English System
Length	mm	0.03937, 0.003281	in., ft
Force	N	0.2247	lb
Torque	mm · N	0.00885	in. · lb
Temperature difference	°C, °K	1.8	°F, °R
Kinematic viscosity	mm ² /sec	0.001076	ft ² /sec
Heat flow, power	W	3.412	Btu/hr
Thermal conductivity	W/mm · °C	577.7	Btu/hr · ft · °F
Heat convection coefficient	W/mm ² · °C	176,100	Btu/hr · ft ² · °F
Pressure, stress	N/mm ² (MPa)	144.98	psi

^aEnglish system units equal Standard International system units multiplied by conversion factor.

TABLE A.2
Equation Constants for Metric and English System Units

Chapter Number	Equation Number	SI System Constant	English System Constant
3	29	47100	6.83×10^6
	30	47100	6.83×10^6
6	39	0.0236	0.0045
	41	0.0236	0.0045
	43	2.79×10^{-4}	1.01×10^{-5}
	52	3.35×10^{-3}	2.78×10^{-4}
7	54	3.84×10^{-5}	4.36×10^{-7}
	8	2.15×10^5	3.12×10^7
	9	8.06×10^4	1.17×10^7

TABLE A.2 (continued)
Equation Constants for Metric and English System Units

Chapter Number	Equation Number	SI System Constant	English System Constant
8	1	4.36×10^{-4}	8.71×10^{-8}
	2	6.98×10^{-4}	2.53×10^{-5}
	3	1.81×10^{-4}	4.33×10^{-6}
	4	7.68×10^{-5}	8.71×10^{-7}
	5	4.36×10^{-4}	8.71×10^{-8}
	6	6.98×10^{-4}	2.53×10^{-5}
	7	5.24×10^{-4}	1.90×10^{-5}
	8	1.81×10^{-4}	4.33×10^{-6}
	9	7.68×10^{-5}	8.71×10^{-7}
	23	0.0472	0.0090
	24	0.0472	0.0090
	25	0.0472	0.0090
	27	1.166×10^{-3}	4.24×10^{-5}
9	1	1.30×10^{-7}	6.20×10^{-12}
	2	5.25×10^{-7}	2.50×10^{-11}
	3	2.52×10^{-7}	1.20×10^{-11}
	4	6.03×10^{-11}	1.98×10^{-17}
	6	23.8	3440
	7	23.8	3440
	9	44.0	6379
	12	220	32150
	21	10^{-7}	1.42×10^{-5}
	22	160×10^{-7}	2.32×10^{-3}
10	28	4.5×10^{-7}	7.043×10^{-7}
	28	0.12	0.0497
	29	4.5×10^{-7}	7.043×10^{-7}
	29	0.016	0.016
	30	3.35×10^{-8}	1.04×10^{-4}
	31	3.35×10^{-8}	1.04×10^{-4}
	34	0.001	0.3855
	35	1.047×10^{-4}	0.0404
	36	10^{-7}	1.42×10^{-5}
	36	30×10^3	8.79×10^3
	38	0.016	35.22
	38	50000	77.5
	39	0.020	44.03
	39	50000	77.5
	67	98.1	7450
11	99	98.1	7450
	100	39.9	3030
	101	98.1	7450
	102	38.2	2900
	104	39.9	3030
	105	39.9	3030
	106	39.9	3030
	132	98.1	7450
	133	98.1	7450
	134	98.1	7450
	135	98.1	7450

continued

TABLE A.2 (continued)
Equation Constants for Metric and English System Units

Chapter Number	Equation Number	SI System Constant	English System Constant
	136	88.2	6700
	138	88.2	6700
	140	59.1	4490
	143	552	49500
	156	207	18600
	157	207	18600
	162	552	49500
	163	469	42100
	169	207	18600
	170	552	49500
	171	469	42100
